NASA Conference Publication 2092

Aeropropulsion 1979

Proceedings of a conference held at
NASA Lewis Research Center
Cleveland, Ohio
May 15-16, 1979

NASA

NASA Conference Publication 2092

Aeropropulsion 1979

Proceedings of a conference held at
NASA Lewis Research Center
Cleveland, Ohio
May 15-16, 1979

National Aeronautics
and Space Administration

**Scientific and Technical
Information Branch**

1979

FOREWORD

The Lewis Research Center has a 37-year heritage of providing advances in aeronautical propulsion from the research activities of its staff and its university and industrial grantees and contractors. These advances have helped create the preeminence in aeronautics that has contributed to our national defense, has provided swift, reliable transportation for our people and their goods, and has so greatly aided our position in international trade.

Although the results of the Center's projects and programs are reported as they are obtained, from time to time a conference such as this one affords the opportunity for a broad overview and an in-depth interpretation of a large body of results and for informal discussions about the subject.

We hope you will find the material given herein informative and useful and that you will inquire further about whatever may be important to you.

John F. McCarthy, Jr.
Director

CONTENTS

I. AIRCRAFT ENERGY EFFICIENCY (ACEE) STATUS REPORT

Donald L. Nored, James F. Dugan, Jr., Neal T. Saunders,
and Joseph A. Ziemianski

National Aeronautics and Space Administration
Lewis Research Center

Efficient air transportation is of national concern since commercial aircraft constitute a primary segment of public transportation. However, the viability of the U.S. air transportation industry and its ability to handle future traffic growth are threatened by rapidly escalating fuel prices. Figure I-1, taken from Civil Aeronautics Board (CAB) data (ref. 1), illustrates the recent trend in fuel prices. From 1973 to 1975, fuel prices essentially tripled internationally and doubled domestically. They have since continued to increase about 12 percent each year. Such increases are directly reflected in the aircraft direct operating cost (DOC).

The major elements of the DOC are shown in figure I-2 (ref. 2). The elements are expressed in cents per available ton-mile of the mix of passengers and cargo for each year. Before 1973, these elements were about equal in their contribution to DOC. Starting in 1973, however, with the OPEC embargo and the subsequent large increases in fuel prices, these historical relationships changed. Fuel prices began to escalate faster than the rate of inflation and even faster than increased productivity could reduce them. As a result, not only has the total DOC increased, but fuel costs have become a much larger percentage of the DOC. For example, as shown in figure I-3 for the Boeing 727 flying commercially in the domestic market, in 1973, fuel contributed about 26 percent of the DOC. By 1977, this fuel percentage had increased to about 41 percent.

The percentage of the DOC related to fuel is expected to continue to increase in the future. Large increases in aircraft fuel needs are projected, as a result of an expected rapid growth in air travel. Aircraft fuel, however, is derived completely from petroleum, a dwindling national resource. Hence, scarcity of fuel and resulting higher prices are foreseen. This situation will be aggravated by various artificial (e.g., OPEC initiated) price increases. Commercial aircraft currently use over 10 billion gallons of fuel per year (ref. 1). This is conservatively projected to more than double by the year 2000. Obviously, an increase in fuel supply would alleviate the problems of cost and availability. For this reason, there is interest in producing

synthetic jet fuel from our large national resources of coal and oil shale. However, such synthetic fuel will not be available in large quantities for some years, and until it is, the aircraft industry must use its petroleum-based fuel more efficiently. Increases in fuel efficiency will help counteract the effect of rising fuel prices on the DOC while also alleviating the critical problem of future fuel availability.

To answer this need, NASA started the Aircraft Energy Efficiency (ACEE) program in 1976. This program is a focused reponse to the current importance of fuel effiency in aeronautics, for fuel conservation in general as well as for its effect on commercial aircraft operating economics. Included in the program are six major projects aimed at providing technology for more fuel-conservative aircraft and propulsion systems for future commercial airline service (ref. 3). Three of the projects - in the areas of aerodynamics and aircraft structures - are managed by the Langley Research Center. These aircraft-related projects are Energy Efficient Transport, Laminar Flow Control, and Composite Structures. The other three projects are propulsion related, as indicated in figure I-4, and are managed by the Lewis Research Center. They are (1) Engine Component Improvement (ECI), directed at improving the engine components and the performance retention of existing engines; (2) Energy Efficient Engine (E^3), directed at providing the technology base for the next generation of turbofan engines; and (3) Advanced Turboprop, directed at advancing the technology of turboprop-powered aircraft to a point suitable for commercial airline service. It is these three projects that are discussed in this paper in some detail.

ENGINE COMPONENT IMPROVEMENT

The ECI project is investigating the potential for reducing fuel usage in existing engines. It is these engines that will use the bulk of the commercial aircraft fuel between now and 1990. This project is expected to result in technology, by 1980 to 1982, that will permit as much as a 5 percent fuel savings over the operational life of the engines. Such fuel savings will be achieved by improving engine performance as well as by minimizing engine performance degradation in service. Thus, the project has two parts: (1) performance improvement and (2) engine diagnostics (fig. I-5).

Performance Improvement

The performance improvement part of the ECI project is directed at developing the technology for improved, more fuel-efficient engine components for early introduction into commercial service. The technical effort is being conducted by the manu-

facturers (General Electric and Pratt & Whitney) of the three engines that power most of the current commercial fleet (fig. I-6). These engines are the Pratt & Whitney JT8D - used on the Boeing 727 and 737 and the Douglas DC-9 - and the Pratt & Whitney JT9D and the General Electric CF6 - used on the Boeing 747, Douglas DC-10, and Airbus Industries A300. Derivatives of these latter two large, high-bypass-ratio engines will also power the newer airplanes such as the Boeing 757 and 767 and the Airbus Industries A310.

The components being investigated are shown in figure I-7, and include most major components of the engine. The specific component improvements will be derived generally from improved aerodynamics, reduced clearances, more effective cooling, and improved materials.

An extensive feasibility and screening analysis was conducted on a variety of concepts by both General Electric and Pratt & Whitney before a specific concept was selected (refs. 4 and 5). This analysis was a team effort, with each engine manufacturer being assisted by NASA, two aircraft manufacturers (Boeing and Douglas), and a number of airlines (United, American, TWA, Pan Am, and Eastern). Technical merits (e.g., performance, weight, and maintenance) as well as economic merits (e.g., airline return on investment, direct operating cost, and payback period) were investigated. From considerations such as potential fuel savings, economic benefits, and cost of development, NASA selected 16 component improvement concepts for technology development by General Electric and Pratt & Whitney.

For the JT8D engine, four concepts were selected (table I-1) for development:

(1) An improved outer air seal for the high-pressure turbine

(2) A new high-pressure-turbine blade cooling concept, wherein the cooling air is discharged at the root of the blade

(3) An aerodynamically improved DC9/JT8D reverser stang fairing that incorporates advanced composite materials for lighter weight

(4) Longer blades and abradable trenched rubstrips on the high-pressure compressor

Concepts 1, 2, and 4 are being developed by Pratt & Whitney; the reverser stang fairing is to be developed by the Douglas Aircraft Co.

Technology development has been completed on the improved JT8D outer air seal. Figure I-8 shows some features of the seal. Through the use of honeycomb seal material plus additional

knife-edges, an improved labyrinth arrangement was effectively added to the seal. Also, the blade cooling flow, which had been discharged completely from the blade tip, was rerouted to permit some discharge from the blade suction surface. Results have been obtained from back-to-back engine tests of both the current and improved configurations, as shown in figure I-9, over a range of thrust levels. At the normal (90 percent) cruise point, a specific fuel consumption (SFC) reduction of 0.6 percent was achieved. This reduction (though small) is equivalent to 6 percent of the total net income of the U.S. domestic airlines in 1977 (at an average fuel cost of 50¢/gallon). It is also equivalent to an airline fuel savings of 200 million gallons by the end of the century, if the seal is incorporated both into new-production JT8D engines and into older engines through retrofit, where economically feasible.

For the JT9D engine, four concepts were also selected (table I-1) for development by Pratt & Whitney:

(1) Active clearance control for the high-pressure turbine

(2) A new fan incorporating only a single shroud along with low-aspect-ratio blades

(3) Ceramic thermal-barrier coatings on the vane end walls in the high-pressure turbine

(4) Ceramic outer air seals for the high-pressure turbine

Development of the active clearance control concept has been completed. As indicated in figure I-10, this is a technique to reduce tip clearances during cruise by cooling, and hence shrinking, the case. During the transient portions of flight (takeoff and landing), the cooling air is reduced or eliminated. This increases the tip clearances between the turbine blade and shroud and minimizes the potential for rubbing.

The current and improved JT9D configurations are shown in figure I-11. The significant features of the improved configuration are

(1) A modified support ring that permits greater reduction in tip clearance

(2) A doubling of the cooling flow

(3) A new configuration for the air supply tubes that provides shorter impingement distances and a more effective use of the cooling air

Results are shown in figure I-12 for back-to-back tests of the improved and current configurations. These results indicate

that cruise SFC can be reduced 0.65 percent over a wide range of cruise thrust settings.

For the CF6 engine, eight concepts (table I-2) were selected:

(1) A short-core nozzle that permits reduction in weight and scrubbing drag

(2) A new front mount that improves the load distribution around the compressor case and results in reduced tip clearances

(3) A new fan with improved aerodynamic design

(4) Improved aerodynamics for the high-pressure turbine

(5) Improved roundness control for the high-pressure turbine

(6) Reduced compressor bleed by recirculation of air in the DC-10 cabin air-conditioning system

(7) Active clearance control for the high-pressure turbine

(8) Active clearance control for the low-pressure turbine

Concept 6 is under development by the Douglas Aircraft Co.; all the other concepts are to be developed by General Electric.

Technology development has been completed on the first three concepts. The changes in the core nozzle resulted in a 0.9 percent SFC reduction at cruise, as demonstrated by flight tests on both the DC-10 and A300 aircraft. The new front mount can provide a 0.3 percent cruise SFC reduction. The improved fan can provide a 2.0 percent cruise SFC reduction. Figure I-13 lists the improved features for the new fan concept: basically, improved airfoils, rearward placement of the current single shroud to minimize blockage, and addition of a fan-case stiffening ring to keep the case round (hence, reducing tip clearances). Results of sea-level engine tests are shown in figure I-14. The indicated 3.2 percent SFC reduction at 40 000 pounds of sea-level thrust is equivalent to a 2 percent cruise SFC reduction.

According to a projection based on various market predictions by the engine manufacturers, the performance improvement part of the Engine Component Improvement project should provide the airline industry with a cumulative fuel savings of at least 7 billion gallons by the year 2000. This savings would occur if all the concepts complete the technology development phase successfully, are carried through the certification phase by the manufacturers, and are successfully introduced into commercial service on future engine models or through retrofit.

Engine Diagnostics

The engine disagostics part of the ECI project is directed at identifying and quantifying the sources of the performance deterioration that occurs with time in the JT9D and CF6 engines. The effort will also provide design methodology and maintenance practices for minimizing such deterioration in current and future engines. As with performance improvement, NASA has major contracts with both Pratt & Whitney and General Electric for testing, data analysis, and modeling.

The major contributors to performance degradation are shown in figure I-15. Examples of these degradation mechanisms are shown in figure I-16. In the cold section of the engine, foreign object damage, erosion, and surface roughness are significant. In the hot section of the engine, thermal distortion is one of the predominant degradation mechanisms - causing, for example, warpage or distortion of vanes. Clearance increases occur through the entire engine, as a result of blades rubbing with the outer shrouds. These clearance increases result in efficiency losses.

In investigating these contributors to performance degradation, the general approach is as follows:

(1) Gather existing (historical) data from airline in-flight recordings and from ground test cells at both airline and engine overhaul shops. (To date, this has been done for about one-third of the world's aircraft that use JT9D and CF6 engines.) Also, conduct inspections on a selected used parts that contribute to performance degradation.

(2) Augment this information with special engine tests and inspections in order to evaluate the effects of deteriorated components, and subsequent refurbishment, on both overall performance and engine module performance. (Overall performance deterioration was evaluated by securing an engine from an airline, testing it, conducting a complete teardown, and inspecting it. The engine was then refurbished and/or reassembled, retested, and returned to the airline. Module performance degradation was evaluated by tests before and after used modules were replaced.)

(3) Assess the causes of performance degradation during the first flight or flights of the aircraft as the engine structure first responds to the flight environment

(4) Assess the causes of long-term performance degradation as a function of both cycles and time

(5) Determine the effects of deteriorated parts on module performance

(6) Establish statistical trends, analytical models, and design criteria, with associated correlations of the effect of maintenance practices on SFC losses

The results of the module replacement and refurbishment test on the CF6 engine are shown in figure I-17. The numbers in parentheses represent the number of test modules. Simply cleaning the fan blades and recontouring the leading edges resulted in a specific-fuel-consumption reduction of 0.3 percent. Replacing the low-pressure turbine with new or refurbished modules resulted in a SFC reduction of 0.4 percent. The high-pressure-turbine results are not available yet, since testing and analysis are still under way.

How the various performance degradation mechanisms - such as clearance increases, erosion and airfoil roughness, and thermal distortion - affect the cruise SFC deterioration of the JT9D engine modules is shown in figure I-18. These results, averaged for a large number of engines, are based on used-parts analysis and prerepair tests (i.e., the historical data). Clearance changes affect all the engine modules from the very first flight. As the engine matures, however, thermal distortion becomes of significance for the high-pressure turbine, and erosion and airfoil roughness become of significance for the high-pressure compressor. Although the data indicate that the high- and low-pressure-turbine modules do not deteriorate much beyond the 1000th flight, this is only because these modules are normally replaced every 1000 to 2000 flights. Thus, what is shown are deterioration values where the high-pressure turbine has been replaced between the 1000th and 3000th flights.

Percent cruise SFC deterioration as a function of the number of flight cycles (where a flight cycle is a takeoff, flight, and landing) is shown in figure I-19. As evident, clearance increases cause more than 50 percent of the overall deterioration experienced in the JT9D engine.

The major causes of these service-related changes in gas-path clearances are the loads on the engine in flight. These are nacelle aerodynamic loads, experienced during airplane rotation, as well as inertia loads, such as "g" and gyroscopic loads. These loads, schematically shown in figure I-20, cause the engine to bend and distort and the blade to rub against the outer shroud. They thus produce increased clearances and attendant performance losses.

Pratt & Whitney and Boeing - in a cooperative program - used a NASTRAN finite-element structural model (fig. I-21) to analyze these flight-load effects on the JT9D engine. The NASTRAN model

was used to calculate the deflections or changes in clearances that occur throughout the engine, for both steady-state and dynamic conditions. These clearance changes were then converted to performance losses. Shown in table I-3 are the NASTRAN theoretical results. In the steady-state case, the nacelle aerodynamic load affected all engine stages and contributed to about 87 percent of the total performance loss. The other two loading conditions were of lesser significance. In the dynamic cases, such as wind gust and hard landings, there were no significant changes from the steady-state results.

To provide a data base for validating the NASTRAN theoretical steady-state load results, Pratt & Whitney will subject a JT9D engine to a simulated aerodynamic loads test. Aerodynamic loads will be simulated by placing a series of supporting bands (bellybands) around the inlet. These bands will then be pulled to exert loads on the inlet to simulate nacelle loading conditions (fig. I-22). As the engine is run through a performance test, X-ray and laser proximity probes will be used to determine changes in tip clearances. Additional instrumentation will be added to the engine to determine the engine and module performance changes that occur as the aerodynamic loads are simulated.

A summary of engine diagnostics results to date for both the JT9D and CF6 engines is shown in figure I-23. Shown are the statistically averaged engine performance deterioration trends as a function of engine cycles. There is about a 3 percent increase in SFC after 3000 flight cycles, and about 1 percent is recovered during a normal overhaul (which is typically done on the engine hot section). Many factors influence the shape and values of the curves: Airline overhaul practice, route structure, derated takeoff, engine module mix, airplane model, and engine location are but a few.

The output of the engine diagnostics effort is expected to provide industry with data necessary to cost effectively restore the performance of current engines. The magnitude and location of performance deterioration will also be pinpointed, and the modular performance analyses techniques required to diagnose the related performance losses associated with the engine will be improved. For derivative and future engines, this effort - by identifying unique degradation mechanisms and developing usage-related deterioration models - will provide design tools for improving performance retention.

ENERGY EFFICIENT ENGINE

The objective of the Energy Efficient Engine (E^3) project is to provide an advanced technology base for a new generation of fuel-conservative turbofan engines for commercial transports. Specifically, this project involves aggressive development of

advanced component technologies, followed by integration and testing as complete systems. A technology readiness date of 1983 has been set for completing these activities. At that time, the advanced component technologies will have been developed and demonstrated to a point where they are suitable for use in a future commercial engine development. In the late 1980's, E^3 technology could appear in new advanced commercial turbofan engines, or perhaps even a few years sooner in advanced derivative versions of current engines. Benefits from E^3 technology would then start to accrue and would grow rapidly during the 1990's.

Goals were established at the outset of the project to guide the selection of engine cycles and configurations and to serve as a focus for the technology efforts. These goals recognized that future engines must be not only fuel efficient, but also economically attractive to the airlines and environmentally acceptable to the public. Goals for fuel savings are

(1) At least a 12 percent reduction in SFC for newly manufactured engines

(2) At least a 50 percent improvement in performance retention over the lives of the engines

To provide economic incentives, NASA established a goal of at least a 5 percent reduction in the DOC. These fuel and economic goals are relative to current high-bypass-ratio turbofan engines (specifically, the JT9D-7A and the CF6-50C engine models).

There is a high degree of uncertainty as to future environmental requirements. As a result, since any future advanced turbofan engine must meet the requirements prevailing at that time, NASA selected, as goals, the most stringent limits for noise and emissions that have been proposed to data by either the Federal Aviation Administration or the Environmental Protection Agency. These are the FAA's FAR-36 (1978) standards for noise and the EPA's proposed 1981 standards for emissions.

The E^3 project is being accomplished through parallel contracts with the two U.S. manufacturers of large, high-bypass-ratio engines: General Electric and Pratt & Whtney. The effort itself is structured and scheduled as shown in figure I-24. The first element involves defining a baseline design for a future advanced propulsion system. This baseline design serves as a focus for defining technology needs, performance potential, component interfaces, and system trade-offs. To arrive at optimum cycle characteristics and engine configurations, both General Electric and Pratt & Whitney conducted trade-off evaluations, in which they concentrated on fuel usage and DOC for E^3 technology engines operating on potential 1990-era aircraft. Each company was assisted by Boeing, Douglas, and Lockheed in conducting

these trade-offs. The initial design effort has been completed, but lower-level work will be conducted during the remainder of the project to support the experimental efforts and to use data from those efforts for refining the initial propulsion-system baseline design. Thus, an on-going appraisal of the technology status and potential will be obtained. Component technology needs have now been well defined, and work has started on the second element of the project. This element - which comprises the major portion of the project - involves design and extensive experimental development of the major engine components. The intent is to substantially improve the performance of each component.

In the third element, the components will be integrated to assess their interactive effects and to work on those mechanical technologies that are unique to the integrated system. First, the high-pressure compressor, the combustor, and the high-pressure turbine will be assembled in a core (or high spool) package. Then the core will be integrated with the low-spool components (fan, booster or low-pressure compressor, low-pressure turbine, and mixer) and a metal "boilerplate" nacelle. This integrated core - low-spool package (ICLS) will then be tested to assess the overall performance, component interactions, and design integrity of the mechanical systems.

General Electric Configuration

The initial baseline propulsion-system design has been finished. Figure I-25 illustrates General Electric's E^3 configuration, which resulted from that effort. Their configuration uses two spools plus a mixer and a long-duct nacelle. A mixer is included because, according to results from the initial performance analyses, exhaust-gas mixing offered the potential for about a 3 percent reduction in SFC from that of an unmixed engine.

Table I-4 lists the cycle characteristics of General Electric's E^3 configuration. As a comparison, values for General Electric's reference engine - the CF6-50C - are also shown. The bypass ratio of the E^3 has been increased substantially, as has the compressor pressure ratio, over those of the CF6-50C. Turbine temperatures have been increased only moderately. Cycle trade-off studies indicated that, if the DOC and performance-retention goals are to be met, only moderate increases could be tolerated even with improved materials. A thrust of 36 500 pounds was used to size the hardware for this project. The technologies, however, are scalable over a wide range; hence, commercial engines based on E^3 technology could have whatever appropriate thrust is required to meet airline needs. For this particular configuration, General Electric predicts a 14.2 percent cruise SFC reduction over the CF6-50C SFC.

The advanced technologies needed for the high-pressure-core components are listed in figure I-26. The aggressive compressor design has a compression ratio of 23 in only 10 stages. So that it can achieve a polytropic efficiency of over 90 percent, it will have advanced, low-aspect-ratio, highly loaded airfoils and will be made of advanced materials. In addition, active clearance control will be used on stages 6 to 10 in order to achieve much tighter clearances than those used in current engines.

The combustor is a two-zone, double-annular configuration. This rather complex configuration is required to meet the stringent emission goals, which will be very difficult to achieve on an engine with an overall pressure ratio of 36. This combustor requires several technology advances, including improved diffuser designs and a segmented (or "shingled") liner, in order to achieve longer life.

The high-pressure turbine has two stages and is designed for an efficiency of over 92 percent at maximum cruise conditions. This high efficiency requires a number of technology advances including low leakages, improved cooling concepts, and advanced active clearance controls. Also, several advances in materials and fabrication processes are required (directionally solidified blades, ceramic shrouds, and near-net-shape rotors that use hot isostatic pressing of powder-metallurgy alloys).

Similar aggressiveness in technology advances is required for the General Electric low-spool components, as shown in figure I-27. Particularly important are the fan and the booster. The fan uses low tip speeds and a low placement of the midspan damper to achieve over 88 percent efficiency. The novel quarter-stage "island" booster design serves a dual function: It aids matching of the fan and core streams, and it centrifuges any foreign objects away from the core stream and thereby helps reduce foreign-object-damage erosion in the core. The five-stage, low-pressure turbine has been specially configured to reduce noise. And, as in the high-pressure compressor and turbine, an active clearance control system will be used to permit closer running clearances. The mixer will be designed to achieve 75 percent mixing effectiveness and very low pressure losses in a short length.

Pratt & Whitney Configuration

The Pratt & Whitney E^3 design that resulted from the initial design and definition effort is illustrated in figure I-28. It is similar to the General Electric design in that it is a two-spool, mixed-flow configuration. This design, like General Electric's, has also stressed greater durability, performance retention, and ease of maintenance. Both designs feature a short, stiff, straddle-mounted core with five main bearings

located in easily accessible bearing compartments. Special attention also has been given to structural load paths in order to minimize the bending and twisting encountered in current engines, thus improving performance retention. Both designs also feature careful attention to active and passive clearance control as an aid in retaining performance.

The cycle characteristics of Pratt & Whitney's baseline design are listed in table I-5. Again, for comparison, values for their reference engine - in this case the JT9D-7A - are also shown. The predicted cruise SFC reduction for the E^3 design is 14.9 percent below that of the JT9D-7A.

Advanced-technology features in the Pratt & Whitney E^3 core configuration are shown in figure I-29. This core includes a 10-stage compressor with a compression ratio of 14. A number of advanced-technology features - including supercritical airfoils, trenched cases, and active clearance controls - help achieve a polytropic efficiency level of over 91 percent. The combustor also depends on a two-zone configuration for emissions control (in a similar manner to General Electric's combustor), but the Pratt & Whitney design has two burning zones arranged axially in series. Several technology advances are also planned for this combustor, including carburetor-type fuel nozzles and an advanced liner configuration that uses improved cooling concepts and segmented panels to extend life.

Pratt & Whitney selected a single stage for the high-pressure turbine in order to gain the cost and maintenance benefits associated with fewer hot-section parts. However, a cooled turbine efficiency of over 88 percent must be reached if the total engine performance required for fuel savings is to be achieved. Reaching this high efficiency in a single stage will require advances in several areas, including advanced airfoil designs for the transonic airflow in this turbine, improved cooling schemes, and several advanced materials. Pratt & Whitney's single-crystal alloys will be used for the blades and vanes. An improved active clearance-control system is also planned for this turbine.

Advanced-technology features in the low-spool components of the Pratt & Whitney E^3 design are shown in figure I-30. The fan blades are unshrouded. Eliminating the midspan dampers, used in the fan blades on all current engines, can improve efficiency and hence reduce SFC nearly 1 percent. However, the designs of unshrouded blades invariably result in very large, long-chord configurations that tend to increase engine weight. Thus, advanced design approaches are needed to generate lighter weight fan-blade configurations that are resistant to both aeroelastic flutter and foreign-object damage. Pratt & Whitney has developed a promising design approach that uses hollow titanium airfoils, and work is now under way to develop the manufacturing

technology for such unique blades. To date, the most promising approach is to fabricate the hollow blades from diffusion-bonded titanium laminates.

The other low-spool components include a four-stage, low-pressure compressor driven by a four-stage, counter-rotating, low-pressure turbine. The approach to exhaust-gas mixing is also extremely aggressive, calling for a design mixing effectiveness of 85 percent and low pressure losses. These design goals are to be achieved by using a short, scalloped mixer to minimize the weight and drag penalties of the required long-duct nacelle.

Component Technology

The component design phase is well under way, and both General Electric and Pratt & Whitney are conducting technology investigations in support of their design work. Figure I-31 illustrates an example of such work at General Electric in support of their fan-frame acoustic design. Current engines have about twice as many vanes as fan blades for minimum fan noise. Also they have an axial spacing of about 1 chord width between the vanes and blades, along with separate struts to carry loads to the fan case. In the E^3 design, General Electric will use a lower vane-blade ratio, as indicated, and a much wider axial spacing. This design permits the vanes to be integrated with the struts and hence reduces fan weight and cost.

Acoustic tests of these two configurations were recently conducted, and the results are shown in figure I-32 for perceived noise level as a function of acoustic angle. The upper plot shows results for the approach condition; the lower plot shows results for the takeoff condition. The two configurations gave very similar acoustic results. Thus, GE's E^3 fan is being designed with a vane-blade ratio of about 1.1 and very wide axial spacing, as illustrated in figure I-31.

Another important series of supporting technology tests conducted by GE involves the combustor design. GE's prime combustor design is the double-annular configuration, shown at the left in figure I-33. Principles of this two-zone design were established under NASA's Experimental Clean Combustor program. The results of that program, when extrapolated to the higher pressure conditions for E^3, indicate that this configuration offers potential for meeting the stringent E^3 emissions goals. However, the two separate combustion zones require rather complex staging of the valves that control the fuel-flow to each zone. Thus, GE proposed an alternative design involving a simpler single-annular configuration. A series of early tests were run on this single-annular configuration in order to assess its potential for meeting the E^3 emissions goals.

The prime resutls of those tests are shown in figure I-34. Plotted are the emissions levels for carbon monoxide (CO), hydrocarbons (HC), and oxides of nitrogen (NO_x). The left bar in each pair shows single-annular combustor results from tests recently run as part of the E^3 project. The right bar in each pair shows estimates for the double-annular combustor: These predictions are based on the earlier test results from the Experimental Clean Combustor program. These results indicate that the single-annular combustor does not meet the E^3 goals for CO and NO_x emissions. Also, these differences might be increased with future broad-specification fuels. Thus, NASA has concluded that the more-complex double-annular combustor is needed to meet the stringent E^3 emissions goals. All efforts are now directed at the double-annular configuration so that the low emissions levels that might be required in future engines can be demonstrated.

Another example of the component technology efforts completed to date involves Pratt & Whitney's single-stage turbine. Early emphasis was on aerodynamic tests in an uncooled turbine-rig so that the best airfoil designs could be selected. Two combinations of vanes and blades were tested; figure I-35 shows the two blades. Results for the uncooled-rig tests are shown in figure I-36. Plotted are the measured efficiency levels as functions of airfoil span for the two airfoil combinations. Both designs achieved good efficiencies, but the 43-percent-reaction airfoils produced higher efficiencies. This reaction value was thus selected for the E^3 turbine design.

Benefits

The fuel savings that have been predicted for the E^3 engines are shown in figure I-37. These are the projections made for both engine designs by three major aircraft manufacturers: Boeing, Douglas, and Lockheed. Using the predicted SFC reductions of 14 to 15 percent, the aircraft companies predicted fuel usages for their own versions of advanced aircraft for various flight missions, and then they compared these to the predicted fuel usages for similar aircraft with current engines. Plotted are the differences in the fuel-usage estimates. (Note the ordinate of the plot starts at 10 percent.) The projected fuel savings for E^3 ranges from 13 to 22 percent. The fuel savings increase with longer flight distances since the prime fuel savings is achieved in the cruise portions of each flight mission. However, even the shorter-range flights with relatively short cruise durations show significant fuel savings.

Projections were also made for the direct operating costs of the same aircraft-engine combinations, and a plot of these results is shown in figure I-38. As might be expected, the projected trends for DOC are similar to those for fuel savings since fuel

costs contribute about 40 percent to the direct operating costs. Also important in these DOC reductions was the emphasis both General Electric and Pratt & Whitney placed on minimizing maintenance costs. For example, the total numbers of airfoils in their engines were drastically reduced from the numbers in the reference engines.

From the current status of the E^3 project, these benefits appear to be realistic. Present E^3 designs indicate that all goals are achievable, with the possible exception of the NO_x emissions goal. The advanced technologies required to meet the goals are scheduled to be demonstrated by 1983.

ADVANCED TURBOPROP

The third ACEE propulsion effort, the Advanced Turboprop project, is directed at establishing the feasibility of radically improving propeller-driven propulsion systems to the point where they can be effectively applied to future commercial air transports. Advanced turboprop propulsion systems promise extremely large fuel savings. And, with an aggressive technology development program - demonstrating the advanced technology in the late 1980's - they would be available for the commercial air transports of the 1990's.

Turboprop-powered aircraft are not new, of course. Turboprops are used today in various military, business, and commuter aircraft, and at one time were used in medium-range commercial air transports. Figure I-39 shows the turboprop-powered Lockheed Electra, which was introduced into medium-range commercial service in the late 1950's. It was a major improvement over the reciprocating-engine, propeller-driven aircraft then in commercial service.

Jet-powered aircraft, such as the Boeing 707 shown in figure I-40 (the first domestic commercial jet), were also introduced in the late 1950's. Such jet-powered aircraft offered better passenger comfort since they flew above the weather and had less noise and vibration in the cabin than the Electra. They were also faster. This, along with their larger size, provided greater productivity and convenience. And, they had newer engines with lower maintenance costs. The 707, and others like it, swept the market. Their major disadvantage was the higher fuel consumption of the turbojet engines. But, in an era of inexpensive fuel - around 5 to 10 cents a gallon at that time - the price of fuel was not a critical factor in propulsion-system selection.

Figure I-41 illustrates this last point. Shown is the fuel consumption for various propulsion systems - expressed in gallons per mile to account for speed differences. These values are

plotted relative to the Electra engine fuel consumption. Also plotted are the dates of introduction into service (or possible introduction). Going from the Mach 0.6 turboprop-powered Electra to the Mach 0.8 turbojet-powered 707 resulted in a 50 percent increase in fuel consumption.

Since the first commercial turbojet was put into service, a number of improvements have increased the efficiency of aircraft gas-turbine engines. Most significantly, the high-bypass-ratio turbofan engine has been a major factor in reducing fuel consumption. The Energy Efficient Engine promises another 15 percent reduction in fuel consumption, primarily through better thermal efficiency. But the curve does appear to be flattening out, an indication of a maturing technology.

Making the next significant step in fuel savings will necessitate a major increase in propulsive efficiency. Such an increase, about 15 percent at Mach 0.8, is offered by the advanced turboprop. Even larger savings would be possible at lower speeds. This propulsion-system concept will be considerably different, however, from the older, more conventional, Mach 0.6 Electra system. Figure I-42 illustrates this difference. The advanced propeller concept is compared with the Electra propeller, to the same scale. The shape, size, and number of blades are all radically different.

The major features of the advanced propeller concept are shown in figure I-43. The advanced propeller would be driven by a large, modern turboshaft engine and a gearbox. The blades of the propeller would be very thin and highly swept to minimize both compressibility losses and propeller noise during high-speed cruise. An area-ruled spinner and an integrated nacelle shape would also be used to minimize compressibility losses in the propeller-blade hub region. A high power loading, and hence a relatively small propeller diameter, would be achieved by using 8 or 10 blades. A final feature worthy of note is that modern propeller blade fabrication techniques would be used to make the thin, highly swept, twisted blades.

The basic reason for the advanced turboprop being such an attractive concept is its potential for high propulsive efficiency in the Mach 0.7 to Mach 0.8 speed range, as shown in figure I-44. Older model turboprops had relatively thick, unswept propeller blades and experienced rapid increases in compressibility losses above Mach 0.6. Current high-bypass-ratio turbofans exhibit their highest propulsive efficiency (about 65 percent) at cruise speeds somewhat above Mach 0.8. The new advanced turboprops are estimated to be about 20 percent more efficient than high-bypass-ratio turbofans at Mach 0.8. At lower cruise speeds, the efficiency advantage of the advanced turboprop is even larger. This high propulsive efficiency of the advanced turboprop makes it an attractive powerplant for many applications.

A number of aircraft studies have been conducted to quantify the benefits promised by the advanced turboprop. Figure I-45 shows some of the passenger aircraft studied to date. Two aircraft are shown: a medium-range wide-body transport with four turboprops mounted on the wing, and a shorter-range narrow-body transport with two turboprops mounted at the rear of the fuselage. Cargo airplanes and military patrol aircraft could also benefit from using advanced turboprops. In every study, the airplanes powered by advanced turboprops used much less fuel than competing turbofan-power airplanes.

These studies are summarized in figure I-46, where the trend in fuel savings with aircraft design range is shown. For short-haul aircraft, where takeoff and descent dominate the fuel fraction, the turboprop fuel savings can be as high as 30 percent. For medium-range aircraft, fuel savings are 15 to 20 percent. For very long-range aircraft, where cruise dominates the fuel fraction, turboprop fuel savings are 17 to 30 percent. These fuel savings for the turboprop are relative to a turbofan-powered aircraft with the same level of component technology. Thus, if an E^3 turbofan will achieve a 15 percent fuel savings over a conventional turbofan in a new medium-range transport, a new turboprop with an E^3 level of component technology would achieve a 30 to 35 percent fuel savings. It is this very large fuel savings potential that prompted NASA to include the Advanced Turboprop project in its ACEE program.

The objective of this project is to develop the technology for efficient, reliable, and acceptable operation of advanced turboprop-powered aircraft at cruise speeds between Mach 0.7 and Mach 0.8. The turboprop goals of minimums of 15 percent fuel savings and 5 percent DOC improvement are relative to turbofans at equivalent levels of technology. The third turboprop goal is a cabin comfort level (noise and vibration) the same as that in modern turbofan-powered aircraft.

To achieve these goals, Lewis began a phased Advanced Turboprop project in 1978. The major elements of phase I (an enabling technology and research phase) are shown in figure I-47. The first element - the propeller-nacelle - is concerned with propeller aerodynamics, acoustics, and structures. The second element addresses the cabin environment. Since the fuselage may be in the direct noise field of the propeller, the noise generated by the propeller must be attenuated by the cabin wall in order to provide a low-noise cabin environment. Also, the turboprop engines must be mounted in such a way that cabin vibration is low. The third major element of phase I, installation aerodynamics, is concerned with an accelerated, swirling propeller slipstream flowing over the wing. Here, there is the challenge of integrating propeller design with wing design to achieve the best combination of engine efficiency and aircraft lift-drag ratio. Also, airplanes powered by advanced turboprop engines

must be configured to have adequate stability and control. The fourth element involves the mechanical components of an advanced turboprop propulsion system: the engine drive, the gearbox, and the advanced propeller. These components must be designed and packaged in such a way that maintenance and reliability will be much improved over that experienced by the first generation of turboprop-powered aircraft. Since these four elements are so strongly interrelated, aircraft trade-off studies must be performed to obtain the match that will best achieve the goals of low fuel consumption, low operating cost, and passenger acceptance.

Propeller-Nacelle

The advanced propeller technology program in phase I is outlined in table I-6. The plan is to test a matrix of eight 2-foot-diameter wind tunnel models. The range of the propeller design parameters is indicated in the table. Eight or 10 blades are used to keep the propeller diameter relatively small. Sweep at the blade tip as high as 60° will be investigated to determine its effect on propeller-generated noise at cruise. The tip-speed range results in transonic relative tip Mach numbers during Mach 0.8 cruise. The high-cruise power loading also results in relatively small propeller diameters. Besides the experimental work on propellers in phase I, an extensive analytical effort is under way to upgrade prediction and design capabilities.

Three blades have been tested and are shown in figure I-48. Each blade is extremely thin over much of its span for minimum compressibility losses during high-speed operation. Also, the blade aspect ratio is relatively low as a result of designing for a relatively small propeller diameter (i.e., high power loading). The blade on the left in the figure is straight, with 0° of tip sweep. The middle blade has 30° of tip sweep. The blade on the right, with 45° tip sweep, was designed with both refined aerodynamic and acoustic design methodology. Indeed, acoustics dictated the rather unique blade planform shape, which has a longer chord and more sweep than the other two blades. This high-sweep propeller model is shown in figure I-49 installed in the Lewis 8- by 6-Foot Wind Tunnel. All three propeller models were tested in this wind tunnel, and all were driven by the strut-mounted air-turbine propeller test rig shown in the background.

Efficiency. - The measured efficiencies of all three propellers are shown in figure I-50 as a function of Mach number. At Mach 0.8 conditions, measured efficiency improved as the tip sweep of the models increased. This confirms that blade sweep does reduce compressibility losses. Also, efficiency improved as Mach number was reduced.

Shown in figure I-51 is a more complete Mach 0.8 performance map of the model with 45° sweep. Blade tip speed and blade pitch angle were changed during testing in order to define lines of constant power loading. An efficiency of 79.5 percent has special significance since this efficiency was assumed in the early studies that indicated the potential of the advanced turboprop. Measured propeller efficiencies exceeded 79.5 percent for a range of power loadings and tip speeds. Since each point on this map represents a unique set of values for propeller efficiency, diameter, weight, and tip speed, an airplane trade-off study must be performed to select the best propeller design for a particular application.

Noise. - The relative noise generated by the three propeller models, as measured in the wind tunnel, is shown in figure I-52. At Mach 0.8 design conditions, the propeller with a tip sweep of 45° was the quietest. Its peak sound pressure level was about 6 decibels lower than that of the straight blade. Because of the many unknowns involved in noise measurements in wind tunnels, particularly in measurements of absolute noise levels, NASA is proceeding with a program that will allow propeller noise to be measured in flight.

A NASA JetStar aircraft that is being modified to accept a small propeller and its air-turbine drive atop the fuselage is shown in figure I-53. The 2-foot-diameter propeller will be driven by an air turbine, whose working fluid is main-engine bleed air. Microphones will be mounted in the JetStar's fuselage to record propeller noise generated at flight conditions from takeoff to Mach 0.8 cruise. Testing is scheduled to begin next year. The data from these tests will be used to upgrade propeller noise prediction programs. The data on noise level, spectral content, and directionality will constitute the input needed to work on fuselage attenuation of propeller noise.

Structural techniques. - Propeller structural techniques are compared in figure I-54. Shown at the top of the figure is the structural design for a current-production fiberglass blade. It has a fiberglass shell, a solid aluminum load-carrying spar, and foam fill. Blades like this were introduced into service in the early 1960's. On the bottom is shown an example of how an advanced blade might be constructed. Materials and fabrication techniques are similar to those for current blades. In place of foam fill, however, honeycomb or some other material is used to give the thin blade more rigidity. This blade construction concept, along with others, will be analyzed in the coming year.

Cabin Environment

The noise inside the cabin depends mainly on the noise generated by the propellers and on the attenuation of this noise by the

fuselage wall and the cabin interior trim. These two conditions are interrelated, as shown in figure I-55.

The maximum-cabin-noise goal is 75 decibels on the A scale (dBA). For a typical propeller design, sound pressure level in the cabin would be 90 decibels. With current conventional cabin treatment, exterior noise could be as high as 110 decibels. With improved fuselage design and cabin treatment, exterior noise of 140 decibels or more could be tolerated according to initial studies conducted by the Langley Research Center. However, the price that must be paid for the higher noise attenuation is an increase in fuselage weight.

Influencing cabin noise, of course, is the propeller noise level. At the moment, there is uncertainty in predicting noise level and also uncertainty in interpreting wind tunnel noise measurements. The absolute noise level of the three models tested thus far is somewhere in the shaded area with a possible lower bound of approximately 140 decibels. With improved propeller design, it may be possible to reduce the noise level to about 130 decibels. Since the two bars overlap, a number of solutions are possible for achieving the desired maximum noise level in the cabin. Thus, it will be necessary to conduct aircraft trade-off studies. Engine location is, of course, another variable in such studies. The optimizations are quite different, for example, when the turboprops are mounted at the rear of the fuselage rather than on the wing.

Installation Aerodynamics

The third major element of the Advanced Turboprop project is installation aerodynamics. So far only the question of drag has been addressed. Drag becomes of concern with the advanced turboprop because, at the Mach 0.7 to 0.8 cruise speeds of interest, large compressibility losses could be encountered on that area of the wing washed by the accelerated slipstream of the propeller.

Preliminary results have been obtained with a propeller slipstream simulator (fig. I-56). This figure shows a wing-body aircraft model installed in an Ames wind tunnel. There were no model turboprops directly on the aircraft model; instead, the ejector device directed a simulated propeller slipstream over the wing. By using this device, slipstream Mach number and slipstream swirl angle were varied independently. It is these two parameters that are peculiar to a turboprop installation.

The results are shown in figure I-57 for two cruise Mach numbers. The aircraft drag at a lift coefficient typical of cruise is the zero reference point. When the simulator was turned on, generating a 0^{o}-swirl slipstream, the increase in drag was

about 2.5 percent. This level was maintained to swirl angles of 7°. At higher swirl angles, drag decreased as the wing recovered some of the swirl and actually became negative between 7° and 11°. Since the amount of swirl of the slipstream increases as power loading is increased, propeller design selection must consider these slipstream effects. Wing design must also be optimized for the recovery of swirl. Such integration may yield an installation drag for the turboprop equal to - or perhaps even lower than - that of the turbofan.

Turboprop installation drag will be accurately assessed in the near future by testing an aircraft model with a 2-foot-diameter propeller, as shown in the artist's sketch of figure I-58. Data from this test will guide the integration of propeller design with wing design.

Mechanical Components

The fourth major element in the Advanced Turboprop project involves the mechanical components. This element was of particular concern at the beginning of the project because of the high maintenance costs for the turboprop propulsion system on the Electra and the general feeling that turbofan maintenance costs would always be substantially lower. For this reason, the Lewis Research Center placed a contract with Detroit Diesel Allison (with Hamilton Standard as a subcontractor) to evaluate the Electra system. Results indicated that the 1970-era turboprop maintenance costs were indeed higher than those for the JT8D turbofan (a representative turbofan), but the difference was mainly in the core engine. The core engine of the turboprop was expensive to maintain largely because it was an older technology core originally designed for military application. It was therefore concluded that overall advanced-turboprop maintenance costs can be competitive with those of an advanced turbofan. Core maintenance costs, based on equal levels of technology, should be about equal. Preliminary conceptual designs were made to evaluate how turboprop maintenance costs could be reduced. The advanced propeller and gearbox can be greatly improved by performing on-condition maintenance instead of scheduled overhauls, by using modular construction, and by emphasizing simplicity and reliability in design.

Future Phases

Results of the subscale testing part of phase I has been very promising. Progress has been achieved in developing design and prediction methodologies. This phase is an enabling technology effort that will take about 3 years to accomplish, with the intent being to establish the feasibility of concepts and a data base for future efforts. As a logical next step, NASA is plan-

ning large-scale component verification tests that will lead to flight verification (fig. I-59). To be evaluated are propeller fabrication, propeller flutter, scale effects relative to propeller-generated noise, and advanced fuselage-noise-attenuation concepts. Operational effects for a full range of flight conditions would be an important feature in demonstrating technological readiness. Thus, at the conclusion of the Advanced Turboprop project, technology would be available for use in designing very efficient turboprop-powered commercial aircraft and in establishing commercial acceptance of this advanced system.

CONCLUDING REMARKS

The technology readiness dates for the three Aircraft Energy Efficiency propulsion projects are shown in figure I-60. By the dates shown, the technology required for beginning commercial development will be demonstrated. Such developments would be expected to yield the fuel savings indicated in the figure. Figure I-61 indicates the potential benefits of the three projects in terms of both direct operating cost and fuel savings. DOC savings are, of course, important since future propulsion systems must be economically attractive to the airlines as well as fuel efficient.

There could be about a 5 percent fuel savings and a 3 percent DOC savings in derivative engines that use Engine Component Improvement (ECI) technology. With a technology readiness data of 1980 to 1982, this project will yield results that are extremely applicable to the near-term needs of the airlines. Energy Efficient Engine (E^3) benefits are about a 15 to 20 percent fuel savings and a consequent 5 to 10 percent DOC savings. These benefits could be realized by the late 1980's in new engines that use E^3 technology to be demonstrated by 1983. Advanced turboprops are expected to provide about 30 to 35 percent fuel savings over current engines, if E^3 technology is used for the turboshaft engine, with a possible 10 to 15 percent DOC savings. These major gains could begin to be achieved in the 1990's, if the technology is successfully demonstrated in the late 1980's. In a future where fuel prices (and possibly even fuel allocations) will influence aircraft design and selection, advanced turboprops are expected to play an important role.

These three projects differ not only in their technology readiness dates but also in the level and type of technology that each is addressing. In going from the ECI project to the E^3 project to the Advanced Turboprop project, the emphasis shifts from the near term to the far term, with progressively larger benefits, but also with more unknown technology, with higher degrees of risk, with more difficulties in integration with the aircraft, and with ultimate applications being clouded as usual

by market and economic uncertainties. The ACEE effort, however, represents a comprehensive approach to resolving these difficulties and unknowns and offers a number of technology options. And, if the ACEE technology advances prove as attractive as expected, this program should have a major impact on future commercial air transportation systems.

REFERENCES

1. Fuel Cost and Consumption, Monthly Reports. Civil Aeronautics Board.

2. Trends in Airline Cost Elements. Second ed., Civil Aeronautics Board, July 1977 plus Supplement, Jan. 3, 1979; and Trends in Airline Unit Costs. Fourth ed., Civil Aeronautics Board, Feb. 1979.

3. Aircraft Fuel Conservation Technology - Task Force Report. NASA-Office of Aeronautics and Space Technology, Sept. 10, 1975.

4. Fasching, W. A.: CF6 Jet Engine Performance Improvement Program: Task I - Feasibility Analysis. (R79AEG295, General Electric Co.; NASA Contract NAS3-20629.) NASA CR-159450, 1979.

5. Gaffin, W. O.; and Webb, D. E.: JT8D and JT9D Jet Engine Performance Improvement Program: Task I - Feasibility Analysis. (PWA-5518-38, Pratt & Whitney Aircraft Group; NASA Contract NAS3-20630.) NASA CR-159449, 1979.

PERFORMANCE IMPROVEMENT CONCEPTS
PRATT & WHITNEY ENGINES

CONCEPTS	% SFC REDUCTION	COMPLETION DATE
P & WA JT8D ENGINE		
HPT OUTER AIR SEAL	0.6	SEP 1978
NEW HPT BLADE	.9	JUL 1980
REVERSER STANG FAIRING	.5	SEP 1980
TRENCHED ABRADABLE HPC	.9	DEC 1980
P & WA JT9D ENGINE		
HPT ACTIVE CLEARANCE CONTROL	.7	NOV 1978
NEW FAN TECHNOLOGY	1.3	JUN 1979
HPT VANE THERMAL COATING	.1	FEB 1981
HPT ABRADABLE OUTER SEAL	.3	OCT 1981

CS-79-1534

Table I-1

PERFORMANCE IMPROVEMENT CONCEPTS
GENERAL ELECTRIC ENGINE

CONCEPTS	% SFC REDUCTION	COMPLETION DATE
GE CF6 ENGINE		
SHORT CORE NOZZLE	0.9	FEB 1979
NEW FRONT MOUNT	.3	MAR 1979
IMPROVED FAN	2.0	MAY 1979
HPT AERO REFINEMENT	1.3	JUL 1979
HPT ROUNDNESS CONTROL	.4	MAY 1980
REDUCED HPC BLEED	.7	SEP 1980
LPT ACTIVE CLEARANCE CONTROL	.3	OCT 1980
HPT ACTIVE CLEARANCE CONTROL	.6	AUG 1981

CS-79-1535

Table I-2

PROPULSION SYSTEM LOADS ANALYSIS RESULTS

STEADY STATE		
LOADS	AREA AFFECTED	% OF TOTAL SFC LOSS
NACELLE AERODYNAMIC	ALL STAGES	87
INERTIA		
"g"	HPT STAGES	8
GYRO	FAN STAGE	5
DYNAMIC		
NO SIGNIFICANT CHANGE FROM STEADY STATE		

CS-79-2089

Table I-3

CYCLE CHARACTERISTICS OF GENERAL ELECTRIC'S ENGINES AT MAX CRUISE CONDITIONS

	EEE	CF6-50C
EXHAUST CONFIGURATION	MIXED	SEPARATE
BYPASS RATIO	6.9	4.3
FAN PRESS. RATIO	1.61	1.72
COMPRESSOR PRESS. RATIO	22.6	12.9
OVERALL PRESS. RATIO	36.1	32.0
TURBINE TEMP, ^{0}F		
HOT-DAY TAKEOFF	2450	2400
MAX CRUISE	2170	2080
TAKEOFF THRUST, SLS-lb	36 500	50 250
INSTALLED SFC, lbm/hr/lbf	0.572	0.666
	$\Delta \approx -14.2\%$	

CS-79-2065

Table I-4

CYCLE CHARACTERISTICS OF
PRATT & WHITNEY'S ENGINES
AT MAX CRUISE CONDITIONS

	EEE	JT9D-7A
EXHAUST CONFIGURATION	MIXED	SEPARATE
BYPASS RATIO	6.6	5.1
FAN PRESS. RATIO	1.71	1.58
COMPRESSOR PRESS. RATIO	13.9	10.0
OVERALL PRESS. RATIO	37.4	25.4
TURBINE TEMP, ^{0}F		
HOT-DAY TAKEOFF	2495	2300
MAX CRUISE	2200	2000
TAKEOFF THRUST, SLS-lb	41 115	46 300
INSTALLED SFC, lbm/hr/lbf	0.576	0.677
	Δ = -14.9%	

CS-79-2067

Table I-5

ADVANCED PROPELLER TECHNOLOGY PROGRAM
PHASE I

DESIGN MATRIX OF EIGHT 2-ft DIAM WIND TUNNEL MODELS

NO. OF BLADES	8 OR 10
SWEEP AT BLADE TIP, deg	0 TO 60
TIP SPEED, ft/sec (RELATIVE TIP MACH NO.)	600 TO 800 (1.0 TO 1.15)
POWER LOADING, hp/ft^2 (RELATIVE DIAM)	26 TO 37.5 (1.2 TO 1.0)

USE DATA TO UPGRADE AERO, ACOUSTIC, & STRUCTURAL ANALYSIS & PREDICTION PROGRAMS

CS-79-2155

Table I-6

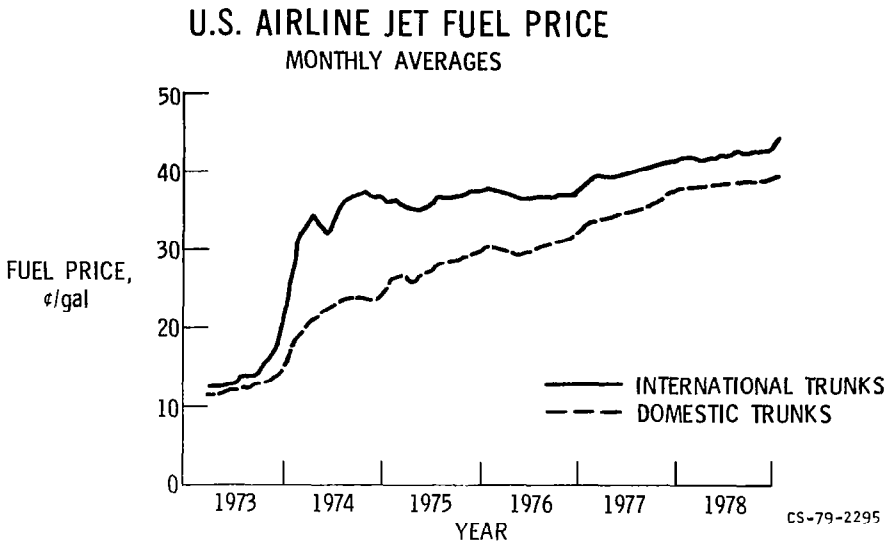

Figure I-1

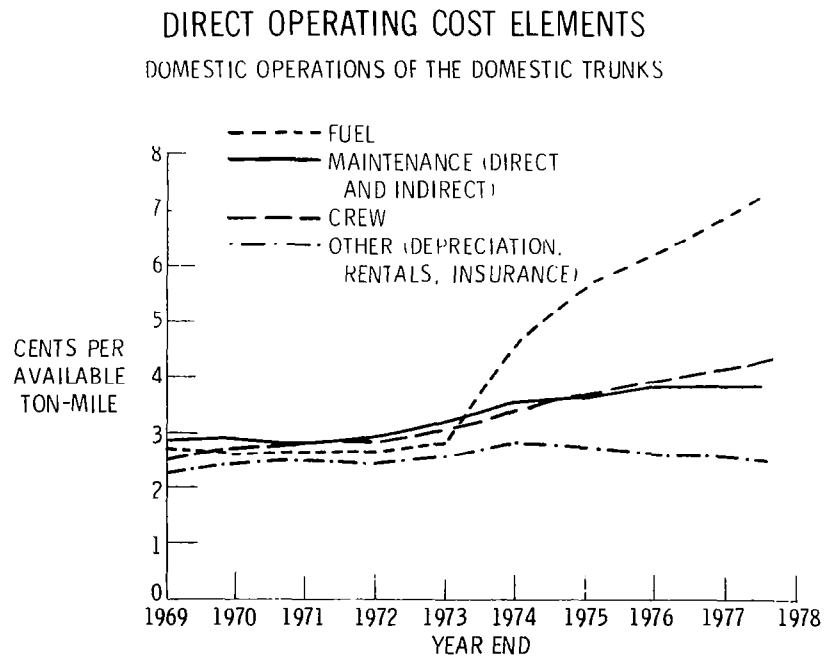

Figure I-2

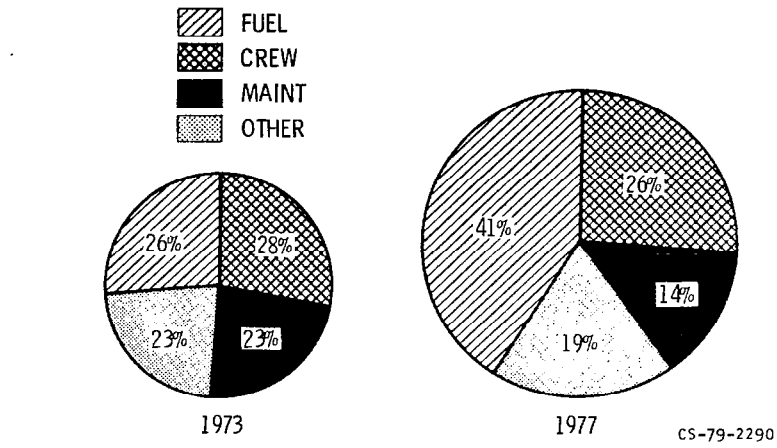

Figure I-3

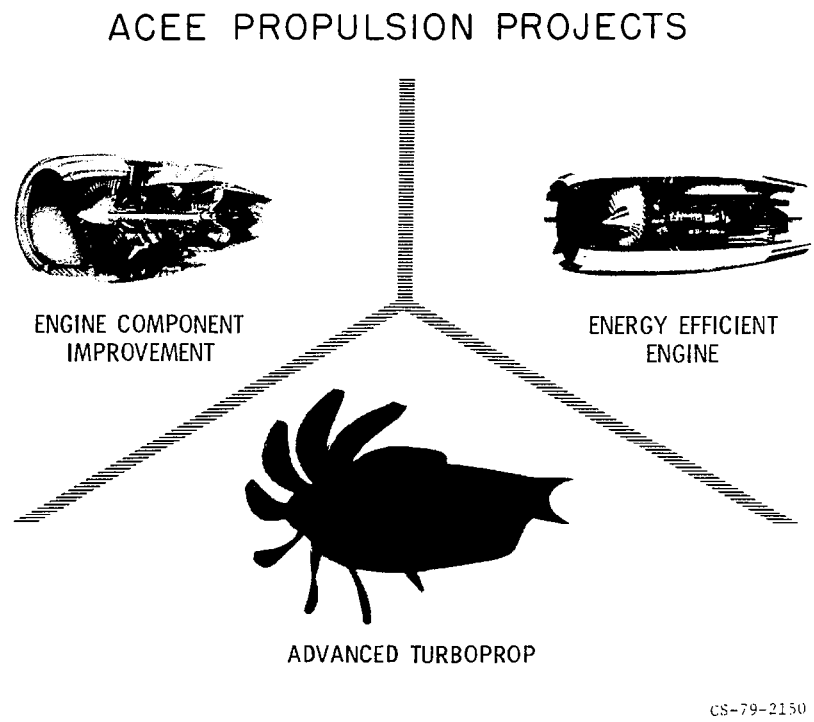

Figure I-4

ENGINE COMPONENT IMPROVEMENT PROJECT

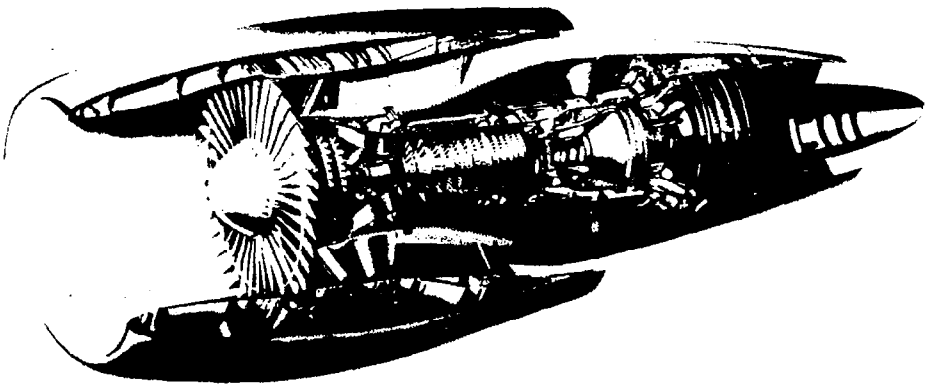

PERFORMANCE IMPROVEMENT

ENGINE DIAGNOSTICS

GOAL OF 5% FUEL SAVINGS

CS-79-2099

Figure I-5

PERFORMANCE IMPROVEMENT

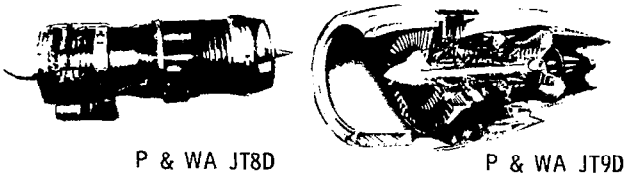

P & WA JT8D

P & WA JT9D

DEVELOP TECHNOLOGY FOR COMPONENTS TO REDUCE FUEL CONSUMPTION IN NEW PRODUCTION OR RETROFIT OF CURRENT ENGINES BY 1980-1982

GE CF6

CS-79-2098

Figure I-6

COMPONENT AREAS

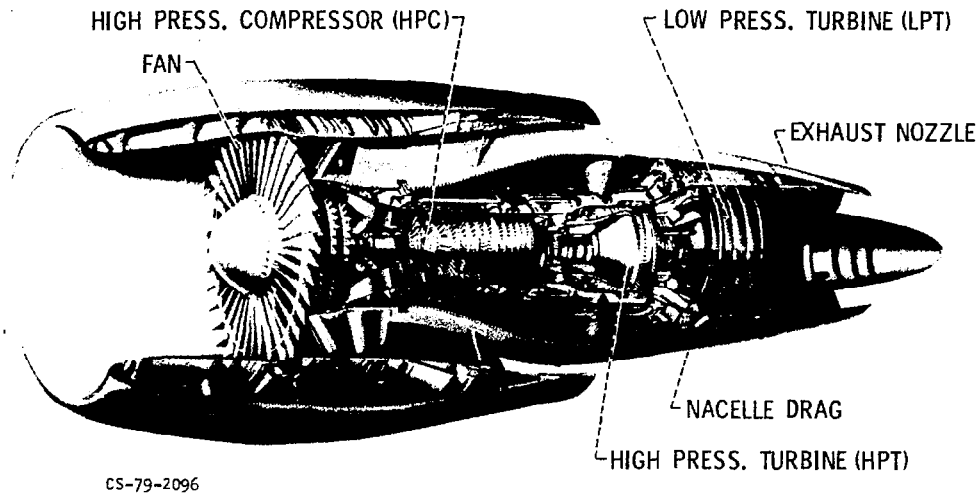

Figure I-7

JT8D HPT OUTER AIR SEAL

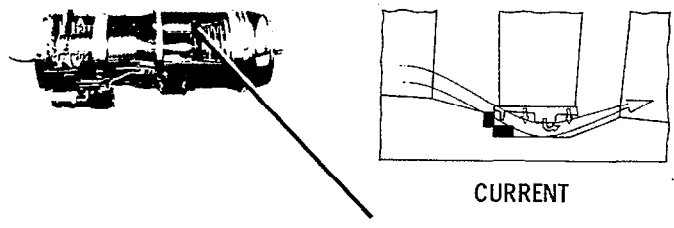

ADDED KNIFE-EDGE SEAL
ADDED HONEYCOMB SEAL
COOLING AIR DISCHARGE RELOCATED
CRUISE SFC REDUCTION, 0.6% DEMONSTRATED

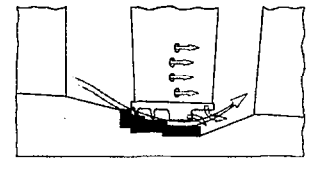

CS-79-2144

Figure I-8

JT8D HPT OUTER AIR SEAL ENGINE TEST

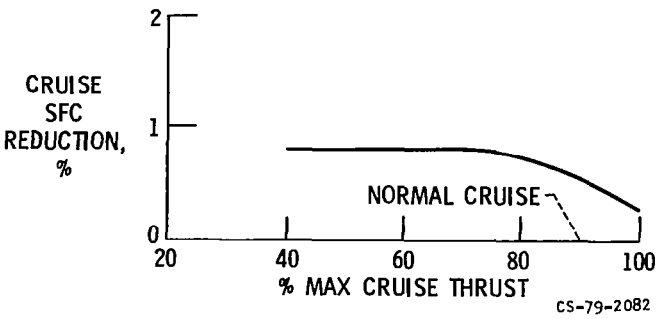

Figure I-9

ACTIVE CLEARANCE CONTROL

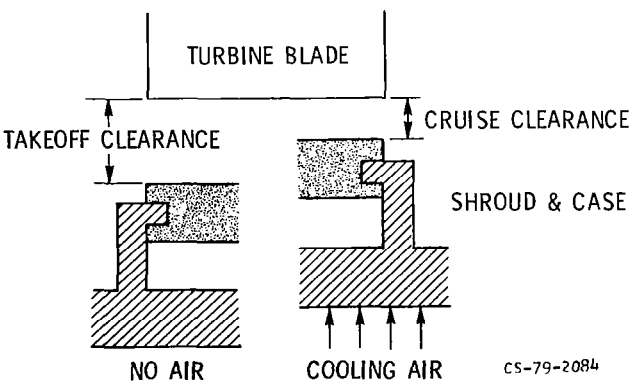

Figure I-10

JT9D HPT ACTIVE CLEARANCE CONTROL

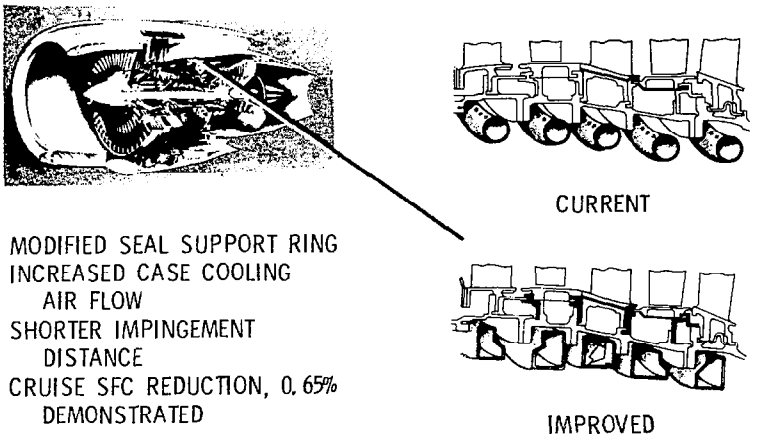

MODIFIED SEAL SUPPORT RING
INCREASED CASE COOLING AIR FLOW
SHORTER IMPINGEMENT DISTANCE
CRUISE SFC REDUCTION, 0.65% DEMONSTRATED

CS-79-2143

Figure I-11

JT9D HPT ACTIVE CLEARANCE CONTROL TEST DATA

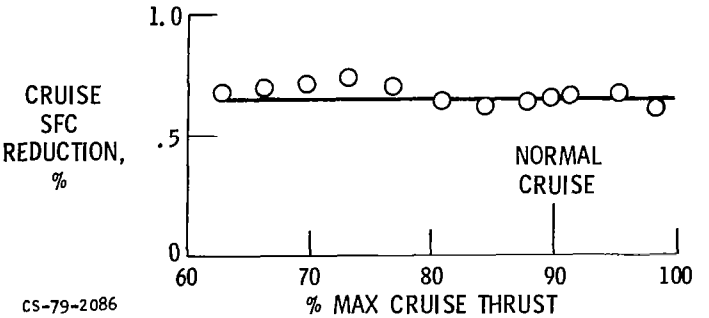

CS-79-2086

Figure I-12

CF6 FAN

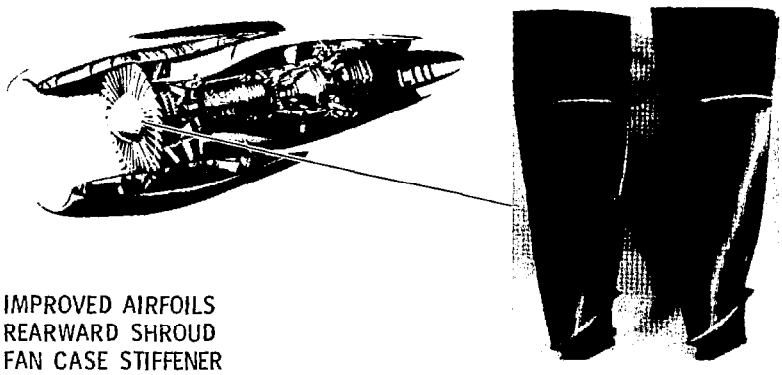

IMPROVED AIRFOILS
REARWARD SHROUD
FAN CASE STIFFENER
CRUISE SFC REDUCTION, 2% DEMONSTRATED

CURRENT IMPROVED

CS-79-2097

Figure I-13

CF6 ENGINE TEST COMPARISON

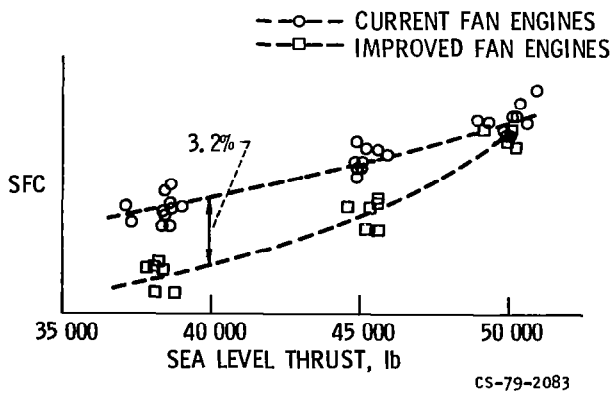

Figure I-14

CONTRIBUTORS TO ENGINE PERFORMANCE DETERIORATION

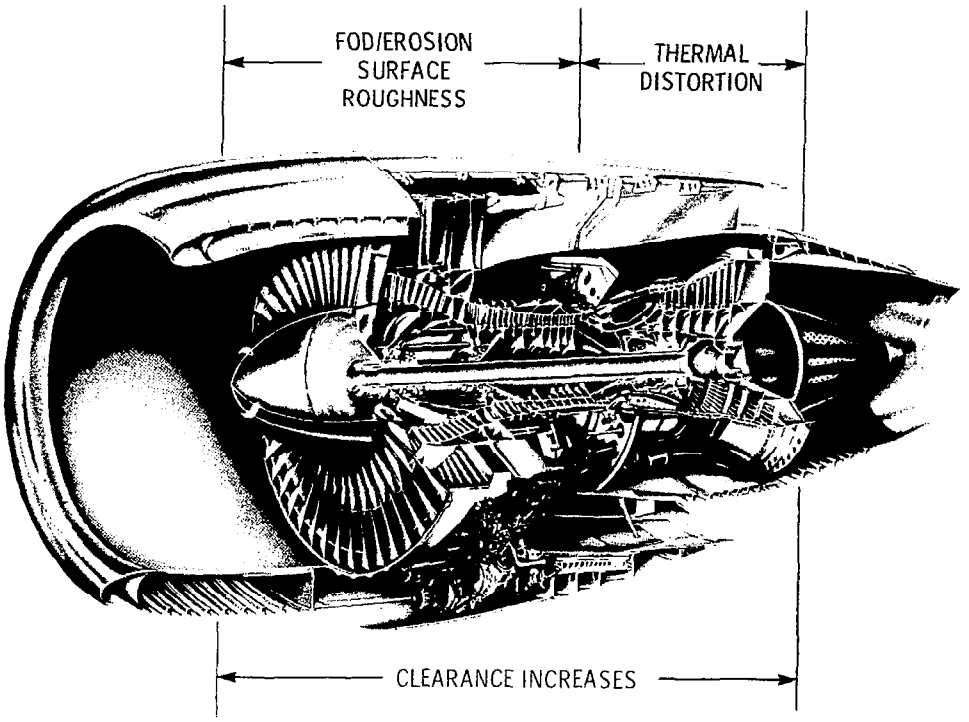

Figure I-15

EXAMPLES OF ENGINE PERFORMANCE DETERIORATION

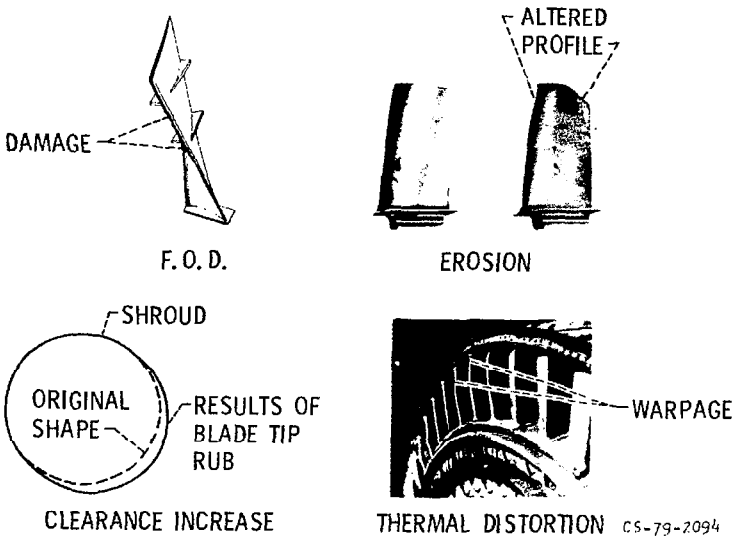

Figure I-16

CF6 MODULE REPLACEMENT/REFURBISHMENT TEST RESULTS

CRUISE CONDITIONS

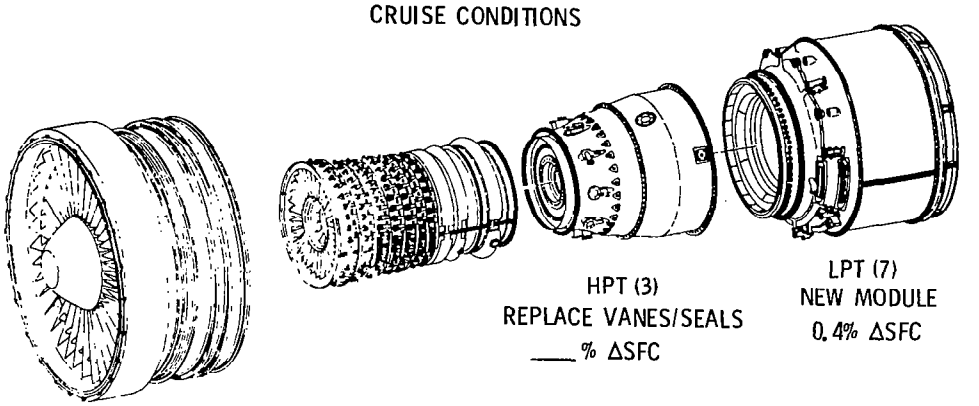

FAN (2)
CLEAN BLADES/RECONTOUR
LEADING EDGE
0.3% ΔSFC

HPT (3)
REPLACE VANES/SEALS
___% ΔSFC

LPT (7)
NEW MODULE
0.4% ΔSFC

CS-79-2093

Figure I-17

JT9D MODULAR PERFORMANCE DETERIORATION RESULTS

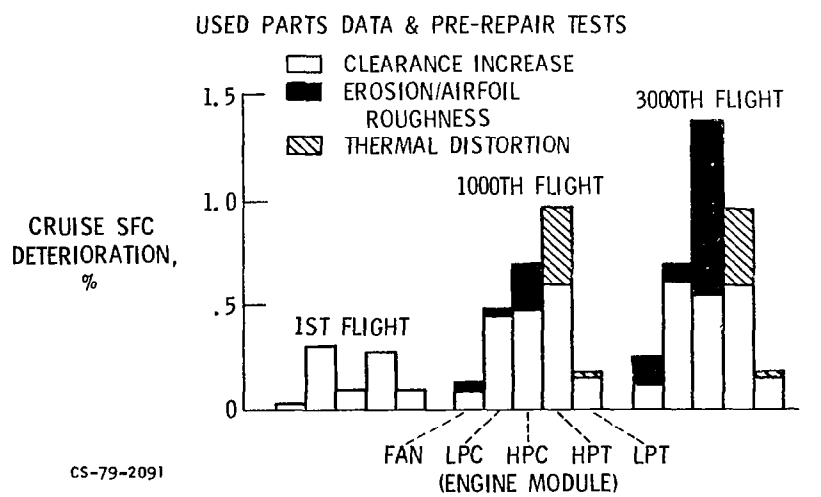

Figure I-18

JT9D PERFORMANCE DETERIORATION BY DAMAGE MECHANISM

CRUISE CONDITIONS

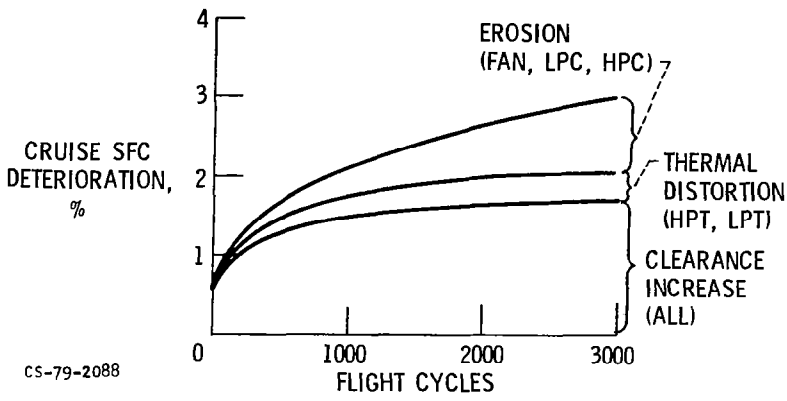

Figure I-19

JT9D EXTERNAL APPLIED LOADS AND REACTIONS

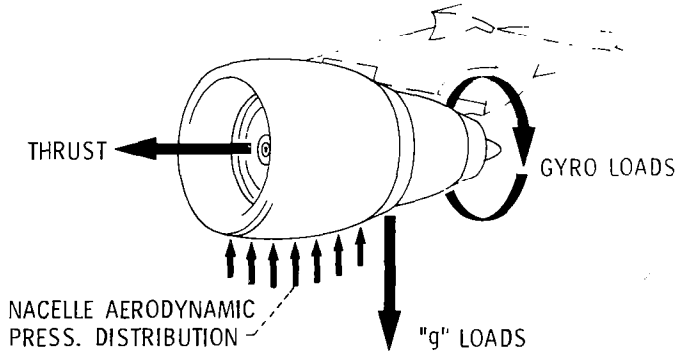

- NACELLE AERODYNAMIC LOADS
- INERTIA LOADS

CS-79-2145

Figure I-20

JT9D/747 PROPULSION SYSTEM STRUCTURAL MODEL

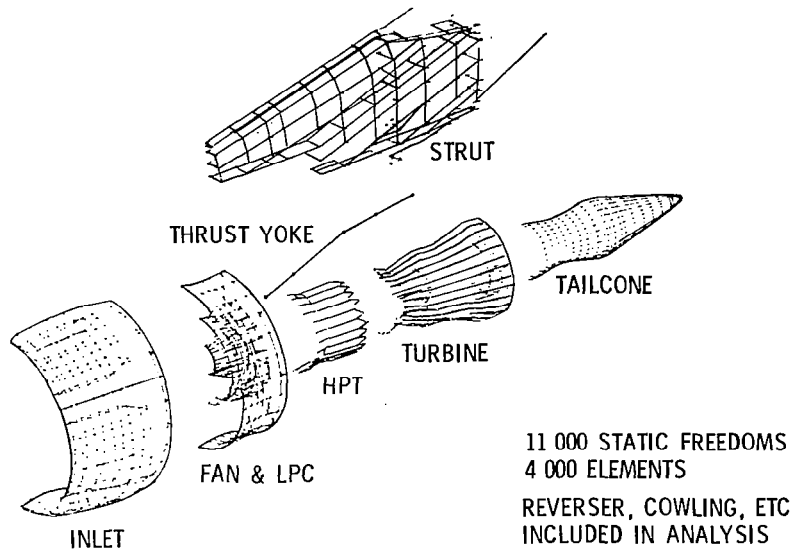

Figure I-21

JT9D ENGINE IN PRATT & WHITNEY X-RAY ENGINE TEST FACILITY

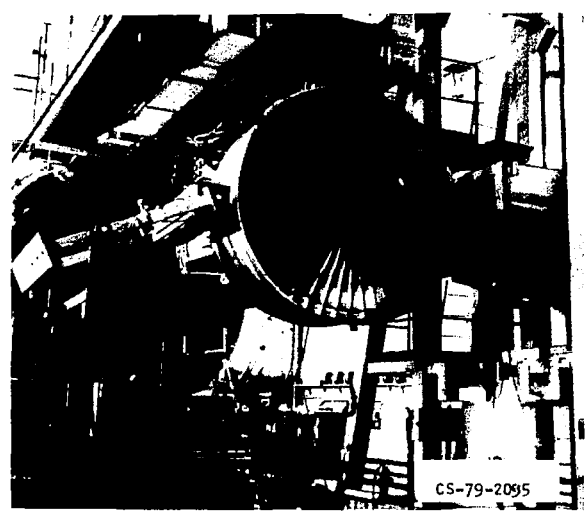

Figure I-22

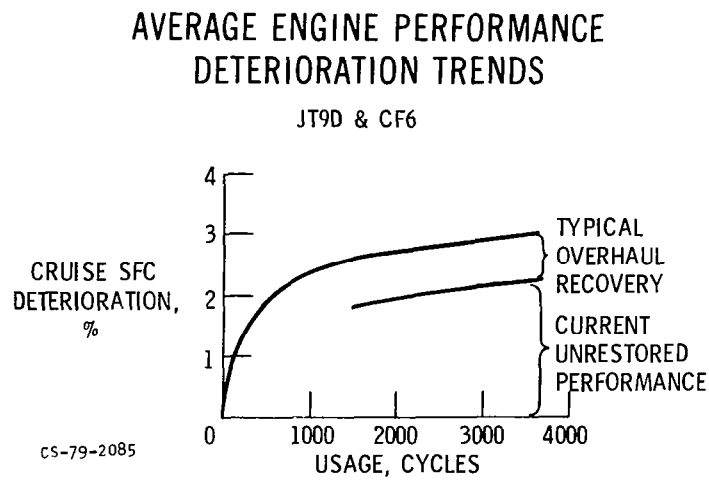

Figure I-23

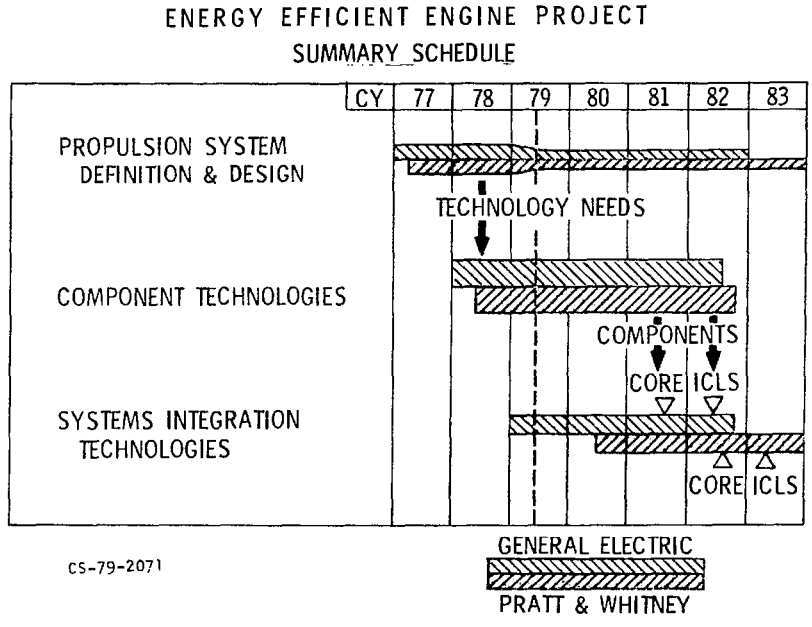

Figure I-24

ENERGY EFFICIENT ENGINE CONFIGURATION

GENERAL ELECTRIC

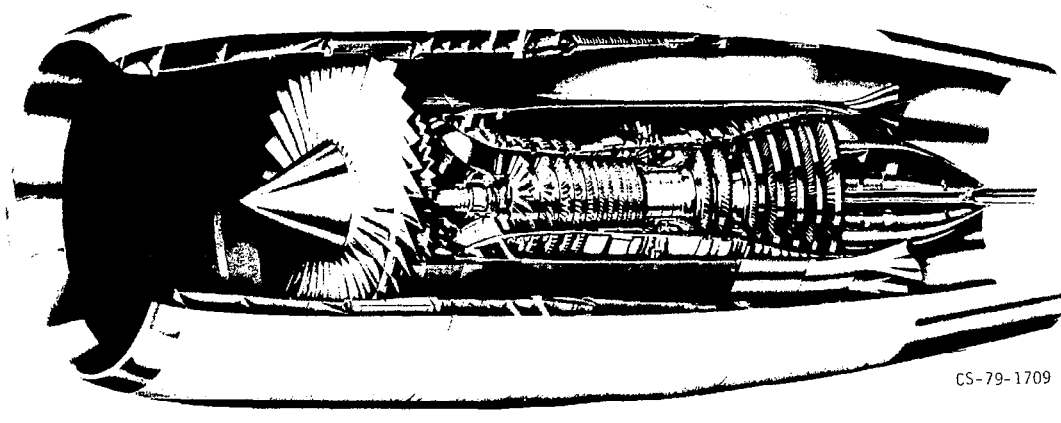

Figure I-25

ENERGY EFFICIENT ENGINE – GENERAL ELECTRIC CONFIGURATION

CORE COMPONENT TECHNOLOGIES

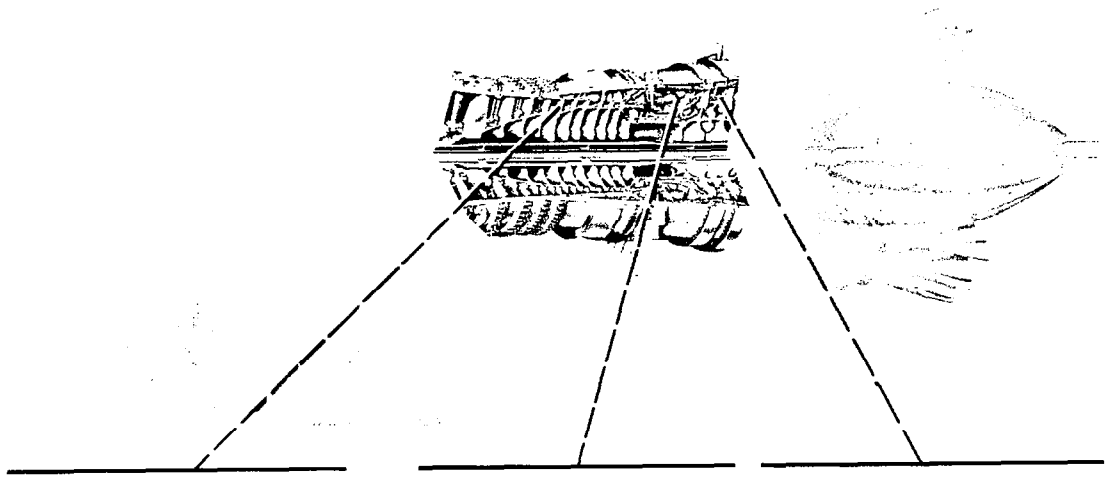

TEN-STAGE H. P. COMPRESSOR
- 23:1 PRESS. RATIO
- HIGH AIRFOIL LOADINGS
- ACTIVE CLEARANCE CONTROL
- ADVANCED MATERIALS

TWO-ZONE COMBUSTOR
- LOW EMISSIONS
- ADVANCED DIFFUSER
- SEGMENTED LINER
- DIGITAL-CONTROL STAGING

TWO-STAGE H. P. TURBINE
- VERY HIGH EFFICIENCY
- LOW LEAKAGE
- IMPROVED COOLING
- ADVANCED MATERIALS
- ACTIVE CLEARANCE CONTROL

CS-79-2187

Figure I-26

ENERGY EFFICIENT ENGINE – GENERAL ELECTRIC CONFIGURATION

LOW-SPOOL COMPONENT TECHNOLOGIES

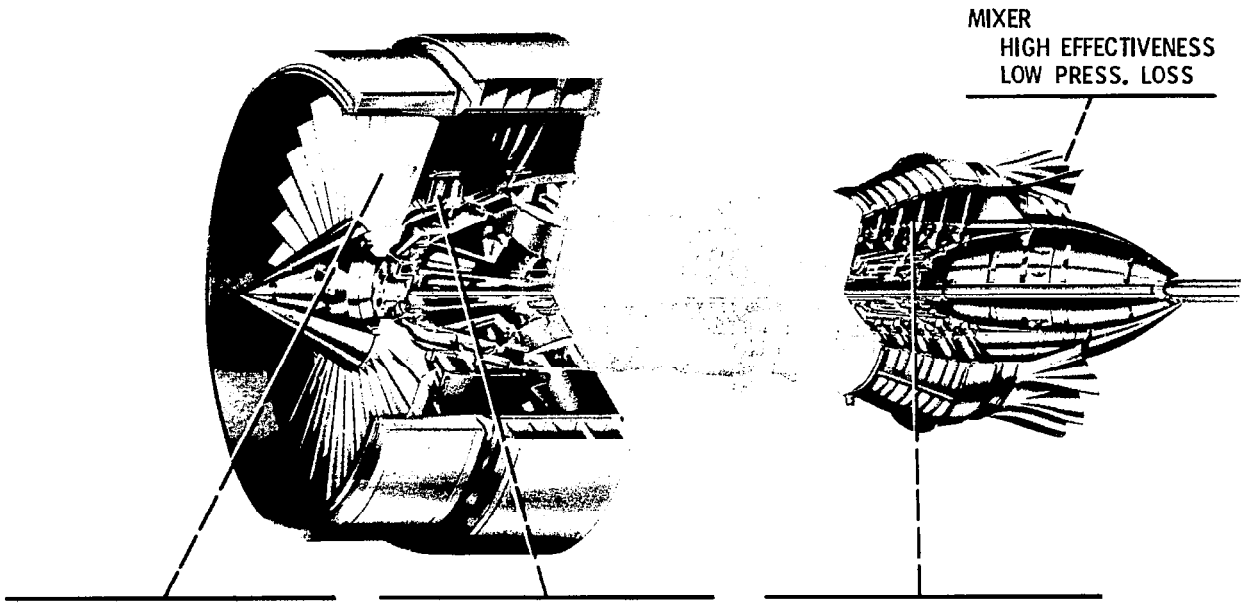

Figure I-27

ENERGY EFFICIENT ENGINE CONFIGURATION

PRATT & WHITNEY

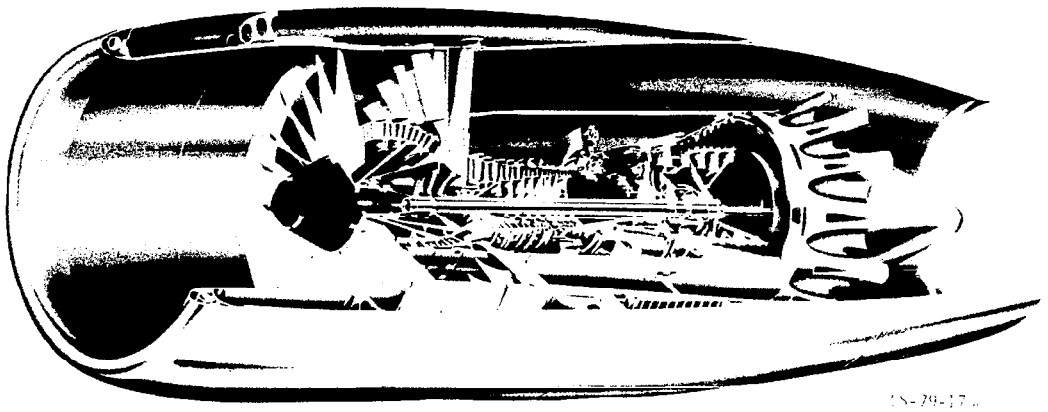

Figure I-28

ENERGY EFFICIENT ENGINE – PRATT & WHITNEY CONFIGURATION

CORE COMPONENT TECHNOLOGIES

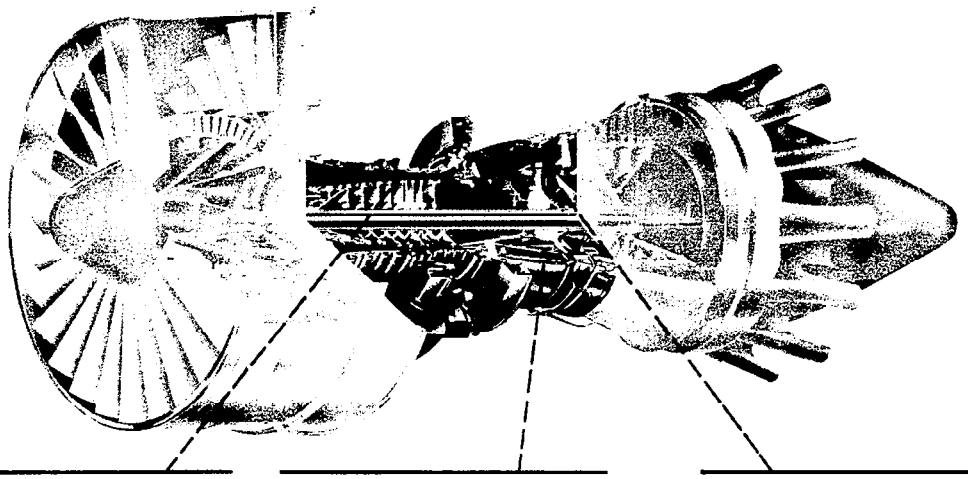

TEN-STAGE H. P. COMPRESSOR
- SUPERCRITICAL AIRFOILS
- TRENCHED CASES
- ACTIVE CLEARANCE CONTROL
- ADVANCED MATERIALS

TWO-ZONE COMBUSTOR
- LOW EMISSIONS
- CARBURETOR FUEL NOZZLES
- ADVANCED LINER
- DIGITAL-CONTROL STAGING

SINGLE-STAGE H. P. TURBINE
- HIGH EFFICIENCY
- TRANSONIC FLOW
- IMPROVED COOLING
- ADVANCED MATERIALS
- ACTIVE CLEARANCE CONTROL

CS-79-2189

Figure I-29

ENERGY EFFICIENT ENGINE – PRATT & WHITNEY CONFIGURATION

LOW-SPOOL COMPONENT TECHNOLOGIES

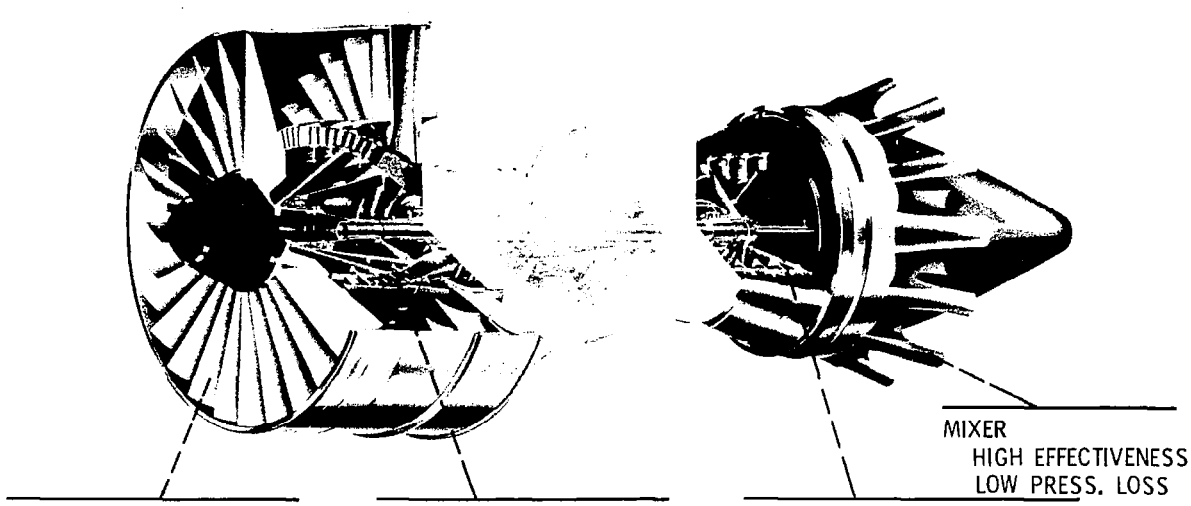

Figure I-30

ENERGY EFFICIENT ENGINE – GENERAL ELECTRIC

FAN-FRAME ACOUSTIC CONFIGURATIONS

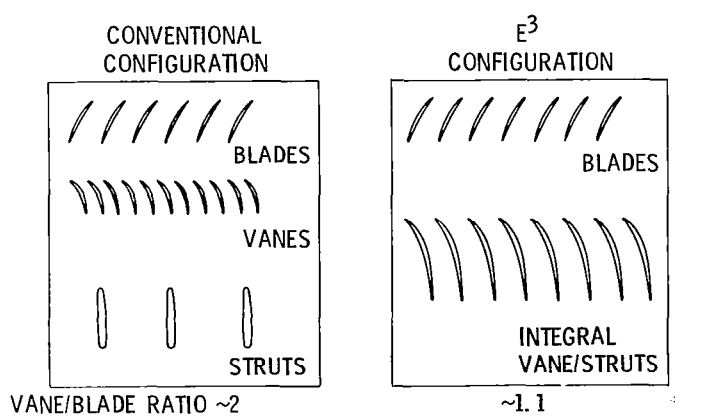

Figure I-31

ENERGY EFFICIENT ENGINE – GENERAL ELECTRIC

FAN-FRAME ACOUSTIC TEST RESULTS

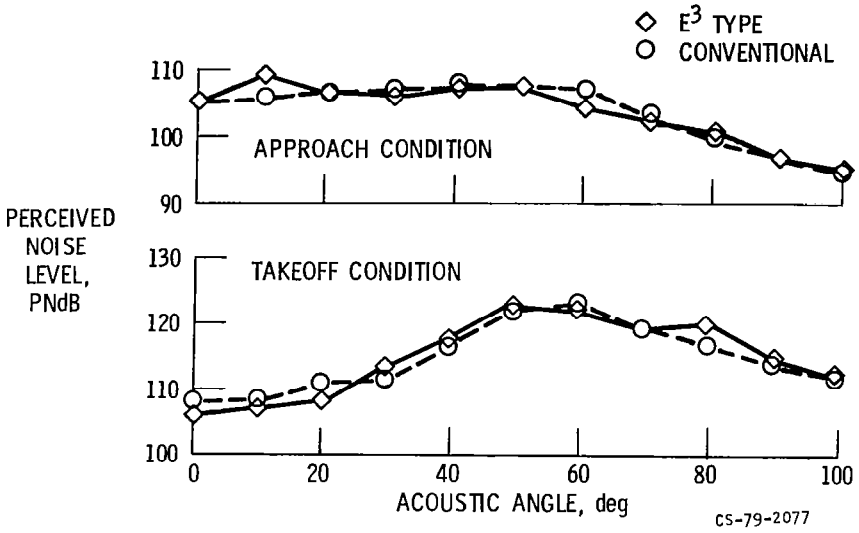

Figure I-32

ENERGY EFFICIENT ENGINE – GENERAL ELECTRIC

COMBUSTOR CONFIGURATIONS

DOUBLE-ANNULAR COMBUSTOR

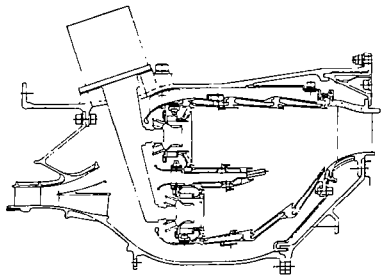

- LOWER EMISSIONS
- MORE COMPLEX

SINGLE-ANNULAR COMBUSTOR

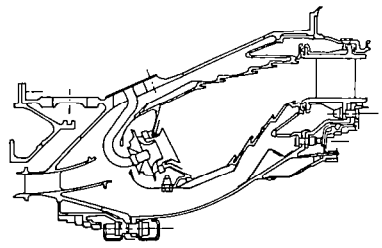

- LOWER COST
- LESS WEIGHT

CS-79-2070

Figure I-33

ENERGY EFFICIENT ENGINE – GENERAL ELECTRIC

COMBUSTOR EMISSION CHARACTERISTICS; 4% IDLE THRUST

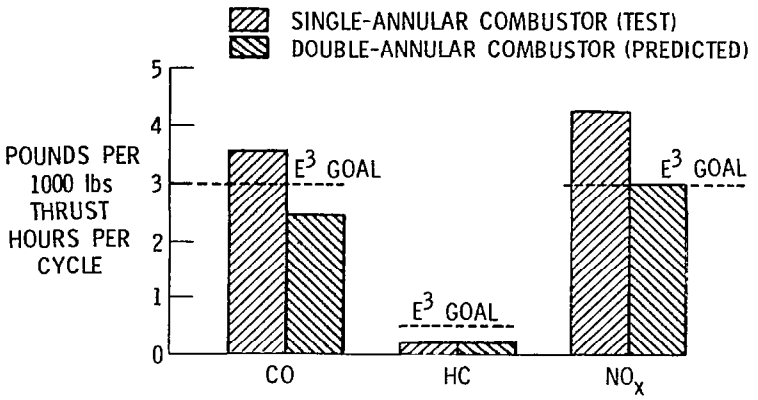

Figure I-34

CS-79-2073

ENERGY EFFICIENT ENGINE – PRATT & WHITNEY

H.P. TURBINE UNCOOLED RIG HARDWARE

35% REACTION BLADE

43% REACTION BLADE

Figure I-35

ENERGY EFFICIENT ENGINE – PRATT & WHITNEY

H. P. TURBINE UNCOOLED-RIG TEST RESULTS

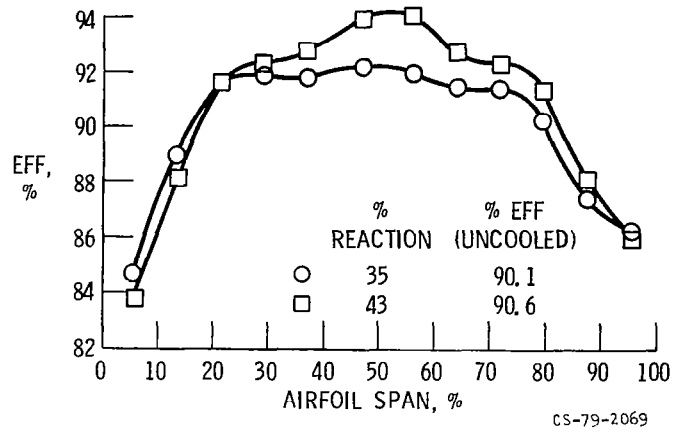

Figure I-36

POTENTIAL FUEL SAVINGS OF ENERGY EFFICIENT ENGINES

RELATIVE TO THE SAME AIRCRAFT WITH SCALED JT9D-7A OR CF6-50C

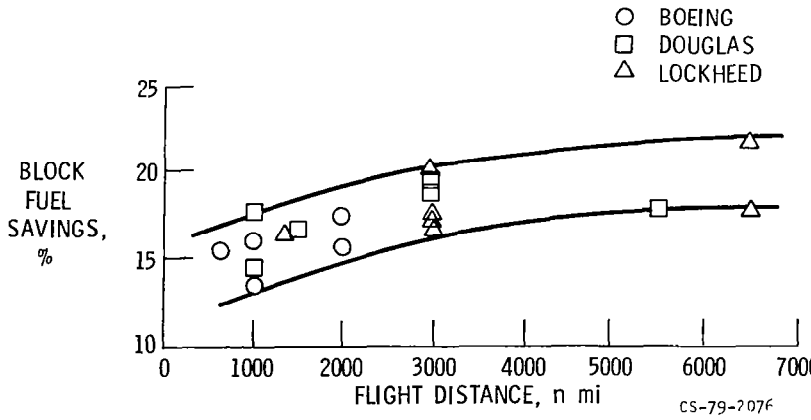

Figure I-37

POTENTIAL DOC IMPROVEMENTS OF ENERGY EFFICIENT ENGINES

RELATIVE TO THE SAME AIRCRAFT WITH SCALED JT9D-7A OR CF6-50C

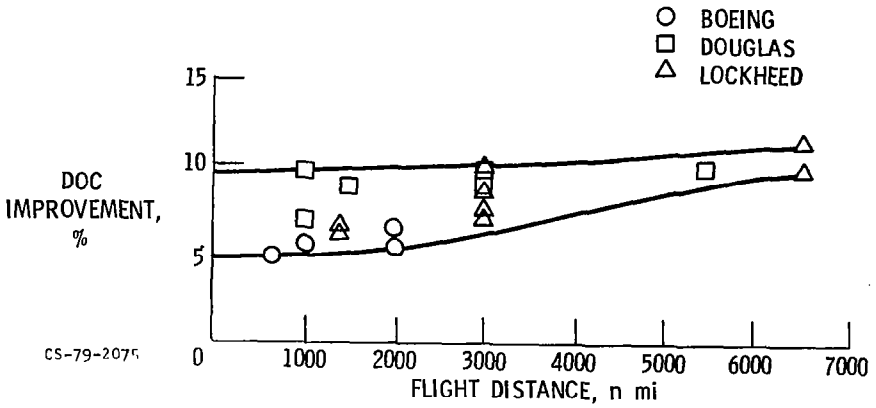

Figure I-38

LOCKHEED ELECTRA AIRCRAFT

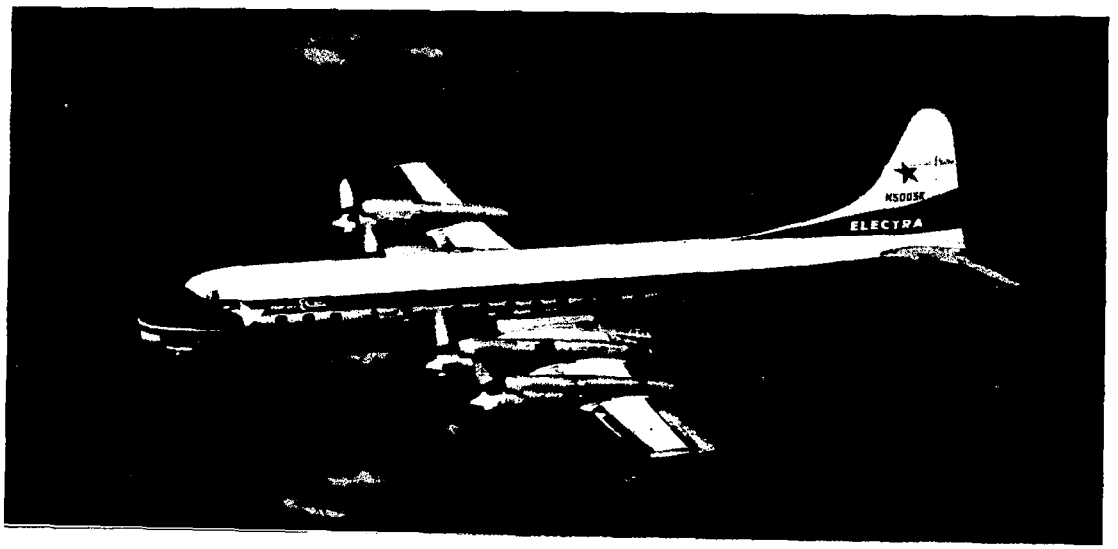

Figure I-39

BOEING 707 AIRCRAFT

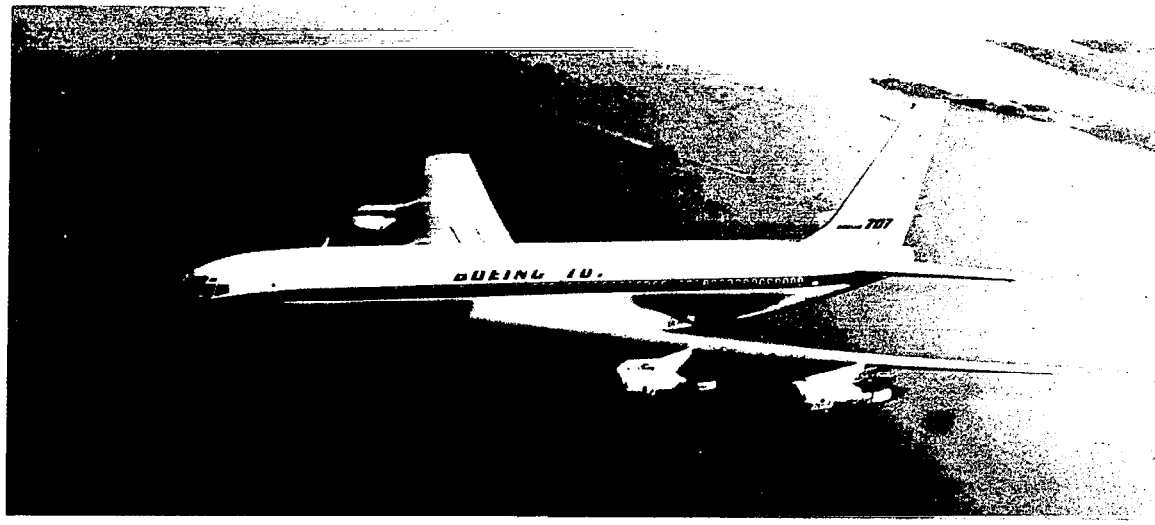

Figure I-40

PROPULSION SYSTEM RELATIVE FUEL CONSUMPTION

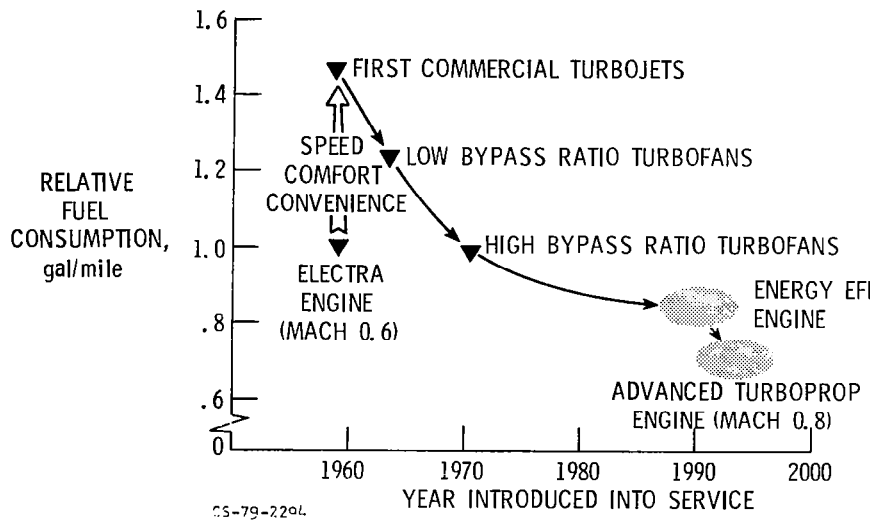

Figure I-41

SIZE/CONFIGURATION COMPARISON

Figure I-42

ADVANCED TURBOPROP PROPULSION SYSTEM

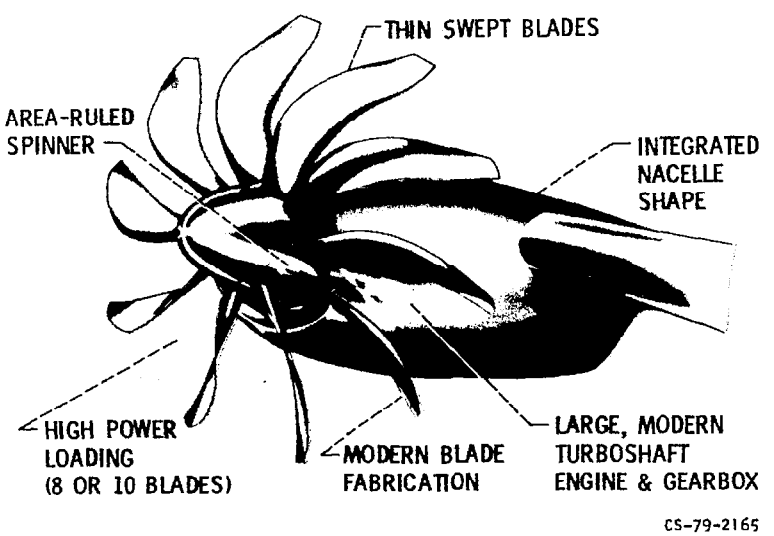

Figure I-43

INSTALLED PROPULSIVE EFFICIENCY AT CRUISE

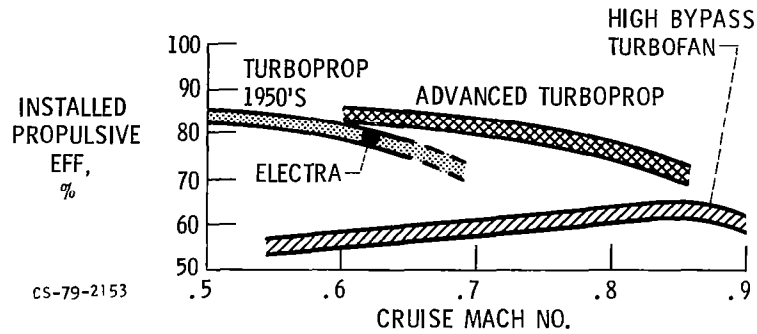

Figure I-44

ADVANCED TURBOPROP PASSENGER AIRCRAFT

Figure I-45

TREND OF POTENTIAL FUEL SAVINGS FOR ADVANCED TURBOPROP-POWERED AIRCRAFT

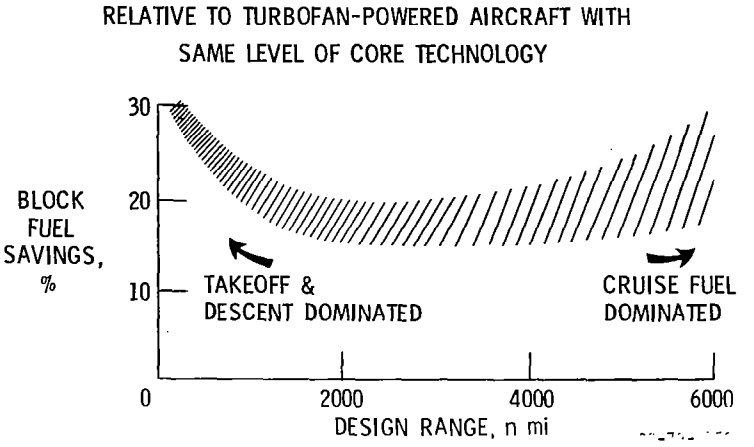

Figure I-46

ADVANCED TURBOPROP PROJECT

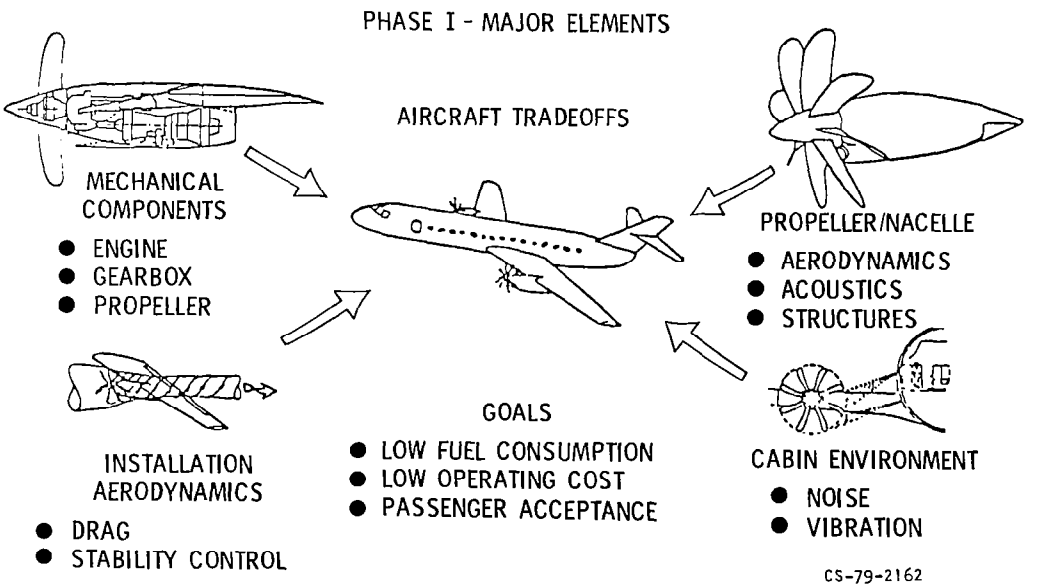

Figure I-47

MODEL PROPELLER BLADES

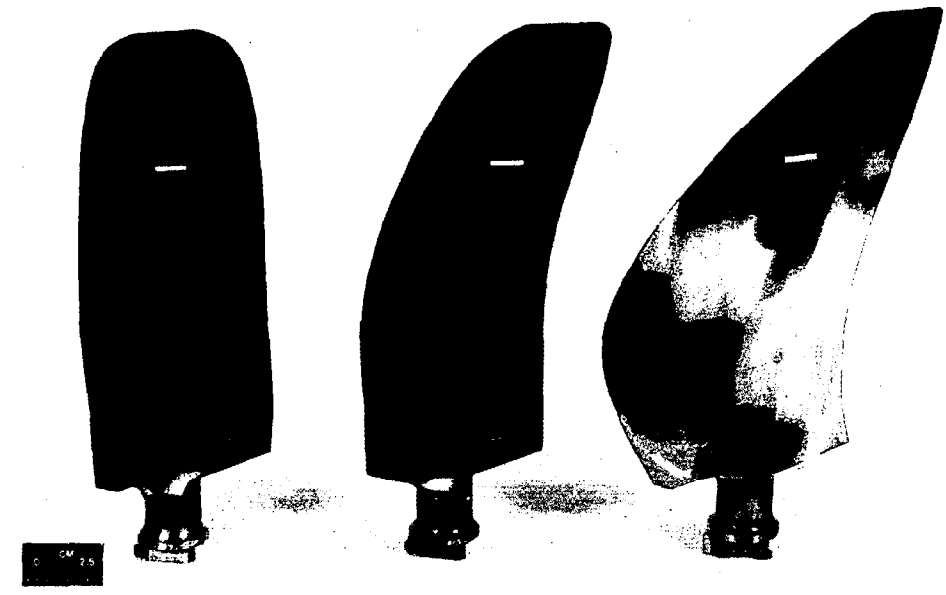

SWEEP 0^0 30^0 45^0

Figure I-48

PROPELLER MODEL TEST IN LEWIS WIND TUNNEL

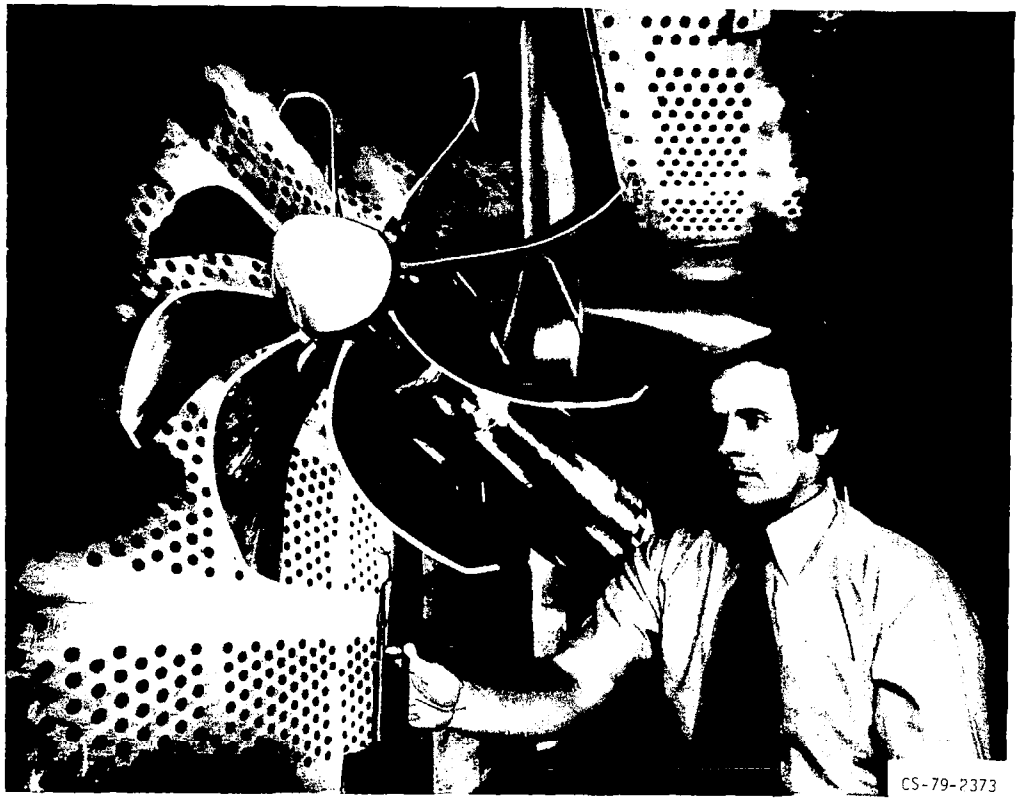

Figure I-49

PROPELLER MODEL EFFICIENCY

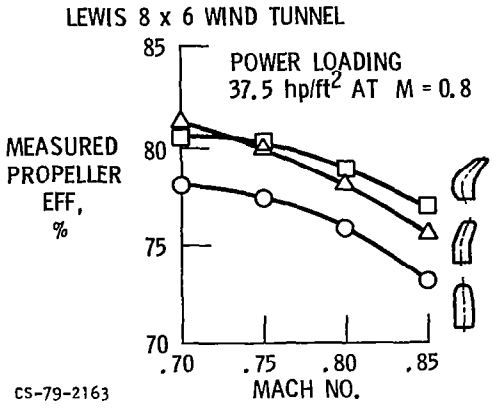

Figure I-50

PROPELLER PERFORMANCE AT MACH 0.8

MODEL WITH 45° TIP SWEEP; LEWIS 8 x 6 WIND TUNNEL

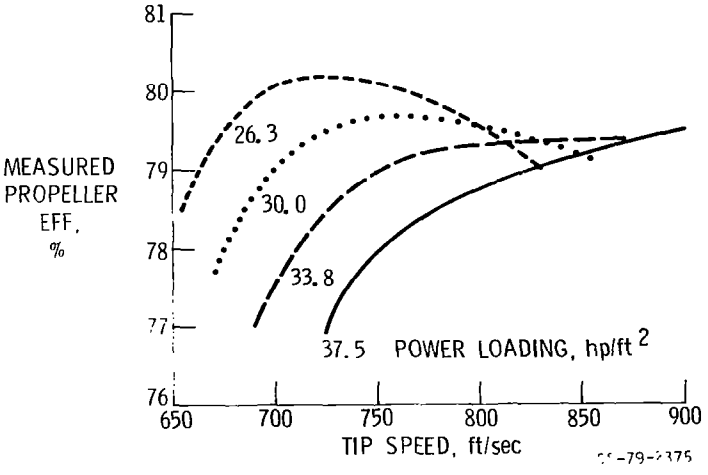

Figure I-51

NOISE COMPARISON OF ADVANCED PROPELLER MODELS

$M_0 = 0.8$ DESIGN CONDITIONS; LEWIS 8 x 6 WIND TUNNEL

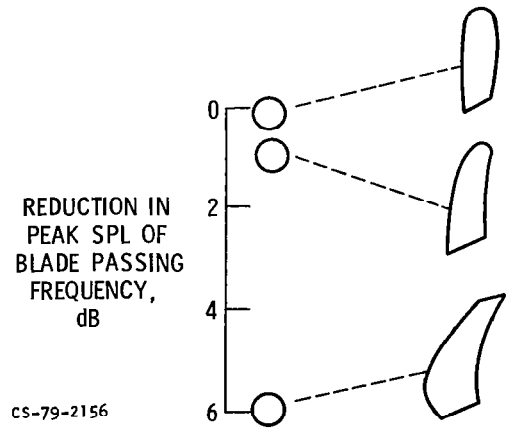

Figure I-52

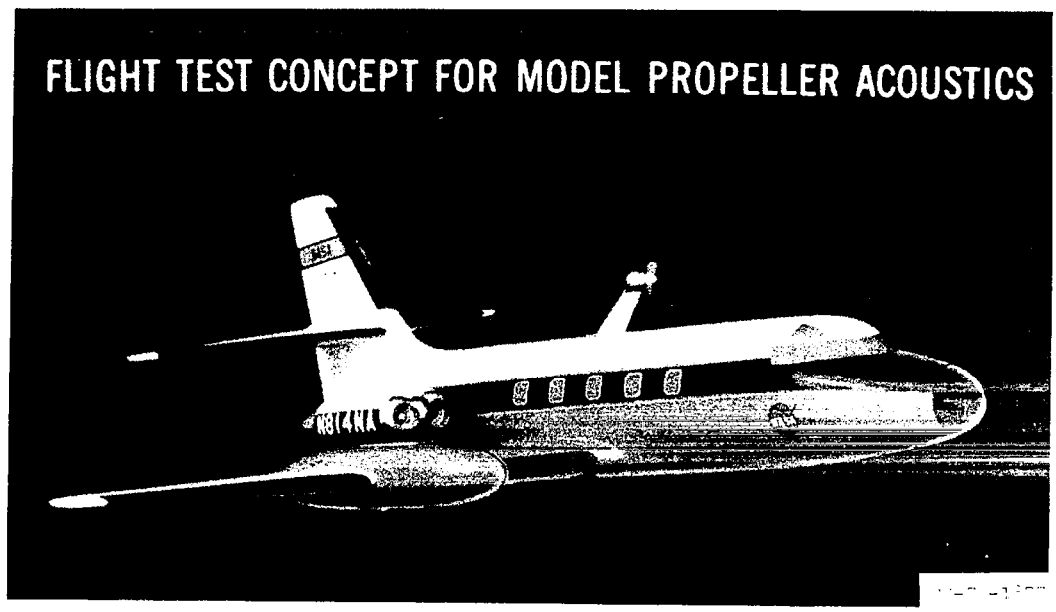

Figure I-53

BLADE FABRICATION COMPARISON

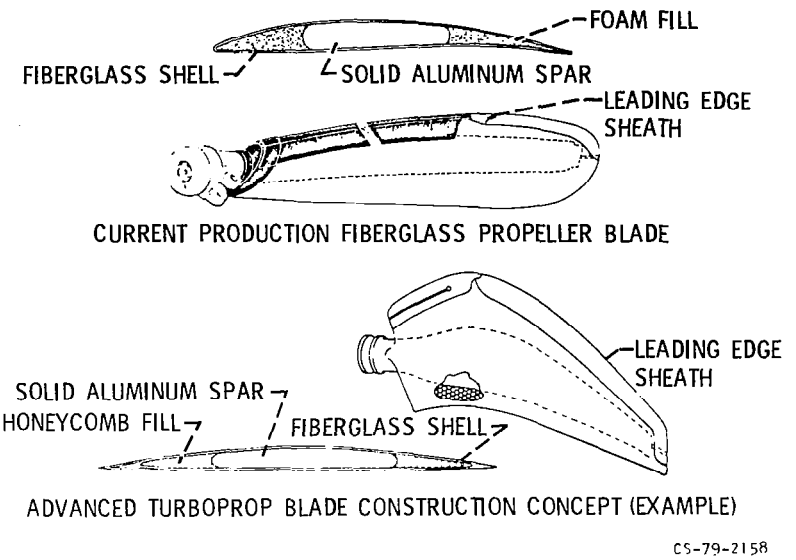

Figure I-54

CABIN NOISE

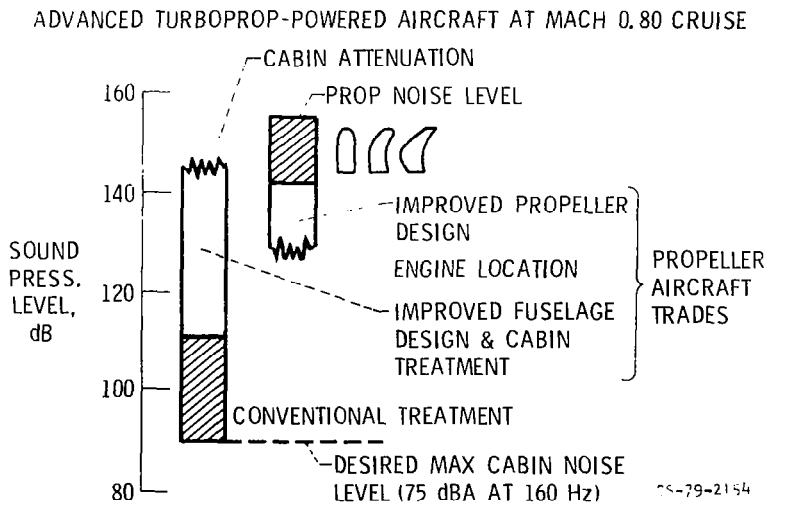

Figure I-55

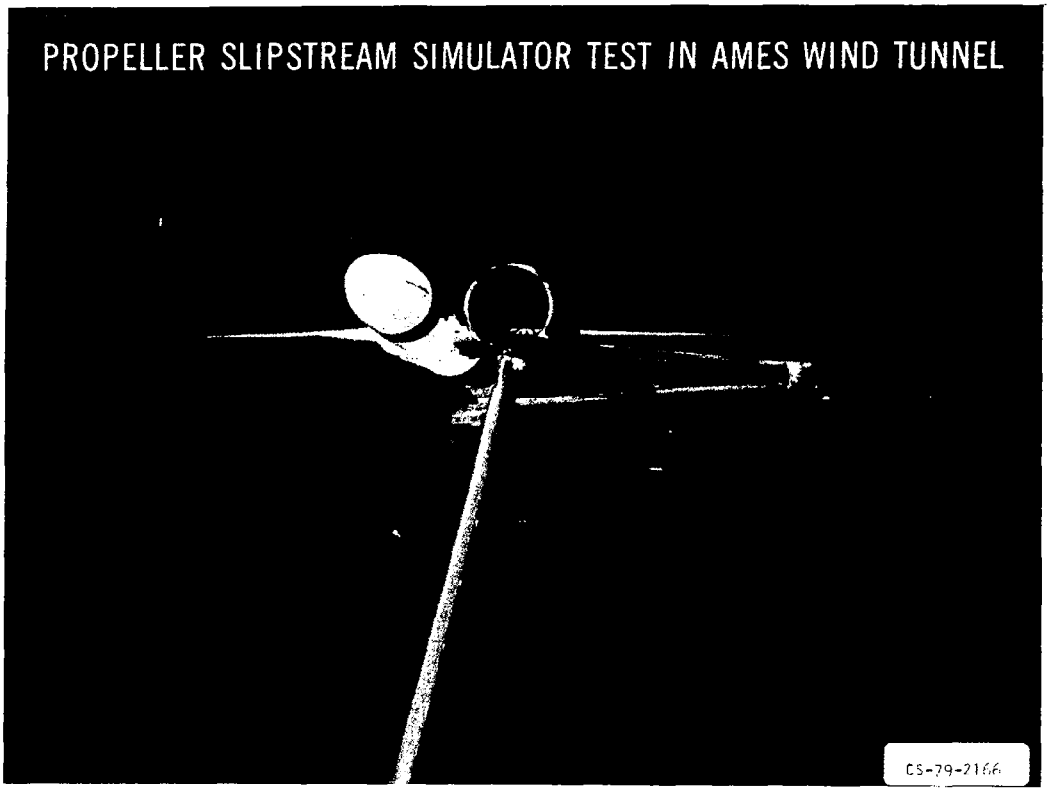

Figure I-56

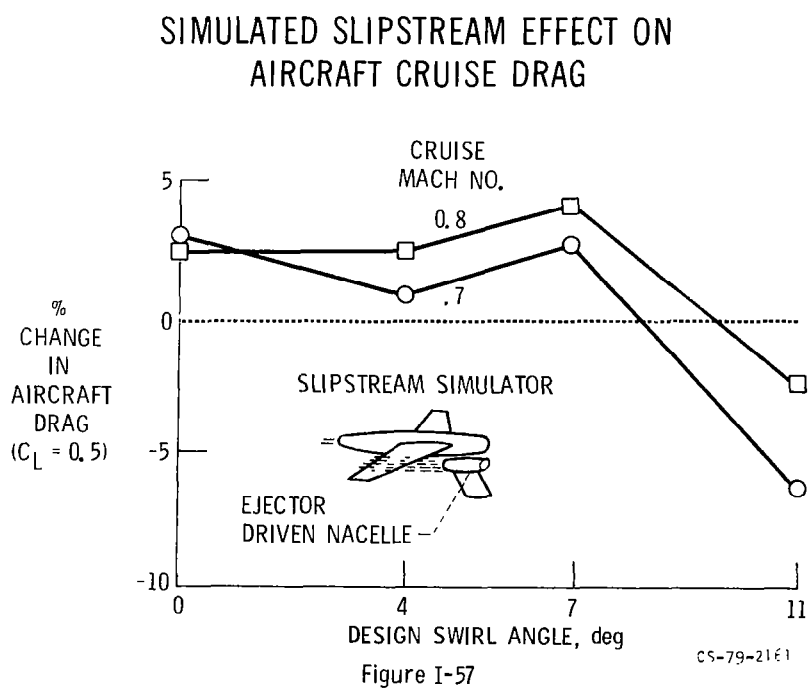

Figure I-57

POWERED-PROPELLER SEMI-SPAN AIRCRAFT MODEL

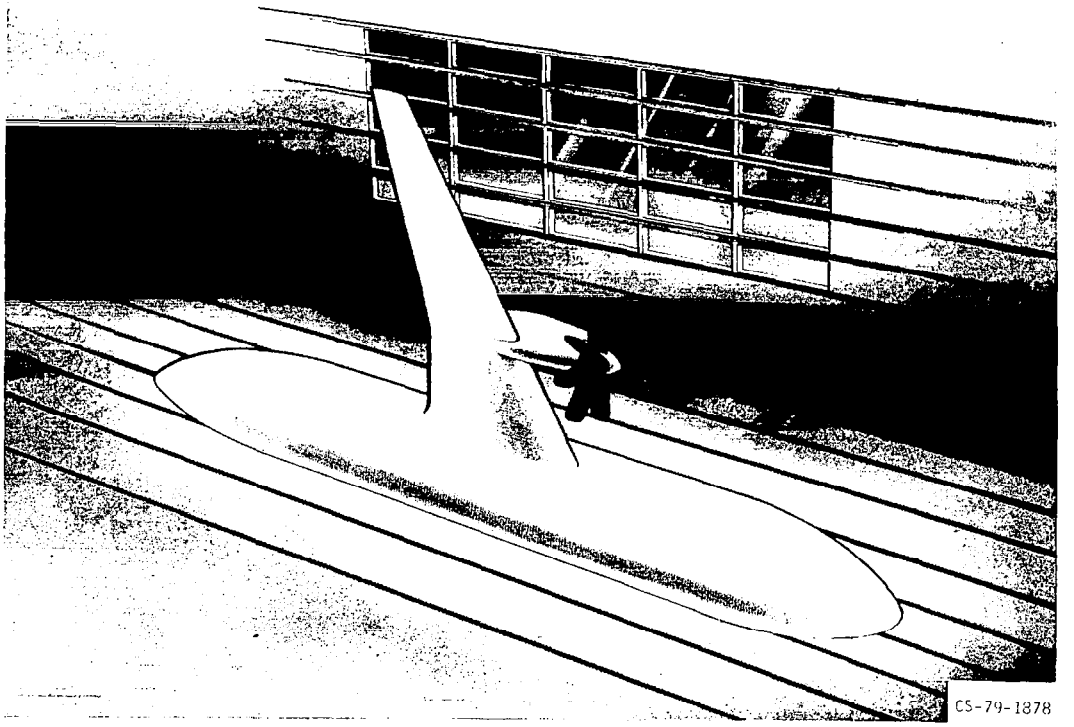

Figure I-58

ADVANCED TURBOPROP

PHASE I - ENABLING TECHNOLOGY

SUBSCALE COMPONENTS

- PROPELLER DESIGN PARAMETERS
- FUSELAGE NOISE ATTENUATION
- AIRFRAME INTERACTIONS

FUTURE PHASES

LARGE-SCALE COMPONENTS - DEVELOPMENT & VERIFICATION

- PROPELLER FABRICATION
- PROPELLER AERO/ACOUSTIC/STRUCTURAL SCALING VERIFICATION
- FUSELAGE SEGMENTS/CABIN ENVIRONMENT
- ADVANCED GEARBOX & PITCH CHANGE SYSTEM
- AIRFRAME INTERACTIONS
- INSTALLED PERFORMANCE
- OPERATIONAL EFFECTS
- ADVANCED ENGINE/GEARBOX/PITCH CHANGE SYSTEM PERFORMANCE

Figure I-59

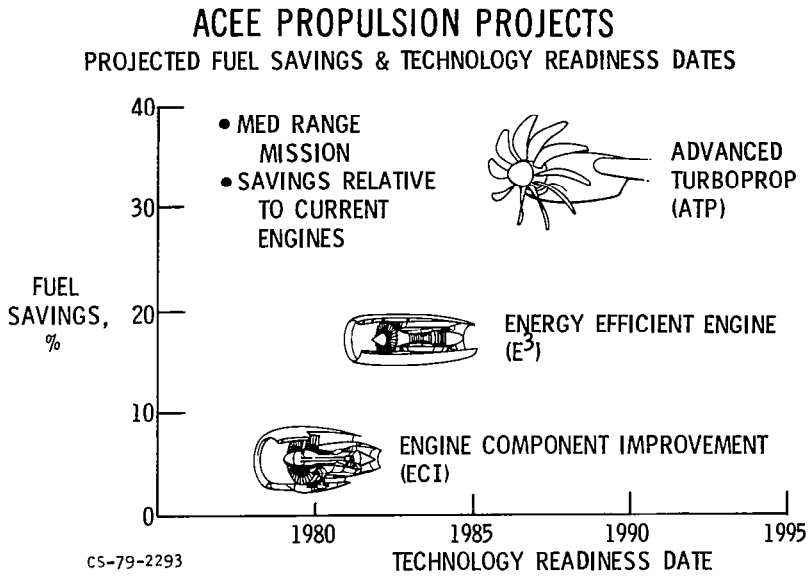

Figure I-60

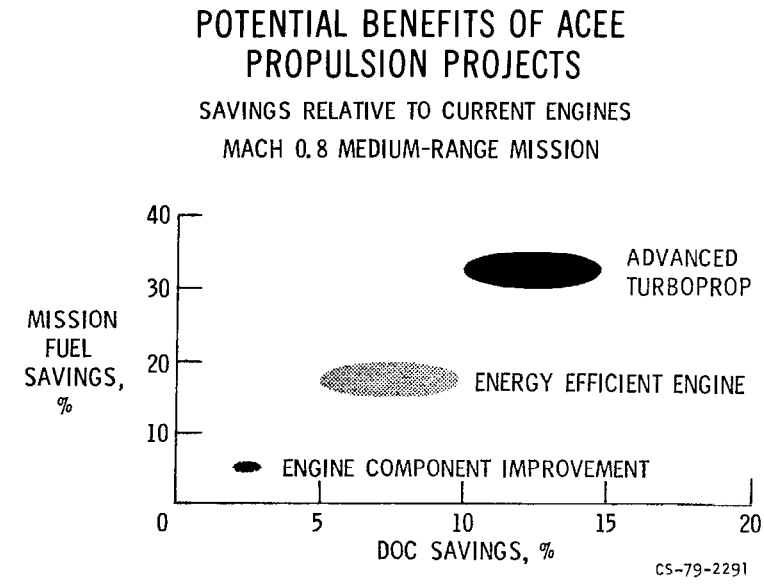

Figure I-61

II. EMISSION REDUCTION

Donald A. Petrash, Larry A. Diehl, Robert E. Jones,
and Edward J. Mularz

National Aeronautics and Space Administration
Lewis Research Center

The quality of life in the United States and in particular the quality of the air we breathe came into focus as a national issue in the 1960's. The Congress in 1970 amended the Clean Air Act to include the control of undesirable gaseous pollutant emissions from aircraft engines. NASA responded by initiating an emissions reduction research and technology program in 1971. This program, the results obtained to date, and its future direction form the basis of this paper. In 1973 the Environmental Protection Agency issued aircraft engine gaseous pollutant emission standards, which were to be implemented by 1979. Since that time the EPA has continuously examined the effect of aircraft engine emissions on air quality and has closely followed the advancing technology for the control of these pollutants. Just last year, the EPA issued a Notice of Proposed Rule Making that would amend the standards. Final action by the EPA has not yet been taken with respect to the proposed amended standards.

The Gaseous Pollutant emission standards in effect today for newly manufactured engines are shown in table II-1. The three gaseous emissions that are controlled are carbon monoxide, unburned hydrocarbons, and oxides of nitrogen. Six engine classes for gas-turbine-powered aircraft have been established. The T1 class applies to turbofan engines of less than 8000 pounds thrust. Into this class fall most engines used in general-aviation aircraft. The T2 class applies to engines having thrust levels greater than 8000 pounds and for the most part applies to engines used in commercial aviation. The T3 and T4 classes are specific to the Pratt & Whitney JT3D and the JT8D engines. The T5 class applies to those engines used to power supersonic commercial aircraft, and the P2 class applies to turboprop engines.

In 1971 NASA took several actions to address the issues of gaseous pollutant emissions. A program was constructed that had both near-term and far-term objectives. The near-term program concentrates on achieving a large and immediate reduction in the pollutant emissions. It addresses engines classes T1, T2, T4, and P2. This program, conducted largely under contract, is essentially complete. The far-term program has the overall goal of developing the technology necessary to define the minimum

pollutant emission levels that aircraft gas-turbine engines can achieve. This program is being conducted both at the Lewis Research Center and through research grants to universities and contracts with industry.

NEAR-TERM PROGRAMS

From 1970 to 1973 considerable effort was directed toward examining various methods of controlling engine emissions. Most of this work, however, was conducted in simplified test rigs. No serious efforts to integrate these emission-reduction methods into actual aircraft-engine combustors had been undertaken. The purpose of the near-term program was to study the various emission-reduction schemes, choose the best of these and evaluate their potential in realistic engine combustor geometries.

By way of background, figure II-1 illustrates schematically an aircraft-engine combustor of the type used in large turbofan engines. Below the sketch are bar graphs illustrating the levels of pollutants typical of these engines. The characteristic features of these combustors are noted in the sketch. They have a single burning stage; the primary zone tends to operate fuel rich; and large amounts of air bypass the combustor primary zone and are admitted further downstream to cool and dilute the combustion products. These combustors all use a step-louver, film-cooled liner, and a large portion of the total combustor airflow is used to cool the liner. The emission levels shown are expressed as values of EPAP (EPA parameter), and are obtained by integrating the engine emissions over the specified landing and takeoff cycle. In general, emissions of carbon monoxide, total hydrocarbons, and oxides of nitrogen are all substantially greater than the EPA standards. Smoke levels are low, well below the level of visibility, which reflects the work done to control smoke in the late 1960's and early 1970's.

Figure II-2 shows the combustion characteristics that cause high pollutant-emission levels and identifies the various emission-reduction techniques that are used.

At low-power conditions, typically engine idle, emissions of carbon monoxide and hydrocarbons are predominant, primarily because of poor combustion efficiency. The combustion characteristics responsible for low-power emissions are quenching of the burning gases near the film-cooled liner walls and quenching of the burning mixture with cold dilution airflows. The combustion stability of the flames is also low, primarily because of the low inlet-air temperature and pressure that characterize the idle operating mode. In addition, poor fuel atomization and distribution contribute to poor combustion stability and low combustion efficiency, which, in turn, contribute to greater emissions of unburned hydrocarbons. The emission-reduction techniques,

itemized on the right of figure II-2, all result in a marked reduction in carbon monoxide and hydrocarbon emissions. Increasing the burning zone residence time will allow time for the complete consumption of the hydrocarbon fuel and carbon monoxide. Reducing the flow velocity is one way to increase the residence time. Delaying the injection of dilution air will result in a longer primary zone and hence increased residence time. Delayed mixing also reduces quenching effects caused by rapid cooling of the burning mixture. Increasing the burning-zone equivalence ratio, that is, adding more fuel to the burning zone, results in a higher local temperature, which accelerates the combustion reactions. Improvements in fuel atomization and distribution prevent large pockets of fuel-rich mixtures from occurring and make for smaller fuel droplets which can be more rapidly consumed.

At high power conditions, typically takeoff and climb, the major pollutants are oxides of nitrogen and smoke. Carbon monoxide and hydrocarbons are present only in very small amounts, as combustion efficiency is virtually 100 percent. Oxides of nitrogen and smoke emissions are formed when residence times are long, when flame temperatures become very high due to the high air pressures and temperatures (which are typical of high-power operation), and where there is poor local fuel distribution, which causes very-high-temperature, fuel-rich pockets or zones. These pollutants can be reduced by decreasing the combustor residence time so that they do not have time to form in any significant amount. This can be done by increasing the velocity or by enhancing mixing, which effectively reduces the length of the burning zone. Decreasing the equivalence ratio, that is, operating fuel lean, reduces the maximum flame temperature and the rate at which these pollutants are formed. Improving fuel atomization and distribution results in a more uniform mixture of the fuel and air.

An examination of the emission-reduction techniques reveals an interesting conflict between those that reduce idle emissions and those that reduce high-power emissions (fig. II-3): With the exception of improved fuel atomization and distribution, the reduction techniques are in opposition. As an example, to reduce low-power emissions, increased residence time is needed; however, to reduce high-power emissions, decreased residence time is needed. This poses a difficult combustor design dilemma. It is as if two different combustors, one for low power and one for high power, are required.

The problems, then, were to determine if these conflicting approaches could be integrated into a real engine combustor without compromising performance and, if so, to determine to what level the resulting pollutants could be reduced. These were the questions to be answered by our near-term emission-reduction program. Put another way, the objectives of this program were to

investigate new combustor concepts with the potential for significantly lower emission levels and to measure the emissions reduction by engine test. Contracts were awarded to major aircraft engine manufacturers to devise and investigate new combustor concepts. In general, these contracts were for a multiphase program. The first phase consisted of the screening of a variety of new combustor concepts to determine those with the greatest emission-reduction potential. Those concepts so identified were refined in the second phase, and finally the best or most "engine ready" combustor design was tested in an engine to measure the emission reduction obtainable. Table II-2 shows the engine manufacturers and the engines selected. The engines are arranged in order of increasing compressor pressure ratio. The EPA engine class designation is shown in the left column.

Near-Term Program Results

The results of the programs conducted with the engines in EPA class T2 are discussed herein. In general, these results are quite similar to those obtained for combustors in the other engine classes. Figure II-4 shows the Vorbix combustor used in the JT9D-7 engine. Vorbix is an acronym meaning vortex burning and mixing. A cross section of this combustor (fig. II-4) shows that there has been a drastic departure from conventional combustors. The Vorbix combustor consists of two burning stages arranged in series: a pilot stage, for low-power emission control, and a main stage, for operation at all engine conditions beyond idle. The main stage is separately fueled; the pilot stage is the ignition source for the main stage. The bar graphs below the drawing compare the emissions of a production JT9D-7 combustor with those obtained with the Vorbix combustor tested in JT9D-7 engine. Carbon monoxide emissions were reduced by more than one-half; total hydrocarbon emissions were reduced by over a factor of 10; and oxides of nitrogen emissions were reduced by over one-half. A photograph of the Vorbix combustor is shown in figure II-5.

Figure II-6 shows the double-annular combustor tested in an experimental CF6-50 engine. This combustor also has two stages, but, here, the pilot and main stages are arranged in parallel, resulting in two annular burning zones. The pilot zone is used at all operating conditions and is designed to control low-power pollutants. The main zone is functional at all engine conditions above idle and is designed to reduce the high-power pollutants. The bar graphs compare the production CF6-50 combustor emissions with those of the double-annular combustor. Carbon monoxide emissions were reduced by about 40 percent; total hydrocarbons by a factor of 10; and oxides of nittrogen by about 30 percent. A photograph of the double-annular combustor is presented in figure II-7.

With the completion of the engine tests, several important achievements had been made. All the gaseous pollutants were significantly reduced with these controlled-emission combustors. These combustors operated the engines in which they were tested to full takeoff power levels and essentially met the required engine acceleration times. In general, combustor performance was excellent, considering the extent of these programs. These combustors are, of course, not ready for manufacture, and many technical areas require further development. A major problem with these two-stage combustors is the coking of fuel in the main-stage fuel lines and injectors. This occurs when the engine is idling and no fuel is flowing through the main-stage injectors. Fuel in the lines or injectors is exposed to compressor-exit air temperatures for some time, resulting in the degradation of the fuel. This fuel degradation can become serious enough to affect the fuel flow and spray quality. Liner durability problems were encountered, particularly around the throat separating the pilot and main stages of the Vorbix combustor. The combustor exhaust-temperature pattern factor can be improved and needs more work.

Figure II-8 summarizes the advances made to control pollutant emissions in these two programs. The combustor sketch illustrates the typical features of controlled-emission combustors. Note the multiple stages: a pilot stage for engine idle emission control and a lean-burning main stage for all higher power operating conditions. Air-blast fuel injectors are often used in the main stage to achieve fine fuel drops intimately mixed with combustion air. Since most of the air is now used in controlling the combustion process, very little air is available for dilution and temperature profile tailoring. Similarly, the amount of air available for liner film cooling is reduced, and other, advanced cooling schemes must be used. Emission performance is summarized below. Carbon monoxide was reduced about 50 percent; total hydrocarbons by about a factor of 10; and oxides of nitrogen by about 35 percent. Good reductions were achieved in carbon monoxide and oxides of nitrogen emissions, but they may not be as low as may be required to meet emission standards. Total hydrocarbons on the other hand, virtually disappeared, which would suggest that no further work is needed to reduce levels of this pollutant. Another aspect of our near-term program concentrated on investigating other techniques to further reduce carbon monoxide emissions at low-power conditions.

Idle Emissions Reduction Program

As mentioned earlier, carbon monoxide and unburned hydrocarbons are emitted from combustors mainly during low-power, or idle, operating conditions. Quenching of the burning fuel and air before combustion is complete is the characteristic most responsible for these emissions. Quenching takes place near the combustor liners and at the dilution air jets. In conventional

combustors, liners are cooled by injecting a film of air onto the liner wall. The interaction of combustion gases with this cool air film sup- presses the completion of the combustion process. Avoiding the use of this cool air film and allowing the liner surface to run hotter would greatly reduce the quenching of the reacting gases.

Quenching can also be reduced by delayed mixing of the dilution-air jets with the combustion gases. If these dilution jets are placed further downstream, the chemical reactions of the burning zone can take place for a longer time, resulting in more complete combustion.

With these facts in mind, the idle emissions reduction program had the objective of investigating new combustor concepts with potential for significantly lower engine-idle emissions.

To achieve this objective a contract was awarded to an engine manufacturer to test and evaluate three new combustor concepts having unconventional design features. The testing and evaluation of the combustor were confined to typical idle conditions; no attempt was made to operate the combustors at the more severe high-power conditions. The application of this technology to a practical combustor system could be realized by using variable-geometry schemes or by using one of these designs as the pilot stage of a multistage combustor.

The three combustor designs were the hot-wall combustor, the recuperative-cooling combustor, and the catalytic-converter combustor.

The main feature of the hot-wall combustor (fig. II-9) is the thermal barrier coating on the inside surface of the combustor liner to reduce wall quenching. These refractory coated surfaces, along with impingement-cooled liners and no film cooling whatsoever, result in greatly reduced quenching losses at the walls. Also, the secondary dilution-air jets are placed farther downstream to further reduce quenching.

The main feature of the recuperative cooling combustor (fig. II-10) is that all of the primary combustion air is first sent through the annular passages of the combustion liners as impingement cooling air before being admitted into the combustor through the air swirlers of the dome or the primary dilution holes. Thus, the combustion air is first used to cool the liners and in this way picks up heat before entering the combustor. This air temperature enhancement reduces pollutant emissions by increasing combustion reaction rates.

The catalytic converter combustor (fig. II-11) consists of a conventional, initial burning zone followed by a ceramic honeycomb catalyst bed. The fuel is first burned in front of the catalyst

bed in a lean fuel mixture. The catalyst then acts as a cleanup reactor for the unburned hydrocarbon and carbon monoxide products in the combustion gas, resulting in very low emissions of these pollutants. A photograph of the actual catalyst bed used in this design is shown in figure II-12. It consists of three sections of a ceramic honeycomb substrate cemented together and placed in a metal housing shaped to fit the 60^{o} sector combustor test hardware. The ceramic honeycomb substrate is approximately 4 inches deep and is impregnated with the catalyst material.

In addition to the main features of each of the combustor designs, they all featured impingement-cooled liners with no film-cooling, and they used improved, air-blast fuel injectors for good fuel atomization, another factor in achieving low idle emissions. Finally, the primary-zone equivalence ratio of these concepts was designed to be very close to stoichiometric, and air dilution was delayed until far downstream for maximum reaction of fuel and air.

The results of this experimental program are shown in figure II-13 in terms of carbon monoxide and unburned hydrocarbon emissions at the design idle condition. These results are compared with those of the controlled-emission combustor at a similar idle condition. All three combustor designs dramatically reduced carbon monoxide emissions and significantly reduced unburned hydrocarbon emissions. The large reduction in idle emissions achieved by these concepts indicates the potential of this technology if it were to be applied into a full combustor design for a gas turbine engine.

Because the hot-wall combustor is the simplest, its design features are shown in figure II-14 as the pilot stage of a hypothetical multistage combustor. The refractory surfaces of the inner liner walls and the use of impingement cooling result in minimized wall quenching effects. The pilot stage is designed for optimum burning rates at the idle operation of the combustor.

The projected emissions of such combustor operating in an engine over a standard landing-takeoff cycle are shown in the lower half of the figure. Carbon monoxide emissions are seen to be dramatically reduced from the controlled-emission combustor. Unburned hydrocarbon emissions are further reduced from the already low levels of the controlled-emission combustor. Oxides of nitrogen are essentially unchanged from the controlled-emission combustor, as expected, because most of this pollutant is generated during high-power operation. To realize the benefits of the reduced idle emissions, work must be undertaken to apply this technology into a full combustor system.

FAR-TERM PROGRAMS

At high-power operation high flame temperature is the most important factor in the formation of oxides of nitrogen. Experimental data as well as analytic predictions indicate that oxides of nitrogen emissions vary exponentially with flame temperature. Therefore, far-term efforts are concentrating on the technique of lean burning in which decreasing the combustion-zone equivalence ratio will lower the flame temperature with a resultant reduction in oxides of nitrogen.

Reducing the combustion-zone equivalence ratio alone may not result in the lowest possible oxides of nitrogen emissions unless several other factors are also considered. Because the local flame temperature is a significant factor in controlling oxides of nitrogen production, fuel distributions with locally rich full pockets must be avoided. This requires the fuel and air to be uniformly mixed throughout the combustion zone. In addition, it may be necessary to prevaporize the fuel. Large fuel droplets in the combustion zone are consumed by a diffusion flame that surrounds the evaporating droplets. This process takes place at near-stoichiometric conditions, and the high temperatures produce excessive oxides of nitrogen emissions. Thus, combustors with provisions to prevaporize the fuel and premix the fuel and air may be necessary to realize the full potential of lean-burning techniques.

Low levels of oxides of nitrogen emissions obtainable by lean, premixed, prevaporized combustion have been demonstrated in experimental flame-tube combustors. The essential features of this type of experiment are shown in figure II-15. Fuel is injected into a preheated airstream upstream of a simple flame-holding device. A vaporization and mixing zone provides sufficient time for the fuel to completely vaporize and mix. In such a well-controlled experiment the fuel-air distribution at the flame holder is uniform. Order-of-magnitude reductions in oxides of nitrogen emissions have been obtained in experiments such as these.

The concept of catalytic combustion offers the potential of even further reductions in pollutant emissions. By using a catalyst bed consisting of a ceramic honeycomb substrate impregnated with catalytic material, stable, efficient combustion occurs at even leaner overall equivalence ratios. When operating in idealized conditions, such as the flame-tube apparatus (fig. II-16), nearly pollutant-free combustion occurs.

Even though lean, premixed, prevaporized combustion and catalytic combustion have the potential for achieving very low emission levels. Considerably more work is required before either technology could be applied to aircraft engine combustion systems.

This then forms the basis for the far-term emission reduction program.

The objective of our far-term program is to evolve the technology needed for the development of combustors with minimum pollutant levels. The achievement of this objective relies heavily on continuing basic and applied research. The degree of risk and overall level of complexity associated with the adaptation of advanced techniques is more severe than that of the near-term programs. Fundamental studies are viewed as a requirement to closing the gaps in our understanding of key areas and to bringing the new technology to a point where a new approach to combustor design is practical. As discussed previously two techniques appear particularly attractive: The lean, premixed, prevaporized and the catalytic combustion techniques. In late 1979 contracts will be awarded to evolve and evaluate both of these combustor concepts.

Before lean, premixed, prevaporized combustors can be used in aircraft engines, additional research is required in several areas. Shown in figure II-17 is a conceptual drawing of a lean, premixed, prevaporized combustor, which is a staged type of design. The pilot stage has been configured to include features, such as a hot-wall liner to minimize idle pollutants. The main stage looks much like a flame-tube rig and contains a fuel injector, a premixing and prevaporizing section, and a flame holder. To maintain a wide operating range, while burning as lean as possible, control of the airflow as well as the fuel flow between the two stages may be required. To achieve this required airflow control, a variable geometry device has been included in the diffuser section.

Key areas requiring additional study are also shown in the figure II-17. Combustor inlet airflow characteristics must be known to assure uniform fuel-air distributions. Engine transient characteristics must be identified and studied to avoid autoignition and flashback in the fuel-air mixing passage. Practical schemes for varying the combustor geometry and controlling the operation of the combustor must be identified. Techniques for predicting and achieving the required fuel distribution and vaporization in the premixing section of the main stage as needed. Autoignition and flashback may also be problems there. More data on these phenomena are needed over the full range of engine operating conditions, including transients. Other areas of the combustor also require study. Lean stability and altitude relight capability need special attention with these advanced concepts. Because most of the combustor airflow must pass through the main stage to satisfy the lean burning requirement, the amount of air available to cool the combustor liner will be less than that of current technology combustors. It therefore appears likely that advanced liner cooling schemes will be required to avoid liner durability problems.

Digital engine controls will likely be required for the additional complexity of variable geometry. It is expected that full-authority digital-control technology will be available in the future. However, additional study is needed to examine the control aspects of variable geometry combustors and to establish transient response requirements.

Figure II-18 indicates the areas requiring research for catalytic combustors. In general, all of the problem areas associated with premixed combustion apply equally well to the catalytic concepts. Problems unique to this concept include the activity of the catalytic materials over wide operating ranges, long-term degradation and poisoning of the catalyst, and thermal durability of the catalyst during continuous and cyclic operation of the catalyst bed. While considerable progress has been made in the last few years on research into catalyst and substrate materials, considerably more is required. It is not the purpose of this paper to fully document the results to date of these fundamental studies in support of our far term program. However, three studies that highlight some of the activities have been selected for discussion.

Studies of the influence of flame-holder geometry on emissions and performance have been undertaken. Figure II-19 shows the flame zone structure for six flame-holder designs that have been evaluated. The designs tested included wire grids, perforated plates, cones, and C-gutters. These open-duct burning photographs were taken only for visualization purposes. Actual testing was done at high pressure in an enclosed flame-tube rig.

Figure II-20 presents data from a high-pressure, lean, premixed, prevaporized flame-tube experiment. Emissions of oxides of nitrogen are shown as a function of the adiabatic flame temperature. When this experiment was completed, several milestones had been passed. First, flame-tube experiments were for the first time conducted at pressures well above 10 atmospheres. In fact, these flame-tube experiments were successfully conducted at pressures to 30 atmospheres and inlet-air temperatures comparable to those of modern engines. Second, although previous data had shown an inconsistentency in oxides of nitrogen emissions with increasing pressure, this experiment demonstrated that, from 10 to 30 atmospheres, pressure had no effect on oxides of nitrogen emissions in lean, premixed, prevaporized, combustors when correlated against adiabatic flame temperature. Third, this experiment verified the emission levels projected from lower pressure tests.

Tests are also underway to determine the characteristics of boundary-layer autoignition and flashback phenomena in premixed fuel-air streams. As discussed earlier, an understanding of autoignition and flashback phenomena are important in the design and operation of the premixer section. Figure II-21 is a photo-

graph taken through the viewing port of a high-pressure flame-tube apparatus with a quartz liner. A variety of test plates can be mounted in the premixed stream to map the autoignition and flashback limits of various boundary-layer profiles for high inlet temperature and pressure conditions. In this particular photograph the inlet temperature and pressure were such that autoignition of the fuel-air mixture occurred in the boundary layer. In another view taken from a high-speed movie sequence (fig. II-22), the flame was observed on the upper surface propagating upstream through the boundary layer. When the inlet-air temperature and pressure are further increased, autoignition occurs in the free stream. An example of this phenomenon is shown in figure II-23. Details of the combustion on the test plate as well as residual droplet burning may also be seen. Studies of this type apply to both premixed and catalytic combustion.

Looking into the future, we can project engine emission levels for lean, premixed, prevaporized and catalytic combustors. The drawing of the combustor in figure II-24 shows some essential features of these designs. The combustor is staged, has variable geometry, and has optimized pilot-stage technology. In the main stage lean combustion occurs downstream of the flame holder or, in the case of a catalyic combustor (see insert), in the catalyst bed.

The bar graphs of carbon monoxide and hydrocarbons show achievable levels which are based on the successful integration of optimized pilot-stage features such as those discussed previously. The emission-control strategies used here were aimed at oxides of nitrogen reduction. The third set of bar graphs shows that, in terms of the integrated EPA parameter, oxides of nitrogen levels may be further reduced from the previous controlled-emission techniques by a factor of 3 to 4. It is interesting to note that the pilot stage, which is necessary for engine startup and wide-range operation, may contribute more oxides of nitrogen during engine idle than the main stage contributes during high-power operation. Thus, the pilot stage is limiting the minimum achievable oxides of nitrogen emission levels for the specified landing-takeoff cycle used in computing the EPA parameter.

The actual levels may be somewhat different when these emission-control techniques are developed into operational engine hardware: Tradeoffs between emissions, performance, altitude-relight capability, durability, maintainability, and complexity will be evaluated in future experimental programs. The influence of the actual engine environment as opposed to carefully controlled rig experiments will be considered.

CONCLUDING REMARKS

The combustion systems found in engines today may well be markedly different in the future if low-pollutant-emission combustion systems are required. Current combustors are characterized by burning in a single stage, film-cooled liners, single-plane fuel injection, and rich burning in the primary zone. Current combustors are all fixed-geometry systems. The prospective minimum pollutant combustors are far different. First, multiple stages will be needed to reduce both low-power and high-power emissions. Advanced liner-cooling concepts will be used, particularly in the pilot stages, to reduce quenching and to control low-power (idle) emissions. The main stage will burn lean to reduce oxides of nitrogen by reducing the flame temperature. To fuel the two stages multiple-point fuel injection will be needed. And last, variable geometry will be incorporated to optimize overall combustion system performance. Much work, however, still needs to be done before these advanced systems can be considered for actual application. Quite obviously there is a price to pay: Low pollutant emission combustion systems are more complex.

These complexities arise from the very items that distinguish the advanced combustor from the current combustor, that is, the need for more injectors to fuel the multiple-burning stages, the more complex liner cooling required, and the variable geometry. The price for this complexity will be higher initial cost. There are benefits however, the most significant of which is the drastic reduction in pollutant emissions. Because of the lower flame temperatures and uniform burning, the combustor-exit pattern factor should be improved over that in current engines, thereby resulting in longer turbine life. Additionally, hot streaks in the combustor should be minimized, thereby increasing combustor liner life. The ability to vary the airflow distribution in the combustor through the use of the variable geometry should improve the altitude relight characteristics of the system.

At present we are a long way from realizing the potential of these advanced combustion systems. Research and technology programs indicated that dramatic reductions in the pollutant emissions of gas turbine engines can be achieved in the near term. Taking that technology and developing it into practical flight systems remains to be accomplished. Continuing research and technology programs must be pursued to validate that the minimum pollutant emission levels found in rig tests can in fact be realized in gas-turbine engine combustion systems.

GASEOUS EMISSION STANDARDS

	ENGINE CLASS	POLLUTANT*		
		HC	CO	NO_x
T1	TURBOJET/TURBOFAN LESS THAN 8000 lb THRUST	1.6	9.4	3.7
T2	TURBOJET/TURBOFAN GREATER THAN 8000 lb THRUST	.8	4.3	3.0
T3	P & W JT3D	.8	4.3	3.0
T4	P & W JT8D	.8	4.3	3.0
T5	TURBOJET/TURBOFAN ENGINES FOR SUPERSONIC AIRCRAFT	3.9	30.1	9.0
P2	TURBOPROP ENGINES	4.9	26.8	12.9

*T STANDARDS AS lb/1000 lb THRUST-hr/CYCLE
P STANDARDS AS lb/1000 hp-hr/CYCLE

CS-79-1758

Table II-1

NEAR TERM EMISSION REDUCTION PROGRAM
SCOPE

ENGINE CLASS	MANUFACTURER	ENGINE
P2	DETROIT-DIESEL-ALLISON	501-D22-A
T1	GARRETT AIRESEARCH	TFE-731-2
T4	PRATT & WHITNEY	JT8D-17
T2	PRATT & WHITNEY	JT9D-7
T2	GENERAL ELECTRIC	CF6-50

CS-79-1747

Table II-2

CURRENT COMBUSTORS

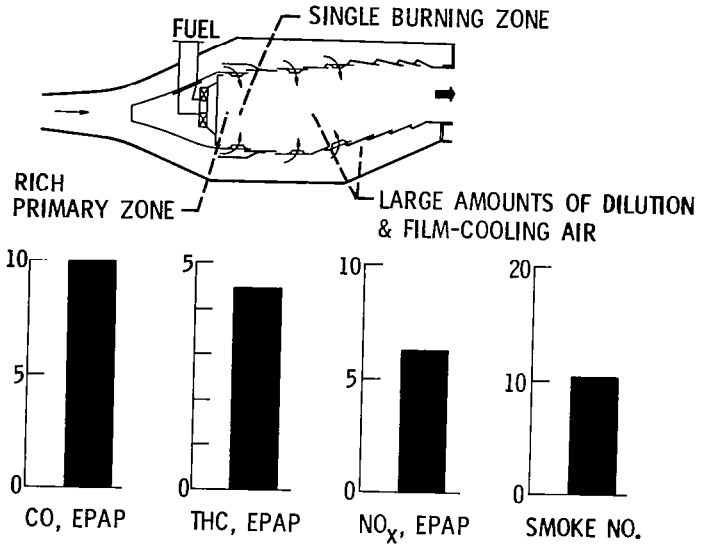

CS-79-2138

Figure II-1

COMBUSTOR EMISSIONS

OPERATING CONDITIONS	COMBUSTION CHARACTERISTICS	POLLUTANTS	REDUCTION TECHNIQUES
LOW POWER/IDLE	QUENCHING POOR COMBUSTION STABILITY POOR FUEL ATOMIZATION & DISTRIBUTION	CARBON MONOXIDE UNBURNED HYDROCARBONS	INCREASE RESIDENCE TIME REDUCE FLOW VELOCITY & DELAY MIXING INCREASE EQUIV RATIO IMPROVE FUEL ATOMIZATION & DISTRIBUTION

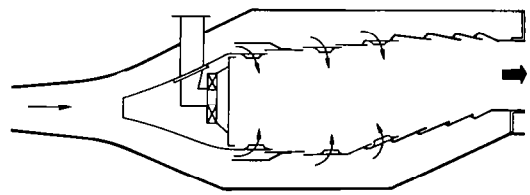

HIGH POWER/ TAKEOFF	EXCESS RESIDENCE TIME HIGH FLAME TEMP POOR LOCAL FUEL DISTRIBUTION	OXIDES OF NITROGEN SMOKE	**DECREASE RESIDENCE TIME INCREASE FLOW VELOCITY ENHANCE MIXING DECREASE EQUIV RATIO IMPROVE LOCAL FUEL DISTRIBUTION**

CS-79-2054

Figure II-2

EMISSION REDUCTION PROBLEM

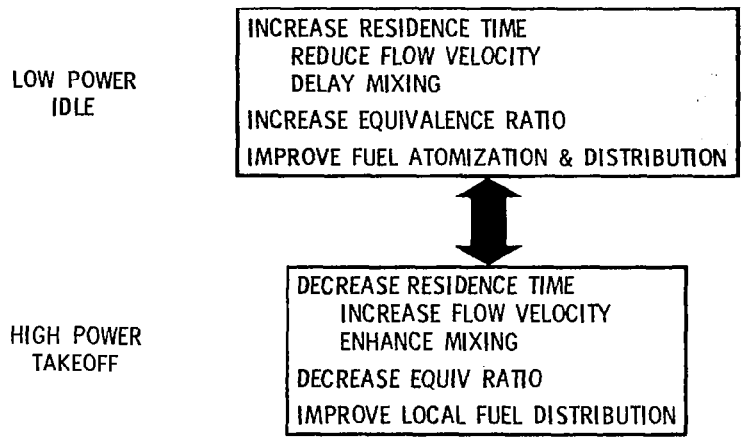

CS-79-2042

Figure II-3

VORBIX COMBUSTOR CONCEPT FOR JT9D-7 ENGINE

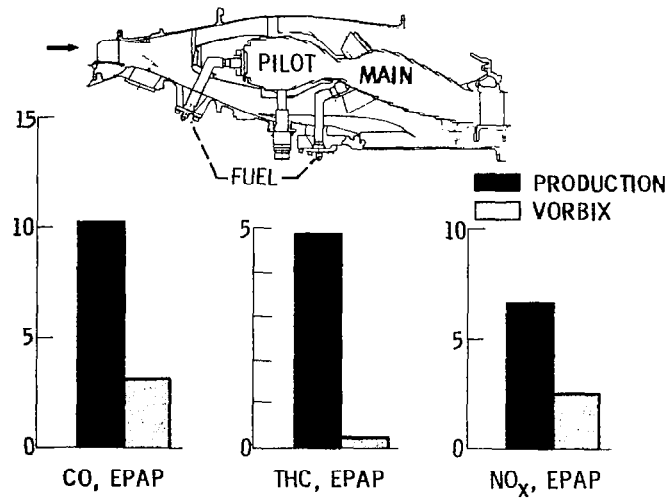

Figure II-4

PROTOTYPE VORBIX COMBUSTOR

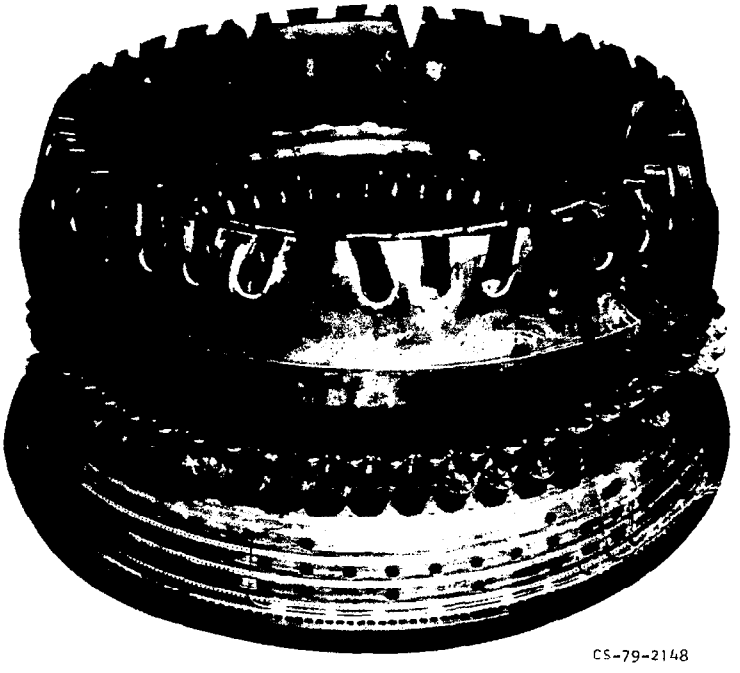

Figure II-5

DOUBLE/ANNULAR COMBUSTOR FOR CF6-50 ENGINE

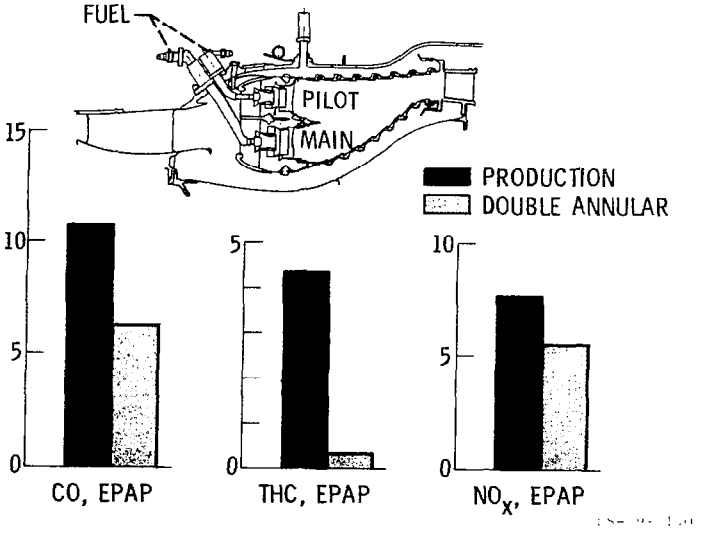

Figure II-6

PROTOTYPE DOUBLE ANNULAR COMBUSTOR

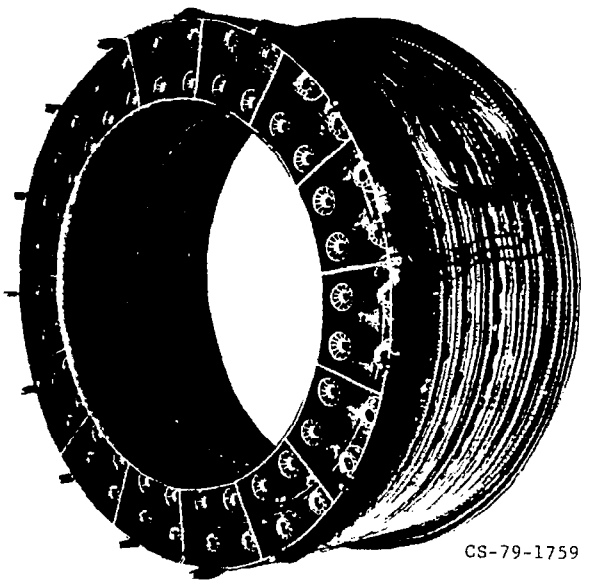

Figure II-7

CONTROLLED-EMISSION COMBUSTOR

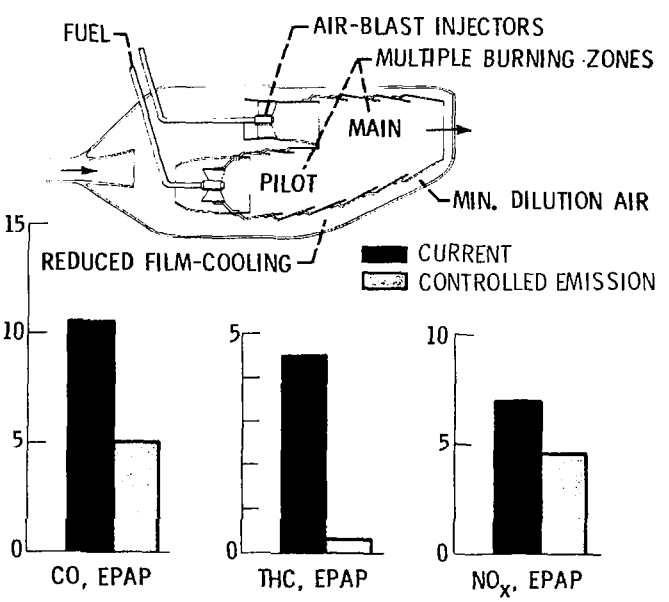

Figure II-8

HOT WALL COMBUSTOR

CONCEPT NO. 1

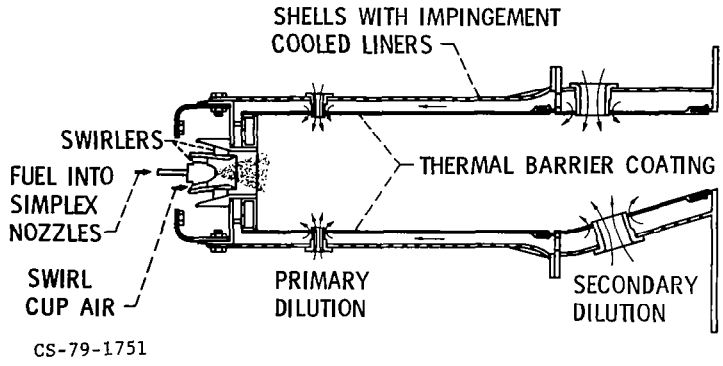

Figure II-9

RECUPERATIVE COOLING COMBUSTOR

CONCEPT NO. 2

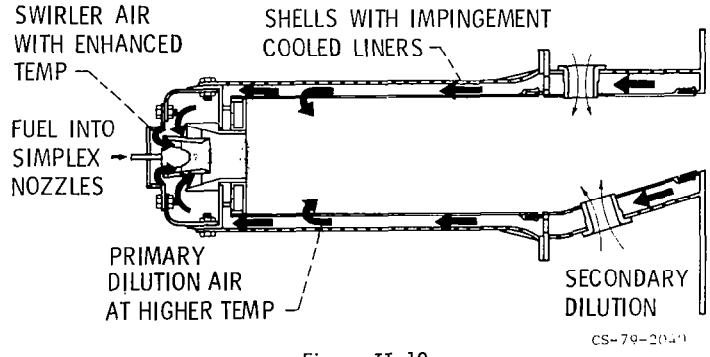

Figure II-10

CATALYTIC CONVERTER COMBUSTOR

CONCEPT NO. 3

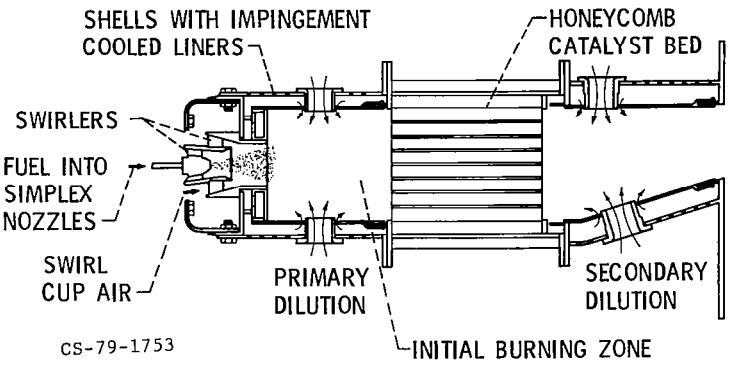

Figure II-11

CATALYTIC COMBUSTOR ASSEMBLY

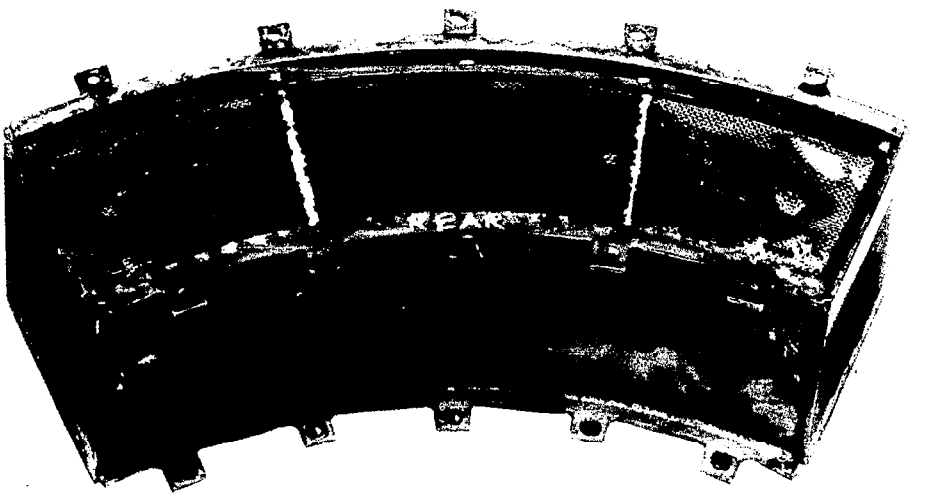

Figure II-12

EMISSIONS AT IDLE

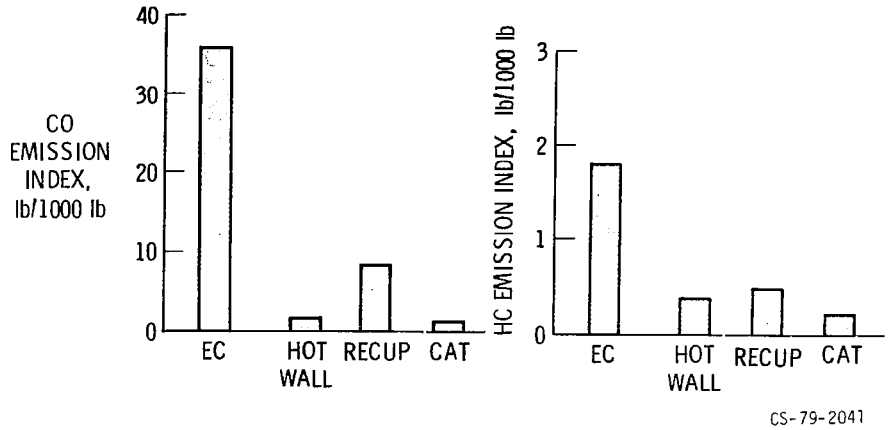

Figure II-13

PROJECTED ENGINE EMISSIONS INCORPORATING IDLE EMISSIONS CONTROL TECHNOLOGY

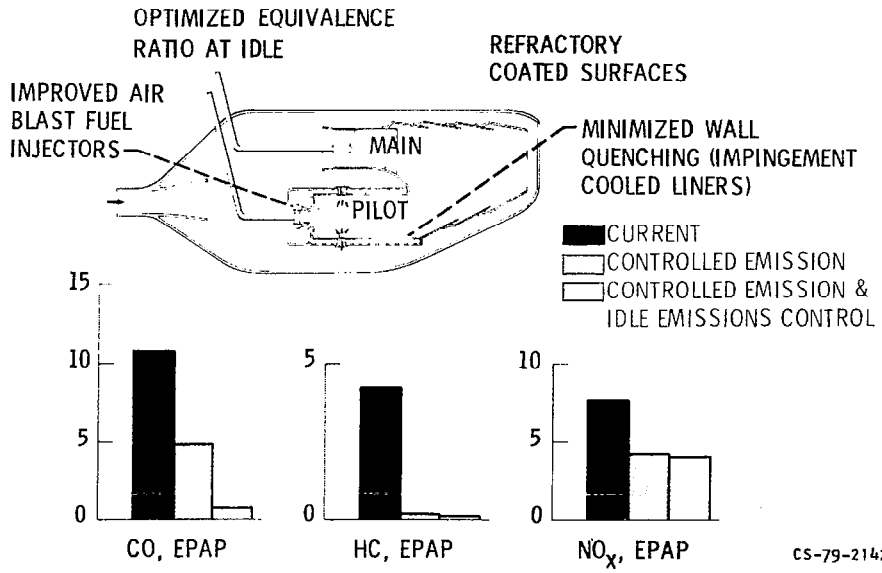

Figure II-14

PREMIX FLAME TUBE COMBUSTOR

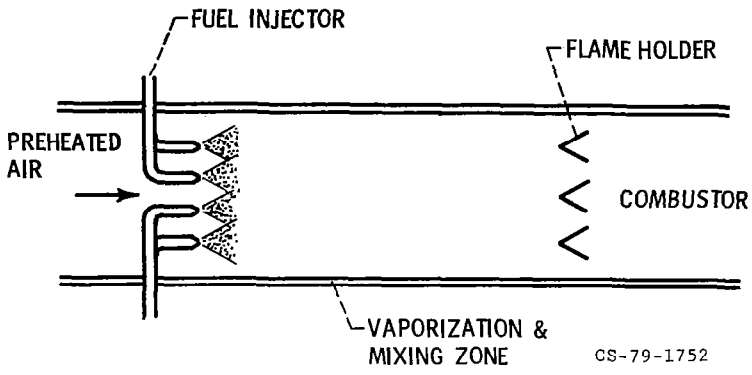

Figure II-15

CATALYTIC FLAME TUBE COMBUSTOR

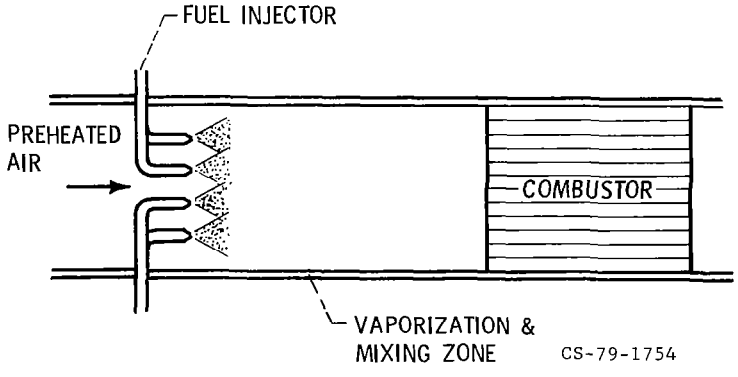

Figure II-16

LEAN, PREMIXED, PREVAPORIZED COMBUSTOR

REQUIRED RESEARCH AREAS

FUEL DISTRIBUTION
FUEL VAPORIZATION
AUTOIGNITION
FLASHBACK

LEAN STABILITY
ALTITUDE RELIGHT
LINER DURABILITY
CONTROLS

AIRFLOW UNIFORMITY
TRANSIENT EFFECTS
VARIABLE GEOMETRY

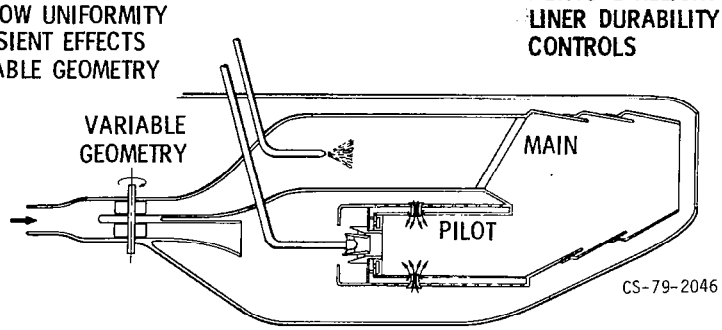

Figure II-17

CATALYTIC COMBUSTOR

REQUIRED RESEARCH AREAS

FUEL DISTRIBUTION
FUEL VAPORIZATION
AUTOIGNITION
FLASHBACK

CATALYST ACTIVITY
CATALYST DEGRADATION
THERMAL DURABILITY
LINER DURABILITY

AIRFLOW UNIFORMITY
TRANSIENT EFFECTS
VARIABLE GEOMETRY

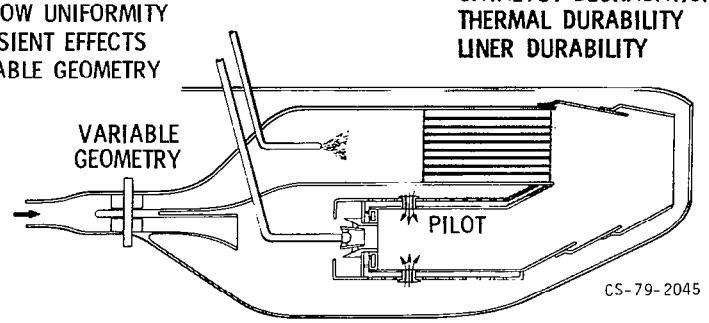

Figure II-18

OPEN DUCT OPERATION OF SIX FLAMEHOLDERS AT 70% BLOCKAGE

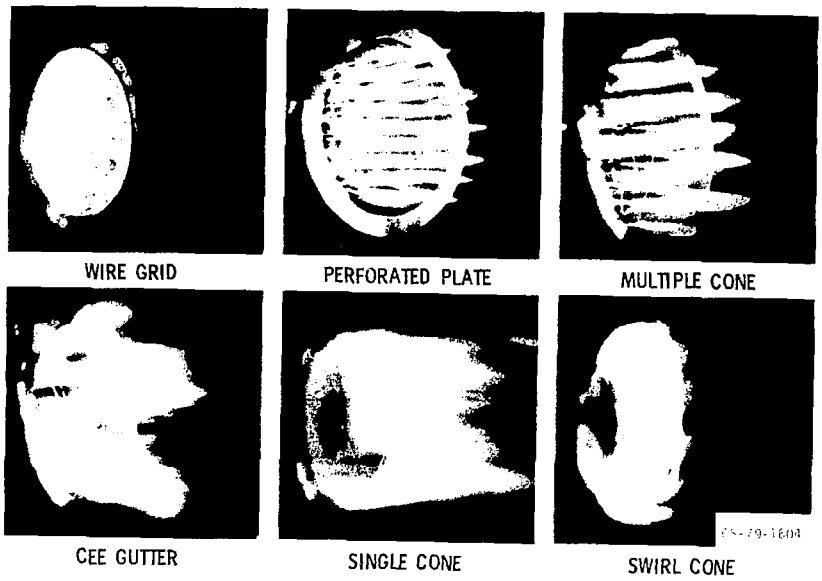

Figure II-19

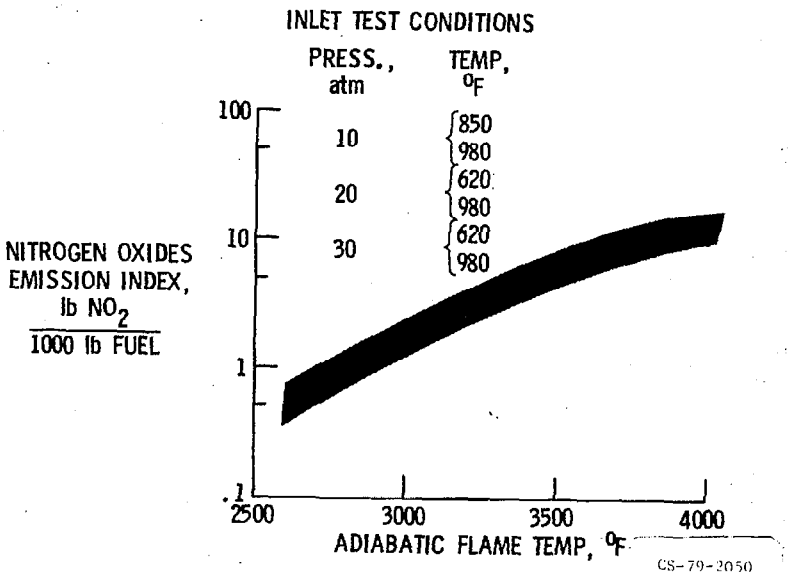

Figure II-20

STUDY OF BOUNDARY LAYER AUTOIGNITION AND FLASHBACK PHENOMENA

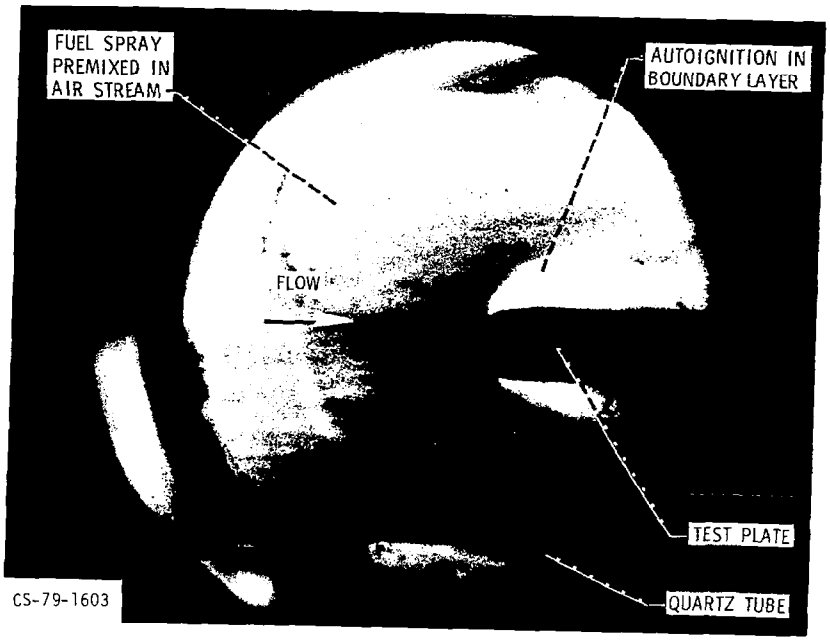

Figure II-21

Figure II-22

Figure II-23

PROJECTED ENGINE EMISSION LEVELS FOR FAR TERM TECHNOLOGIES

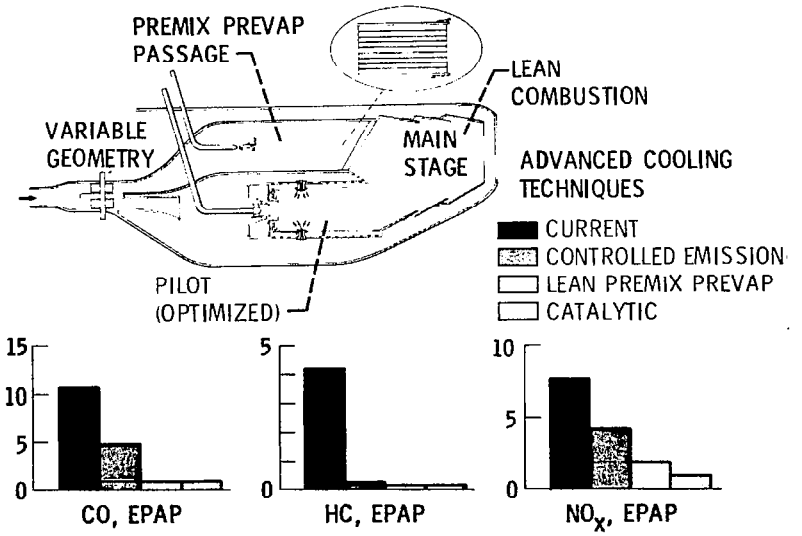

Figure II-24

CS-79-2141

III. NOISE REDUCTION

Charles E. Feiler, John F. Groeneweg, Francis J. Montegani,
John P. Raney*, Edward J. Rice, and James R. Stone

National Aeronautics and Space Administration
Lewis Research Center

Aircraft noise has been a major national environmental concern for a number of years. One indication of the public pressure to reduce noise is the number of major airports around the world that have noise restrictions. Some data are shown in figure III-1 for the years 1968, 1973, and 1978 (ref. 1). In 10 years the number of airports with restrictions doubled. The restrictions take several forms: curfews on nighttime operations; flight routing and operating restrictions; and the use of preferential runways. During this time, the Federal Aviation Administration (FAA) has issued increasingly stringent noise certification standards that are critical design constraints on new aircraft. To help with the problem, NASA has been engaged in research-and-technology studies to advance the state of the art in aircraft noise reduction. The primary noise source is the turbofan engine.

Propulsion noise research is focused on understanding the turbofan engine's noise-producing components so that noise can be reduced in efficient and economical ways that do not penalize the engine performance or weight significantly. An additional objective is to develop prediction procedures for each source that will allow aircraft noise to be estimated accurately.

The noise sources from a turbofan engine are illustrated in figure III-2. The sources are both internal and external to the engine. The internal sources are the fan, the compressor, the turbine, the combustor, and flow over the support struts. The last three sources have usually been considered collectively as engine core noise. Sound from the internal sources must propagate through the engine ducts and nozzles, where it can be reduced with acoustic treatment. Thus, acoustic treatment and the sound propagation in ducts are very important elements in engine noise reduction.

*NASA Langley Research Center, Hampton, Va.

The external noise sources are the high-velocity jets mixing with each other and with the ambient air. An important aspect of the engine noise problem is the effects of flight on the various noise sources. As will be shown, the effects of flight, or forward velocity, differ with the noise source.

The discussion presented herein is based on recent research. The topics discussed are fan noise, acoustic suppression, jet noise technology, combustor noise, and aircraft noise prediction.

FAN NOISE

The fan is a dominant noise source in current high-bypass-ratio turbofan engines, particularly during the landing approach. Furthermore, advanced turbofan design studies, such as those associated with the Energy Efficient Engine program, indicate that the fan will continue to be a dominant noise source in future engines. The ultimate objectives of fan noise research are to propose noise-reducing fan design features that are compatible with good aerodynamic performance and to experimentally confirm the acoustic effectiveness of those designs. Our approach includes research to understand the generation mechanisms and to describe in detail the fan source characteristics. Describing the source is important because propagation, suppression, and radiation all strongly depend on the initial conditions at the source. An important constraint on experimental work in static facilities is that the test environment must lead to noise levels that correctly simulate flight.

Two primary source mechanisms that are addressed in research to reduce fan noise are shown in the turbofan cross section in figure III-3. Rotor-stator interactions in the form of rotor wakes and vortices impinge on the stators and can be particularly important noise generators at the subsonic tip speeds that occur during landing approach. The corresponding narrowband spectrum is shown in the upper portion of figure III-4. The blade passing tone and its harmonics, which are due to periodic interactions of the rotor wakes with the stator blades, are superimposed on the broadband levels that result from interactions involving random flow disturbances. Rotor-alone noise production occurs because of nonuniformities in the rotor-locked shock wave patterns which form at the leading edges at supersonic tip speeds. These patterns radiate multiple pure tones during takeoff and have a spectrum of the type shown in the lower portion of figure III-4. Multiple pure tones can occur at all multiples of the shaft rotation frequency, and some of the individual tone levels often exceed the level of the blade passing frequency and its harmonics.

One of the concepts that has been investigated to reduce shock-generated, multiple-pure-tone noise is to sweep the rotor-blade leading edges. An experimental swept-rotor fan designed to explore the acoustic performance of swept blades is shown in figure III-5. The acoustic design of this fan was performed by Bolt Beranek and Newman Inc., and the aerodynamic and mechanical designs were done by the Lycoming Division of AVCO Corp. (refs. 2 and 3). The fan was acoustically tested at the NASA Lewis Research Center (ref. 4). The blade leading edges are swept forward to midspan and then backward to the tip in order to limit the maximum blade stresses at the blade roots. These stresses would be unacceptably high if the sweep were only in one direction.

The aerodynamic concept involved, which is used in supersonic swept-wing aircraft, is shown in figure III-6. The components of the blade leading-edge Mach numbers are shown in the planform view of the swept blade, and the variation of these components along the blade span is shown in the plot. Distance along the span is plotted vertically to correspond with the blade sketch. It is the component of Mach number normal to the blade leading edge that controls leading-edge shock formation. The sweep rate at each spanwise location is designed to keep the normal component of blade-inlet relative Mach number subsonic over the entire span. Even though the total inlet relative Mach number is supersonic over the outer three-fourths of the swept blade, the normal component is limited to a maximum Mach number of about 0.9. Except for blade end effects and the sweep reversal point, this should eliminate a major portion of the strong leading-edge shock system and thereby reduce the multiple-pure-tone noise.

The acoustic results obtained with this swept design are shown in figure III-7. The multiple-pure-tone power levels for a unswept fan and the swept-rotor fan are compared as a function of fan-tip relative Mach number. Rotor sweep delayed the onset of multiple pure tones to higher Mach numbers (about 1.25 instead of 1.0) and reduced the levels over a large portion of the tip-speed range, including speeds representative of takeoff. These initial results are encouraging, and refinement of the aerodynamic design may lead to further multiple-pure-tone reductions.

In addition to the rotor-alone and rotor-stator interaction sources, another strong source of noise is present in all static testing: rotor interaction with inflow disturbances, as shown in figure III-8. The rotor blades cut externally produced turbulence, wakes, or vortices that are drawn into the inlet. At subsonic tip speeds, this source often obscures or completely masks the rotor-stator interaction source.

The reasons for the prominence of the inflow source statically and its greatly reduced importance in flight (ref. 5) are illustrated in figure III-9. The nature of the fan-inlet flow field for static and flight cases is shown on the left side of figure III-9, and the corresponding fan spectra are shown on the right. Statically, turbulence in the atmosphere and wakes and vortices from the proximity of the test stand and ground plane are drawn into the inlet through greatly contracting stream tubes. The contraction intensifies transverse turbulent fluctuations and stretches the disturbances axially so that the rotor blades cut each intensified disturbance many times. Tone bursts are generated that appear as a strong blade passing tone and harmonics in the fan spectrum. In contrast, with forward velocity in flight, the stream tubes no longer contract to intensify and elongate atmospheric turbulence, and test-stand and ground-plane disturbances are not present. Thus, for fan stages that have been designed to limit noise caused by rotor-stator interaction, the tone levels - particularly those of the fundamental tone - are greatly reduced.

To eliminate extraneous inflow disturbances during static tests, passive inflow control devices of the type shown in figure III-10 are being developed (refs. 6 to 8). A hollow, hemispherical structure surrounds the fan inlet to damp incoming turbulence and to smooth out local distortions. The structure consists of layers of honeycomb and screen. The honeycomb cells are essentially alined along streamlines, and the size of the structure (about 4 fan diameters) was chosen to keep the pressure drop low and to avoid affecting the acoustic transmission to the far field. The frontal view shows that a segmented construction was used to approximate a hemisphere.

The segmented honeycomb surface of the inflow control device is shown in figure III-11. This device has been studied in both indoor anechoic chamber fan tests and outdoor engine tests. Figure III-12 shows the device mounted around the fan inlet in the Lewis anechoic chamber.

Typical aeroacoustic results obtained in the anechoic chamber tests are shown in figure III-13 in terms of measured inlet turbulence intensities and scales and the narrowband fan noise spectra. With inflow control the transverse turbulence intensities were reduced by more than a factor of 5. Axial length scales were also reduced and this indicates much less axial elongation of inflow disturbances. The narrowband spectra show large fan-tone reductions, particularly at the blade passing frequency. The fan tested was designed to minimize rotor-stator interaction and the results show that a large portion of the rotor-inflow disturbance noise that controlled the tone levels without inflow control was removed.

Development of inflow control methods (ref. 9) is also proceeding on the outdoor engine stand shown in figure III-14. A JT15D engine is shown fitted with the inflow control device. An exhaust muffler is used so that the inlet noise can be measured separately. These tests are part of an intercenter program involving the Lewis, Ames, and Langley Research Centers. Related NASA-sponsored work is also going on at engine and aircraft manufacturers. The purposes of the program are to measure the effects of forward velocity on fan noise and to develop static test methods that correctly simulate the measured flight behavior. A key feature of the program is the use of the same turbofan engine source in four test situations: the outdoor static engine tests and the indoor anechoic chamber fan tests, both to be done at Lewis; wind tunnel tests at Ames; and flyover noise measurements at Langley. The flight noise will be obtained by using an OV-1 aircraft as a flying testbed, as illustrated in figure III-15, which shows an artist's conception of the planned JT15D engine installation under the wing. The flight results will serve as the standard by which the adequacy of the ground-test methods can be verified.

As the inflow control methods are perfected, the rotor-stator interactions and any other sources controlling flight fan noise will be clearly revealed in static tests. These are the sources to be minimized by fan design. They also define the source characteristics that are the starting point for acoustic suppressor analyses and experiments.

ACOUSTIC SUPPRESSION

Basic research on noise suppressors is aimed at making them more efficient. It is believed that the weight gains and engine performance losses they cause can be reduced. This research is going on at the NASA Langley and Lewis Research Centers and at all the major engine and airframe companies.

Summary of Sound Propagation Theory

The components of suppressor analysis are shown in figure III-16. The noise source is pictured at the far right. The characteristics of the source must be known to build a good suppressor. Some of the other phenomena are illustrated as the sound waves move to the left. The sound is scattered at the interface between the hard wall and the acoustic liner. The sound is absorbed as it passes through the liner. More details of the liner as a boundary condition are shown later. The usual duct geometry includes a variable area so that the sound is scattered and reflected, and possibly refracted because of the velocity gradients. The sound reaches the inlet lip, is further scattered, and finally radiates to the far field. The far-field

sound level directivity is most important since the far field is where the observer is located. All the elements mentioned have an influence on far-field directivity. One approach to solving the complete problem is to attack the entire system at once by using numerical techniques. This is a long-range solution that will not be considered here. Just a few of the elements on this figure are briefly discussed here.

A simplified picture of a single sound wave traveling in a duct is shown in figure III-17. Of course, many such waves at different angles would be present. Two angles associated with this wave are very important. The incidence angle of the wave on the liner is labeled. The other angle, between the wavefront normal and the duct axis, is called the axial propagation angle. The incidence angle correlates the optimum wall impedance (ref. 10); the axial propagation angle is related to the far-field radiation direction (ref. 11). The two angles, together with the wall impedance, determine the suppression that can be obtained.

The correlation of optimum resistance with incidence angle is shown in figure III-18 (from ref. 10). All possible modes or angles of propagation were considered. Frequency and Mach number were held constant. A cylindrical duct was used with three boundary-layer thicknesses. For each boundary-layer thickness the calculated "best resistance for maximum damping" is very well correlated. Also, the boundary layer has an effect only for incidence angles above 65°, which corresponds essentially to axial propagation. Similar correlations could be shown for the other component of wall impedance - the imaginary part, or reactance. Equations are available to describe the optimum impedance behavior illustrated here (ref. 12).

The axial propagation angle can be used to modify the existing inlet radiation theory, which is quite limited. Only zero flow or the same flow inside and outside the duct can be handled exactly. In a static engine test, there is a large flow Mach number in the inlet but essentially zero flow outside the duct. The radiation theory must therefore be modified (ref. 11). The results of such a modification are shown in figure III-19 (ref. 13), in which sound pressure level is plotted against the angle from the inlet axis. Forty-one rods mounted in front of the rotor of a JT15D engine produced a single mode or angle of propagation to keep the experiment simple. The previous theory, which does not fit the data, is shown by the dashed line. The modified theory, which uses the axial propagation angle and fits the data quite well, is shown by the solid line. An additional correction for refraction appears necessary when the principal lobe of radiation falls near the inlet axis (ref. 13).

The improvement in liner efficiency with the newer suppressor concepts is illustrated in figure III-20 (from ref. 14). Sound

power reduction in the highest 1/3-octave band is plotted against the liner length-diameter ratio. The two liners were tested on Quiet Engine C and the Lycoming YF-102 engine, which happened to be the available engines at the time of the tests. The old liner (plane-wave design) was quite long and was tested in three lengths. The new liner (spinning-mode design) was very short and only one length was used. The increased suppression was quite dramatic, about a 3-to-1 improvement. This improvement comes about by a better match of the liner to the estimated properties of the noise source.

Extended-Reaction Liners

The final subject covered is sound propagation within the suppressor material itself and the resultant effect on the far-field sound pressure level suppression. As illustrated in figure III-21 the liner acts as a boundary condition that must be applied to the propagating sound waves within the duct.

Two broad distinctions in the type of liners that can be built are shown in figure III-22. On the left is shown a liner made of perforated plate bonded to honeycomb. This is a point-reaction liner, which means that sound can travel in the liner only in the direction normal to the liner. This type of suppressor provides an acoustic impedance type of boundary condition (as implied in fig. III-21) and is the liner commonly used in aircraft applications. Other variations could use wire mesh or other fibers bonded to the faceplate. The point-reaction liner is often called a single-degree-of-freedom (SDOF) liner. A second type of liner, called an extended-reaction liner or bulk absorber, is shown on the right. Sound is free to travel in all directions in the bulk absorber, and impedance boundary conditions no longer apply. The wave equation must be solved both in the bulk material and in the duct, and these solutions must be matched at the common interface. The bulk absorber has been known for quite some time to provide a wider attenuation bandwidth than the point-reaction liner. The problems with this liner have been associated with its wicking properties, or the ease with which it soaks up water, oil, and fuel. This causes the liner to lose its sound-absorbing properties and can also be a safety problem. Recent work at NASA Langley (ref. 15) and in the aircraft industry has shown that some fibrous materials can be made nonwicking and thus flightworthy. Therefore, a detailed study of the physics of bulk absorbers is justified and is being done under a university grant at the University of Texas, Austin, and under a contract with Hersh Acoustical Engineering, as well as in house.

A Lycoming YF-102 engine on a test stand where bulk absorber inlets were tested is shown in figure III-23. The large aft

suppressor assures that aft fan and jet noise do not contaminate the inlet noise. Three densities of Kevlar were tested in the inlet suppressor panels over the full speed range of the engine.

The sound power attenuation as a function of frequency is shown in figure III-24 for the best bulk-absorber and perforated-plate honeycomb liners that were tested. More extensive results are reported in reference 16. Both liners were designed for a blade passing frequency of 5000 hertz, and their attenuations are about the same at that frequency. At higher and lower frequencies the bulk absorber has a larger attenuation. The higher frequency improvement can be explained by the difference in the acoustic reactance between the two materials. However, at the lower frequencies both materials have about the same acoustic impedance characteristics. The extended-reaction properties of the Kevlar liner must be invoked to explain the low-frequency improvement.

Just a few of the efforts to better understand the details of suppressor performance have been discussed in this paper. This improved understanding has resulted in better suppressors, and it can be expected that even more efficient suppressors will evolve.

JET NOISE TECHNOLOGY

For jet-powered aircraft the most important noise source at takeoff is usually the jet exhaust noise. Considerable research has been conducted over the last several years on the jet noise problems of subsonic aircraft. This section summarizes some recent advances in jet noise technology applicable to advanced supersonic cruise aircraft and progress toward understanding flight effects on jet engine exhaust noise.

Inverted-Velocity-Profile Coannular Jets

A few years ago, inverted-velocity-profile coannular jets were identified as a breakthrough in jet noise suppression applicable to advanced supersonic cruise aircraft (e.g., ref. 17). As illustrated in figure III-25, this approach is to exhaust the higher velocity stream through an annulus, with the lower velocity stream in the middle. Such velocity profiles can be obtained by crossducting the fan and core streams (e.g., ref. 18) or by burning in the fan duct and thereby increasing the fan stream velocity above that of the core stream (e.g., ref. 19). Engines incorporating these approaches are further described in paper XI, SUPERSONIC PROPULSION TECHNOLOGY.

The noise benefits of the inverted velocity profile are shown in figure III-26. The normalized peak perceived noise level is

plotted against the mass-averaged jet velocity (ideal specific thrust) for several of the many configurations tested (refs. 20 and 21). A reference curve is also shown for a hypothetical, perfectly mixed conical nozzle. For all these coannular nozzle data, the outer-stream velocity is 1.5 to 2.0 times that of the inner stream. Noise reductions with the coannular nozzles, relative to the conical nozzles, generally improve as the ratio of the inner diameter to the outer diameter of the outer stream increases. The area ratio and the velocity ratio between the two streams also influence the noise levels at a given mass-averaged velocity. Further results are discussed in references 20 to 32.

Since the noise is a complicated function of flow-field and geometric parameters, it is necessary to go beyond simple plots such as figure III-26 to correlate the data (e.g., refs. 33 to 35). The complexity of the inverted-velocity-profile jet-noise-generating processes is illustrated in figure III-27. As many as four noise-generating regions must be considered. The low-frequency noise is generated well downstream of the nozzle, where the two flows have mixed and can no longer be distinguished; this is the merged region. The higher frequency jet mixing noise is generated near the nozzle exit, where the individual jets can still be identified; this is the premerged region. When either or both streams are supersonic, noise can be generated by turbulent eddies passing through shock waves; thus, we must in general consider both inner-stream and outer-stream shock noise.

We have developed empirical models relating these noise-generating processes to those of a simple conical nozzle (refs. 33 to 35). Small-scale, plugless, coaxial-nozzle experimental spectra (ref. 30) are compared with predictions based on the empirical model of reference 33 in figures III-28 and III-29. In figure III-28, sound pressure level is plotted against frequency for an angle of 120°, in the rear quadrant. For this case both streams are supersonic, so all four noise sources must be considered. But it is the jet mixing noises that dominate. The shock noises, predicted by an empirical modification to the theory of Harper-Bourne and Fisher (ref. 36), contribute somewhat in the high-frequency range, but not as much as the premerged mixing noise. Figure III-29 shows results for the same conditions, but in the forward quadrant at 75°. Shock noise becomes much more important here. The inner-stream shock noise dominates the midfrequency range and determines the peak sound pressure level. The outer-stream shock noise controls the high-frequency range. Although the relative contributions of the various sources differ in the forward and rear quadrants, the spectra at both angles are predicted with good accuracy.

Typical results for an engine with a coannular plug nozzle are shown in figure III-30. The perceived noise level is plotted as a function of angle at a typical sideline distance. The symbols denote model-scale experimental data obtained by General Electric under NASA Lewis sponsorship (contract NAS3-19777) scaled up to engine size. The solid curve represents the total noise predicted from the empirical model of reference 33, the dash-dotted curve represents the predicted mixing noise from both the merged and premerged regions, and the dashed curve represents the predicted shock noise from both streams. Although the jet mixing noises are most important in this case, the shock noises do contribute somewhat in the forward quadrant. At higher power settings and in flight, the shock noises become even more important and can contribute significantly to the effective perceived noise level.

As discussed in paper XI, SUPERSONIC PROPULSION TECHNOLOGY, these results have now been verified statically at larger scale on the NASA/General Electric variable-cycle-engine testbed. It is also quite significant that the inverted-velocity-profile noise benefits have been verified under simulated flight conditions in model-scale tests conducted by Pratt & Whitney under NASA Lewis sponsorship (ref. 37).

Flight Effects on Jet Noise

The subject of flight effects on jet noise has been a rather controversial one in recent years. Some of the terminology needed to describe flight effects is defined in figure III-31. The cases considered herein are level flyovers at an airplane velocity of V_0. The observer is located at an angle θ from the engine inlet axis. In the present discussion, only the effect of flight on the overall sound pressure level is considered. Spectral effects, which usually are not very significant, are not discussed. Only conventional engines are considered, although analogous results have been obtained with inverted-velocity-profile jets.

According to classical jet noise theory, in-flight jet noise should follow a fairly simple relation, as the velocity arrows at the bottom of figure III-31 suggest. For a given absolute jet velocity V_j (shown by the upper, longer arrow), increasing the flight velocity V_0 (shown by the lower arrow) reduces the velocity of the jet relative to the air. This reduces the shear, and therefore the noise should be less in flight.

The current interest in flight effects was greatly stimulated a few years ago when Rolls-Royce (refs. 38 and 39) reported results like those shown in figure III-32, where the overall sound pressure level is plotted as a function of angle. The

static case is shown by the solid curve, and the corresponding flight case is shown by the dash-dotted curve. The noise in the rear quadrant was reduced, as expected. However, in some cases, such as the one shown here, the noise in the forward quadrant increased in flight. Further confusing the issue is the fact that model-jet simulated flight tests indicate that in-flight noise should be reduced at all angles, as shown by the dashed curve. Studies conducted or sponsored by NASA suggest that these apparent anomalies can be resolved when the engine internal noise is considered (refs. 40 to 46). The internal noise is amplified in the forward quadrant in flight by a sufficient amount (ref. 47) that the total in-flight noise exceeds the static level even though the jet noise is reduced.

As can be inferred from the preceding discussion, the type of flight effects to be expected depends on the relative levels of jet mixing noise and internal noise. To demonstrate this point, figure III-33 shows the flight effects for engines with different levels of internal noise relative to jet mixing noise. On the left are overall sound pressure level (OASPL) data as a function of angle for an HS-125 airplane with a Viper 610 engine at relatively low jet velocity, about 1100 feet per second (ref. 38); this represents relatively "high" internal noise. The predictions are based on semiempirical NASA methods (ref. 43). For this case a forward-quadrant noise increase is both predicted and observed. On the right is a similar plot for a DC-9 airplane with refanned JT8D engines at a jet velocity of about 1500 feet per second (ref. 41); this represents relatively "low" internal noise. For this case, noise reductions in flight are predicted and observed at all angles. Comparing improved prediction methods (ref. 48) with flight data shows agreement, with a standard deviation of about 1.5 decibels.

The major developments in jet noise technology can be summarized as follows: Inverted-velocity-profile noise reductions have been demonstrated for a wide range of nozzle geometries at model scale and have now been verified statically at larger scale on the variable-cycle-engine testbed. Furthermore, inverted-velocity-profile noise reductions have been verified under simulated flight conditions in model-scale tests. Flight effects have proven to be predictable with reasonable accuracy when all the noise sources are properly accounted for.

COMBUSTOR NOISE

After the fan and the jet, the engine core is the next most significant source of noise. Figure III-34 shows data from the YF-102 engine that illustrates this fact. When fan noise is reduced, the engine noise signature tends to be dominated by low-frequency noise, which is shown in figure III-34 as acoustic power data. This low-frequency noise comes from the jet and the

core. Moreover, the levels of the jet and core noises are comparable and intersect somewhere in the normal operating range of the engine, as shown. As a result, at low engine power settings, core noise tends to dominate. Low-frequency core noise is essentially all from the combustor. Consequently, this discussion focuses on combustor noise generation and propagation.

Research for other engine noise sources is fairly mature and is focused on specific critical problems. Combustor noise research at Lewis is in a formative stage characterized by rather general objectives at this time. These objectives include the acquisition of a valid noise data base and information on the nature of combustor noise generation and propagation. From this information, empirical or analytical models of noise generation and propagation can be developed to give a predictive capability that in part will support the NASA noise prediction objectives discussed here. The entire program, of course, points toward the ultimate goal of developing noise reduction methods.

Examination of engine operation reveals a number of problem areas associated with combustor noise research. Principal among these is the combustor itself. Since the combustor is an acoustic source, the noise generated is influenced by the environment in which it operates - in acoustical terms, by the impedances at its boundaries. Operation of a combustor outside an engine in general will be acoustically different from in situ operation. Therefore, definitive information on combustor noise-generation characteristics must be derived from actual engine operation. Once the noise is generated, it must propagate through the turbine and then through the nozzle, both of which can subject it to attenuation. It then propagates through the flow and shear layers of the jet, where refraction and scattering are possible, before it radiates to the far field. Obviously, actual engine operation also is the only definitive source of combustor far-field noise. This creates an additional problem area since it requires some ingenuity to discriminate and measure only combustor noise in the presence of the other engine noises.

As a practical matter, testing engines is costly and this prohibits parametric investigations. Therefore, component tests are mandatory in conducting research. (This is true of combustor source noise research as well as of turbine and nozzle propagation research.) Combustor component tests allow parametric investigations of noise-generating mechanisms at tolerable cost. Also, they can be used to obtain acoustic power measurements. However, since it is likely that a combustor will generate a different noise in a rig than in an engine, an important problem associated with component testing is the need to understand any anomalies of combustor operation in test rigs. Some preliminary findings relating to this point are given in reference 49.

Direct Measurement of Combustor Far-Field Noise by Correlation Techniques

An important problem is the detection and measurement of only combustor far-field noise in the presence of noise from other engine sources. Figure III-35 schematically illustrates the YF-102 engine and microphones used to obtain far-field noise. The usual method of obtaining engine combustor noise is to measure the total noise signature and then to use the properties shown in figure III-34 to infer from the changing slope of the data with engine speed when the noise is dominated by the core. This method has obvious drawbacks, one of which is the limited range of power settings for which it is useful.

A more direct way of measuring far-field combustor noise from an engine has been demonstrated. It has the advantage of being more definitive than the traditional method and is not limited to engine power settings where combustor noise is dominant. The method makes use of internal fluctuating pressure and the total far-field noise to obtain the far-field combustor noise.

Some results from YF-102 engine tests are shown in figure III-36. The top graph shows the coherence between the internal and far-field signals. The coherence is the square of the cross-spectrum between the internal and far-field signals normalized by the product of the internal and far-field spectra. It is the frequency-domain analog of the cross-correlation function. The coherence function can have a value only between 0 and 1 and can be interpreted in this case as the fraction of mean-square acoustic energy in the far-field signal due to the internal signal. In the bottom graph, the upper curve is the engine total far-field spectrum as measured directly by a single far-field microphone. By applying the coherence function to this spectrum, that portion which is identifiable with the combustor is extracted, as shown. This measurement technique is not novel, but this is thought to be its first use to obtain combustor noise from a complete engine. A significant contributor to the success of the technique was the development of the probes used to obtain the fluctuating internal pressure. This method provides a direct way of measuring combustor far-field noise from engines in order to contribute to a valid data base. This work is discussed more completely in references 50 to 52.

Combustor Acoustic Power

A central problem in the combustor noise field is to determine the acoustic energy generated by the source. An analytical capability to do this is far beyond the state of the art, and current efforts are directed at developing empirical methods from test data. Figure III-37 shows much of the available data

and how the acoustic power generated is related in some manner to the heat release rate. Data have been generated for a variety of combustor types, and these data are largely from component rig tests. Equally important as the quantity and variety of data is the discovery of normalizing parameters for the acoustic power and the heat release rate that collapse the data onto a reasonable curve. The normalizing parameters are not explicitly noted, for simplicity, but they involve the various design and operational variables of the combustors. Although some data scatter remains, it is not unreasonable considering the wide variety of combustors included and the present state of the art. This empirical correlation is a significant step toward developing a combustor model. The correlation and its development are discussed fully in reference 53.

In addition to combustor far-field noise and combustor source acoustic power, propagation of low-frequency core noise through the turbine, nozzles, and jet flow is receiving attention. Significant programs have been completed or are under way in these areas under contracts to the General Electric Co. and the Lockheed-Georgia Co. Recent work completed is reported in references 54 and 55.

AIRCRAFT NOISE PREDICTION: STATUS AND FUTURE APPLICATIONS

Designers of new aircraft have been forced in recent years to accept propulsion noise as a critical design constraint. Tradeoffs among many variables, including noise, must be considered before an aircraft that meets all mission requirements emerges from the preliminary design process. An accurate, validated system for aircraft noise prediction is clearly required.

As indicated in figure III-38, aircraft noise prediction is based on three calculations. First, the aircraft trajectory must be calculated from engine cycle and aerodynamic data. Next, the noise characteristics of the various propulsion system components must be calculated and summed. Finally, atmospheric propagation and ground effects must be calculated to represent the properties of the noise that actually reaches an observer (or microphone) on the ground.

A comprehensive computer program, the Aircraft NOise Prediction Program (ANOPP), that implements the steps shown in the first figure has been developed by NASA (ref. 56). The diagram shown in figure III-39 illustrates the computational flow. From engine cycle and aircraft aerodynamic data, the aircraft trajectory is computed as a function of time. From the engine thermodynamic state variables together with certain physical data, the component noise characteristics are calculated. For

example, the noise-critical parameters required by the combustor-noise prediction module include the mass flow rate, the combustor inlet temperature and pressure, and the turbine inlet and exhaust temperatures. For each time interval or aircraft position, the component noise characteristics are calculated and summed to give the total noise produced by the engine. Propagation and ground effects are then calculated to produce received-noise characteristics in the form of 1/3-octave spectra at one or more arbitrary observer positions. Levels for any of the subjective noise scales are then calculated and plotted.

The ANOPP noise prediction modules have been developed by the Langley, Lewis, and Flight Research Centers and are maintained and updated by Langley and Lewis.

ANOPP is currently operational at Langley, where it is also available to other NASA Centers through remote terminal access. ANOPP is available to other users through the Control Data Corp. Cybernet commercial data processing network.

Some recent comparisons of ANOPP-predicted noise levels with measured data are shown in figures III-40 to III-42. The first comparison, shown in figure III-40, is for the turbojet-powered Concorde. There is good agreement between calculated and measured perceived noise levels plotted as a function of the directivity angle to the engine inlet θ. The spectra at a directivity of 130^{o} agree well up to about 1 kilohertz. The discrepancy at higher frequencies may be due to the omission of turbomachinery noise from the calculated levels.

The next comparison, shown in figure III-41, is for the low-bypass-ratio-powered DC-9. The calculations for tone-corrected perceived noise levels agree well with the measured data except for peak levels at a directivity of 120^{o} where a 3- to 5-PNdB difference exists. ANOPP underpredicts the effective perceived noise level by 1.2 EPNdB. The predicted and measured spectra at a directivity angle of 120^{o} would be nearly coincident except for the unexplained consistent difference in level.

The final comparison, shown in figure III-42, is for the high-bypass-ratio-powered DC-10 at takeoff. The tone-corrected perceived noise levels and spectral comparisons show a slight average overprediction. ANOPP overpredicts the effective perceived noise level by 1.6 EPNdB. The noise levels shown in this figure are based on data from McDonnell-Douglas, who also made the ANOPP calculations.

For all the previous aircraft, NASA had no role in the data acquisition and reduction process; and, for all cases, the values of the noise-critical parameters were not available as

recorded data but were estimated by others ex post facto. Considering the uncertainties inherent in the measured noise levels and in the estimated values of the engine cycle parameters, the agreement between the measured flyover noise levels and the ANOPP-predicted levels is encouraging. However, because severe economic penalties result from each decibel of noise design margin, the highest level of prediction accuracy is absolutely essential. ANOPP should continue to be developed until this goal has been met.

As indicated, propulsion noise must be treated as a critical constraint during the preliminary aircraft design process. The application of ANOPP to preliminary design systems studies or parametric analyses is illustrated in figure III-43.

A few of the key dimensionless variables are the thrust-weight ratio T/W, which sizes the propulsion system; the lift-drag ratio C_L/C_D, which represents the aircraft's aerodynamic characteristics; and the normalized specific thrust $T/\dot{m}C_a$, which is an indicator of source noise. The interrelationships among these and other dimensionless variables must be carefully studied before the ultimate compromise between noise at the FAA certification points, performance, and economics can be reached.

System trade-off studies involving aircraft noise often result in the identification of noise-generating phenomena or propagation effects that require individual research before final conclusions can be reached. The role of ANOPP in identifying critical noise research areas has been illustrated in a recent International Civil Aviation Organization (ICAO) study related to future SST noise standards.

As indicated in figure III-44, the effects of shock cell noise, advanced or automated flight procedures, and excess ground attenuation all emerged from the ICAO study as areas with unacceptably high levels of uncertainty. For example, the intensity of shock cell noise when the exhaust nozzle is operating at off-design conditions is not fully understood. Likewise, the noise reductions actually obtainable from the use of flight-profile optimizing techniques have never been demonstrated. Finally, the actual amount of excess ground attenuation, expecially at shallow angles, is the subject of a great deal of controversy. Research activities that focus on each of these phenomena are in progress at the Langley Research Center.

The value of ANOPP for design studies and, consequently, for quantifying the benefits of proposed noise reduction technology has been established. The Langley and Lewis Research Centers are committed to continued cooperative development and improvement of ANOPP for application to future parametric and pre-

liminary design studies of advanced aircraft system concepts. This would include executive system improvements, new prediction modules, and component and system validation.

SUMMARY

Fan Noise

Shock-related multiple-pure-tone noise from fans can be controlled to some extent by sweeping the rotor-blade leading edges. The concept is also applicable to the high-speed turboprop (see paper I, ACEE Status Report).

Inflow control devices appear to be an adequate approach to simulating the in-flight characteristics of fan noise in static testing. Experiments relating to the development of inflow control devices have also provided a great deal of insight into the several sources of fan noise that had not been fully appreciated.

Acoustic Suppression

Substantial advances have been made in understanding suppressor behavior and in simplifying suppressor concepts. The results show that, when the various factors in a suppressor design are adequately accounted for, there can be a large improvement in suppressor performance. It now appears that improved understanding of suppression, coupled with the new understanding of fan source noise, will soon permit us to achieve the long-standing objective of jointly optimizing the acoustic suppression and the fan design for low noise.

Jet Noise Technology

The noise reductions associated with inverted-velocity-profile coannular jets have been demonstrated for a large number of nozzle geometries at model scale and have now been verified at larger scale on the variable-cycle-engine testbed. These inverted-velocity-profile noise reductions have also been verified under simulated flight conditions in model-scale tests.

Flight effects on jet noise and low-frequency noise are now fairly well understood, with experimental static-to-flight noise increments agreeing with prediction within a standard deviation of about 1.5 decibels.

Combustor Noise

Combustor noise has been fairly well defined over the past few years. The sampling of results discussed is representative of a larger collection of new data and findings that has been developed. These new findings relate to the combustor acoustic power generation, acoustic transmission through the turbine and nozzle, and the development of new measurement techniques and a data base. From these new results a fairly comprenensive model of combustor noise can be developed. This is a necessary step toward reducing this noise.

Aircraft Noise Prediction

A working ANOPP computer program is now available that appears to provide an acceptable level of accuracy for CTOL aircraft with low- or high-bypass-ratio engines and for SST aircraft. The usefulness of the program in defining areas needing research has also been demonstrated.

REFERENCES

1. Russell, R. E.: The State of Aircraft Noise Technology. Presented at the EPA Noise Technology Research Symposium, Dallas, Texas, Jan. 29, 1979.

2. Bliss, D. B.; et al.: Design Considerations for a Novel Low Source Noise Transonic Fan Stage. AIAA Paper 76-577, July 1976.

3. Hayden, R. E.; et al.: Analysis and Design of a High Speed, Low Noise Aircraft Fan Incorporating Swept Leading Edge Rotor and Stator Blades. (BBN-3332, Bolt Beranek and Newman Inc., NASA Contract NAS3-18512.)

4. Lucas, J. G.; Woodward, R. P.; and MacKinnon, M. J.: Acoustic Evaluation of a Novel Swept-Rotor Fan. AIAA Paper 78-1121, July 1978. (Also NASA TM-78878.)

5. Feiler, C. E.; and Groeneweg, J. F.: Summary of Forward Velocity Effects on Fan Noise. AIAA Paper 77-1319, Oct. 1977. (Also NASA TM-73722.)

6. Shaw, L. M.; et al.: Inlet Turbulence and Fan Noise Measured in an Anechoic Wind Tunnel and Statically with an Inlet Flow Control Device. AIAA Paper 77-1345, Oct. 1977. (Also NASA TM-73723.)

7. Woodward, R. P.; et al.: Effectiveness of an Inlet Flow Turbulence Control Device to Simulate Flight Fan Noise in an Anechoic Chamber. NASA TM-73855, 1977.

8. Kantola, R. A.; and Warren, R. E.: Reduction of Rotor-Turbulence Interaction Noise in Static Fan Noise Testing. AIAA Paper 79-0656, Mar. 1979.

9. Jones, W. L.; McArdle, J. G.; and Homyak, L.: Evaluation of Two Inflow Control Devices for Flight Simulation of Fan Noise Using a JT15D Engine. AIAA Paper 79-0654, Mar. 1979. (Also NASA TM-79072.)

10. Rice, E.J.: Modal Propagation Angles in Ducts with Soft Walls and Their Connection with Suppressor Performance. AIAA Paper 79-0624, Mar. 1979. (Also NASA TM-79081.)

11. Rice, E. J.; Heidmann, M. F.; and Sofrin, T. G.: Modal Propagation Angles in a Cylindrical Duct with Flow and Their Relation to Sound Radiation. AIAA Paper 79-0183, Jan. 1979. (Also NASA TM-79030.)

12. Rice, E. J.: Optimum Wall Impedance for Spinning Modes - A Correlation with Mode Cutoff Ratio. J. Aircr., vol. 16, no. 5, May 1979, pp. 336-343.

13. Heidmann, M. F.; Saule, A. V.; and McArdle, J. G.: Analysis of Radiation Patterns of Interaction Tones Generated by Inlet Rods in the JT15D Engine. AIAA Paper 79-0581, Mar. 1979. (Also NASA TM-79074.)

14. Jones, W. L.; and Groeneweg, J. F.: State-of-the-Art of Turbofan Engine Noise Control. NOISE-CON 77, G. C. Maling, Jr., ed., Noise Control Foundation, 1977, pp. 361-380.

15. Smith, C. D.; and Parrott, T. L.: An Experimental Study of the Effects of Water Repellant Treatment on the Acoustics Properties of Kevlar. NASA TM-78654, 1978.

16. Heidelberg, L. J.; and Homyak, L.: Full-Scale Engine Tests of Bulk Absorber Acoustic Inlet Treatment. NASA TM-79079, 1979.

17. Willis, Edward: Variable-Cycle Engines for Supersonic Cruise Aircraft. Variable Geometry and Multicycle Engines, AGARD CP-205, 1976, pp. 7-1 to 7-19.

18. Krebs, J. N.: Advanced Supersonic Technology Study - Engine Program Summary: Supersonic Propulsion - 1971 to 1976. Proceedings of the SCAR Conference, NASA CP-001, Part 1, 1976, pp. 353-370.

19. Howlett, Robert A.: Variable Stream Control Engine Concept for Advanced Supersonic Aircraft - Features and Benefits. Proceedings of the SCAR Conference, NASA CP-001, Part 1, 1976, pp. 341-352.

20. Lee, Robert: Coannular Plug Nozzle Noise Reduction and Impact on Exhaust System Design. Proceedings of the SCAR Conference, NASA CP-001, Part 2, 1976, pp. 505-524.

21. Goodykoontz, Jack H.; and Stone, James R.: Experimental Study of Coaxial Nozzle Exhaust Noise. AIAA Paper 79-0631, Mar. 1979. (Also NASA TM-79090.)

22. Stone, James R.; Goodykoontz, Jack H.; and Gutierrez, Orlando A.: Effects of Geometric and Flow-Field Variables on Inverted-Velocity-Profile Coaxial Jet Noise and Source Distributions. AIAA Paper 79-0635, Mar. 1979. (Also NASA TM-79095.)

23. Sarohia, V.: Effect of Density on Noise Radiated from Inverted Velocity Profile Jets. AIAA Paper 79-0634, Mar. 1979.

24. Tanna, H. K.; Tester, B. J.; and Lau, J. C.: The Noise and Flow Characteristics of Inverted-Profile Coannular Jets. (Lockheed-Georgia Co.; NASA Contract NAS1-15018.) NASA CR-158995, 1979.

25. Strout, Frank G.: Flight Effects on Noise Generated by the JT8D Engine with Inverted Primary/Fan Flow as Measured in the NASA Ames 40- by 80-Foot Wind Tunnel. NASA CR-2996, 1978.

26. Cargill, A. M.; and Duponchel, J. P.: The Noise Characteristics of Inverted Velocity Profile Coannular Jets. AIAA Paper 77-1263, Oct. 1977.

27. Crouch, R. W.; Coughlin, C. L.; and Paynter, G. C.: Nozzle Exit Flow Profile Shaping for Jet Noise Reduction. AIAA Paper 76-511, July 1976.

28. Dosanjh, D.S.; et al.: Supersonic Jet-Noise Suppression by Coaxial Cold/Heated Jet Flows. AIAA Paper 76-507, July 1976.

29. Knott, P. R.; et al.: Acoustic Tests of Duct-Burning Turbofan Jet Noise Simulation. NASA CR-2966, 1978.

30. Kozlowski, Hilary; and Packman, Allan B.: Aerodynamic and Acoustic Tests of Duct-Burning Turbofan Exhaust Nozzles. NASA CR-2628, 1976.

31. Gutierrez, Orlando A.: Aeroacoustic Studies of Coannular Nozzles Suitable for Supersonic Cruise Aircraft Applications. Proceedings of SCAR Conference, NASA CP-001, Part 2, 1976, pp. 471-490.

32. Kozlowski, Hilary: Coannular Nozzle Noise Characteristics and Application to Advanced Supersonic Transport Engines. Proceedings of the SCAR Conference, NASA CP-001, Part 2, 1976, pp. 491-504.

33. Stone, James R.: An Empirical Model for Inverted-Velocity-Profile Jet Noise Prediction. NASA TM-73838, 1977.

34. Pao, S. Paul: A Correlation of Mixing Noise from Coannular Jets with Inverted Flow Profiles. NASA TP-1301, 1979.

35. Larson, R. S.: A Jet Exhaust Noise Prediction Procedure for Inverted Velocity Profile Coannular Nozzles. AIAA Paper 79-0633, Mar. 1979.

36. Harper-Bourne, M.; and Fisher, M. J.: The Noise from Shock Waves in Supersonic Jets. Noise Mechanisms, AGARD-CP-131, 1974, pp. 11-1 to 11-13.

37. Kozlowski, Hilary; and Packman, Allan B.: Flight Effects on the Aerodynamic and Acoustic Characteristics of Inverted Profile Coannular Nozzles. NASA CR-3018, 1978.

38. Brooks, J. R.; and Woodrow, R. J.: The Effects of Forward Speed on a Number of Turbojet Exhaust Silencers. AIAA Paper 75-506, Mar. 1975.

39. Bushell, K. W.: Measurement and Prediction of Jet Noise in Flight. AIAA Paper 75-461, Mar. 1975.

40. Stone, J. R.: On the Effects of Flight on Jet Engine Exhaust Noise. NASA TM X-71819, 1975.

41. Merriman, J. E.; et al.: Forward Motion and Installation Effects on Engine Noise. AIAA Paper 76-584, July 1976.

42. Blankenship, G. L.; et al.: Effect of Forward Motion on Engine Noise. (MDC-J7708, Douglas Aircraft Co., Inc.; NASA Contract NAS3-20031) NASA CR-134954, 1977.

43. Stone, James R.: Prediction of In-Flight Exhaust Noise for Turbojet and Turbofan Engines. Noise Contr. Eng., vol. 10, no. 1, Jan.-Feb. 1978, pp. 40-46.

44. Stone, J. R.: On the Use of Relative Velocity Exponents for Jet Engine Exhaust Noise. NASA TM-78873, 1978.

45. Ahuja, K. K.; Tester, B. J.; and Tanna, H. K.: The Free Jet as a Simulator of Forward Velocity Effects on Jet Engine Noise. NASA CR-3056, 1978.

46. Burcham, F. W., Jr.; Lasagna, P. L.; and Oas, S. C.: Measurements and Predictions of Flyover and Static Noise of a TF-30 Afterburning Turbofan Engine. NASA TP-1372, 1978.

47. Morse, P. M.; and Ingard, K. U.: Theoretical Acoustics. McGraw-Hill Book Co., Inc., 1968.

48. Stone, J. R.: An Improved Method for Predicting the Effects of Flight on Jet Mixing Noise. NASA TM-79155, 1979.

49. Reshotko, M.; and Karchmer, A. M.: Combustor Fluctuating Pressure Measurements In-Engine and in a Component Test Facility: A Preliminary Comparison. NASA TM-73845, 1977.

50. Reshotko, M.; et al.: Core Noise Measurements of a YF-102 Turbofan Engine, AIAA Paper 77-21, Jan. 1977.

51. Karchmer, A. M.; and Reshotko, M.: Core Noise Source Diagnostics on a Turbofan Engine Using Correlation and Coherence Techniques. NASA TM X-73535, 1976.

52. Karchmer, A. M.; and Reshotko, M.; and Montegani, F. J.: Measurement of Far Field Combustion Noise from a Turbofan Engine Using Coherence Functions. AIAA Paper 77-1277, Oct. 1977. (Also NASA TM-73748.)

53. von Glahn, U. H.: Correlation of Combustor Acoustic Power Levels Inferred from Internal Fluctuating Pressure Measurements. NASA TM-78986, 1978.

54. Doyle, V. L.; and Matta, R. K.: Attenuation of Upstream-Generated Low Frequency Noise by Gas Turbines. (R77AEG482, General Electric Co.; NASA Contract NAS3-19435.) NASA CR-135219, 1977.

55. Matta, R. K.; and Mani, R.: Theory of Low Frequency Noise Transmission Through Turbines. (R77AEG570, General Electric Co.; NASA Contract NAS3-20027.) NASA CR-159457, 1979.

56. Raney, J. P.: Noise Prediction Technology for CTOL Aircraft, NASA TM-78700, 1978.

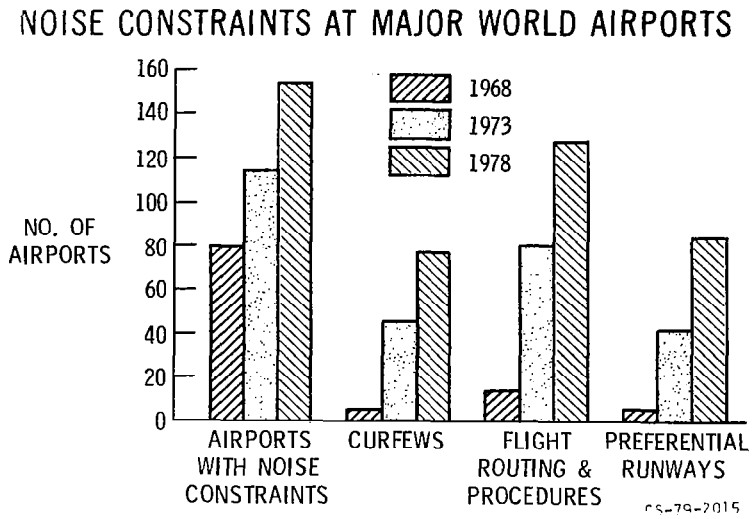

Figure III-1

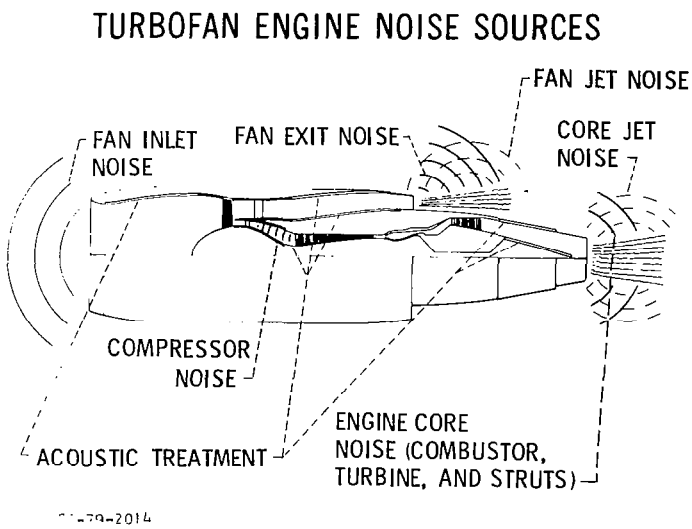

Figure III-2

FAN NOISE SOURCES

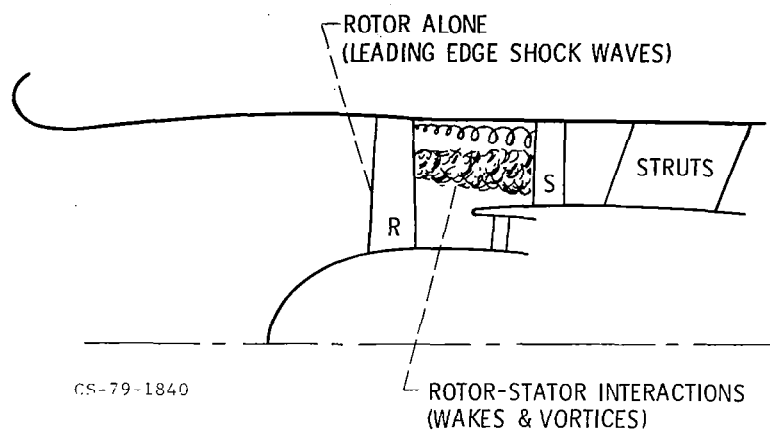

Figure III-3

FAN NOISE SPECTRA AT SUBSONIC AND SUPERSONIC TIP SPEEDS

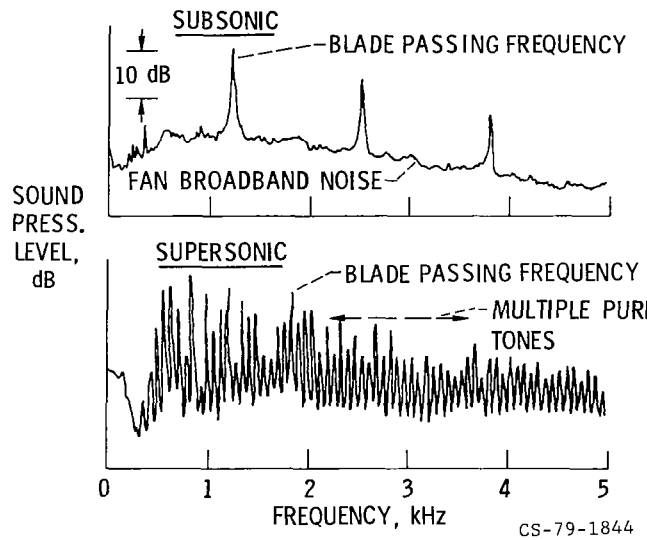

Figure III-4

SWEPT-ROTOR FAN

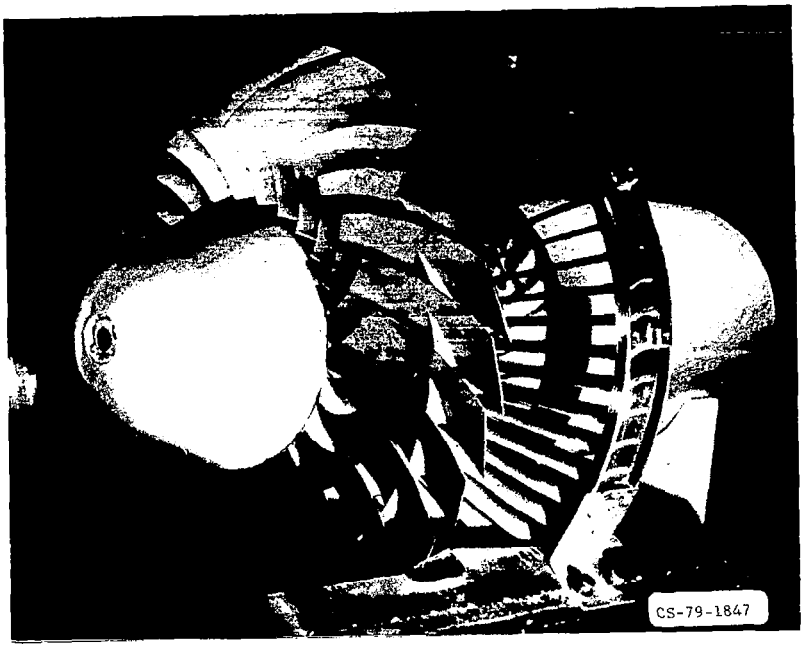

Figure III-5

SWEPT ROTOR BLADE

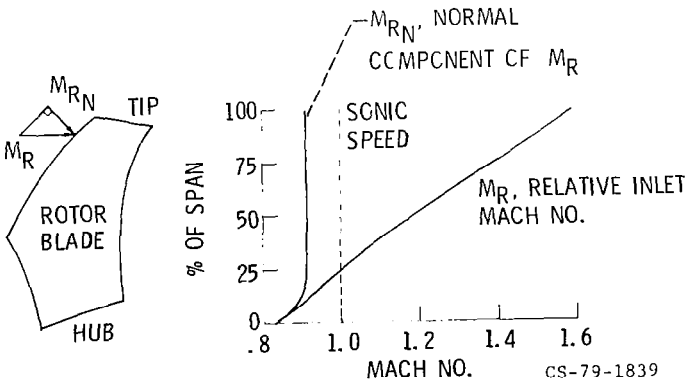

Figure III-6

MULTIPLE PURE TONE GENERATION OF UNSWEPT AND SWEPT-ROTOR FANS

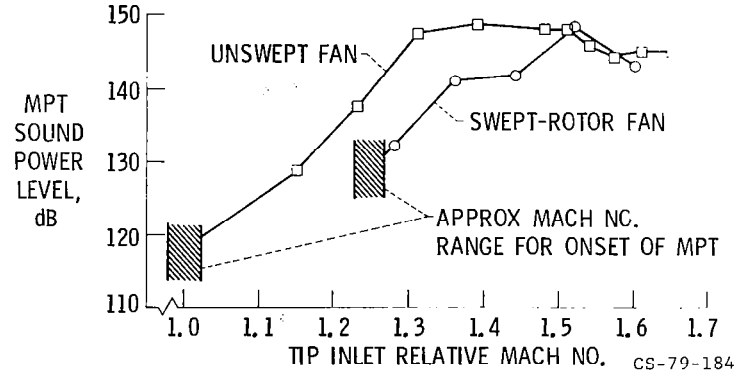

Figure III-7

FAN NOISE SOURCES

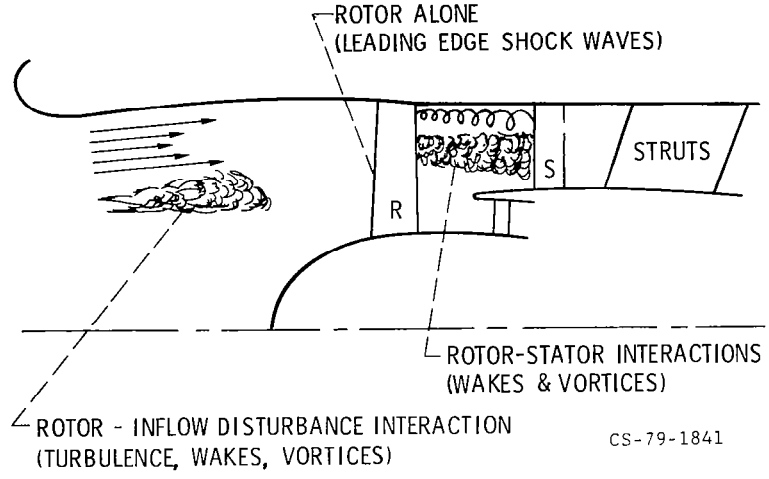

Figure III-8

FORWARD VELOCITY EFFECTS ON INLET FLOW AND NOISE

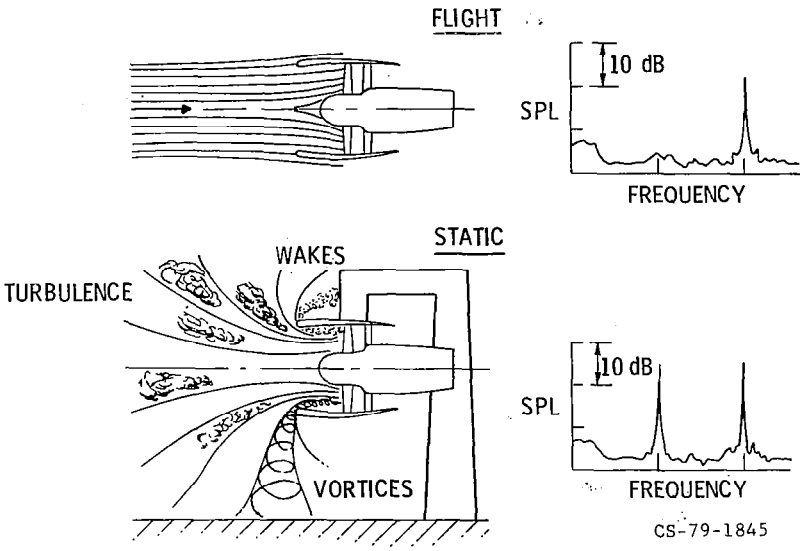

Figure III-9

INFLOW CONTROL DEVICE

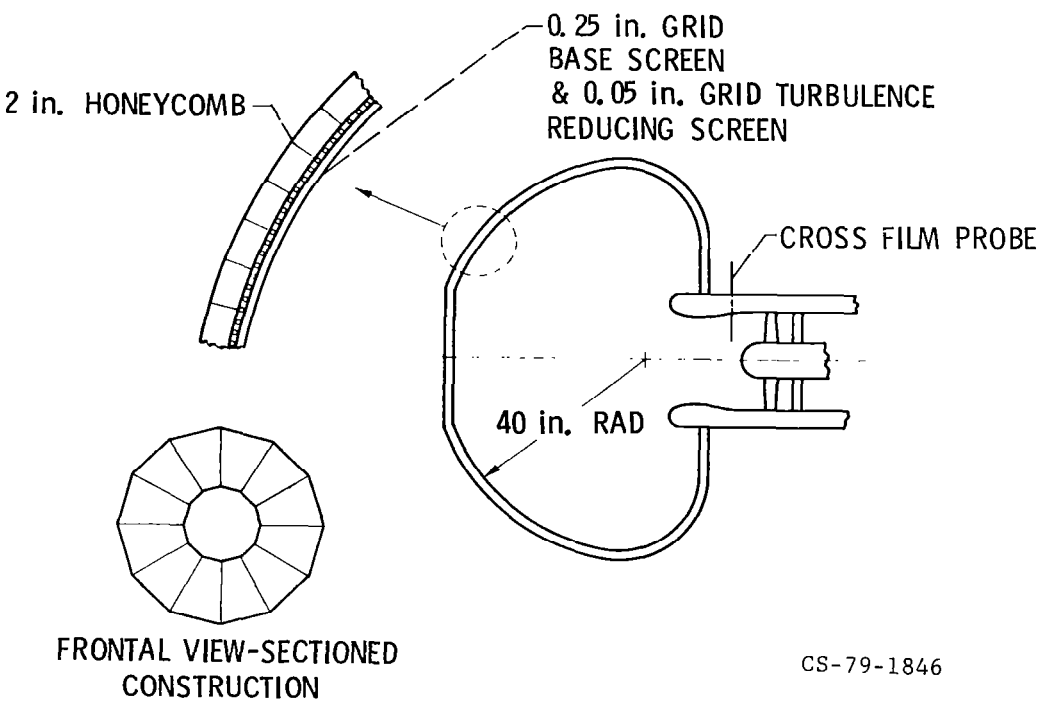

Figure III-10

INFLOW CONTROL DEVICE

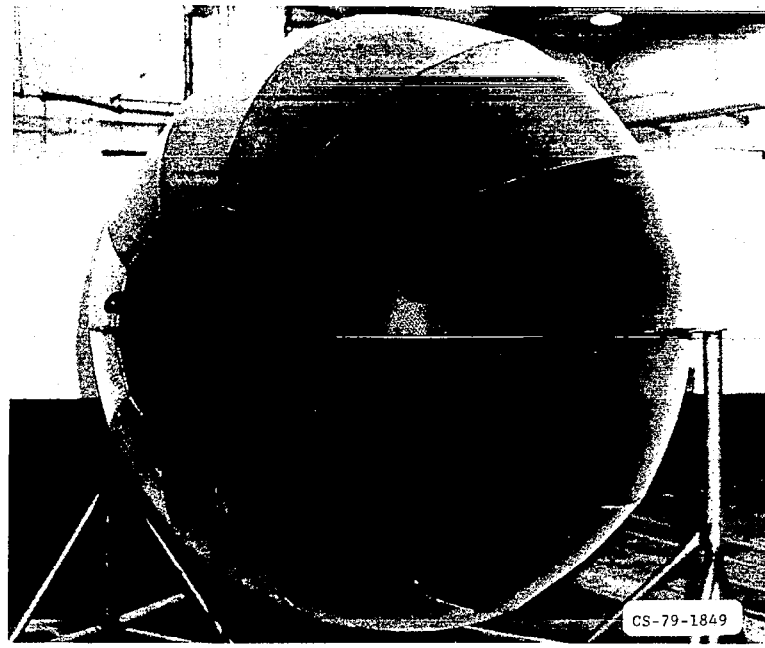

Figure III-11

INFLOW CONTROL DEVICE IN ANECHOIC CHAMBER

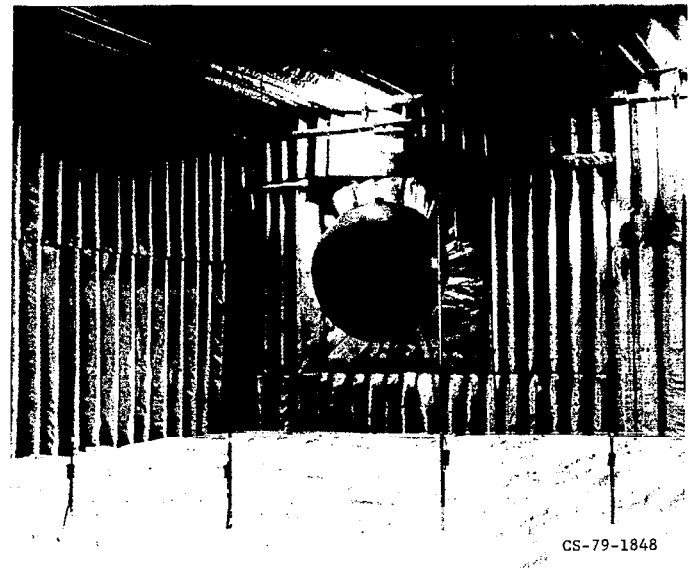

Figure III-12

AEROACOUSTIC EFFECTS OF INFLOW CONTROL DEVICE

	INLET TURBULENCE	
INFLOW CONTROL DEVICE	TRANSVERSE INTENSITY, %	AXIAL LENGTH SCALE, ft
—— WITHOUT	1.1	18.7
---- WITH	.2	3.3

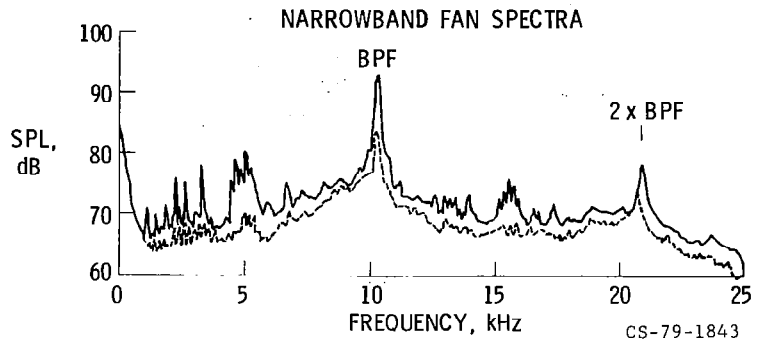

Figure III-13

INFLOW CONTROL DEVICE INSTALLED ON JT15D ENGINE

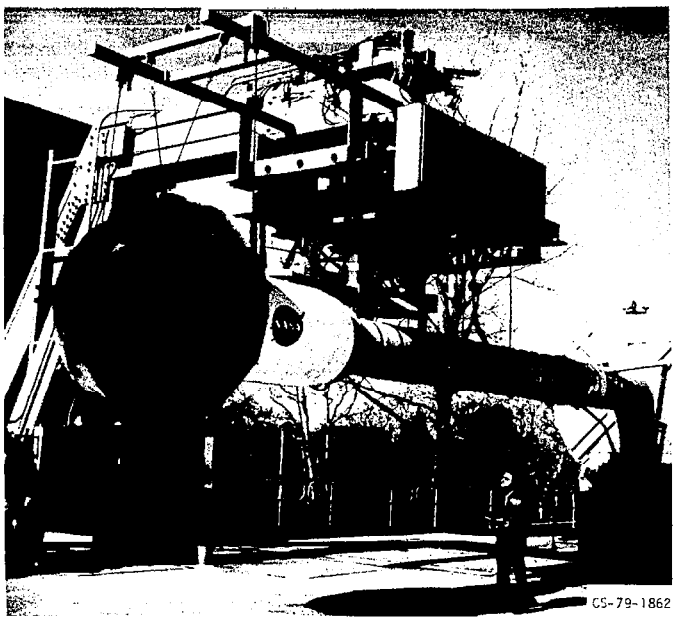

Figure III-14

OV-1 AIRCRAFT TO BE USED FOR JT15D FLYOVER NOISE TESTS

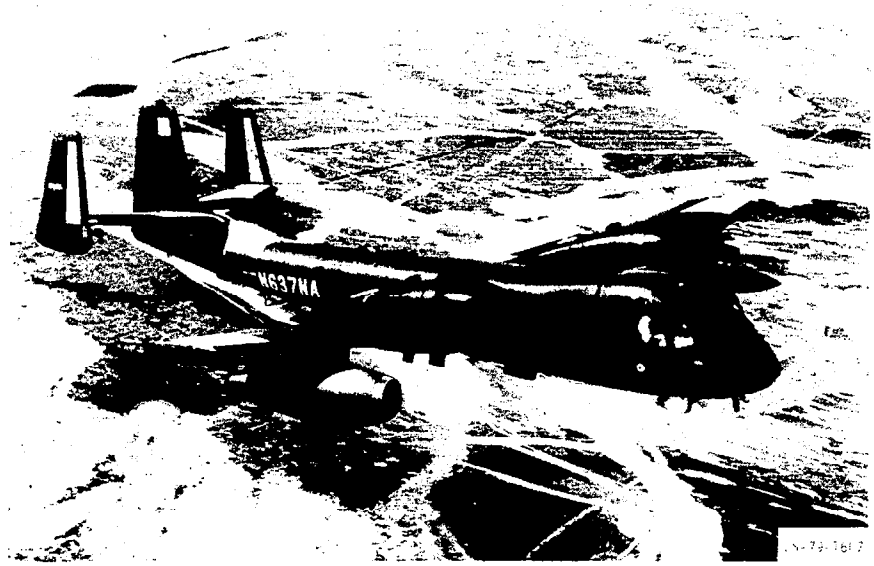

Figure III-15

COMPONENTS OF SUPPRESSOR ANALYSIS

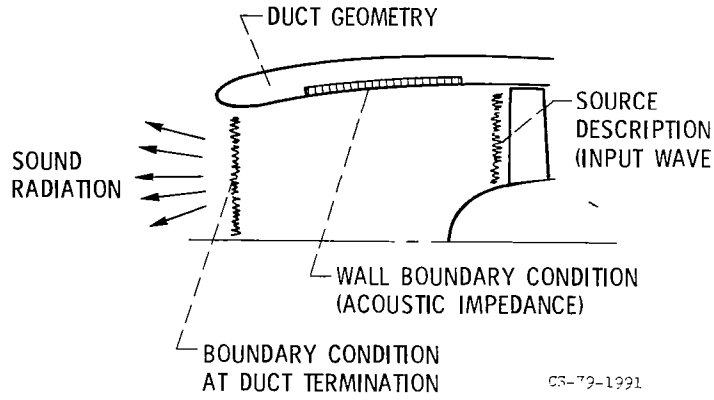

Figure III-16

COMPONENTS OF SUPPRESSOR ANALYSIS

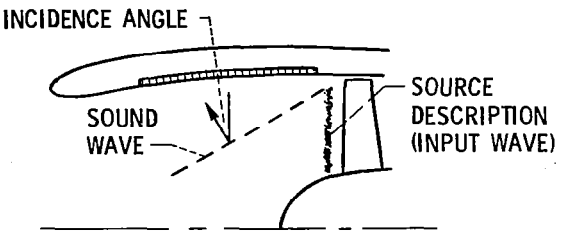

CS-79-1988

Figure III-17

EFFECT OF BOUNDARY LAYER THICKNESS UPON OPTIMUM RESISTANCE – INCIDENCE ANGLE CORRELATION

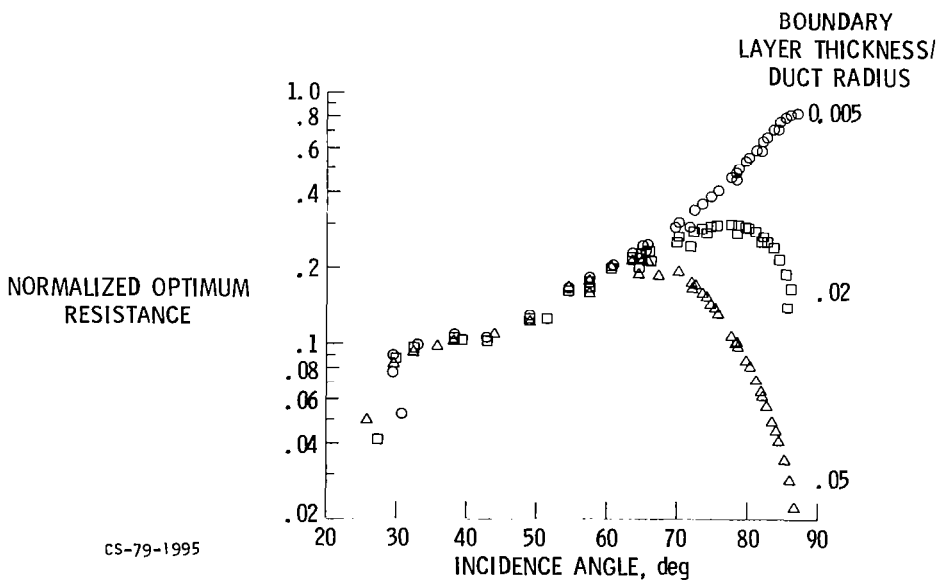

CS-79-1995

Figure III-18

COMPARISON OF MEASURED AND PREDICTED TONE DIRECTIVITIES

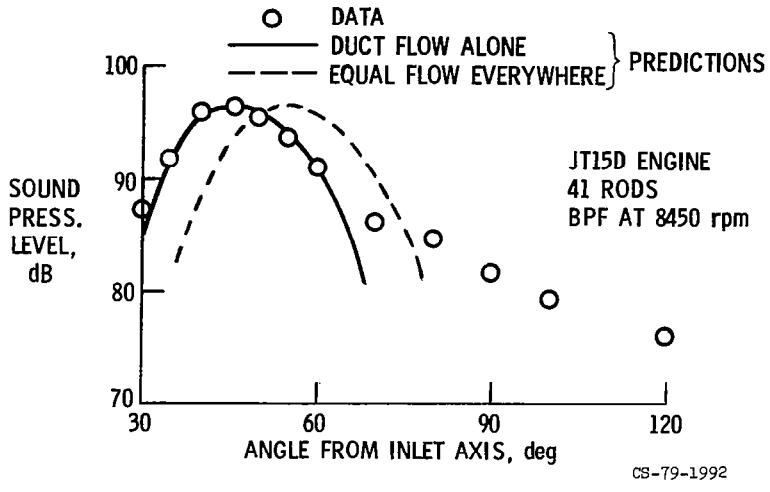

Figure III-19

PERFORMANCE OF SUPPRESSORS BASED ON TWO DESIGN METHODS

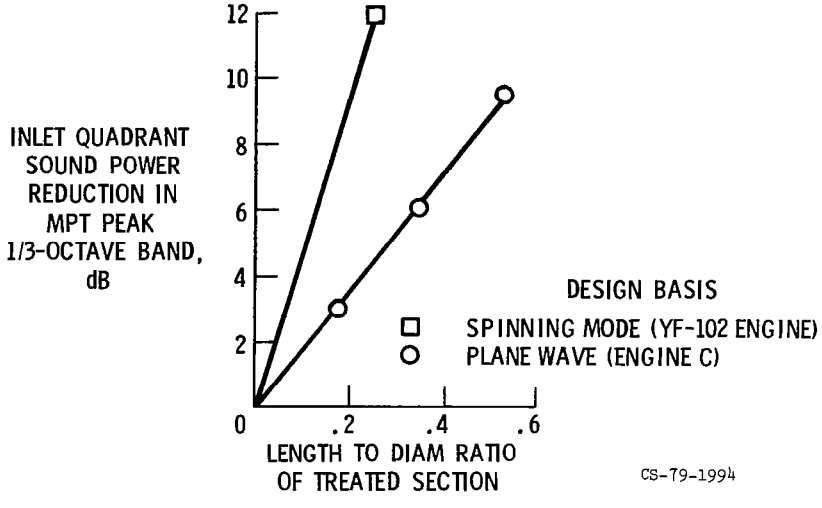

Figure III-20

COMPONENTS OF SUPPRESSOR ANALYSIS

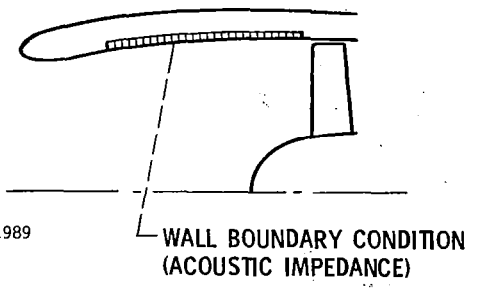

Figure III-21

LINING MATERIALS AND CONSTRUCTION

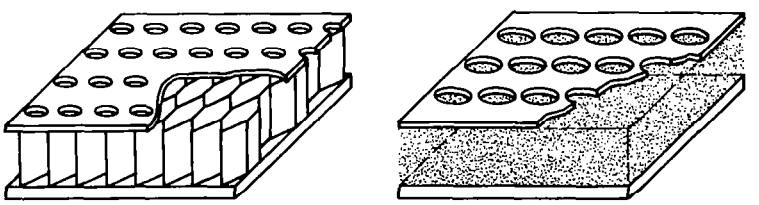

Figure III-22

AVCO-LYCOMING YF-102 ENGINE ON TEST STAND

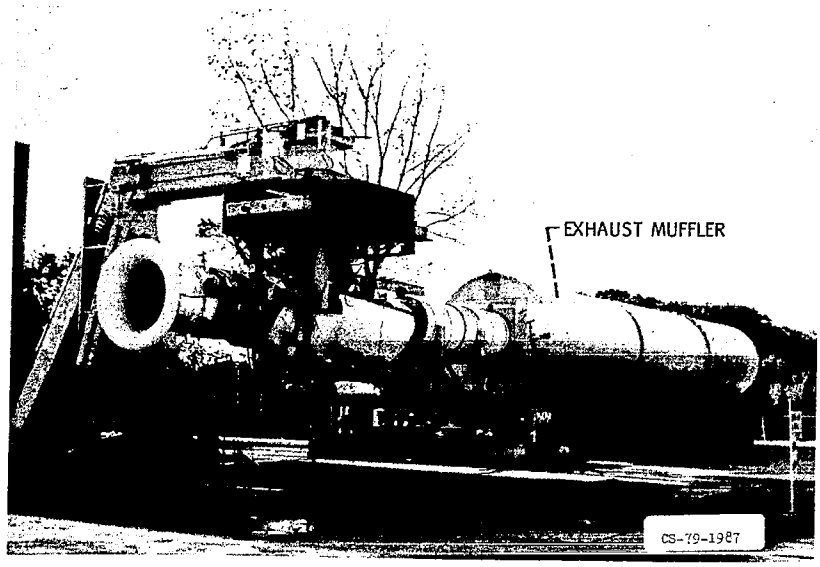

Figure III-23

COMPARISON OF SOUND POWER ATTENUATION SPECTRA FOR BULK AND SDOF LINERS

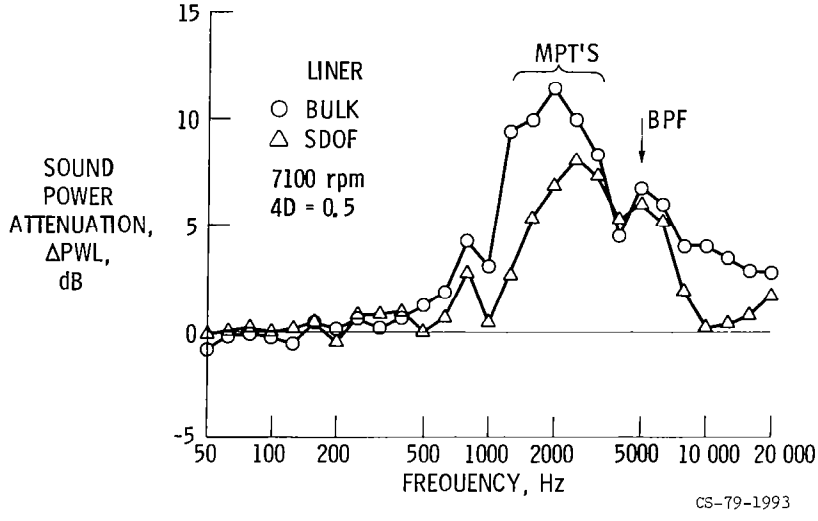

Figure III-24

INVERTED-VELOCITY-PROFILE COANNULAR JETS

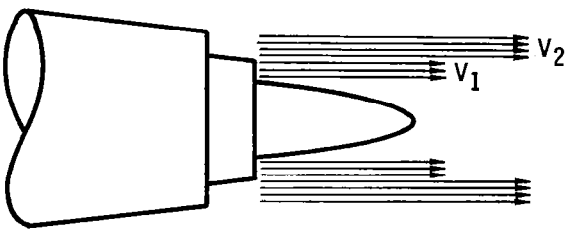

CS-79-1850

Figure III-25

NORMALIZED PEAK PNL AS FUNCTION OF MASS-AVERAGED JET VELOCITY

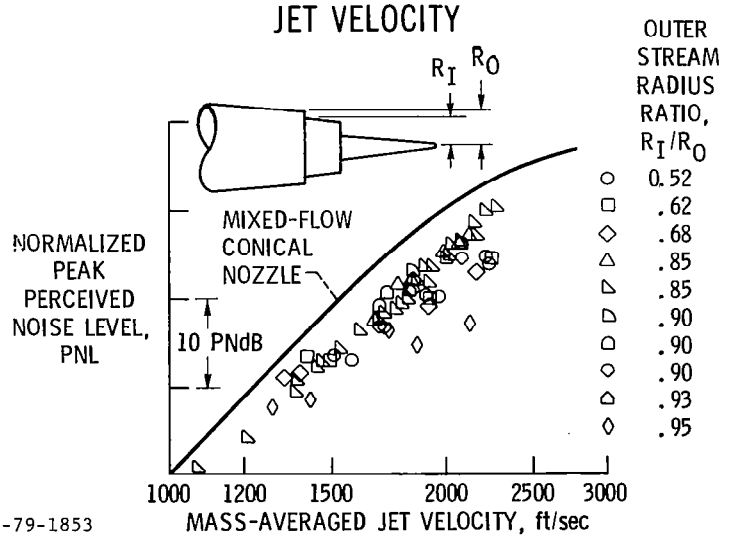

CS-79-1853

Figure III-26

INVERTED-VELOCITY-PROFILE JET NOISE SOURCES

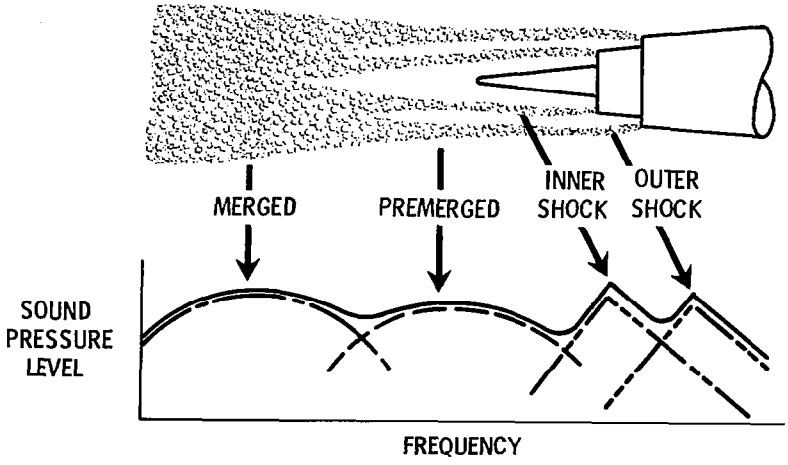

Figure III-27

COMPARISON OF INVERTED-VELOCITY-PROFILE JET NOISE PREDICTION WITH STATIC MODEL EXPERIMENTAL DATA

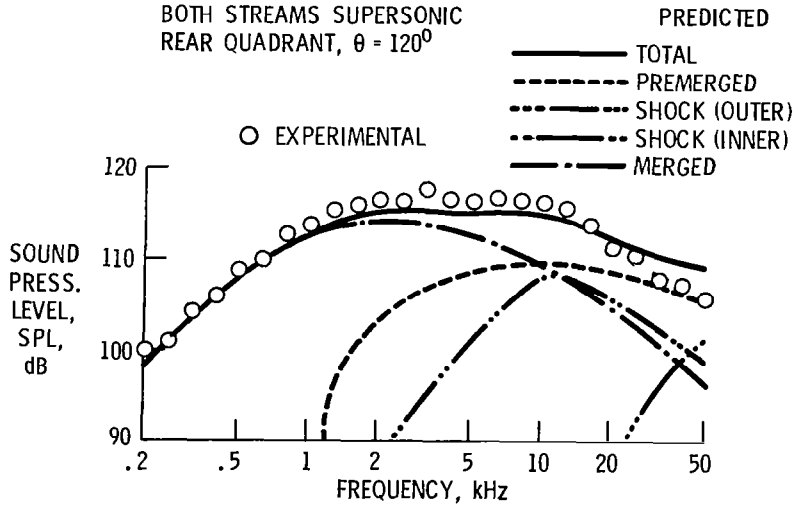

Figure III-28

COMPARISON OF INVERTED-VELOCITY-PROFILE JET NOISE PREDICTION WITH STATIC MODEL EXPERIMENTAL DATA

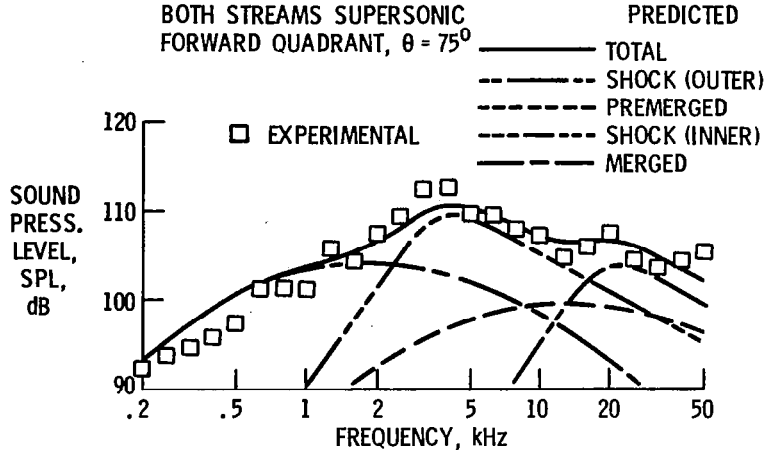

Figure III-29

COMPARISON OF EXPERIMENTAL AND PREDICTED PNL DIRECTIVITY

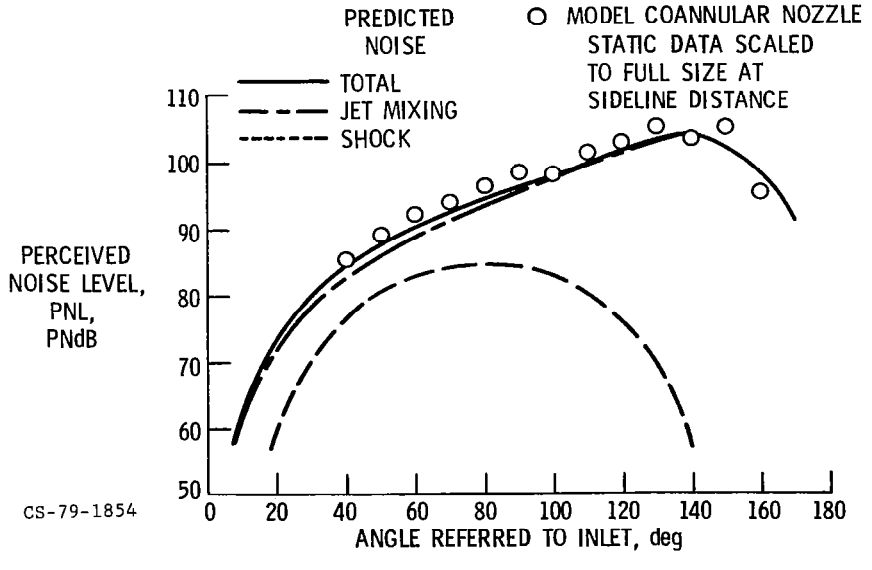

Figure III-30

FLIGHT EFFECTS ON EXHAUST NOISE

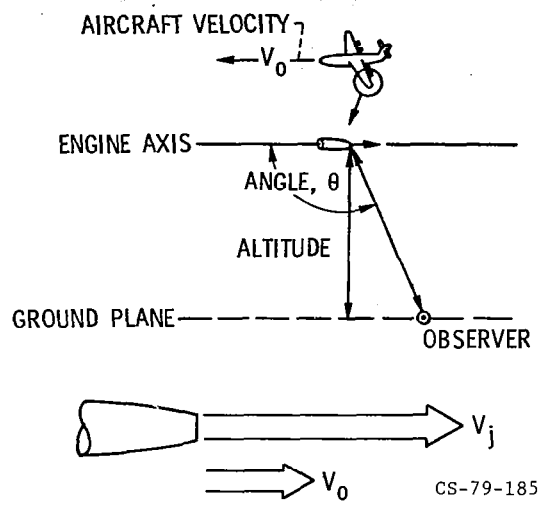

Figure III-31

TYPICAL FLIGHT EFFECTS ON EXHAUST NOISE

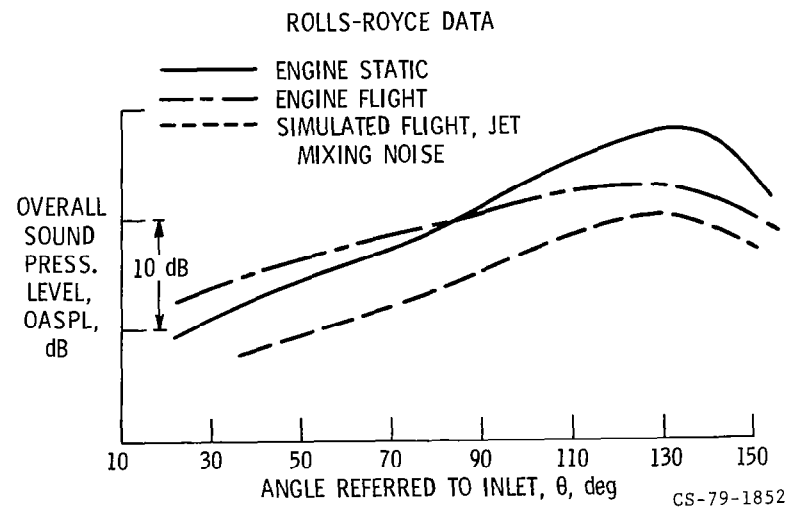

Figure III-32

STATIC AND FLIGHT DIRECTIVITIES FOR DIFFERENT TYPE ENGINES

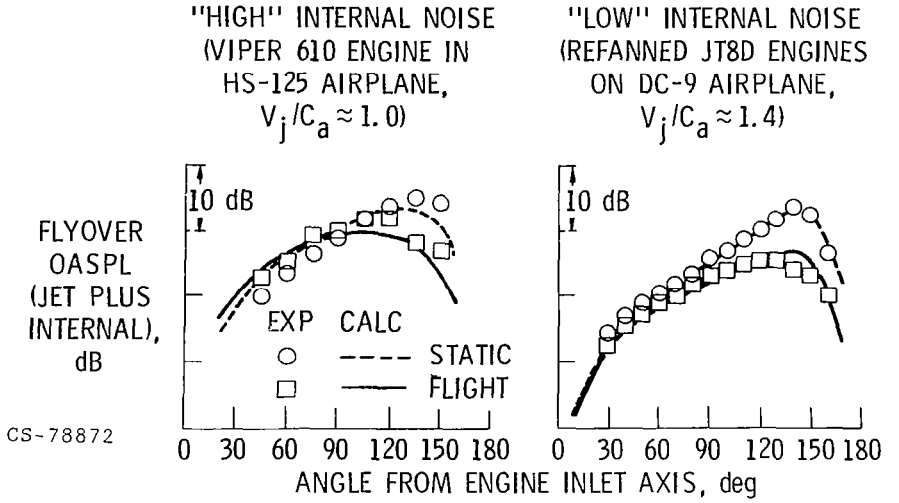

Figure III-33

YF-102 ENGINE FAR-FIELD ACOUSTIC POWER

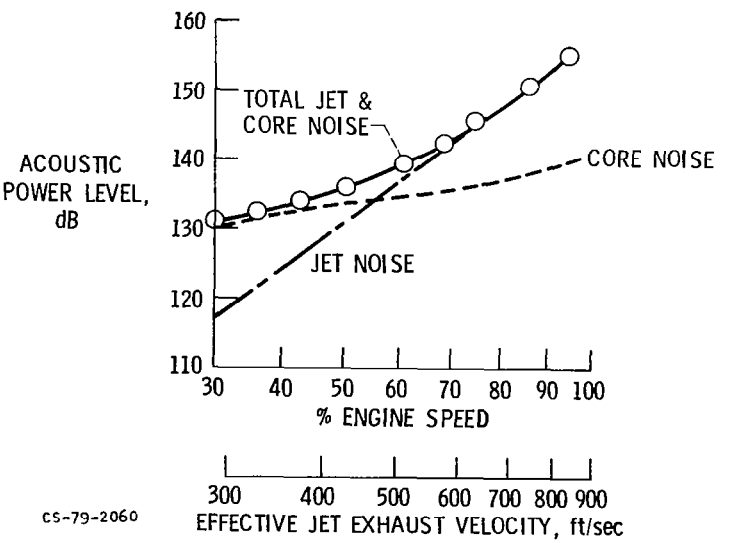

Figure III-34

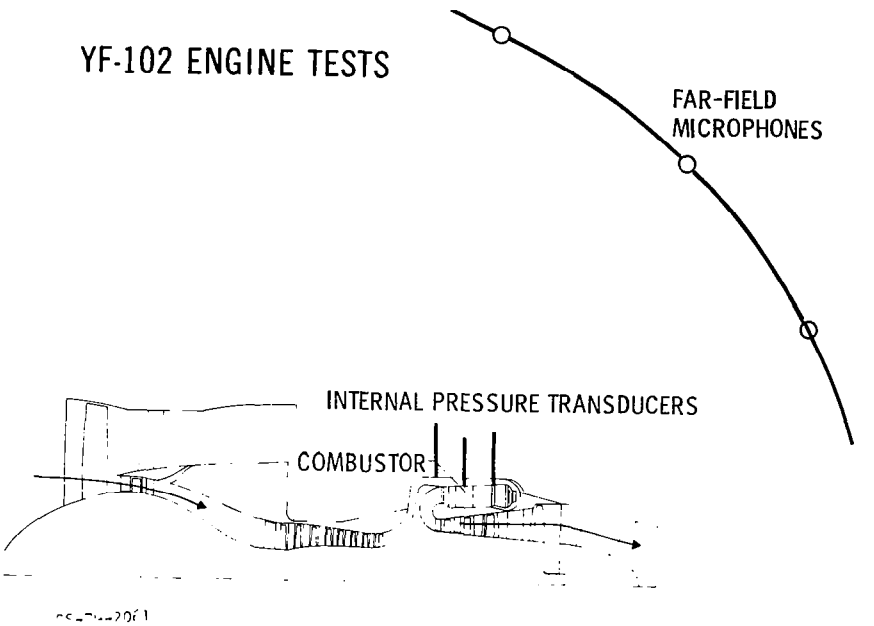

Figure III-35

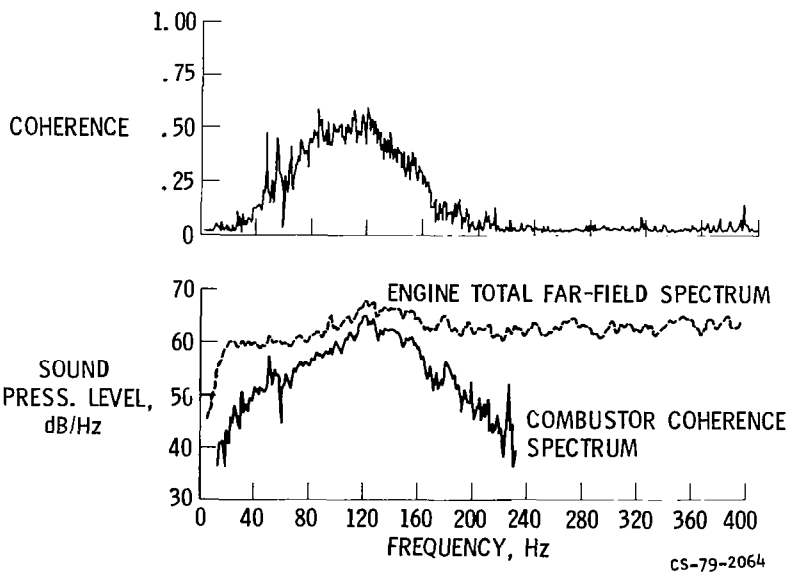

Figure III-36

CORRELATION OF COMBUSTOR ACOUSTIC POWER LEVELS INFERRED FROM INTERNAL FLUCTUATING PRESSURE MEASUREMENTS

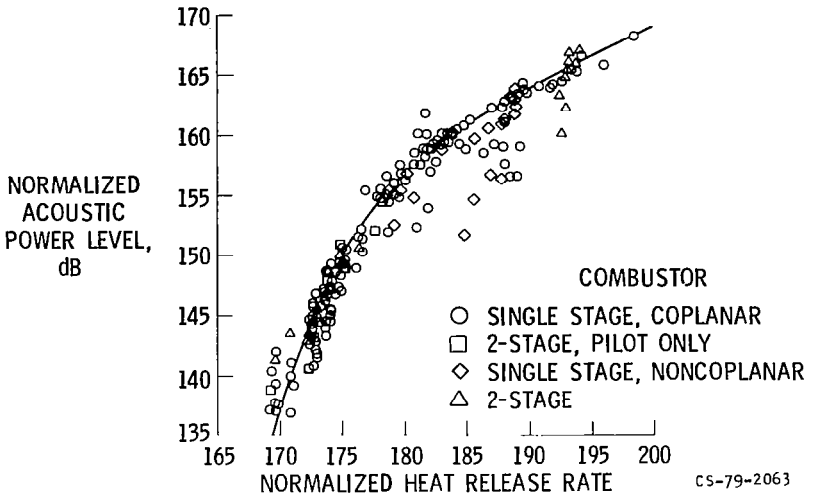

Figure III-37

PREDICTION METHODOLOGY

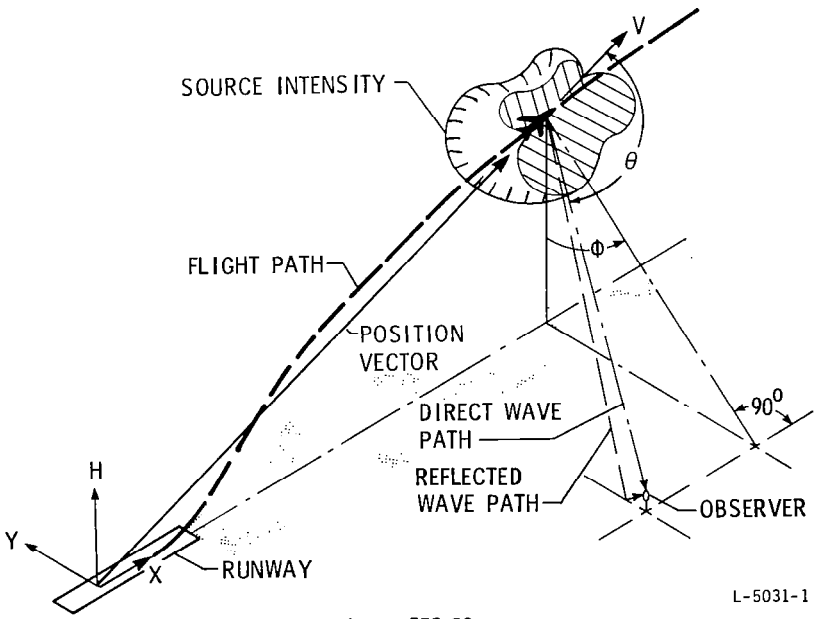

Figure III-38

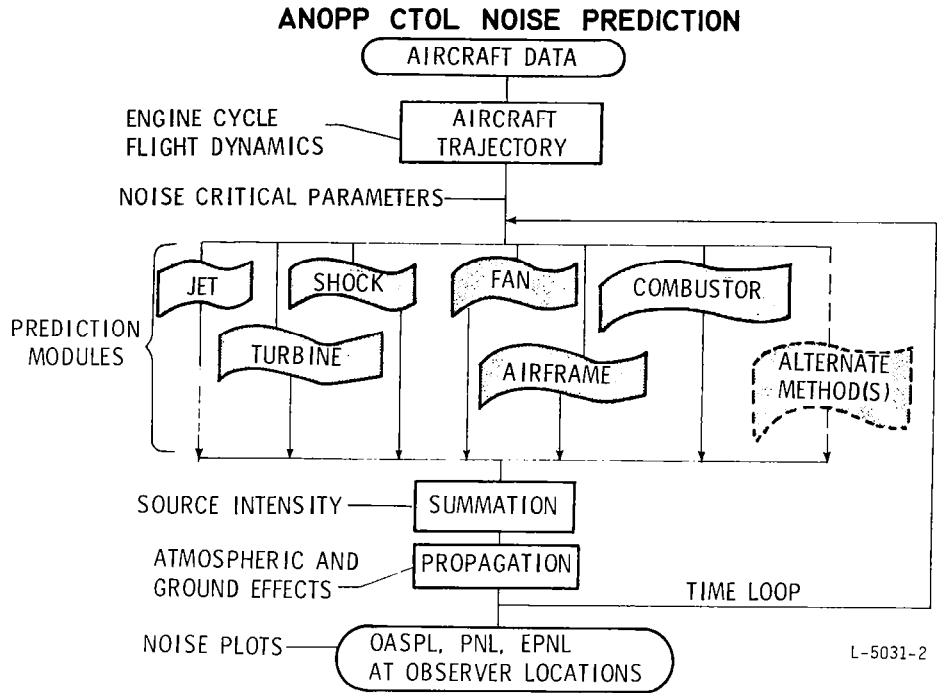

Figure III-39

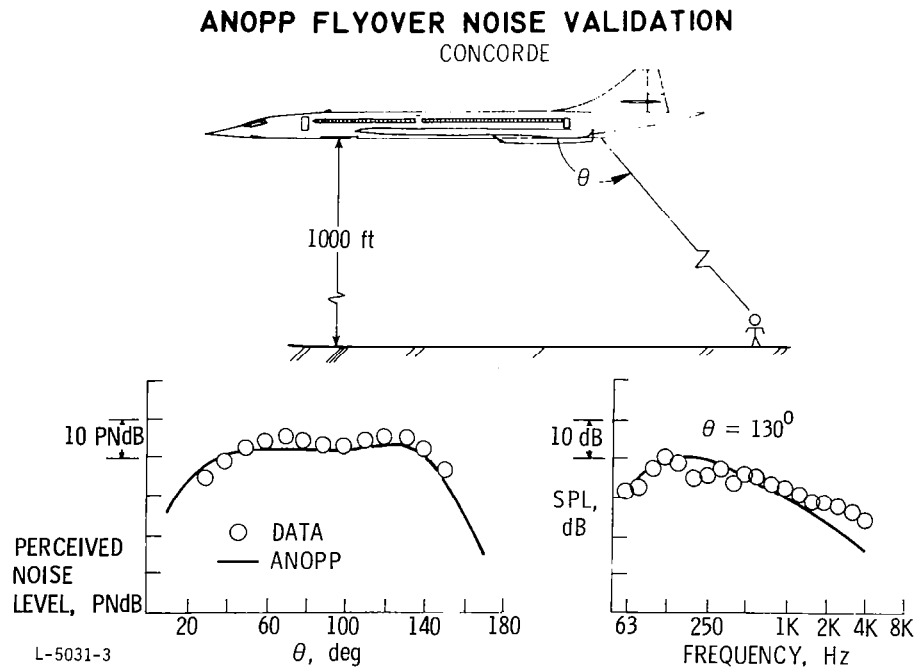

Figure III-40

ANOPP FLYOVER NOISE VALIDATION

DC-9

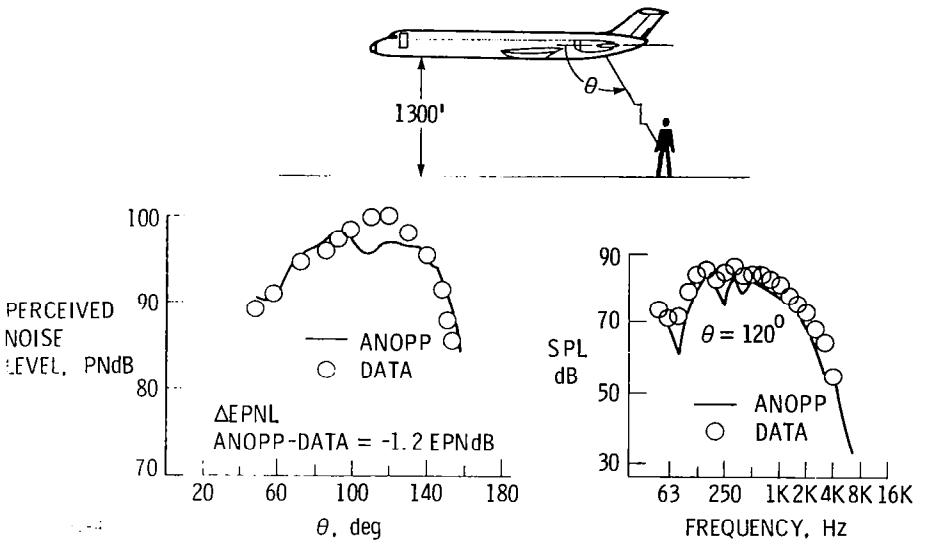

Figure III-41

ANOPP FLYOVER NOISE VALIDATION

DC-10

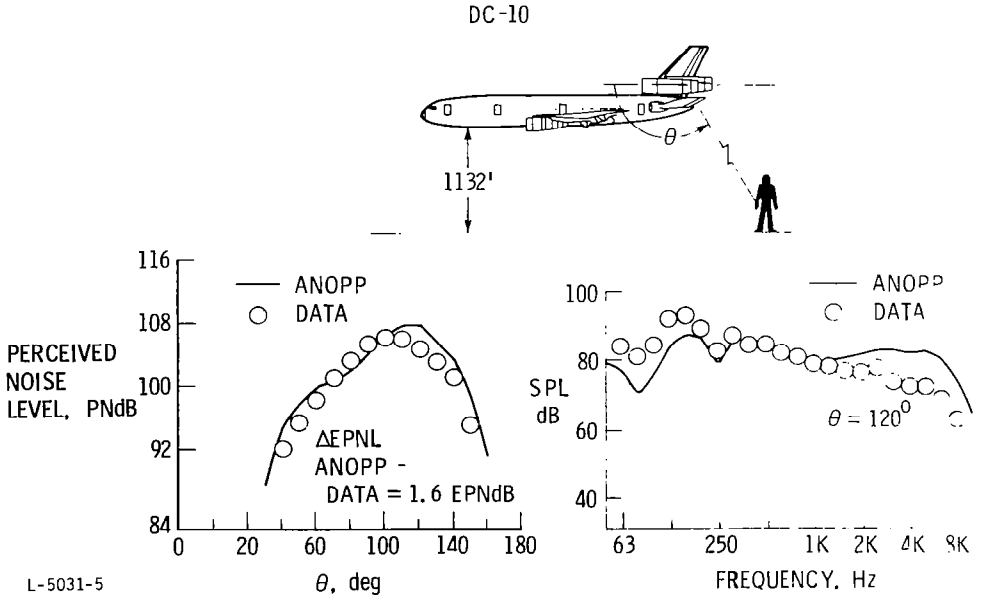

Figure III-42

ANOPP PRELIMINARY DESIGN SYSTEMS STUDIES

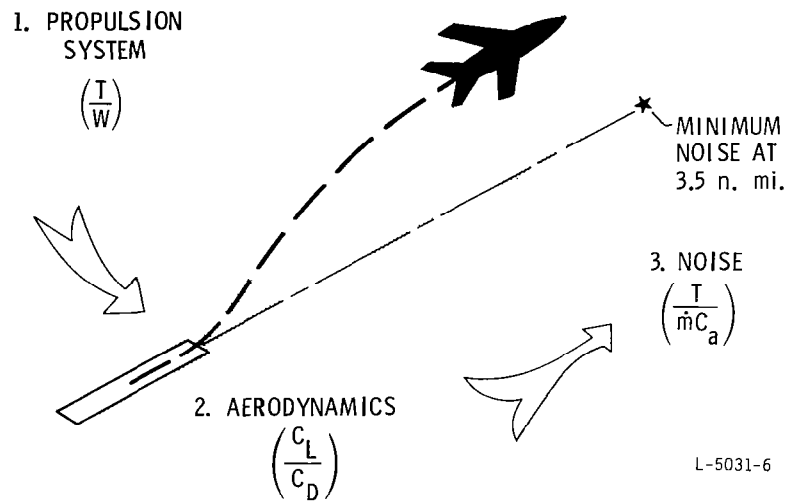

Figure III-43

ANOPP RESEARCH IDENTIFICATION

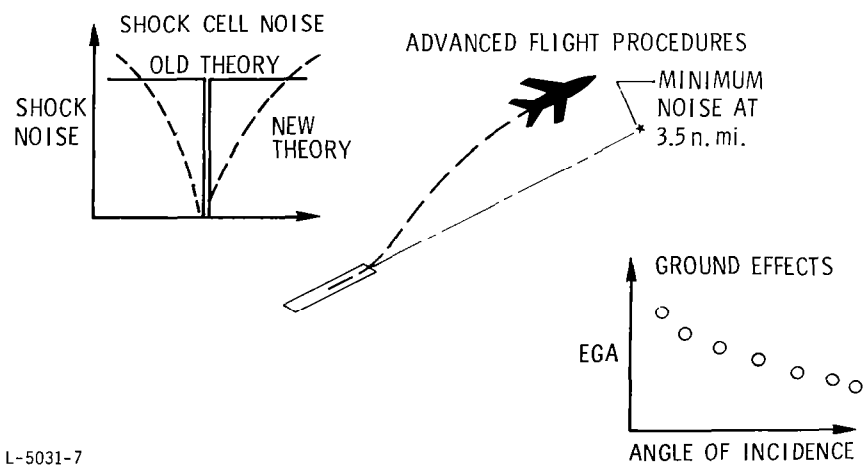

Figure III-44

IV. ALTERNATIVE JET AIRCRAFT FUELS

Jack Grobman

National Aeronautics and Space Administration
Lewis Research Center

The first paper in this conference discusses NASA's research efforts to evolve energy-efficient aircraft technology and emphasizes the fact that jet fuel costs have become the dominant factor affecting aircraft direct operating costs. The diminishing reserves of petroleum aggravate the problem of rising costs and, in addition, lead to concern about how we will be able to meet the growing need for jet fuel in the future.

This paper discusses the changes in jet fuel properties that may occur in the future as a result of shifts in the supply and demand for fossil fuels, the effects that varying fuel properties would have on aircraft engines and fuel systems, and, finally, the technology that would be required to use these fuels.

POTENTIAL CHANGES IN FUEL PROPERTIES

The options that we might have for producing jet fuel in the future are illustrated in figure IV-1. For the present, the aircraft industry is totally dependent on petroleum as a source of jet fuel. Jet fuel is currently produced by straight distillation followed by mild hydrotreating for removal of sulfur. Trends in the aromatic content of jet fuel produced in this manner are shown in figure IV-2. Aromatics, which have about half the hydrogen content of saturated hydrocarbons, have undesirable combustion characteristics as a jet fuel. An increase in aromatic content results in a corresponding reduction in the hydrogen content of a jet fuel. The average aromatic content has increased steadily over the past several years. This increase is due to the increased proportion of high-aromatic crude oils being used to produce jet fuel (ref. 1). The aromatic content is limited to a maximum of 20 percent by the current ASTM Jet A fuel specification; however, Jet A produced from some of the available sources of crude oil exceeds this limit. Jet A refined from a heavy Arabian crude oil has had aromatic contents as high as 22 percent, and projections indicate that Jet A refined from Alaskan crude oil may have aromatic contents as high as 25 percent. A waiver currently in effect permits the limited use of jet fuels with aromatic contents as high as 25 percent.

There is increasing pressure to raise the specification limit for aromatic content as a result of these trends.

As the demand for the middle-distillate fuels such as jet fuel, diesel fuel, and heating oils increases, the supply of these natural distillation products will be exceeded by the demand (fig. IV-1). Then it will become necessary to crack the heavier ends of the barrel to increase the middle-distillate pool. Energy-intensive hydrocracking will be required to limit the aromatic content of jet fuel produced in this manner (ref. 2).

As the supply of natural petroleum diminishes, the next likely domestic source of fossil fuel would be shale oil. The production of jet fuel from shale oil requires relatively severe hydrotreating to remove undesirable impurities and to upgrade the hydrogen content. For shale oil, nitrogen removal is particularly important because of the relatively large quantity of organic nitrogen present in comparison with that in petroleum. Nitrogen is undesirable because it reduces the chemical stability of the fuel and because it may be converted to the pollutants oxides of nitrogen (NO_x) during combustion. Ultimately the Nation's large reserves of coal could be used as a source of jet fuel. The use of coal syncrudes, which have very high concentrations of aromatics, would require even more severe hydrogenation for the production of jet fuel. The cost of producing jet fuel to current specifications will certainly rise as we use less desirable feedstocks and more-energy-intensive refining processes. Rising production costs will be an increasing incentive to broaden jet fuel specifications in order to minimize energy consumption and reduce total fuel costs.

The degrees to which fuel properties may change within the next 20 years are shown in table IV-1 (ref. 3). The ranges of properties for a potential broad-specification fuel are compared with those for a typical current Jet A fuel. These are the more significant changes to be expected in terms of their effects on aircraft engines and fuel systems. The increase in aromatic content is approximately equivalent to the reduction in hydrogen content. Increasing the final boiling point as indicated generally leads to the increase in freezing point shown. The thermal stability, which is a measure of the degree to which the fuel may be heated without incurring deposits within the fuel system, might become marginal in terms of current-day standards. The properties of the potential broad-specification fuel approach those of a number 2 diesel fuel.

The feasibility of using cryogenic fuels such as liquid hydrogen is being studied (ref. 4); however, the use of this fuel is a long way off. The general consensus is that liquid-hydrocarbon fuels will be used to fuel jet aircraft for many years to come, but that less stringent specifications may be necessary in the future for the reasons discussed previously. Therefore the al-

ternative jet aircraft fuels considered in this paper are liquid-hydrocarbon fuels with the range of properties indicated for the potential broad-specification fuel in table IV-1.

EFFECTS OF FUEL PROPERTY CHANGES ON AIRCRAFT ENGINES AND FUEL SYSTEMS

The effects that the property changes shown in table IV-1 would have on the performance and durability of aircraft engines and fuel systems are discussed in references 5 to 7. Reduced hydrogen content along with lower volatility and higher viscosity would adversely influence the combustion characteristics of jet fuel. A higher concentration of reactive constituents would lower the thermal stability of the fuel. A higher freezing point along with a higher viscosity would adversely influence the low-temperature flow and pumping characteristics.

Combustion Characteristics

Decreases in hydrogen content have a pronounced effect on exhaust smoke and liner temperatures. Combustor tests have been conducted with prepared fuel blends having varying hydrogen contents. At simulated cruise and takeoff conditions typical for a JT8D engine, exhaust smoke increases significantly as the hydrogen content of the fuel decreases (fig. IV-3). There is a corresponding effect of hydrogen content on maximum liner temperature (fig. IV-4). As the hydrogen content is lowered, the flame becomes more sooty and more luminous; thus the heat radiated to the liner walls is increased. The rate of increase in maximum liner temperature as the hydrogen content is lowered is much greater at cruise than at takeoff. The increases in liner wall temperature at cruise would have a larger influence on liner durability because of the much larger exposure time during cruise. Higher liner temperatures reduce liner life as a result of accelerated metal fatigue and oxidation. Other combustor performance and durability criteria that could be adversely affected by reduced hydrogen content, lower volatility, and higher viscosity include ignition and relight capability, gaseous exhaust emissions, and carbon deposition.

Fuel Thermal Stability

The effects of reactive constituents in the fuel on thermal stability were discussed at a recent workshop sponsored by the Lewis Research Center. The amount of reactive constituents in the fuel may increase as fuel specifications are broadened or as fuel is produced from alternative sources such as shale oil or coal (ref. 8). Figure IV-5 shows tubes that were heated to various temperatures with fuel flowing over the outside of them.

They represent heated passages within a fuel injector or fuel-oil heat exchanger. The figure illustrates what can occur with jet fuels that are not thermally stable at the temperatures they encounter on their way through the fuel system to the combustor. The deposits shown on the tubes result from the auto-oxidation of the reactive constituents in the fuel. Deposit build-up in a fuel injector may cause nonuniform fuel sprays, which can lead to local hotspots on the liner or nonuniformities in the exit temperature profile. The effects of both temperature and nitrogen content of the fuel on the rate of deposit formation are illustrated in figure IV-5. As the temperature increases, the rate of deposition increases, and at similar temperature levels, the fuel with the higher nitrogen content has a much higher rate of deposition.

Similar results, shown in figure IV-6, were obtained in the study described in reference 9. The effect of temperature on the deposit formation rate for a Jet A fuel containing negligible amounts of nitrogen is compared with that for a Jet A fuel doped with 0.1 percent nitrogen. Both fuels display a rapid increase in deposit formation rate as temperature is increased, but the fuel containing 0.1 percent nitrogen shows a much greater acceleration of deposit formation rate with increasing temperature.

Fuel Pumpability at Low Temperature

Fuel stored in aircraft tanks can reach very low temperatures during long flights. Figure IV-7 shows a correlation of in-flight minimum fuel temperatures for Boeing 707 and 747 aircraft flying polar route missions. Data were obtained from about 1100 missions. Each mission was greater than 4000 nautical miles. The probability that the temperature of fuel in the tank will fall below a given minimum value is plotted against minimum fuel temperature. The minimum temperature that the fuel may reach during flight is lower than -15° F for half of these missions. For 10 percent of these flights, the temperature may be lower than -30° to -40° F. The differences in temperature between the two types of aircraft are mainly attributed to differences in flight Mach number or flight envelope. For a probability of 1 day per year, the minimum fuel temperature is as low as about -45° to -55° F. Airlines have always avoided potential fuel freezing problems by using fuels with low freezing points and, when necessary, altering flight conditions.

Lockheed conducted an experimental study under a NASA contract to determine the flow behavior of fuels cooled below their freezing points in a simulated flight environment. The experimental fuel tank simulator used for this study is shown in figure IV-8. It represents a section of a Lockheed L-1011 wing tank. Cooling was provided at the top and bottom of an insula-

ted tank to simulate the in-flight cooling of the upper and lower surfaces of a section of the wing. Fuel sloshing could be simulated by rocking the tank with a mechanical agitation system. After being cooled, fuel was discharged from the tank by the boost pump. Conditions in the tank were observed through viewing ports on each side of the tank. Figure IV-9 shows an interior view of the tank loaded with a test fuel at a temperature above the freezing point of the fuel. A surge box was located at the inlet to the boost pump to maintain a constant pressure head. Ejector tubing connected to the pump inlet provided a means for removing fuel from the bottom of the tank. Temperature was measured at various locations by thermocouples. Stringers were located at the top and bottom to simulate the structural design of the wing tank. The effects of cooling a fuel below its freezing point are illustrated in figure IV-10, which shows the frozen and liquid fuel remaining in the tank after pumpdown. During the initial part of the pumpdown, the two-phase mixture of wax and liquid fuel may be removed by the boost pump, but eventually the pump inlet becomes plugged by this slushy mixture, and the remaining fuel cannot be pumped from the tank. The low-temperature flow behavior of fuels in the fuel-tank simulator was assessed by measuring the percentage of a full load of fuel that could not be pumped from the tank as temperature was lowered. The percentage of fuel held in the tank was a function of boundary-layer temperature, as shown in figure IV-11. The boundary-layer temperature was measured about 1/2 inch from the lower surface of the tank. Data are shown for three fuels. While the boundary-layer temperature for a specific percentage of fuel holdup is lower for both lower-freezing-point fuels, the rate of increase in fuel holdup as the boundary-layer temperature is reduced is different. The holdup for the Jet A fuel refined from a paraffinic petroleum increases more rapidly as the boundary-layer temperature is reduced than that for either the naphthenic Jet A or the broad-specification fuel. This may be attributed to the larger concentration of high-molecular-weight, long-chain paraffin waxes contained in this fuel. This kind of research data enables us to have a better understanding of the low-temperature behavior of fuels in aircraft fuel systems. Nevertheless, for the present, any amount of solid fuel formed in the fuel tank is unacceptable to an airline and is avoided by routinely maintaining the fuel tank temperature about 5° F above the freezing point of the fuel being used.

COMBUSTOR AND FUEL SYSTEM TECHNOLOGY NEEDS

The potential problem areas described previously are identified in the sketch of a typical combustor shown in figure IV-12. The higher liner temperatures associated with the use of fuels with higher aromatic content could be reduced or tolerated by evolving improved construction, improved cooling effectiveness, ad-

vanced alloys, or ceramic coatings. Increasing the proportion of air used to cool the liner would be unacceptable, however, because this approach would reduce the amount of air available for control of the exit temperature profile. Increasing coolant airflow might also increase carbon monoxide and unburned-hydrocarbon emissions.

Approaches which are successful in reducing exhaust emissions, such as lean burning or improved fuel atomization (paper II), can also be effective in reducing liner temperature by minimizing luminous flame radiation. These approaches could also prevent carbon deposition and reduce exhaust smoke. Multizone combustion or variable geometry, besides enabling the control of emissions at both high and low power levels, could also ensure reliable ignition and relight. Several multizone designs, including the Pratt & Whitney vorbix and the General Electric double annular combustors, are described in paper II. A cutaway drawing of the double annular combustor is shown in figure IV-13. During idling and at low power, fuel is fed only to the outer annulus, and combustion occurs in a relatively fuel-rich zone. At high power levels, fuel is fed to both the inner and outer annuli, and combustion occurs at relatively fuel-lean conditions. Both the double annular and vorbix combustors have been evaluated with several fuel blends varying in hydrogen content (refs. 10 and 11). The liner temperatures measured in tests of the double annular and vorbix multizone combustors are compared with data from several production combustors in figure IV-14. Since the various data were not all obtained at the same combustor-inlet conditions, the data are plotted as the difference between maximum liner temperature and combustor-inlet temperature. The curves for the production combustors exhibit a strong dependence of maximum liner temperature on hydrogen content of the fuel. The data for the multizone combustors show a relative insensitivity of maximum liner temperature to hydrogen content. Most of these data were obtained in combustor rig tests at pressures of 10 atmospheres or less; however, the two data points shown were obtained in the evaluation of the double annular combustor in the CF6-50 engine at takeoff conditions. While these findings represent limited laboratory tests and their practicality requires demonstration in a full development program, they do indicate that it may be possible to make important advances in the ability of aircraft gas turbine engines to use low-hydrogen-content fuels.

Additional combustor design concepts for broad-specification fuels being evaluated under a NASA contract with General Electric are shown in figure IV-15. Several variations of the double annular combustor are being investigated. Both of the modified configurations shown employ improvements in fuel nozzle design, including air atomization. A shorter main combustion stage is incorporated in one configuration to reduce liner surface exposure and to minimize smoke and NO_x emissions. Pre-

mixing of fuel and air in the main stage will be studied in the second configuration to reduce luminous flame radiation and exhaust emissions.

Prevention of Fuel System Fouling

Preventing fuel gumming and coking in the engine fuel system becomes more and more difficult as compressor discharge temperatures increase as a result of increasing engine pressure ratios or as fuel systems become more complex as a result of multistage combustion. Many approaches to preventing fuel system fouling are already in use. For example, designers attempt to limit the maximum fuel temperature by insulating the parts of the fuel manifold exposed to high temperatures. The control of reactive constituents in the fuel is attempted by the addition of antioxidants during the final stages of refining. However, further design improvements must be sought to limit fuel exposure temperature. Research is needed to obtain a better understanding of the effects of constituents in the fuel on fuel degradation. The dissolved oxygen in the fuel plays an important part in these reactions. While the removal of this oxygen may be impractical, more efficient antioxidant additives could be developed and the removal of certain reactive or catalytic impurities might be effective. Fuel system purging could be investigated as a means of minimizing fuel deposits in multizone combustors.

Fuel System Technology for Fuels With Higher Freezing Points

Modifications to aircraft fuel systems that might be necessary to permit the use of a higher-freezing-point fuel are being investigated (refs. 12 and 13). A number of fuel tank heating sources plus insulation have been evaluated as approaches to keeping the fuel in the tanks above the freezing point (fig. IV-16). Insulation of the fuel tanks is currently not practical because it entails a large weight penalty; however, future aircraft wing designs may permit the use of effective lightweight insulation. The use of a tailpipe heat exchanger is undesirable because of design complexity. Fuel heating by means of compressor air bleed has the disadvantage of having a relatively high cycle penalty. The use of either boost pump recirculation or a heat exchanger in the cabin air conditioning system is limited by the amount of heat that either could provide. Two systems are considered worthy of further study: the lubrication oil heat exchanger and an electric heat exchanger powered by an engine-driven generator.

The existing lubrication oil heat exchanger system would be modified by adding a second heat exchanger that would return heated fuel to the tank (fig. IV-17). The recirculation valve could be shut off when fuel tank heating would not be required. This

system has the advantages of using existing components, being low in cost, having a low cycle penalty, and being a simple system requiring only a relatively minor modification to the existing lubrication oil heat rejection system. The calculated fuel temperatures for a long-range flight using this system are compared with the temperatures for an unheated fuel tank in figure IV-18. Heating the fuel permits the minimum in-flight fuel temperature to be raised from about -45° to -25° F. The latter value points out the disadvantage of this system. The heat rejection limit of about 2800 Btu per minute would not be applicable to fuels with freezing points greater than -30° F, allowing for a 5° F operating margin. In addition, the heat available would be variable and would depend on the engine operating point.

The electrical fuel heating concept would overcome these disadvantages by providing much higher heating rates to permit the use of fuels with freezing points up to 0° F (fig. IV-19). Heater control would be independent of engine operating point, and this system would be adaptable to layover heating by means of auxiliary ground power. In-flight power would be obtained by installing a generator on each engine. An inert fluid would be heated by an electric resistance heater. The heated fluid would then be pumped to another heat exchanger in order to reject heat to the fuel tank. A disadvantage of this system is that it involves major modifications and additions to the engines and aircraft. Furthermore there would be a significant weight penalty and a cycle penalty when the system is used. The judgment to use such a fuel heating system will depend partly on the relative cost reduction of using a broad-specification fuel compared with its installation and operating costs.

CONCLUDING REMARKS

Projected shifts in the supply and quality of refinery feedstocks warrant the consideration of broadening jet aircraft fuel specifications. Advanced combustor and fuel system technologies that will be required to counteract adverse fuel property effects if fuel specifications are broadened are currently being evaluated. A considerable effort will be necessary by both government and industry to assemble the data base that must be developed in order to establish an acceptable tradeoff between future fuel specifications and aircraft engine technology.

REFERENCES

1. Dukek, W. G.; and Longwell, J. P.: Alternative Hydrocarbon Fuels for Aviation. Exxon Air World, vol. 29, no. 4, 1977, pp. 92-96.

2. Longwell, J. P.; and Grobman, J.: Alternative Aircraft Fuels. J. Eng. Power, vol. 101, no. 1, Jan. 1979, pp. 155-161.

3. Longwell, John P., ed.: Jet Aircraft Hydrocarbon Fuels Technology. NASA CP-2033, 1978.

4. Witcofski, Robert D.: Progress on Coal-Derived Fuels for Aviation Systems. CTOL Transport Technology, 1978. NASA CP-2036, Pt. 2, 1978, pp. 927-950.

5. Grobman, Jack S.: Impact of Broad-Specification Fuels on Future Jet Aircraft. CTOL Transport Technology, 1978. NASA CP-2036, Pt. 1, 1978, pp. 217-233.

6. Blazowski, W. S.; and Jackson, T. A.: Evaluation of Future Jet Fuel Combustion Characteristics. AFAPL-TR-77-93, Air Force Aero Propulsion Lab., 1978. (AD-A060218.)

7. Rudey, R. A.: Effect of Broadened-Specification Fuels on Aircraft Engines and Fuel Systems. NASA TM-79086, 1979.

8. Reynolds, Thaine W.: Thermal Stability of Some Aircraft Turbine Fuels Derived from Oil Shale and Coal. NASA TM X-3551, 1977.

9. Taylor, William F.: The Study of Hydrocarbon Fuel Vapor Deposits. GR-10-VDP-69, Esso Research and Engineering Co., 1969. (AFAPL-TR-69-77, AD-863604.)

10. Gleason, C. C.; and Bahr, D. W.: Experimental Clean Combustor Program, Alternate Fuels Addendum, Phase II. (R76AEG268, General Electric Co., NASA Contract NAS3-18551.) NASA CR-134972, 1976.

11. Roberts, R.; Peduzzi, A.; and Vitti, G. E.: Experimental Clean Combustor Program, Phase II. (PWA-5370, Pratt & Whitney Aircraft; NASA Contract NAS3-18544.) NASA CR-134970, 1976.

12. Pasion, A. J.; and Thomas, I.: Preliminary Analysis of Aircraft Fuel Systems for Use with Broadened Specification Jet Fuels. (D6-44538, Boeing Commercial Airplane Co.; NASA Contract NAS3-19783.) NASA CR-135198, 1977.

13. Friedman, Robert: High Freezing Point Fuels Used for Aviation Turbine Engines. NASA TM-79015, 1979.

POTENTIAL CHANGES IN FUEL PROPERTIES

PROPERTY	CURRENT JET A	POTENTIAL BROAD-SPEC FUEL
AROMATICS, vol %	17 → 25	30 → 35
HYDROGEN, wt %	14 → 13.5	13.0 → 12.5
FINAL BOILING POINT, °F	500 → 530	550 → 630
FREEZING POINT, °F	-50 → -40	-30 → -20
THERMAL STABILITY	ACCEPTABLE	MARGINAL

CS-79-1558

Table IV-1

JET FUEL PRODUCTION ALTERNATIVES

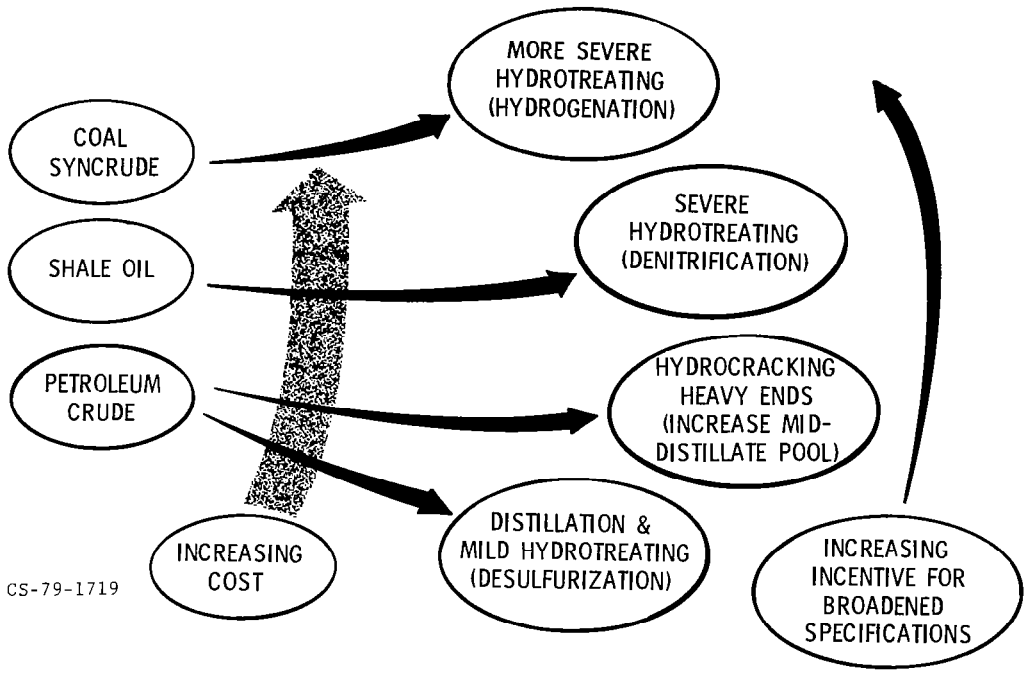

Figure IV-1

TRENDS IN AROMATIC CONTENT OF COMMERCIAL JET A FUEL

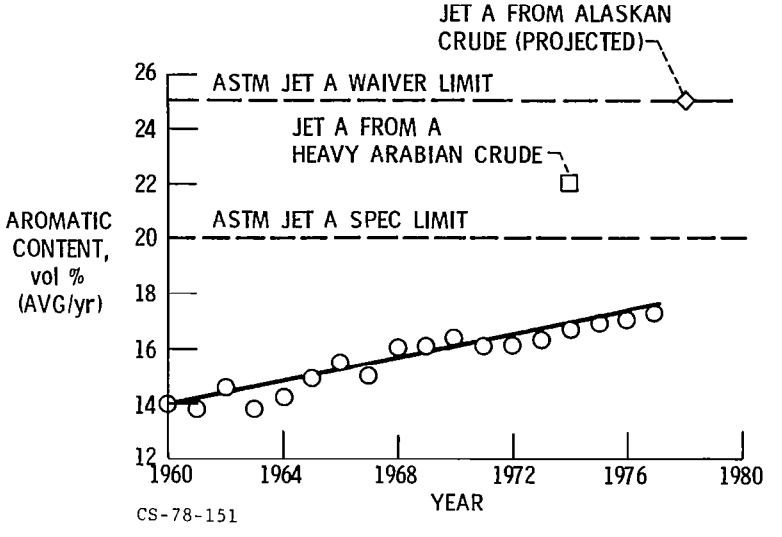

Figure IV-2

EFFECT OF HYDROGEN CONTENT OF FUEL ON SAE SMOKE NUMBER

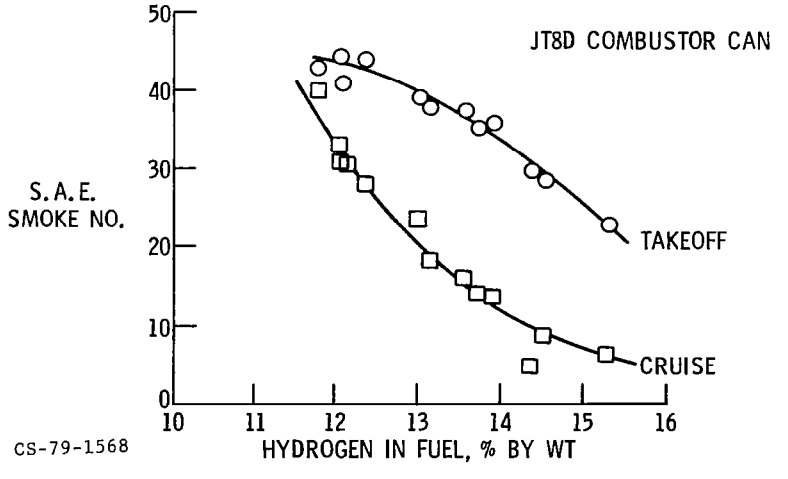

Figure IV-3

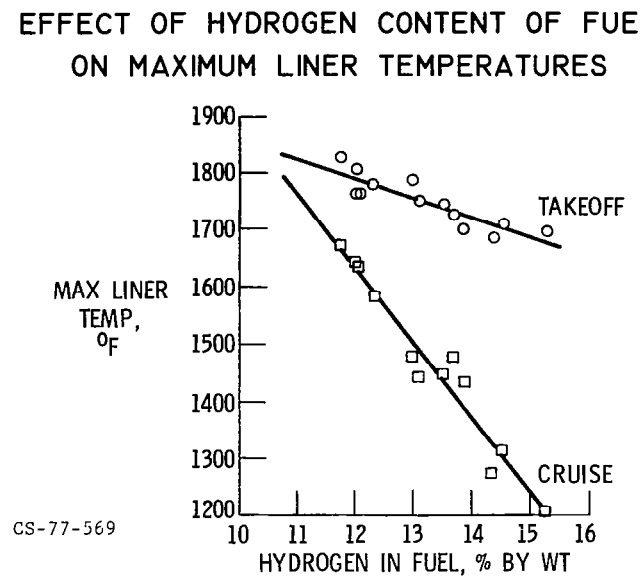

Figure IV-4

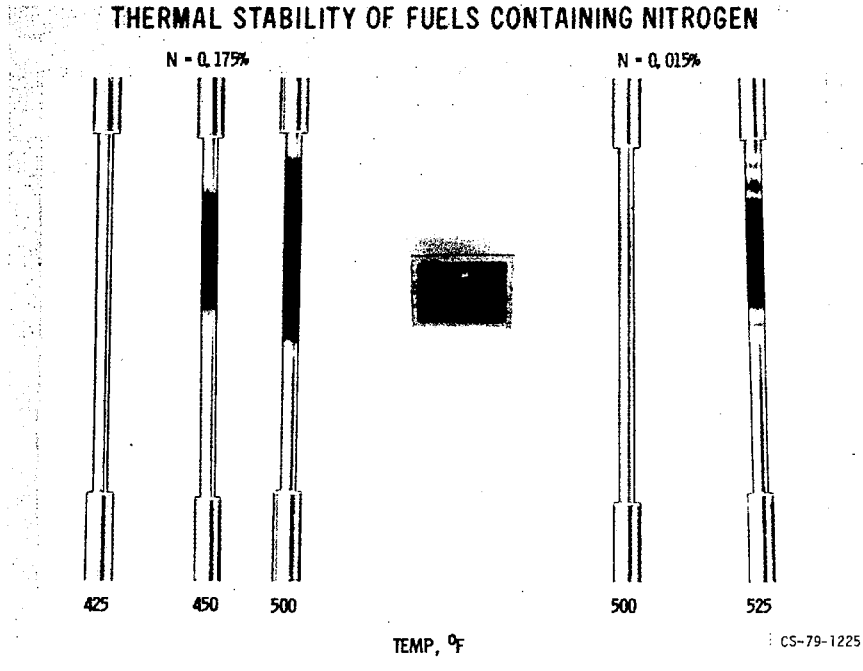

Figure IV-5

EFFECT OF FUEL NITROGEN CONTENT ON THERMAL STABILITY

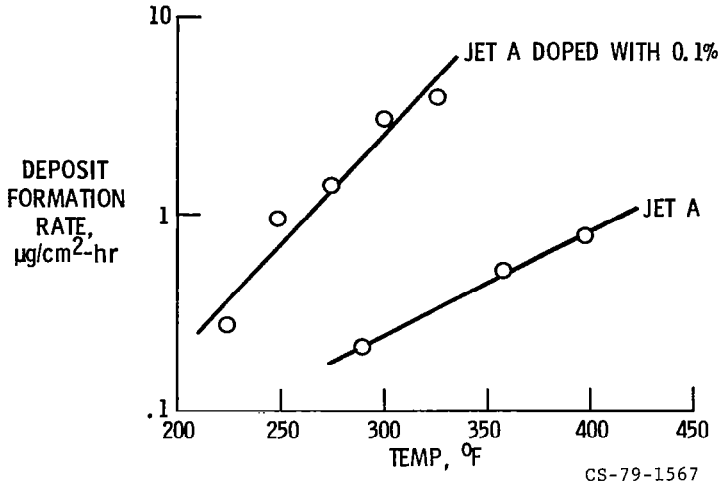

Figure IV-6

SUMMARY OF IN-FLIGHT MINIMUM FUEL TEMPERATURES

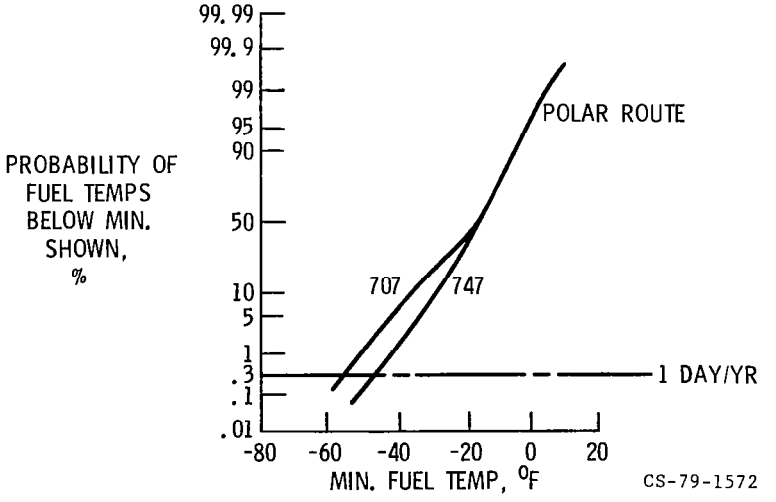

Figure IV-7

LOW TEMPERATURE FUEL TANK SIMULATOR

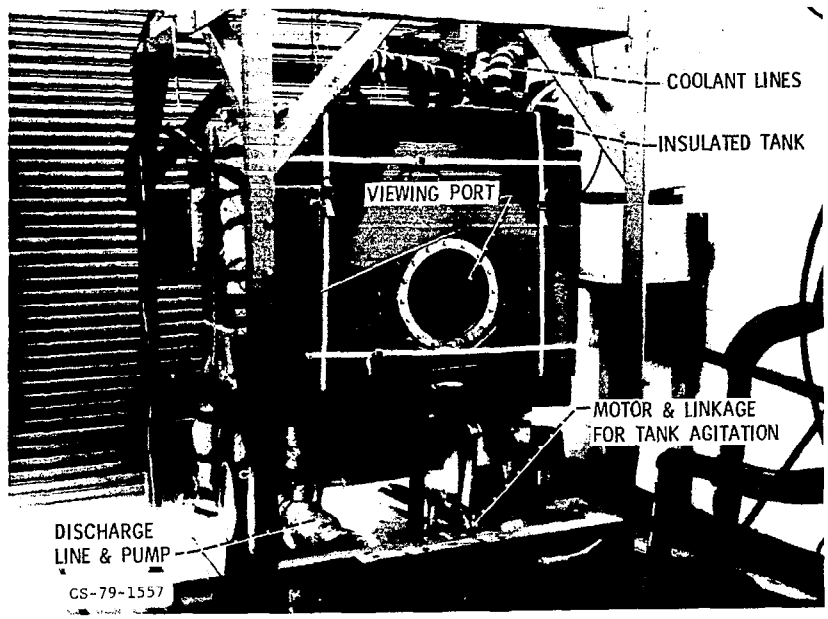

Figure IV-8

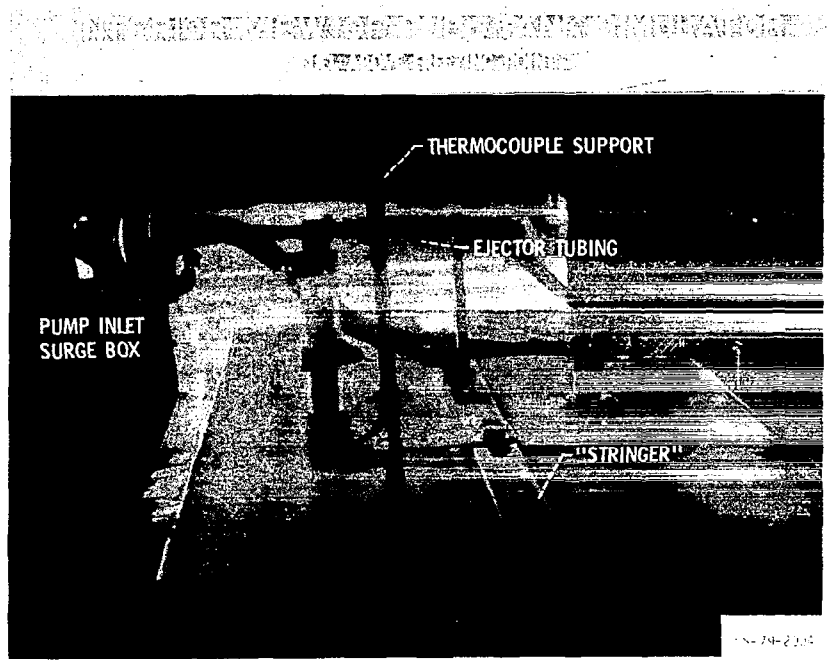

Figure IV-9

INTERIOR VIEW OF FUEL TANK SIMULATOR

FUEL COOLED DOWN BELOW FREEZING PT

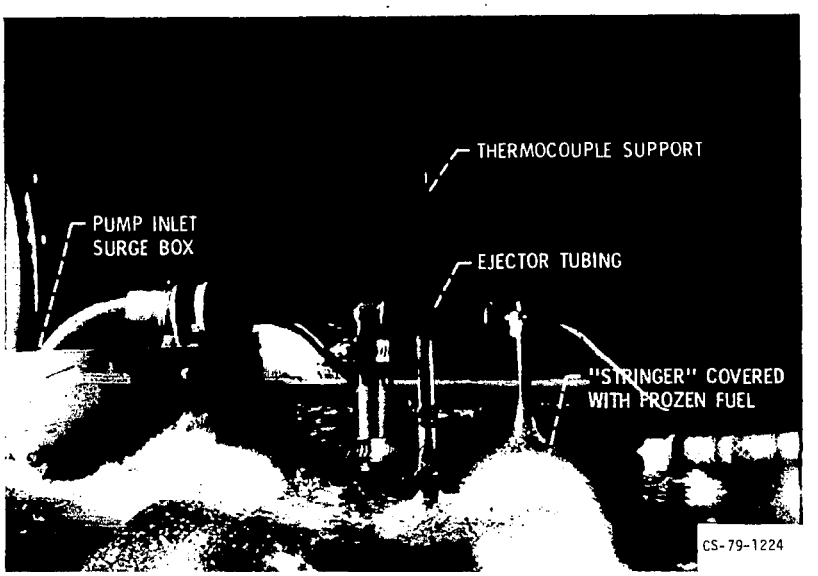

Figure IV-10

LOW TEMPERATURE FUEL TANK BEHAVIOR

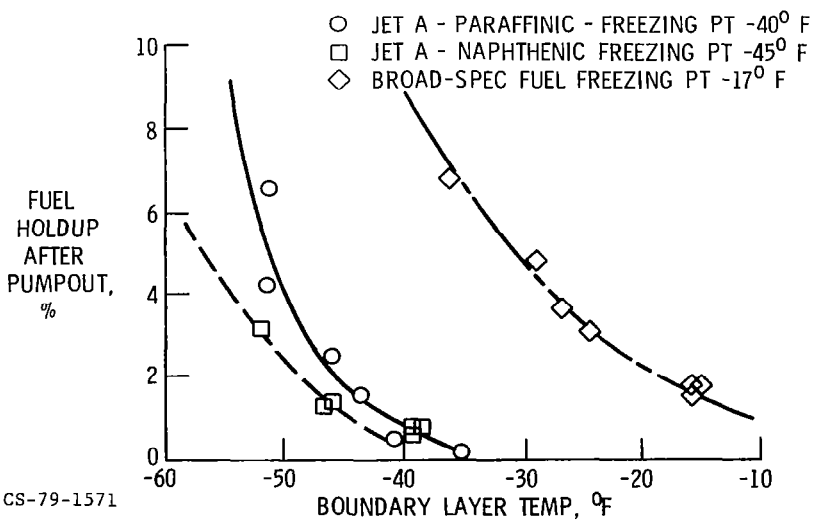

Figure IV-11

COMBUSTOR TECHNOLOGY REQUIRED TO USE BROAD-SPEC FUELS

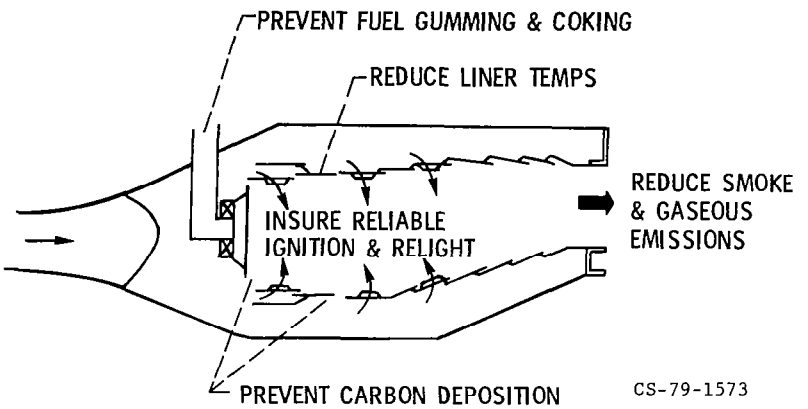

Figure IV-12

DOUBLE ANNULAR COMBUSTOR

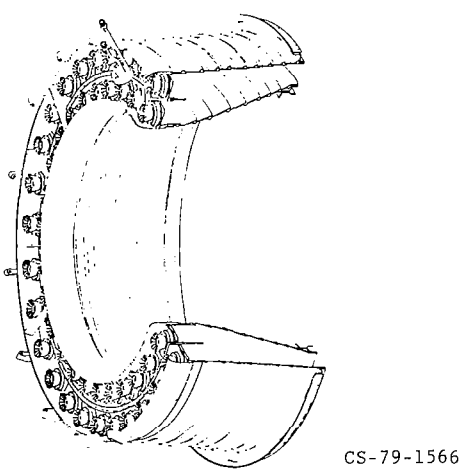

Figure IV-13

EFFECT OF HYDROGEN CONTENT OF FUEL ON LINER TEMPERATURE FOR DIFFERENT COMBUSTORS

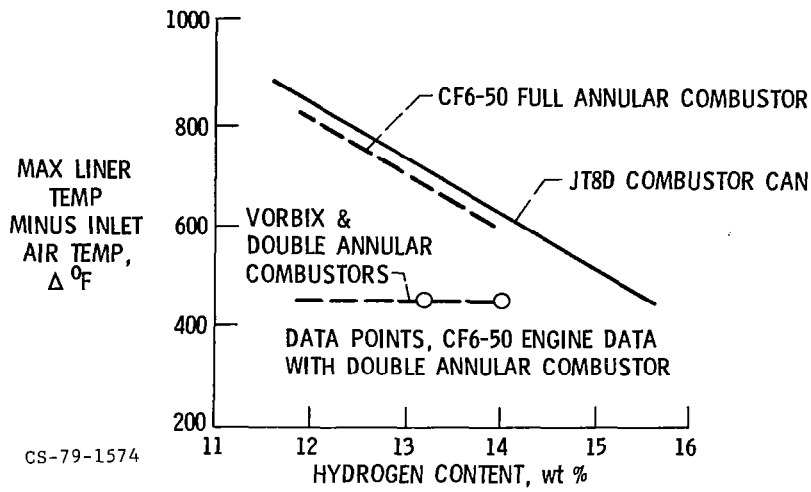

Figure IV-14

COMBUSTOR DESIGN CONCEPTS FOR BROAD-SPEC FUELS

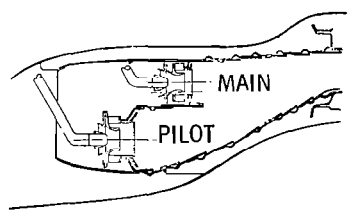

DOUBLE/ANNULAR WITH AXIAL STAGED BURNING ZONES

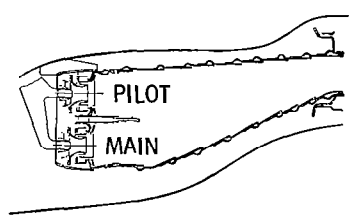

DOUBLE/ANNULAR BASELINE

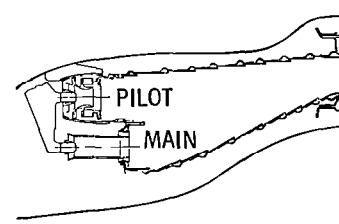

DOUBLE/ANNULAR WITH PREMIXED MAIN STAGE

CS-79-1575

Figure IV-15

FUEL TANK HEATING SOURCES

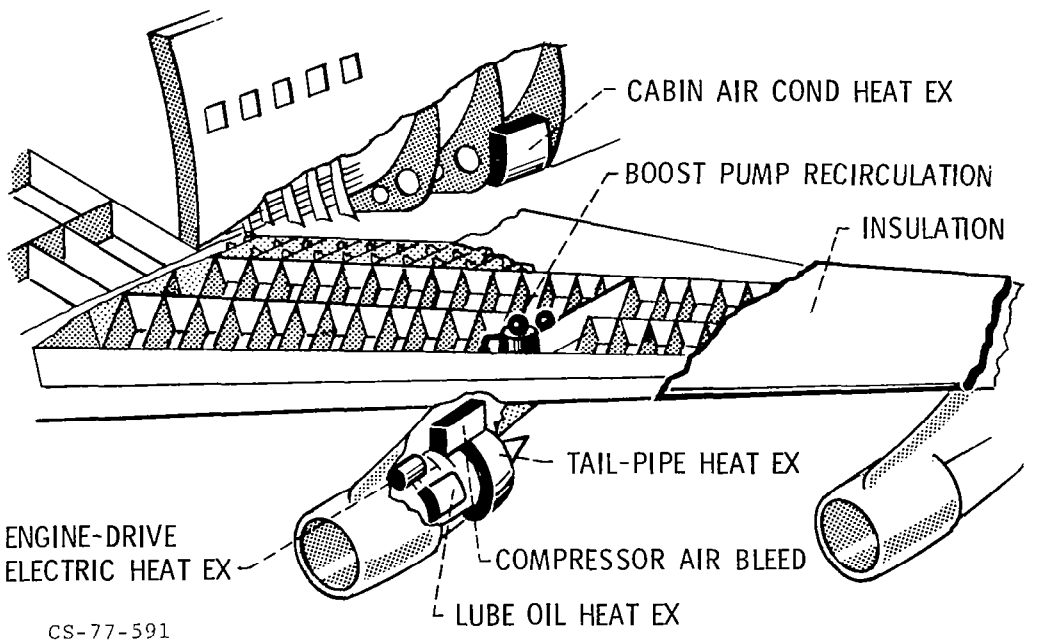

Figure IV-16

FUEL HEATING SYSTEM STUDY - BOEING

FUEL/OIL HEAT EXCHANGER SYSTEM

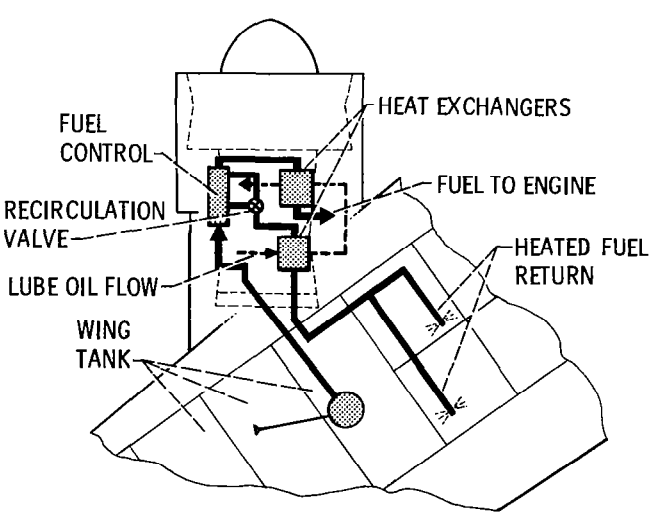

ADVANTAGES

- USES EXISTING HEAT REJECTION HARDWARE
- LOW COST - LOW PENALTY
- SIMPLE SYSTEM, RELATIVELY MINOR MODIFICATION

DISADVANTAGES

- LIMITATION TO QUANTITY OF HEAT AVAILABLE (-30^{0} F FREEZE PT MAX.)
- VARIABLE HEAT AVAILABLE, DEPENDENT ON ENGINE OPERATING POINT

CS-78-2880

Figure IV-17

PERFORMANCE OF LUBE-OIL HEATER FOR IN-FLIGHT FUEL HEATING

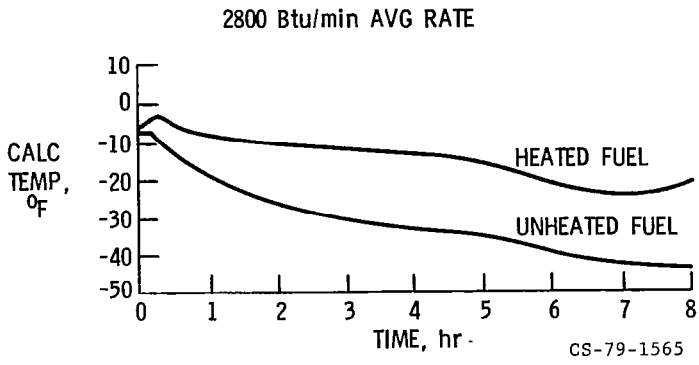

Figure IV-18

ELECTRICAL FUEL HEATING CONCEPT - BOEING

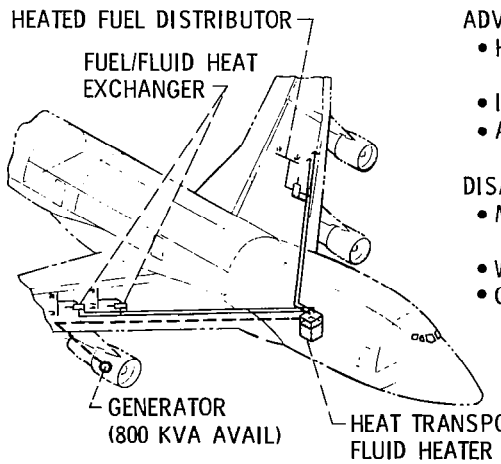

ADVANTAGES
- HEAT AVAIL FOR FUEL WITH 0^{0} F FREEZE PT
- INDEPENDENT CONTROL
- ADAPTABLE TO GROUND HEATING FOR LAYOVER

DISADVANTAGES
- MAJOR MODIFICATION-ADDITIONAL SYSTEM
- WEIGHT PENALTY
- CYCLE PENALTY WHEN USED

Figure IV-19

V. MATERIALS AND STRUCTURES TECHNOLOGY

Robert A. Signorelli, Thomas K. Glasgow, Gary R. Halford, and Stanley R. Levine

National Aeronautics and Space Administration
Lewis Research Center

There are several major thrusts of our materials and structures research for aircraft turbine propulsion systems. First, we must understand the materials and structures performance limitations, particularly for the hot section of the engine in which these limitations limit the life of components. To do so, it is necessary to understand the failure modes for components such as blades, vanes, and combustors and how they are affected by the environment for such components.

Second, we are attempting to improve the materials used for such components using several approaches. Turbine components with high strength at higher temperatures are being achieved through the application of directional structures. Improved coatings are being applied to hot section parts to increase oxidation and corrosion resistance. The higher specific properties of composite materials are being applied to increase strength and stiffness with reduced weight. Also, more cost effective processing such as near net shape powder methods are being applied to disks.

Third, we are attempting to employ these advanced materials more effectively by developing more accurate life prediction techniques. These techniques will enable the designer to predict component life more accurately in advance of service and also to incorporate advanced structural concepts in design.

In addition to these structural concepts, structures work is an area of growing importance at Lewis. We are increasing our effort and resources in this area, and in the future we anticipate that there will be much to report in the field of engine structural dynamics.

In this paper, hot section components are discussed first since they operate under a severe combination of stress, temperature, and environmental attack. After describing the various aspects of our program to improve materials and structures for the hot section, the work directed toward improving the intermediate temperature and cold section components of turbine engines will be discussed.

HOT SECTION COMPONENTS

We consider first the major structural materials requirements for the engine hot section components. Because of the complexity of the loadings imposed and the environmental conditions to which these components are exposed, it is vital to understand the nature of these requirements in order for the engine designer to proceed effectively.

Material Requirements

There are three major structural materials requirements for hot section components: strength, thermal fatigue resistance, and resistance to environmental attack.

Strength. - The traditional strength requirements are, of course, short time yield and tensile strength. At high use temperatures, long time creep and rupture strength become an additional important consideration. Strength requirements generally dictate the sizing of a component part. Since the historic trend is to increase use temperatures, it is mandatory that alloys be identified that have higher strength to keep pace with these higher use temperatures. Examples of such alloys will be discussed in a later section.

Thermal fatigue. - The second and third requirements are not as familiar as the first. This is primarily because thermal fatigue and environmental attack are more complex phenomena and are not as readily understood. Thermal fatigue cracking, nevertheless, is a common failure mode in hot section components of gas turbine engines. An example involving a film-cooled inlet guide vane is shown in figure V-1. Thermal fatigue cracks have initiated and propagated as a direct result of the cyclic thermal strains caused by the repeated heating and cooling on each engine startup and shutdown cycle. Thermal fatigue in engines usually involves a combination of fatigue and creep which can interact to seriously reduce cyclic lifetime.

Figure V-2 dramatizes the cyclic life degradation brought about by the interaction of creep with fatigue. At lower temperatures and short times per cycle, the creep effect is not present and the cracking mode is transgranular and representative of classical fatigue cracking. However, as the temperature and the time per cycle increase, the creep influence increases and the cracking shifts to the more detrimental intergranular mode following along transverse grain boundaries (ref. 1). As may be seen from the figure, cyclic life is reduced substantially. By recognizing the mode of thermal fatigue cracking, we are in a much better position to cope with this crucial problem by providing materials with no transverse grain boundaries and by

developing life prediction methods which can accurately account for the creep-fatigue interaction.

Environmental attack. - In addition to being mechanically demanding, the gas turbine environment is chemically aggressive toward materials. High temperatures, pressures, gas velocities, and severe thermal cycles can cause rapid oxidation attack. Impurities in the gas stream can further accelerate the process by inducing hot corrosion and erosion. These reactions can also accelerate the creep-fatigue cracking process. Since the oxidation process is unavoidable, the approach to controlling environmental attack is to select materials which react slowly to form an adherent, protective corrosion product.

Three basic modes of oxidation attack are possible (ref. 2) as shown in figure 3. For parabolic oxide growth, an adherent oxide is required. In this case, a plot of oxide thickness squared against time is linear. Hence, the term parabolic oxide growth. NiO, which forms on most turbine blade alloys, grows parabolically at unacceptably high rates. Cr_2O_3, which is volatile, can be useful as a protective scale at lower hot section temperatures but not at the highest temperatures. Here nonvolatile oxides such as Al_2O_3 are most desirable. However, because of a thermal expansion mismatch with turbine materials, Al_2O_3 is subject to spalling.

In figure V-4, the hot corrosion and erosion failure modes (ref. 2) are illustrated. These potentially more aggressive modes of environmental attack are induced by impurities in the air and fuel. The hot corrosion process is caused by the reaction of airborne impurities, such as sea salt with sulfur, in the fuel. At certain temperature, pressure, and concentration levels, sodium sulfate and other salts can condense as a liquid phase, react with and flux protective oxide scales, and cause rapid sulfidation attack of turbine alloys. Because the hot corrosion process is induced by a liquid, it can be far more damaging than oxidation even though the temperature is typically several hundred degrees lower.

A second potentially catastrophic problem can be caused by impurities which form heavy solid deposits. Such deposits can plug film cooling holes and lead to component overtemperature.

Finally, the impact of carbon or ingested dirt particles on turbine components causes metal loss via the erosion process.

The seriousness of the hot corrosion problem for the first-stage vanes of a helicopter gas turbine is illustrated in figure V-5. Here, hot corrosion attack along the leading edges has contributed to the formation of longitudinal cracks. In addition, heavy impurity deposits have formed near pressure surface film cooling holes.

Improved Hot Section Component Materials

Of the hot section components, turbine blades are subject to the most severe combination of temperature, stress, and oxidation and corrosion attack. Consequently, a substantial portion of the materials effort at NASA Lewis is devoted to turbine blade applications. Figure V-6 illustrates the use temperature trend for turbine blade materials. Some specific data points are shown for alloys subjected to typical blade operating conditions of 30 000 psi stress and a rupture life of 5000 hours. Conventional cast alloys with random polycrystalline microstructure developed in the 1950's and 1960's had use temperatures ranging from 1400° to 1600° F under these conditions.

Directional structures. - To go to higher temperatures for the same stress and life, materials having distinct directional structures are being developed. These include single crystal superalloys, oxide dispersion strengthened superalloys (ODS), and fiber reinforced superalloys (FRS). Beyond the metals, ceramic materials offer considerable potential, though at this time we do not have the design skills required for their use as turbine blades. However, their use for stationary or nonload bearing components such as seals and coatings will occur much sooner than shown in figure V-6.

Two of the cast directional structures under development in our Materials for Advanced Turbine Engines (MATE) program at Garrett AiResearch are shown in figure V-7. The first blade is a conventional casting; it has randomly oriented grain boundaries hidden in this view by a coating applied for oxidation protection. By directional solidification, the grain boundaries are alined in the major stress direction. And, of course, in the single crystal there are no grain boundaries to weaken the blade.

In past practice, to maintain a turbine inlet temperature of 1920° F the conventional casting required cooling air and thus the complexity of casting a hollow blade. If directional solidification is used, a simpler, solid blade capable of withstanding the same turbine inlet temperature can be employed with no cooling as shown in the figure. If a single crystal blade is used, it is anticipated that the turbine inlet temperature can be increased to 1965° F without requiring cooling (ref. 3).

Oxide dispersion strengthened superalloys. - For higher use temperatures a new development, an oxide dispersion strengthened superalloy, offers considerable potential. In oxide dispersion

strengthened alloys such as MA-6000E, the traditional superalloy strengthening mechanisms are augmented by a dispersion of fine, stable oxide particles (ref. 4). The particles are especially effective in improving high temperature properties.

The process steps by which an oxide dispersion strengthened superalloy is made are shown in figure V-8. Metal powders, elemental and prealloyed, are mixed together with oxides in a high energy stirred mill which kneads the fine oxides thoroughly into the metal. The very homogeneous powder that results is sealed in cans and consolidated by extrusion. Optionally, hot rolling may follow. Finally, the hot worked product is given its elongated microstructure by recrystallization in a thermal gradient.

The macro and microstructures of the oxide dispersion strengthened alloy MA-6000E are shown in figure V-9. The highly elongated grain structure shown in the macrograph is oriented in the direction of highest applied stress. It can be noted that there are essentially no transverse grain boundaries available at which thermal fatigue cracks can initiate. The microstructure shows both cubic gamma prime precipitates, the traditional strengthening phase in superalloys, and the very fine oxide particles that are within both the gamma prime and gamma phases. This oxide dispersion strengthened alloy MA-6000E has generated a great deal of interest among engine manufacturers, particularly for the smaller engines that are relatively difficult to cool.

The stress rupture properties of this alloy account for much of this interest (fig. V-10). The grain structure of each alloy is illustrated schematically in the figure. Alloy B-1900 is typical of current conventionally cast gas turbine blades. Directionally solidified cast alloys, polycrystalline and single crystal, provide some advantage. And the addition of an oxide dispersoid adds a considerable increment so that one can envision using the oxide dispersion strengthened alloys at temperatures of 2000^{o} F or higher.

It should be mentioned that extending the use temperature of superalloys to higher values aggravates the oxidation attack. Alloy MA-6000E will require a coating for extended life at high temperature. As will be discussed later, the process required to identify the best alloy/coating combination has already begun.

In addition to the improved stress rupture capability, the oxide dispersion strengthened alloy MA-6000E has demonstrated very good thermal fatigue resistance (fig. V-11). Thermal fatigue testing is conducted by alternately immersing wedge-shaped specimens in hot and cool fluidized beds. Thermally induced strains crack typical current blade materials after relatively few cycles. For example, B-1900 and directionally solidified Mar 200

cracked after only 800 and 2300 cycles, respectively. MA-6000E is still being tested and has yet to show any cracks after 6500 cycles (ref. 5). It must already be considered among the very best of thermal fatigue resistance materials.

Another hot section component, the combustor, may use a different ODS alloy. Work on the advanced combustor is being performed by Pratt & Whitney in our Materials for Advanced Turbine Engines (MATE) program. As shown in figure V-12, the outside cooler portion of the combustor is to be formed of the conventional alloy Hastelloy X. The interior, hotter portion will be lined with an ODS sheet alloy based on the FeCrAlY or the NiCrAlY system (ref. 6). Another use for oxide dispersion strengthened alloys is as vanes; in fact, one alloy is already specified as bill-of-material in an advanced military engine.

Fiber reinforced superalloys. - The next higher level of use temperature (fig. V-6) capability, above that of the oxide dispersion strengthened alloys, is occupied by the fiber reinforced superalloys (FRS). These are composite materials in which we can take advantage of the high strength at high temperature of reinforcing fibers, such as tungsten, and the ductility of superalloys as a matrix to achieve an outstanding combination of properties. The 1000-hour density-compensated rupture strength of several fiber reinforced superalloy or FRS composites is shown in figure V-13 along with a typical superalloy for comparison. The relative strength advantage of each composite is controlled by the wire used to reinforce the superalloy. The composite using unalloyed tungsten lamp filament, such as 218 alloy wire, achieves a modest improvement, while the composite with WReHfC alloy wire, developed as part of the Lewis Research Center FRS program, has more than a fourfold advantage in strength - density at 2000° F over conventional superalloys (refs. 7 and 8).

In addition to high temperature strength, FRS has the added advantages of high thermal conductivity and low thermal expansion as shown in figure V-14. The high thermal conductivity of tungsten provides a typical FRS composite with a thermal conductivity about twice that of conventional superalloys (ref. 9). This advantage can be used to increase the effectiveness of cooled turbine components by increasing life at a given cooling airflow or by reducing cooling airflow to increase engine efficiency. The lower thermal expansion of FRS compared with nickel and cobalt superalloys also aids in reducing the severity of the creep-fatigue interaction discussed previously.

A question that has been addressed is how such a complex composite blade would be fabricated. Figure V-15 shows schematically the process employed for turbine blade fabrication. This process is based on the technology evolved for boron-aluminum

fan blades. A filament mat and matrix alloy foil are combined to form composite monotape, which is cut into plies. These plies are stacked in a die and then diffusion bonded at temperature to form a blade.

Figure V-16 shows how a cooled turbine blade has been made using a modification of the basic process just described. A solid steel core was used along with monotapes and root blocks. After diffusion bonding, the steel core was removed by acid leaching to form a hollow internal cavity. An impingement cooling insert can be used to provide more complex cooling passages to improve cooling effectiveness. The photograph in figure V-17 shows a JT-9D blade with an unmachined oversized base fabricated using this process. The blade, about 4 inches long, was designed to the same external contour as the bill-of-material blade and to within 10 percent of the weight of the superalloy blade (ref. 10). The wall thickness was modified to take advantage of composite properties. This illustrates the feasibility of fabricating cooled hot section parts such as blades and vanes using the FRS process concept.

Other hot section parts such as combustor liners are attractive candidates and are being explored for possible application of FRS. Unfortunately, as the operating temperature goes up, the severity of environmental effects such as oxidation and hot corrosion also increases.

Improved Environmental Protection Systems

The development of stronger alloys, often at the expense of resistance to the oxidation and hot corrosion attack processes, has made surface protection problems extremely challenging.

Metallic coatings. - Over the past 15 years, metallic coating selection criteria have been devised by a combination of analytical and experimental approaches.

Figure V-18 shows a simplified oxidation resistance map on the left for three key elements affecting the oxidation resistance of superalloys nickel, chromium, and aluminum (ref. 11). Most cast superalloys fall in the poor area and the lower part of the fair area. The two composition areas exhibiting good oxidation resistance define two major coating classifications. Simple aluminide coatings, which have compositions near the apex of the diagram, are typically formed by reaction between the alloy and a source of aluminum (ref. 12). Overlay or add-on coatings, which can be deposited by such methods as electron-beam evaporation (ref. 13) or cladding (ref. 14), typically fall near the center of the diagram.

A second factor to consider in coating selection is hot corro-

sion resistance. As discussed previously, hot corrosion is caused by impurities in the air reacting with sulfur in the fuel to form a condensed fluxing liquid. The hot corrosion map (ref. 15) for the same three elements near the apex of the diagram can be undesirable for hot corrosion protection while coating compositions falling across the center of the diagram are good. The most favorable coating for a given application can be selected by properly balancing coating composition with additional factors such as ductility (ref. 16) and processing cost. The need for high ductility at low temperature generally favors compositions near the center of the maps while cost considerations favor aluminide coatings having compositions near the apex. The same principles can also be applied in the selection of cobalt-base coating compositions (ref. 17).

The significant degree to which metallic coatings can extend oxidation life compared to bare superalloys is illustrated by the burner rig data of figure V-19. Here, life in a Mach 1 burner rig is plotted as a function of temperature. Simple aluminide coatings which fall toward the lower end of the coated specimen range offer more than a fourfold extension of life (ref. 18) whereas overlay coatings offer as much as a fiftyfold extension in life. The effectiveness of overlay coatings as protection against hot corrosion is illustrated in figure V-20. Here specimen weight loss (ref. 19) in a Mach 0.3, Jet A fueled burner rig is shown. Hot corrosion is induced by injecting sea salt at a 5 ppm concentration based on air flow. In this accelerated test, most uncoated cast nickel-base alloys suffer immediate and rapid hot corrosion attack. A NiCrAlY overlay affords protection for 1100 hours.

Coatings are also highly effective in suppressing the initiation of creep-fatigue induced cracks as illustrated in figure V-21 by the log scale plot of cycles to crack initiation. The data were obtained in a fluidized bed (ref. 20). The random polycrystalline cast MM-200 alloy exhibits low life. The addition of an aluminide coating more than doubled life. Directional solidification to obtain a more crack resistant strulcture dramatically improves thermal fatigue resistance. The addition of an overlay coating to this stronger alloy more than doubled life.

Our current efforts in metallic coatings are aimed at developing better coatings for airfoil cooling passages, improving plasma spray deposited coatings so that they are equivalent in performance to the more costly electron beam evaporated coatings, and developing coatings for advanced alloys such as MA-6000E.

Thermal barrier coatings. - Another concept undergoing rapid development is the thermal barrier coating (refs. 21 to 24). The conventional metallic coated blade illustrated on the left in

figure V-22 can operate in gas turbines under conditions where the gas temperature is above the high temperature strength capability of the superalloy and even above its melting point because of air cooling. If a 15-mil insulating oxide ceramic layer or thermal barrier is added (as shown on the right in fig. V-22), the difference between the gas and metal temperatures can be increased by 200° to 600° F without additional cooling. The vital glue that locks the oxide onto the superalloy is an oxidation resistant metallic bond coating as can be seen from the optical photomicrograph. Both the bond coat and the oxide layers shown in figure V-22 were deposited by a plasma spray process. The concepts discussed earlier for metallic coating selection are also being applied to bond coat selection. Besides proper selection of the bond coat composition, the selection of the oxide composition is key to the durability of the NASA thermal barrier coating (refs. 21 and 23).

Because of the large temperature drop through the oxide layer, thermal barrier coatings are not just another new family of protective coatings. The thermal barrier coating is a revolutionary concept that can be applied to turbine airfoils in many ways. An example of the calculated benefits of a 10-mil oxide coating applied to the cooled components of a high bypass engine is shown in table V-1. Cooling air reductions to the first and second stages are shown in the center column as a percent of engine airflow. The 6.1 percent total cooling air saving yields a net thrust specific fuel consumption improvement of 1.3 percent. Alternatively, blade life can be improved by more than four times at the baseline coolant flow because of lower metal temperatures and less severe transient thermal stresses.

Looking ahead, thermal barrier coatings may also provide gains in efficiency by permitting higher gas temperatures without increasing the coolant flow. Thus, thermal barrier coatings can greatly extend the capability of conventional superalloys as well as of advanced material concepts such as single crystals, ODS superalloys, and FRS alloys.

The durability of the thermal barrier coating is illustrated by the cyclic Mach 1 burner rig data shown in figure V-23. The ZrO_2 12 weight percent Y_2O_3 NASA coating lasts about 1-hour cycles at a surface temperature of 2640° F. This is the coating that survived on turbine blades for 500 cycles between full power and flameout in a J-75 engine (ref. 25). Reducing the yttria content to 8 weight percent to obtain a tougher, stronger oxide resulted in a dramatic life improvement as shown by the two lower bars in figure V-23. This improved coating lasted 2000 hours without failure at a 40° higher surface temperature. Finally, at a surface temperature of 2860° F, which is well above levels anticipated in any current engine, the coating survived over 700 1-hour cycles.

Recent JT-9D engine tests conducted on a cooperative basis with Pratt & Whitney Aircraft (ref. 26) indicate that the original 1976 NASA coating is not yet engine ready as an add-on for first-stage turbine blades. Currently, our efforts are directed toward improving coating durability by further composition and process refinement, and toward developing a design methodology which treats the coating and airfoil as an integral system. The aerodynamic and heat-transfer aspects of thermal barrier coatings are covered in the TURBOMACHINERY TECHNOLOGY paper of this conference proceedings.

Abradable seal materials. - Besides applying our understanding of the environmental resistance of NiCrAl alloys to coatings, we have used it to develop an improved first-stage turbine abradable shroud material. This powder metallurgy material, known as Genaseal, was developed under NASA contract by the General Electric Company (ref. 27).

An engine-tested shroud segment filled with Genaseal is compared to two types of shroud segments filled with Bradelloy in figure V-24. The Genaseal segment is in better condition than either of the Bradelloy segments. Genaseal offers improved abradability and oxidation resistance at temperatures about 150° F above Bradelloy. Consequently, turbine efficiency can be improved by reducing the cooling air to the shrouds. Also, turbine efficiency can be retained by preferential wear of the shrouds rather than wear of the blades during rubs. Genaseal is now the bill-of-material shroud in one aircraft gas turbine engine and is under consideration for a number of others. The development of an even higher temperature capability oxide ceramic turbine shroud is covered in the MECHANICAL COMPONENTS paper of this conference proceedings.

Development of Life Prediction Methods

Of prime importance to the engine designer is the availability of techniques for predicting the life of engine hot section components. The creep-fatigue behavior is one major aspect that must be taken into account in order to achieve accurate component life prediction in advance of service.

Strainrange Partitioning. - A promising method has been under development at the NASA Lewis Research Center during the past several years called Strainrange Partitioning (ref. 28). The method serves two primary functions: it is a method for characterizing the creep-fatigue behavior of materials, and then, once characterized, it can be used to predict the thermal fatigue lives of components made of those materials.

The creep-fatigue behavior of any material which undergoes cyclic inelastic deformation can be characterized by means of

the Strainrange Partitioning method. Figure V-25 represents the relationship between the cyclic strainrange imposed on a laboratory test specimen and the number of times the cycle can be repeated before failure occurs by cracking. Four curves are shown; each represents whay may happen when creep is imposed in different ways. When no creep is present, the uppermost curve, which represents the pure fatigue condition, results. Creep imposed in only the compressive half of the cycle reduces the cyclic life. Creep in both the tensile and compressive halves of the cycle gives rise to further life reductions. Finally, when only tensile creep occurs, the greatest life loss is suffered, and the lower bound on cyclic life is established. Any conceivable reversed strain cycle can be broken down or partitioned into components of the four types of strainrange shown. Then, by employing a damage rule, the lifetime of any cycle can be predicted.

Considerable experience has been gained in using Strainrange Partitioning to characterize the creep-fatigue behavior of high temperature engineering alloys. An international symposium (ref. 29) was held recently during which organizations from six NATO nations presented the results of a 2-year evaluation program of Strainrange Partitioning. By and large, the method proved to be a satisfactory approach for characterizing the creep-fatigue resistance of high temperature alloys.

To date, over 50 engineering alloys have been studied using the Strainrange Partitioning method of characterization. In general, the cyclic lives can be correlated to within a factor of 2. Considering that the scatter in cyclic life measurements is also on the order of a factor of 2, the correlation capabilities of the method are highly satisfactory.

The second important aspect of Strainrange Partitioning is its ability to predict thermal fatigue lives. The method is currently being used to predict the cyclic lifetimes of hot section components which are life limited by thermal fatigue cracking. Under contract, the General Electric Company will be applying the method to the life prediction of a CF6-6 first-stage high pressure turbine blade squealer tip. Over the past few years Pratt & Whitney has been making life predictions of combustor liners in high bypass ratio engines using a rudimentary form of Strainrange Partitioning (ref. 30). A recently initiated contract program with Pratt & Whitney calls for a more sophisticated use of the method in making liner life calculations.

Figure V-26 illustrates the severity of thermal fatigue cracking in combustor liners. Cracks have initiated and propagated from the lip edge of the louvered liner construction. The accuracy with which the thermal fatigue lives of combustor liners can be predicted is shown in figure V-27 (ref. 31). Observed lives are on the order of a few thousands of cycles to failure, with vari-

ations due to different flight missions. These missions result in different operating temperatures, strainranges, and times. Strainrange Partitioning takes into account these variations directly and accordingly predicts greater or lesser lives depending on the severity of the flight mission. Predicted lives agree with the observed lives to within factors of 2 as indicated in the figure. This accuracy is considered remarkably good since the correlation of laboratory specimen data is also within a factor of 2.

Oxidation and corrosion prediction. - Considerable progress has also been made in developing techniques for predicting the degree of environmental attack at high temperatures. At NASA Lewis a technique known as COREST (corrosion estimation) has been developed for predicting oxidation attack of bare superalloys. COREST is available as a computer program (ref. 32). With COREST the depth of oxidation attack can be estimated from weight change data. Estimated depths of oxidation attack for a number of high temperature alloys were calculated by using an early version of COREST, and these estimations are compared with actual depths of attack in figure V-28 (ref. 33). In many cases the measured values exceed the estimated values because the estimation does not take grain boundary oxidation into account. However, most actual values fall within a factor of 3 of the predictions. COREST can also be applied to predict long-time depth of attack from short-time oxidation data.

In the area of hot corrosion, we are in the early stages of developing a method for predicting attack of bare superalloys. The basis for this method is a series of statistically designed, 100-hour, Mach 0.3 burner rig experiments. The variables are the corrosive elements and their concentration and the temperature. In figure V-29 good agreement between predicted 200-hour attack and measured attack is shown for four superalloys exposed to a complex combination of corrosive elements. These limited results are most encouraging.

The prediction of coating life is far more complex than for bare metals. The microstructure of an as-deposited NiCrAlY coating on an oxide dispersion strengthened superalloy is shown on the left in figure V-30. The protective oxide scale forming elements, aluminum and chromium, are concentrated in the darkly etched particles. After 200 hours of cyclic Mach 0.3 burner rig exposure at 2000° F, shown on the right of figure V-30, some protective elements are consumed by the oxidation reaction as can be seen from the disappearance of the darkly etched phase from the thin layer at the surface. However, the diffusion reaction between the coating and alloy has resulted in a greater loss of coating protective capability than has the reaction with the environment. We have developed a method for predicting the diffusion reaction kinetics in simple model alloy systems (ref.

34). Further research with this method and adaptation of the environmental attack like prediction methods already discussed are key approaches to obtaining a comprehensive coating life prediction methodology.

INTERMEDIATE TEMPERATURE COMPONENTS - DISKS

Disks operate at lower temperatures than the hot section components thus far discussed. However, they are a critical component in that failure poses a serious threat to safe aircraft operation. Until recently, disk materials were confined to wrought alloys and these provided definite limitations as to strength, fabricability, and cost. However, with the advances in powder metallurgy techniques, very significant progress is being made in this area as well.

The requirements for alloys to be used as disks are somewhat different from those of the hot section components. Environmental attack, for example, is minimized by the lower temperatures. Since disks are highly loaded parts, the first concern must be with strength - especially uniformity of strength - so that we can design to the greatest advantage without some small weaker area developing a crack prematurely. Disks are large and heavy; therefore, cost, including material use efficiency, is a factor. And the loading on a disk is cyclic, so fatigue resistance must also be considered.

The traditional practice of manufacturing disks has been to cast and then forge. This process wastes material. Also, nonuniformities inherent in the casting process are carried through forging and weaken production disks. The powder metallurgy process offers the potential of increased alloy additions without harmful segregation. Work on this process has also been part of NASA's MATE program.

The process itself is illustrated in figure V-31. Prealloyed metal powders are loaded into a can shaped like the final product. The powder is consolidated by the combined effects of heat and pressure in a hot isostatic press. After removal of the can by etching, only minimal machining is required to bring the part into the shape necessary for quality assurance by sonic inspection. It should be noted that the scale marker below the two disks in figure V-31 is 12 inches long. So the diameter of the disks is 19 inches, more than double that which had previously been processed by powder metallurgy techniques.

A finished disk made by the powder metallurgy process is illustrated in figure V-32. This disk would be used in a large commercial engine to hold the first stage of blades. As already indicated, the primary advantage of making the disk by powder metallurgy is uniformity; highly alloyed parts can be made with

confidence that all portions are similar in strength (ref. 35). The process is also conservative of materials, reducing machining by 34 percent, and is projected to result in cost savings on the order of 25 percent.

As part of the continuing efforts at NASA Lewis to provide materials for hotter and more efficient engines, we are seeking to identify advanced disk materials. These are evaluated at temperatures well above current disk use temperatures. Consequently, the creep-fatigue mechanisms described previously become very important. As shown in table V-2, the ultimate tensile strength attainable has been increased from about 180 000 for conventional wrought disk alloys to 221 000 pounds per square inch by means of powder metallurgy materials. Also, the number of cycles to first crack has increased dramatically from 8000 to 165 000 cycles (ref. 36). Unfortunately, the number of cycles to propagate such cracks to test specimen failure has decreased It would, of course, be desirable to improve all the alloy properties. As is the case in all our material programs, determining the optimum balance of properties for a component, in this case a disk, continues to be a major area of investigation.

COLD SECTION COMPONENTS

Thus far the hot section and the intermediate temperature engine components have been discussed. It is appropriate to conclude by considering some of the advances being made with composite materials for the engine cold section components. Some of the components where composites can and to some extent are being used in this part of the engine include rotating fan blades and static structures such as the frame-containment ring and the exhaust nozzle flaps.

A number of benefits can be gained by using composites, both polymer matrix and metal matrix, for these components. The lower density of composites combined with their greater stiffness and strength permits designers to tailor these materials to meet component requirements while improving performance and decreasing component weight. In addition, costs may be reduced by decreasing the number of parts needed for an engine. For example, the number of blades per stage or the number of stages may be reduced, thereby lowering costs.

Fan Blades

The major impediment to using composite fan blades remains that of inadequate resistance to large object foreign object damage (refs. 37 and 38). Figure V-33 shows a number of design variations and materials combinations under study to apply composites

to fan blades. The designs include solid and hollow blades, a spar-shell configuration with a leading edge or central spar, and a composite patch design wherein the midspan damper is removed and a composite patch substituted for vibration dampening. Three types of composite materials are being used - polymer matrix, boron-aluminum, and superhybrids. The latter is a combination of polymer and metal matrix composites. Improvements are being made to overcome the foreign object damage limitation to composite fan blades.

Engine Static Structures

There is a more immediate opportunity for application of composites to static engine structures. Figure V-34 illustrates a graphite-epoxy fan frame for a quiet, clean, short-haul experimental engine (QCSEE) program (refs. 39 and 40). The QCSEE program conducted by NASA has been described in previous conferences held at NASA Lewis. It is expected that weight savings up to 30 percent can be achieved by this approach compared to current frames. The composite frame includes a composite containment ring. This component is designed to prevent a failed fan blade from penetrating the engine case. A heavy steel ring has been replaced by a lightweight fiber composite to satisfy the containment requirement.

Figure V-35 shows a recent application of a graphite-polyimide composite for the nozzle flaps of the F-100 engine. The standard flaps are titanium, and the substitution of composite flaps is intended both to increase service life and to decrease weight. The figure shows a composite flap installed in an F15 aircraft at Edwards Air Force Base to evaluate service performance. In addition to flaps, graphite-polyimide composites are being applied to the thrust reverser stang of the JT-8D engine on the DC-9 aircraft. PMR polyimide, developed at the Lewis Research Center, is used as the matrix for that component.

Thus, composites appear to have a bright future for achieving significant increases in component durability, reducing weight, and ultimately engine cost. Further research in this area is continuing to fully realize their potential.

SUMMARY

The advances of materials and structures for propulsion systems are now summarized.

We have made major strides in developing a better understanding of hot section component failure modes such as thermal fatigue and environmental attack, and we have used this understanding to

provide components with improved performance potential. Directionally structured materials, such as ODS superalloys and FRS, have demonstrated the potential for significant increases in hot section component use temperature (up to 2100° F). Coatings, both metallic and thermal barrier, can be used to increase the use temperature by retarding environmental attack and by thermally insulating components. Improved materials for abradable seals permit increases in service temperature (as much as 150° F) with reduced leakage losses. Accurate life prediction techniques for failure modes, such as thermal fatigue, oxidation, and corrosion, are being developed for use by designers to utilize more of the service life potential of the improved materials for the engine hot section components.

Powder metallurgy fabrication processing of disks, one of the key intermediate temperature engine components, permits lower fabrication costs and increased strength up to 220 ksi at 1200° F. Cold section components can be made lighter and stiffer by using composite materials. Composites also afford the potential for reduced cost through reduction of the number of required parts.

Thus, it is apparent that major strides are being made in advancing the state-of-the-art of the engine materials and structural concepts which are so key to achieving the performance gains desired in advanced turbine engines.

REFERENCES

1. Manson, S. S.; Halford, G. R.; and Hirschberg, M. H.: Creep-Fatigue Analysis by Strainrange Partitioning. Design for Elevated Temperature Environment. American Society for Mechanical Engineers, 1971, pp. 12-24.

2. Grisaffe, S. J.; Lowell, C. E.; and Stearns, C. A.: High Temperature Environmental Effects on Metals. NASA TM-73878, 1977.

3. Sink, L. W.; Hoppin, G. S., III, and Fujii, M.: Low-Cost Directionally-Solidified Turbine Blades, Vol. 1. (AIRESEARCH 21-2953-1, Airesearch Manufacturing Company of Arizona; NASA Contract NAS3-20073.) NASA CR-159464, 1979.

4. Benjamin, J. S.: Dispersion Strengthened Superalloys by Mechanical Alloying. Metall. Trans., vol. 1, no. 10, Oct. 1970, pp. 2943-2951.

5. Glasgow, T. K.: An Oxide Dispersion Strengthened Alloy for Gas Turbine Blades. NASA TM-79088, 1979.

6. Eng, R. D.; and Evans, D. J.: Manufacture of Low Carbon Astroloy Turbine Disk Shapes by Hot Isostatic Pressing, Vol. 1. (PWA 5574-12, Pratt and Whitney Aircraft Group; NASA Contract NAS3-20072.) NASA CR-135409, 1978.

7. Petrasek, D. W.; and Signorelli, R. A.: Stress Rupture Strength and Microstructural Stability of Tungsten-Hafnium-Carbon-Wire-Reinforced Superalloy Composites. NASA TN D-7773, 1974.

8. Signorelli, R. A.: Review of Status and Potential of Tungsten Wire: Superalloy Composites for Advanced Gas Turbine Engine Blades. NASA TM X-2599, 1972.

9. Winsa, E. A.; Westfall, L. J.; and Petrasek, D. W.: Prediction of Inlet Gas Temperatures for Tungsten-Fiber Reinforced Superalloy Turbine Blades. NASA TM-734842, 1978.

10. Petrasek, D. W.; et al.: Tungsten Fiber Reinforced FeCrAlY: A First Generation Composite Turbine Blade Material. NASA TM-79094, 1979.

11. Barrett, C. A.; and Lowell, C. E.: Resistance of Ni-Cr-Al Alloys to Cyclic Oxidation at 1100° and 1200° C. Oxid. Met., vol. 11, no. 4, 1977, pp. 199-223.

12. Levine, S. R.; and Caves, R. M.: Thermodynamics and Kinetics of Pack Aluminide Coating Formation on IN-100. J. Electrochem. Soc., vol. 121, no. 8, Aug. 1974, pp. 1051-1064.

13. Talboom, F. P.; Elam, R. C.; and Wilson, L. W.: Evaluation of Advanced Superalloy Protection Systems. (PWA-4055, Pratt & Whitney Aircraft; NASA Contract NAS3-12415.) NASA CR-72813, 1970.

14. Gedwill, M. A.; and Grisaffe, S. J.: Oxidation Resistant Claddings for Superalloys. Met. Eng. Q., vol. 12, no. 2, May 1972, pp. 55-61.

15. Santoro, G. J.; and Barrett, C. A.: Hot Corrosion Resistance of Nickel-Chromium-Aluminum Alloys. J. Electrochem. Soc., vol. 125, no. 2, Feb. 1978, pp. 271-278.

16. Strangman, T. E.; Felten, E. J.; and Benden, R. S.: Refinement of Promising Coating Compositions for Directionally Cast Eutectics. (PWA-5441, Pratt & Whitney Aircraft; NASA Contract NAS3-18920.) NASA CR-135103, 1976.

17. Barrett, C. A.; and Lowell, C. E.: The Cyclic Oxidation Resistance of Cobalt-Chromium-Aluminum Alloys at 1100° and 1200° C and a Comparison with the Nickel-Chromium-Aluminum Alloy System. Oxid. Met., vol. 12, no. 4, 1978, pp. 293-311.

18. Grisaffe, S. J.: Protective Coating for Superalloys. Aerospace Structural Materials, NASA SP-227, 1969, pp. 305-316.

19. Lowell, C. E.; and Deadmore, D. L.: High Velocity Oxidation and Hot Corrosion Resistance of Some ODS Alloys. NASA TM X-73656, 1977.

20. Bizon, P. T.; and Spera, D. A.: Comparative Thermal Fatigue Resistances of Twenty-Six Nickeland Cobalt-Base Alloys. NASA TN D-8071, 1975.

21. Stecura, S.: Two-Layer Thermal Barrier Coating for High Temperature Components. Am. Ceram. Soc. Bull., vol. 56, no. 12, Dec. 1977, pp. 1082-1085, 1089.

22. Stepka, F. S.; Liebert, C. H.; and Stecura, S.: Summary of NASA Research on Thermal Barrier Coatings. SAE Paper 770343, 1978.

23. Stecura, S.: Effects of Compositional Changes on the Performance of a Thermal Barrier Coating System. NASA TM-78976, 1979.

24. Hodge, P. E.; et al.: Thermal Barrier Coatings: Burner Rig Hot Corrosion Test Results. DOE/NASA/2593-78/3, NASA TM-79005, 1978.

25. Liebert, D. H.; et al.: Durability of Zirconia Thermal-Barrier Ceramic Coatings on Air-Cooled Turbine Blades in Cyclic Jet Engine Operation. NASA TM X-3410, 1976.

26. Sevcik, W. R.; and Stoner, B. L.: An Analytical Study of Thermal Barrier Coated First Stage Blades in a JT9D Engine. (PWA-5590, Pratt & Whitney Aircraft Group; NASA Contract NAS3-21033.) NASA CR-135360, 1978.

27. Bessen, I. I.; Rigney, D. V.; and Schwab, R. C.: Improved High Pressure Turbine Shroud. (R77AEG481, General Electric Co.; NASA Contract NAS3-18905.) NASA CR-135181, 1977.

28. Hirschberg, M. H.; and Halford, G. R.: Use of Strainrange Partitioning to Predict High-Temperature Low-Cycle Fatigue Life. NASA TN D-8072, 1976.

29. Characterization of Low Cycle High Temperature Fatigue by the Strainrange Partitioning Method. AGARD CP-243, 1978.

30. Vogel, W. H.; Soderquist, R. W.; and Schlein, B. C.: Application of Creep-LCF Cracking Model to Combustor Durability Prediction. Fatigue Life Technology, T. A. Cruse, ed., American Society of Mechanical Engineers, 1977, pp. 23-31.

31. Schlein, B. C.: Reliability Prediction for Combustors and Turbines. FR-8187-Vol. 1, Pratt and Whitney Aircraft Group, 1977. (AFAPL-TR-77-8-Vol. 1, AD-A045670.)

32. Barrett, C. A.; and Presler, A. F.: COREST: A FORTRAN Computer Program to Analyze Paralinear Oxidation Behavior and its Application to Chromic Oxide Forming Alloys. NASA TN D-8132, 1976.

33. Barrett, C. A.; and Lowell, C. E.: Comparison of Isothermal and Cyclic Oxidation Behavior of Twenty-Five Commercial Sheet Alloys at 1150° C. NASA TN D-7615, 1974.

34. Levine, S. R.: Reaction Diffusion in the NiCrAl and CoCrAl Systems. Metall. Trans., vol. 9A, Sept. 1978, pp. 1237-1250.

35. Eng, R. D.; and Evans, D. J.: Manufacture of Low Carbon Astroloy Turbine Disk Shapes by Hot Isostatic Pressing. (PWA-5574-12-Vol. 1, Pratt and Whitney Aircraft Group; NASA Contract NAS3-20072.) NASA CR-135409, 1978.

36. Cowles, B. A.; Sims, D. L.; and Warren, J. R.: Evaluation of the Cyclic Behavior of Aircraft Turbine Disk Alloys. (PWA-FR-10299, Pratt and Whitney Aircraft Group; NASA Contract NAS3-20367.) NASA CR-159409, 1978.

37. McDanels, D. L.; and Signorelli, R. A.: Improved Impact-Resistance of Boron/Aluminum Composites for Use as Turbine Engine Fan Blades. NASA TM X-71875, 1976.

38. Signorelli, R. A.; and Blankenship, C. P.: Advanced Materials Research for Long-Haul Aircraft Turbine Engines. CTOL Transport Technology-1978, NASA CP-2036, Part 1, 1978, pp. 187-204.

39. QCSEE - Under the Wing (UTW) Engine Composite Nacelle Test Report. (R78AEG573, Vol. 1. Summary, Aerodynamic and Mechanical Performance, General Electric Co.; NASA Contract NAS3-18021, Proj. FEDD.) NASA CR-159471, 1979.

40. Quiet Clean Short-Haul Experimental Engine - Under the Wing Final Design Report. (General Electric Co.; NASA Contract NAS3-18021.) NASA CR-134847, 1977.

POTENTIAL BENEFITS OF 10 MIL THERMAL BARRIER COATINGS ON HIGH BYPASS ENGINE

COMPONENT	COOLANT REDUCTION, % ENGINE AIRFLOW	TSFC, %
1ST VANES	4.2	-0.4
1ST BLADES	1.2	-.4
2ND VANES	.6	-.3
2ND BLADES	.1	-.2
	6.1	-1.3

ALTERNATIVELY, 4X LIFE IMPROVEMENT AT BASELINE COOLANT FLOW.

CS-79-1612

Table V-1

ADVANCED DISK ALLOY PROPERTIES

	WROUGHT WASPALOY	WROUGHT ASTROLOY	POWDER METALLURGY IN 100	POWDER METALLURGY NASA II-B7
1200^{0} F UTS, ksi	183	197	196	221
CYCLES TO INITIAL CRACK	8000	24 000	64 000	165 000
CYCLES TO PROPAGATE CRACK TO FAILURE	725	265	75	<10

Table V-2

CS-79-1509

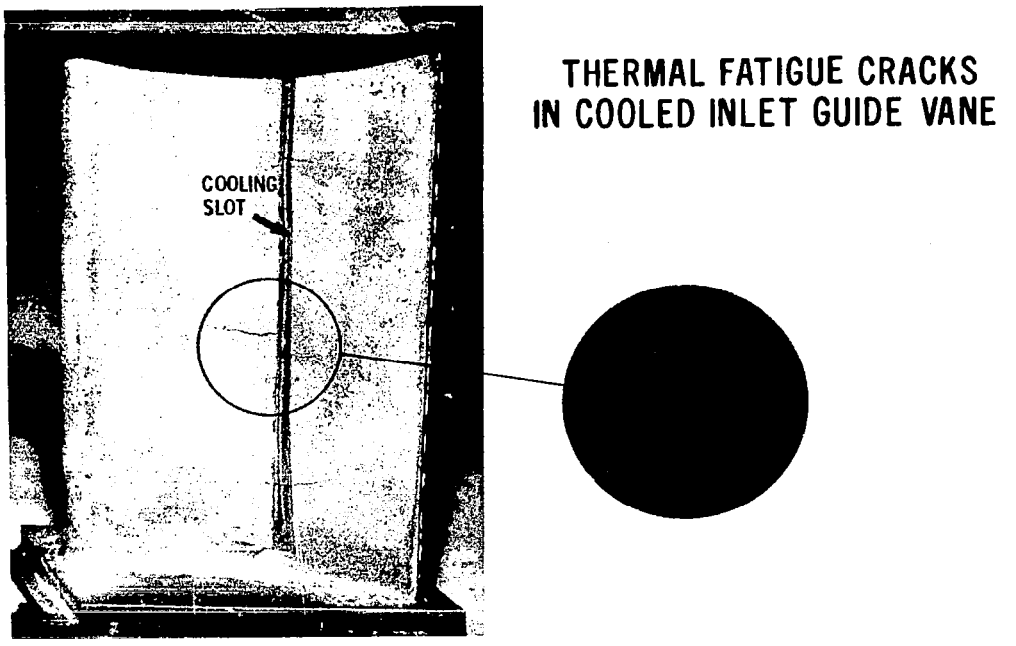

Figure V-1

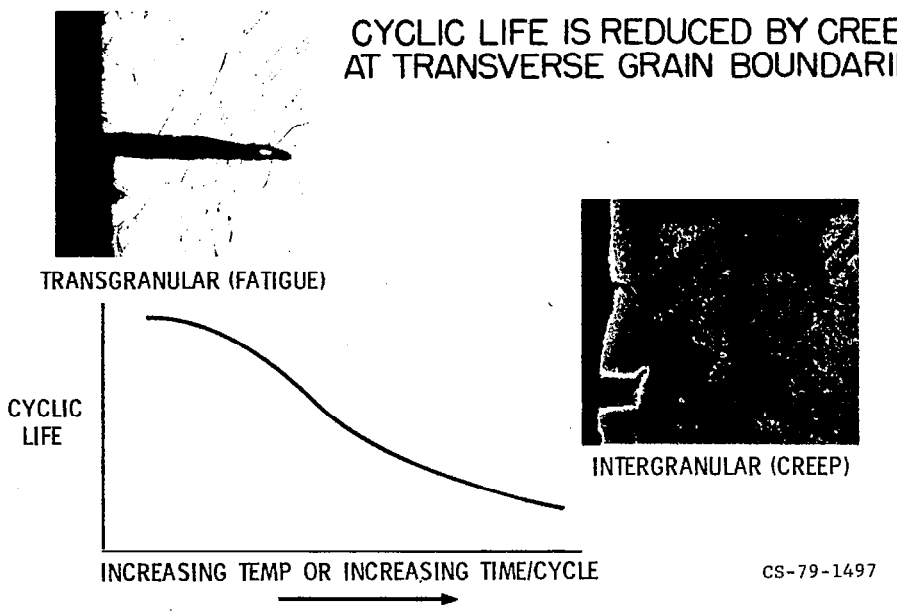

Figure V-2

SCHEMATIC OF MODES OF OXIDATION ATTACK

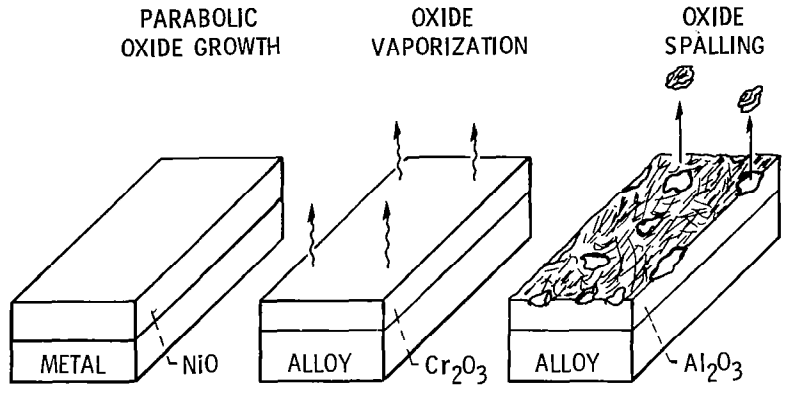

CS-79-1618

Figure V-3

SCHEMATIC OF MODES OF HOT CORROSION/EROSION ATTACK

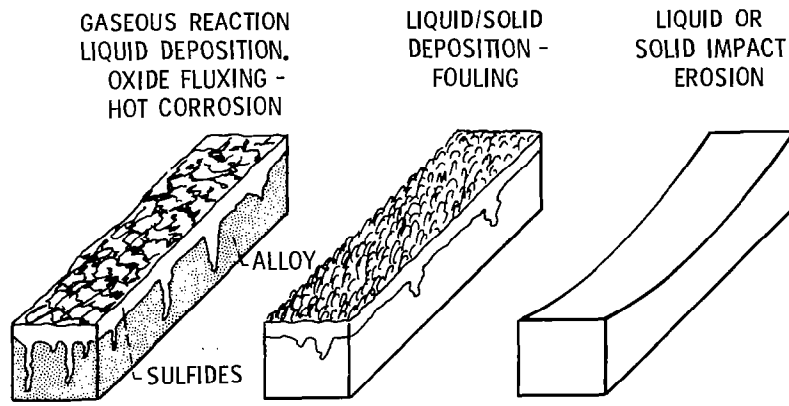

CS-79-1620

Figure V-4

HOT CORRODED TURBINE VANES

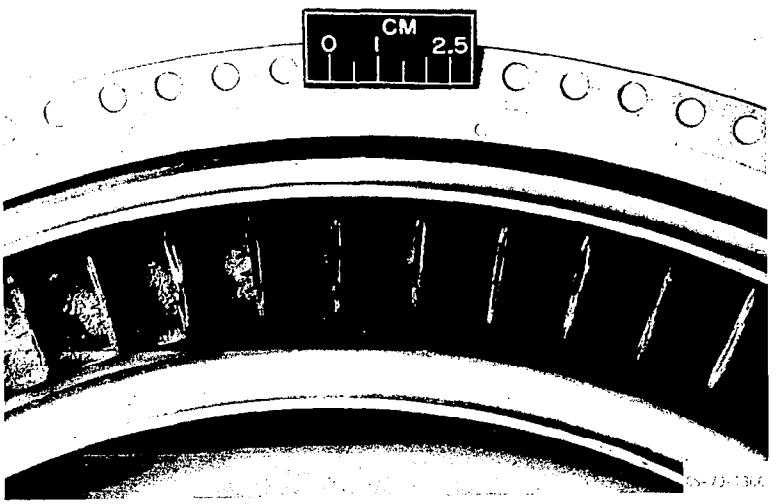

Figure V-5

PROJECTED USE TEMPERATURES FOR TURBINE BLADE MATERIALS

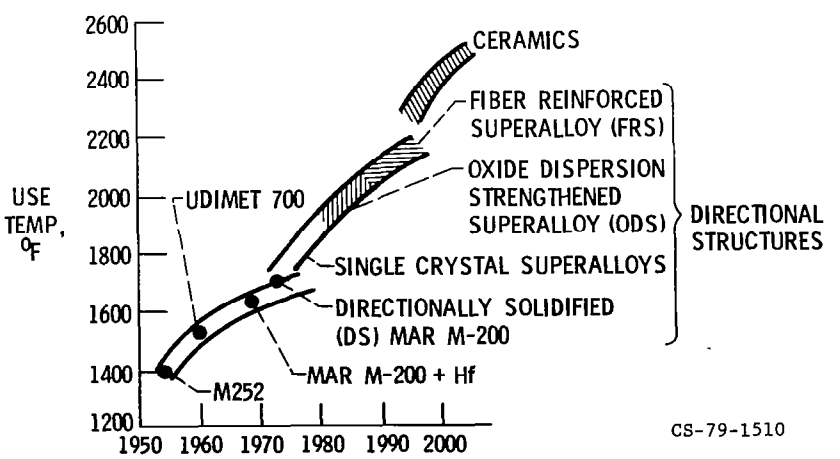

Figure V-6

CAST TURBINE BLADES

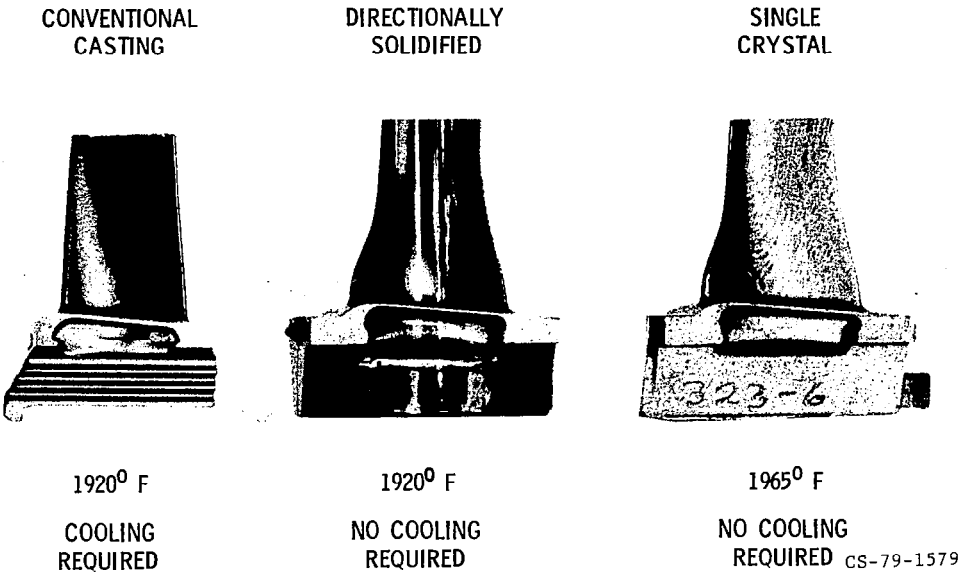

Figure V-7

MECHANICAL ALLOYING PROCESS

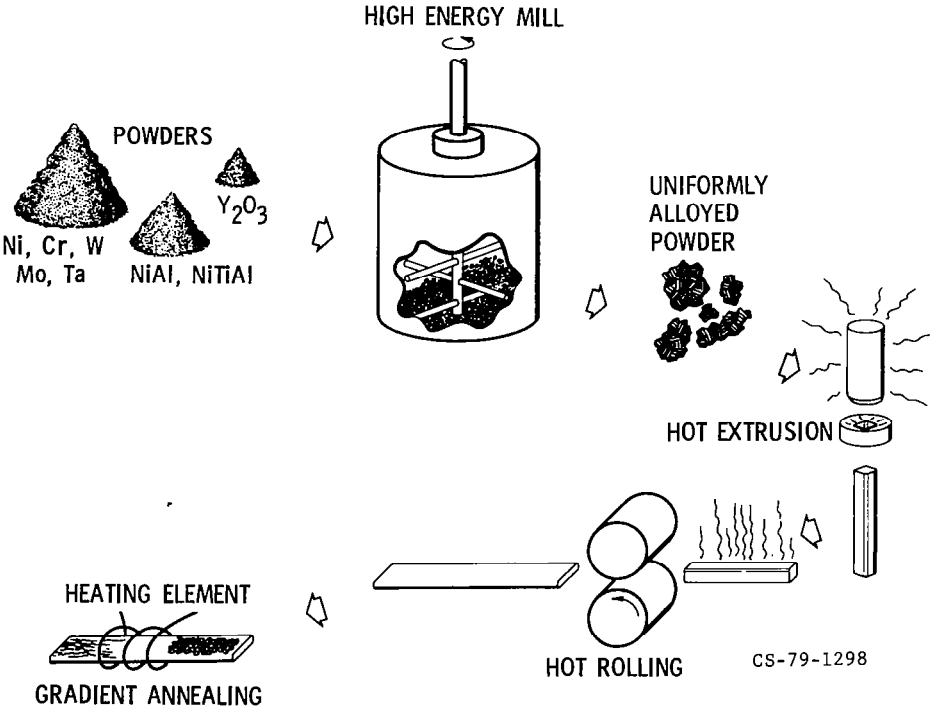

Figure V-8

MACRO AND MICROSTRUCTURE OF AN OXIDE DISPERSION STRENGTHENED SUPERALLOY, MA-6000E

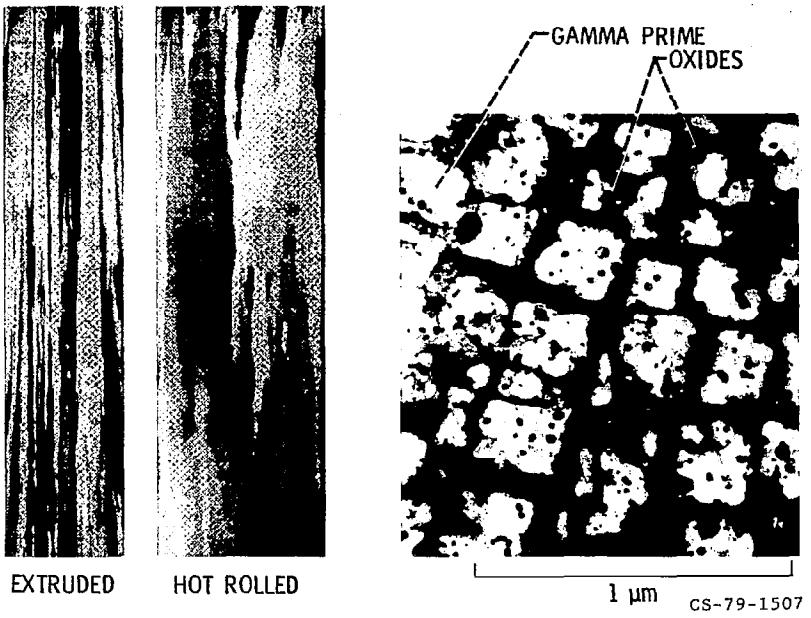

Figure V-9

USE TEMPERATURE ADVANTAGE OF ODS SUPERALLOYS

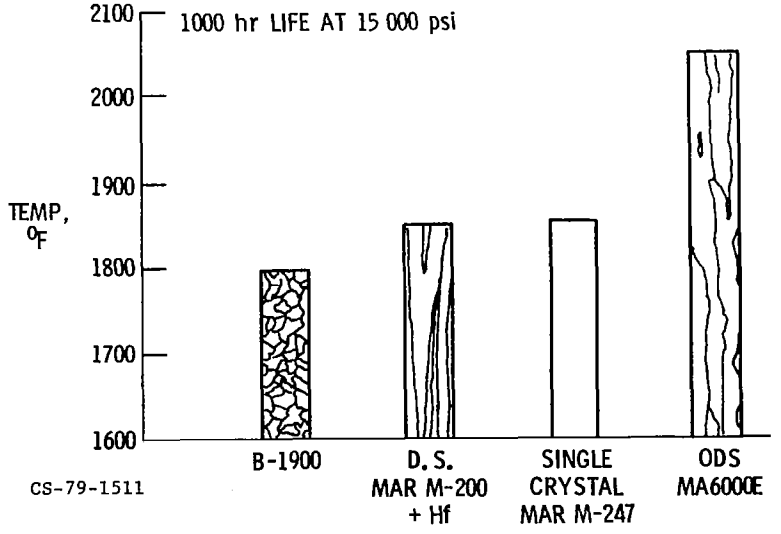

Figure V-10

SUPERIOR THERMAL FATIGUE RESISTANCE OF MA-6000E ODS SUPERALLOY

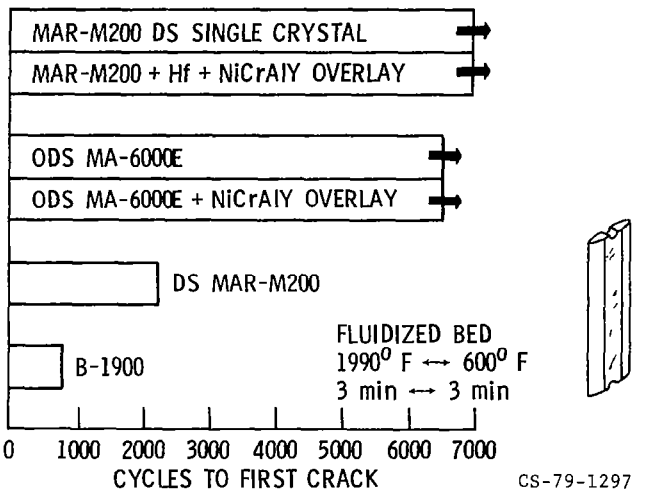

Figure V-11

EXPERIMENTAL SEGMENTED ODS COMBUSTOR DESIGN

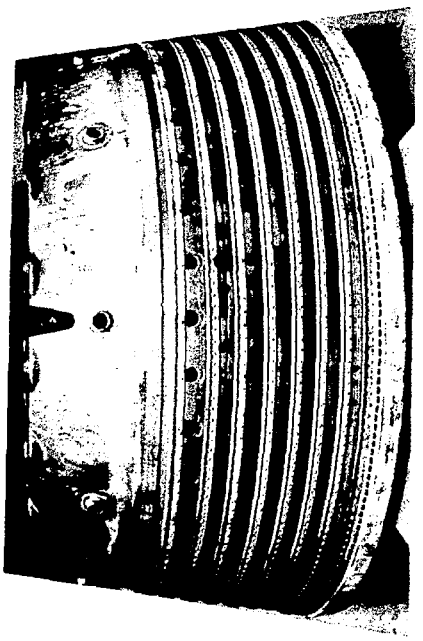

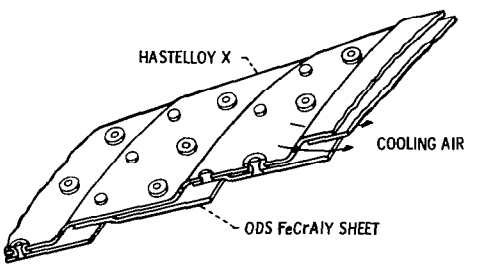

Figure V-12

STRENGTH ADVANTAGE OF TUNGSTEN FIBER REINFORCED SUPERALLOY (FRS)

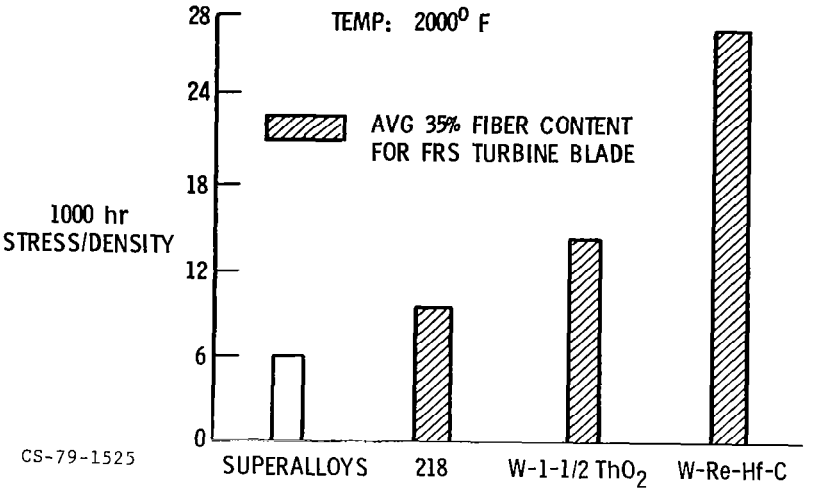

Figure V-13

RELATIVE THERMAL CONDUCTIVITY AND THERMAL EXPANSION ADVANTAGE OF FRS OVER SUPERALLOYS

CONDITION: TYPICAL TURBINE BLADE TEMPS

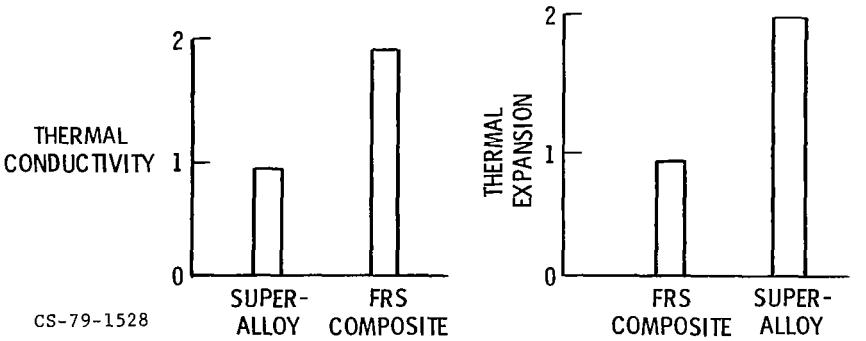

Figure V-14

FIBER REINFORCED SUPERALLOY FABRICATION PROCESS

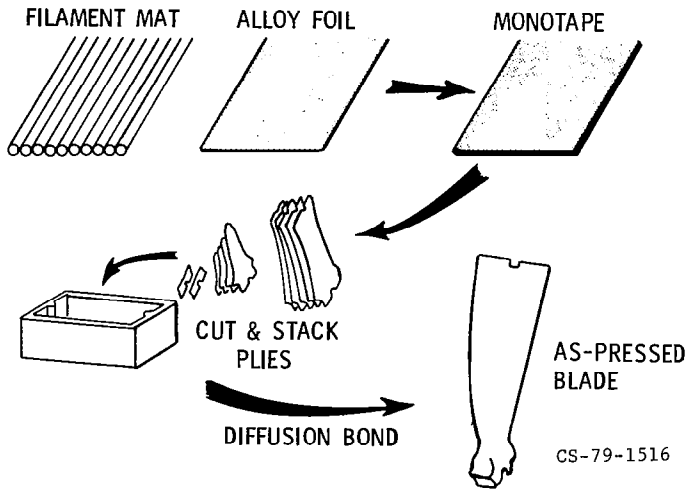

Figure V-15

COMPOSITE BLADE ASSEMBLY SCHEMATIC

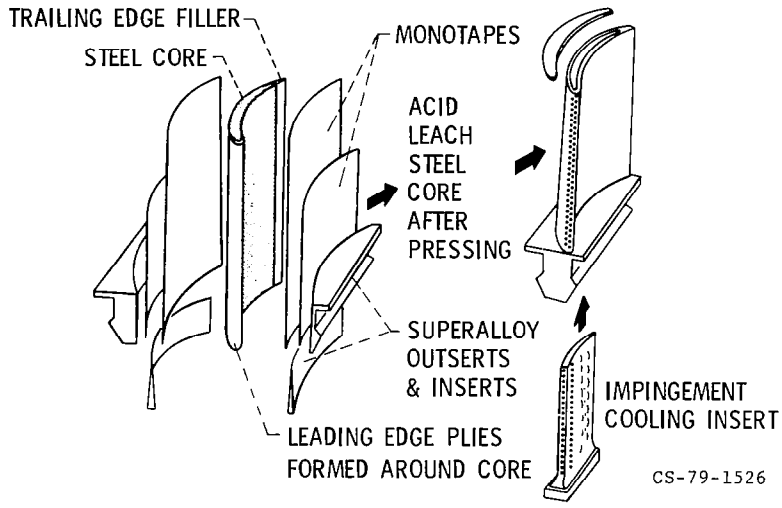

Figure V-16

COOLED FIBER REINFORCED SUPERALLOY
TURBINE BLADE

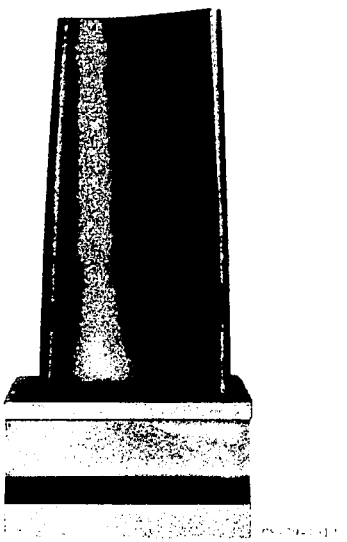

Figure V-17

METALLIC COATING SELECTION METHOD

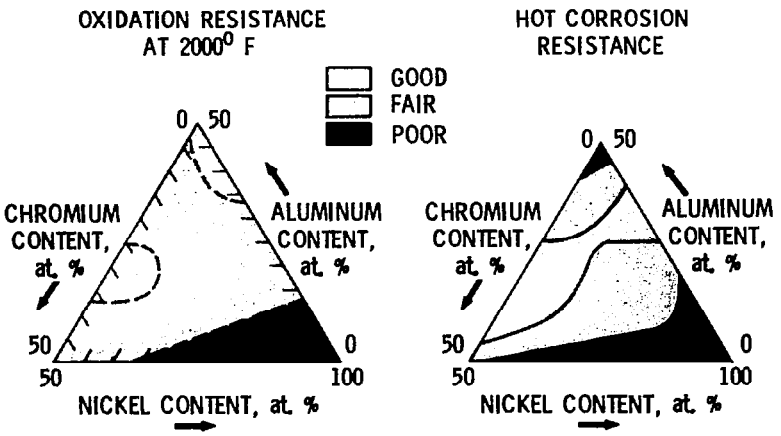

Figure V-18

CS-79-1305

METALLIC COATINGS EXTEND OXIDATION LIFE OF SUPERALLOYS

MACH 1 BURNER, 1 hr AT TEMP ≠ 3 min AT RT

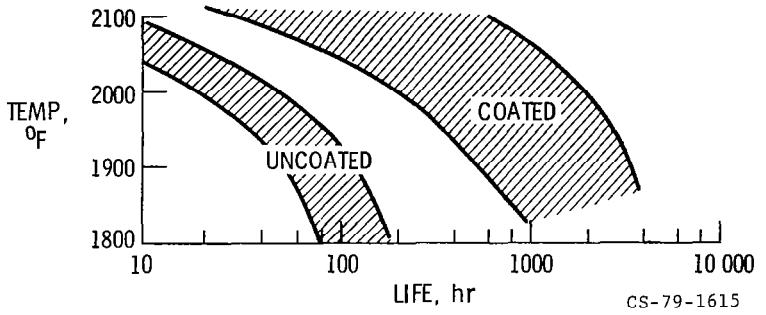

Figure V-19

METALLIC COATINGS EXTEND HOT CORROSION LIFE OF SUPERALLOYS

M 0.3 BURNER RIG, 1 hr AT 900° C ≠ 3 min AT RT; 5 ppm SEA SALT

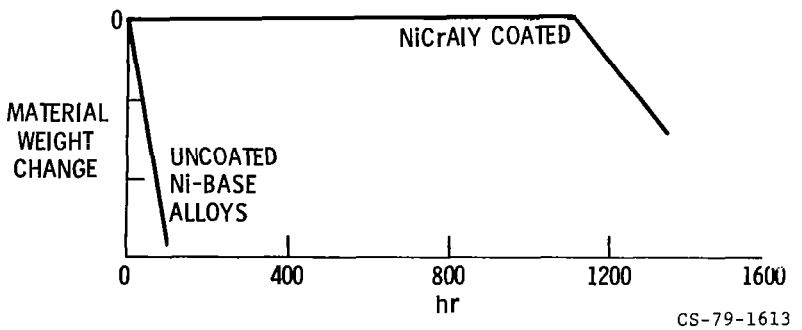

Figure V-20

METALLIC COATINGS EXTEND THERMAL FATIGUE LIVES OF SUPERALLOYS

FLUIDIZED BED TEST; 2000° F (3 min) ⇄ 600° F (3 min)

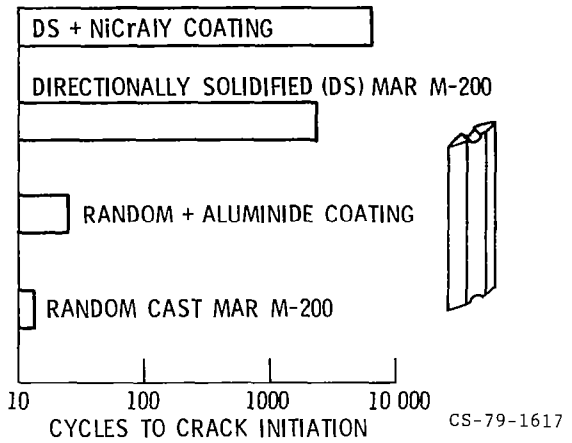

Figure V-21

SCHEMATIC OF THERMAL BARRIER COATING CONCEPT

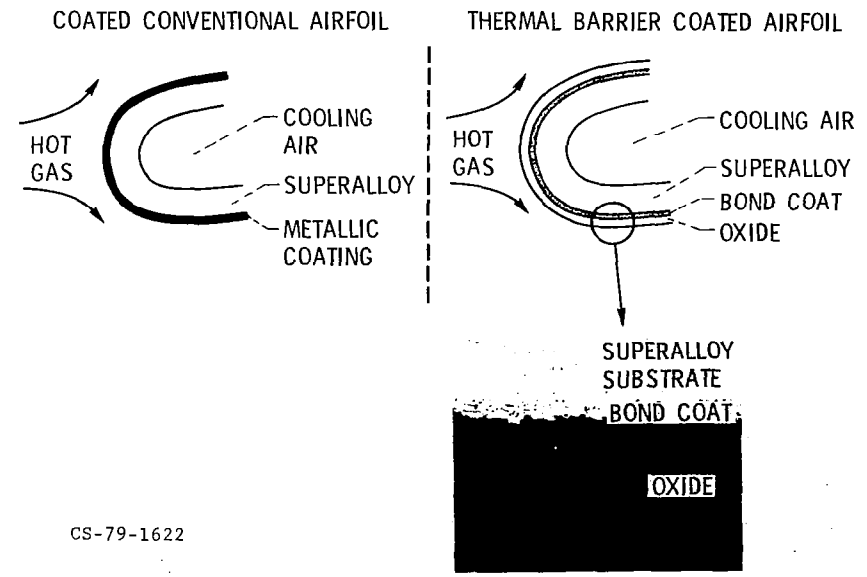

Figure V-22

THERMAL BARRIER COATINGS OFFER LONG LIVES AT VERY HIGH TEMPERATURES

MACH 1 BURNER RIG; 1 hr HOT ⇄ 70° F (30 sec)

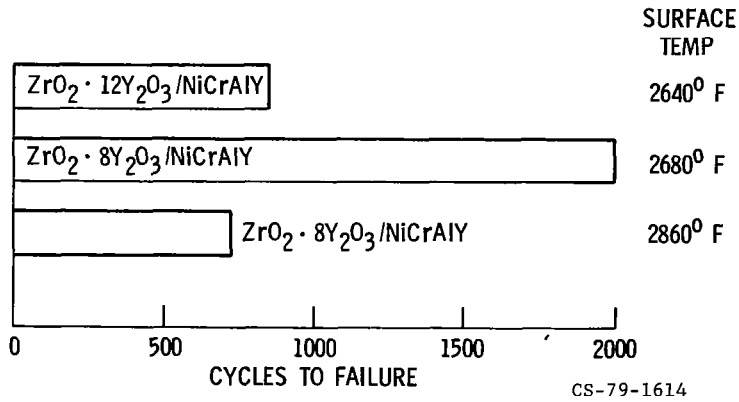

Figure V-23

GENASEAL IS IMPROVED SHROUD MATERIAL

CF6-50C ENGINE GROUND TEST RESULTS

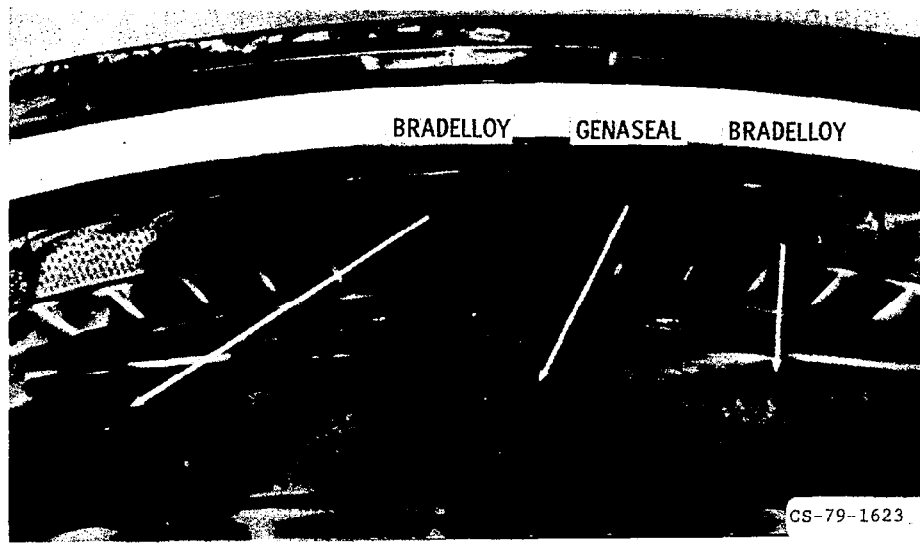

Figure V-24

CHARACTERIZATION OF CREEP-FATIGUE BEHAVIOR BY STRAINRANGE PARTITIONING

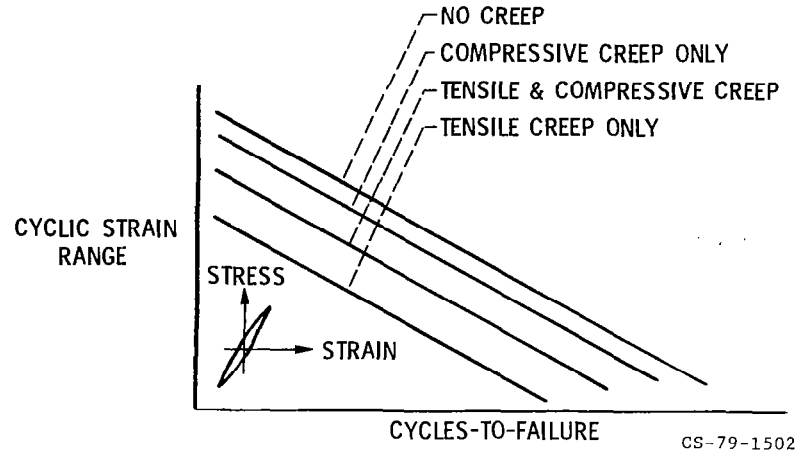

Figure V-25

THERMAL FATIGUE CRACKS IN COMBUSTOR LINER

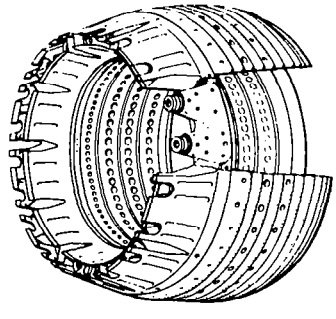

CS-79-1496

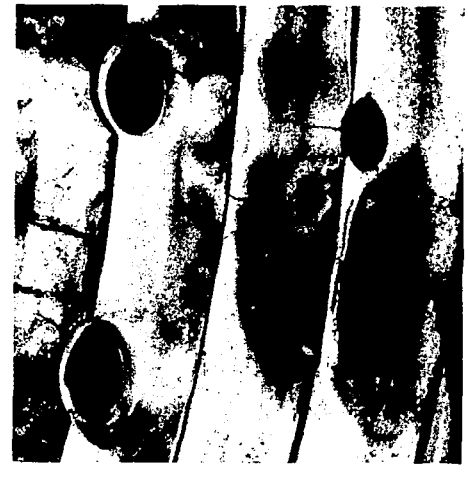

Figure V-26

ACCURACY OF STRAINRANGE PARTITIONING IN PREDICTING COMBUSTOR LINER LIFE IN HIGH BYPASS RATIO ENGINES

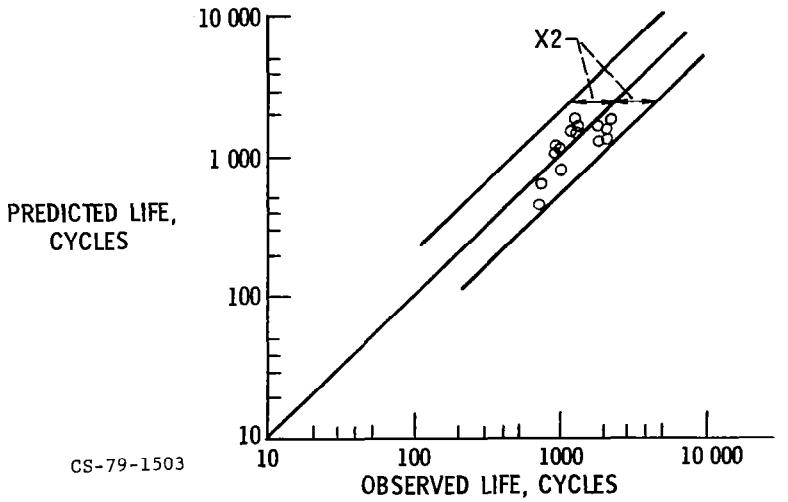

Figure V-27

PREDICTION OF OXIDATION ATTACK BY COREST

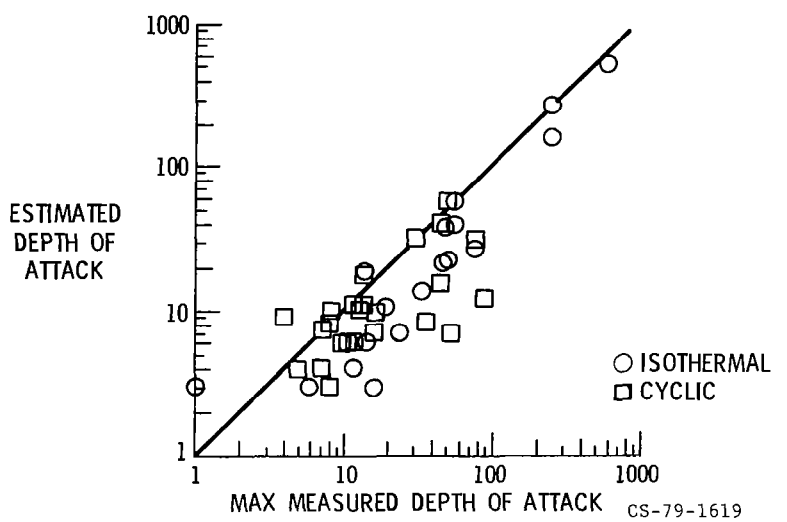

Figure V-28

PREDICTION OF HOT CORROSION ATTACK

MACH 0.3 BURNER RIG, 1 hr 1740° F ⇄ 3 min RT, 200 CYCLES
FUEL IMPURITIES IN ppm: 0.9 Na, 0.9 K, 0.45 Ca, 0.45 Mg

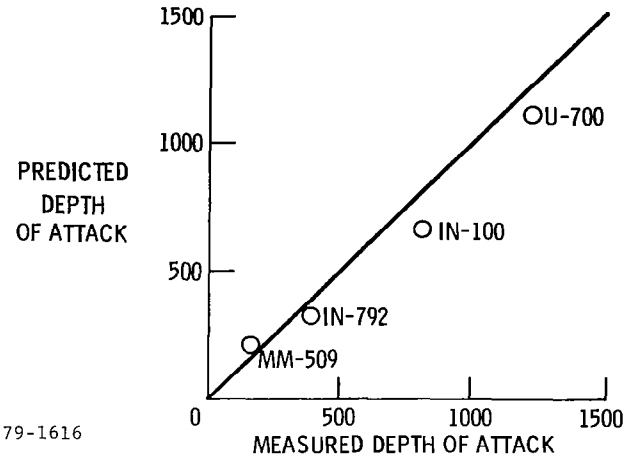

CS-79-1616

Figure V-29

ENVIRONMENTAL AND SUBSTRATE REACTIONS DEGRADE COATINGS

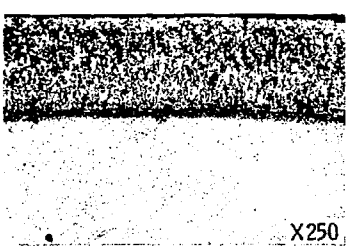

AS-DEPOSITED NiCrAlY COATING

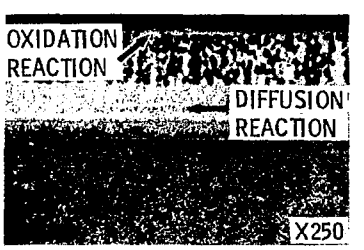

AFTER 200 hr AT 2000° F

CS-79-1621

Figure V-30

HOT ISOSTATIC PRESSING OF LARGE DISK

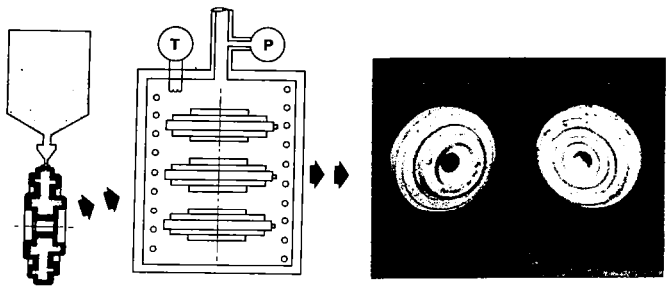

Figure V-31

FIRST STAGE TURBINE DISK FOR COMMERCIAL ENGINES

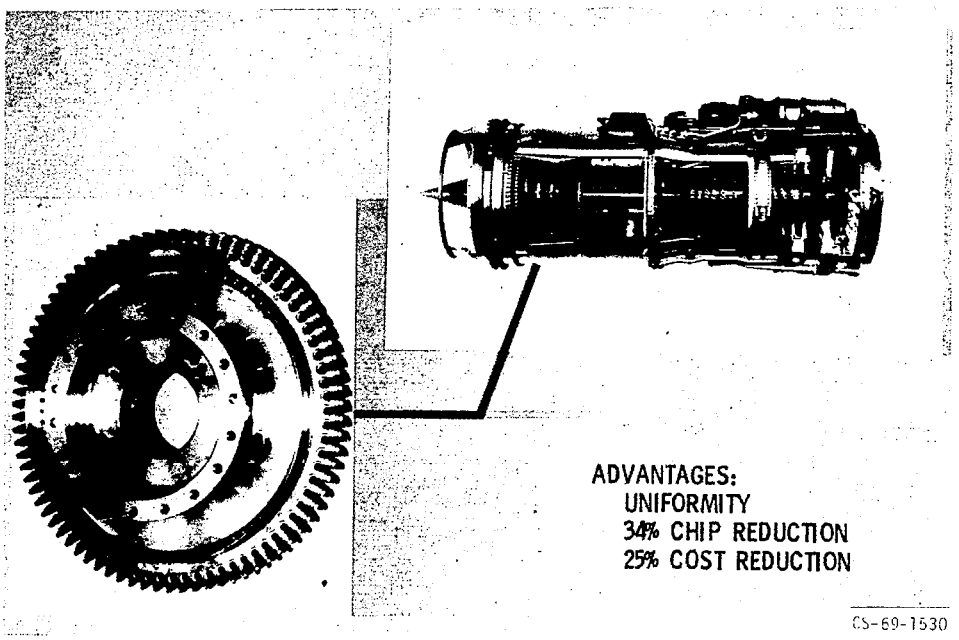

Figure V-32

COMPOSITE FAN BLADE

MATERIALS & DESIGNS

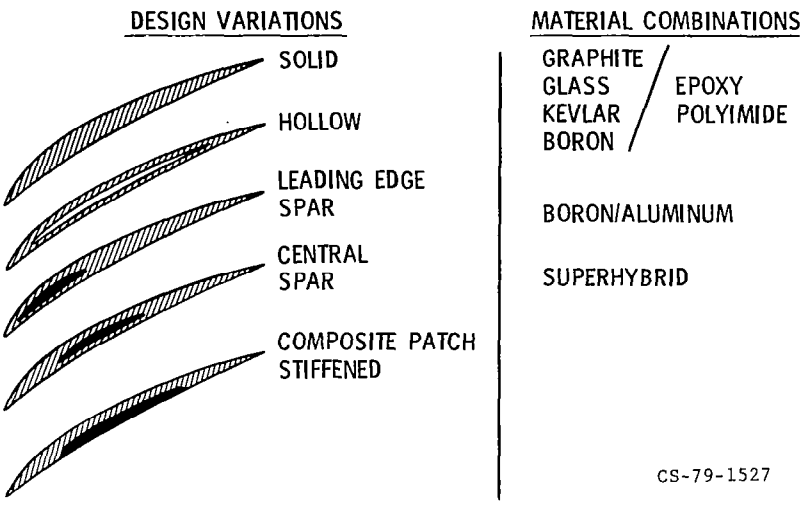

Figure V-33

COMPOSITE FAN FRAME/CONTAINMENT RING

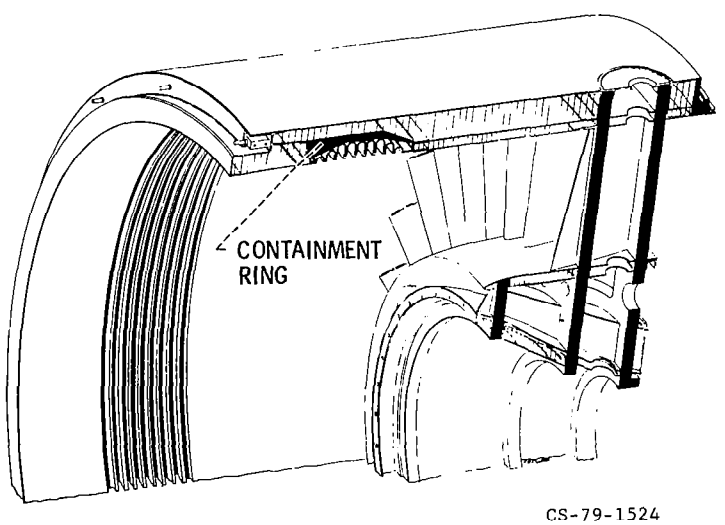

Figure V-34

COMPOSITE NOZZLE FLAP FOR F-100 ENGINE

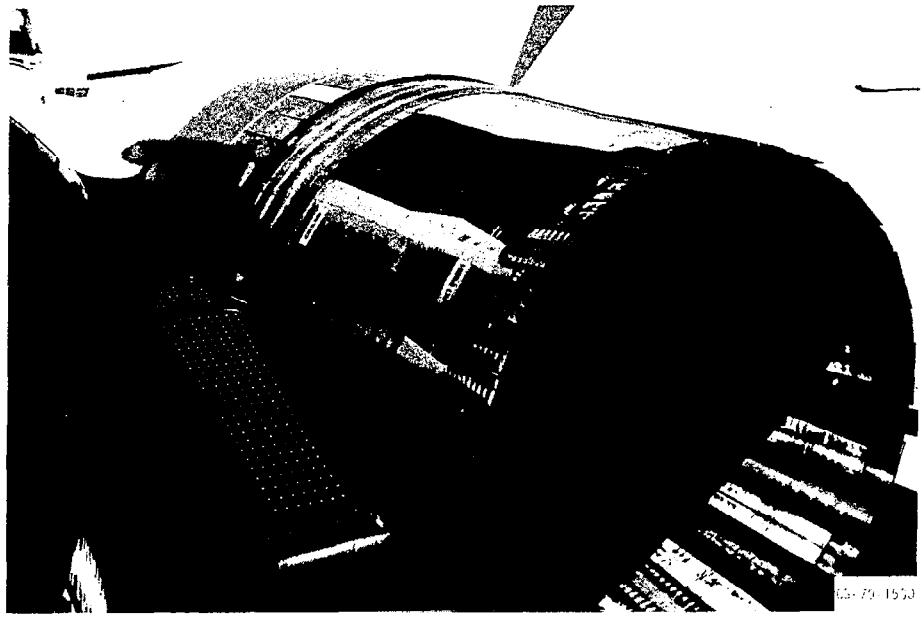

Figure V-35

VI. COMPUTATIONAL FLUID MECHANICS OF INTERNAL FLOW

David N. Bowditch, William D. McNally, Bernhard H. Anderson,
John J. Adamczyk, and Peter M. Sockol

National Aeronautics and Space Administration
Lewis Research Center

Computational fluid mechanics, a method for determining the internal flows of a propulsion system, shares many solution techniques with external-flow computations. However, internal flows present unique problems that require different procedures in applying those solution techniques or, in some cases, completely different approaches. Some of these problems are illustrated by the variable-cycle propulsion system for supersonic cruise shown in figure VI-1. The internal flows of this propulsion system include supersonic, transonic, and subsonic flows in the inlet and nozzle and speed variations from subsonic to supersonic on a single fan blade row. The viscous layers are very important for internal flows. This is particularly true where the annulus heights are small and the adverse pressure gradients are large, such as in a compressor or an inlet, which can have pressure ratios of 20 or higher. The latter stages of the compressor encounter boundary layers over a major portion of the passage. These boundary layers interact with the flow-field curvature to create secondary flows in the blade rows. Therefore, the propulsion-system flow analysis poses many problems that are different from those encountered in computing the external flows around the aircraft. This paper discusses some major solution techniques for internal computational fluid mechanics and presents some examples from the Lewis Research Center program. It then discusses the major steps involved in developing a large computer code.

Until recently, internal aerodynamics has relied on a combination of analysis and empirical correlations that were obtained from many hours of testing. Testing is becoming increasingly expensive as component performance becomes more demanding in order to satisfy the requirements of complex engines such as the variable-cycle engine in figure VI-1. While the cost of testing has been increasing, the relative computation cost has been decreasing, as shown in figure VI-2, where the relative computation cost for many of the computers introduced in the last 25 years is plotted at the year each new computer became available. A value of 1 corresponds to the IBM 360-67 cost. Currently, computation costs are one-hundredth of that cost and are still declining. Therefore, internal computational fluid mechanics becomes more attractive as computation costs continue to decline.

The goals for the Lewis program include rapid simulation of complex flows combined with detailed flow-field descriptions. Computations provide much more detailed information about the flow than most researchers can afford to measure. The goals also include simulation of flows that are too costly to duplicate experimentally and rapid configuration optimization. Meeting these goals will reduce the cost, time, and risk to arrive at improved designs.

SOLUTION TECHNIQUES USED IN INTERNAL COMPUTATIONAL FLUID MECHANICS

The major solution techniques used in internal computational fluid mechanics are shown in figure VI-3. The most complex equations are the full viscous equations. Solving these equations for turbulent flow requires calculating all the eddies shown in the upper left of figure VI-3. This photograph was taken with a camera that was moving with the flow. Even with the special-purpose computers currently planned, solving these equations would require so long that it could only be done for research in fluid mechanics.

Therefore, the first of many efforts to model the flow is done in a manner that simplifies the equations so that they can be solved more quickly. The effect of the eddies on the flow is simulated with a turbulence model so that the viscous profiles shown on the right in figure VI-3 can be calculated. This gives the Reynolds-averaged Navier-Stokes, or viscous, equations. These are still complex enough that current computers can only economically calculate relatively simple two- and three-dimensional flows.

For less time-consuming solutions, more modeling is needed to obtain the methods shown at the bottom of figure VI-3. Additional modeling can provide faster viscous marching methods. By separating the viscous layer from the free-stream flow, we can model each separately and can still obtain certain interactions by using interacting free-stream - viscous methods. By neglecting all viscous effects and using numerical inviscid methods, we can concentrate the computation effort on defining the shocks and the large flow gradients in regions like the leading edge of a compressor blade. For some time-dependent flows, such as those associated with flutter and forced vibration, solutions must be obtained in seconds. Therefore, further modeling is required to obtain analytical methods. In the following discussion, these methods are described, and examples from the Lewis program are presented.

Analytical Methods for Unsteady Flow

Unsteady linearized aerodynamic theory has been used at Lewis to analyze the onset of supersonic flutter in axial-flow fan and compressor stages. These models assume that detailed steady-state flow physics is not required to model supersonic flutter. In addition, the unsteady flow field generated by the blades is viewed as a small perturbation superimposed on a steady base flow. From these assumptions, analytical solutions were developed for the supersonic flutter problem (refs. 1 to 3). These solutions are computationally efficient and, hence, can be used in conjunction with large structural dynamic codes to perform parametric aeroelastic design studies.

In figure VI-4 the flutter regions analyzed at Lewis are shown superimposed on a typical fan performance map. The abscissa on this figure is the weight flow entering the fan. The ordinate is the ratio of exit to inlet total pressure. A typical operating line is shown. The stable operating range of the machine extends up to the stall line. A region of supersonic unstalled flutter extends from near the stall line to wide-open discharge. This unstalled flutter region forms a barrier that potentially limits the design of efficient, high-speed fan stages. At high back pressure the flutter mode in the unstalled flutter region is usually the bending mode. At low back pressure the flutter mode is primarily torsion. At moderate back pressure the flutter mode tends to be a combination of the two. The flutter region shown paralleling the stall line is supersonic stall flutter. The flutter mode in this region is primarily the bending mode.

Supersonic unstalled flutter. - The supersonic flutter analyses developed at Lewis analyze the unsteady flow field surrounding a cascade of airfoils like those in the tip region of a high-speed fan or compressor. A physical model of the cascade flow field at low back pressure is shown in figure VI-5. The relative Mach number approaching and exiting the cascade is supersonic. The shock waves in the entrance, passage, and exit regions are weak and oblique. An analytical model of this flow field is shown on the right of the figure. The steady flow is a uniform, supersonic stream entering and exiting the cascade. The airfoils in the cascade are represented as flat plates oscillating in simple harmonic bending and torsional motion. This motion is the source of the unsteady flow perturbations.

A physical model of the flow field at moderate back pressure is shown in figure VI-6. The entrance-region shock structure is essentially unchanged from its configuration at low back pressure. In the exit region of the passage a normal shock exists. Downstream of this shock the flow field is subsonic. In the analytical model the steady flow entering the cascade is a uniform supersonic stream. A normal shock located at the exit of

the passage takes the flow down to a uniform subsonic stream. The airfoils are again assumed to be harmonically oscillating flat plates. The shape and position of the shock at an instant in time are determined as part of the solution.

A physical model of the flow field at high back pressure is shown in figure VI-7. At this level of back pressure, the normal shock is located at the entrance, with subsonic flow downstream. In the analytical model the steady flow entering the cascade is again a uniform, supersonic stream shocked down to a uniform, subsonic stream by the normal shock at the passage entrance. The motion of this shock, as in the previous model, is determined as part of the solution. The airfoils in the cascade are flat plates harmonically oscillating in time.

The results of applying these three analytical models to a cascade of airfoils oscillating in torsional motion are shown in figure VI-8. The aerodynamic work performed by the airstream on an airfoil during a cycle of motion is shown as a function of interblade phase angle at three levels of back pressure. The interblade phase angle parameter is directly related to the relative displacement between adjacent airfoils in a cascade. If this parameter is 0^{o} or 360^{o}, all the airfoils in the cascade oscillate in unison; if this parameter is 180^{o}, alternate airfoils in the cascade oscillate in unison. When the aerodynamic work is positive, the airstream is supplying energy to the airfoils. Unless this energy is dissipated by damping within the rotor structure, any small motion imparted to the cascade will cause it to flutter. When the aerodynamic work is negative, the airfoils are supplying energy to the airstream. Hence, any small motion imparted to the airfoils will be quickly damped. These results show that in moving from a region of high back pressure to a region of low back pressure, the aerodynamic work becomes positive and this positive work causes torsional flutter. This result is consistent with the experimental observations shown in figure VI-4.

The results of the analytical models applied to a cascade of airfoils in bending are shown in figure VI-9. At low and moderate back pressures the aerodynamic work is always negative. Hence, bending flutter should not occur at these operating conditions. However, if the cascade were operated at high back pressure the analysis predicts that the aerodynamic work would become positive over a range of interblade phase angle. If damping in the rotor assembly is not sufficient to dissipate this energy, the cascade will experience bending flutter. The prediction of supersonic unstalled bending flutter at high back pressure is consistent with the experimental observations shown in figure VI-4. Experimental measurements are currently being obtained in the Detroit Diesel Allison supersonic cascade wind tunnel to validate the supersonic unstalled flutter analyses.

Supersonic stalled bending flutter. - As the operating point of the fan stage is moved toward its stall limit, supersonic stalled bending flutter can occur. The flow-field model for this flutter regime is shown in figure VI-10. The flow approaching the cascade is supersonic. The analytical model for this flow field represents the cascade as a deforming actuator disk that changes the direction and energy of the flow. The motion of an airfoil in the cascade is represented by a combination of simple harmonic bending and chordwise motion. This motion is related to the deformation of the actuator disk in space and time. Strong detached shocks exist near the stall line at the entrance to the cascade. The strength of these waves is sufficient to cause the turbulent boundary layer on the suction surface of the airfoils to separate. The effects of these shocks and the separated flow regions on the unsteady flow field are modeled by using empirical rotor-blade-element loss and turning correlations.

Results of a study using this supersonic stalled flutter model are shown in figure VI-11. The cascade geometry and the steady-state flow field were chosen to represent the tip region of the General Electric Fan C from the NASA Quiet Engine Program. The maximum aerodynamic work predicted over the entire range of interblade phase angle is shown as a function of weight flow and wheel speed. Also shown is the estimated energy dissipated in the rotor assembly during a cycle of motion. Flutter is assumed to occur if the aerodynamic work exceeds the energy dissipated in the structure. Transforming this stability boundary to the Fan C performance map yielded the results shown in figure VI-12. The agreement between theory and experiment is quite good. Currently, General Electric, under contract to NASA, is performing aeroelastic experiments on a 1/3-scale model of Fan C. This program will supply additional data for validating the semi-empirical stalled flutter model.

Current Lewis in-house research in unsteady aerodynamics involves developing analytical models to assess the effects of airfoil geometry on flutter and developing analyses to predict unsteady air-loads caused by flow irregularities.

Numerical Inviscid Methods

Several methods of solving the full inviscid equations are shown in figure VI-13. The full inviscid equations, or Euler equations, cannot handle viscous dissipation such as boundary layers or mixing. However, they do retain the ability to handle total-pressure variations, entropy changes across shock waves, and compressibility. Solving these equations for subsonic flow requires successive calculations through the mesh to relax the solution or to march it in time to converge to a steady-state solution. Time-marching solutions, discussed in a later sec-

tion, are applicable to either subsonic or supersonic flow. If the flow is supersonic, it can also be simulated with the method of characteristics. By further modeling the flow to get the potential equations, solutions are limited to isentropic flow. Finite difference methods can be used to simulate compressible flows with weak shocks. Further modeling to an incompressible flow allows paneling procedures to be used. Examples of these methods are described in the following sections.

Three-dimensional paneling method. - The three-dimensional paneling method represented in figure VI-14 was recently acquired by Lewis from Douglas Aircraft Corp. so that we could design three-dimensional subsonic inlets (ref. 4). Paneling methods are different from all the other steady-state techniques to be described in that any solution can be a linear combination of four fundamental solutions.

The fundamental solutions require a large amount of computer time. However, for a given inlet geometry, the solution for any combination of angle of attack, yaw, and inlet mass flow can be obtained quickly by properly combining the four fundamental solutions. This computational technique is thus ideally suited for parametric studies.

This new analysis gives Lewis the ability to predict the nonuniform pressure on three-dimensional inlets like the scoop inlet shown in the figure. The surface static pressure is for the inlet operating at zero angle of attack. The pressure distribution at the top of the inlet indicates an overexpansion and recompression. The pressure distribution at the side of the inlet shows less overexpansion, and that at the lower lip shows almost no overexpansion. By combining these pressure distributions with boundary-layer analysis, it is possible to estimate the operating limits of the inlet.

Two-dimensional potential-flow finite difference method. - Another potential-flow problem on which progress has been made is the solution to the full potential-flow equation for two-dimensional blade-to-blade flow through compressor blade rows. A calculation obtained with a finite difference relaxation solution, developed at Lewis, to the full potential equation is shown in figure VI-15. The solution is for flow through a cascade of thin blades at a 60° setting angle and a 3° angle of attack. One of the keys to the success of this new method is the use of a unique body-fitted solution grid that is drawn on the blades at the left side of the figure. The effect of the solution grid used on the accuracy of the computed results is discussed in more detail later. Calculated results are presented in figure VI-15 in terms of blade-surface relative Mach number as a function of distance along the blade chord. These results show the ability of the method to automatically capture

shocks in the transonic region of the flow field. In the past, when time-marching techniques were used with the Euler equations, this type of calculation took much more computer time.

Three-dimensional method of characteristics. - Potential-flow solutions are used for subsonic and transonic flows, but the method of characteristics is used primarily for supersonic flows. The three-dimensional method-of-characteristics analysis presented in figure VI-16 was developed at Purdue University (refs. 5 and 6) and is used for computing the flow field in supersonic, mixed-compression inlets operating at the angle of attack. In this method, the shock waves are computed by a discrete shock-wave-fitting scheme.

At the bottom of figure VI-16, the centerbody surface static pressures on the windward and leeward sides are plotted as a function of distance from the cowl lip. These results are for a mixed-compression inlet operating at Mach 3.3 and 3^{o} angle of attack. The data for the leeward side are compared with the solid calculated line. Good agreement is obtained to just ahead of the second shock pressure rise. At this point, viscous effects apparently feed the shock pressure rise forward over a wide region. Although the current inviscid analysis predicts significant differences between the windward and leeward sides, a viscous interaction must be added to obtain better agreement at the second shock near the inlet throat. This additional effort is currently planned for next year.

Three-dimensional time-marching methods. - Time-marching solutions to the full inviscid, or Euler, equations are very useful for analyzing transonic flows with shock waves and have been used at Lewis for analyzing propeller and compressor flow fields.

Transonic propeller: The three-dimensional solution developed at Ames for the eight-bladed turboprop configuration shown in figure VI-17 will be used to support design studies for the Advanced Turboprop Project Office. Calculating the flow through the blade passage starts with an initial guess of the flow field in a coordinate system attached to the blade and progresses through time to a steady-state solution.

For this transonic propeller operating at a free-stream Mach number of 0.8 and a relative tip Mach number of 1.15, static-pressure distributions are shown in figure VI-18 for the hub, mean, and tip sections. All the distributions reveal substantial regions of supersonic flow along the blade section. The sharp changes in the static-pressure coefficient at the hub, mean, and tip sections of the blade indicate that the shock extends over the entire span. Substantial spanwise variation in blade loading is indicated by the differences in the areas be-

tween the suction- and pressure-surface curves. Experiments are planned to provide test data to verify this computer code.

1800-Foot-per-second rotor: Another time-marching solution has been developed for NASA at MIT (refs. 7 and 8). This code is for analyzing flow in a three-dimensional compressor blade row, such as the one shown in figure VI-19. This solution of the full inviscid (Euler) equations permits analysis of three-dimensional flow with strong shocks in a rotating blade row that contains midspan dampers. The general three-dimensional solution region includes the interblade passage and the nearby entrance and exit regions.

A midpassage flow surface in the hub-to-shroud direction is also shown. Figure VI-20 shows a contour plot of pressure on this midpassage flow surface for an 1800-foot-per-second-tip-speed fan. The darker regions indicate high pressure and low velocity and the lighter regions, low pressure and high velocity. The closely spaced contours near the front of the passage show the bow shock, which crosses the passage to the suction side of the blade. The contour lines around the damper indicate flow deceleration on the upper side and flow acceleration on the bottom side. This flow variation is caused by a negative flow incidence at the damper of approximately 5°. This information can be used to reset the damper for lower losses.

1600-Foot-per-second rotor: The time-marching technique has been applied to calculating three-dimensional flow in a 1600-foot-per-second-tip-speed fan rotor. A blade-to-blade surface for flow near the tip of this blade row is shown in figure VI-21. Calculated and experimental results are compared for this blade in figure VI-22.

The experimental results at the right in figure VI-22 were obtained at MIT with a unique laser-fluorescence technique in which seed particles in the test gas are excited with a flat sheet of laser light. The resultant fluorescent illumination is photographed and can be directly related to the density of the flow. These experimental results show the presence of two shocks in the passage: a strong normal shock at the exit region and a detached bow shock crossing the passage from the leading edge of the upper blade to the suction surface of the adjacent blade. The presence of two shocks in the passage was unexpected, yet the calculated contours shown at the left in the figure confirm that two shocks should be present. These are evident from the concentration of density contours at the exit region of the passage and also at the leading edge. The analytical density ratio across the bow shock is in agreement with experiment to within 2 percent; the agreement is within 10 percent for the in-passage shock.

Interacting Free-Stream - Viscous Methods

About 70 years ago, Prandtl divided flow near surfaces into a free-stream region and a viscous region, as shown in figure VI-23. This permitted modeling in each region and simplified each solution technique. In many internal flows, it is often desirable to determine the interaction between the viscous and free-stream regions. There are many ways to determine this interaction, but only boundary-layer displacement of the inviscid flow region and matched fluid properties at the interface between the two regions are described here.

Boundary-layer displacement - two-dimensional cascade. - The prediction of fluid turning and loss for two-dimensional blade sections is a key ingredient in most compressor design systems. Figure VI-24 shows schematically the inviscid and viscous regions in a two-dimensional cascade flow and indicates the possible presence of a separation near the trailing edge. In this vicinity the coupling between viscous and inviscid effects can be quite strong. The present method uses separate finite-difference solutions in each region and couples them by means of the displacement effect, which is modeled as a surface injection of fluid (ref. 9).

Experimental and analytical values of fluid turning angle and loss coefficient are compared as a function of angle of attack in figure VI-25 for subsonic flow in a cascade. Also shown is the location of the calculated separation point on the blade suction surface. Although the agreement with the data, for both turning and loss, is only qualitative, the results show that the strong upturn in the experimental and predicted losses corresponds to the rapid shift of the separation point toward the leading edge. Work on this method is continuing at Iowa State University.

Boundary-layer displacement - blade-passage end wall. - Another boundary-layer displacement approach is being developed here at NASA Lewis to analyze flows in the end-wall regions of axial compressors. Most losses in turbomachinery occur in these end-wall regions. The flow along the end wall of a rotating blade row is shown in figure VI-26. A two-dimensional turbulent velocity profile is shown at the inlet. The turning of this flow by the blades generates a passage vortex that in turn modifies the local blade loading and produces a three-dimensional velocity profile at the exit. The present method (ref. 10) uses a pitch-averaged, integral, boundary-layer procedure in the viscous region. This procedure uses an approximate solution for the secondary flow in order to evaluate many of the three-dimensional effects. The inviscid solution is currently obtained from a quasi-one-dimensional model. The two solutions are iteratively coupled by means of the displacement effect.

Experimental and analytical values of equivalent blockage and end-wall loss are shown in figure VI-27 as a function of axial distance for flow through a cascade. For this case the dramatic increase in blockage inside the passage is well predicted by the method, but the agreement for end-wall loss is only qualitative.

Supersonic-subsonic viscous interaction method. - A different approach to the interaction of the viscous layer with the free stream is used in the supersonic-subsonic viscous interaction method depicted in figure VI-28. The method was initially developed in a joint program between Lewis and Case Western Reserve University (refs. 11 and 12). The numerical solution for the flow in the supersonic viscous region is obtained by applying the method of characteristics to a system of equations that includes some viscous terms. The system of equations for the subsonic viscous region includes, in addition to the classical boundary-layer terms, the effects of transverse curvature and normal pressure gradients. Coupling the supersonic and subsonic viscous regions at the interface requires an iteration to match the streamwise and normal velocities as well as the static and total pressures and temperatures.

Although this interaction analysis is still under development at Lewis, some preliminary results are shown in figure VI-29. The calculation was performed on an axisymmetric waisted body, which is shown in the lower part of the figure. The upper part of the figure shows Mach number profiles plotted as a function of distance from the surface at various stations along the waisted body. The calculation was able to pick up the embedded shock wave emanating from the waist region. It is in this particular region that it is very important to include the normal pressure gradients across the boundary layer in the viscous solution.

Viscous Methods

The fully viscous methods under study at Lewis include both the viscous marching methods and the full Reynolds-averaged viscous equations (fig. VI-30). The solutions to the Reynolds-averaged viscous equations require successive calculations through the mesh in order to relax the solution or to march it in time to a steady solution. They typically require very long run times. Since run time increases with the number of mesh points in the flow, only a moderate number can be used and this results in limited flow resolution. Through flow modeling the problem can be partially separated into two steps: An inviscid solution is used to obtain upstream effects on the subsonic flow field, and then the viscous equations are marched down the flow field to define the viscous effects. Faster run times for these marching methods permit the use of more mesh points, and this results in

better flow resolution. Some recent results from these viscous marching methods and a solution to the full Reynolds-averaged viscous equations are described in the following section.

Axisymmetric viscous marching method. - An axisymmetric viscous marching method (refs. 13 and 14) was developed at United Technologies Research Center to analyze annular flows in configurations like the nozzle depicted in figure VI-31. This method treats the entire flow field in any annular duct with a single set of viscous equations. It constructs a mesh like that shown in the figure, with the stream function as the normal coordinate and the velocity potential as the streamwise coordinate. Since the inviscid-flow streamlines approximate the viscous-flow streamlines, the fully viscous equations can be reduced to a set of boundary-layer-like equations that can be solved by a forward marching method. The solution mesh for the curved nozzle shown in figure VI-31 is a typical mesh that is necessary to properly resolve the flow.

Velocity profiles at different stations within the curved nozzle are shown in figure VI-32. Because of channel divergence, the flow initially diffuses until it nearly separates on the inner wall. Then the flow rapidly accelerates and the boundary layer thins as the flow turns. Finally the flow rapidly diffuses until it again nearly separates at the nozzle exit. Also clearly evident in the figure is the significant flow shift from one side of the passage to the other.

Three-dimensional viscous marching method. - An application of viscous marching methods to three-dimensional flows is described in figure VI-33. This method, developed by Scientific Research Associates, was specifically designed for configurations with large geometric curvature (refs. 15 and 16). Such flows are common in both diffusers and turbomachinery. Another variation of this numerical analysis, which uses generalized coordinates (refs. 17 and 18), can compute flows in duct geometries with cross-sectional transitioning and off-set bends.

The ability of the present method to predict the formation and development of secondary flows is of primary interest here. A sample calculation was made on a circular-arc duct with a square cross section (fig. VI-33) in order to evaluate the present state of development of this method. For this calculation, a 20x20 mesh was used in the transverse plane and 45 streamwise stations were used in the forward marching direction. This gave a step size THETA of 5.0°. The flow was assumed to be symmetric about the half-span plane.

A computer motion picture made of the calculations shows the development of the secondary flows in the transverse planes. Sample frames from this motion picture are shown in figure VI-34 for angular positions (THETA) of the cross plane every 30°.

Initially, there is no secondary flow entering the bend (THETA = 0). The secondary flows along the top and bottom surfaces begin to move toward the suction surface so that at THETA = 30° two large counter-rotating vortices have been well established. These secondary flows are caused by the transverse pressure gradients associated with the turning of the primary flow. By THETA = 60°, a second vortex pair has been formed close to the pressure, or right, surface. This vortex pair is convected toward the suction, or left, surface so that by THETA = 90° it has merged with the first vortex pair. A third vortex pair is forming near the plane of symmetry close to the pressure surface. This vortex pair builds up in strength (THETA = 120°) and moves toward the main vortex pair. This allows a smaller vortex pair to form in the corner near the pressure surface (THETA = 150°). This vortex pair grows in strength (THETA = 180°) and translates toward the suction surface to join the initial vortex pair (THETA = 210°).

These results demonstrate the complexity of geometry-driven secondary flows that stem from the curvature and the associated pressure field. To verify that the calculations represent a real flow, we have begun an experimental effort to obtain Doppler velocimeter measurements in a similar configuration.

Forced mixer nozzle: In support of the Lewis Engine Component Improvement program, a three-dimensional compressible viscous marching code is under development at Scientific Research Associates. It will be used to analyze the flow in lobed mixer nozzles of the type depicted in figures VI-35 and VI-36. In the lobed mixer nozzle, the hot core flow passes up through the lobed section and the cooler fan flow passes down through the valleys. Very simply, this nozzle increases mixing by providing a much greater interface between the hot core flow and cooler fan flow. By mixing the core and fan flows in this manner, a small but significant performance gain can be realized. The level of the gain depends on the trade-offs between the degree of mixing of the two streams and the viscous losses incurred in the mixing process.

The present analysis concentrates on the actual mixing process downstream of the lobe exit plane. Although the present analysis is preliminary in that only laminar flow is considered, it addresses the important underlying fundamentals of lobed mixer flows.

A sample laminar calculation was performed with this preliminary deck in order to evaluate the overall method in its present state of development and to demonstrate the potential of this method for predicting the flow and the mixing process in lobed mixers. The solution was computed for the geometry shown in figure VI-36. The Reynolds number based on the hot-stream velocity and the inlet casing diameter was 900, the Mach number

of the inlet plane was 0.35 in both streams, and the temperature ratio between the streams was 2. Because of nozzle symmetry, only a pie-shaped computational segment covering a half lobe had to be analyzed. The computational mesh within this segment consisted of 20 points in the radial direction and 10 points in the circumferential direction. A computer motion picture was made showing the development of total temperature and streamwise vorticity at successive axial stations. Several simulated frames showing profiles of temperature and streamwise vorticity are presented as figure VI-37. The locations are identified by the station number, which increases from 0 at the lobe exit to 32 at the mixer nozzle exit.

At station 0, there is no streamwise vorticity, and the total-temperature plots clearly define the lobe geometry. As the solution begins to move downstream, there is relatively little change in the total temperature. Vortices are generated on both sides of the radial interface between the core flow and the fan flow (station 6). As the solution progresses downstream, the vortices initially generated in the core flow dissipate and the fan vortex pairs dominate (station 12). As the vortex pairs intensify near the end of the plug (station 19), faster mixing appears to take place. The overall effect is to enhance mixing. The vortex intensity and resulting enhanced mixing are probably due to the curvature of the flow at the end of the plug. This suggests that the centerbody shape is important to the mixing process through the generation of streamwise vorticity. Downstream of the plug (station 32), the streamwise vorticity dissipates.

Three-dimensional full viscous method. - The final example is a solution to the full Reynolds-averaged viscous equations. The solution is for flow in a blade passage of the centrifugal impeller shown in figure VI-38.

There is currently considerable interest in centrifugal compressors for small jet engines and for automotive applications. The flows in these devices are quite complex and often contain large separated regions. The present technique was developed under an NASA contract with Thermo Mechanical Systems (ref. 19). It solves the steady viscous equations, first on blade-to-blade surfaces that are swept from hub to shroud and then on cross-sectional surfaces that are swept from inlet to exit. By alternating between these two sweep directions, the full solution can eventually be obtained. The method is quite time consuming and takes several hours on the fastest computer that is now available.

A velocity-profile plot of the solution on a blade-to-blade surface of a centrifugal impeller is shown in figure VI-39. The calculation is for laminar flow and exhibits a large separation on the suction surface near the trailing edge. A turbulence

model has recently been added to the code, and further development is now under way.

DEVELOPMENT OF A COMPUTER CODE

The steps in the development of a computer code and some of its key elements are shown in figure VI-40. Developing a code from a basic algorithm to a design-analysis code can take many years and includes geometry and graphics work that may have little to do with fluid mechanics. The process usually starts with the basic algorithm, which is a numerical scheme to solve the appropriate equations for a relatively simple geometry and flow. For example, the initial code may only treat laminar flow on a flat plate. To extend that capability to more practical flows and to obtain what we call a research code require considerable effort. Initial and boundary conditions, a turbulence model, and more complex geometry and mesh are all part of this effort.

Geometry and Mesh

Geometry and mesh generation are often a major roadblock to the use of a research code. The geometry often needs to be quite detailed and smooth, and the mesh characteristics often affect the computed results. Therefore, computer assistance is frequently needed to overcome this barrier.

Enrichment techniques. - Experience with three-dimensional potential-flow paneling techniques has indicated that the large number of panels depicted on the right in figure VI-41 are required to describe the inlet geometry in sufficient detail to obtain an accurate calculation. Typically, over a thousand panels can be necessary for complex inlet geometries. However, it is difficult and time consuming to input all the necessary information by hand. Therefore, techniques have been developed at Lewis to smooth and enrich the input geometry, that is, to input a few points and have the computer enrich and construct the necessary number of panels.

Effect of mesh geometry. - In addition to describing the geometry of a configuration to the computer, there is the subsequent problem of generating an appropriate grid, if a finite-difference solution is to be used. In numerical code development, the solution grid, or mesh, can greatly influence the accuracy of the calculated results. Shown in figure VI-42 are two finite-difference meshes applied to the same cascade of thin blades. At the left is a conventional sheared mesh of throughflow lines and blade-to-blade lines that has been used successfully with a number of numerical methods. When applied with the new full-potential relaxation scheme described previously, this mesh yielded

the surface Mach number distribution in figure VI-43. The terminal shock expected at the end of the supersonic zone was completely smeared by the numerical algorithm applied on this sheared mesh. The spike near the blade trailing edge is another result of the poor performance of the sheared mesh. A proposed solution to this shock resolution problem was the application of a less conventional wraparound mesh, shown at the right in figure VI-42. Although this mesh is more difficult to generate, it has the advantages of grid lines nearly normal to the blade surface in a direction alined with the shock and of clustering grid points near the leading and trailing edges of the blades, where flow gradients are strong. The improved resolution of the terminal shock to the supersonic bubble is very evident in figure VI-44, which now has the solution for the wraparound mesh superimposed on the original solution for the sheared mesh.

Graphics and Data Handling

In addition to dealing with complex geometries and generating grids tailored to finite-difference schemes, there is the problem of extracting meaningful information from the tremendous volume of output generated by the large three-dimensional and viscous codes. Sophisticated computer graphics and data-handling techniques such as those shown in figure VI-45 are required to alleviate this problem. These techniques include profile development, x-y plots, contour representation, geometry and vector plots, streamline tracing, and three-dimensional function representation. To make graphical techniques available to all Lewis flow analysis codes, we have modified them to build a standard bulk data file. This file can be accessed by any of the graphical techniques represented in this figure.

It is also very important that the engineer have a variety of graphical hardware available to display data. These might include a Calcomp plotter, cathode ray tubes, microfilms, and motion pictures. Color capability must also be included because it can be used very effectively to enhance the meaning of graphical representations.

Much work still has to be done in developing data-handling and graphics techniques, particularly for three-dimensional steady and unsteady flow fields.

Benchmark Experiments

In addition to the coding efforts previously outlined, there is the important problem of verifying the accuracy of the codes. Carefully planned and executed (benchmark) experiments are re-

quired to prove that the models incorporated in the coding represent the physics of the real flows.

Effective benchmark experiments have the following characteristics: First, they are conducted in simple geometries that isolate a particular flow phenomenon. The flow situation is simplified initially so that various aspects of the numerical algorithm can be verified. Geometry and boundary and initial conditions are clearly defined. Redundant measurements are often conducted with differing kinds of instrumentation in order to give credibility to the results. Finally, the results must be well documented and available to everyone. NASA Lewis recognizes the extreme importance of this type of activity and will be emphasizing benchmark experiments in the near future.

Design-Analysis Codes

A large effort is required to obtain a verified production code. However, for the designer to use this code, additional assistance is needed. The code can require long computer run times; and therefore, for efficient use, the number of full solutions obtained must be minimized. This can be done by using the interpolation and optimization techniques described in the following paragraphs.

Numerical optimization procedures. - So that long-running codes can be used for design, procedures must be developed to aid the user in selecting an optimum configuration. A numerical optimization procedure was developed at Lewis so that the computer could be used, instead of the wind tunnel, to search for the best inlet bleed configuration. This computer code is diagrammed in figure VI-46. Data are introduced to initialize the decision variables, which are the bleed rates at the shock - boundary-layer interaction regions. The optimization routines make changes in these decision variables, and these changes are evaluated by the aerodynamic programs, subject to the objective and constraint functions. The objective function in this problem is maximum range; the constraint function is avoiding boundary-layer separation. This process is repeated until an optimum, or final, design has been reached.

The variation in range decrement and total bleed rate as a function of the number of iterations is shown in figure VI-47. Forty iterations were required to obtain a minimum range decrement, or a maximum range. The bleed rate obtained in the wind tunnel for a Mach 2.5 mixed-compression inlet agreed with the results of the computer optimization procedure. This was accomplished in about 30 minutes of computing time on the Univac 1110; this compares to several weeks of varying the individual bleed zones on the inlet model in the 10- By 10-Foot Supersonic Wind Tunnel.

Fast-perturbation solutions for design. - There is also a need to assist the designer in using long-running codes throughout the design process. Information from existing solutions can be used to predict other solutions at slightly perturbed flow conditions or with slight changes in geometry. This approach is particularly helpful in blade profile design, where parametric studies are often conducted over a range of flow conditions and geometry perturbations.

A method has been developed for NASA Lewis by Nielsen Engineering (ref. 20). In this method, perturbation solutions can be obtained easily and rapidly for changes in a number of flow and geometry parameters. These solutions use previously calculated base solutions from the longer running codes. In figure VI-48, the two dashed-line solutions represent the two base solutions obtained with traditional analysis codes. These were run on a parabolic-arc blade profile for angles of attack of 3.0° and 4.0°. The perturbation code, which uses information from these base solutions, was then run to obtain a solution at an angle of attack of 3.75°. This solution is represented by the circular symbols in the figure, and it was obtained in less than 1 percent of the computer time used by either of the base solutions. So that its accuracy can be evaluated, it is compared in the figure to a third full-base solution for an angle of attack of 3.75°; and it is evident that the agreement is excellent. Results for perturbations of other variables show just as good agreement in the same short computer time. This code will soon be extended to perturb several design variables simultaneously.

CONCLUDING REMARKS

As discussed in the examples, many internal flows can now be analyzed by using computational fluid mechanics. A large effort is required to develop the computer codes needed to analyze these flows from a basic algorithm to a code that can be used reliably for designing aircraft hardware. Most of the results discussed in the text are from codes that are only part way through that development cycle. Therefore a lot of work is still required to compile the library of codes needed to analyze all the internal flows in a propulsion system. The Lewis Research Center is convinced that the effort is worthwhile and is currently constructing the Research Analysis Center shown in figure VI-49 to house new computer facilities that will support this work. The results of the effort should allow the designer to produce a better product cheaper, faster, and with less risk.

REFERENCES

1. Goldstein, M. E.; Braun, W.; and Adamczyk, J. J.: Unsteady Flow in a Supersonic Cascade with Strong In-Passage Shocks. Fluid Mech., vol. 83, Dec. 5, 1977, pp. 569-604.

2. Adamczyk, J. J.; and Goldstein, M. E.: Unsteady Flow in a Supersonic Cascade with Subsonic Leading-Edge Locus. AIAA J., vol. 16, no. 12, Dec. 1978, pp. 1248-1254.

3. Adamczyk, J. J.: Analysis of Supersonic Stall Bending Flutter in Axial-Flow Compressor by Actuator Disk Theory. NASA TP-1345, 1978.

4. Hess, J. L.; Mack, D. P.; and Stockman, N. O.: An Efficient User-Oriented Method for Calculating Compressible Flow About Three-Dimensional Inlets. (Douglas Aircraft Co., Inc.; NASA Contract NAS3-21135.) NASA CR-159578, 1979.

5. Vadyak, J.; and Hoffman, J. D.: Calculation of the Flow Field in Supersonic Mixed-Compression Inlets at Angle of Attack Using the Three-Dimensional Method of Characteristics with Discrete Shock Wave Fitting. (TSPC-78-1, Purdue Univ.; NASA Grant NGR-15-005-162, NGR-15-005-191.) NASA CR-135425, 1978.

6. Vadyak, J.; Hoffman, J. D.; and Bishop, A. R.: Calculation of the Three-Dimensional Flow Field in Supersonic Inlets at Angle of Attack Using a Bicharacteristic Method with Discrete Shock Wave Fitting. AIAA Paper 79-379, Jan. 1979.

7. Epstein, A. H.; Kerrebrock, J. L.; and Thompkins, W. T., Jr.: Shock Structure in Transonic Compressor Rotors. AIAA J., vol. 17, no. 4, Apr. 1979, pp. 375-379.

8. Thompkins, W. T.; and Epstein, A. H.: A Comparison of the Computed and Experimental Three-Dimensional Flow in a Transonic Compressor Rotor. AIAA Paper 76-368, July 1976.

9. Hansen, E. C.; Serovy, G. K.; and Sockol, P. M.: Axial-Flow Compressor Turning Angle and Loss by Inviscid-Viscous Interaction Blade-to-Blade Computation. ASME Paper 79-GT-5, Mar. 1979.

10. Sockol, P. M.: End-Wall Boundary Layer Prediction for Axial Compressors. NASA TM-78928, 1978.

11. Anderson, B. H.; Tassa, Y.; and Reshotko, E.: Characteristic Procedure for Supersonic Flows Including Consideration of Viscous Contribution to Flow Rotationality. AIAA Paper 76-426, July 1976.

12. Tassa, Y.; Anderson, B. H.; and Reshotko, E.: Finite Difference Procedure for Boundary Layers Including Effects of Longitudinal and Transverse Curvatures. AIAA Paper 76-427, July 1976.

13. Anderson, O. L.: A Comparison of Theory and Experiments for Incompressible, Turbulent, Swirling Flows in Axisymmetric Ducts. AIAA Paper 72-42, Jan. 1972.

14. Anderson, O. L.: Finite Difference Solution for Turbulent Swirling, Compressible Flow in Axisymmetric Ducts with Struts. NASA CR-2365, 1974.

15. McDonald, H.: Computational Fluid Dynamic Aspects of Internal Flows. AIAA Paper 79-1445, July 1979.

16. Briley, W. R.; and McDonald, H.: Computation of Three-Dimensional Viscous Subsonic Flows with Large Streamwise Vorticity. AIAA Paper 79-1453, July 1979.

17. Levy, R.; McDonald, H.; and Briley, W. R.: Calculation of Three-Dimensional Turbulent Subsonic Flows in Transition Ducts. 6th International Conference on Numerical Methods in Fluid Dynamics, Springer-Verlag, 1979, pp. 184-192.

18. Eisman, P.: A Unification of Unidirectional Flow Approximations. 6th International Conference on Numerical Methods in Fluid Dynamics, Springer-Verlag, 1979, pp. 72-79.

19. Walitt, L.; Liu, C. Y.; and Harp, J. L., Jr.: An Alternating Direction Explicit Method for Computing Three-Dimensional Viscous Flow Fields in Turbomachines. SAE Paper 781001, Nov. 1978.

20. Stahara, S. S.; Chaussee, D. S.; and Spreiter, J. R.: Perturbation Solution for Transonic Flow on the Blade-to-Blade Surface of Compressor Blade Rows. NASA CR-2941, 1978.

INTERNAL COMPUTATIONAL FLUID MECHANICS FOR PROPULSION SYSTEMS

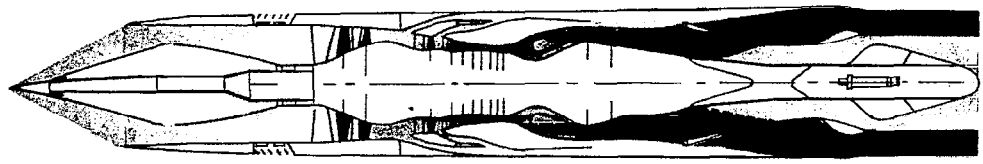

- SOLUTION TECHNIQUES
- DEVELOPMENT OF A COMPUTER CODE

CS-79-2346

Figure VI-1

TREND IN COMPUTATION COST

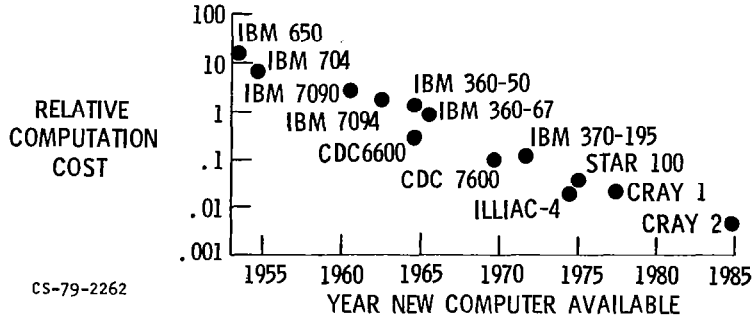

CS-79-2262

Figure VI-2

INTERNAL COMPUTATIONAL FLUID MECHANICS SOLUTION TECHNIQUES

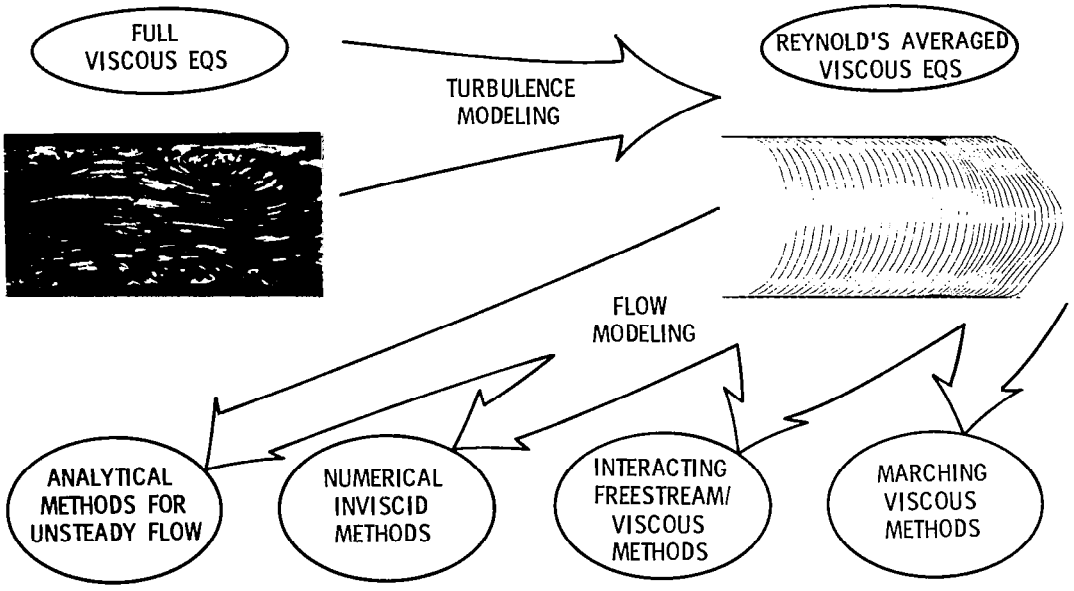

Figure VI-3

CS-79-1819

REGIONS OF COMPRESSOR FLUTTER

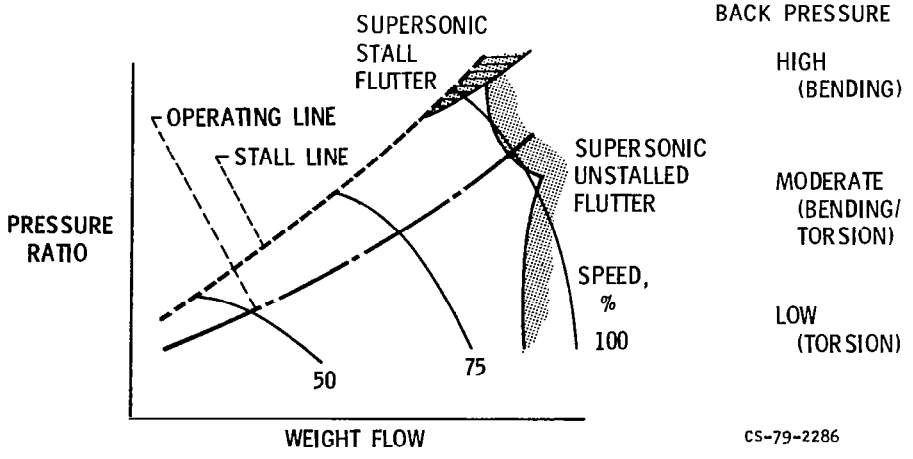

CS-79-2286

Figure VI-4

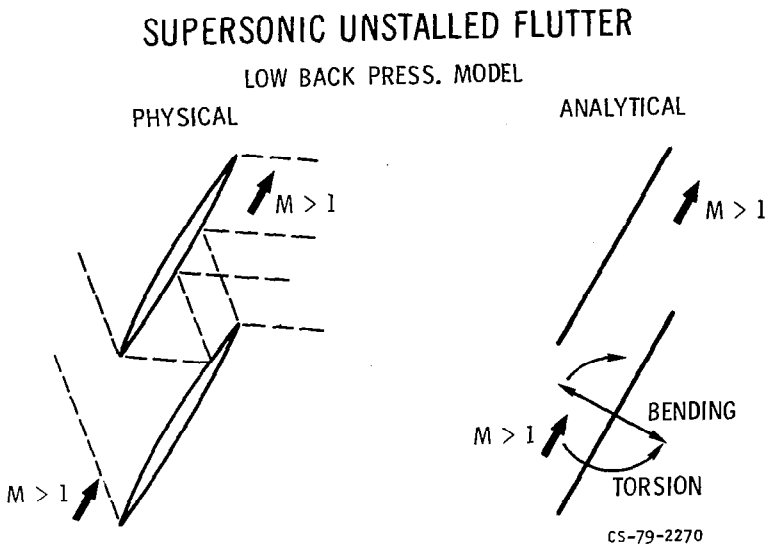

Figure VI-5

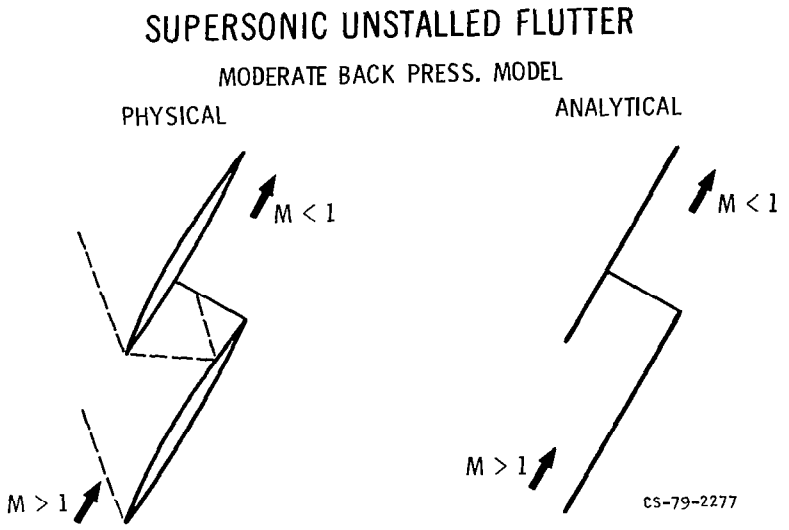

Figure VI-6

SUPERSONIC UNSTALLED FLUTTER

HIGH BACK PRESS. MODEL

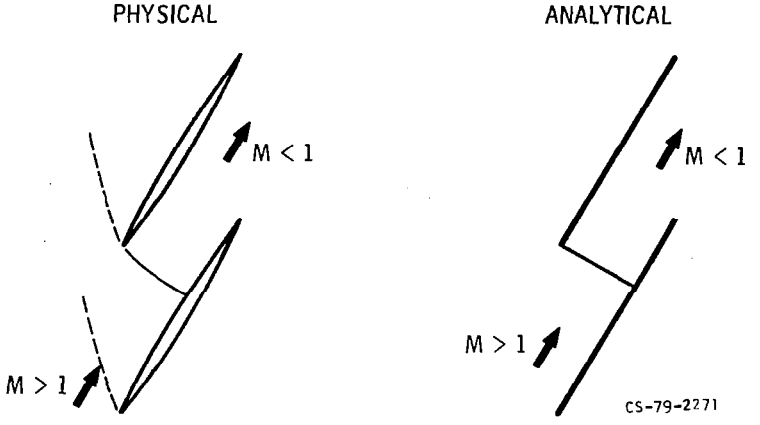

Figure VI-7

SUPERSONIC UNSTALLED FLUTTER ANALYSES

PREDICTION FOR TORSIONAL MOTION

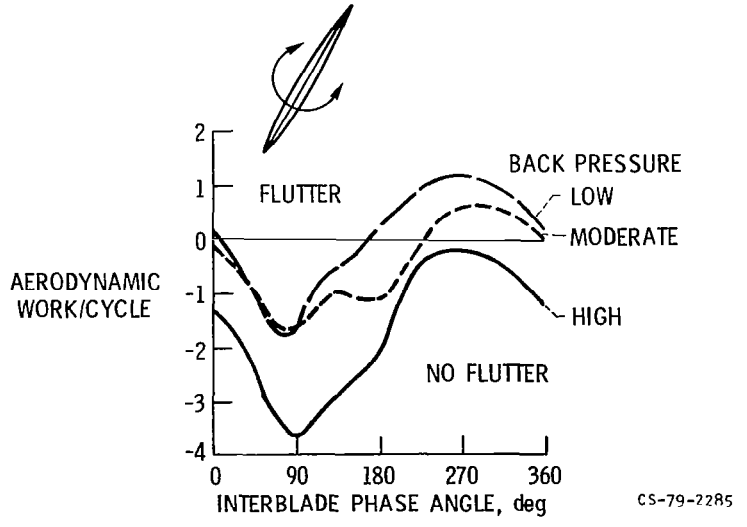

Figure VI-8

SUPERSONIC UNSTALLED FLUTTER ANALYSES

PREDICTION FOR BENDING MOTION

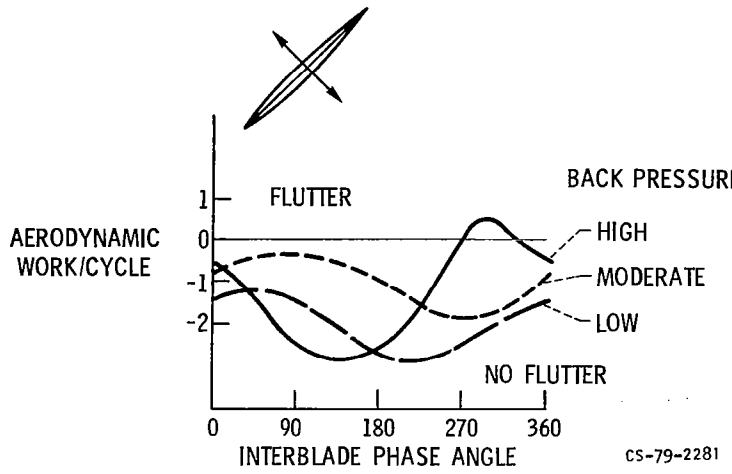

Figure VI-9

SUPERSONIC STALLED BENDING FLUTTER SEMIEMPIRICAL ANALYSIS

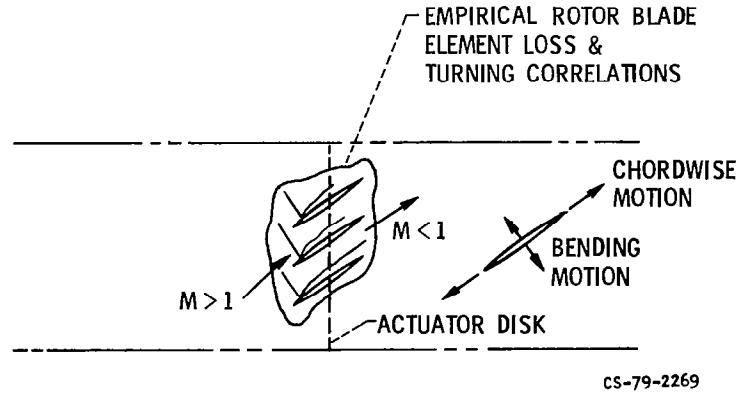

Figure VI-10

SUPERSONIC STALLED BENDING FLUTTER

PREDICTION FOR NASA QUIET ENGINE FAN C

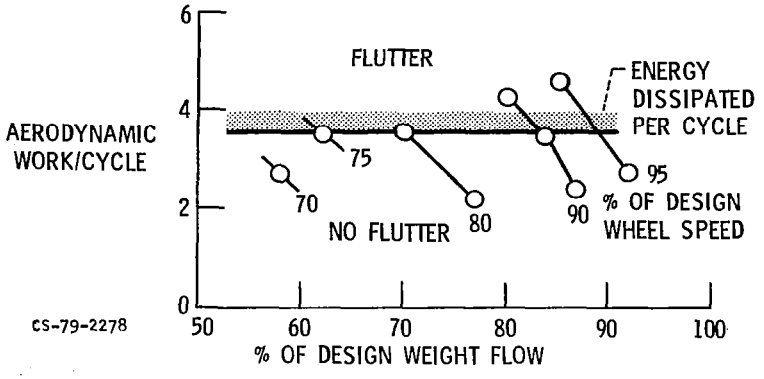

Figure VI-11

SUPERSONIC STALLED BENDING FLUTTER

COMPARISON OF ANALYSIS & EXPERIMENT; NASA QUIET ENGINE FAN C

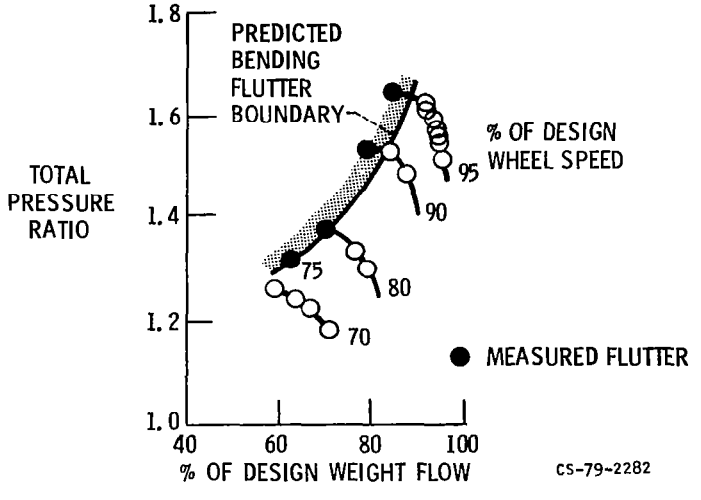

Figure VI-12

NUMERICAL INVISCID METHODS

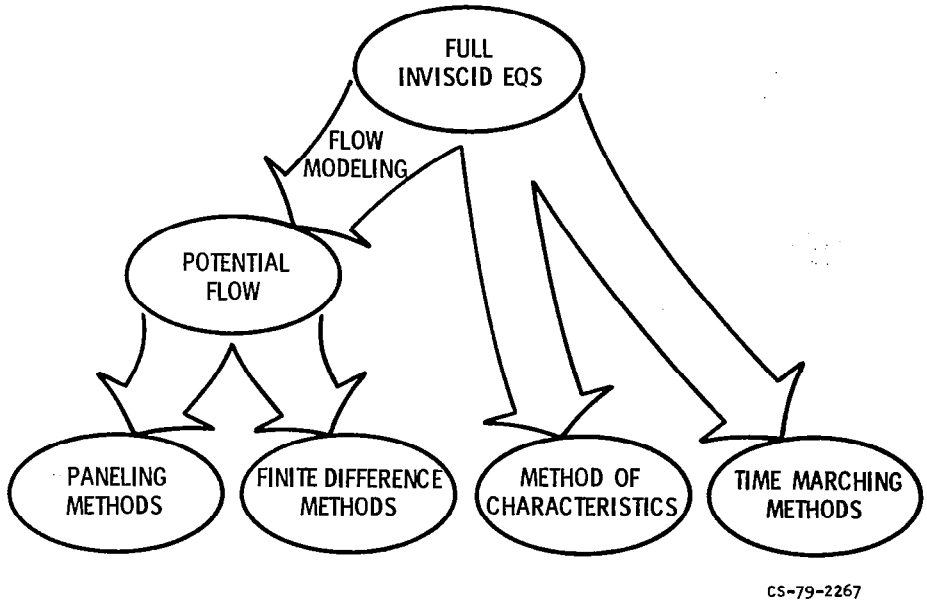

Figure VI-13

3-D POTENTIAL FLOW PANELING METHOD

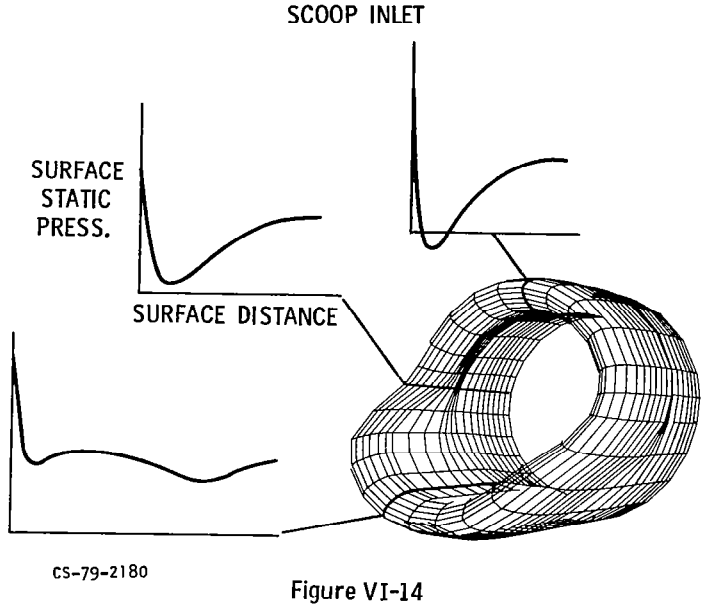

Figure VI-14

2-D POTENTIAL FLOW FINITE DIFFERENCE METHOD

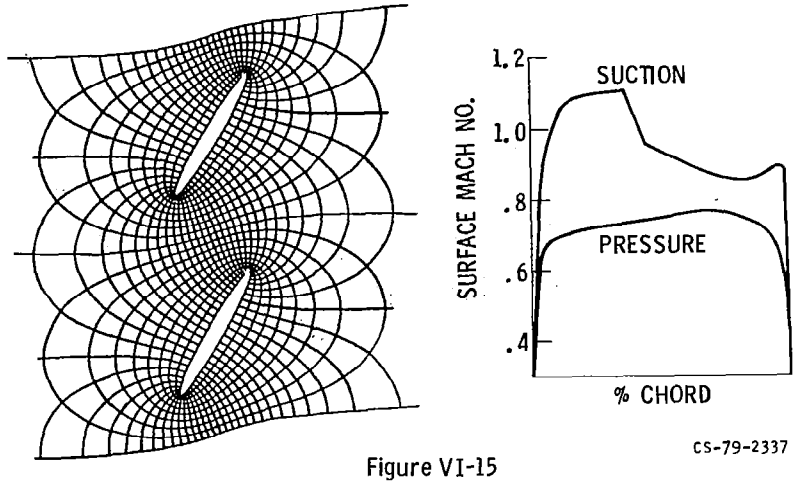

Figure VI-15

3-D METHOD OF CHARACTERISTICS

INLET AT 3° ANGLE OF ATTACK

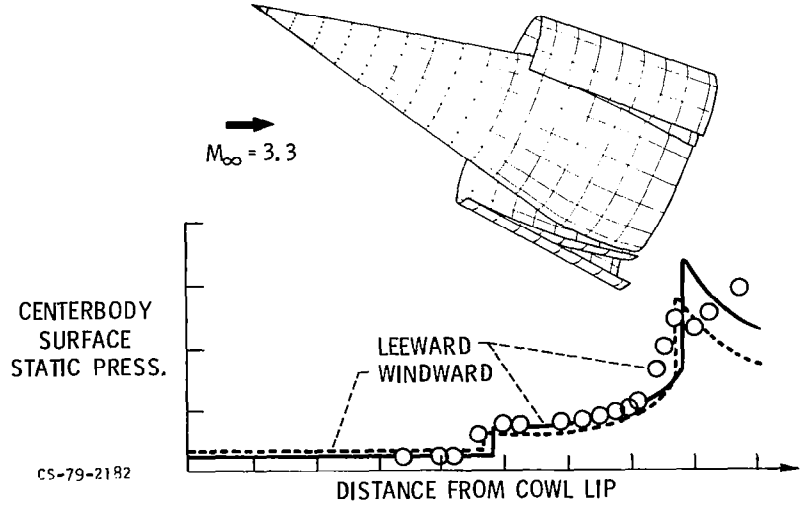

Figure VI-16

3-D TIME MARCHING METHOD

TRANSONIC PROPELLER; $M_\infty = 0.8$, $M_{TIP} = 1.15$

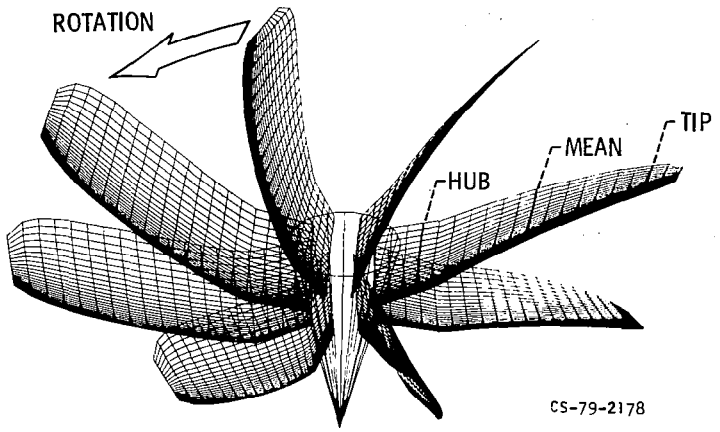

Figure VI-17

3-D TIME MARCHING METHOD

TRANSONIC PROPELLER

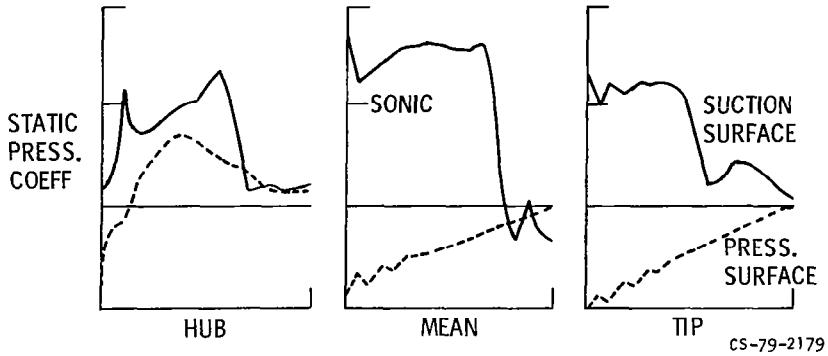

Figure VI-18

3-D TIME MARCHING METHOD

1800 fps ROTOR

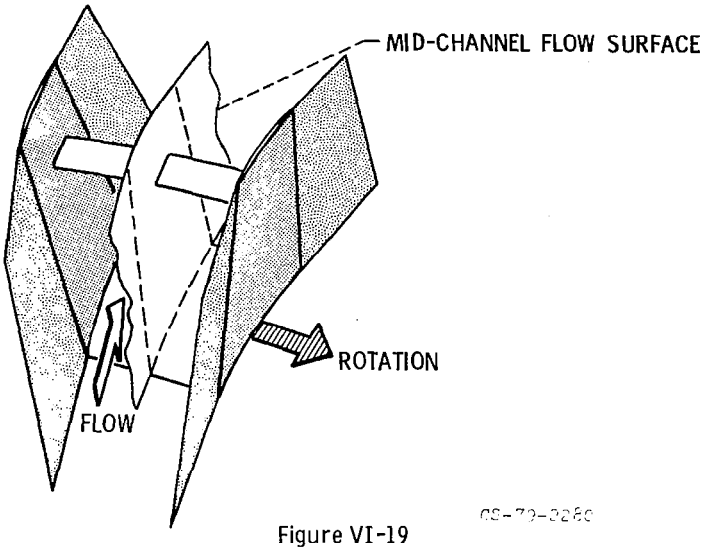

Figure VI-19

3-D TIME MARCHING METHOD

1800 fps ROTOR PRESSURE CONTOURS

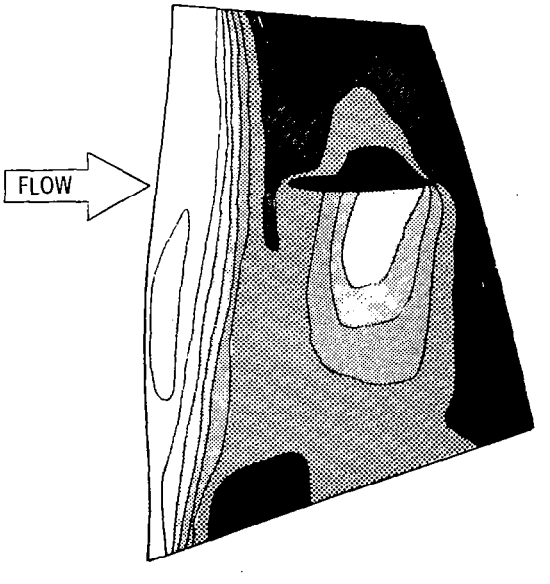

Figure VI-20

3-D TIME MARCHING METHOD

1600 fps ROTOR

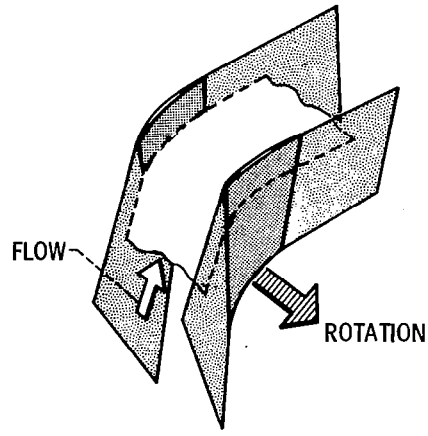

BLADE-TO-BLADE FLOW SURFACE

CS-79-2273

Figure VI-21

3-D TIME MARCHING METHOD

1600 fps ROTOR

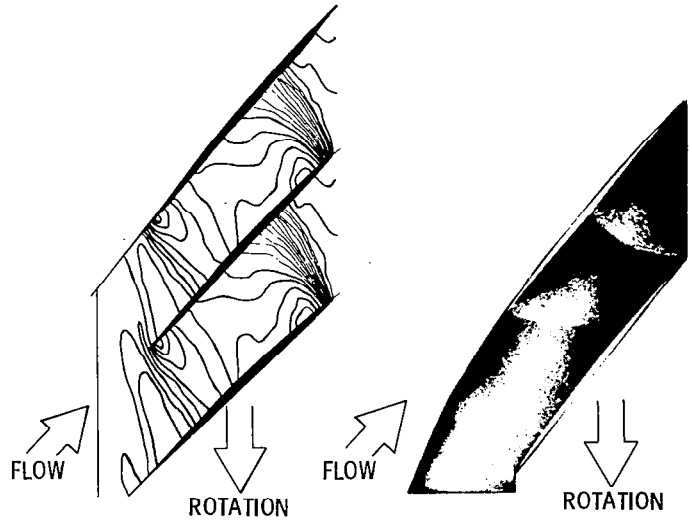

CALCULATED DENSITY CONTOURS

EXPERIMENTAL SHOCK LOCATIONS

CS-79-2288

Figure VI-22

INTERACTING FREE-STREAM - VISCOUS METHODS

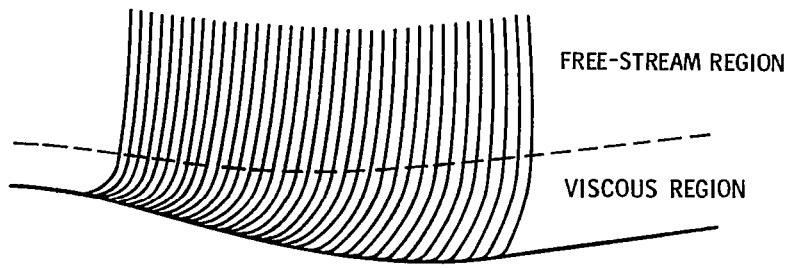

INTERACTION TECHNIQUES

BOUNDARY-LAYER DISPLACEMENT OF INVISCID REGION

MATCHED FLUID PROPERTIES AT INTERFACE

CS-79-2264

Figure VI-23

INTERACTING INVISCID/VISCOUS METHOD

BOUNDARY LAYER DISPLACEMENT - 2-D CASCADE

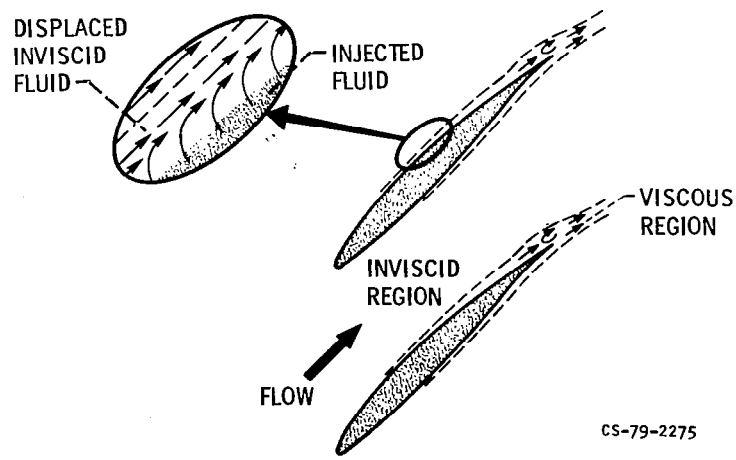

CS-79-2275

Figure VI-24

INTERACTING INVISCID/VISCOUS METHOD

EXPERIMENTAL/ANALYTICAL COMPARISON - 2-D CASCADE

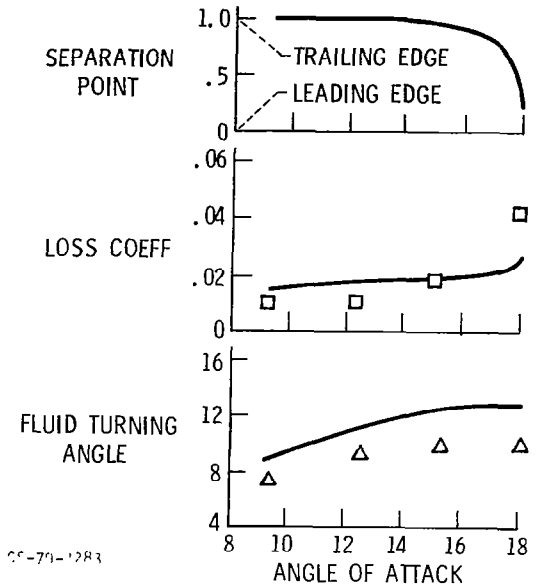

Figure VI-25

INTERACTING INVISCID/VISCOUS METHOD

BOUNDARY LAYER DISPLACEMENT - BLADE-PASSAGE END WALL

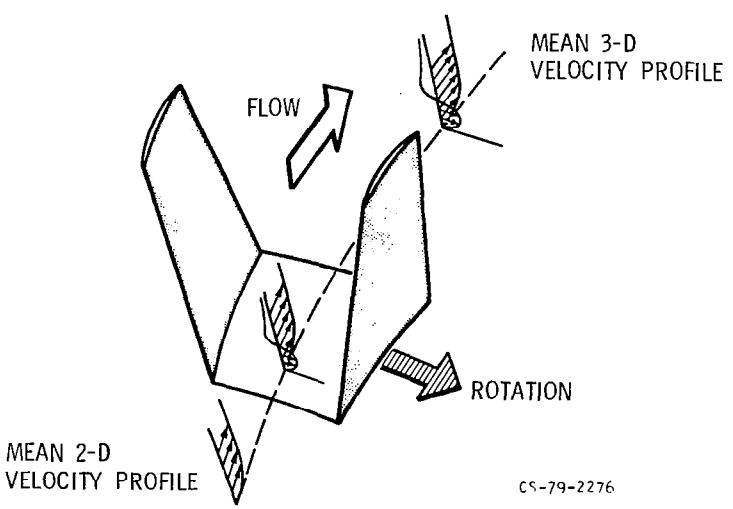

Figure VI-26

INTERACTING INVISCID/VISCOUS METHOD

EXPERIMENTAL/ANALYTICAL COMPARISON BLADE-PASSAGE END WALL

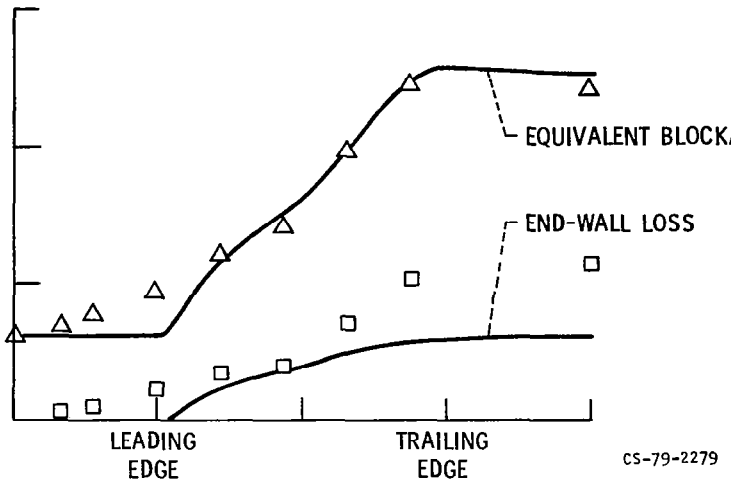

Figure VI-27

INTERACTING SUPERSONIC/SUBSONIC VISCOUS METHOD

MATCHED FLUID PROPERTIES AT INTERFACE

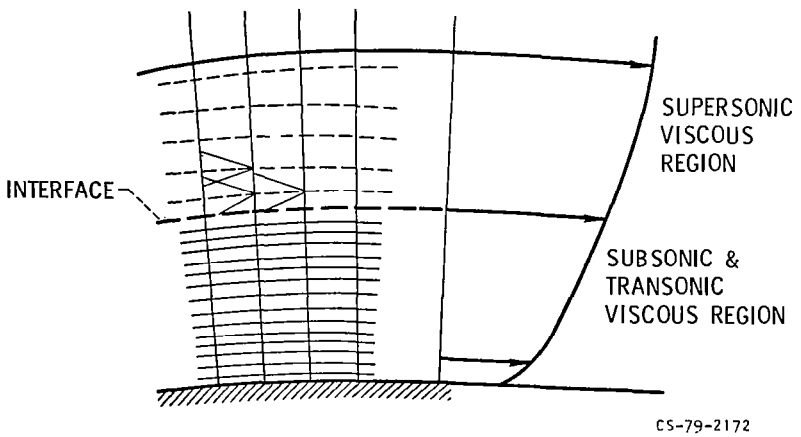

Figure VI-28

INTERACTING SUPERSONIC/SUBSONIC VISCOUS METHOD

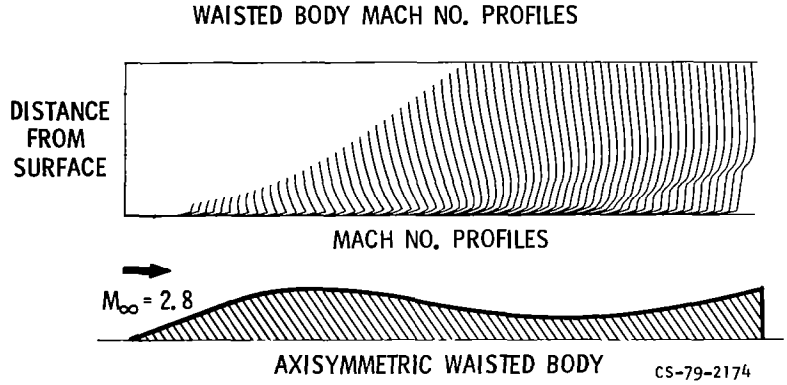

Figure VI-29

VISCOUS METHODS

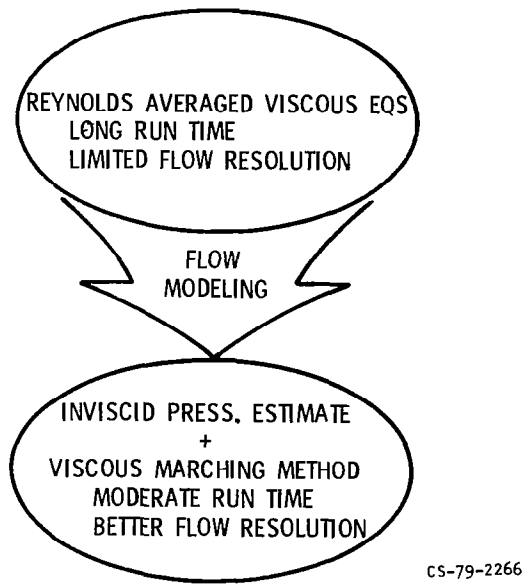

Figure VI-30

AXISYMMETRIC VISCOUS MARCHING METHOD

CURVED NOZZLE SOLUTION MESH

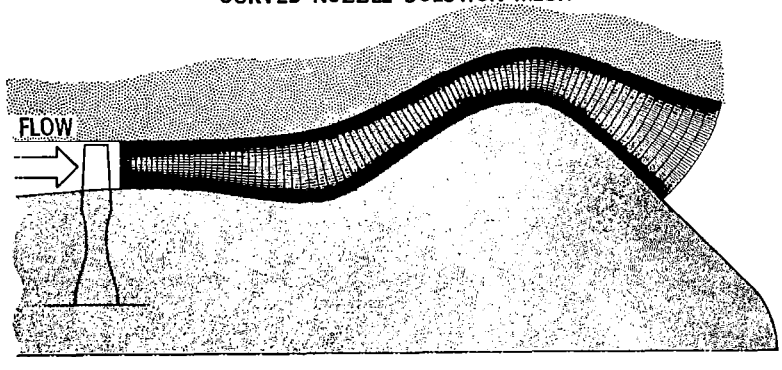

CS-79-2176

Figure VI-31

AXISYMMETRIC VISCOUS MARCHING METHOD

CURVED NOZZLE VELOCITY PROFILES

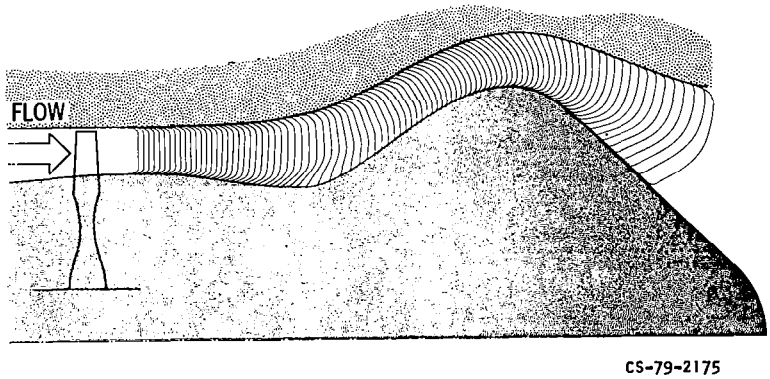

CS-79-2175

Figure VI-32

3-D VISCOUS MARCHING METHOD

CIRCULAR ARC DUCT

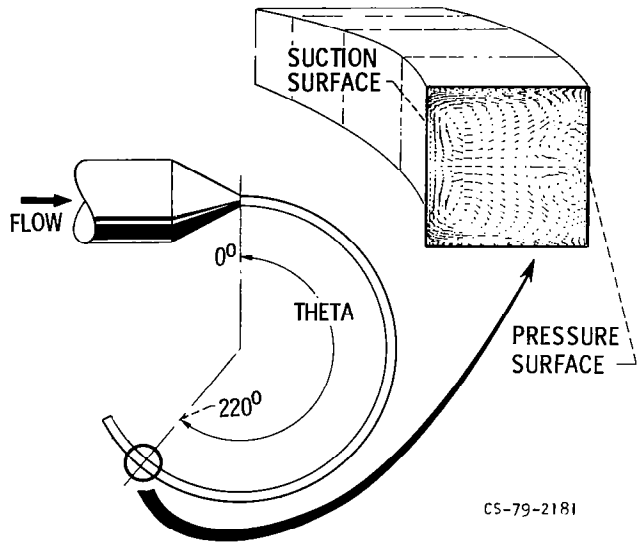

Figure VI-33

3-D VISCOUS MARCHING METHOD

CIRCULAR-ARC DUCT

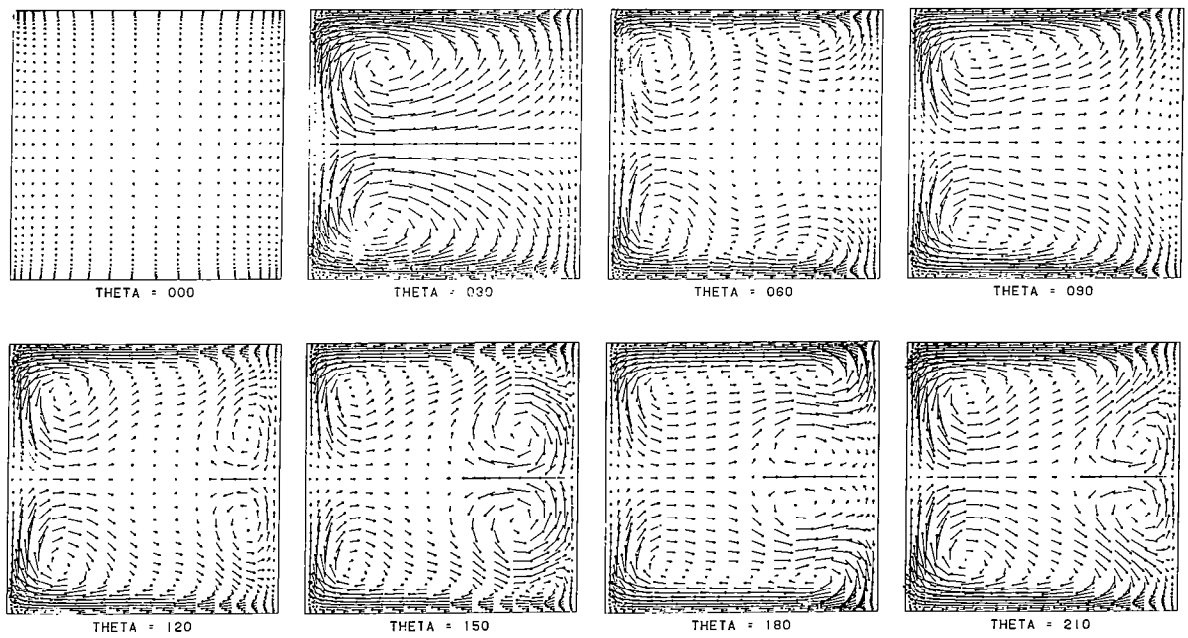

Figure VI-34

MIXER NOZZLE LOBE GEOMETRY

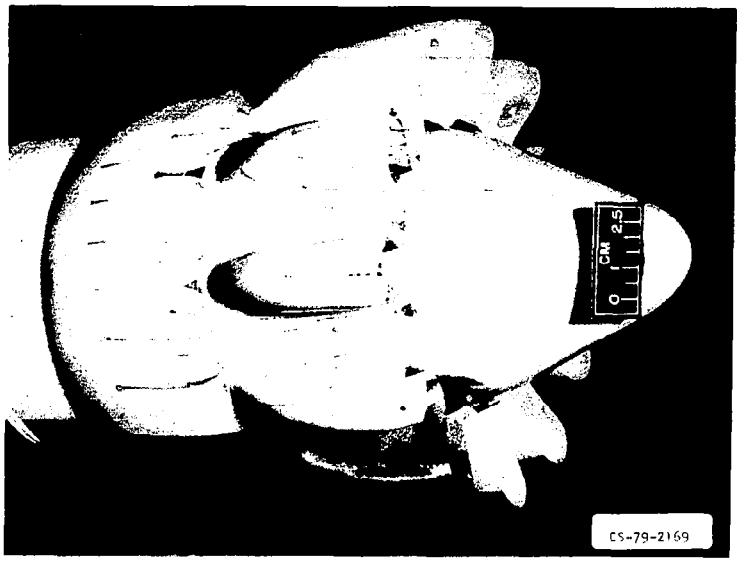

Figure VI-35

3-D VISCOUS MARCHING METHOD

MIXER NOZZLE SOLUTION MESH

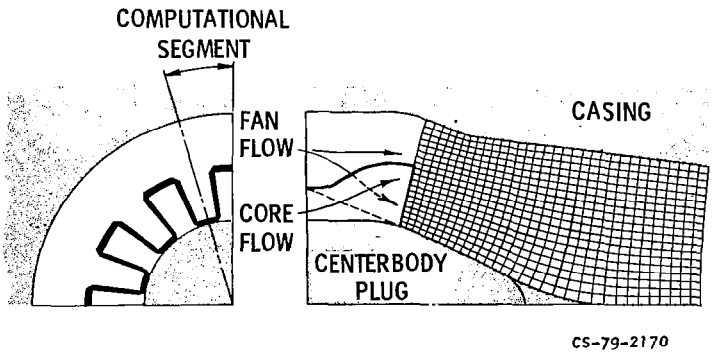

Figure VI-36

3-D VISCOUS MARCHING METHOD

MIXER NOZZLE

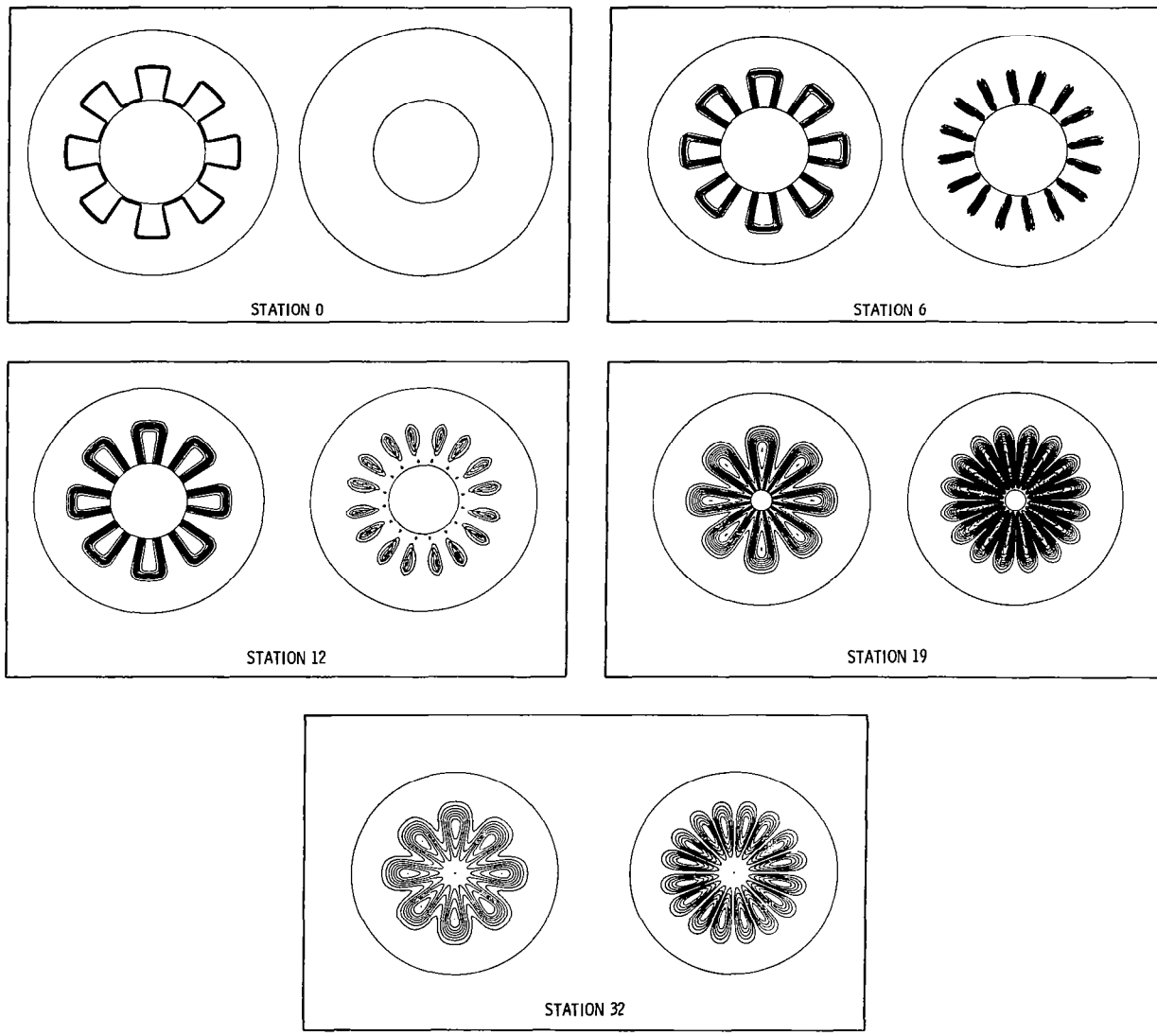

Figure VI-37

3-D FULL VISCOUS METHOD

BLADE PASSAGE IN CENTRIFUGAL IMPELLER

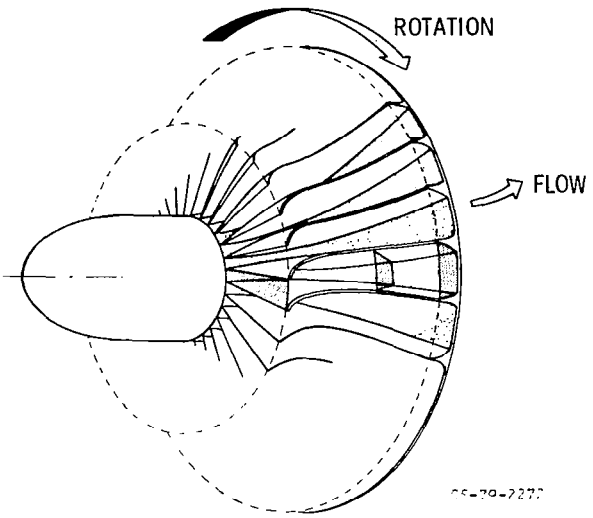

Figure VI-38

3-D FULL VISCOUS METHOD

VELOCITY PROFILES ON BLADE-TO-BLADE SURFACE

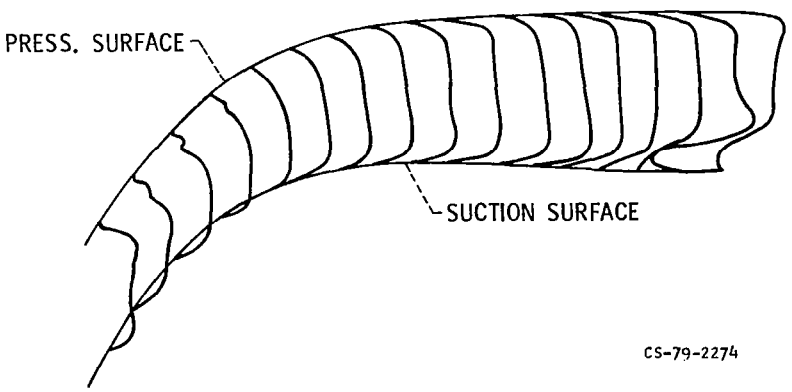

Figure VI-39

DEVELOPMENT OF A COMPUTER CODE

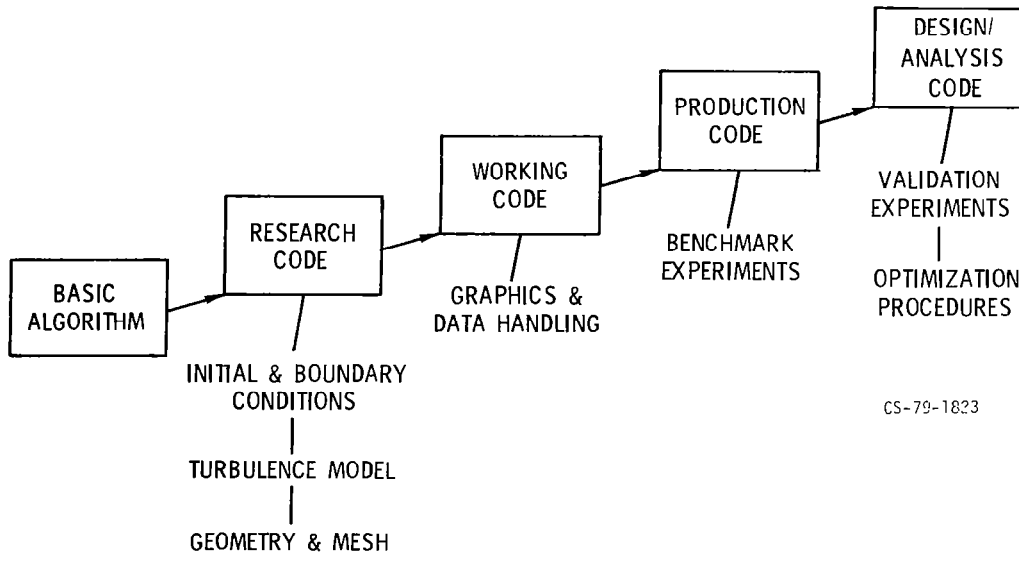

Figure VI-40

GEOMETRY ENRICHMENT

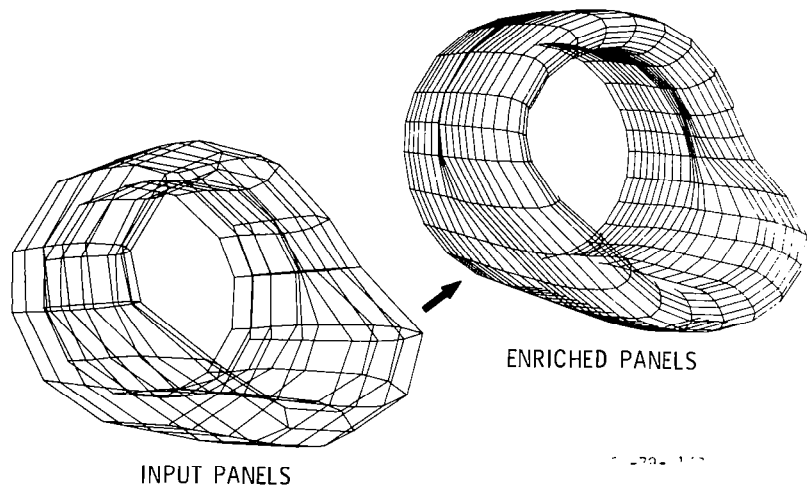

Figure VI-41

EFFECT OF MESH GEOMETRY

TRANSONIC CASCADE FLOW

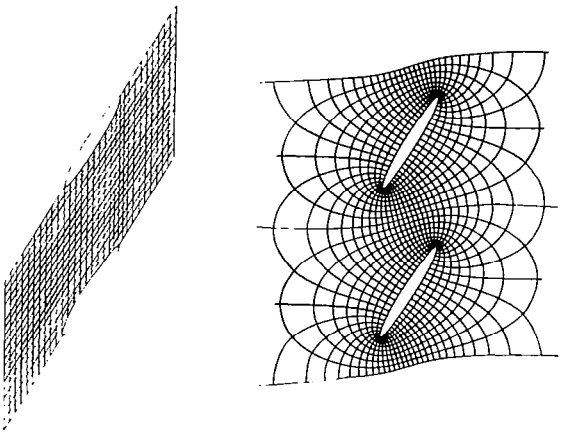

SHEARED MESH WRAPAROUND MESH

Figure VI-42

EFFECT OF MESH GEOMETRY

SHEARED MESH RESULTS

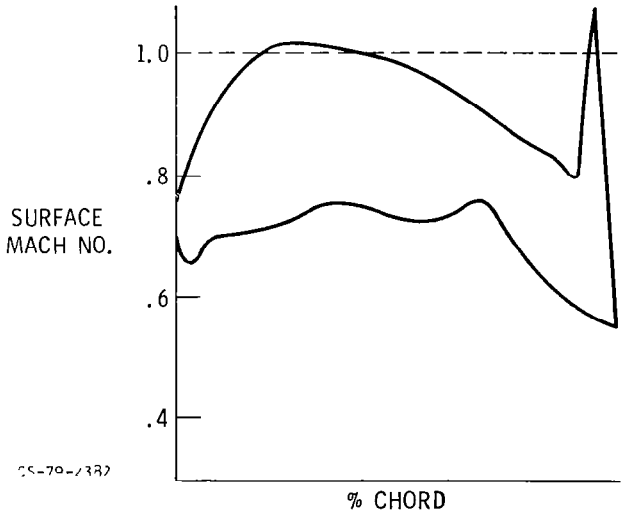

Figure VI-43

EFFECT OF MESH GEOMETRY

COMPARISON OF SHEARED & WRAPAROUND MESH RESULTS

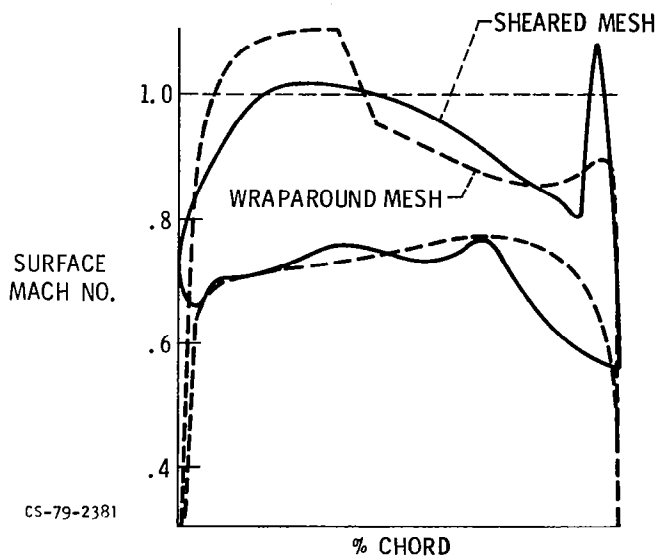

Figure VI-44

DATA HANDLING AND GRAPHICS

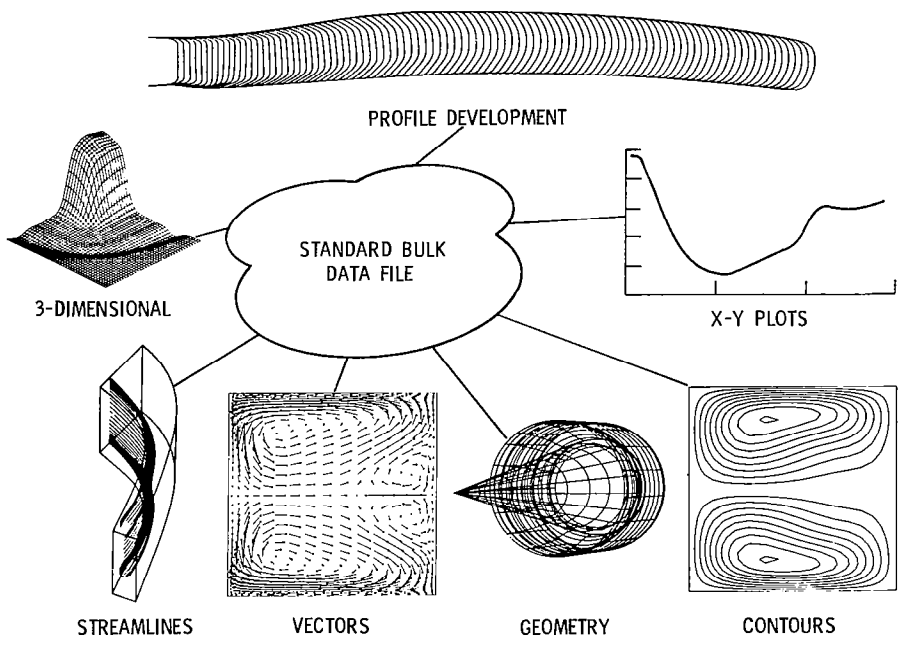

Figure VI-45

NUMERICAL OPTIMIZATION FOR DESIGN

LOW BLEED INLET

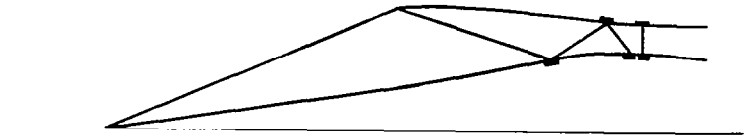

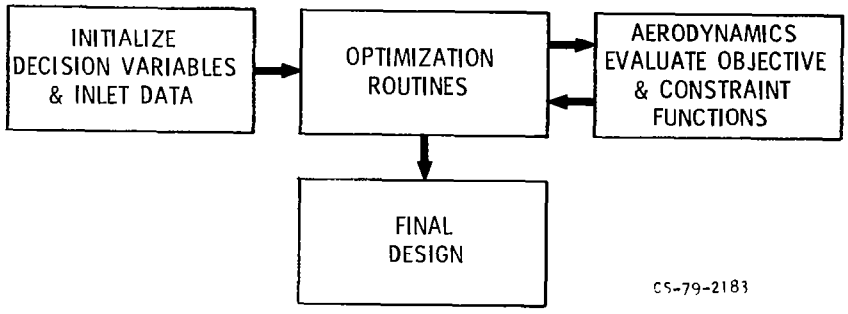

Figure VI-46

NUMERICAL OPTIMIZATION FOR DESIGN

LOW BLEED INLET

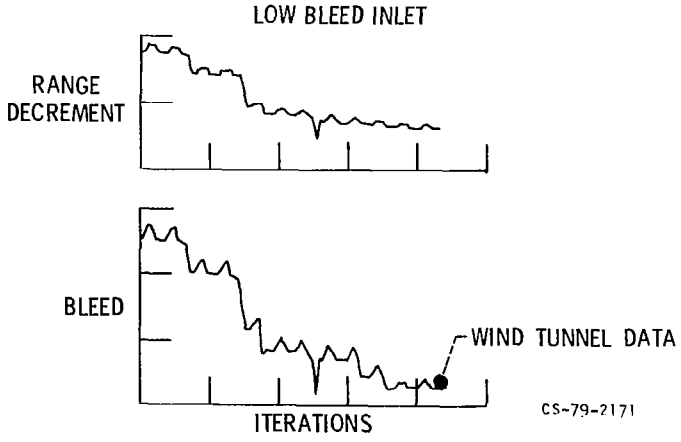

Figure VI-47

FAST PERTURBATION SOLUTIONS FOR DESIGN

PARABOLIC ARC BLADE ROW

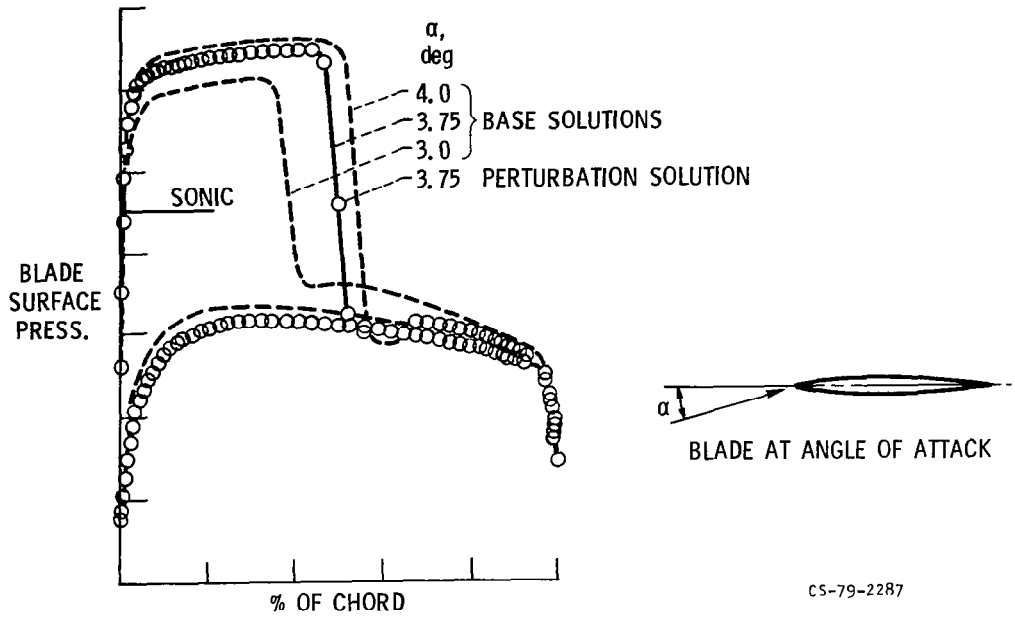

Figure VI-48

NASA LEWIS RESEARCH ANALYSIS CENTER

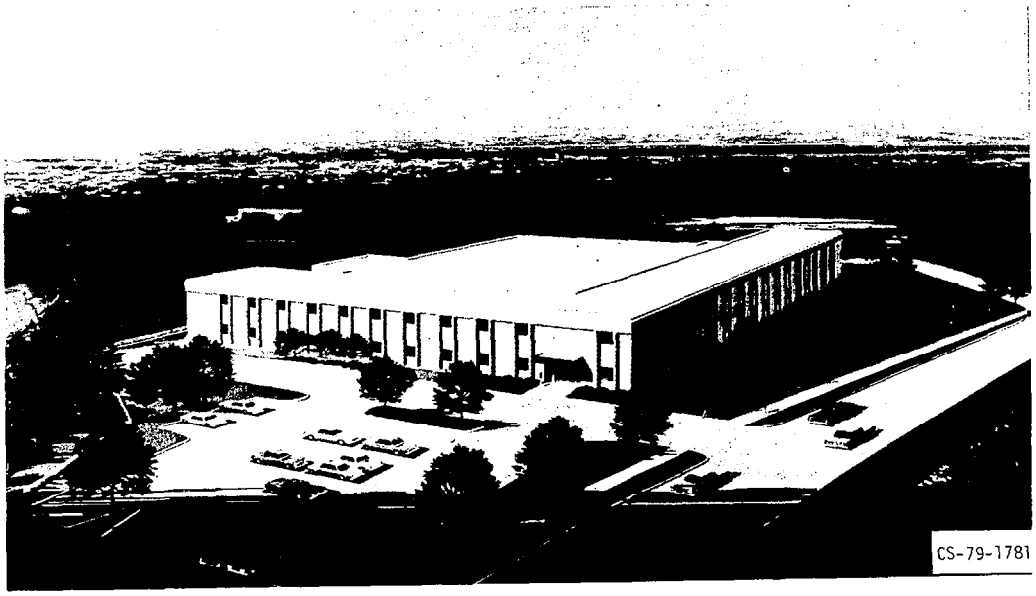

Figure VI-49

VII. TURBOMACHINERY TECHNOLOGY

Cavour H. Hauser, Jeffrey E. Haas*, Lonnie Reid,
and Francis S. Stepka

National Aeronautics and Space Administration
Lewis Research Center

The goal of Lewis Research Center studies of turbomachinery is to provide the basic technology for the design of the fan, compressor, and turbine components for future advanced aircraft engines. These engines will be quieter and more efficient and will require less maintenance largely because of improvements in their turbomachinery components. The example of an advanced engine shown in figure VII-1 is one of the engines of the Aircraft Energy Efficiency (ACEE) program. These engines represent the next forward step in engine component improvement. A wide range of research activities to support the ACEE program and to develop further advanced design concepts for each of the turbomachinery components is underway. An understanding of the basic flow characteristics in compressors and turbines and the heat-transfer phenomena in cooled turbines is necessary to our goal. This understanding is being attained through a combination of analytical studies and new experimental techniques.

The core compressor and the high-pressure turbine are the key elements in the heart of the engine. They have a large effect on engine performance, on fuel consumption, and on maintenance costs. The results of research projects for these two components are presented herein. The attainment of improved engine cycle efficiency requires increased pressure ratio for the core compressor and higher inlet temperature in the turbine. Advanced engines will achieve greater economy through overall pressure ratios as high as 40 to 1 and turbine inlet temperatures to 3000° F.

For the core compressor the aerodynamic blading design techniques must be refined so that the required high-pressure ratios can be obtained with high overall efficiency. Further, the compressor must be designed to avoid engine flow instability and to retain its good performance even after thousands of hours of operation. Losses in efficiency due to erosion and wear of components should be reduced. Significant cost reductions may

*U.S. Army Research and Technology Laboratories (AVRADCOM), Cleveland, Ohio.

be attained if the total number of blades in the compressor can be reduced. With higher tip speed a higher pressure ratio per stage may be attained. In the inlet stages the blading must be tailored to accept high-Mach-number flow if high efficiency is to be obtained. Low-aspect-ratio blades, that is, blades that have relatively long chord as compared with their radial span, are effective in extending the useful flow range of high-Mach-number, highly loaded stages. For middle and rear stages the through-flow velocities are not constant over the blade height, but fall off in the hub and tip region. Stages in which the blade profiles in the end-wall regions are designed to account for this velocity profile are being studied. A recessed casing contour over the rotor blading is shown to reduce tip clearance losses.

The laser velocimeter has recently been applied to the measurement of local velocities within the rotating blades of experimental compressor stages. Some early results show that measured velocities verify calculated values from analytical codes.

For the high-pressure turbine minimizing the cooling requirements for the desired increased temperatures is the dominant engineering challenge. Overhaul and replacement of the turbine hot parts is the largest cost in the long-term maintenance of an engine. Thus increased turbine durability is a high priority goal. For the turbine temperatures of interest, film cooling, where the coolant is bled out over the blade surfaces, is required. Cooled-blade configurations must be evolved so that the minimum coolant flow is required and so that a minimum penalty in aerodynamic efficiency, due to the coolant discharge over the blade surface, are incurred. Recent progress in heat-transfer studies on cooling, ceramic thermal barrier coatings, and the effect of the film-coolant effluent on the turbine aerodynamic performance, are discussed. Finally, as for the compressor, it has been found that turbine tip clearance losses can be reduced with a recessed casing.

CORE-COMPRESSOR INLET STAGE STUDY

An experimental study was made to evaluate the performance of inlet stages of an advanced core compressor. These stages have high blade loadings and must operate in a transonic-flow environment. Rotor blading must be designed to accommodate high supersonic inlet relative Mach numbers and to diffuse the flow to subsonic exit velocities. To achieve good efficiency and flow range with these stages, it is necessary to carefully consider the flow physics within the blade row and to establish a rationale for the selection of the blade design parameters. A model of transonic flow through a compressor rotor-blade row is shown in figure VII-2. For supersonic inlet relative Mach numbers a bow shock exists at the blade leading edge and extends upstream of the adjacent blade. The bow shock is followed by a

series of expansion waves. The blade-passage throat occurs a short distance downstream of the passage shock. For these highly loaded blade rows the velocity just downstream of the passage shock is subsonic. These subsonic velocities must be diffused to a lower velocity at the exit of the blade passage.

In the design of the blading it is necessary to minimize the amount of supersonic expansion ahead of the passage shock to avoid high shock losses and severe shock-boundary-layer interaction. This can be achieved by minimizing the amount of flow turning or blade camber ahead of the passage shock. The blade passage throat area must be large enough to pass the design mass flow. The throat size is strongly influenced by the selection of camber distribution. The requirement of low blade camber ahead of the passage shock necessitates relatively high camber downsream of the passage shock to achieve the overall flow turning through the blade row. The blade surface pressure distributions for this transonic flow model are shown in figure VII-3 where the ratio of local static pressure to the inlet relative total pressure is plotted as a function of blade chord. The pressure gradients on the blade pressure surface are relatively mild. However, the pressure gradients on the suction surface are quite severe and merit special considerations. Near the blade leading edge the flow is subsonic, due to the strong bow shock. The sharp drop in static pressure near the leading edge on the suction surface corresponds to local acceleration of the flow to supersonic conditions. This is followed by a gradual drop in static pressure, which represents the supersonic expansion or flow acceleration on the suction surface. The large pressure rise is indicative of the strong shock. The flow condition just downstream of the shock is subsonic. The static pressure rise from that point to the blade exit is indicative of the amount of subsonic diffusion that is required to reach the blade-exit conditions.

Blade surface pressure distributions are shown in figure VII-4 for two blades with the same design blade shape and with the same inlet and exit flow conditions, but with different chord lengths. The strength of the shock or sharp static-pressure rise on the suction surface is the same for both blades. However, the static-pressure rise from downstream of the shock to the blade exit, or subsonic diffusion, occurs over a longer distance for the blade with the longer chord. Therefore, the rate of subsonic diffusion is lower for the blade with the longer chord. This lower rate of diffusion reduces the tendency for severe boundary-layer separation and high diffusion losses and implies that long-chord, or low-aspect-ratio, blading might perform well for these high-Mach-number, highly loaded stages.

An experimental evaluation of the effects of blade aspect ratio has been made using two high-Mach-number, highly loaded stages

that are suitable as inlet stages of an advanced core compressor. The rotors for the compressors are shown in figure VII-5. One rotor has low-aspect-ratio blading; the other has moderate-aspect-ratio blading. Both compressors were designed for a pressure ratio of 2.05, a rotor tip speed of 1500 feet per second, and a rotor-inlet relative Mach number of 1.48. A photograph of corresponding individual rotor blades is shown in figure VII-6. The aspect ratio is 1.2 for the low-aspect-ratio blade and 1.6 for the moderate-aspect-ratio blade. These stages were tested in the Lewis single-stage compressor facility (fig. VII-7).

A performance comparison of the two stages is shown in figure VII-8. Performance data are presented at speeds from 0.5 of design speed to design speed. The low-aspect-ratio stage has a substantially greater flow range than the moderate-aspect-ratio stage. Both stages have about the same maximum flow for a given speed but the low-aspect-ratio stage operates at a much lower flow and higher pressure ratio before it encounters the stall limit. The overall efficiency levels for the two stages are comparable. The results from this particular study show that for this high pressure ratio and high-inlet-relative Mach number good efficiency and stall margin can be achieved with low aspect ratio blading.

CORE-COMPRESSOR MIDDLE AND REAR STAGE STUDIES

Reduced Losses in End-Wall Regions

Research studies on the middle and rear stages of core compressors are aimed at reducing the losses in the end-wall regions near the hub and tip of the blades and also reducing the tip-clearance losses. Some fundamental experimental studies of these areas are being carried out in a contract program with the General Electric Co. using the facility shown in figure VII-9. Because the flow in compressor rear stages is subsonic, the performance of these stages may be modeled in this low-speed, large-scale facility where detailed measurements of the flow can be obtained. The rig includes survey instrumentation that rotates with the rotor blades, allowing loss source to be identified. Tests are conducted using four successive, identical stages (fig. VII-10), so that the forward stages set up a true multistage environment for the latter stages and typical multistage loss mechanisms are simulated. The primary objective of the program is to develop middle- and rear-stage blade designs with improved efficiency through reduced losses in the end-wall boundary-layer regions. Blade design concepts that show promise of reducing these end-wall losses are evaluated.

Part of the study is aimed at an evaluation of the best distribution of velocity over the surfaces of the rotor blades. Two

rotor-blade designs (rotor A and rotor B) are compared. In figure VII-11 the blade-tip profiles are superimposed, and the design velocity distributions on these two profiles are compared. The velocity distributions were calculated using a blade-to-blade analysis code; the velocity field over a circumferential surface between adjacent blades was analyzed. The blade profile for rotor A is standard, having essentially circular arc curvatures over the suction and pressure surfaces. Rotor B was designed for the same velocities and flow angles both upstream and downstream of the blade row but the distribution of camber is changed to give higher blade loading in the rear portion and a more rapid diffusion of the velocity along the suction surface near the trailing edge. For the velocity distribution of rotor B, the maximum difference in velocity between the suction and pressure surfaces is reduced. This corresponds to a smaller pressure difference from the pressure to the suction surface across the tip of the blade over the forward portion of the blade chord. It is thought that this reduced pressure difference will reduce the strength of the tip clearance leakage vortex and thereby reduce the resulting losses.

The objective of the second part of the study was to determine what distribution of axial velocity from the hub to the tip over the blade height would give the better performance. Two different stators were designed (stator A and stator B) to vary the velocity distribution (fig. VII-12). The axial velocity component is generally lower in the hub and tip regions, and the radial distribution for stator A is conventional. Stator B is designed to give the design axial velocity distribution shown in figure VII-12 with higher velocities over the midportion of the passage and lower velocities in the hub and tip regions than stator A. Stators A and B have essentially the same airfoil sections, but the sections in the hub and tip regions of stator B are twisted toward the tangential direction, which increases the flow angle β in these regions. These changes in twist at the extremities of stator B are evident in figure VII-13. The axial velocity distribution has less effect on rotor blade angles, and the two rotors were designed for either of the velocity distributions.

To evaluate the relative performance for the two stators, the measurements were taken in the third stage of the four-stage group. These measurements confirmed that the desired velocity distributions had already been set up for each case by the inlet guide vanes and the first two stages. Thus the performance comparison of the stages with stators A and B is an evaluation of which of these two radial distributions of axial velocity is preferable.

The relative performances of the two stages are presented in figure VII-14. For these low-speed experimental stages performance is expressed in terms of pressure coefficient and flow

coefficient. Pressure coefficient is the rise in casing static pressure normalized by one half the density times the square of the tip speed. The flow coefficient is the ratio of inlet axial velocity to tip speed. The stage performance of rotor A-stator A is considered as the baseline. The various combinations of rotors and stators were run, but rotor B-stator B gave the best overall performance. Apparently, the design characteristics for both rotor B and stator B were desirable. This stage had higher pressure coefficient at each flow, a greater flow range at high efficiency, and a more desirable pressure coefficient characteristic as stall conditions were approached. The drop in pressure coefficient at low flow for rotor A-stator A probably results from a significant flow breakdown and separation, which has been observed to occur in the hub region.

Reduced Tip Clearance Loss

The effect of a casing with a recessed clearance configuration, as shown in figure VII-15, was evaluated for rotor B-stator B. Such a recessed clearance has proved effective in reducing the tip clearance losses in turbines. The actual running clearance is the same for the standard casing and for the recessed clearance configuration. In the recessed clearance configuration, the blade is longer so that the tip is line-on-line with the upstream and downstream casing. As indicated in figure VII-16, the recessed clearance configuration apparently does reduce the losses in the tip clearance region. A further small increase in efficiency at the higher flows and a higher pressure coefficient over the whole range of flow was obtained with the recessed clearance.

EXPERIMENTAL VERIFICATION OF ANALYTICAL CODES

With the laser Doppler velocimeter, detailed measurements throughout the blade passages for both the rotor and the stator may be obtained. This makes possible direct verification of the analytical codes and thereby gives a far more comprenensive understanding of the complex physical phenomena occuring within the blade rows of turbomachinery. It is most promising.

A photograph of the velocimeter installed in the compressor facility of figure VII-7 is shown in figure VII-17. The compressor test section is on the left. Two laser beams are projected through a window in the compressor casing and cross one another at a point within the rotating blade row. The velocity of microscopic particles passing through this intense point of light is measured by the instrument.

The data shown in figure VII-18 are direct reproductions of online output from the velocimeter. The location of the measurement station is shown in the two diagrams of figure VII-19.

As indicated, the circumferential survey of figure VII-18 was taken at a station about one-third chord length downstream of the blade leading edges and near the blade tip. The axial component of velocity VZ is plotted against circumferential position stations for each blade passage. The cross-hatched regions represent the blade locations. Each of the points of this plot represents the measured axial velocity within the blade passage. Similar measurements of the tangential velocity are obtained so that the distribution of the relative velocity across the blade passage can be calculated. This relative velocity distribution averaged over 20 blade passages is shown in the lower plot. Measurements are taken at other stations through the passage to obtain the relative velocity contour plots shown in figure VII-20. A blade-passage flow analysis code was used to obtain the velocity contours shown on the left. In this case the agreement with the measured contours on the right is quite good. Codes that can be used at higher velocities where there are shock patterns in the passage are under development. The ability to obtain detailed velocity measurements throughout the blade passages is an invaluable aid in verifying the results of analytical design codes.

TURBINE COOLING

The gas temperature levels of current and advanced engines are above the melting point of turbine-blade materials; turbine cooling is, therefore, required. This cooling is provided by air that is bled from the engine compressor and ducted to the base of blades and then through cooling passages within the blades. Bleeding air from the compressor, however, results in engine performance losses. The primary research objective is to provide the technology to minimize the cooling requirements and thus these losses. It is desired to obtain a fundamental understanding of the flow and heat-transfer phenomena for the more effective cooling methods and to improve the accuracy of predicting blade-wall temperatures so that the cooling air is effectively distributed.

Cooled blades will typically use combinations of cooling methods. For example, the blade in figure VII-21 is convectively cooled in the midchord region by the airflow through radial passages. Part of this air passes through holes in an internal wall to impinge and cool the leading edge. It is then ejected through holes in the blade wall to form an insulating film layer on the blade surface. The other part of the air from the midchord is directed to passages in the rear to convectively cool the trailing edge.

The various methods of cooling or insulating turbine blade walls are schematically illustrated in figure VII-22. Convection cooling with augmented surface area is the simplest means of

cooling. Another method is impingement cooling, wherein air from a row, or many rows of small holes from an insert within a blade, impacts the blade wall and reduces its temperature. For advanced engines these cooling methods alone are not adequate at some locations on the airfoil and need to be combined with local film cooling, wherein the addition of a thin layer of cool air insulates the blade from the hot gas stream. For temperatures envisioned for future engines full-coverage film cooling consisting of additional film cooling air from a multitude of small holes will be required. A thermally more efficient extension of full-coverage film cooling is transpiration cooling, wherein a cool layer of air is deposited on the blade surface after passing through a porous or woven wall material. Another method of reducing blade wall temperatures is to insulate the blade from the hot gases by a thermal barrier, that is, a low conductivity ceramic coating deposited on the gas side of the blades.

The need for the more effective cooling methods is indicated in figure VII-23. Coolant flow requirements rise rapidly for convection cooling when turbine-inlet gas temperatures and pressures increase. The conditions of current engines are indicated by the vertical line on the abscissa. Obviously, more complex cooling methods, for example, full-coverage film cooling or transpiration cooling, will be required to reduce cooling-air flow requirements in future engines. The use of thermal-barrier coatings on cooled turbine parts can further reduce the cooling-air requirements.

Although heat-transfer studies have been conducted for all of the methods depicted in figure VII-22, only research results on impingement cooling, full-coverage film cooling, and the thermal-barrier coating will be discussed.

Impingement Cooling

In order to effectively utilize impingement cooling, the interrelationship of flow and geometry variables on heat transfer must be known. The schematic of an impingement-cooled wall configuration in figure VII-24 shows that, in addition to the impingement jet flow, a crossflow of cooling air is often present. This air is from previous cooling of the blade upstream of the jet array or from the flow that has accumulated with distance downstream of the initial impinging jets. The research on impingement cooling discussed herein was conducted under a grant to Arizona State University. Experimental studies were conducted at conditions that simulate those of advanced core turbine vanes. Some of the variables under investigation included arrangements of the jet arrays, hole spacing, hole-diameter-to-wall-distance ratios, and impingement-to-crossflow velocity ratios.

A photograph and a schematic of the test apparatus are shown in figures VII-25 and VII-26. Air enters the plenum, exits through hole arrays in an interchangeable jet plate, and then impinges upon the test wall. The test wall consists of individually heated and insulated copper strips. The local heat-transfer coefficients for each strip are obtained from measurements of the electrical heat input into the strip and the temperatures of the strip and impinging air. For the tests described herein, only the test strips beneath the jet plate were used.

One of the purposes of the investigation was to evaluate the relative cooling effectiveness of in-line rows of jets and staggered rows of jets. Initial results are shown in figure VII-27 where the change in relative heat-transfer coefficient with distance is plotted. High coefficients are desirable so that heat will be taken from the blade wall and reduce wall metal temperatures. The results show that the coeficient is highest at the first row of holes and then decays with distance downstream for both the in-line and staggered jet arrays. Of greater significance, and contrary to initial expectations, the in-line jet array is more effective than the staggered array for the same coolant flow rate and hole density. At the farthest downstream row of jets the in-line array has a 60 percent higher heat-transfer coefficient than the staggered array. This superiority of the in-line array was greatest when the hole density was the highest, that is, when the hole spacings were four and five diameters and when the jet-to-wall distances were two and three hole diameters. Test are continuing to obtain more data on this cooling method. The current study is concentrated on developing the analysis that will correlate the many variables in the investigation so that optimum impingement-cooling configurations can be designed.

Full-Coverage Film Cooling

Research on full-coverage film cooling has been conducted to obtain the experimental thermal performances of selected film-cooling hole arrays and to develop analytical methods to predict their performances. The study was conducted under a contract with Stanford University. A photograph and a schematic of the test appratus are shown in figures VII-28 and VII-29. In the test tunnel film-cooling air and main-stream gas-flow conditions simulate those over a turbine vane. Cooling air is injected into the main stream through 11 rows of holes in the test wall. The film-cooling holes extend over only the initial portion of the tunnel length. The tunnel test wall consists of individually insulated and heated copper strips. The heat-transfer coefficient for each strip is obtained (as in the impingement cooling study) from measurements of the electrical energy input to the individual strips and of the temperatures of the strip and main-stream air. This apparatus gives the flexibility to

investigate various hole geometries, spacings, and orientations. The two hole arrays discussed herein are shown in figure VII-30. The holes in both arrays are inclined 30° to the wall surface. The array on the right has these holes alined in the direction of the main-stream flow (in-line injection). The holes in the other array are alined at an angle of 45° to the main stream (compound-angle injection). The compound-angle injection was included in the study because Lewis flow-visualization studies indicated that improved cooling might be obtained.

The results of detailed measurements of the relative heat-transfer coefficients as a function of distance downstream of the test-section inlet for no air injection and for in-line and compound-angle injection are given in figure VII-31. For these data, which represent conditions on the gas-side surface of a turbine blade, a low coefficient is desirable so that less heat will be transferred from the gas stream to the blade wall and thus give lower blade metal temperatures. Clearly, in-line injection significantly reduces the heat-transfer coefficient. Compound-angle injection is even more effective beyond 25 hole diameters downstream of initial injection. However, beyond the region of film injection, the heat-transfer coefficient for the compound-angle injection increases rapidly.

As part of the study at Stanford, a two-dimensional boundary-layer computer program called STANCOOL was developed to predict heat-transfer coefficients with film cooling. Figure VII-32 shows a comparison of analytical predictions with experimental heat-transfer coefficients for no injection and for in-line hole injection. The agreement is good. For no film injection the prediction line runs through the experimental data. For film injection the cyclic pattern of the predicted local coefficients across each of the strips (between rows of film cooling holes) agrees well with the measured average coefficients for the individual strips.

To evaluate the performance of the in-line and compound-angle hole arrays on an actual turbine vane a Lewis investigation was conducted using the turbine cascade shown in figure VII-33. One of the vanes in the center of the cascade had five rows of in-line holes and another had five rows of compound-angle holes on the suction surface. The schematic of the airfoil in the figure shows the location of the rows of holes. Downstream of each row a copper strip with thermocouples was installed to obtain the average spanwise temperature for each row. The results of the test confirmed the superiority of the compound-angle injection over the in-line injection for all of the rows. Evidence of this superiority is shown in figure VII-34 in the plots of cooling effectiveness as a function of mass flux ratio for the second and last row of holes on the vanes. Cooling effectiveness is the ratio of the reduction of vane metal temperature

below the gas temperature to that ideally possible at a given cooling-air temperature. The mass flux ratio is proportional to cooling-air flow rate. The superiority of the compound-angle injection is particularly evident at mass flux ratios above about 0.5 for the last row of holes where the cooling effectiveness of the in-line injection begins to decline while that of the compound-angle injection increases.

Thermal-Barrier Coating

The thermal-barrier coating is a means for reducing blade metal temperatures and/or coolant flow. The two-layered, thermal-barrier coating applied to a convection-cooled turbine blade is shown in figure VII-35. The first layer is a metallic bond coat that is typically about 0.004 inch thick, and the second layer is yttria stabilized zirconia that is typically 0.005 to 0.020 inch thick.

Figure VII-36 shows turbine vane leading-edge metal wall temperatures obtained over a range of coolant-to-gas-flow ratios in a research engine for both an uncoated vane and one with a 0.011 inch thickness of the ceramic. The circles and squares are experimental data and the lines are analytical predictions. The gas temperature for these tests was 2500° F and the cooling-air temperature was 115° F. The results illustrate that significant reductions of as much as 340° F in vane wall metal temperatures were obtained with the coating. The tests also showed the ability to predict this reduction analytically, thus indicating that the thermal conductivity data for the plasma-sprayed-on coating is adequate for design purposes. The figure also shows that at a given metal temperature a threefold reduction in coolant flow was obtained.

Although large metal temperature or coolant-flow reductions can be obtained with the coating, there was concern about the effect of the coating on aerodynamic loss. Figure VII-37 shows the kinetic energy loss coefficient (which is a measure of loss in aerodynamic efficiency) for coated and uncoated vanes as obtained in a cold-air cascade. The data show that the as-sprayed coating gave very high losses compared with an uncoated vane. However, when the coating was smoothed by abrasive polishing, the loss was only about 0.7 of a point larger than that for the uncoated vane. This loss was attributed to the 38 percent thicker trailing edge caused by the coating. Redesign of the blade for a thinner trailing edge would reduce this loss.

TURBINE COOLING AERODYNAMICS

Ejecting air from film-cooling holes such as those shown on the vane in figure VII-38 disturbs the boundary layers along the blading and end walls and causes significant decreases in turbine efficiency. The design problem becomes one of devising means for ejecting the coolant from the blading and end walls so that it effectively insulates the blade yet causes a minimum disturbance to the boundary layers.

Two-Dimensional Cascade Program

Several programs to investigate the effect of film-coolant injection on stator-vane performance have been conducted using the cascade shown in figures VII-39 and VII-40. This cascade consists of 12 constant-section vanes, the middle three of which are cooled. The main-stream air enters the cascade from the right, and the air that is used to simulate coolant is introduced to the middle three vanes through the coolant manifold and associated piping. A survey probe is mounted downstream of the blading and traverses parallel to the plane of the vane trailing edges. The flow is discharged from the cascade through exhaust piping attached to the cascade base. Variables that have been investigated in the research programs include coolant hole size, the angle orientation of the coolant holes with respect to both the vane surface and the main-stream flow direction, and the location of the coolant ejection holes on the vane surface.

One of the experimental film-cooled vanes is shown in figure VII-41. There were 12 rows of coolant holes oriented in-line with the main-stream - 6 rows on the pressure surface and 6 rows on the suction surface. There were about 80 holes per row. The blading was hollow and of constant cross section.

A summary of the effect of coolant ejection from individual locations on vane efficiency is shown in figure VII-42. In these tests the coolant was ejected individually from each of the 12 rows of coolant holes. These tests were conducted for a condition where the coolant temperature was equal to the main-stream temprature and the coolant pressure was equal to the main-stream pressure. The numbers in the figure refer to the percentage loss in efficiency for a 1 percent coolant flow from each row of coolant holes. For example, a value of 0.20 indicates that the vane efficiency would decrease by 0.20 percent for 1 percent coolant ejection from that row of coolant holes alone. For this vane configuration the largest losses occurred on the suction surface, particularly in the region of maximum diffusion. In this region the local surface static pressure is lower than the static pressure downstream of the vane. Ejecting coolant into the boundary layer in this region of diffusion where an adverse

pressure gradient exists thickens the boundary layer considerably and causes large loss in vane efficiency.

It is of interest to know whether the total vane efficiency loss can be predicted by adding the individual single-row losses. Figure VII-43 shows that the single-row results do add together quite well. This figure compares the additive single-row losses with the multirow losses for coolant holes open on the pressure surface, on the suction surface, and around the entire vane. The numbers next to the blocks for the additive, single-row results indicate the location of the film cooling hole rows. The good agreement for all three cases indicates that coolant ejection from upstream rows of coolant holes has little effect on coolant ejected from downstream coolant rows.

Analytical methods that can be used to predict the effect of coolant on the aerodynamic performance are being developed. A comparison of results from one of these methods (the previously mentioned STANCOOL computer analysis) with experimental results is shown in figure VII-44. The STANCOOL results, given in terms of efficiency loss, are compared with experimentally obtained efficiency losses from different multirow coolant ejection locations. The case where the coolant holes were sealed (labeled "solid vane" in the fig.) is included as a reference. The next two bars show the predicted loss with the holes open only on the suction surface and then on the pressure surface. The last bar indicates that, with the use of all of the coolant holes, the efficiency loss is 5 percent. The STANCOOL program predictions agree very well with the experimental data.

Another observation can be made from these results. If the solid vane loss of 2 percent is subtracted from each of the other three cases, the remaining loss is that due to the film cooling. It can be seen that the individual film cooling losses for the suction and pressure surfaces add together to equal the total cooling loss.

Stator End-Wall Film Cooling

In another program the effect of stator end-wall film cooling on stator-vane performance was investigated in a cold-air, full-annular cascade. In figure VII-45 the end-wall coolant-hole patterns can be seen on the hub and tip hollow vane rings. Figure VII-46 shows the arrangement of the end-wall cooling holes with respect to the vane passage. Again, it is desirable to eject the coolant with the least disturbances of the main-stream flow.

The radial variation in vane total-pressure ratio with and without end-wall coolant is compared in figure VII-47. The coolant and main-stream pressures were equal, resulting in a 1-percent

coolant flow. The low momentum coolant apparently migrates to the passage vortex regions that are formed from the movement of secondary flows in the vane passage and increases the losses as compared with those for the solid end walls. This increase in total-pressure loss corresponds to an approximate 0.8 percent decrease in vane efficiency. Other configurations are being studied in an effort to reduce these losses.

Effect of Temperature Ratio on Vane and Turbine Efficiency

The results presented thus far have been from cold-air experimental studies where air at or near the same temperature as the main-stream flow was used to simulate cooling air. The tests were conducted in this manner because the test facility and test hardware costs were markedly lower and because the tests could be performed more rapidly and with fewer problems. However, a questions arises as to whether these tests accurately model the actual engine operating condition. A method was developed to predict the aerodynamic performance at actual engine operating conditions from results obtained where the coolant and main-stream temperatures were equal. The primary assumption used in this method is that the aerodynamic performance at the actual engine operating condition will be modeled if the ratio of the coolant momentum to that of the main-stream flow is held constant between the test condition and the engine operating condition.

The results from this prediction method are first compared with experimental data for a full film-cooled vane (fig. VII-48). The vane efficiency is plotted against the ratio of the main-stream temperature to the coolant temperature. In a core turbine application this ratio will approach a value of three. Shown in this figure is the variation in vane efficiency for three values of coolant-supply to main-stream total-pressure ratio. The agreement between the results of the prediction method and the experimental data is good. At a pressure ratio of 1, which is typical of a first-stage vane, the efficiency is constant with temperature ratio. At higher pressure ratios, which correspond to coolant ejected from downstream vanes in a multistage turbine, the efficiency increases with increasing temperature ratio.

The results from this prediction method are compared with experimental data for a core turbine in figure VII-49. As with the vane results, there is good agreement. Of special interest is that the turbine efficiency remains almost constant as the temperature ratio increases. This indicates that the performance at the actual temperature ratio condition can be modeled quite well from reduced temperature ratio results.

TURBINE ROTOR TIP CLEARANCE EFFECTS

The problem of maintaining good aerodynamic efficiency with film cooling of the stator and rotor blading is the most critical problem associated with the core turbine. However, because the core turbine has small-blade-height, low-aspect-ratio blading, other aerodynamic design considerations are also important. As in the core compressor, the rotor tip losses are significant. Several studies have been conducted at Lewis to investigate the rotor-tip clearance loss. Two rotors that were tested are shown in figure VII-50.

Two tip-clearance configurations were investigated. The inset on the left in figure VII-51 shows a recessed casing configuration. In this configuration the rotor-blade tip was in line with the upstream and downstream casing, and the tip clearance was varied by changing the casing recess depth. In the conventional, reduced-blade-height configuration, which is shown in the inset on the right, the casing was not recessed, and the tip clearance was varied by cutting back the rotor-blade height.

The tip-clearance losses for the two configurations are compared in figure VII-52. The recessed casing configuration was tested with the 5-inch tip-diameter rotor. The reduced-blade-height configuration was tested with both rotors. For a given rotor tip clearance, the loss for the recessed-casing configuration is less than the loss for the reduced-blade-height configuration. The difference in loss for the two rotors having a reduced-blade-height configuration is attributed to a difference in the level of rotor reaction. Using a recessed-casing configuration instead of a reduced-blade-height configuration could result in a core turbine efficiency improvement of approximately 1.0 to 1.5 percent.

TURBOMACHINERY TECHNOLOGY GOALS

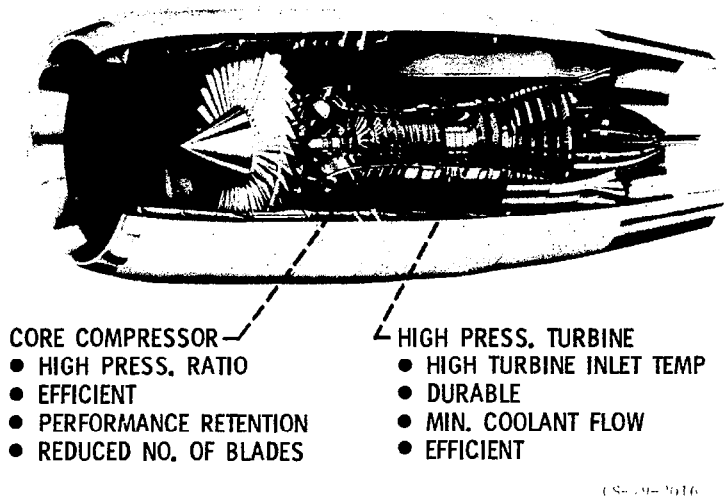

Figure VII-1

TRANSONIC COMPRESSOR FLOW MODEL

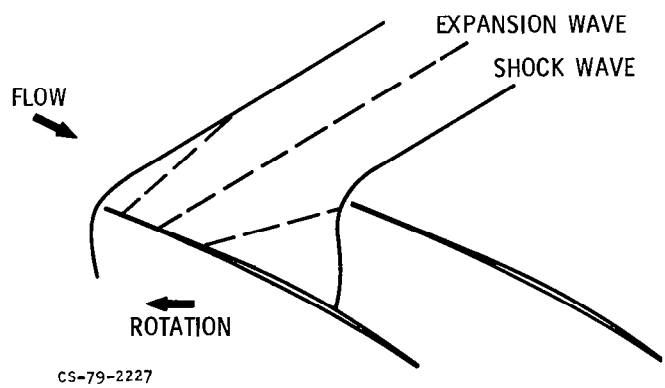

Figure VII-2

BLADE SURFACE PRESSURES

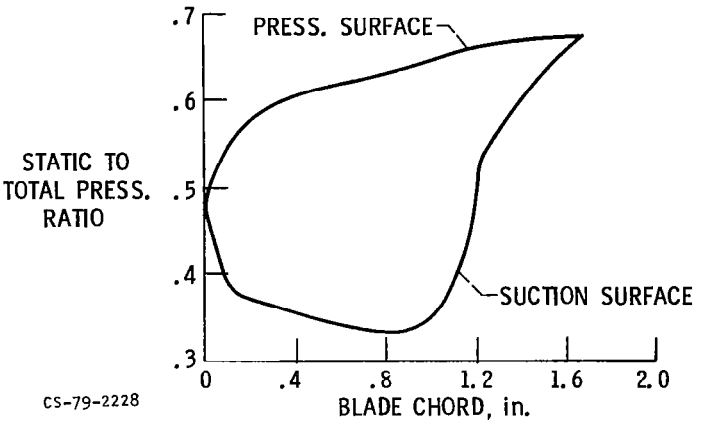

Figure VII-3

BLADE SURFACE PRESSURES

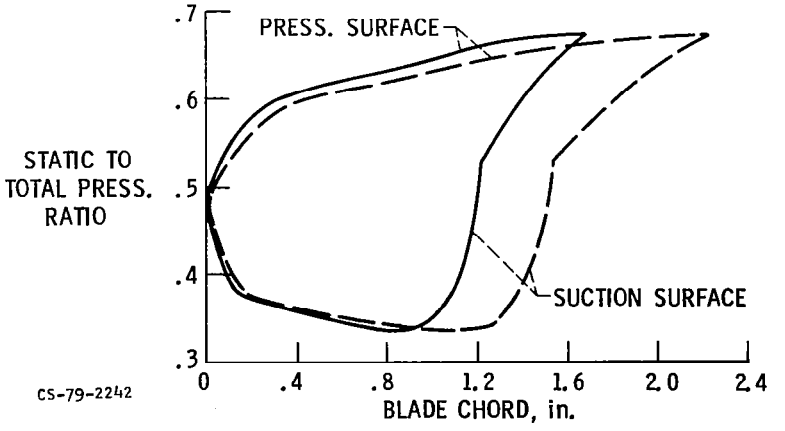

Figure VII-4

LOW AND MODERATE ASPECT RATIO COMPRESSOR ROTORS

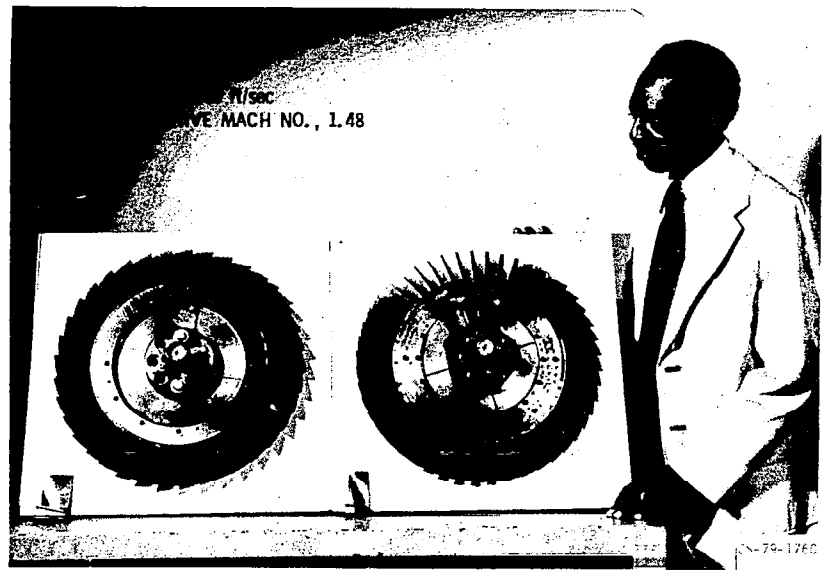

Figure VII-5

LOW AND MODERATE ASPECT RATIO COMPRESSOR ROTOR BLADES

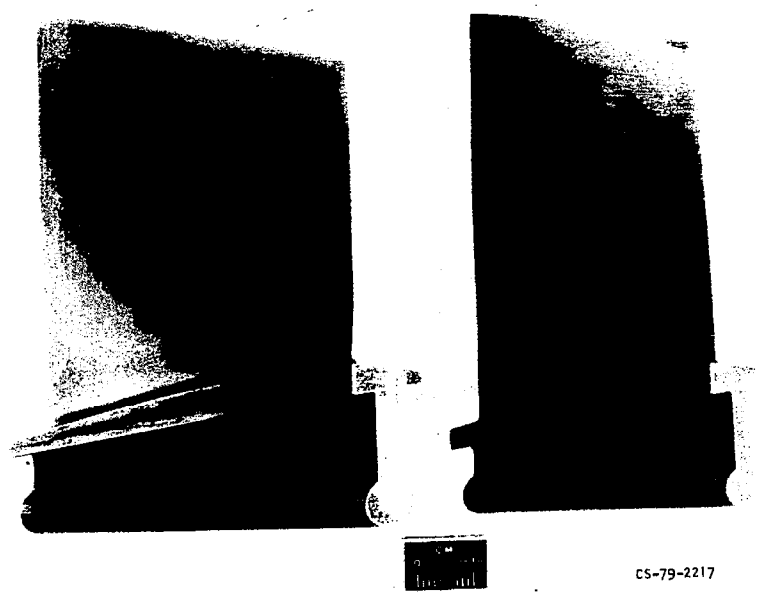

Figure VII-6

LEWIS SINGLE STAGE COMPRESSOR FACILITY

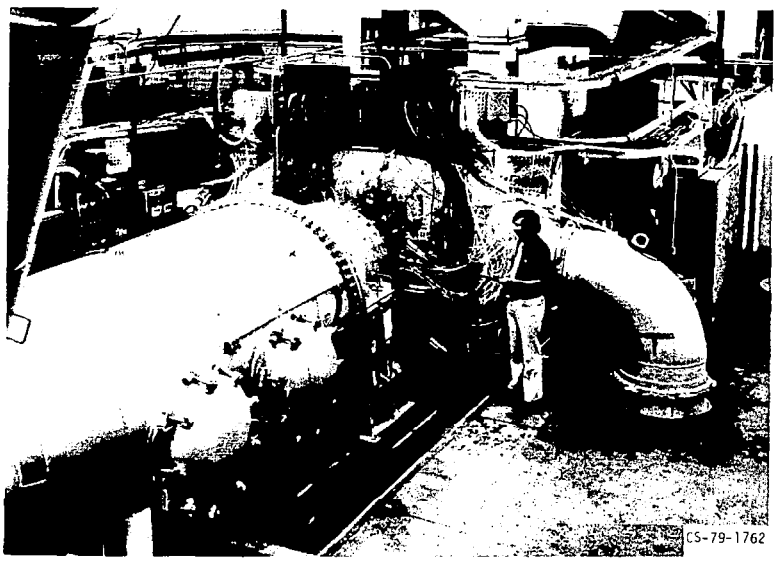

Figure VII-7

STAGE PERFORMANCE COMPARISON

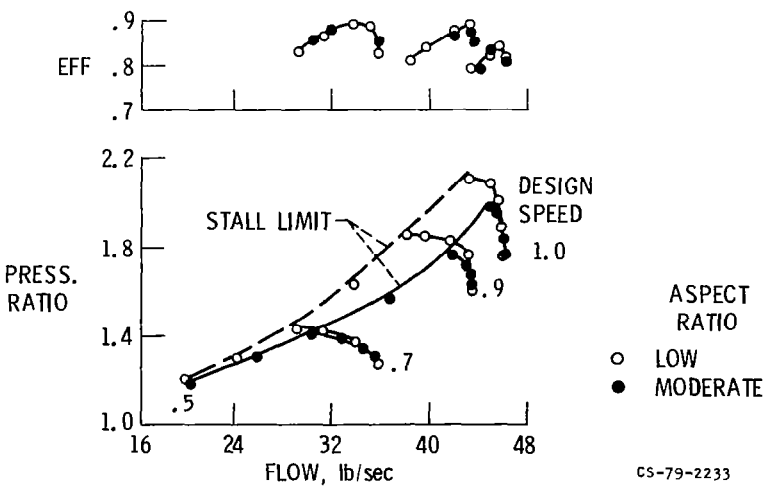

Figure VII-8

LOW SPEED COMPRESSOR FACILITY

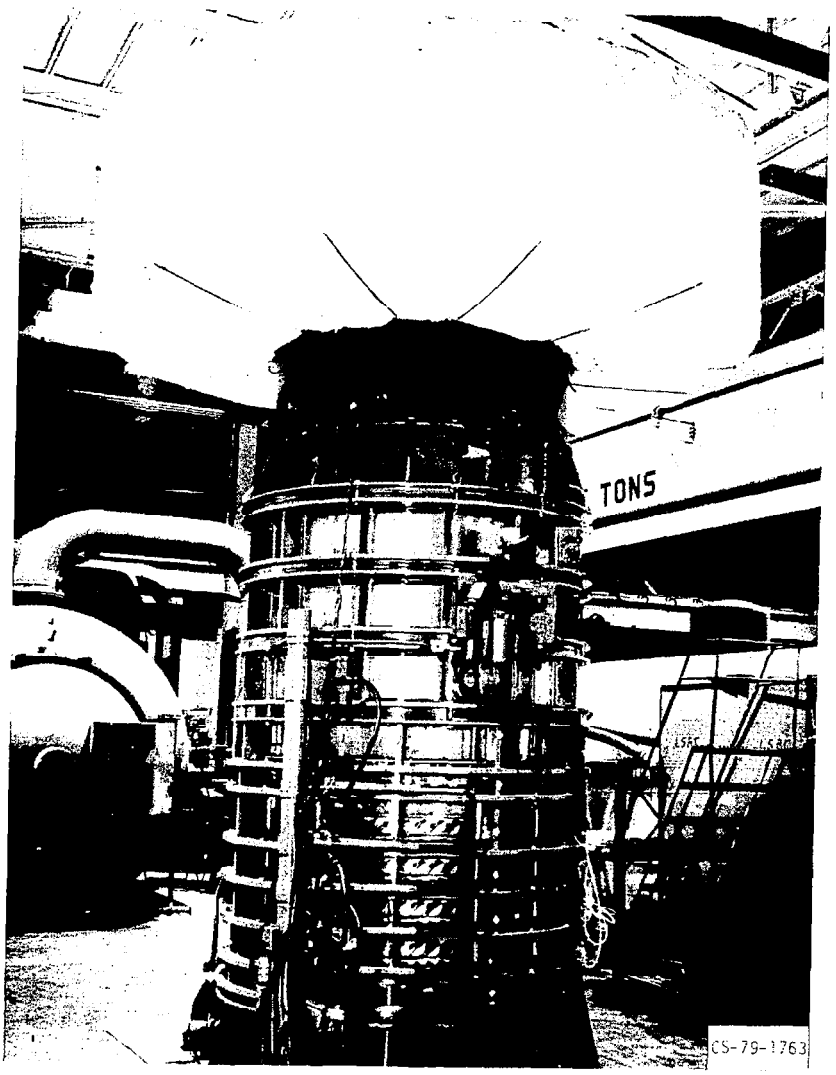

Figure VII-9

LOW SPEED COMPRESSOR BLADE ROWS

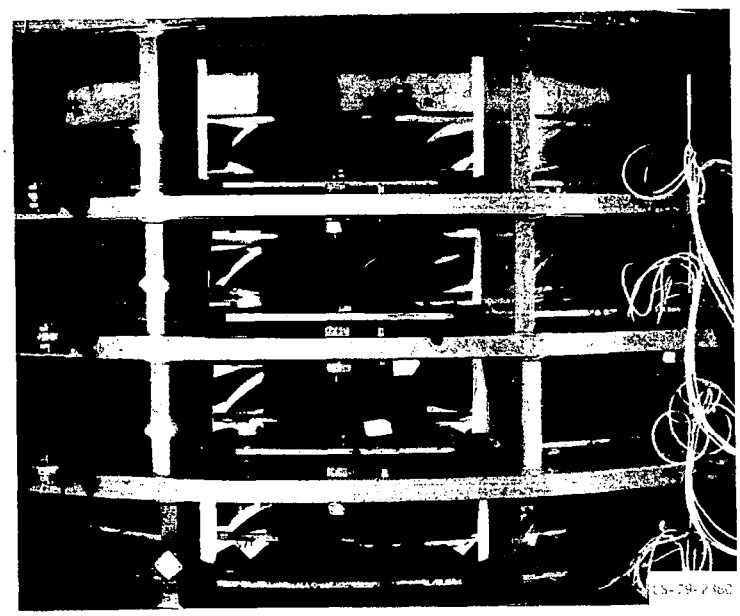

Figure VII-10

SURFACE VELOCITY COMPARISON

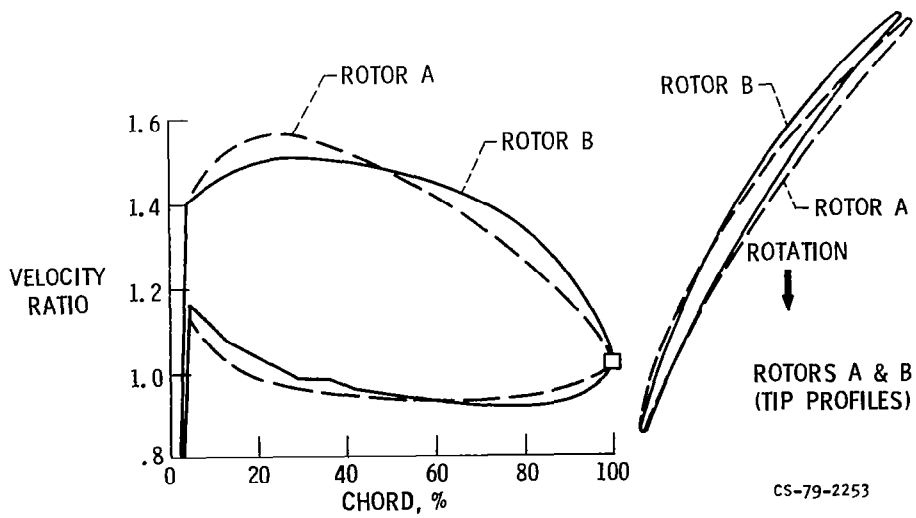

Figure VII-11

COMPARISON OF RADIAL VARIATION OF AXIAL VELOCITY

STATORS A & B

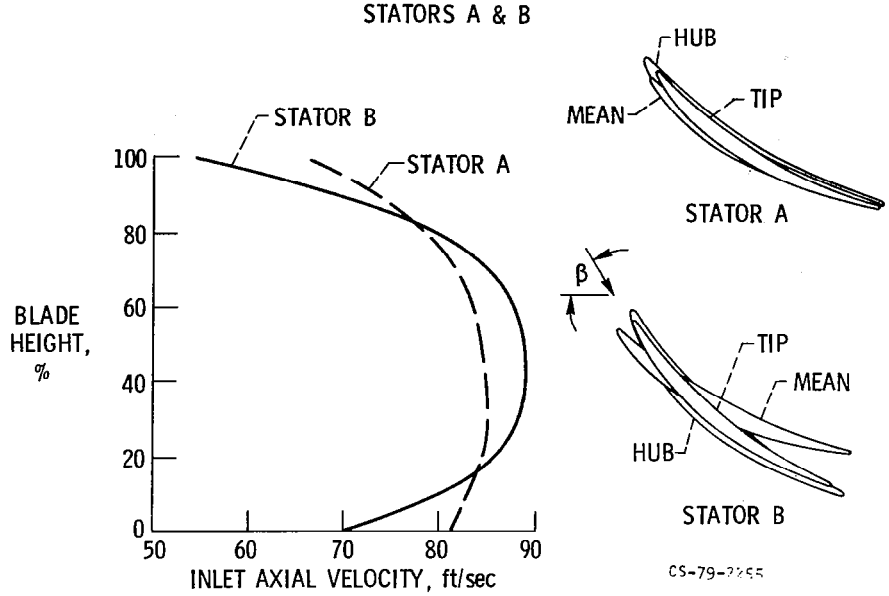

Figure VII-12

REAR STAGE BLADING

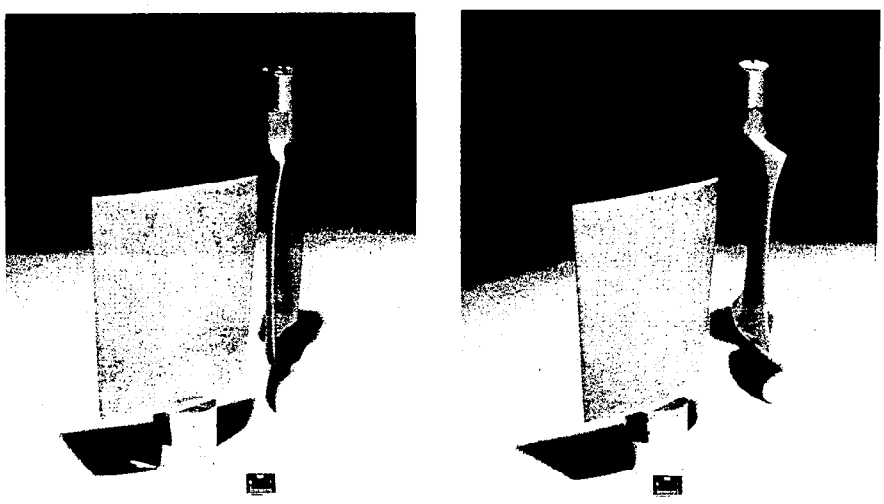

ROTOR A – STATOR A

ROTOR B – STATOR B

CS-79-2208

Figure VII-13

STAGE OVERALL PERFORMANCE

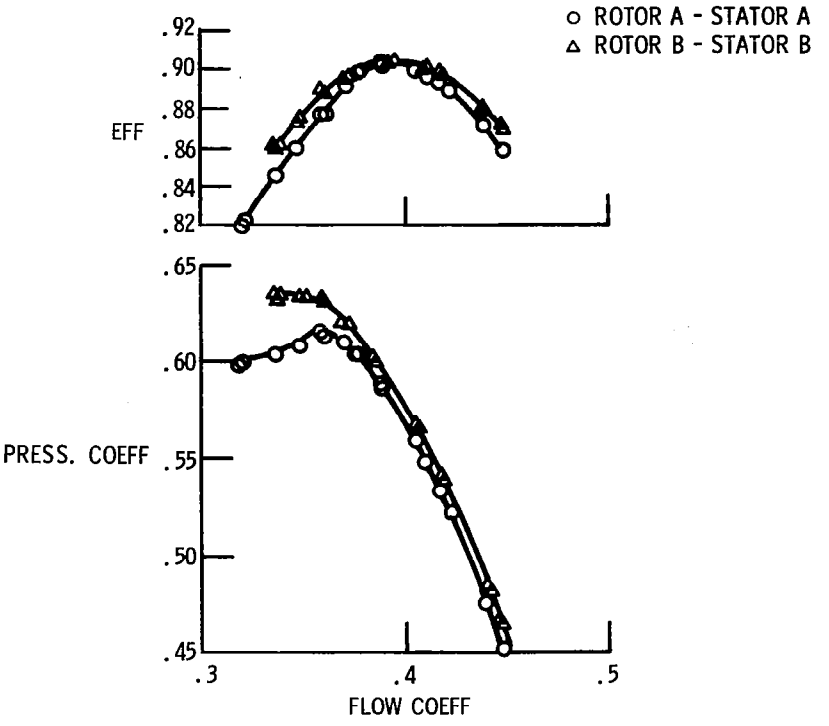

Figure VII-14

CASING WITH RECESSED CLEARANCE

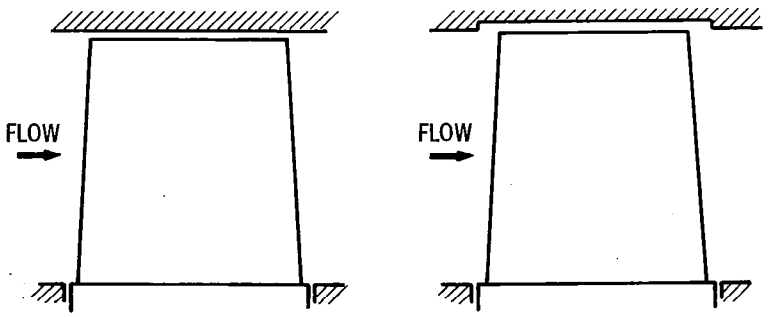

Figure VII-15

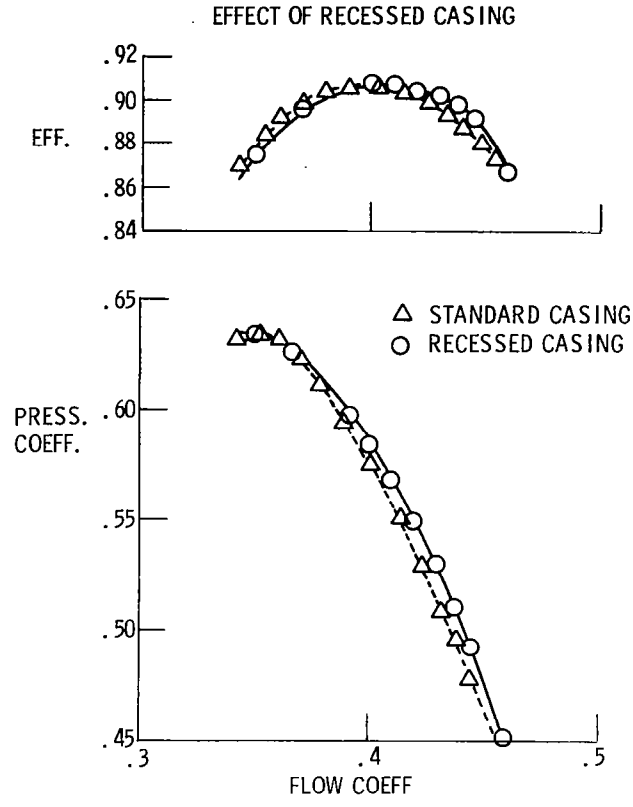

Figure VII-16

COMPRESSOR FACILITY WITH LASER VELOCIMETER

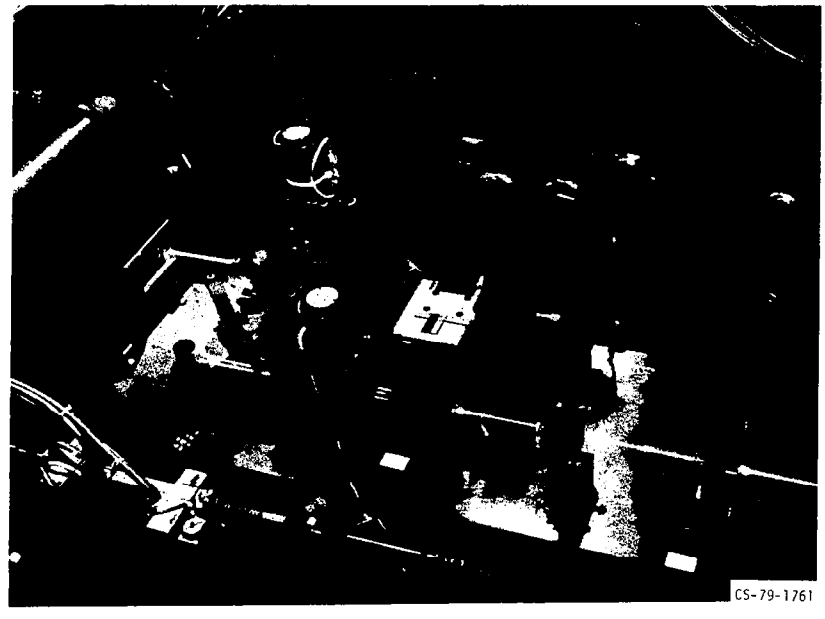

Figure VII-17

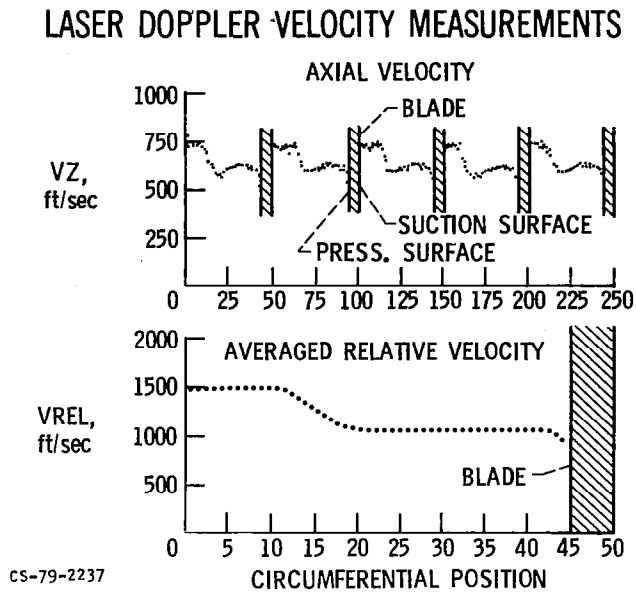

Figure VII-18

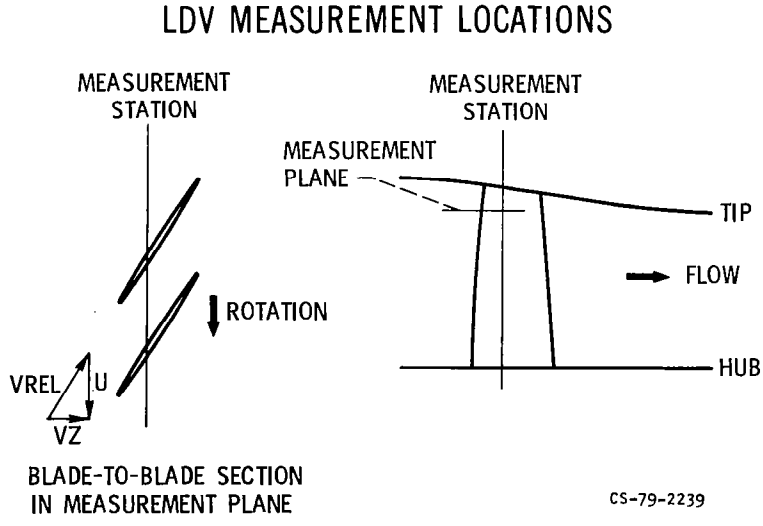

Figure VII-19

CALCULATED AND MEASURED VELOCITY CONTOURS

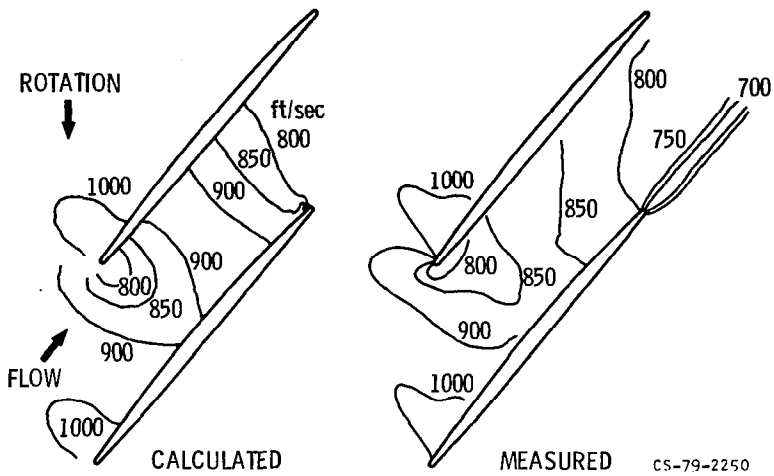

Figure VII-20

SCHEMATIC OF COOLED TURBINE BLADE

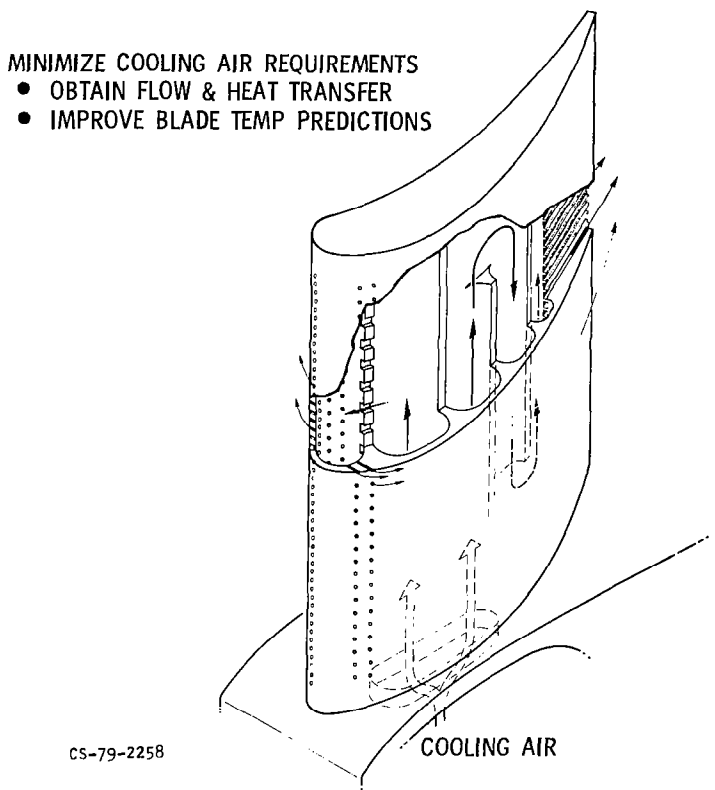

Figure VII-21

TURBINE BLADE WALL COOLING TECHNIQUES

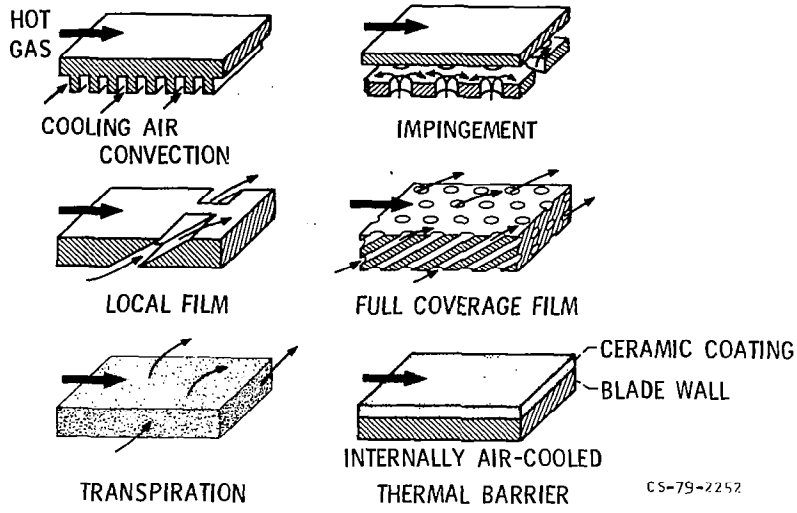

Figure VII-22

TURBINE COOLING REQUIREMENTS

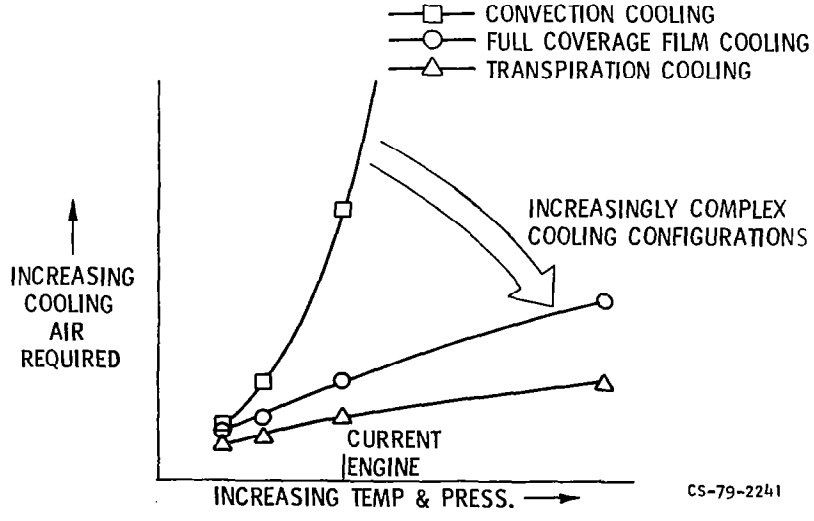

Figure VII-23

IMPINGEMENT COOLING

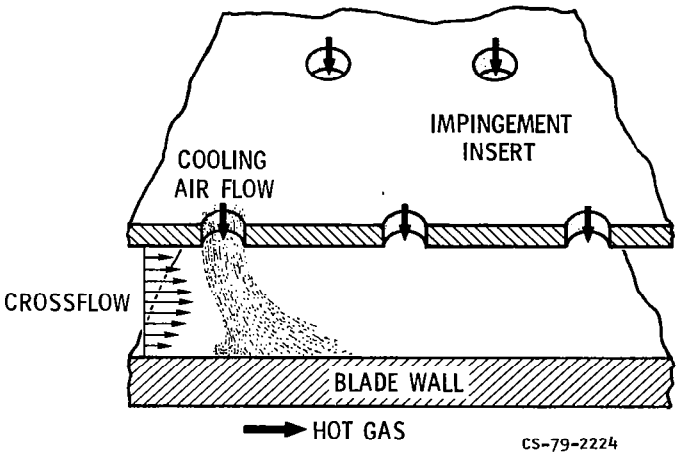

Figure VII-24

IMPINGEMENT COOLING APPARATUS

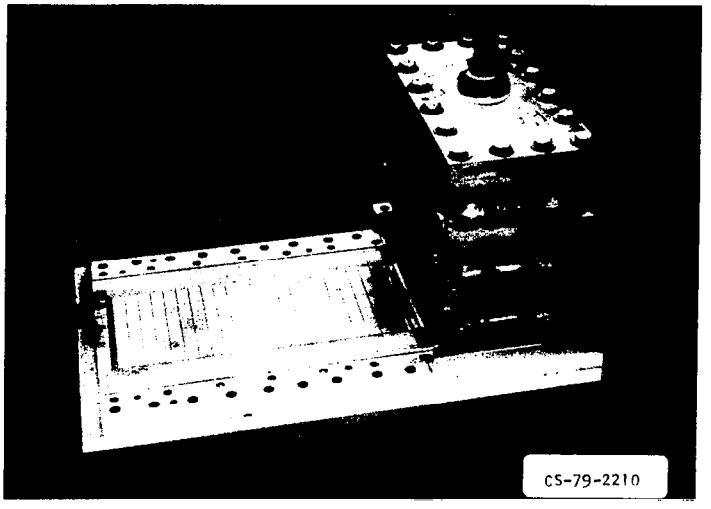

Figure VII-25

SCHEMATIC OF IMPINGEMENT COOLING APPARATUS

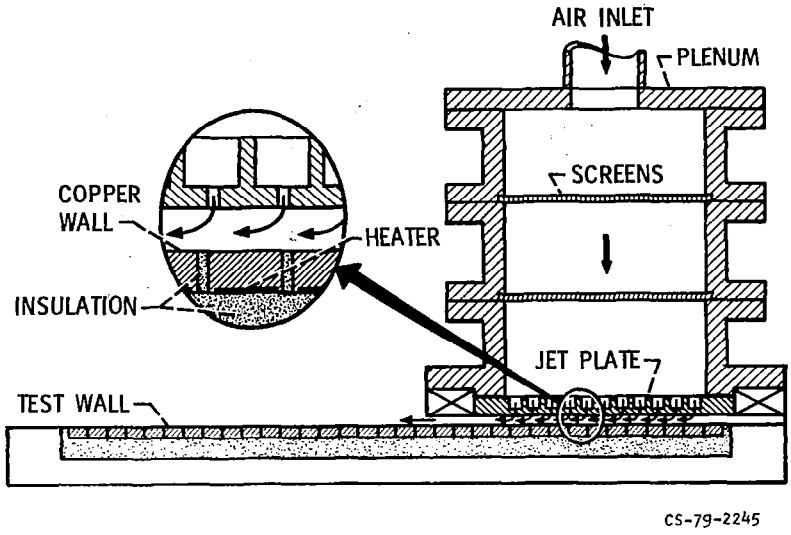

Figure VII-26

IMPINGEMENT COOLING HEAT TRANSFER

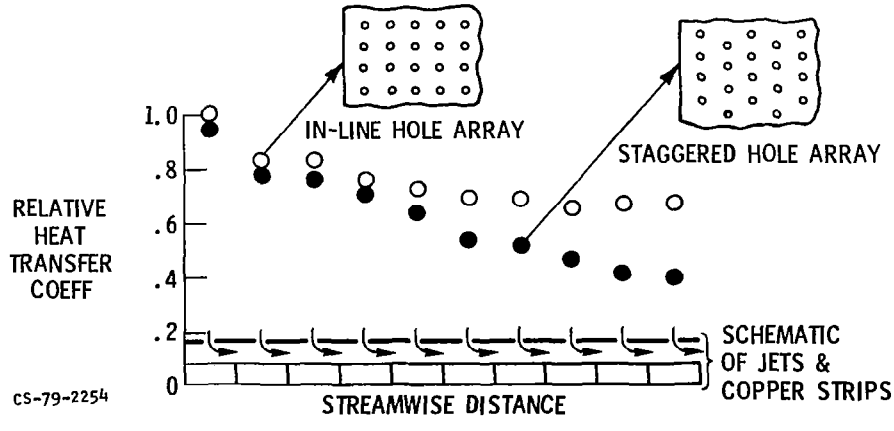

Figure VII-27

FILM COOLING APPARATUS

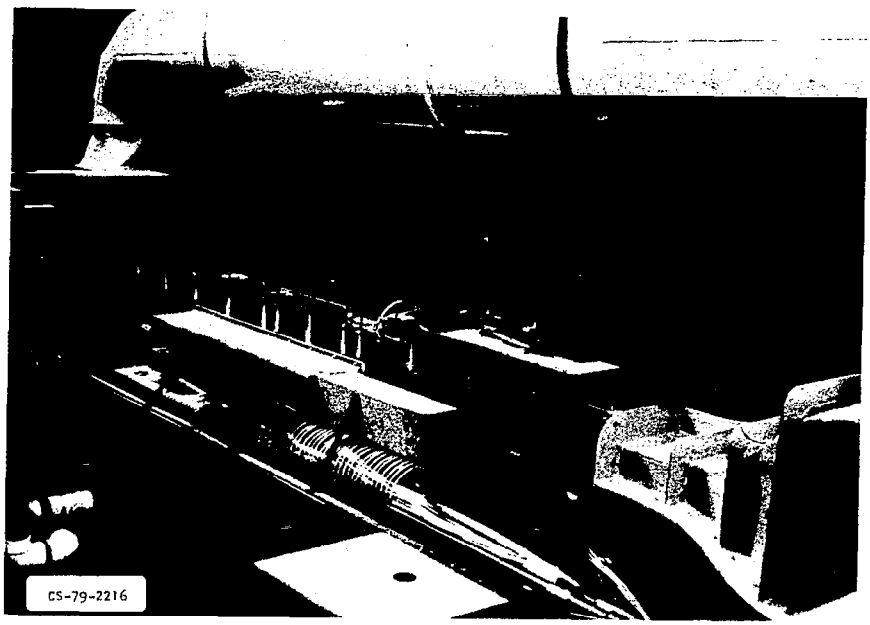

Figure VII-28

SCHEMATIC OF FILM COOLING APPARATUS

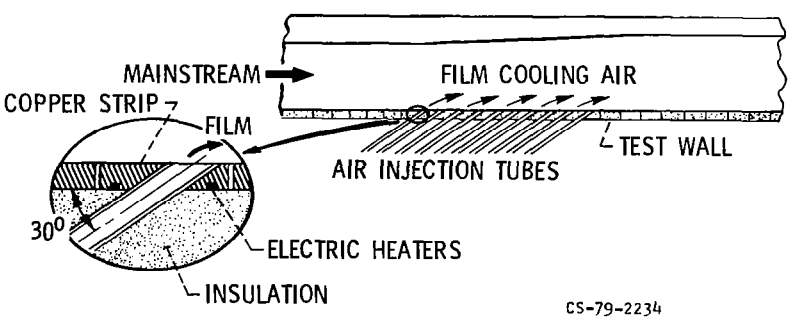

Figure VII-29

FILM COOLING HOLE ARRAYS

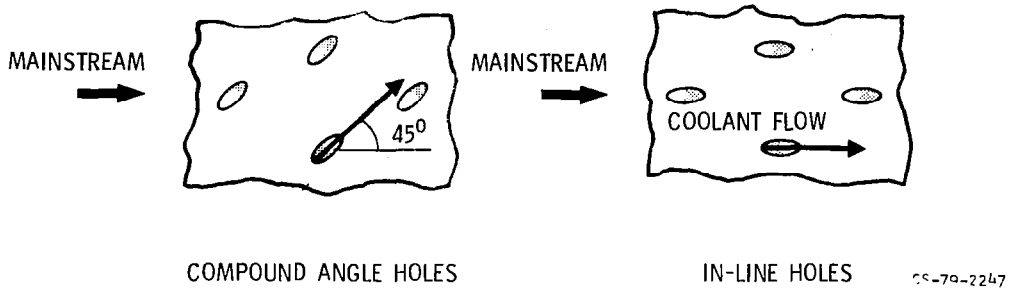

Figure VII-30

EFFECT OF FILM COOLING

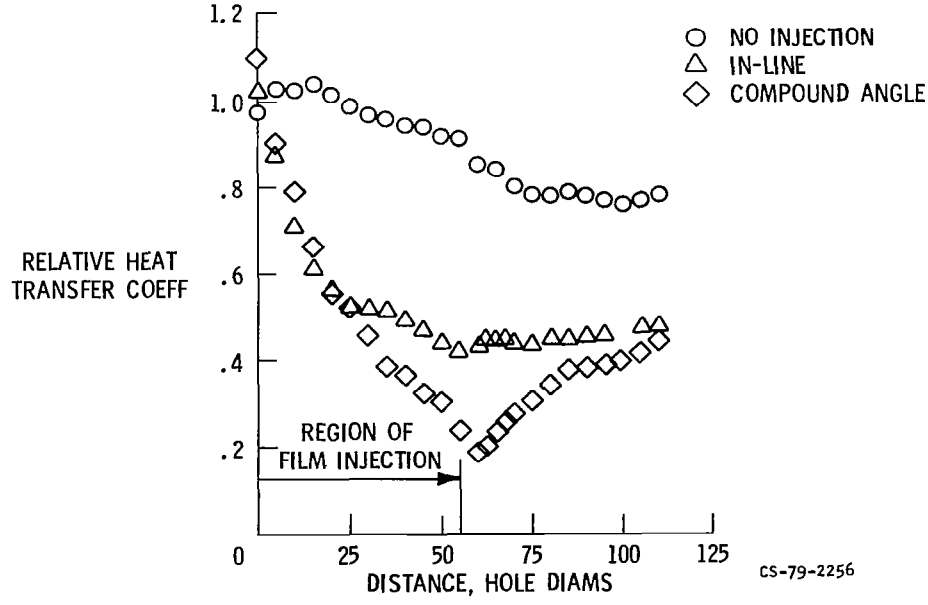

Figure VII-31

EXPERIMENTAL AND PREDICTED FILM COOLING

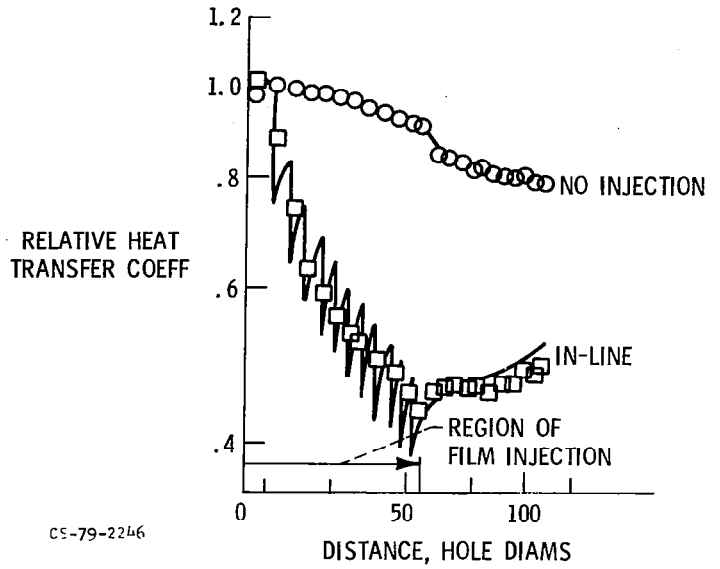

Figure VII-32

CASCADE TESTS OF FILM COOLING

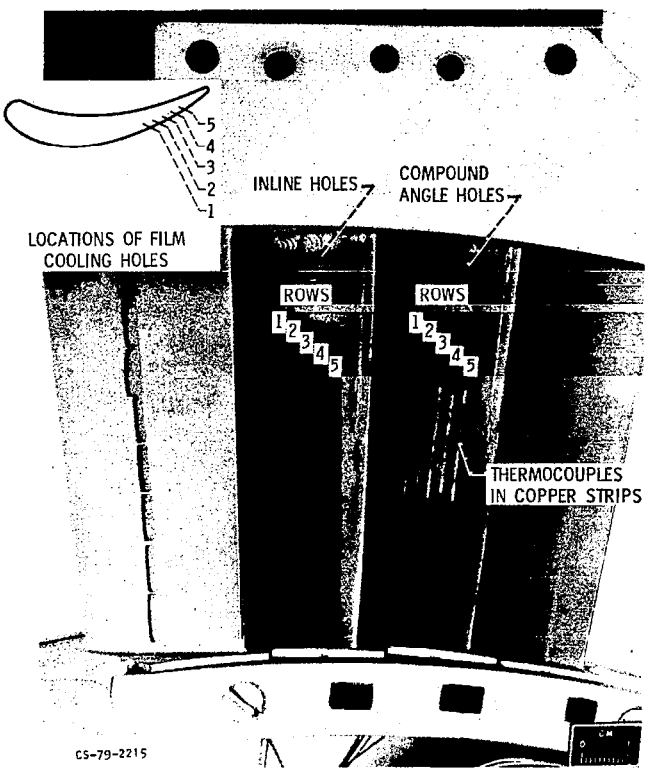

Figure VII-33

FILM COOLING OF TURBINE VANE IN CASCADE

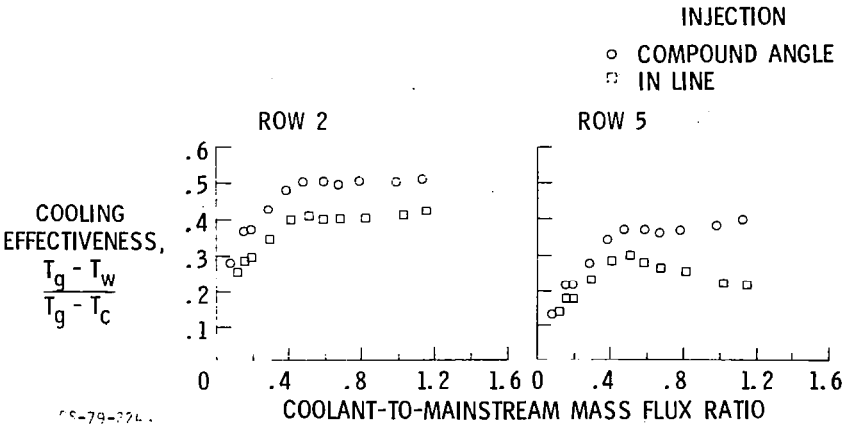

Figure VII-34

THERMAL BARRIER COATED TURBINE BLADE

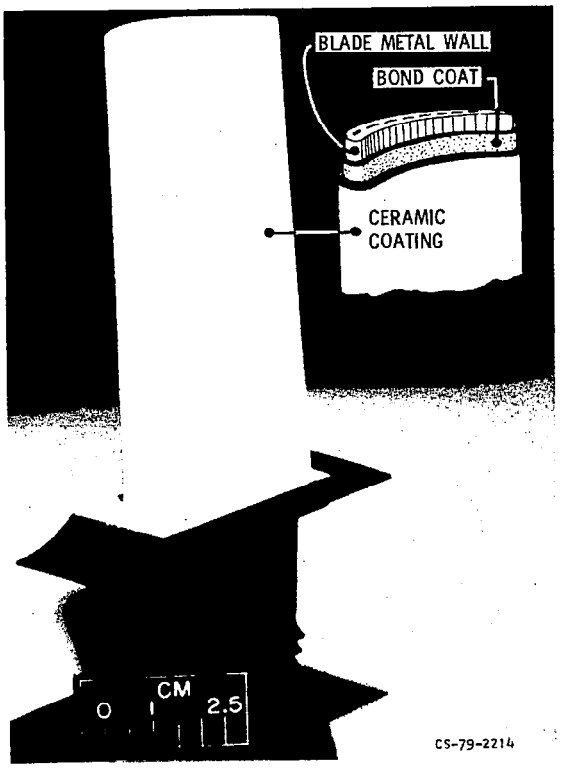

Figure VII-35

EFFECT OF THERMAL BARRIER COATING ON VANE METAL TEMPERATURES

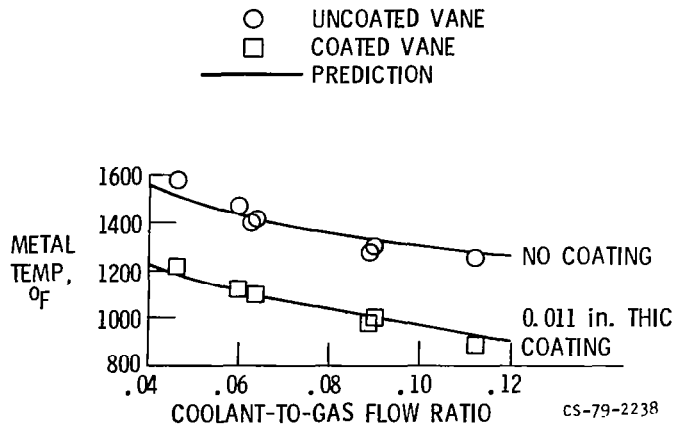

Figure VII-36

EFFECT OF THERMAL BARRIER COATING ON VANE LOSSES

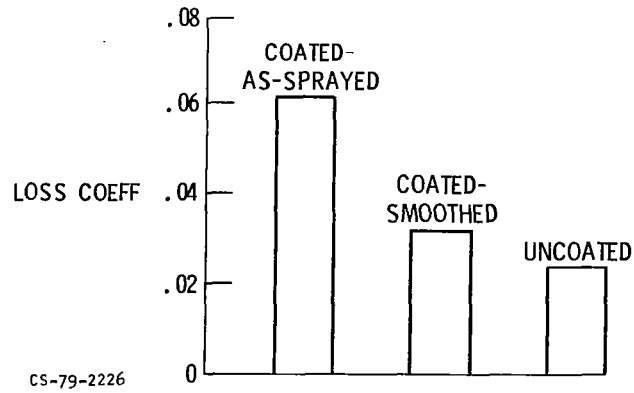

Figure VII-37

FULL-FILM COOLED VANE

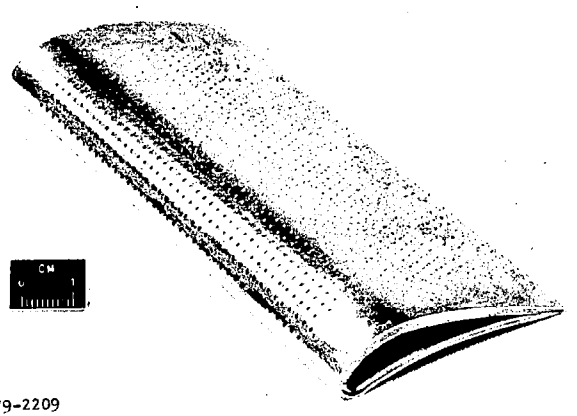

CS-79-2209

Figure VII-38

STATOR VANE CASCADE

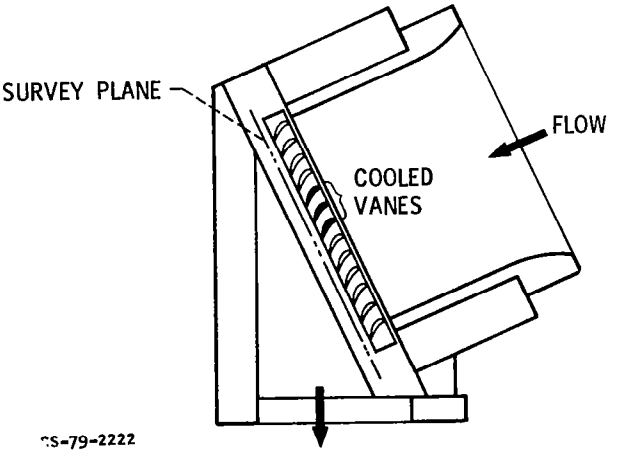

CS-79-2222

Figure VII-39

STATOR VANE CASCADE

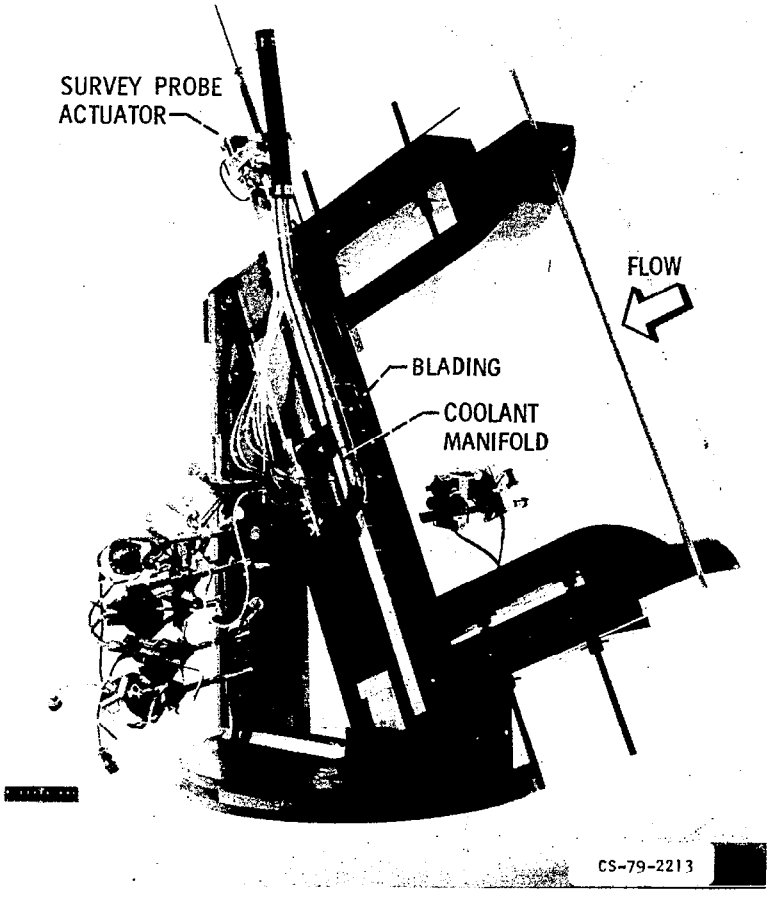

Figure VII-40

FILM-COOLED VANE

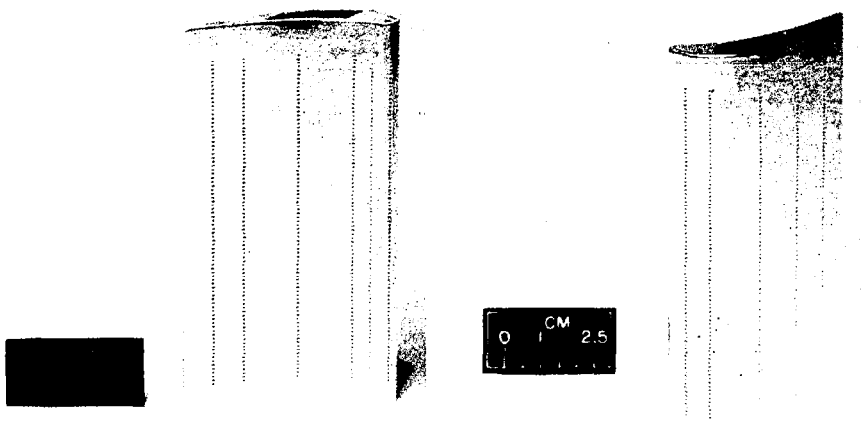

CS-79-2220 PRESS. SURFACE SUCTION SURFACE

Figure VII-41

EFFICIENCY LOSS FOR 1% COOLING AIR EJECTION

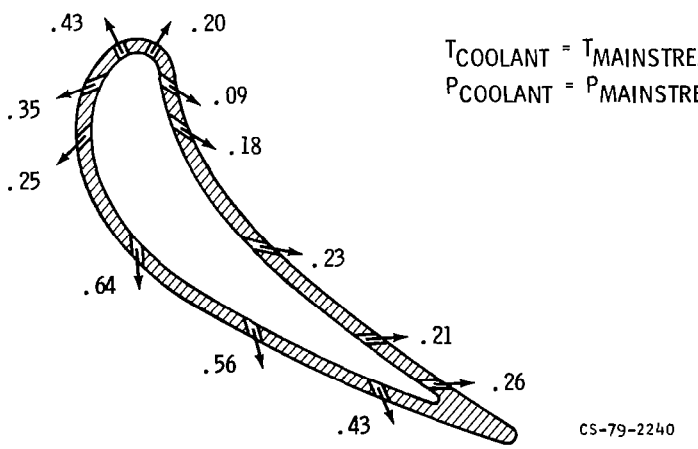

Figure VII-42

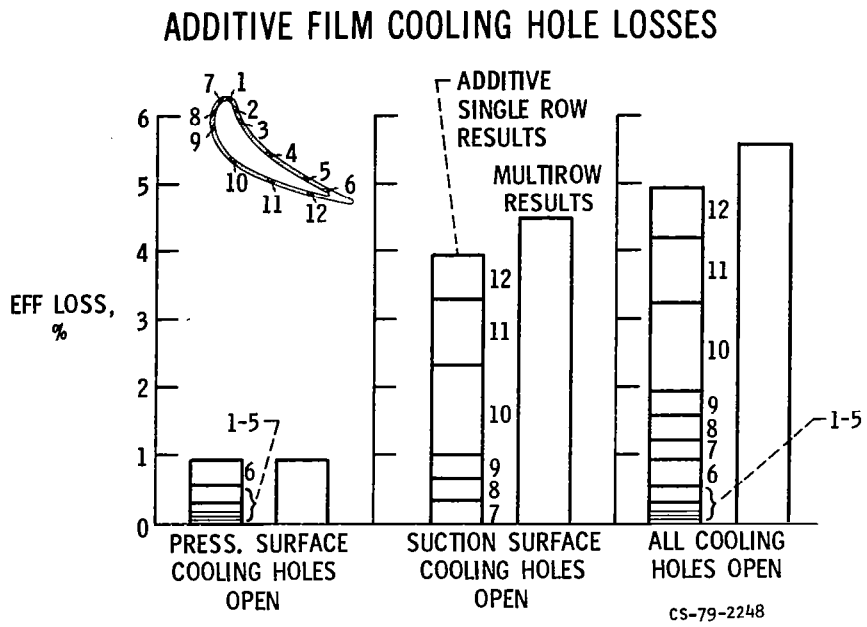

Figure VII-43

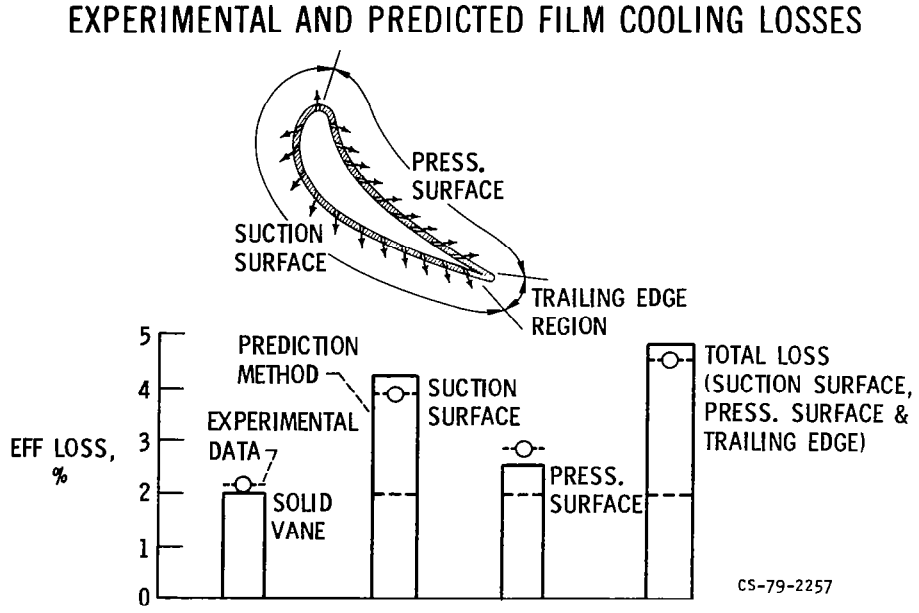

Figure VII-44

VANE RINGS SHOWING ENDWALL COOLING HOLES

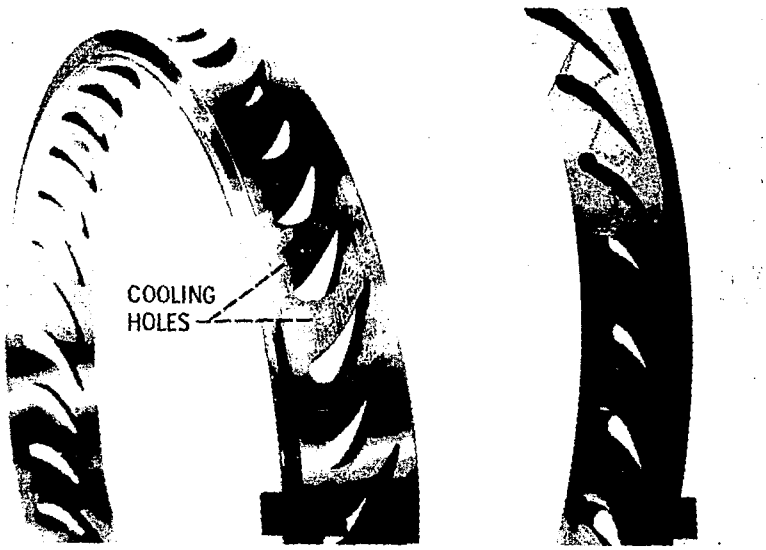

Figure VII-45

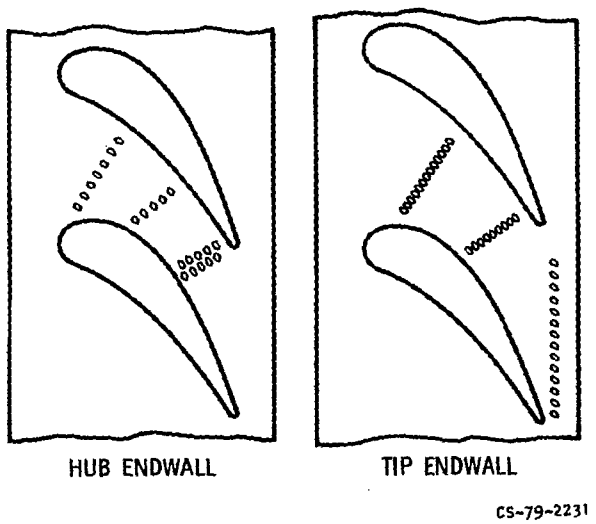

Figure VII-46

VANE TOTAL PRESSURE RATIO WITH ENDWALL COOLING AIR

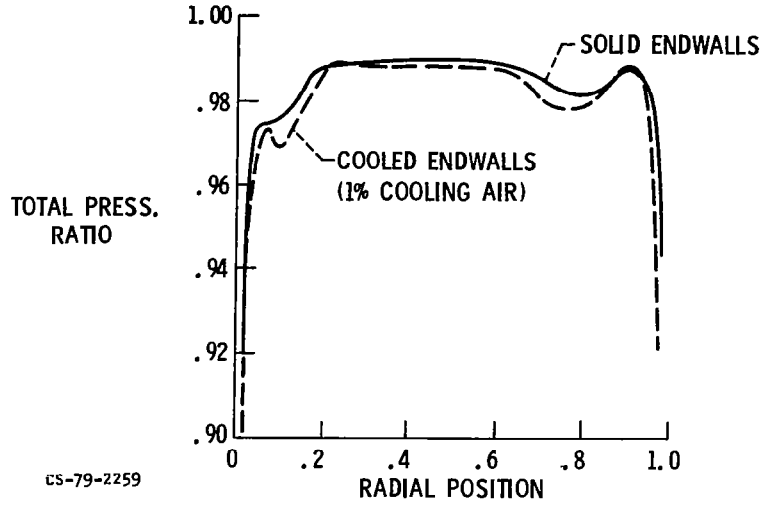

Figure VII-47

EXPERIMENTAL AND PREDICTED VANE EFFICIENCIES

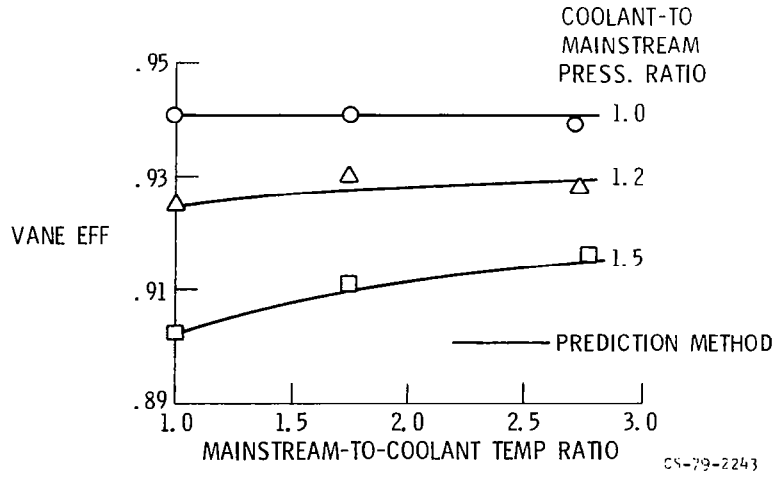

Figure VII-48

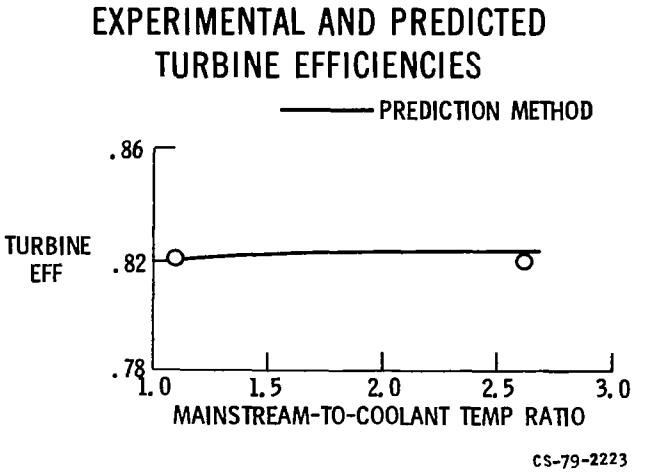

Figure VII-49

TURBINE ROTORS USED IN TIP CLEARANCE INVESTIGATIONS

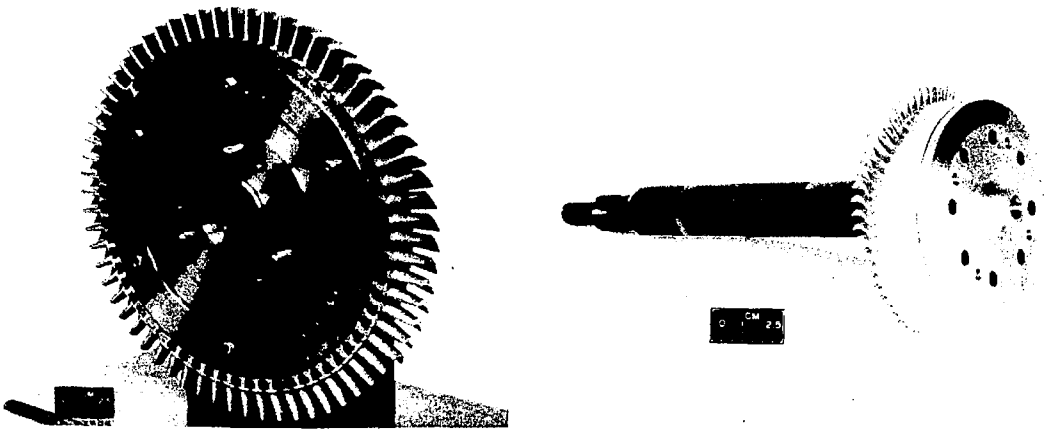

10-in. TIP DIAM ROTOR

5-in. TIP DIAM ROTOR

Figure VII-50

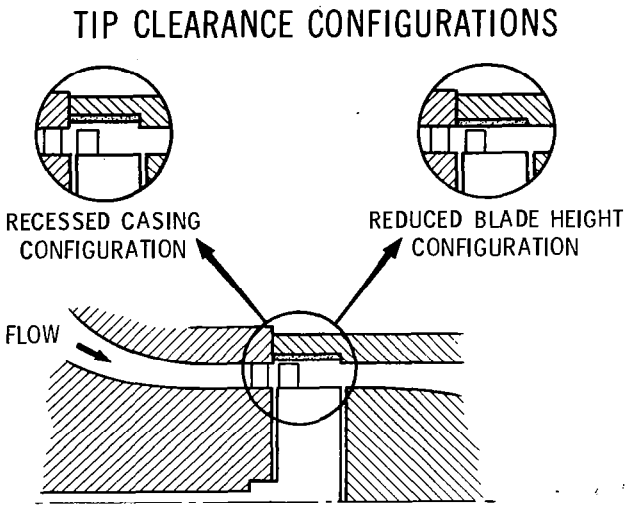

Figure VII-51

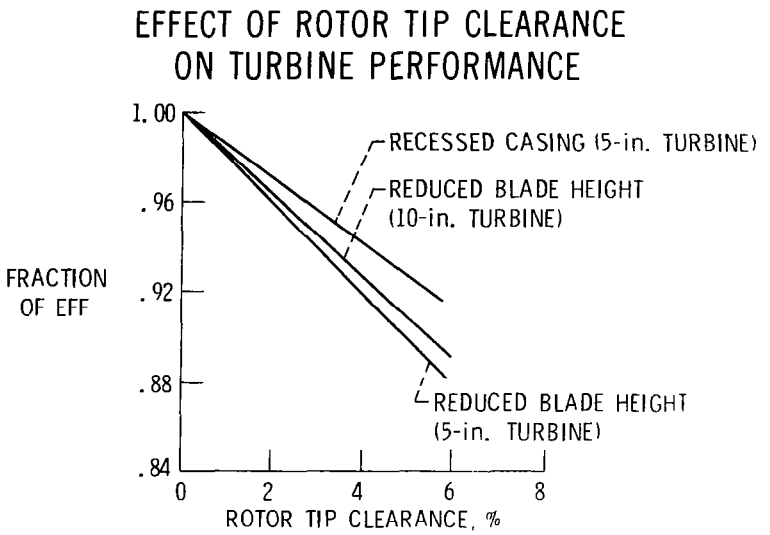

Figure VII-52

VIII. MECHANICAL COMPONENTS

William J. Anderson, Robert C. Bill, John J. Coy,
and David P. Fleming

National Aeronautics and Space Administration
Lewis Research Center

The term mechanical components incorporates machine elements such as bearings, gears, seals, clutches, and shafts or rotors. In this paper, some research on bearings, gears, seals, and rotor dynamics (specifically high-speed balancing and dampers) is reported. This research pertains to problems in both aircraft turbine engines and helicopter transmissions.

TURBINE ENGINES

In turbine engines, the concerns are with main-shaft bearings, dampers, shaft seals, and gas-path seals at the tips of the compressor and turbine blades and between the compressor stages. The locations of these components are shown in figure VIII-1.

Main-Shaft Bearings

In turbine engines, main-shaft bearings are either ball or cylindrical-roller bearings. In present engines, they are required to operate at DN values up to about 2.4 million. DN is a speed severity parameter consisting of the product of bearing bore diameter, D, in millimeters, and the rotative speed, N, in rpm. Engine designers would like to have main-shaft bearings with a DN capability of 3 to 3.3 million for advanced engines. Extensive work has been done in conjunction with the General Electric Company to define and solve the problems associated with operating ball bearings at 3 million DN. Approximately 70 000 operating hours have been accumulated at 3 million DN.

The bearing design and lubrication problems associated with operating at 3 million DN have been solved, but catastrophic fracturing of the bearing inner ring occurs as a result of fatigue pitting. Figure VIII-2 shows one-half of the inner ring of a ball bearing run at 3 million DN. Fatigue pitting is the normal failure mode for rolling bearings. At lower speeds, it is a benign type of failure which can be detected by small chips in the oil. The bearing is then replaced. At very high speeds, the hoop stress in the rotating ring causes minute cracks in the

fatigue pits to propagate through the ring and cause fracture and complete failure.

Engine bearings are traditionally made of through hardened steels, which have low fracture toughness. One approach to this problem might be to use carburized materials with a hard surface layer and a soft core. Tapered roller bearings made of carburized materials are currently being tested at high speeds for transmission applications. This research may have application to engine bearing problems.

The problem of bearing material fracture toughness is one that is confined to the extremely high speeds contemplated for future, advanced engines. A much more mundane problem that is present every day in the operation of all machinery is dirt ingestion into the lubrication system. With the steady improvements that have been made in bearing material quality, more and more failures are traceable to contaminants in the lubrication system. For this reason, a research program was conducted to determine the effect of lubricant filtration on bearing life.

Figure VIII-3 shows the bearing fatigue life results for these tests. The lives are statistical lives, each being obtained with a group of 65-millimeter ball bearings. First a new, clean oil was used to determine a baseline life. Then a test series was run with the oil purposely contaminated to simulate the normal operating conditions of a turbine engine in a real environment. A different filter size was used for each of four test groups. Using a 105-micrometer filter resulted in premature failure due to severe wear. With progressively finer filter mesh sizes, fatigue life continued to improve, although the gains were modest. In fact, even with the finest (3-μm) filter, fatigue life was only about one-half as long as when the system was perfectly clean and free of contaminants. Although the improvement in fatigue life with finer filtration was rather modest in these tests, it may be more significant in other systems.

Another factor was the dramatic difference in appearance among the bearings in the different groups. Bearing surface distress and wear were much more prevalent in the tests run with coarser filters, indicating that wear could be the mode of failure for many of the longer running bearings with coarser filtration. Normally 30- to 40-micrometer filters are used in aircraft engine and transmission lubrication systems. Use of finer filters could result in increased bearing life.

Shaft Seals

In present engines, shaft seals operate at sliding speeds up to approximately 450 feet per second. Usually noncontact labyrinth seals are used because of wear and durability problems associ-

ated with contact or rubbing seals. Engine designers would like to have contact seals capable of operating at 700 to 800 feet per second. Sliding velocities of conventional contact seals are limited by the wear and heat generation associated with high-speed rubbing. The development of self-acting or film-riding seals has been pioneered at NASA. Early work on self-acting seals which incorporate Rayleigh pads to create a separating film was reported at the 1975 Aeronautical Propulsion Conference (ref. 1). Figure VIII-4 shows the spiral-groove self-acting seal, which utilizes shallow spiral grooves in the face of the stationary seal member to pump fluid and to establish a very thin film which prevents direct rubbing contact between the stationary and rotating seal elements. This design significantly reduces friction and temperature rise at high sliding speeds. A spiral-groove seal has been operated successfully for 100 hours at sliding speeds up to 800 feet per second. A seal of this type is presently being designed for retrofitting into a 1500-horsepower turboshaft engine in a helicopter.

Gas-Path Seals

At the present time, an intensive program for the development of ceramic seals for the turbine blade shroud is being carried out. Present engines have metal shrouds which must be cooled with engine airflow. They also have low rub tolerance, which necessitates large tip clearances. These two factors - the need for cooling air and the need for large tip clearances - result in performance losses.

Figure VIII-1, although simplified, shows the locations of the gas-path seals. A large engine contains over 50 dynamic sealing locations. The purpose of gas-path sealing is to minimize leakage from the primary flow path through the compressor, burner, and turbine. This leakage occurs across the blade tips and at the labyrinth seals between stages; it has a very significant cumulative effect, not only on specific fuel consumption, but also on compressor stall margin and engine thrust. Furthermore gas-path sealing becomes more critical as engines advance to higher pressures and temperatures. One of the sealing locations most critical to specific fuel consumption is the high-pressure-turbine blade tip, which is shown in detail in figure VIII-5.

From a sealing standpoint, the operating environment is the most severe with gas temperatures near 2600° F and with pressures near maximum. In small engines, the turbine rub shroud is a single ring; in large engines, it is constructed of segments in order to reduce thermal strains. Typically each segment is impingement cooled and is held in place by a cooler outer case structure.

Figure VIII-6 indicates the problems induced by the high pressures and temperatures of advanced engines. These problems include

(1) High cooling requirements, which can be 2 to 3 percent of flow through the compressor

(2) Low durability, which shows up in the form of wear, erosion, cracking, and warping

(3) Lack of abradability, which means the shroud out-of-roundness or eccentricity cannot be corrected by being worn down by the turbine blades (illustrated in fig. VIII-7)

For engine efficiency, minimum clearance between the blade and shroud is desired. However, the high-pressure-turbine shroud out-of-roundness, exaggerated in figure VIII-7, is common because of

(1) Nonuniform temperatures

(2) Nonaxisymmetric structures

(3) Flange leakage

(4) Nonuniform distribution of cooling air

(5) Localized flow, in particular, hot gas recirculation

An important point is that the out-of-roundness is often greater than the desired operating clearance. Therefore, with conventional blade and shroud construction, either the initial assembly clearance must be large enough to preclude rubbing or the out-of-roundness will cause blade wear. In either case, the out-of-roundness results in an increased clearance which can be as large as 1 to 2 percent of the blade height. This clearance, in turn, can result in a significant penalty in terms of specific fuel consumption.

Typically in a modern, highly loaded turbine, a clearance change of 1 percent of blade height changes the specific fuel consumption by 1.5 to 2.0 percent. Each 1 percent of specific fuel consumption is a very significant figure because fuel costs account for nearly 50 percent of the direct operating cost, which is most of the ticket price. A 1-percent change in specific fuel consumption applied to the Nation's commercial fleet represents about 150 000 000 gallons of fuel per year. A significant portion of the fuel loss due to large out-of-roundness clearances could be saved if the local bumps were abraded away without blade wear as indicated in figure VIII-8.

Several new shroud concepts are being developed with the goal of mitigating the problems of high cooling requirements, low durability, and lack of abradability. Abradable metal shrouds have been developed for use in present engines. Ceramic shrouds for even higher temperatures are under development. Ceramic shroud development is not yet complete, but some very interesting results have been obtained.

The most challenging and immediate problem connected with the use of ceramic materials in the high-pressure-turbine seal application is retention of mechanical integrity under conditions of severe thermal gradients imposed by the engine operating cycle. Currently being evaluated are two approaches to ensuring mechanical integrity of ceramic seals, both based on plasma-sprayed zirconium oxide (ZrO_2).

One approach, shown in figure VIII-9, incorporates metal-ceramic composite intermediate layers between the alloy substrate and the fully ceramic layer adjacent to the gas path. The function of the metal-ceramic intermediate layers is to mitigate thermal stresses imposed on the brittle ceramic by gradually varying the thermal expansion and mechanical properties from those of the metal substrate to those of the ceramic layer. Variations on this approach include nickel or cobalt alloys with chromium, aluminum, and yttrium (NiCrAlY or CoCrAlY) as the metal constituent and different arrangements and compositions of intermediate layers. Pioneer analytical and experimental work on this approach was conducted under NASA contract by the Pratt & Whitney Division of United Technologies Corporation.

The other approach, shown in figure VIII-10, employs a strain isolator pad of porous metal with ZrO_2 sprayed on top. The strain isolator pad, in this case a Brunswick fiber metal, looks very sparse on a microscopic scale, but is structurally very sound and protects the ceramic from the thermal expansion difference between the ceramic and the metal. The grey ceramic is the ZrO_2. Other strain isolator pad systems being evaluated include alternate fiber and metal layers, low-density sintered metals, and low-density plasma-sprayed metals.

The durability of the ceramic shroud materials is being investigated in thermal cycling tests in which the surface temperature of the ceramic is held at 2400° F. As illustrated in figure VIII-11, an oxyacetylene torch is used, and the ceramic is cycled into the torch and then into a stream of cold air. The ceramic is alternately heated to 2400° F and cooled to about 500° F. In the heating portion of the cycle, the temperature of the ceramic surface reaches 2000° F in about 20 seconds and 2400° F in another 10 seconds. Cooling air is directed onto the metal backing so that the backing temperature is about 1100° F. The hot portion of each cycle lasts about $3\frac{1}{2}$ min-

utes. The thermal gradients in this test are more severe than those imposed by the engine.

Figure VIII-12 shows a graded layer specimen after 1000 thermal cycles. The shroud segment is in excellent condition; needless to say, a metal shroud that had been at 2400° F would be in very poor condition. Similar results were obtained with the strain isolator pad specimen, shown in figure VIII-13 after 600 cycles. There is no delamination cracking of the bond between the ceramic and the porous metal substrate.

The effect of high cooling flow requirements on engine core flow is illustrated in figure VIII-14. The cooling flow requirement of a conventional shroud, which must be held to about 1800° F, can be as high as 3 percent of the engine core flow; this is a significant penalty. In contrast, a ceramic shroud can be operated at a higher temperature and requires less cooling. The immediate goal is 2400° F, and for this shroud temperature, the cooling flow requirement is only $\frac{1}{2}$ percent of the engine flow. The difference in cooling flow requirements in this typical illustration is $2\frac{1}{2}$ percent, which translates into a specific fuel consumption decrease of about 1 percent. For this reason alone, the ceramic shroud concepts are very attractive.

Another aspect of durability is erosion resistance to particles in the hot gas stream; generally these particles have an impingement angle of about 15°, as illustrated in figure VIII-15. One inherent advantage of ceramics as compared with metals is that the erosion resistance at low impingement angles, like 15°, is generally good. At high impingement angles, ceramics are generally less erosion resistant than metals. Fortunately the impingement angles are small.

The test setup used in work performed under NASA contract by Pratt & Whitney to measure erosion is shown in figure VIII-16. The specimens are positioned at the end of a combustor nozzle at an angle that approximates the impingement angle in an engine. The surface temperature is brought up to 2400° F, and then hard particles are introduced at a controlled rate. Some results are shown in figure VIII-17. The zirconium oxide was held at 2400° F; the metallic system was held at 2000° F. The erosion rate of the metal was significantly higher.

The problem of lack of abradability is being investigated, and one approach is shown in figure VIII-18. Abradability is obtained by bonding abrasive grits to the turbine tips. The turbine then acts as a grinding wheel. At this time, only preliminary results have been obtained. A second approach is to make the ceramic layer more abradable by introducing porosity. Some methods of doing this are currently being evaluated under NASA contract by Detroit Diesel Allison Division of General Motors Corporation. Figure VIII-19 shows a porous ceramic specimen

that has been rather cleanly cut by turbine blades without significant wear to the blades.

In summary, gas-path sealing becomes more critical as engine pressures and temperatures increase. A particularly critical sealing location is the high-pressure-turbine blade tip. Here the ceramic shroud offers a solution to the problems of high cooling airflow requirements, low durability, and lack of abradability in advanced engines, where the potential reduction in specific fuel consumption is a very significant 2 to 4 percent.

Rotor Dynamics

One of the keys to achieving better fuel economy is to make the seal clearance small. The minimum seal clearance is limited by the vibration amplitude of the rotor; that is, clearance has to be greater than the dynamic motion of the rotor or it will rub. The art and science of controlling rotor vibrations is called rotor dynamics.

There are three principal goals in rotor dynamics. The first is to minimize vibration amplitudes. The second is to minimize vibratory forces on the rotor support bearings. Obviously achieving this will increase bearing life. The best rotor support system for low amplitude is not always the best one for low bearing forces, so the design has to be a compromise. The third goal is to reduce stresses due to vibration in the rotor and support structure.

Rotor dynamics must be considered more and more in designing and operating rotating machinery because of two principal factors: first, engine and airframe structures are lighter and more flexible, and second, machines are being operated at high speeds, so that the power per pound increases. The effect of these two factors is that rotors are now running above one or more bending critical speeds. A bending critical speed is a resonance where a significant part of the motion that occurs is bending of the rotor itself, as opposed to deflection of the bearings or other static structures. Figure VIII-20 illustrates a bending critical speed.

When the rotor speed is higher than a bending critical speed, the rotor is operating supercritically. Supercritical operation is more difficult than subcritical. The problem occurs not in running supercritically, but in passing through the critical speed because the rotor is not balanced perfectly; that is, the mass axis, or center of gravity axis, does not coincide with the axis of rotation. Because the rotor is not balanced perfectly, there is a rotating force applied to the rotor, and at resonant speeds, the vibration amplitude can be quite large.

Certain things can be done to make supercritical operation feasible. First, the rotor can be balanced very accurately to reduce the exciting force. Second, the rotor can be accelerated through the critical speed rapidly so that the amplitude does not have time to build up. Third, the rotor supports can be modified to keep the amplitudes and bearing forces tolerable even with an imperfectly balanced rotor. This modification entails designing appropriate stiffness and damping in the supports between the bearing and the engine case (fig. VIII-1). Actually both accurate balancing and properly designed supports are needed; research is being carried out in both areas. The acceleration rate often cannot be chosen, so that option usually is not available.

High-Speed, Multiplane Balancing

Under NASA contract, Mechanical Technology, Inc., has been working on applying the influence coefficient method of high-speed, multiplane balancing. Most recently the research has included the use of a laser to do the actual balancing. Figure VIII-21 shows a laser beam firing at a test rotor being balanced. A computer controls the laser and gives it the right number of pulses to remove the proper amount of material. With the laser, the rotor can be balanced while spinning; it does not have to be stopped as when grinding or drilling is used.

Typical results of the experimental laser balancing are shown in figure VIII-22. Successive corrections were made to reduce the rotor vibration amplitude. More than one run is needed because the calculated required number of laser shots was based on a trial of only a few pulses. When a large number of pulses were fired, the amount of metal removed per pulse decreased.

In this work, a fairly small laser was used. It puts out a pulse every 2 seconds, and each pulse takes off about 2 milligrams of rotor material. The next phase of this work will involve larger scale rotors and a more powerful laser.

High-speed, multiplane balancing has also been applied to the power turbine of the T55 engine, shown in figure VIII-23. It looks substantial, but an analysis shows a good deal of bending at the critical speeds. As shown in figure VIII-24, there is not as much bending at the first critical, 12 000 rpm, as at the second, 21 000 rpm. A rotor response analysis showed that at the normal operating speed, 16 000 rpm, the rotor mode shape is that of the second critical speed. So even though normal operation is at 5000 rpm below the second critical speed, bending still occurs and causes trouble. In the laboratory experiments, high-speed balancing did a good job of smoothing out this rotor; even a rotor that was previously low-speed balanced was a lot quieter. A high-speed balancing rig is presently being in-

stalled at the Army's overhaul depot at Corpus Christi. The rig can accommodate power turbine rotors of the T55 engine and also the smaller T53 engine.

Although the T55 rotor is rather thick and rigid, rotors in some of the new engines are much more flexible. A current-technology turboshaft engine rotor is shown in figure VIII-25. This rotor is about 3 feet long. It has to run through two bending critical speeds on the way up to its normal operating speed. The manufacturer balances this rotor by using traditional methods, but high-speed balancing may be advantageous, particularly if it is coupled with a laser in an automated procedure.

There are several areas in which computer-controlled laser balancing might be applied. It can be most easily used for component balancing, as an automated replacement of present methods. The real potential, though, may be in high-speed balancing of complete rotor assemblies. The best balancing would be done on an assembled engine because the balance would not be disturbed by disassembly and reassembly. Most present engines are not designed for this procedure. It will have to be planned for when the engine is designed. Access to the balancing areas will be needed as well as enough sacrifical material that can be removed by the laser. If force or displacement sensors were placed in the engine permanently, rotors could be rebalanced even with the engines still installed on the airplane. This balancing would provide smoother running engines; there would be fewer unscheduled removals for high vibration, and engines could be expected to run longer between overhauls.

Elastomer Dampers

One means of allowing supercritical operation is to properly tailor the stiffness and damping properties of the rotor support. Getting stiffness is quite easy with mechanical springs, so most of the research effort has been on dampers. Some of the functions of bearing support dampers are (1) to absorb vibrational energy, and in so doing reduce vibration amplitudes and bearing forces; (2) to allow an engine to shut down safely if it loses a blade; and (3) to allow less accurate balancing, because dampers lower vibration amplitudes and bearing forces.

There are three basic types of dampers used in rotating machinery. The first, the dry-friction or Coulomb damper, is not really suitable for high-speed machinery.

The second, the hydrodynamic or squeeze-film damper, has been applied very successfully in many different applications. Many turbine engines would hardly run without them. Two principal disadvantages are that an external oil supply is needed and that

the damping coefficient increases very sharply for large damper motions.

The third, the elastomer damper, largely eliminates these disadvantages. It is self-contained and, for the range of amplitude usually designed for, does not exhibit the stiffening effect of the squeeze-film damper. Of course, it has some disadvantages of its own, but for some applications, it can perform very well. For the past 7 years, a technology effort has been carried out by Mechanical Technology, Inc., under NASA contract, to study the properties of damping materials from an engineer's point of view rather than a physicist's or a chemist's. At first, measurements were made from simple shear specimens on a shaker. Then the basic properties were used in designing a damper for a rotor support system. The damper design, shown in figure VIII-26, is extremely simple and versatile. In a typical application, the rotor turns in a ball bearing whose outer race is pressed into the inner damper housing. Between the inner and outer damper housing, three or more buttons of elastomer material are placed.

This damper was evaluated on a rig simulating a power turbine rotor. The rotor was balanced very carefully and then run with varying known unbalance to evaluate damper performance. As a final test, the elastomer buttons were removed from the damper and replaced with steel blocks. The change in rotor behavior was quite dramatic. Figure VIII-27 shows a plot of rotor vibration amplitude over a range of speed. With the elastomer support, there were no amplitude peaks in the operating speed range, though when discrete unbalances were used, a critical speed was noted at about 10 000 rpm. On rigid supports, the critical speed shifted up to about 19 000 rpm, and the amplitude increased to almost 10 mils. So the elastomer support was extremely effective in reducing vibration amplitude.

In another comparison, both a squeeze-film damper and an elastomer damper were designed for a long drive shaft that was intended to run supercritically. The two dampers were run successively with identical shaft balance. Figure VIII-28 shows a plot of vibration amplitude as a function of speed. The squeeze-film damper was more effective in limiting rotor amplitude at the first critical speed, but the elastomer damper was more effective at the second critical. So, overall, the elastomer and squeeze-film dampers performed comparably.

As discussed in this section, elastomer dampers have several advantages: they are self-contained; the design can be very simple; dimensional tolerances are not as critical as in other dampers; and the stiffness and damping do not increase rapidly as the amplitude increases. Elastomer dampers have limitations too: many rubbers have to be kept away from any oil; elastomer properties can change with age; and elastomers are sometimes

severely affected by temperature change (this effect can be crucial, since the vibration energy absorbed by the damper is converted to heat, which raises the damper temperature). For some applications, though, an elastomer damper is the best kind.

HELICOPTER TRANSMISSIONS

A transmission is nothing more than an assembly of bearings, gears, shafts, and seals which transfers power mechanically, usually from a high speed to a low speed. In a helicopter, it transfers power from the engine to the main rotor and to the tail rotor drive. The goals of transmission research are to increase life and reliability; reduce maintenance intervals; reduce weight, noise, and vibration; and increase efficiency and allowable operating temperature. In the area of gearing, new gear steels are being tested, and new methods of predicting gear reliability are being developed which will result in more reliable gears with longer lives. Also being investigated are improved gear designs which will increase gear life and reliability and also reduce noise and vibration. High-speed photography is being used to study ways of more effectively lubricating gears for more efficient operation and better cooling.

Improvements in one area are expected to benefit that area and others as well. For instance, reductions in impact loading of gear teeth through improved design methods will increase gear life and at the same time reduce noise and vibration.

Transmission Tests

Helicopter transmission tests are currently being conducted at Lewis by using the test rig shown in figure VIII-29. The figure shows a view from the control room, looking through the observation window into the test cell. The helicopter transmission is mounted in the test stand.

The general method used is to first research bearing and gear components by using analysis and experimental bench testing. When a component looks promising after this testing is done, it is put into the transmission system for further testing and evaluation.

Figure VIII-30 shows a cross section of the helicopter transmission currently being tested. This transmission consists of a high-speed input shaft with a spiral bevel gear driving the intermediate shaft by transmitting power through a planetary gear train. The planetary gear train consists of a sun gear, three planet gears, and a ring gear. The overall reduction ratio is approximately 17.5:1. This transmission contains 8 gears and 14 bearings. Note the stack of three ball bearings supporting the

input pinion shaft. This is one of the complexities designers would like to eliminate because proper load sharing in a three-tandem-bearing array is difficult. Even if the bearings are made with perfect geometric accuracy, thermal and mechanical distortions can result in one bearing carrying more than its share of the load and in premature bearing failure.

Figure VIII-31 shows the transmission retrofitted with advanced components. These components will offer improved reliability and higher power transmission capacity. Improved tapered roller bearings on the input and output shaft will be used, as will improved spiral bevel gears and high-contact-ratio gears with improved bearings for the planetary train. After these changes are made, the transmission will be tested and compared with the standard transmission.

Gear Research

Figure VIII-32 shows the spur test gears used at Lewis in the gear fatigue test rig. These gears are 3.5 inches in pitch diameter and have 28 teeth. They are run in the spur gear test rig shown in figure VIII-33. Four such rigs are used to perform long-term endurance tests. The effects of materials, lubrication, and design on gear life are being studied.

Several different types of gear failures occur, as shown in figure VIII-34. Scoring is caused by poor lubrication and high-temperature operation. Tooth fracture is caused by high tooth bending stresses and is aggravated by poor heat treatment. Fracture usually begins at the root of the tooth, but may also originate at a surface fatigue pit. Surface fatigue pitting is caused by repeated application of contact stress. The higher the contact stress, the more rapidly failure occurs.

Gear materials. - Scoring and fracture failures may be controlled by proper design, but fatigue pitting is an intrinsic problem in gear applications. Pitting is an unavoidable event that eventually ends the useful life of a gear. Figure VIII-35 shows data for test gear failures due to pitting fatigue. The failure points are plotted on Weibull coordinates, which give the cumulative percentage of failed specimens as a function of running time. The notable feature of presenting the data this way is that it emphasizes the relation between life and reliability. For instance, the life at which 10 percent of the gear specimens have failed is denoted the L-10 life. This is conceptually identical to the B-10 life for bearings. The L-10 life corresponds to 90 percent reliability; the L-50 life corresponds to 50-percent reliability. Other life numbers may be defined as the degree of reliability required changes.

In figure VIII-35, the fatigue data for two gear steels are compared. The L-10 life of CBS 1000 steel is twice that of AISI 9310 steel, which was used as a baseline material.

Figure VIII-36 shows the results from the fatigue tests of six gear steels. AISI 9310, the baseline for comparison, is assigned a relative life of 100 percent. In the tests, only pitting fatigue failures occurred in this material. The CBS 600 gears had an L-10 life 7.5 times that of the AISI 9310 gears. The failure mechanism was primarily pitting. In some cases, the cracks near the pitting failure propagated through the tooth to cause fracture. The forged M-50 material behaved similarly, with a life six times that of the baseline AISI 9310. The M-50 and CBS 1000 gear steels have good high-temperature hardness retention, which results in longer life at elevated operating temperatures.

Gear designs. - High-contact-ratio gears are being investigated, since they have potential for improving life and reliability as well as reducing dynamic loading of gear teeth. Figure VIII-37 shows test gears of high-contact-ratio and standard-ratio designs. Contact ratio is simply the average number of teeth in meshing contact. High contact ratios are ratios greater than 2, and low contact ratios are those between 1 and 2.

High-contact-ratio and standard gears were tested at the same power level to compare performance. The results are presented in figure VIII-38. Compared with standard gears, high-contact ratio gears show a 300-percent improvement in L-10 life. The improvement in fatigue life, however, is not without a price. As found in additional tests, high-contact-ratio gears are more susceptible to scoring by a 22-percent margin in allowable load. The bending endurance fracture limit is 15 percent lower because the teeth of the high-contact-ratio gear are more slender. Also these gears run hotter because of increased sliding of the longer teeth. With proper lubrication and design, though, the high-contact-ratio gear can be used to achieve longer life and more reliability.

Gear lubrication. - Research into lubrication of high-speed gears has been conducted by using high-speed photography. The lubricant in a high-speed, highly loaded gear system has two functions: to provide a lubricant film between the meshing teeth and to provide cooling of the gears. The effectiveness in performing these two functions is directly related to the depth of penetration of the jet of lubricant between the gear teeth.

Lubrication jets may be tangentially directed into the mesh exit side of the gear pair, as shown in figure VIII-39, or directed radially, as shown in figure VIII-40. High-speed photography showed that more effective penetration to the dedendum, or root region, of the tooth was achieved with the radially directed

jet. From the results of the lubrication study, an analytical model was developed. From the model, a lubricant supply system can be tailored to provide the desired penetration of the lubricant jet and thus assure good lubrication and cooling of the gear teeth.

Tapered Roller Bearings

Tapered roller bearings can support high radial and thrust loads, so they can, in theory at least, be used to replace a stack of two or three ball bearings, such as used in conventional transmissions (fig. VIII-30). This replacement would simplify mechanical design. Conventional tapered roller bearings are not designed for high-speed operation, however, so it has been necessary to upgrade both bearing design and lubrication. A tapered roller bearing designed for high-speed operation is shown in figure VIII-41.

Proper lubrication is especially important in high-speed bearing applications. Figure VIII-42 shows the experimental results obtained with two high-speed tapered roller bearing designs and three lubrication systems. Bearing temperature is plotted as a function of speed for an optimized high-speed design and a more conventional design. The test objective was to operate at high speed without exceeding temperature limits.

First the baseline design bearing was jet lubricated in the conventional manner with a flow of 3 gallons per minute. Next the flow was split so that 2 gallons per minute was jetted in and 1 gallon per minute was introduced into the cone-rib area through a series of equally spaced radial holes in the inner ring. With this change in the lubrication system, considerably higher speeds could be achieved without exceeding the temperature limits.

Further gains were achieved with the optimized high-speed bearing. This design consists of redesigned rolling elements and a new inner ring riding cage. A new lubrication scheme was also used; the lubricant flow of 3 gallons per minute was equally divided among circumferentially spaced holes, from which it lubricates the cage running surface as well as the critical heat generation zones of the rollers.

The new design makes it possible to run at shaft speeds twice as fast as with the baseline design without exceeding the operating temperature limits.

A contractor is now conducting endurance tests of tapered roller bearings at the high speeds required for advanced transmissions.

SUMMARY

Some of our program results and their potential impact on aeronautics are as follows:

(1) Finer lubricant filtration should be considered for all rotating machinery, especially where dirt ingestion, wear, and premature failures occur. The investment is modest, and the payoffs can be significant.

(2) Self-acting seals offer tremendous promise for improved seal performance and life in high-speed rotating machinery. The 4-inch-diameter seal Lewis is retrofitting into the 1500-horsepower turboshaft engine will save 32 horsepower because of reduced leakage.

(3) Successful application of abradable ceramic turbine blade tip seals would save the use of 150 to 600 million gallons of fuel per year by the Nation's commercial airline fleet.

(4) Control of rotor vibration is one of the essential elements entering into successful operation of all high-speed machines. High-speed, multiplane balancing is more effective than conventional low-speed, two-plane balancing. Supercritical operation of shafting is feasible with good balancing and proper use of dampers. Elastomer dampers can be very effective in attenuating rotor vibrational amplitudes in the regions of critical speeds.

(5) High operating cost is one of the major impediments to expanding the market for helicopters. Extended gear life can be achieved with new gear materials. High-contact-ratio gear designs may also extend life and may reduce noise. Improved gear lubrication and the use of advanced-technology tapered roller bearings will increase transmission efficiency and reliability.

REFERENCE

1. Aeronautical Propulsion. NASA SP-381, 1975.

MECHANICAL COMPONENTS AREAS OF RESEARCH

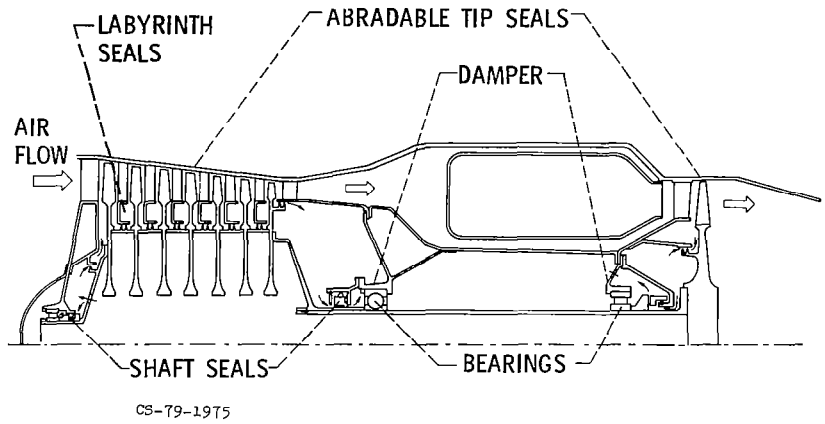

Figure VIII-1

FRACTURED INNER RING FROM BEARING

RUN AT 3 MILLION DN

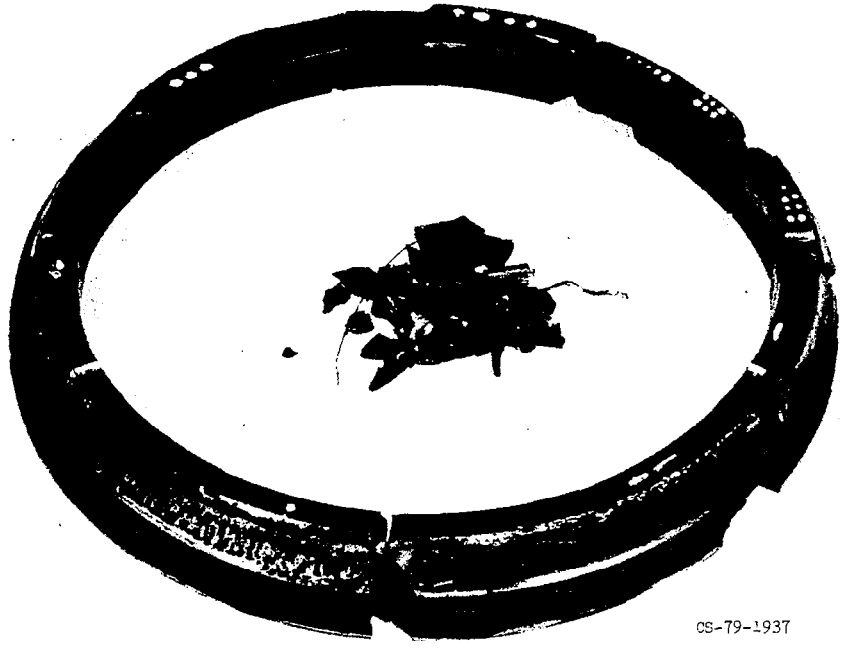

Figure VIII-2

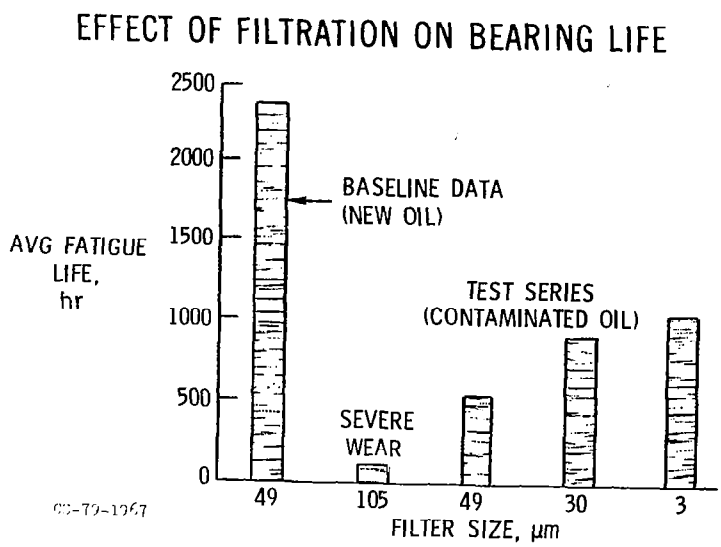

Figure VIII-3

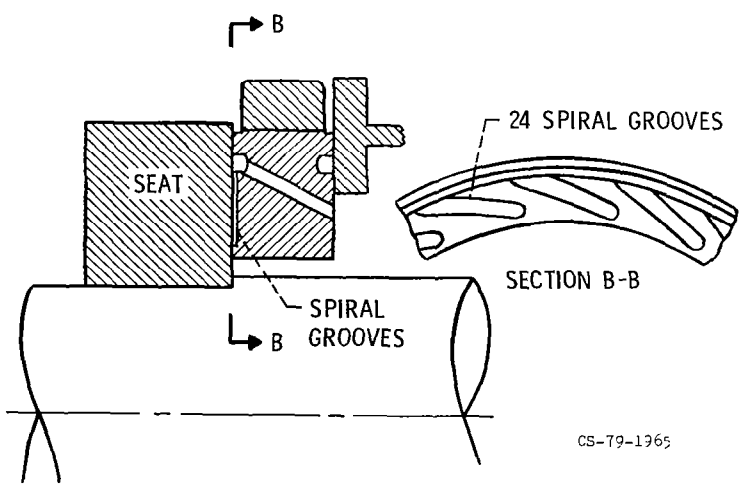

Figure VIII-4

TURBINE GAS PATH SEALING

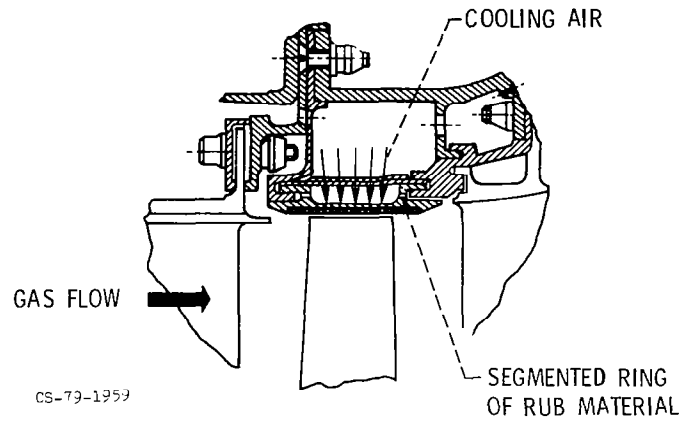

Figure VIII-5

TURBINE GAS PATH SEALING PROBLEMS

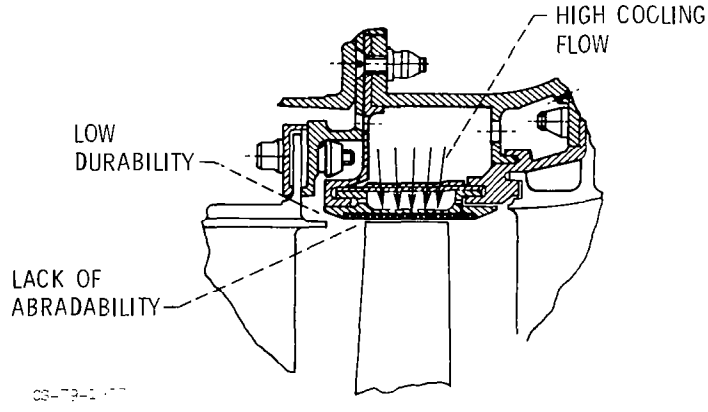

Figure VIII-6

TURBINE BLADE TIP CLEARANCE

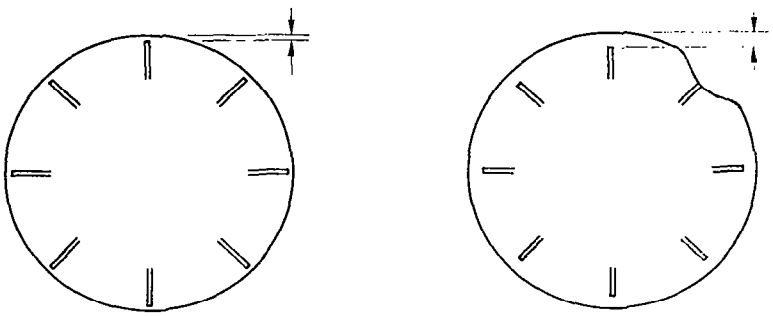

IDEAL CONCENTRIC

OUT-OF-ROUND
NONABRADABLE

Figure VIII-7

ABRADABLE TURBINE SHROUD CLEARANCE

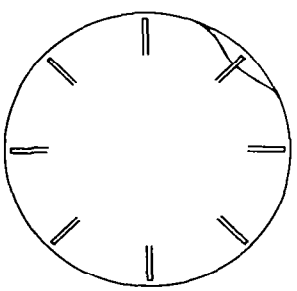

OUT-OF-ROUND ABRADABLE

Figure VIII-8

GRADED LAYER CERAMIC SHROUD

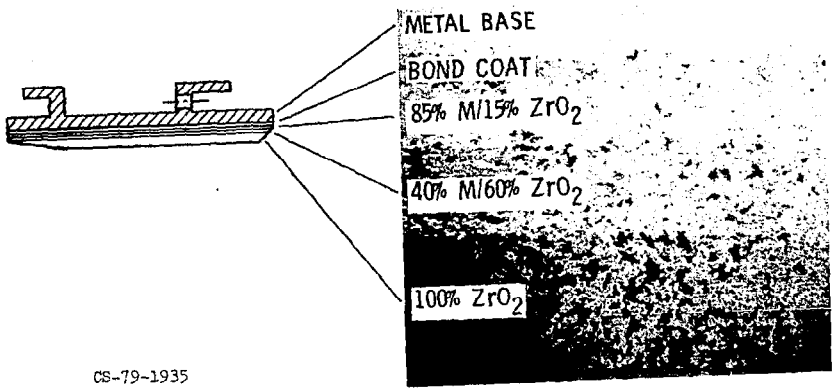

Figure VIII-9

TURBINE SHROUD
STRAIN ISOLATOR PAD CONCEPT

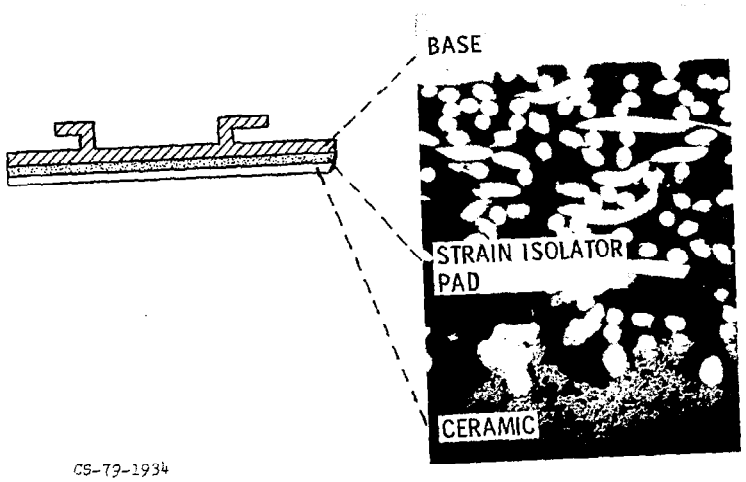

Figure VIII-10

THERMAL CYCLING TEST

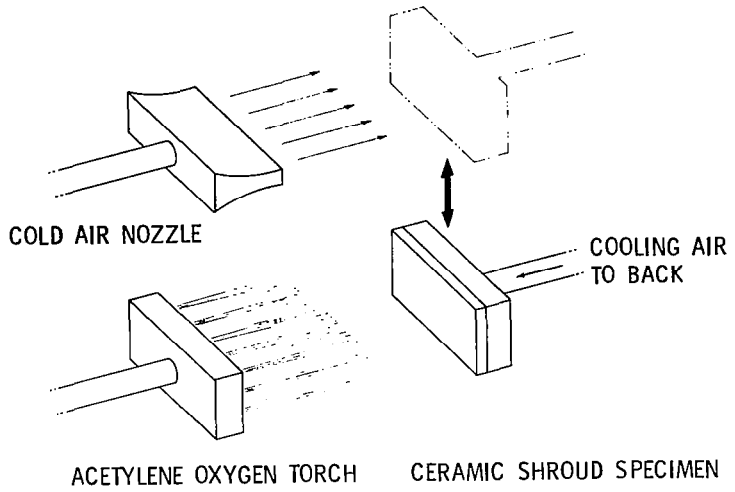

CS-79-1961

Figure VIII-11

GRADED LAYER CERAMIC SHROUD

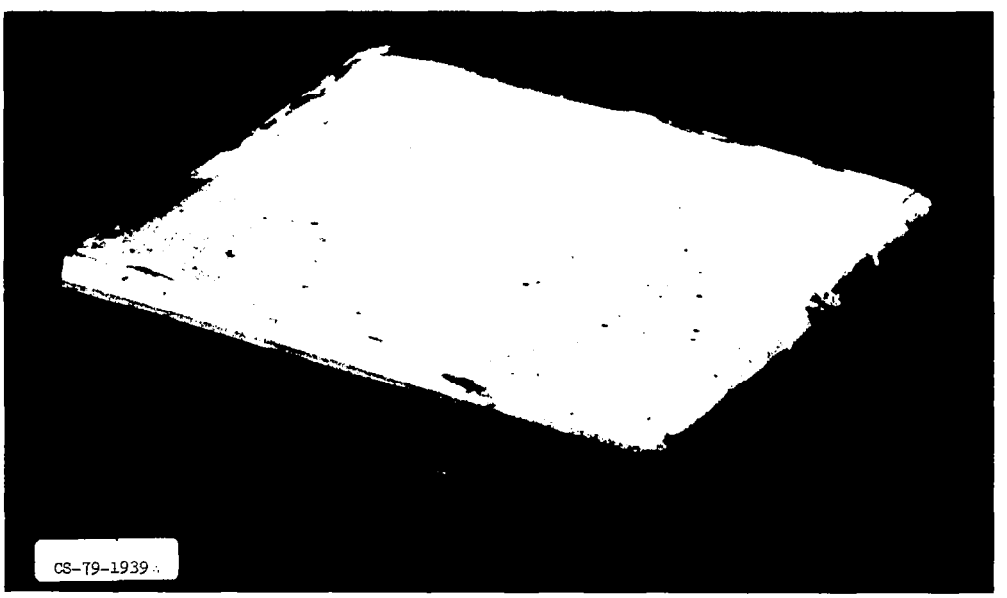

Figure VIII-12

STRAIN ISOLATOR PAD SHROUD

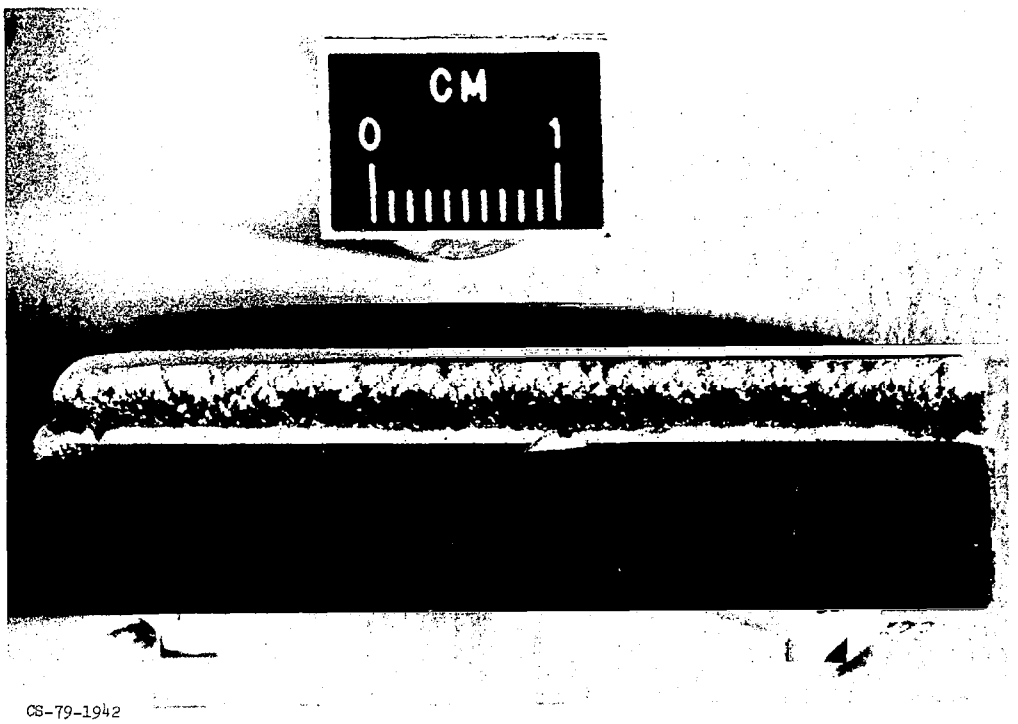

CS-79-1942

Figure VIII-13

COOLING FLOW REQUIREMENTS

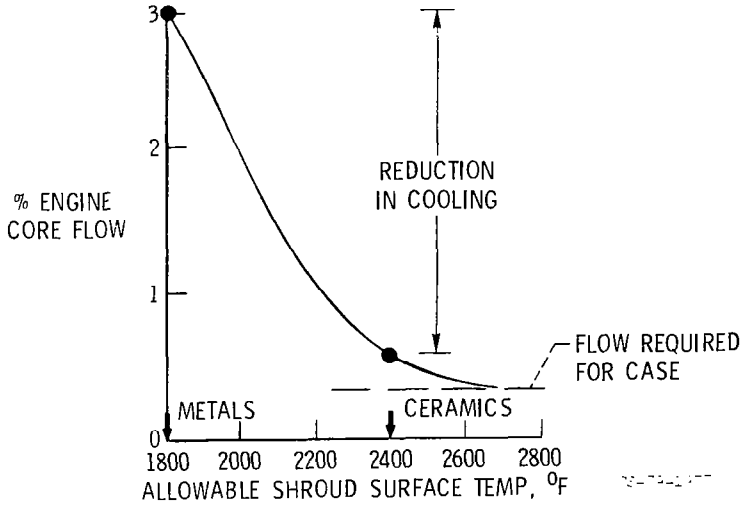

Figure VIII-14

TURBINE SHROUD EROSION

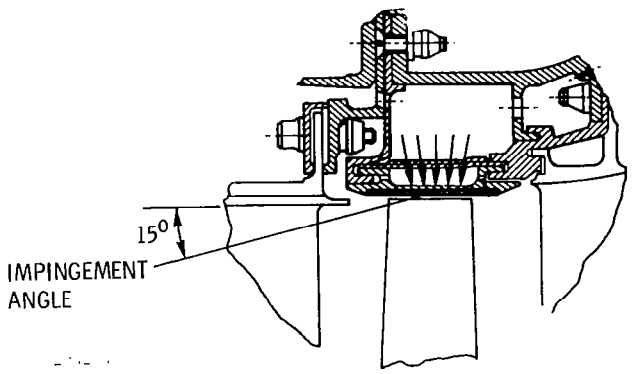

Figure VIII-15

EROSION RIG

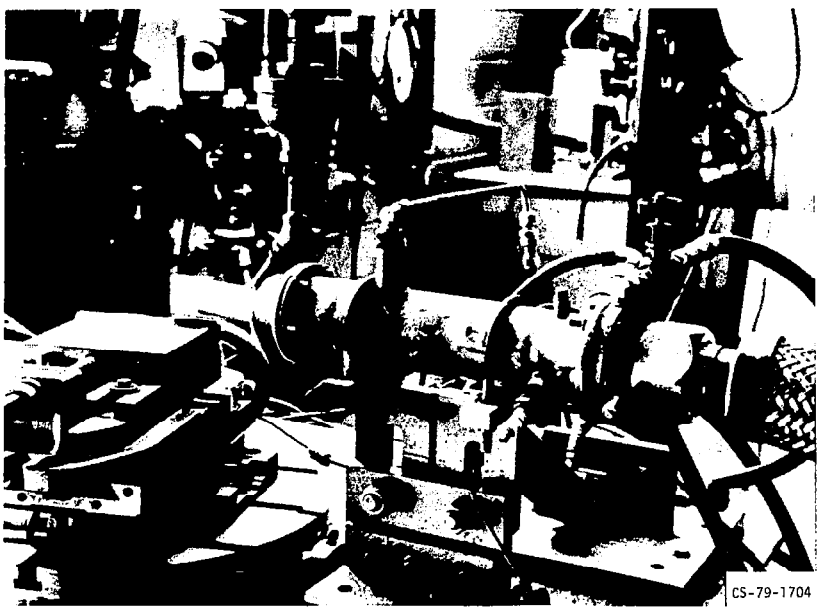

Figure VIII-16

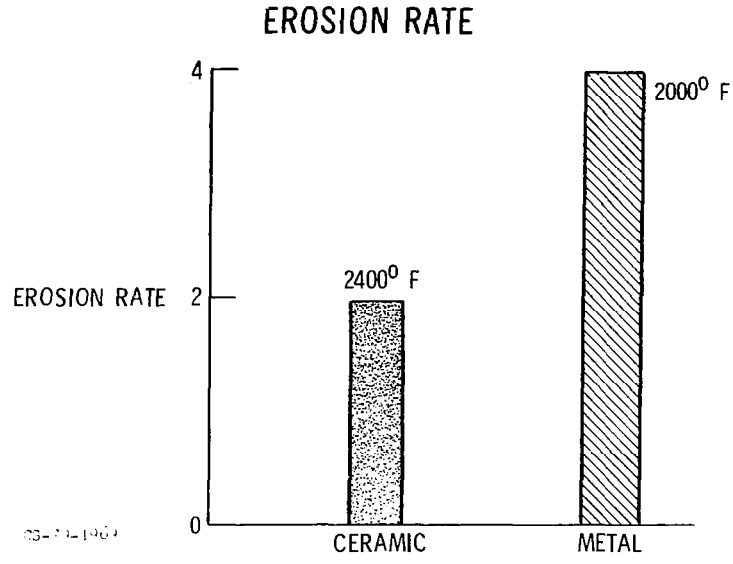

Figure VIII-17

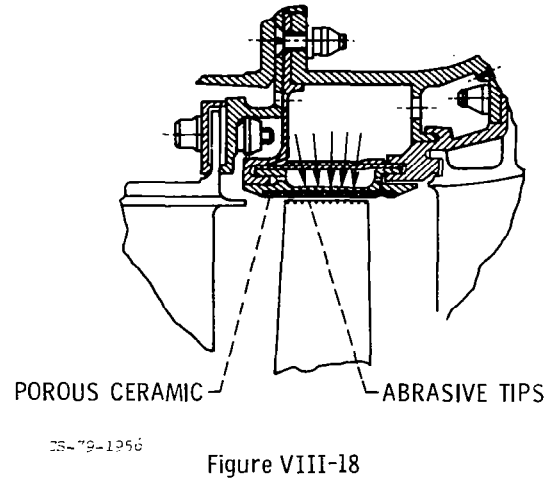

Figure VIII-18

ABRADABLE CERAMIC

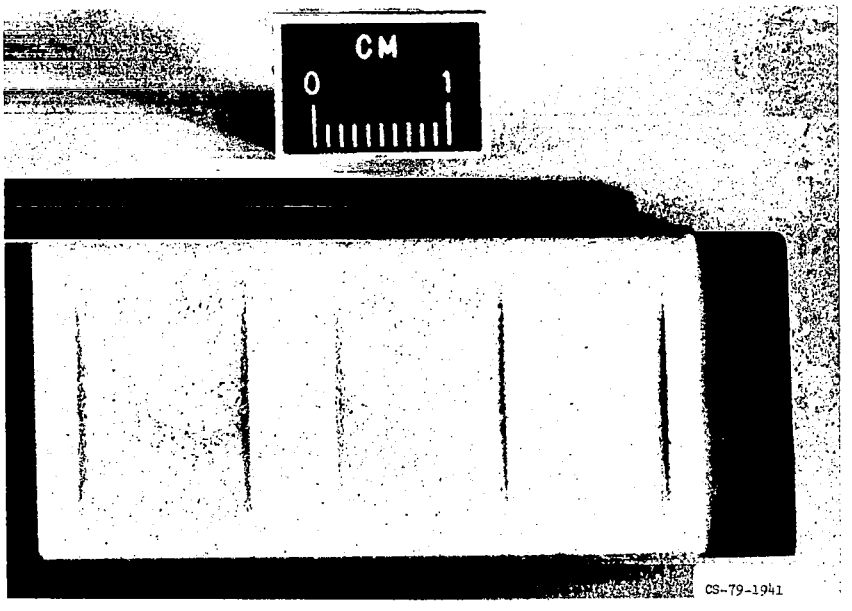

Figure VIII-19

BENDING CRITICAL SPEED

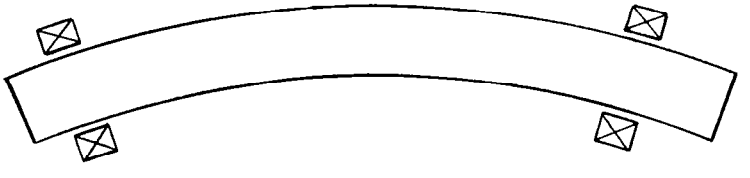

Figure VIII-20

LASER REMOVING METAL FROM TEST ROTOR

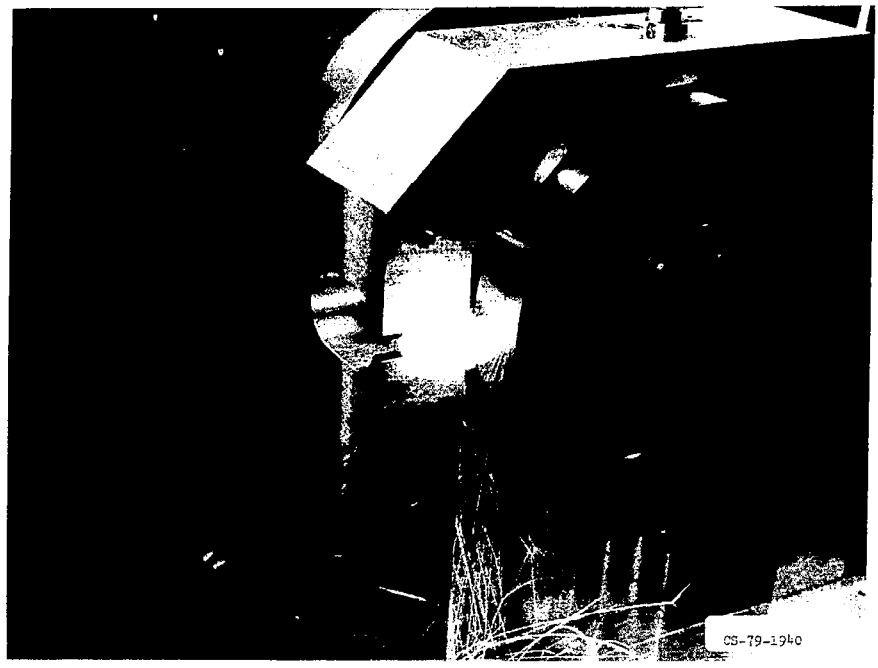

Figure VIII-21

RESPONSE OF TEST ROTOR TO LASER BALANCING

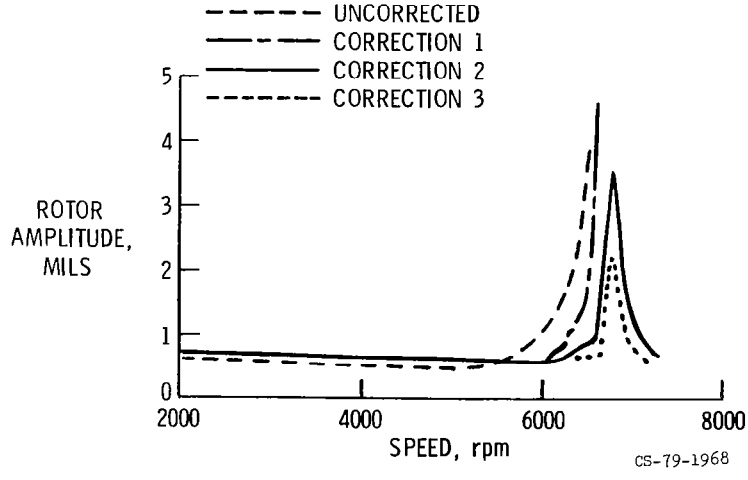

Figure VIII-22

T55 POWER TURBINE ASSEMBLY

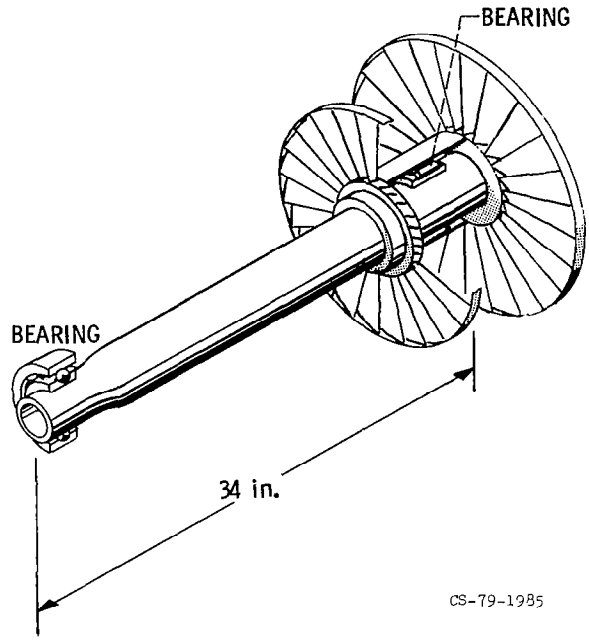

Figure VIII-23

T55 POWER TURBINE CRITICAL SPEED MODE SHAPES

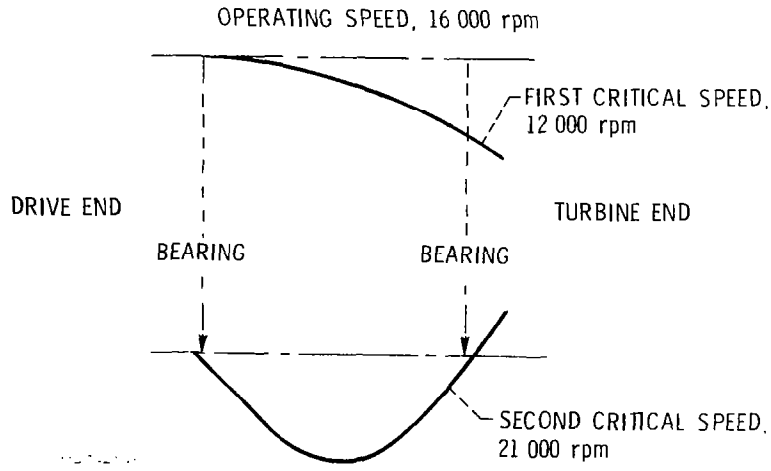

Figure VIII-24

POWER TURBINE OF CURRENT TECHNOLOGY TURBOSHAFT ENGINE

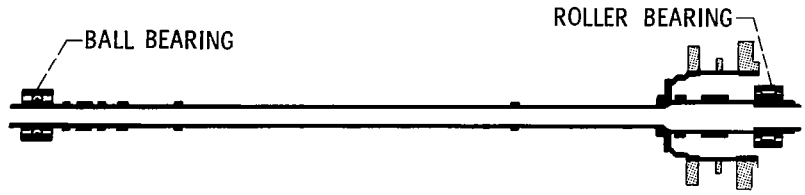

CS-79-1980

Figure VIII-25

ELASTOMERIC DAMPER

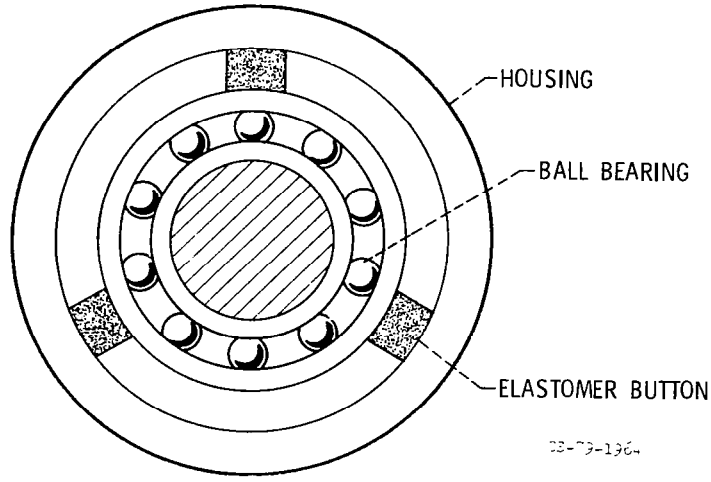

Figure VIII-26

VIBRATION AMPLITUDE WITH ELASTOMER AND RIGID SUPPORTS

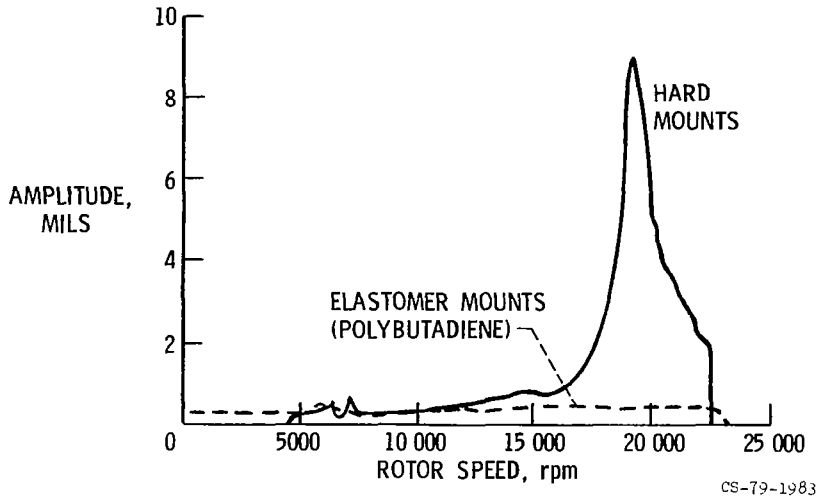

Figure VIII-27

VIBRATION AMPLITUDE OF SUPERCRITICAL DRIVE SHAFT

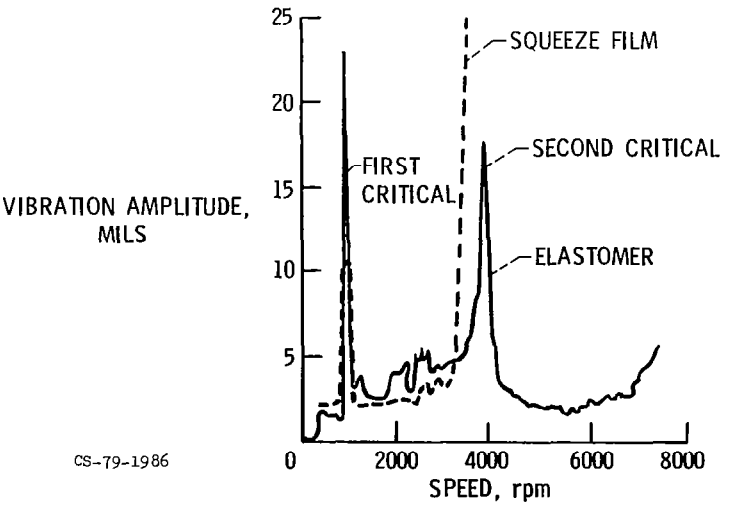

Figure VIII-28

HELICOPTER TRANSMISSION TEST RIG

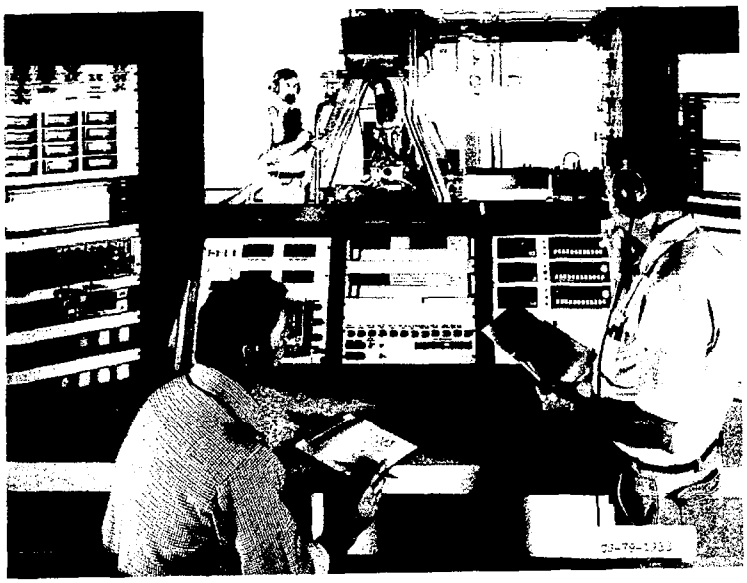

Figure VIII-29

HELICOPTER TRANSMISSION WITH STANDARD BEARINGS AND GEARS

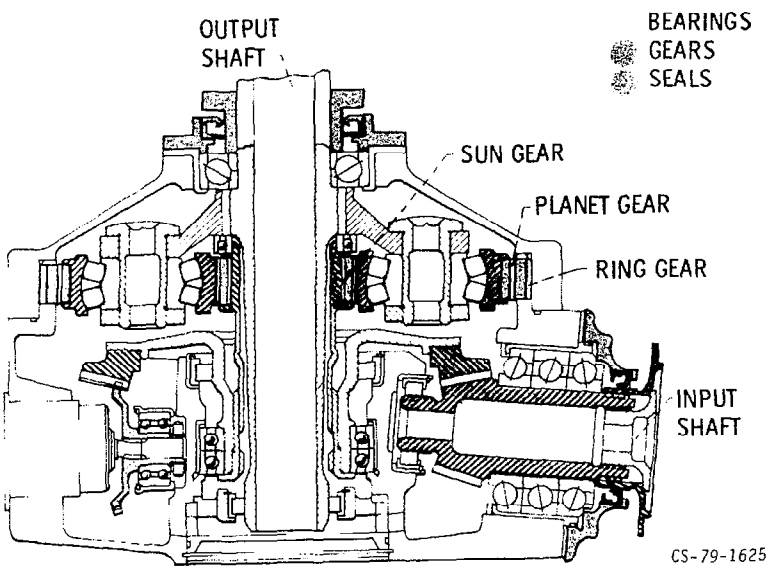

Figure VIII-30

HELICOPTER TRANSMISSION WITH ADVANCED BEARINGS AND GEARS

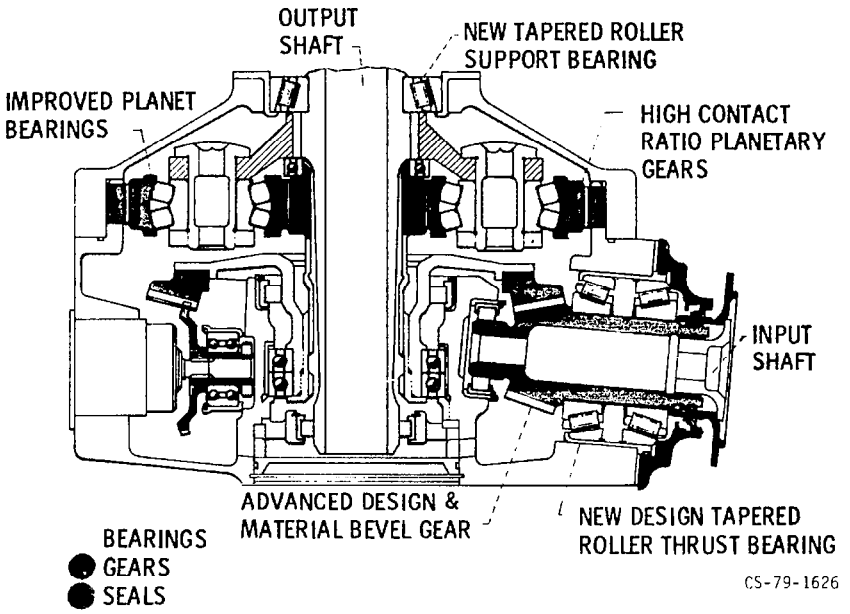

Figure VIII-31

TEST GEARS

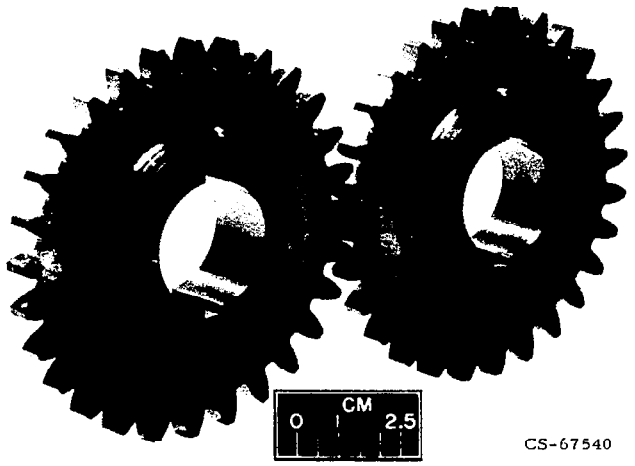

Figure VIII-32

SPUR GEAR TEST RIGS

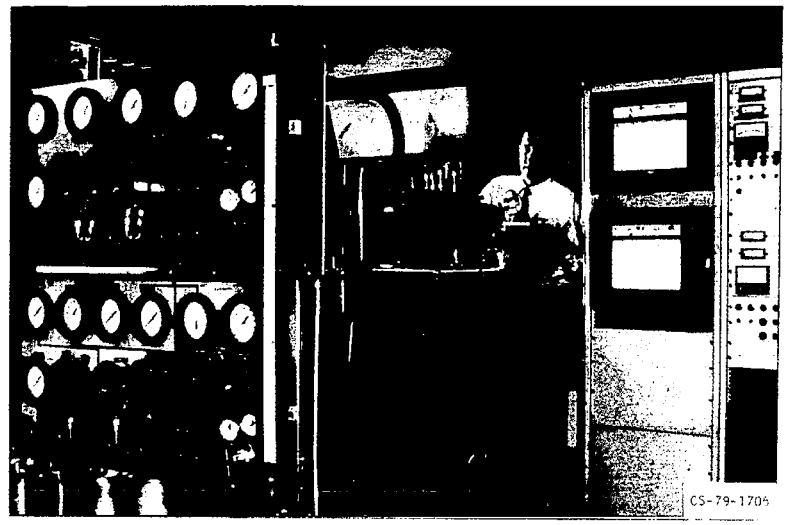

Figure VIII-33

TYPICAL GEAR TOOTH FAILURE MODES

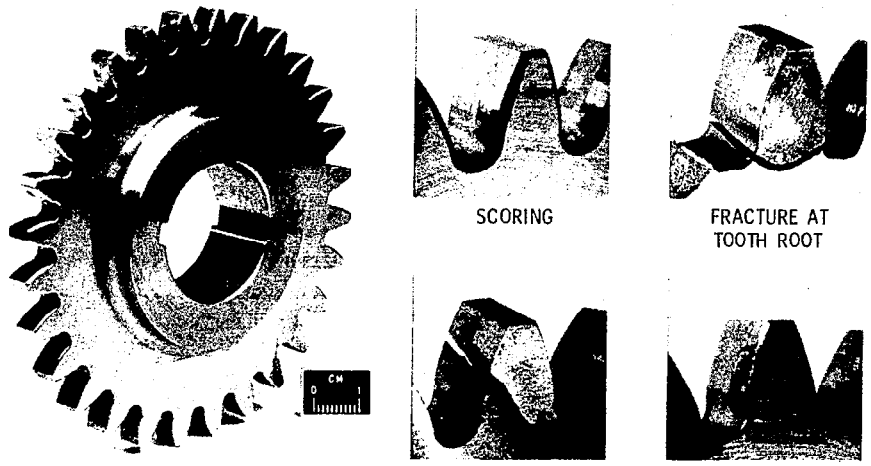

Figure VIII-34

WEIBULL PLOT - GEAR PITTING FATIGUE

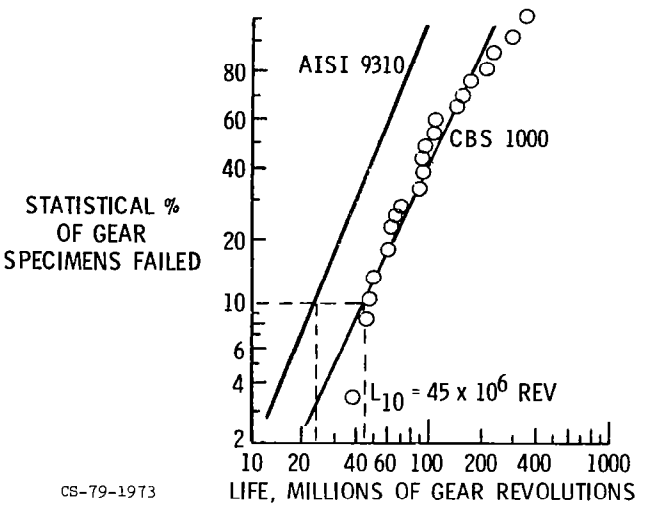

Figure VIII-35

GEAR FATIGUE TEST RESULTS

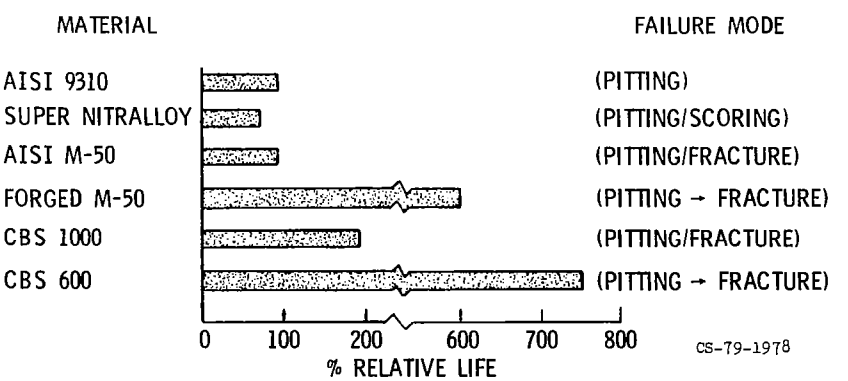

Figure VIII-36

HIGH CONTACT RATIO & STANDARD GEARS

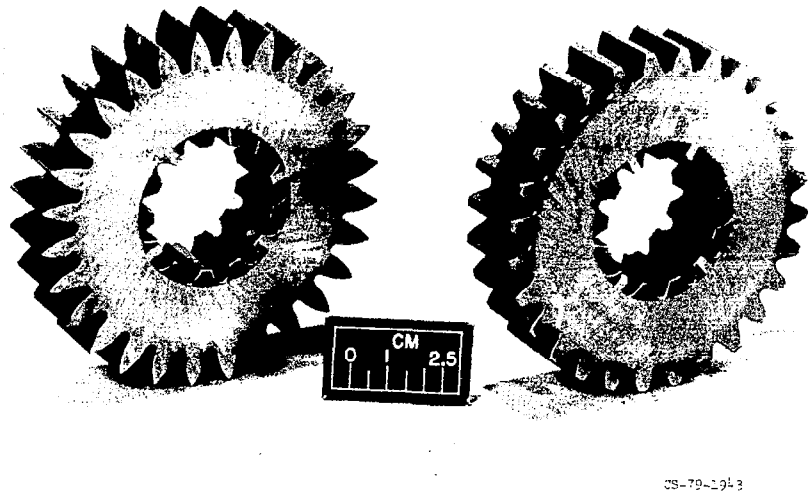

Figure VIII-37

PERFORMANCE COMPARISON
HIGH CONTACT RATIO GEARS VS STANDARD GEARS

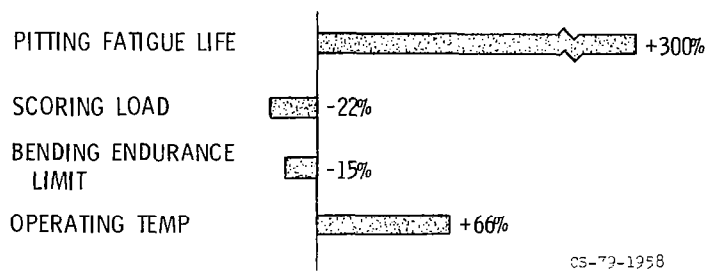

Figure VIII-38

OUT-OF-MESH JET LUBRICATION

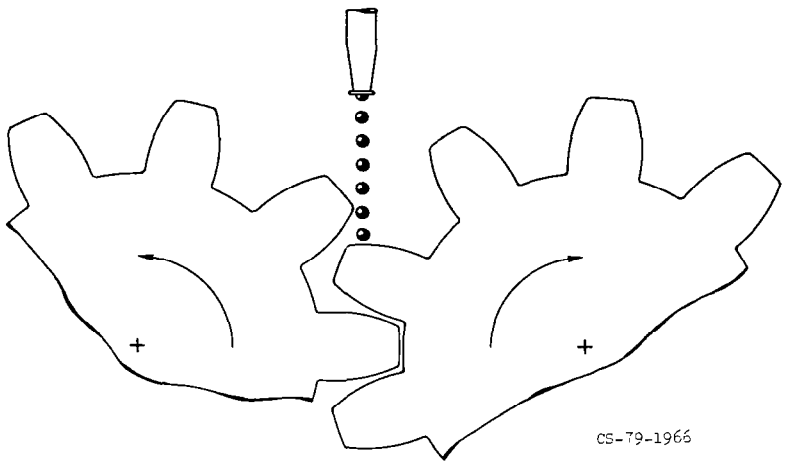

Figure VIII-39

RADIAL JET LUBRICATION

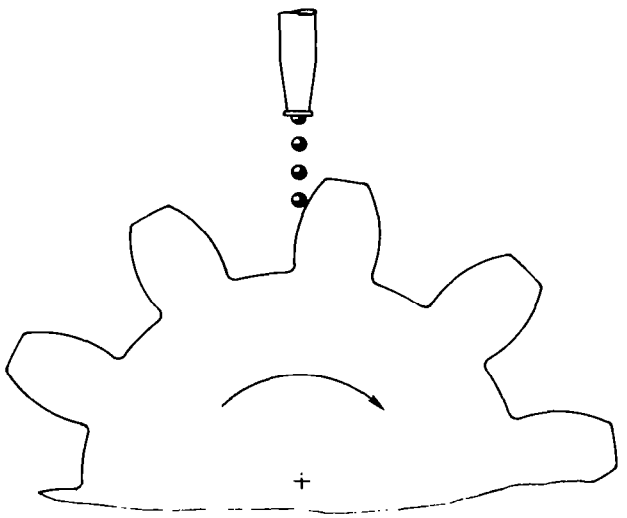

Figure VIII-40

TAPERED ROLLER BEARING

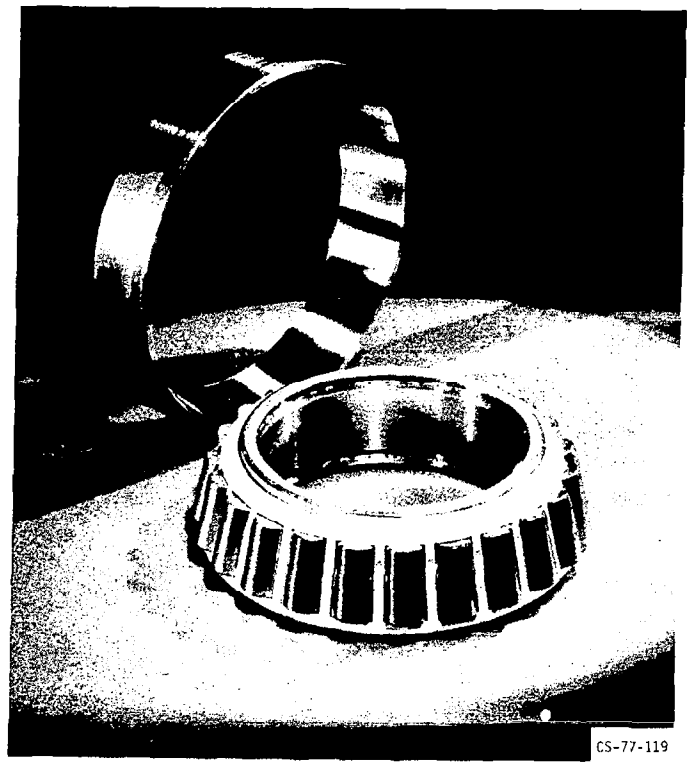

Figure VIII-41

TAPERED ROLLER BEARING TEST RESULTS

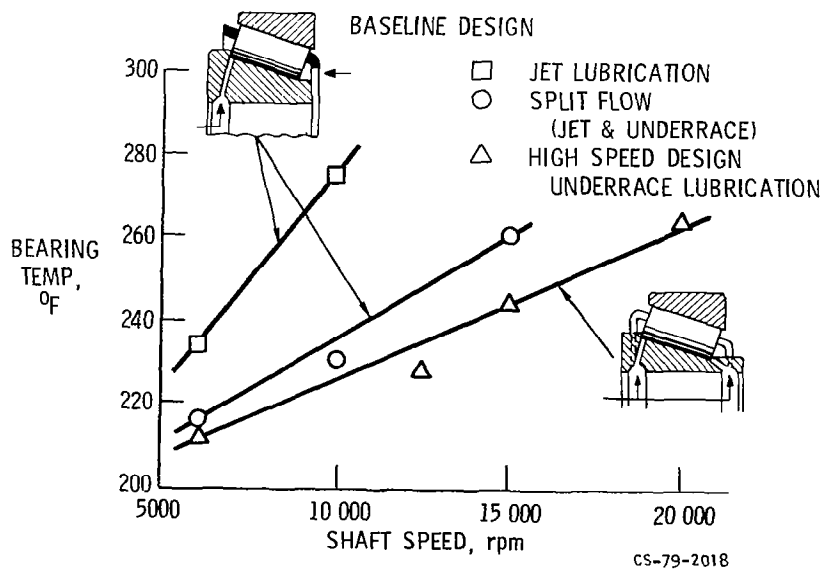

Figure VIII-42

IX. INSTRUMENTATION TECHNOLOGY

William C. Nieberding, David R. Englund, Jr.,
and George E. Glawe

National Aeronautics and Space Administration
Lewis Research Center

Current propulsion instrumentation needs are characterized by the requirement to make measurements under more severe conditions than in the past - such as at higher temperatures, on the rotating parts, in a higher vibration environment, or in very small passages. There is also a need to get more high-frequency data such as dynamic pressure, flow velocity and angle, temperature, strain, stress, and blade position. This leads to vast quantities of data. To be of any practical use, these data must be processed and reduced to humanly understandable form very rapidly. This usually means some form of on-line data processing coupled with an easily interpreted display.

Those are the problems. Fortunately, new technological advances can and are being exploited to solve these problems. Two of the most significant technological advances affecting new measurement system development are optics and microelectronics.

The field of optics with its lasers, fiber optics, and electro-optic devices makes possible noncontacting, nonintrusive, and environmentally tolerant sensors and transmission schemes. The field of microelectronics extends from the ultra-small semiconductor sensors for dynamic measurements to the data-handling power and economics of the computer, especially the small computer.

This paper describes some of the efforts made at Lewis in applying these new tools to today's measurement problems. The topics covered in this paper were selected as representative of the areas Lewis is working in. The first topic is a blade-tip clearance system. The second topic is a pulsed-thermocouple system used to measure gas temperature with a thermocouple at temperatures above the melting point of the thermocouple. The next topic is an optical technique for measuring blade flutter. This is followed by the results of work aimed at measuring unsteady pressure on rotating blades. The last two topics deal with flow measurement. The first is a probe for dynamic flow and flow angle measurement, and the second is a laser anemometer system for rapidly mapping the flow profiles between the blades of a rotating compressor.

BLADE-TIP CLEARANCE MEASUREMENT

One of the conclusions of the Aircraft Energy Efficiency (ACEE) program, described earlier in this conference publication, is that increased blade-tip clearance is one of the major contributors to performance deterioration in modern commercial aircraft engines. The importance of blade-tip clearance is also emphasized by the work described in the preceding paper on abradable rub strips to reduce the effect of blade rubs. It is important to be able to accurately measure the tip clearance of fan, compressor, and turbine blades in an operating engine.

An optical blade-tip clearance measuring system developed by Pratt & Whitney Aircraft under an NASA contract is described here. The objective of the development program and the performance goals for the system are listed in table IX-1. The range of measurement was to be from 0.005 to 0.125 inch, accuracy was to be within 0.002 inch, and resolution was to be within 0.001 inch. The probe was to be cooled so that it could operate in a turbine environment with a wall temperature as high as 1900° F.

The probe used in this system works on the light triangulation principle shown in figure IX-1. With this technique a spot of laser light is focused onto a blade tip. If the blade moves up to the dashed-line position, which indicates a reduction in tip clearance, the spot of laser light moves from point A to point B. An objective lens projects an image of the light spot onto the detector array. With the blade in the original position, the image falls at point A on the detector; with the blade in the dashed-line position, the image is at point B. The detector is a linear array of photodiodes that puts out a signal only from the diodes that are illuminated. Thus the system provides a discrete signal that indicates the blade-tip clearance.

This technique has the advantage that the output signal is not determined by the magnitude of the light falling on the detector but rather by its position. This means that a variation in the reflectance of the blade tips does not cause an error; the only requirement is that sufficient light be reflected to provide a signal.

The actual system is shown schematically in figure IX-2. The engine-mounted sensor is a cylinder less than an inch in diameter. The relatively small diameter is achieved by placing a prism in the tip of the probe. This makes the incoming laser beam and the reflected light beam more nearly parallel to the probe axis. For use at high temperatures the prism is made of sapphire, and nitrogen gas is passed through the probe for cooling. The gas exits over the face of the prism to keep it clean. Fiber optics are used to couple the probe to a remote package that contains the laser and the detector. This arrangement results in a smaller probe and a more acceptable environ-

ment for the contents of the remote package. The fiber optic bundle carrying the reflected light signal is a coherent bundle so as to preserve the relative position of the light spot. An image intensifier is inserted between the coherent fiber optic bundle and the detector array in order to provide sufficient light at the detector for measurements of individual blades. The detector has 256 photodiodes in a 1/4-inch array to provide the required resolution. The output signal from the detector is fed into a data system incorporating a small computer that correlates clearance with blade number. More detail on the design and operation of this system is available in reference 1.

The system has been delivered to Lewis and is being evaluated in the laboratory. Test results show that the performance goals have been met, including accuracy within 0.002 inch and resolution within 0.001 inch. The probe mounted in a test fixture under a compressor wheel is shown in figure IX-3.

Future plans in tip clearance measurement include the development of a multiple-probe system so that a number of optical probes can be used with a single data-handling package. Also, advanced capacitance systems are being considered with the hope of developing lower cost, flyable, tip clearance instrumentation.

PULSED THERMOCOUPLE

In selecting a thermocouple for measuring high-temperature gases, one important limiting consideration is the melting point of the thermocouple material. Also to be considered are physical and chemical changes that degrade the thermocouple and shorten its useful life when it operates continuously at high temperatures and pressures. A pulsed-thermocouple system has been designed to alleviate these problems (ref. 2).

A representative sketch of a pulsed-thermocouple probe is shown in figure IX-4. It has a simple "V"-shaped thermocouple element, which is cooled by a jet of inert gas coming out of a nozzle on the leading edge of the probe body. The curve in figure IX-4 shows the operating cycle on a temperature-time plot. The top horizontal line represents gas temperature, and the second horizontal line represents the melting point of the thermocouple material. The initial part of the curve during the cooling-on time period shows the temperature level to which the thermocouple is initially cooled by the gas jet.

When a measurement is to be taken, the cooling jet is turned off and the thermocouple begins to heat up. Before the thermocouple reaches its melting point, cooling is automatically reapplied. This heating curve is recorded by a high-speed digital system. The data are then sent to the computer, where they are curve fit and extrapolated. The extrapolated curve shows the indicated

equilibrium temperature that the thermocouple would have attained if its melting point would have allowed it to do so.

A three-element pulsed-thermocouple probe used in a recent research combustor program is shown in figure IX-5. The probe was run in a 3800° F gas stream, where the extrapolated temperature steps were each about 300 degrees F. The thermocouple element is "V"-shaped and extends from a cone-shaped nozzle, which brings the cooling jet within 1/8 inch of the junction.

Data taken from an actual computer printout are shown in figure IX-6. Here the thermocouple was initially cooled to 2240° F. When the cooling was turned off, the thermocouple temperature rose to 3200° F, as shown by the solid line (the recorded data curve). Cooling was reapplied at 3200° F. The recorded data were sent to the computer and curve fit (circular symbols on the data curve). From the data curve-fit, the computer program generated the extrapolated curve (diamond symbols) extending to 3500° F. The extrapolation involves a complex computer program for curve fitting. To estimate the accuracy of the extrapolation, we operated the system at a lower temperature.

A combustor run at a lower temperature level, where the thermocouple can go through the full heating curve without burnout, is shown in figure IX-7. The data of the full heating curve (solid line) were recorded. Then as a check on the computer program, the computer is instructed to curve fit only the first 65 percent of the temperature rise (circular symbols) and then to extrapolate the rest (diamond symbols). Since the full curve has already been recorded, this is an in-situ check of the entire system that can be made just before a series of extrapolated runs. The agreement between the final computed temperature and the measured temperature is better than 1.5 percent, which is good agreement at this level.

In conclusion, it looks as if the pulsed-thermocouple probe, which extends both the life and temperature range of thermocouples, will help make the necessary measurements in the new generation of combustors operating at high temperatures and high pressures. The idea of a pulsed-thermocouple system has been around for some time, but advances in data acquisition and microelectronics have finally made it practical. Work is continuing on this system to upgrade probe design, data acquisition, and computer software.

OPTICAL MONITORING OF BLADE FLUTTER

A previous paper in this conference publication deals with the work being done on aerodynamic instability of blades, commonly called flutter. If flutter might occur, planned or not, in a fan or compressor stage during testing, it is crucial that it be

carefully monitored.

The most common method of monitoring flutter has been to mount as many strain gages as possible on as many blades as possible. The gages are usually located at spots preselected for maximum strain. The problem with the strain-gage technique is that the available slip-ring capacity prevents the application of nearly enough gages to cover all the suspected modes on all the blades. In addition, gages did not last long in Lewis engine tests.

Although the strain-gage technique has been used at Lewis, we felt that it should be supplemented with something better. An optical blade-tip detection scheme was further developed for this purpose. It has some significant advantages. Each blade tip is sensed on every revolution. This means that a researcher does not have to be lucky enough to have a strain gage on the blade that is fluttering with maximum amplitude. The optic probes are case mounted, so they provide the dual advantage of a noncontacting measurement without any sensors on the rotor.

System operation is illustrated in figure IX-8. Shown is the compressor, or fan, whose blades are to be monitored. From the shaft a once-per-revolution synchronization pulse is picked up. One or more optical probes (two in this illustration) are mounted in the engine casing. Each probe consists of a bifurcated fiber optic bundle. Half the fibers conduct light from a source to the blade tips; the other half return light reflected from the tips to a photodetector. Both the detectors and the light source are outside the test tank.

The inset in figure IX-8 shows more detail of the probe installation. A lens focuses the incoming light onto a tiny spot on the blade tip. It also collects light reflected from this spot and directs it onto the end of the fiber bundle. Thus, a pulse of light is generated in each probe for each blade passage. In this illustration, one probe senses the trailing edge of each blade tip; the other probe senses near midchord. The photodetector signals and the once-per-revolution pulse are fed to an electronics box that uses television-like techniques to generate a display on an oscilloscope. Two oscilloscope displays - one during no flutter, the other during flutter - are shown in figure IX-9.

The idea is to measure the time of arrival of the blade at the probe location relative to the once-per-revolution pulse. The display consists of one horizontal line for each blade, much like a television raster. On each line is a brightened spot whose horizontal position is proportional to the arrival time of that blade at the probe. If the blade is not fluttering, the spot stays still. If the blade is fluttering, the spot moves back and forth by a distance proportional to the tip motion

caused by the flutter. By using various combinations of the probe signals and the once-per-revolution signal, the system can be set up to monitor a selected flutter mode of the blades, such as torsion or bending.

The displays depicted in figure IX-9 were taken during monitoring of an F-100 fan for the first torsion mode of flutter. It is obvious from this display that all the blades must be monitored because some blades flutter a lot more than others. At any one time during this particular test, the blade showing maximum flutter on this display exhibited an amplitude five times that of the blade showing maximum flutter based on strain-gage signals.

This system is now used for all Lewis engine testing whenever flutter is a possibility. In some tests we have even been able to detect stalls and rubs from the display characteristics.

UNSTEADY PRESSURE ON ROTATING BLADES

Previous papers in this conference publication have presented discussions on fan noise and blade flutter. Both these problems have generated great interest in measuring the unsteady pressure on the surfaces of the rotating blades. Fluctuating pressure (and therefore lift) is a source of both noise and flutter (vibration). A recently completed contract effort with Pratt & Whitney Aircraft to develop improved techniques for measuring unsteady pressure on rotating compressor blades is described here.

The objectives of the program were to design configurations for mounting pressure transducers on the blades and then to identify and quantify the sources of measurement error. The mounting configurations included surface mounting of a subminiature, flat pressure transducer and more complex mountings that required a recess or hole in the blade but resulted in less disturbance of the aerodynamic shape of the blade.

Figure IX-10 shows examples of two of these mountings on JT15D fan blades that will be tested here at Lewis as part of the forward velocity effects program that is described in paper III, NOISE REDUCTION. Surface-mounted transducers are shown on the second and fourth blades, counting from left to right. The diaphragm of the surface-mounted transducer appears as a white dot near the left end of the mounted assembly. Epoxy-coated lead wires are routed along the blade surface. The white material surrounding the transducer is silicone rubber, which is used to fair the installation to the blade surface. Soft rubber is used for this rather than epoxy in order to isolate the transducer from local strain in the blade. The total thickness of this mounting is about 0.015 inch and this, of course, represents a

disturbance of the aerodynamic surface at the point of measurement. A second configuration is shown on the first and third blades. In this case the transducer is mounted with its diaphragm facing the blade and centered over a 0.06-inch-diameter hole, which acts as a pressure tap. This means that the point of measurement is on the opposite surface of the blade. The installation is about 0.018 inch thick on the transducer side of the blade, but there is no disturbance on the side of the blade from which the measurement is made, except for the pressure tap. More detailed information on these mountings and the pressure transducers is available in references 3 and 4.

The environmental conditions specified for this work included up to 90 000 g's centripetal acceleration. This is the acceleration expected on the blade of a 20-inch-diameter compressor operating at 18 000 rpm. The temperature was limited to 300° F, which is the maximum operating temperature of the diffused silicon pressure transducer. Finally, because the interest in this work originated with aeroelastic flutter, in which there is considerable blade vibration, dynamic strain up to ±1000 microstrain was included as part of the environment. The transducers and mountings survived in the environment, and measurement errors for a typical application are estimated to be ±6 percent of reading due to sensitivity changes and ±0.02 psi due to vibration and dynamic strain. The 0.02 psi is a signal that is induced in the transducer and that cannot be differentiated from the pressure signal. This signal determines the minimum unsteady pressure signal that can be measured. The 6-percent sensitivity error is a combination of a sensitivity change due to the rotating environment and uncertainty in calibrating the mounted transducers. Periodic recalibration after mounting is advisable; appreciable calibration shifts were encountered in mounting and testing these transducers.

One further conclusion from this work is that, for most applications, it is probably not feasible to measure steady-state pressure with blade-mounted transducers of the configurations used in this work. Zero shifts of up to 2 psi were measured under conditions that were aimed at minimizing zero drift. It is expected that normal test conditions would lead to totally unacceptable zero drift errors.

Further detail on this work is available from references 3 and 4.

DRAG FORCE ANEMOMETER

Over the past few years, there have been more and more requests for instrumentation to make dynamic measurements in turbomachines. Two parameters of particular interest are the dynamic flow angle and the dynamic flow rate, which is related to dynam-

ic velocity head. A device to make such measurements has been developed. It is called a drag force anemometer (ref. 5).

The operation of the device is depicted in figure IX-11. The measuring element is a cantilevered beam exposed to the flow. The drag force due to the flow over the beam generates a bending moment that is measured with strain gages at the base of the beam. The equation in figure IX-11 shows that the drag force is the product of the drag coefficient, the exposed area, and the velocity head. The drag coefficient varies with flow angle, as shown in this plot. For flow angles from about 60° to 90°, the drag coefficient is constant. This means that when the beam is approximately perpendicular to the flow (as shown in the sketch), the anemometer signal is only a function of velocity head. Conversely, when the flow angle is below 40°, the drag coefficient is proportional to flow angle. Thus, when the beam is approximately parallel to the flow, the anemometer can be used to measure flow angle.

A number of drag force anemometers have been built with both silicon and steel beams. A probe that has a silicon beam purchased from a semiconductor transducer manufacturer is depicted in figure IX-12. The beam is mounted on a pedestal inside the hollow tip of the probe so as to protect the strain gages. The beam is 10 mils thick and the exposed part of the beam is 60 mils on a side. The probe support is 1/4 inch in diameter.

The advantages of the silicon beam are its small size and its high-frequency response. The natural frequency of the silicon beam is 40 kilohertz; this gives a flat frequency response to about 8 kilohertz. The disadvantages of the silicon beam are its susceptibility to breakage by particles entrained in the flow and its relatively poor zero stability. Steel beams with conventional metal-foil strain gages minimize these problems, but the frequency response is roughly half that of silicon.

Different designs of the drag force anemometer have been used in a variety of applications. Fluctuating flow was measured downstream of the F-100 fan during flutter testing. By using the anemometer signals, along with other measurements, it is possible to identify flutter frequencies and rotating nodal patterns. A number of anemometer probes were also used in a compressor dynamics experiment. One of these was a high-sensitivity beam to measure inlet flow at a velocity as low as 100 feet per second. Other measurements included dynamic flow angles downstream of a turbine and turbulence intensity.

In summary, it appears that the drag force anemometer is a very versatile addition to the group of instruments used for dynamic flow measurements. The output of the anemometer is linear with velocity head up to a Mach number of 0.6. The device can measure transient flow even with flow reversals. It can measure dy-

namic flow angle over a range of $\pm 40^{o}$ and, finally, it has high-frequency response.

LASER ANEMOMETER

The laser anemometer (sometimes called the laser Doppler velocimeter) is used extensively in mapping flow velocity fields. In engine and engine component testing, it used to be enough to obtain the velocity map upstream and downstream of the stage. Mathematical models were then used to get the map within the stage. This is no longer good enough. Real data are needed between the blades to verify the models. The laser anemometer has recently been applied to the acquisition of the velocity map within the rotating stage, that is, between the blades. Lewis has developed a system that obtains these data rapidly and efficiently.

A previous paper in this conference publication gives some of the results obtained with this system. The major optical components of the system are shown in figure IX-13. It works in the following way. The laser beam is split into two beams that, by means of a lens, are caused to intersect at a location within the compressor blade row. This location is called the probe volume. Within this tiny volume the two beams interfere to produce a series of parallel planes that are alternately bright and dark. These planes are perpendicular to the plane of the figure. Tiny seed particles, a micrometer or less in diameter, are intentionally injected into the flow upstream of the stage. Laser light is scattered from any of these particles that happen to pass through the probe volume. Some of this scattered light is collected by the receiving optics and focused on the photomultiplier tube. As the particle traverses the series of light and dark planes, the scattered light flashes on and off. The frequency of this flashing is proportional to the particle velocity component perpendicular to the planes. Thus, for each particle that happens to pass through the probe volume, a burst of signal comes from the photomultiplier with a frequency proportional to this velocity component. Since it is really airflow that is being measured, the particles must be small to follow the flow.

The hardware in the Lewis instrument test facility is shown in figure IX-14. The two beams cross to define the probe volume within the blade row. Recall that the data are obtained from this tiny probe volume, which is essentially a point in space. As the stage rotates, data can be obtained from all the points on a circumferential line as they pass through the probe volume. To get at other circumferential lines, stepper motors, as shown in the figure, are used to reposition the whole optics package and hence the probe volume. Thus, the whole stage can be mapped.

A simplified block diagram of the system is shown in figure IX-15. Shown is the rotor with its blades and a once-per-revolution pickup for synchronization. Each time a particle passes through the probe volume, a burst of signal comes from the photomultiplier. The laser anemometer processor converts the signal burst into a digital number proportional to velocity. This number is fed to the minicomputer.

The trick is to tell the computer where, on the circumferential segment, this velocity number was obtained. To solve this problem, we invented an electronic device that we call an electronic shaft-angle encoder. It always has at its output a digital number that is proportional to the shaft angular position relative to the once-per-revolution pulse. In other words, it gives the position on the circumference at any time. Each time a velocity event occurs, as signaled by the processor box, both the velocity and the angle are fed into the computer. These velocity-angle data pairs are stored, sorted, and processed by the computer.

A key component is a CRT terminal, which presents graphics data to the experimenter in practically real time. From it he can tell whether the data are any good and what he should do next.

The equipment in the control room is shown in figure IX-16. Shown are the minicomputer, the laser anemometer signal processor, the electronic shaft-angle encoder, and the operator working at the graphics CRT terminal. The optics system installed in the compressor facility is shown in figure IX-17. The laser beam travels through the optics and enters a specially contoured window in the compressor housing.

The primary contribution to the state of the art with this system is rapid data acquisition. Data are accepted over a whole circumferential segment at whatever time they arrive. Previously reported systems gated the electronics to accept the data from only one point at a time until enough velocity events were recorded for good statistics. This system, as currently operating, accepts the data from 1000 different locations at rates from 5000 to 150 000 points per minute. Thus, it is orders of magnitude faster. This, coupled with the graphics to guide decisionmaking, cuts running time significantly.

CONCLUDING REMARKS

This paper has illustrated the application of optic and microelectronic technology to propulsion instrumentation. Other topics as well as other technology fields, could have been covered. The point to be made is that the solution to measurement problems depends heavily on drawing from a wide variety of technologies.

REFERENCES

1. Ford, M. J.; et al.: Advanced Optical Blade Tip Clearance Measuring System. (PWA FR-10200A, Pratt & Whitney Aircraft Group; NASA Contract NAS3-20479.) NASA CR-159402, 1978.

2. Glawe, George E.; Will, Herbert A.; and Krause, Lloyd N.: A New Approach to the Pulsed Thermocouple for High Gas Temperature Measurements. NASA TM X-71883, 1976.

3. Grant, H. P.; and Lanati, G. A.: Instrumentation for Measuring the Dynamic Pressure on Rotating Compressor Blades. (PWA 5558-12, Pratt & Whitney Aircraft Group; NASA Contract NAS3-20296.) NASA CR-159466, 1978.

4. Englund, D. R.; Grant, H. P.; and Lanati, G. A.: Measuring Unsteady Pressure on Rotating Compressor Blades. NASA TM-79159, 1979.

5. Krause, Lloyd N.; and Fralick, Gustave C.: Miniature Drag Force Anemometer. NASA TM X-3507, 1977.

BLADE TIP CLEARANCE

OBJECTIVE

DEVELOP LASER PROBE SYSTEM TO MEASURE INDIVIDUAL BLADE TIP CLEARANCE

PERFORMANCE

RANGE OF MEASUREMENT	5 TO 125 MILS
ACCURACY	2 MILS
RESOLUTION	1 MIL
TEMP	UP TO 1900° F

CS-79-1553

Table IX-1

OPTICAL TIP CLEARANCE PROBE

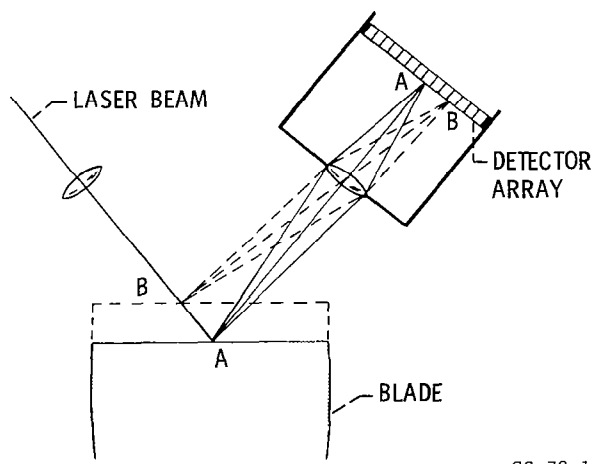

CS-79-1552

Figure IX-1

OPTICAL TIP CLEARANCE SYSTEM

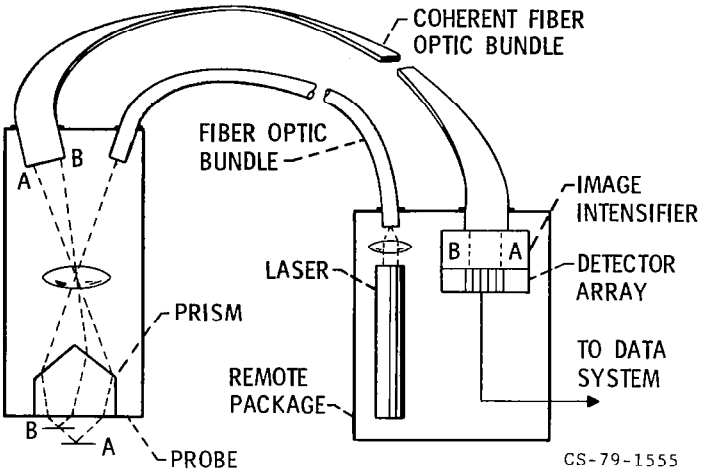

Figure IX-2

BLADE-TIP-CLEARANCE PROBE MOUNTED IN TEST FIXTURE

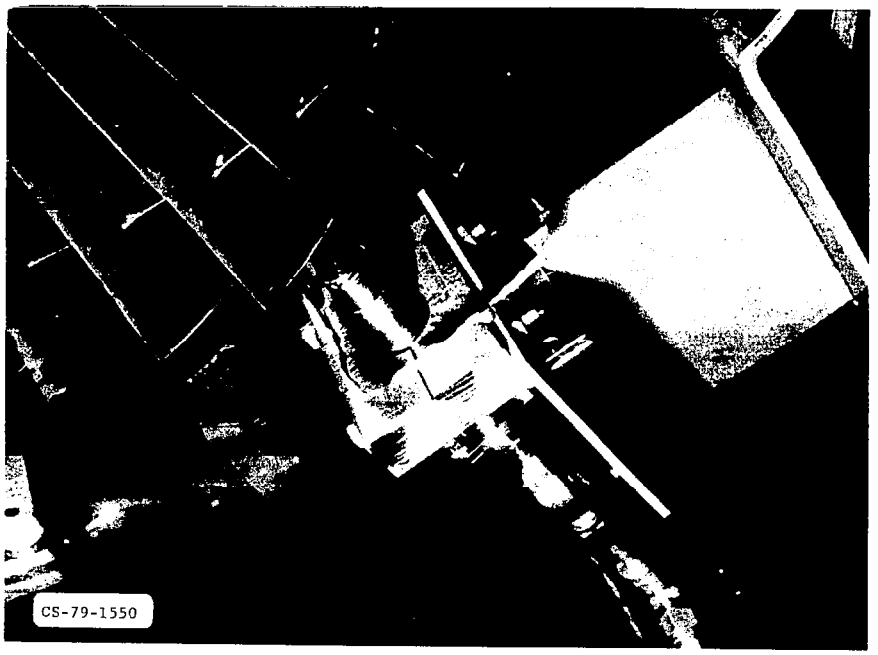

Figure IX-3

PULSED-THERMOCOUPLE SYSTEM

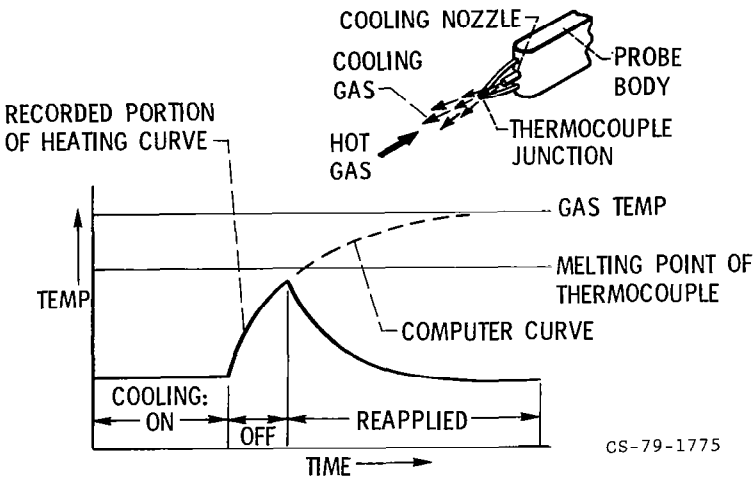

Figure IX-4

THREE-ELEMENT PULSED THERMOCOUPLE PROBE

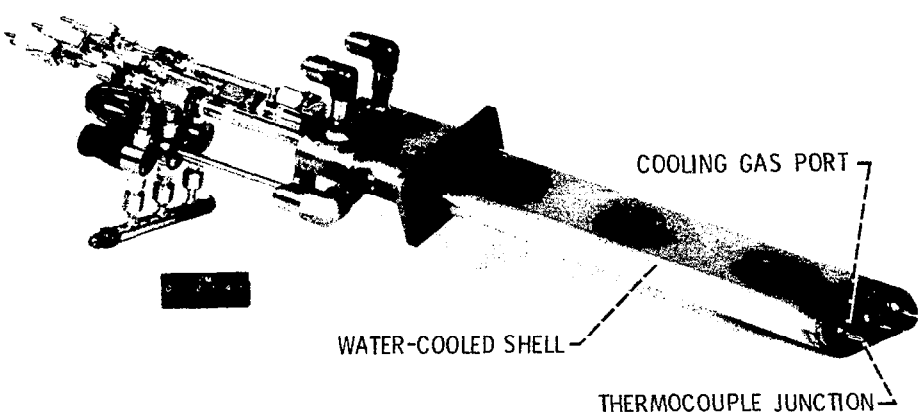

Figure IX-5

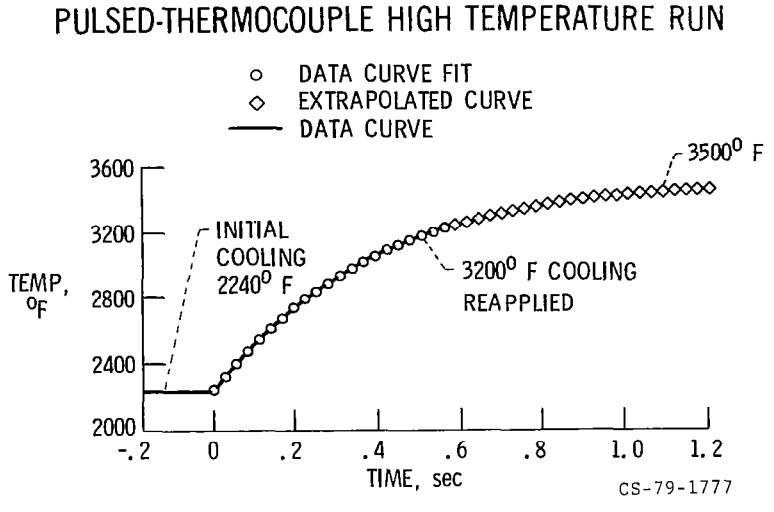

Figure IX-6

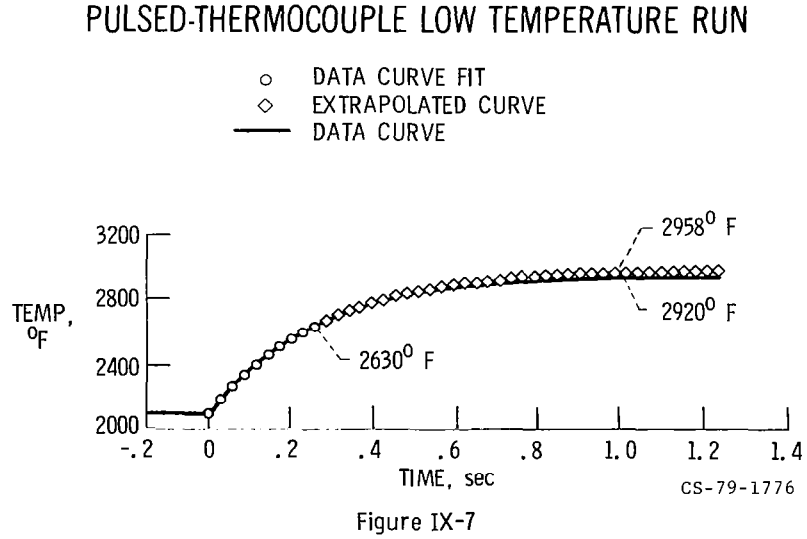

Figure IX-7

OPTICAL DETECTION OF BLADE VIBRATION AMPLITUDE

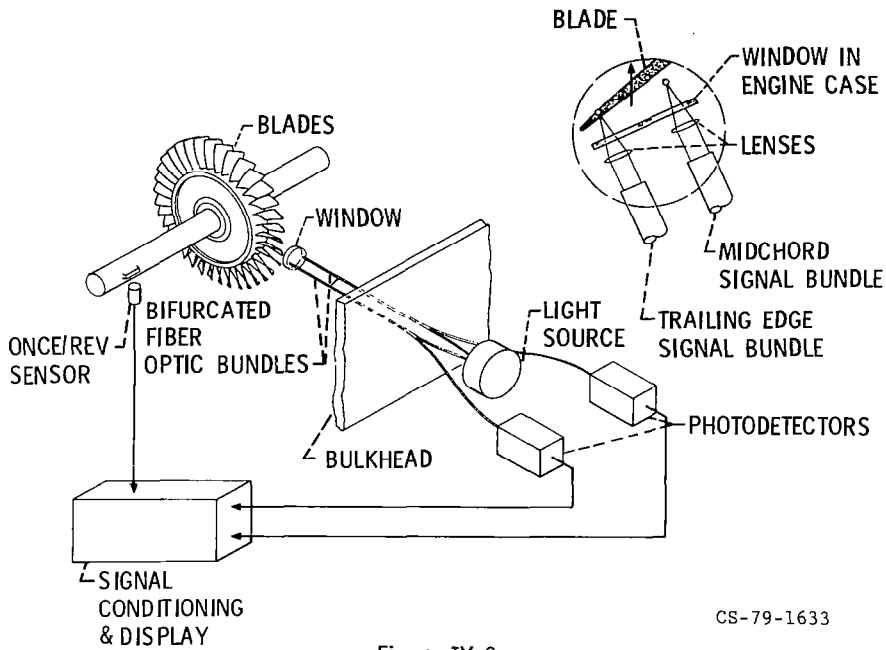

Figure IX-8

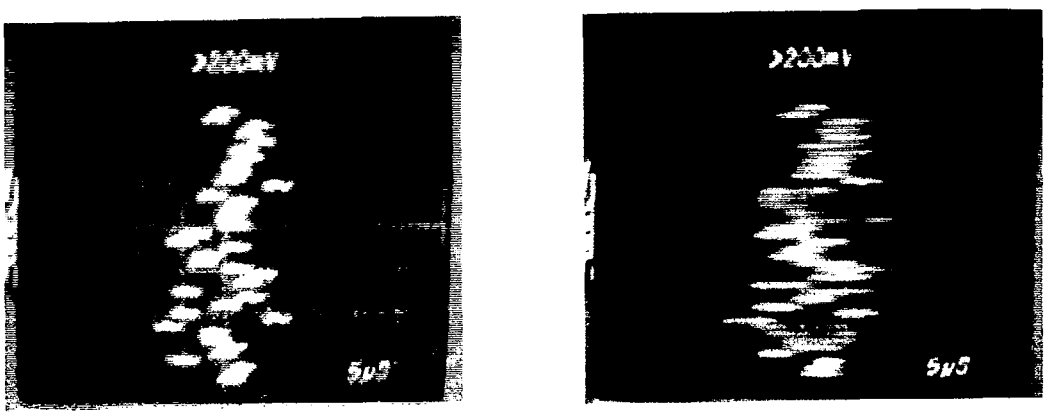

DISPLAY DURING QUIET RUNNING CONDITION

DISPLAY DURING FLUTTER

CS-79-1634

Figure IX-9

PRESSURE TRANSDUCERS MOUNTED ON JT15D FAN BLADES

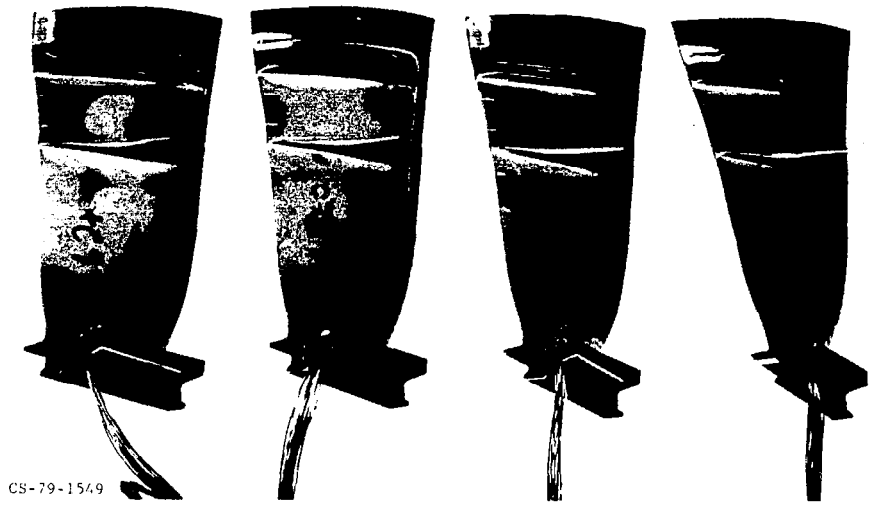

Figure IX-10

DRAG FORCE ANEMOMETER

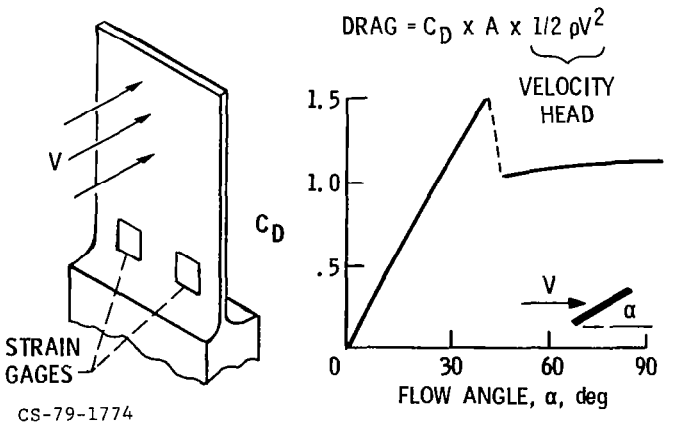

Figure IX-11

DRAG FORCE ANEMOMETER PROBE

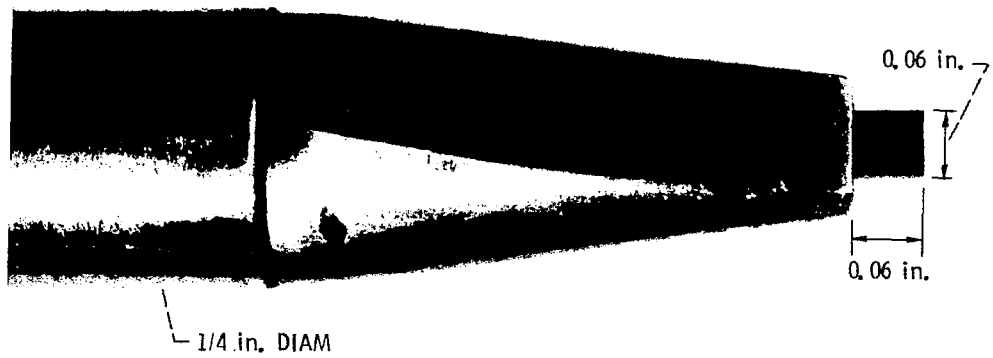

CS-79-1778

Figure IX-12

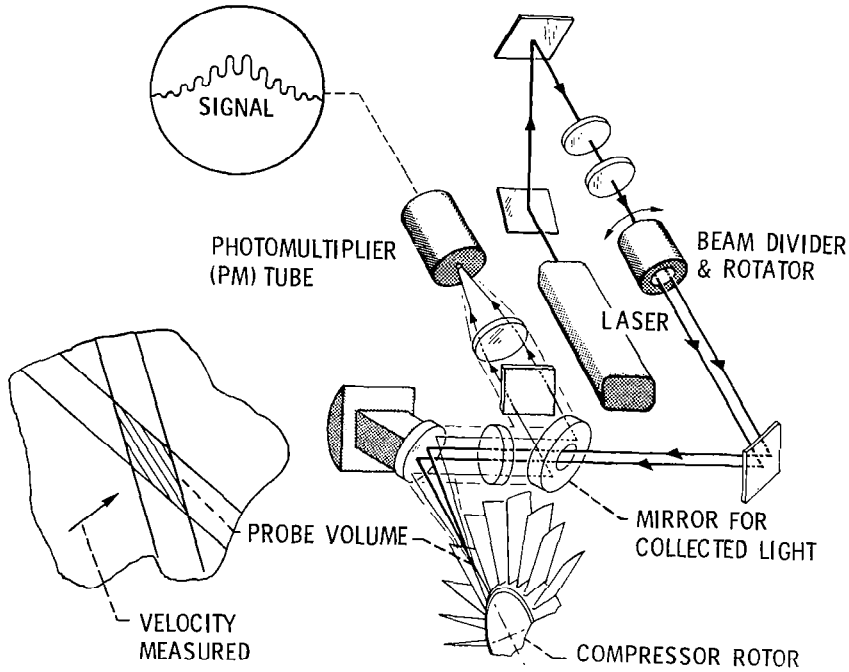

CS-79-1632

Figure IX-13

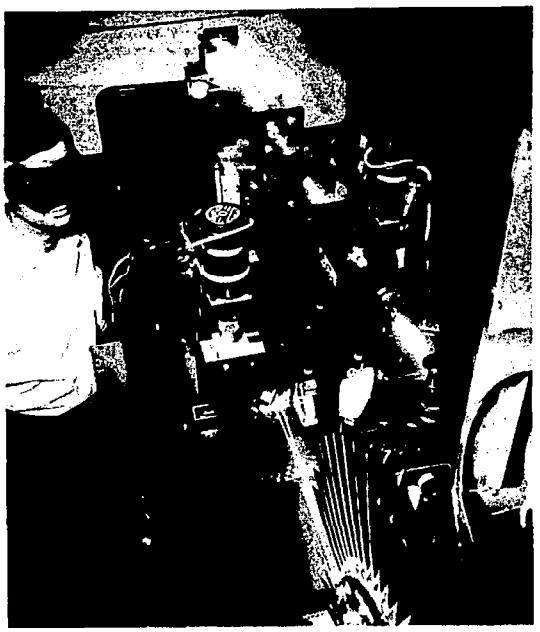

Figure IX-14

CS-79-1610

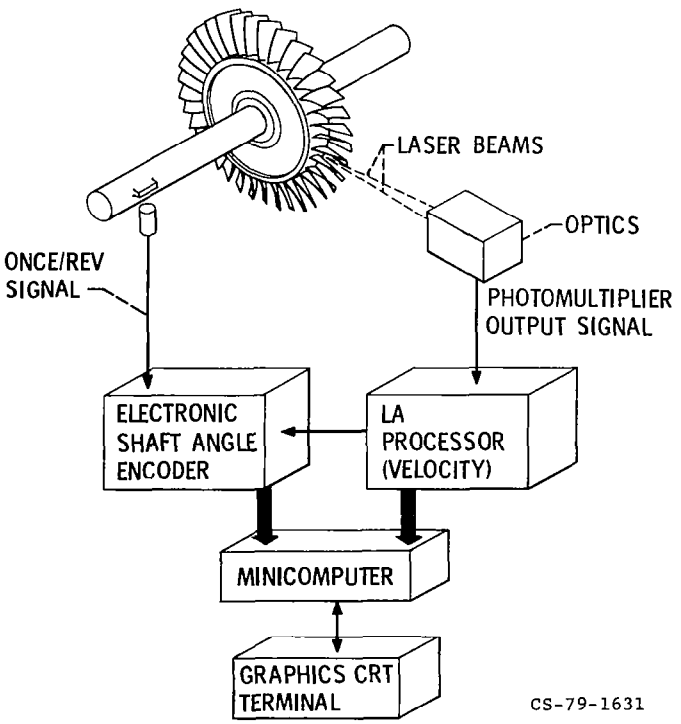

CS-79-1631

Figure IX-15

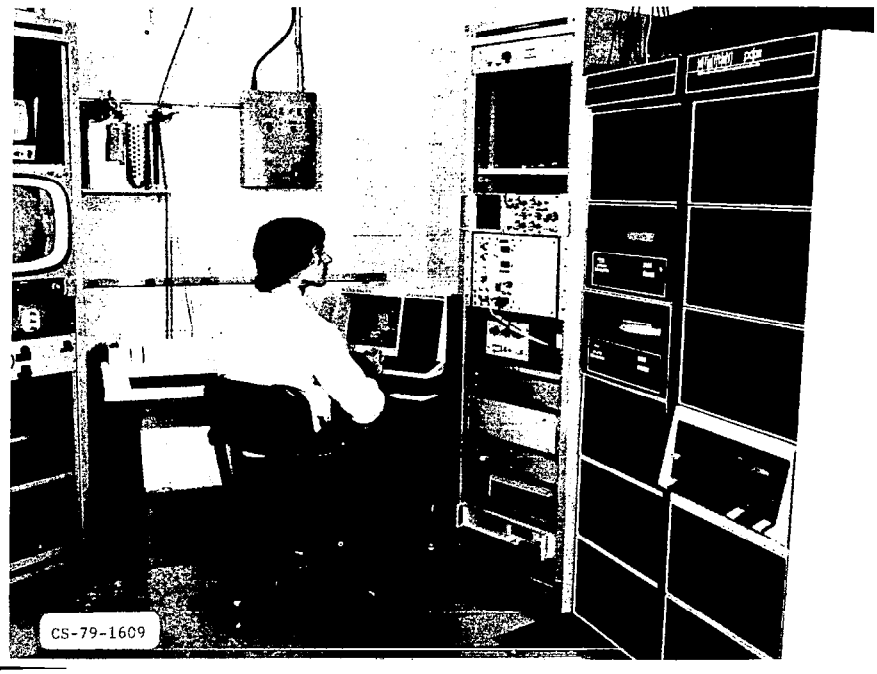

Figure IX-16

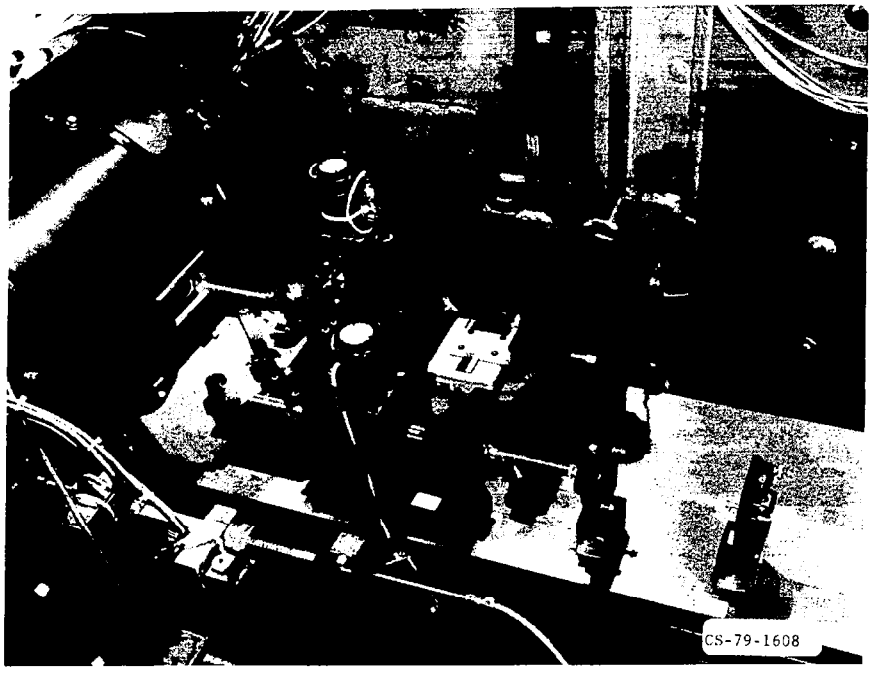

Figure IX-17

X. CONTROL TECHNOLOGY

John R. Szuch

National Aeronautics and Space Administration
Lewis Research Center

Today propulsion control technology is advancing at a tremendous pace, and, as a result, there are dramatic changes taking place both in the things one can expect the control system to do and in the equipment that is becoming available to do the controls job. This paper focuses on gas turbine engine controls by providing an overview of engine control technology and a glimpse of where this technology is heading. The role of the government, and NASA in particular, in advancing this technology is also discussed.

CONTROL REQUIREMENTS

The basic functions that have to be performed by the engine control system include starting the engine, accelerating and decelerating the engine from one thrust level to another, regulating or governing the engine speed to maintain a desired thrust, providing some form of overspeed protection, metering and shutting off the fuel flow to the engine, and providing control for other engine variabl such as compressor vanes and bleed.

These functions have been and still are, for the most part, being performed by hydromechanical control systems such as the one shown in figure X-1, which is a cutaway of a Pratt & Whitney F-100 engine fuel control. This hydromechanical control is similar to an automotive fuel control system in that it uses cams, springs, levers, and valves to deliver the right fuel flow for a given combination of throttle setting, engine speed, and ambient conditions. The hydromechanical units are rugged, dependable, and generally capable of performing the basic control functions. However, there are practical limits on the number and types of calculations one can reasonably expect from a hydromechanical computer before paying a significant penalty in control weight, cost, performance, and reliability (refs. 1 and 2). One factor that is dictating a search for new ways to control engines is the continuing trend (fig. X-2) toward more complex and demanding propulsion systems. If the number of controlled variables is used as a measure of system complexity, it can be seen that over the last two to three decades we have gone from simple turbojets like the J47 with only fuel flow to control to today's

high-performance, afterburning turbofans like the F-100 which has seven control variables. This trend, which can be attributed to requirements for increased thrust to weight ratios, reduced fuel consumption, and lower life-cycle costs, can also be seen in the commercial engines as well. And if one looks ahead to the next generation of variable-cycle engines and engines for VTOL propulsion (refs. 3 and 4), there probably will be 10 or more variables that have to be controlled.

DIGITAL ENGINE CONTROLS

It is generally accepted that hydromechanical controls will be unable to satisfy the multivariable control requirements of future propulsion systems. As a result, the Government and the propulsion industry are aggressively pursuing the use of electronics for both military and commercial engine control applications (refs. 5 and 6). In addition to multivariable control, electronic engine controls offer new opportunities for automatic thrust rating, temperature limiting, self-trim capability, engine condition monitoring, fault tolerance, and communication with the other aircraft systems.

Figure X-3 illustrates how this move from hydromechanical controls toward electronic controls has been progressing. For military engines, we have already seen the introduction of control systems having some form of electronic supervisory trim capability - either analog or digital. Figure X-4 shows the F-100 engine controls. A hydromechanical control unit performs all the basic control functions, while an engine-mounted digital computer trims the fuel flow and exhaust nozzle area commands to increase thrust and to give better thrust regulation at high power conditions throughout the flight envelope. The trim computer, or EEC as it is referred to, also has full authority control of the fan inlet guide vanes.

After demonstrating the suitability of digital electronics for trimming hydromechanical controls, it would seem logical to turn more and more of the control tasks over to the digital computer. As shown in figure X-3, successive steps might include a full authority digital control with a simple hydromechanical backup to provide flyback capability in the event of an electronics failure and, finally, a full-authority digital control with backup provided by complementary or redundant electronics. This same evolutionary process is expected to occur with commercial engine controls but at a somewhat slower pace due to the simpler engines. The new Boeing 757 and 767 aircraft will have hydromechanical controls with supervisory digital electronics. There is a possibility that commercial engine manufacturers will then be able to go directly to all-electronic controls. A lot depends on the outcome of the Navy's FADEC program and the ongoing reliability flight tests of dual channel electronic controls

on the 727 aircraft (ref. 6). In any case, programs such as QCSEE (ref. 7) and the Energy Efficient Engine program (refs. 8 and 9) indicate that digital electronic controls will play a prominent role in future commercial aircraft.

DIGITAL CONTROL RELIABILITY

While the future for digital engine controls looks bright, the question of their reliability remains a major stumbling block to their widespread acceptance for man-rated systems. Of particular concern are future VTOL applications where the engine controls will become, in effect, the flight controls.

Figure X-5 gives a quantitative look at the reliability of both the propulsion and flight controls on modern fighter-attack and commercial transport aircraft. Reliability is expressed as the mean time between control system failures (MTBF). It can be seen that the commercial transports exhibit higher control reliability than do the military aircraft. This is due, in part, to the simpler commercial engines. As an example, the hydromechanical control system on the Pratt & Whitney JT9-D engine, which powers many of today's wide-bodied transports, has an MTBF in excess of 10 000 hours. By comparison, the F-100 engine, with its supervisory digital control, exhibits an MTBF of about 1000 hours. Later this paper will describe a number of technology programs aimed at bridging this reliability gap and thus making possible the development of full-authority digital controls for future, more complex commercial engines. Figure X-5 indicates that the reliability of flight controls is orders of magnitude higher than propulsion control reliability (refs. 10 and 11). This poses a significant problem in the development of electronic controls for future VTOL propulsion systems since it is reasonable to expect that flight control reliability requirements will be imposed on the VTOL propulsion controls. The current approach to achieve this high reliability in flight controls is to use many levels of redundancy. However, this approach may result in severe penalties in control system cost and weight when considered for the engine control application. Therefore, it is expected that a significant number of improvements in control technology will be required if electronic controls are to become a reality for VTOL aircraft.

CONTROL TECHNOLOGY PROGRAMS

A number of technology areas have been identified as having a significant effect on the reliability of electronic controls. One is the computer itself. This includes such things as computer design, parts selection, fabrication, packaging, and test procedures. Another area is computer software. Given the digital computer and its capabilities, one can reevaluate how con-

trol laws are designed and how one can use digital logic to provide the desired level of reliability without resorting to many levels of redundancy. The third area involves computer interface components such as sensors and actuators. Here it is important to start thinking in terms of digital-compatible components that do not require a lot of signal conditioning electronics that can adversely affect the system reliability. And finally, there is control integration. While one usually thinks in terms of the performance benefits of integrated controls, communication between the various aircraft computers can improve control system reliability since it opens up possibilities for computer health monitoring and the trading off of control functions if faults are detected.

NASA, in fulfilling its obligations to fund high-risk research and technology programs and to provide unique facilities for this research, has been active in all of these technology areas.

Both separately funded and jointly funded NASA-DOD programs have been conducted to make maximum use of available resources and to avoid duplication of effort. Each program is contributing to the evolution of reliable electronic control systems.

ADVANCED TECHNOLOGY DEMONSTRATOR ENGINE (ATDE) PROGRAM

The Army's Advanced Technology Demonstrator Engine (ATDE) program is a 4-year effort to provide a technology base for developing an 800-horsepower turboshaft helicopter engine in the mid-1980's. As part of the ATDE program, the engine developers (AVCO Lycoming and Detroit Diesel Allison) are using engine-mounted, full-authority electronic controls. Even though the ATDE only has two control variables, fuel flow and inlet guide vanes, the Army recognizes the potential payoff from electronic controls in terms of improved performance and lower costs. The computer technology being used has evolved from a number of Army programs (refs. 12 and 13). Figure X-6 shows the internal construction of the hybrid (part-digital, part-analog) control unit developed by Chandler-Evans that was tested in 1976 on the Pratt & Whitney Small Advanced Gas Generator (STAGG). The STAGG technology subsequently formed the basis for the ATDE design. Also shown in figure X-6 are a burner pressure sensor and detector circuitry for use with an optical pyrometer to measure turbine blade temperatures. A more advanced version of the control is being developed for the ATDE and will be undergoing engine tests in 1979.

QUIET, CLEAN, SHORT-HAUL EXPERIMENTAL ENGINE PROGRAM

The NASA-sponsored Quiet, Clean, Short-Haul Experimental Engine (QCSEE) program was covered in detail at the 1978 NASA Powered

Lift Conference (ref. 7). It should be noted that General Electric did develop a full-authority digital control for the QCSEE OTW engine. General Electric, by using the state-of-the-art computer technology and sophisticated software techniques, was able to show in sea level tests at Lewis a number of performance and operational benefits of using digital controls for powered-lift propulsion systems. These included thrust-rating control, rapid thrust response (essential for the powered-lift application), failure identification and corrective action software, engine condition monitoring, and an aircraft computer interface, which would allow integration of the engine and aircraft controls.

FULL-AUTHORITY DIGITAL ELECTRONIC CONTROL PROGRAM

Probably the most ambitious of the computer hardware-oriented programs is the Navy's Full-Authority Digital Electronic Control (FADEC) program (ref. 5). In this program, which began in 1976, a dual-channel, full-authority digital control system is being developed to operate advanced variable-cycle engines (VCE) for future supersonic aircraft. In this case, the variable-cycle engines will have as many as 13 controlled variables. Both Pratt & Whitney and General Electric are designing, fabricating, and testing FADEC systems. The stated FADEC goals are to reduce control life cycle costs by 30 percent, control acquisition costs by 25 percent, control weight by 25 percent, and control maintenance time by 50 percent, and to achieve an MTBF of 2000 hours. This reliability goal represents a significant improvement relative to the F-100 EEC experience and the reliability that could be expected from a QCSEE-type computer operating the more complex VCE. This is illustrated in figure X-7 where the computer (or processor) MTBF is plotted against control complexity. Complexity is expressed as a function of both the number of control inputs and the number of control outputs. In this case, the VCE would be represented by a complexity of about 350. Data are plotted for both a hydromechanical computer and a QCSEE-type computer utilizing medium-scale integration of circuits and multilayer circuit board construction. From figure X-7 two things are obvious. First, while hydromechanical controls may be preferred for less complex control tasks, they are out of the question for the VCE task. Second, using QCSEE circuit technology would result in less than half the desired FADEC computer reliability. As a result, both Pratt & Whitney and General Electric have had to take advantage of the latest advancements in large scale integration of circuits and advanced circuit board construction techniques to try to reduce the number of potentially troublesome circuit interconnections. Indications are that the FADEC design goals will be met or exceeded. Altitude tests of the Pratt & Whitney FADEC are being conducted at the NASA Lewis Research Center on an F-401 engine;

engine tests of the General Electric FADEC are to begin in late 1979.

MULTIVARIABLE CONTROL SYNTHESIS PROGRAM

The Multivariable Control Synthesis (MVCS) program was sponsored by the NASA Lewis Research Center and the Air Force Aeropropulsion Laboratory. This joint program began in 1975 and was completed early in 1979. In the MVCS program, it was decided to abandon the idea of merely implementing conventional control laws in the digital computer and instead to exploit the capabilities of the computer to handle sophisticated control algorithms such as those coming out of the so-called modern or optimal control theories. This marked the first application of Linear Quadratic Regulator (LQR) theory (ref. 14) to the design of controls for a modern turbofan engine - in this case, the Pratt & Whitney F-100. This also involved a computer-aided design process whereby the control designer could specify a design criteria or measure of performance and have a high-speed digital computer then compute the set of optimum gains for the control. Systems Control, Inc. (Vt) was contracted to develop the control logic which was then programmed on a NASA minicomputer (ref. 15). The control was then verified using a real-time hybrid computer simulation of the F-100 engine (refs. 16 and and 17). Figure X-8 shows a photograph of the NASA hybrid computer system that was used in the MVCS studies. This approach to software verification has proved to be very convenient and cost effective in that it allows one to debug, modify, and fully evaluate the control software prior to engine testing. Following the hybrid computer studies, the same control hardware and software were used to remotely control the operation of an F-100 engine in the NASA Propulsion Systems Laboratory (PSL). Figure X-9 shows a controls engineer monitoring the MVCS engine tests from the hybrid facility where the control computer was located. Figure X-10 shows the F-100 engine installed and instrumented in the NASA altitude chamber. The engine tests were tremendously successful; they represented a free world first for the LQR control concept.

CONTROL INTERFACE COMPONENTS

Recognizing the importance of the control interface components to the overall control system, the NASA Lewis Research Center began a long-range research program in 1975 aimed at advancing the state of the art in reliable, digital-compatible sensors and actuators. Several contracts are underway to promote research in these areas. Central to these activities is the extensive use of fiber optics with its inherent advantages of simplicity, low weight, passivity, and compatibility with the digital computer. Devices being considered for the engine control applica-

tion include pulse-width-modulated fuel valves, optical tachometers, tip clearance sensors, and optical temperature sensors. Figure X-11 shows a photograph of the Fabry-Perot optical temperature sensor being developed for NASA by Rockwell. The sensor is quite small. Light from a source in the computer enters the sensor through a fiber optic bundle. The thermal expansion of a small brass ring at the tip of the sensor changes the size of an internal air gap and produces a filtering effect on the light which is reflected back to a receiver in the computer (also through a fiber optic bundle). The frequency content, or color of the reflected light, is a measure of the temperature. Figure X-12 shows results from laboratory tests of this sensor. Distinguishable color patterns have been produced over a 14^{o} temperature range. The next steps in the development of this promising concept will be to extend the temperature range and come up with a suitable detecting and decoding scheme to convert the color patterns to digital words that can be used in a control.

INTEGRATED PROPULSION CONTROL SYSTEM (IPCS) PROGRAM

In 1973, the Air Force and NASA initiated the Integrated Propulsion Control System (IPCS) program (ref. 18). The objective was to demonstrate in flight the benefit of integrating engine and air inlet controls on a high performance supersonic aircraft. Figure X-13 shows the F-111 aircraft that was used for the IPCS flight tests. An onboard digital computer provided full-authority control of the inlet and the TF-30 gas generator, afterburner, and exhaust nozzle. The IPCS flight tests resulted in improved aircraft maneuverability, better steady-state and transient thrust performance, lower fuel consumption, and expanded stall-free operation.

INTEGRATED PROPULSION-AIRFRAME CONTROL (IPAC) PROGRAM

While the IPCS program showed that integrating the inlet and engine controls could improve performance, a number of studies have indicated that even more benefits can be derived by integrating all the aircraft control systems, including the engine, inlet, and flight controls. Recognizing a need for research in this area, NASA, the Navy, and the Air Force have joined to sponsor the Integrated Propulsion-Airframe Control (IPAC) program. This program is aimed at developing a flexible flight research facility for conducting flight evaluations of concepts related to controls integration. In addition to these integrated control studies, the facility will be ideal for conducting research in energy management, full-authority digital electronic controls, engine diagnostics, failure accommodation, electronic and optical data bus technology, and other advanced control hardware and software. The IPAC system will be built on the

NASA F-15 aircraft (fig. X-14). The IPAC schedule calls for initial flight tests of the Navy FADEC control system in 1983 with integrated multivariable control research tests to follow.

CONCLUDING REMARKS

This paper has dealt with the increasing demands on propulsion control systems and a number of ongoing programs aimed at developing the required technology base. Results to date indicate that significant advancements in computer technology are being made which should provide future control designers with an almost unlimited computational capability. This will permit using sophisticated control algorithms, like LQR, and other software features, such as fault accommodation, engine diagnostics, and integrated control functions. Also, there is every reason to believe that the work going on in advanced sensors and actuators will result in a number of simple, yet accurate and reliable, devices. These will then mesh with the improved computer hardware and software to form electronic control systems to provide better performance, higher reliability, and lower costs.

REFERENCES

1. Kuhlberg, J. F.; and Newirth, D. M.: The Digital Electronic Propulsion Control System - Problems and Payoffs. AIAA Paper 74-1068, Oct. 1974.

2. Sevich, G. J.; and Newirth, D. M.: Economic Benefits of Digital Electronic Propulsion Controls for Advanced Commercial Aircraft. SAE Paper 760508, May 1976.

3. Gertsma, L. W.; and Zigan, S.: Propulsion System for Research VTOL Transports. ASME Paper 73-GT-24, Apr. 1973.

4. Lieblein, S.: Problem Areas for Lift Fan Propulsion for Civil VTOL Transports. Presented at the Deutsche Gesellschaft Fuer Luft-und Raumfahrt. Symposium on VTOL Propulsion (Munich, West Germany), Oct. 22-23, 1970.

5. Barclay, B. A.; Lenox, T. G.; and Bosco, C. J.: Full Authority Digital Electronic Control - Highlights of Next Generation Propulsion Control Technology. ASME Paper 78-GT-165, Apr. 1978.

6. Kamber, P. W.; and Welliver, A. D.: Electronic Propulsion Controls for Commercial Aircraft. AIAA Paper 74-1065, Oct. 1974.

7. Quiet, Powered-Lift Propulsion. NASA CP-2077, 1978.

8. Johnston, R. P.; et al.: Energy Efficient Engine - Preliminary Design and Integration Studies. (R78AEG510, General Electric Co.; NASA Contract NAS3-20627.) NASA CR-135444, 1978.

9. Gray, D. E.: Energy Efficient Engine - Preliminary Design and Integration Studies. (PWA-5500-18, Pratt & Whitney Aircraft Group; NASA Contract NAS3-20628.) NASA CR-135396, 1978.

10. Boudreau, J. A.: Integrated Flight Control System Design for CCV. AIAA Paper 76-941, Sept. 1976.

11. Helfinstine, R. F.; Montague, L. L.; and Seller, G. L.: Reliability and Redundancy Study for Electronic Flight Control Systems. Honeywell-21718-FR, Honeywell, Inc., 1972. (AD--902445.)

12. White, A. H.; and Wills, D. F.: Advanced Engine Control Program - Design, Fabrication and Test of Electronic Engine Control System for Small Turboshaft Engines. R-492-31, Chandler Evans, Inc., 1972. (USAAMRDL-TR-72-59, AD-758173.)

13. Hearn, R. J.; Cole, M. A.; and White, A. H.: Advanced Engine Control Program - Using Computerized Electronic Equipment. R-492-45, Colt Industries, Inc., 1973. (USAAMRDL-TR-73-81, AD-773660.)

14. Bryson, A. E.; and Ho, Y.: Applied Optimal Control, Blaisdell Publ. Co., 1969.

15. Dehoff, R. L.; et al.: F100 Multivariable Control Synthesis Program. Vol. 1: Development of F100 Control System. AFAPL-TR-77-35-VOL-1, 1977. (AD-A052420.)

16. Szuch, John R.; Seldner, Kurt; and Cwynar, David S.: Development and Verification of Real-Time, Hybrid Computer Simulation of F100-PW-100 (3) Turbofan Engine. NASA TP-1034, 1977.

17. Szuch, John R.; et al.: F100 Multivariable Control Synthesis Program - Evaluation of a Multivariable Control Using a Real-Time Engine Simulation. NASA TP-1056, 1977.

18. Lampard, G. W. N.; and Batka, J. J.: Development of an Integrated Propulsion Control System. AIAA Paper 75-1178, Sept. 1975.

CUTAWAY OF F-100 HYDROMECHANICAL CONTROL

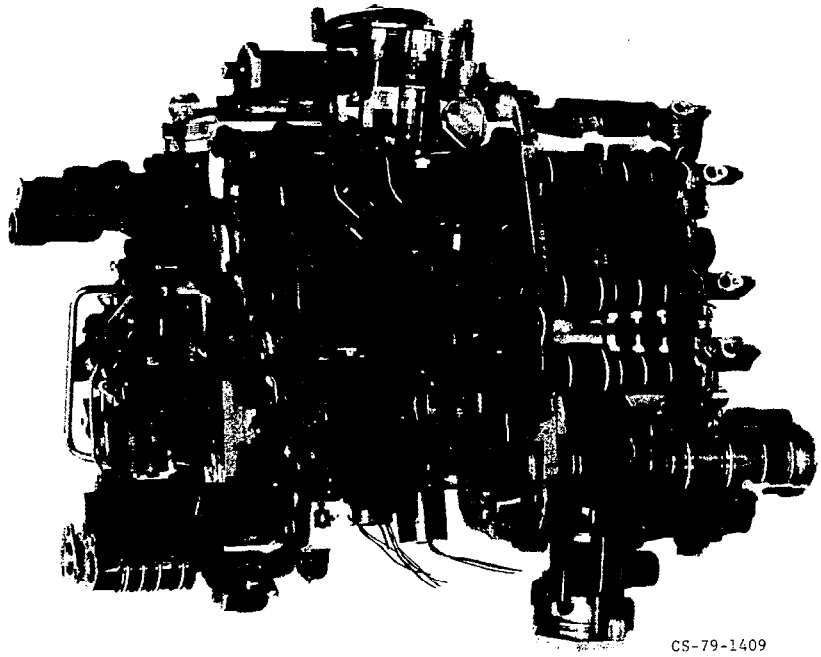

Figure X-1

TRENDS IN CONTROL COMPLEXITY

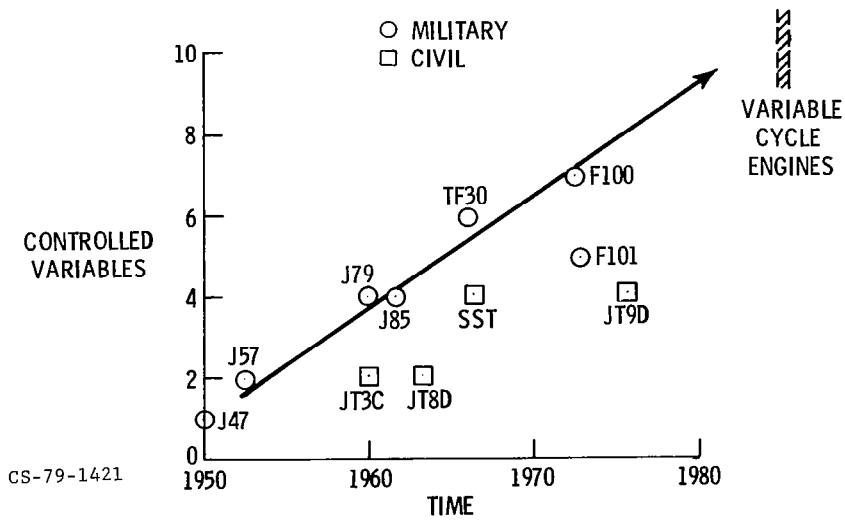

Figure X-2

EVOLUTION OF ENGINE CONTROLS

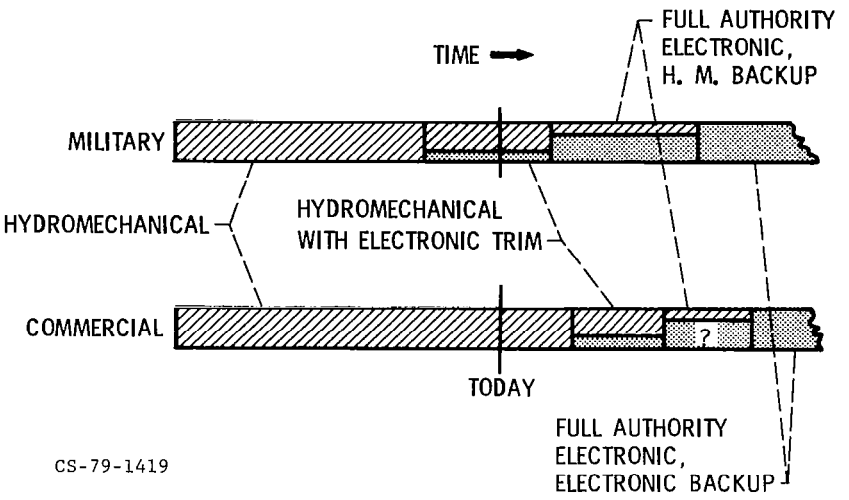

Figure X-3

HYDROMECHANICAL ENGINE CONTROL WITH ELECTRONIC TRIM - F-100

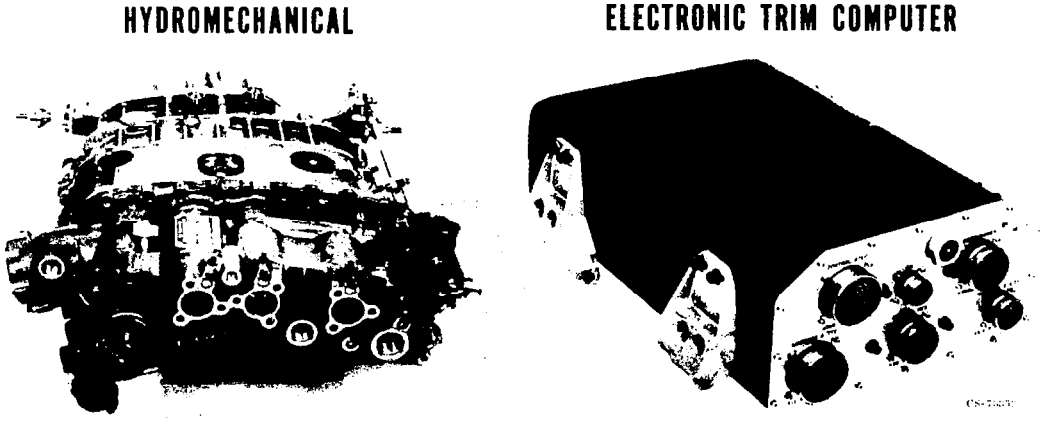

Figure X-4

CONTROL SYSTEM RELIABILITY

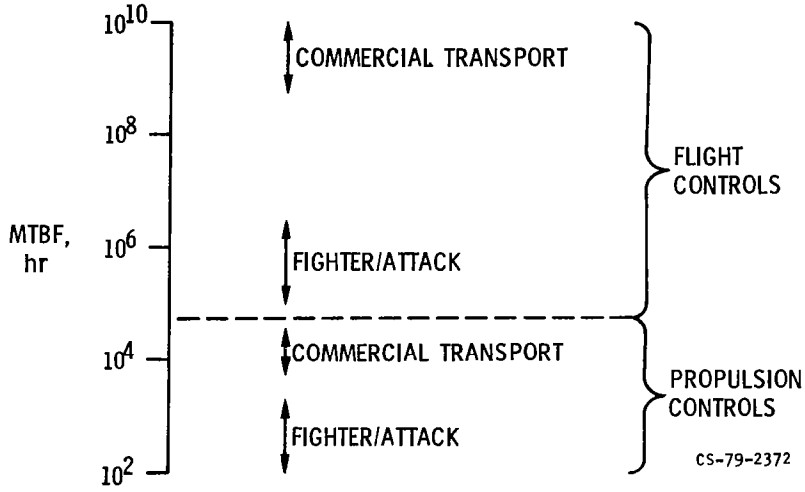

Figure X-5

STAGG ELECTRONIC CONTROL CONSTRUCTION

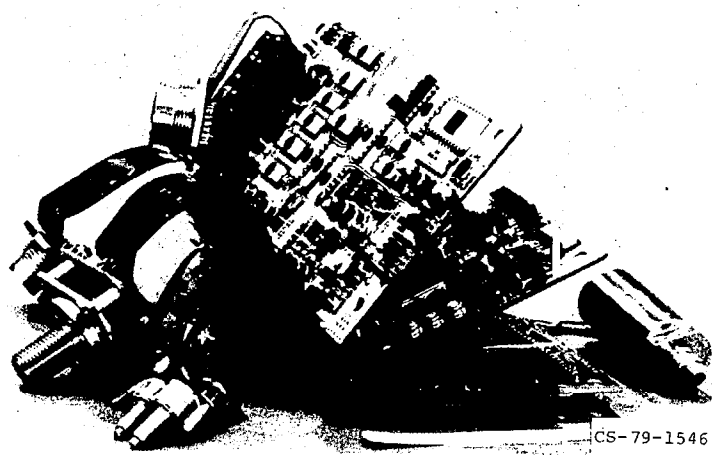

Figure X-6

FADEC COMPUTER RELIABILITY

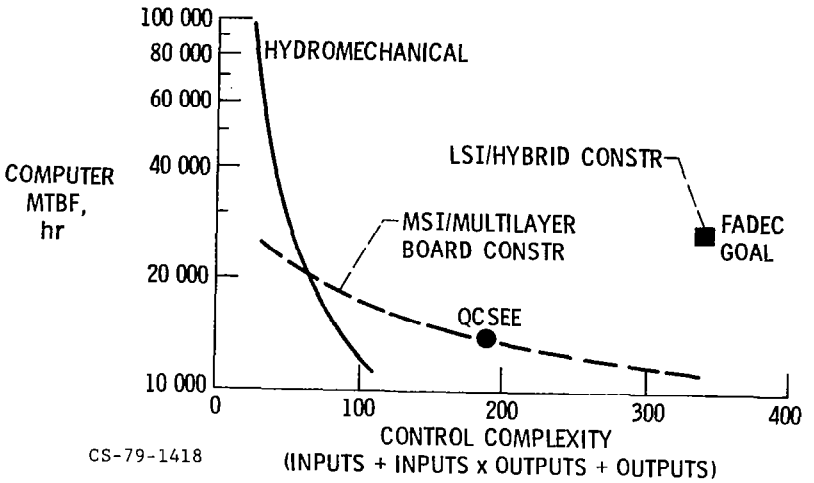

Figure X-7

LeRC HYBRID COMPUTING SYSTEM

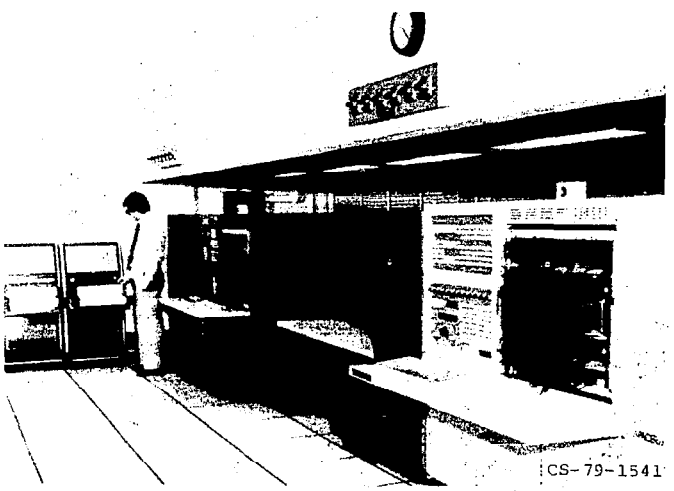

Figure X-8

F-100 MULTIVARIABLE CONTROL TESTS

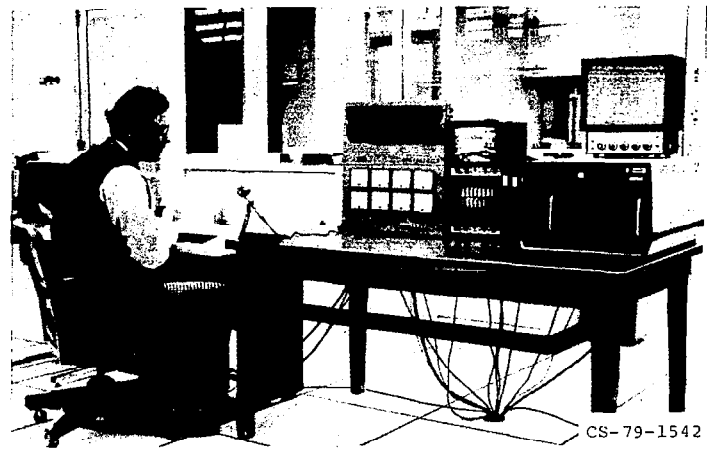

Figure X-9

F-100 TURBOFAN IN LeRC ALTITUDE CHAMBER

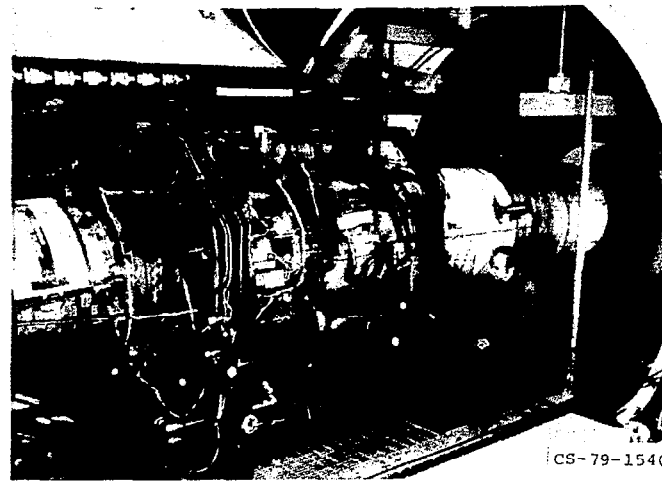

Figure X-10

COMPLETE FIBER-OPTIC FABRY-PEROT TEMPERATURE SENSOR

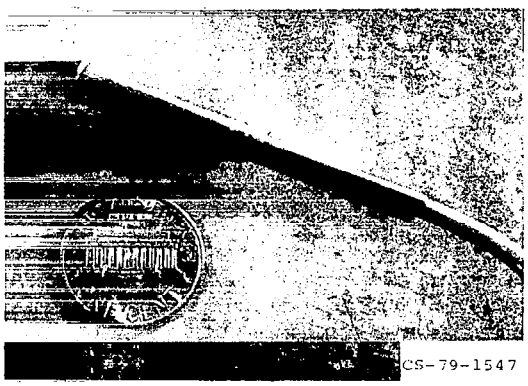

Figure X-11

FABRY-PEROT TEMPERATURE SENSOR TEST RESULTS

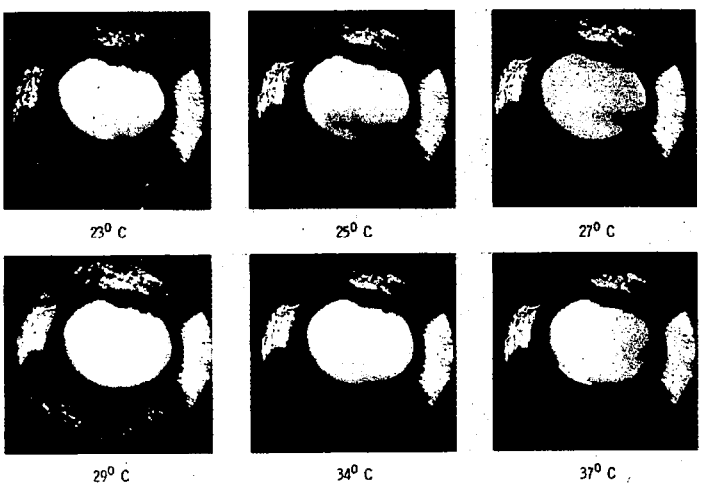

Figure X-12

INTEGRATED PROPULSION CONTROL SYSTEM

COMBINED INLET, ENGINE
EXHAUST NOZZLE CONTROL

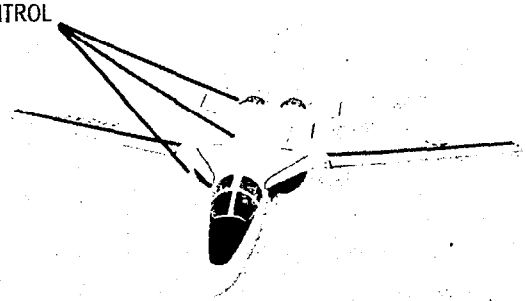

- GREATER MANEUVERABILITY
- MAXIMUM THRUST PERFORMANCE
- IMPROVED FUEL CONSUMPTION
- EXPANDED STALL FREE OPERATION

CS-79-1545

Figure X-13

NASA F-15 IPAC RESEARCH AIRCRAFT

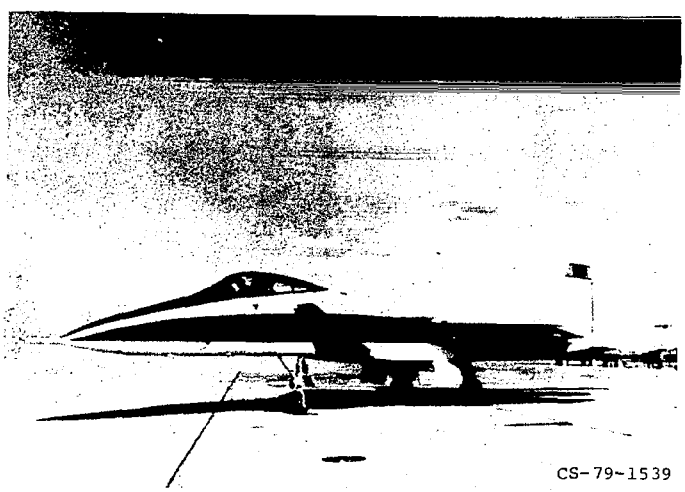

CS-79-1539

Figure X-14

XI. SUPERSONIC PROPULSION TECHNOLOGY

Albert G. Powers, Robert E. Coltrin, Leonard E. Stitt,
Richard J. Weber, and John B. Whitlow, Jr.

National Aeronautics and Space Administration
Lewis Research Center

At the close of the U.S. attempt in the commercial supersonic transport market in the early 1970's, both the government and aircraft industry recognized that significant technical advancements would be required to make a second generation supersonic aircraft economically viable and environmentally acceptable. Consequently, in 1972, NASA initiated a limited effort to advance supersonic technology. The intent of the Supersonic Cruise Research (SCR) program is to investigate areas requiring new and improved technology that will lead to substantial improvements in performance, social acceptability, and cost effectiveness.

The Langley Research Center, the lead center for the overall SCR program, is working closely with three airframe contractors, Boeing, McDonnell Douglas, and Lockheed. Reference aircraft (fig. XI-1) configurations are being studied that show improvements in range, payload, gross weight, and, hence, cost effectiveness. As indicated in figure XI-2, these improvements are results of recent advancements in structures and materials (including manufacturing techniques), airframe aerodynamics, system integration and advanced control concepts, and propulsion, which is obviously the major environmental culprit.

To adequately cover the progress of the overall SCR program, the Langley Research Center is planning a four-day conference in November 1979. However, since this is primarily a propulsion conference, this report concentrates on propulsion and a few closely related disciplines.

PROPULSION SYSTEM STUDIES

In 1971 the national SST program was still in progress (fig. XI-3). Boeing was designing a preprototype airplane that was powered by a General Electric afterburning turbojet. Full-scale engines had actually been built and were being tested. However, in retrospect, this engine was borderline in performance and was a poor neighbor in terms of noise and pollution. This was recognized even at that time, and alternative cycles for the production airplane were just starting to receive serious attention when Congress terminated the SST program.

Determining the best propulsion system for a supersonic transport is not a simple matter because of the diverse requirements that must be satisfied. Figure XI-4 illustrates a typical flight path and identifies the critical operating requirements. The airplane must, of course, be capable of efficient, sustained supersonic cruising. Also, there is the controversial need to limit NO_x emissions to avoid damage to the ozone layer. The best supersonic engine tends to be a low-bypass turbofan, possibly even a turbojet, and augmentation is often desirable.

On the other hand, for low-noise takeoff and efficient subsonic climb, plus at least some amount of occasional subsonic cruising, a high-bypass-ratio turbofan that is similar to those used in modern wide-body transports is preferred.

These conflicts in engine requirements necessitate a search for some type of compromise design that can best suit the airplane on the average. Alternatively, one can in theory imagine an engine that is so versatile that it can modify its mode of operation during flight so as to best match the requirements of the airplane from moment to moment. This is the concept of the variable cycle engine (VCE). In practice, of course, providing this versatility causes penalties in weight, complexity, and component efficiencies; therefore, it is not entirely obvious that the VCE is really the final solution.

As already mentioned, NASA started its SCR program in 1972. Since there were no longer the constraints of a rigid time schedule of a true development program, it was possible to reexamine the engine situation with a fresh approach. As shown in figure XI-5, an extensive series of propulsion studies was initiated with General Electric and Pratt & Whitney. The goal was to screen all the engine concepts that seemed to have any merit. These included all the usual, conventional turbojets and turbofans plus a wide variety of VCE's. In successive years, the studies weeded out the least promising approaches and analyzed the survivors in progressively more detail. This process produced a small number of favored concepts that are presently being studied for such refinements as differences in complexity and maintainability and the technology requirements of the particular components.

The relationship of these studies to other phases of the SCR program is indicated in figure XI-6. The propulsion results are fed into the Langley system studies, and they in turn help identify the desirable engine types and the particular versions needed to match the various airplane configurations. The engine studies were also supported by research in the key environmental areas of emissions and noise. By 1976 the engine concepts were understood well enough for large-scale experimentation; also, work has begun

on the inlets and nozzles necessary to match the engines that have evolved.

Some of the surviving engine concepts are illustrated in figures XI-7 and XI-8. Figure XI-7 shows a fairly conventional turbofan; its bypass ratio is so low, however, that this turbofan is practically a turbojet. Figure XI-8 shows the presently favored VCE offerings of the two contractors. They are both versions of turbofans and capitalize on the coannular noise benefit that was described in paper III.

Because of the unusual features of these two VCE's, they were selected for investigation in the large-scale experimental program. However, this is not intended to suggest that one of these is necessarily the engine that would be chosen by industry if an actual development and production program were started in the future. Considerations of development risk, cost, reliability, technology readiness, and so forth are more properly the responsibility of the manufacturer and his customer than they are of the government. Later sections will describe the operation of these VCE engine concepts and the experimental program that is now underway.

The projected performance of these engine types, as applied to a typical supersonic transport mission, is shown in figure XI-9. Airplane takeoff weight for a fixed range and payload is used as the figure of merit. The independent parameter is the unsuppressed takeoff noise generated by the engines. The circled point on the far right shows the capability of the 1971 turbojet, which is much noisier than the noise constraint that until recently was imposed on new subsonic transports (Federal Air Regulation 36, 1969). The present VCE concepts are competitive with each other and can reach the general level of FAR 36 (1969). It should be stressed, however, that these calculations are probably rather optimistic, and the noise goal is not attained with enough margin to create much confidence. The more conventional engine is inherently somewhat noisier, but if it were fitted with an advanced jet noise suppressor it could possibly achieve similar performance to the VCE's.

Despite the significant improvement since 1971 (fig. XI-9), there are no grounds for complacency. The FAA has announced its intent to subject future supersonic transports to the same noise limits as those that will apply to new subsonic transports of the same time period. The latest subsonic limit, shown at the left side of figure XI-9, is about 8 decibels lower than the 1969 rule, which is barely achievable. Consequently, satisfying the new FAA goal poses quite a challenge.

To elaborate on this important issue, consider figure XI-10, which shows the noise of a typical VCE at the three FAA measuring points: sideline, community, and approach. The open bars pre-

sume that jet noise is reduced by the coannular effect. Compared to the 1969 rule, sideline noise is high, but community and approach noise are low. Hence, after trades are made, the traded limit is just about met. But this is not good enough for the 1978 goal.

One way to improve the situation is to combine the coannular nozzle with a simple mechanical suppressor in the outer stream only. This is represented by the shaded bars. Since the situation is considerably improved, this is a useful direction to pursue. A later section will comment further on jet noise suppressors.

A different type of noise is involved in the bar labeled approach. At this flight condition, the engine is throttled back, and a major noise contributor is the fan, rather than just the exhaust jet. With the present technology the multistage, high-pressure-ratio fan used in these engines is very noisy. However, in this figure it was presumed that a reduction of 15 to 20 decibels was achieved by such techniques as inlet choking and wall treatment. These techniques may also be needed at the community point. The section on inlet design discusses this requirement.

It was mentioned when discussing figure XI-9, that the VCE's and the suppressed conventional engines were competitive. But this conclusion is influenced by the mission selected for the airplane which, for figure XI-9, is an all-supersonic-cruise case. Variations in the mission are examined in figure XI-11. Direct operating cost is used as the figure of merit, and what is plotted is the value of that parameter for a conventional low-bypass engine (LBE) relative to the value for a VCE. These data were all generated by a single contractor to minimize the influence of different technology assumptions. For a full-range, all supersonic mission (circled point), the two engines yield similar performance (fig. XI-9). However, when one looks at how airplanes are actually used once in the fleet, they rarely fly their maximum-range capability. In fact, the average range for these long-distance vehicles is more like 70 percent of maximum. This slightly enhances the importance of the always present subsonic phases involved with takeoff and descent; hence, the LBE suffers slightly with respect to the VCE. This effect really becomes noticeable if substantial amounts of subsonic cruise become necessary to avoid sonic boom exposure over land areas. After all, not all airports are located next to seacoasts. For the example shown, the LBE is 12 percent more expensive to operate than the VCE at the average-range point. The significance of this factor must again be assessed by the manufacturer and the customer airline when selecting a production engine.

To summarize, it seems fair to say that major strides in propulsion have been achieved since the old SST program by means of both imaginative cycle concepts and improved engine components.

VARIABLE CYCLE ENGINE COMPONENT PROGRAM

During the propulsion optimization studies, two unique and attractive VCE concepts were identified as possible solutions to the conflicting propulsion requirements for supersonic transports. These VCE concepts incorporate unique components and unusual flowpath arrangements. Certain technologies were identified as critical to the successful development of these engines. To assess the feasibility of the concepts and to develop the most critical of the engine components, the Lewis Research Center initiated a VCE component program in 1976 through a series of contracts with Pratt & Whitney and General Electric. The next two sections describe these engine cycles and address a few of the critical technology components.

Variable Stream Control Engine

Figure XI-12 is a schematic showing the basic arrangement of the major engine components of the Pratt & Whitney variable stream control engine (VSCE). Also shown is an illustration of the inverted jet velocity profile at takeoff. The engine is a twin-spool configuration similar to a conventional turbofan but with the added feature of a burner in the fan duct. The VSCE derives its name from its ability to independently control the primary and bypass streams. The fan and compressor both have variable geometry components and are driven by advanced technology turbines. The main burner and duct burner both use low-emissions, high-efficiency combustor concepts, based on NASA's Clean Combustor program. The coannular nozzle provides variable throat areas for the core and fan duct flow and also includes an ejector - thrust-reverser system.

The flexibility of this concept to meet the diverse requirements of low jet noise at takeoff and good fuel consumption at cruise can best be illustrated by describing the operation at its three most critical operating conditions: takeoff, subsonic cruise, and supersonic cruise (fig. XI-13).

At takeoff, the primary stream is throttled to an intermediate power setting while the duct burner is operated at its maximum design temperature. The independent control of the two streams provides the unique inverted velocity profile that is needed to take advantage of the coannular nozzle noise benefit. The bypass jet velocity is about 60 to 70 percent higher than the primary jet velocity. This inverted velocity profile provides a significant reduction in takeoff jet noise.

At subsonic cruise, the main burner is throttled to a low temperature and the duct burner is turned off. Variable geometry features are used to "high flow" the engine to match the inlet airflow and thus reduce both the inlet spillage drag and the nozzle

boattail drag. The velocity profile is nearly flat, and the engine approaches the performance level of a moderate bypass ratio turbofan engine designed strictly for subsonic operation.

At supersonic cruise, the primary burner temperature is increased relative to takeoff, and the duct burner is operated at part power. The resulting velocity profile again is nearly flat for good propulsive efficiency, and this concept then provides a fuel consumption that approaches that of a turbojet cycle designed exclusively for supersonic cruise.

VSCE/F-100 component testbed program. - A comparison of the VSCE with Pratt & Whitney's component testbed configuration is shown in figure XI-14. The NASA component testbed program at Lewis began in 1976 to provide a large-scale evaluation of some of the unique and critical components of the selected VCE concepts. To keep the costs to a minimum, the critical component hardware is applied to existing high-technology engines. In the Pratt & Whitney program, the testbed system is designed to provide a large-scale evaluation of two of the most critical technology components of the VSCE - the low-emissions duct burner and the low-noise coannular nozzle. These components are added at the back of an F-100 engine which is used as a gas generator. The F-100 engine has the best potential to simulate the desired exhaust conditions of the VSCE without any major modifications.

Low-noise coannular nozzle. - Model nozzle tests are being conducted concurrently to support the component testbed program. An aero/acoustic design procedure for coannular nozzles was applied to several candidate exhaust systems to identify the most attractive nozzle for the VSCE. A schematic of the selected design is shown in figure XI-15. At supersonic cruise, the nozzle is a conventional convergent-divergent configuration. Two internal clamshells are positioned to provide the initial portion of the expansion surface of the ejector shroud. Variable throat areas are provided for both the primary and fan flows. At low-speed conditions, the nozzle converts to an auxiliary inlet ejector. Actuated inlet flaps are opened to admit external airflow into the shroud. Panels located immediately downstream of the double-hinged doors are translated aft to provide additional area for the ejector, and the internal clamshells are alined with the inlet flow. Floating tail feathers are aerodynamically positioned to provide the proper exit flow area. The clamshells are also used for thrust reversal by rotating them back to the nozzle centerline. The reversed flow is then expelled through the open inlet doors.

Scale models of this nozzle configuration have recently been tested in the Lewis 8 by 6 Foot Wind Tunnel (fig. XI-16). Thrust performance levels were established for this nozzle design at both subsonic and supersonic speeds. The results of this experimental investigation are shown in figure XI-17. The measured

nozzle thrust coefficients are compared to the SCR study goals at three critical flight conditions - takeoff, subsonic cruise, and supersonic cruise. The supersonic cruise point is simulated at Mach 2.0, the highest Mach number available from the wind tunnel. The performance at this flight condition is very good. This is encouraging since this is the most critical operating point for the exhaust system. The low-speed performance was disappointing, especially at subsonic cruise when the measured performance levels are from 5 to 6 counts lower than the study goals. Diagnostic tests of the subsonic cruise configurations showed that the lower performance levels were the result of an aerodynamic flow separation over the inlet doors of the ejector. It is obvious that additional work is required to improve the off-design performance of this ejector nozzle concept.

Low-emissions duct burner. - Segment rig tests are also being conducted concurrently to evaluate the performance and emissions characteristics of duct burner configurations. An analytical screening study of low-emissions, high-performance duct burner concepts indicated that a three-stage burner, operating on the vortex burning and mixing concept (vorbix), offered the best configuration for the testbed engine within its risk and schedule constraints. A schematic of the selected configuration is shown in figure XI-18. The requirement that the duct burner be capable of operating smoothly over a wide range of fuel-air ratios leads to the need for a multistage combustor system. The first, or pilot prechamber, stage is sized for stable operation at very low fuel-air ratios to provide a soft light and to minimize disturbances to the fan operation. The combined first two stages (pilot prechamber and pilot secondary) are designed to operate at supersonic cruise, and the third, or high power, stage is designed to operate only during takeoff and transonic climb.

Emissions and performance measurements have been obtained for this three-stage vorbix configuration in both a two-dimensional segment rig test and more recently in the F-100 testbed engine. Emissions measurements from these experimental tests at two simulated flight conditions, takeoff and supersonic cruise, are shown in figure XI-19. The design goals for carbon monoxide (CO) and unburned hydrocarbons (THC) are based on a combustion efficiency of 99 percent. These goals are intended only as a standard for comparison and are not related to any proposed or established regulation for advanced supersonic aircraft. Since the measured combustion efficiencies are very high (near a value of 1.0), the emissions levels for CO and THC are well below the design goals. The design goal for oxides of nitrogen (NO_x) is the lowest value that can be obtained with this duct burner concept and assumes complete mixing. The measured NO_x emissions levels are quite low and very near the goals at both takeoff and supersonic cruise. It should be pointed out that the duct burner only contributes a small part of the overall engine NO_x emis-

sions when compared to the main burner, as can be seen in figure XI-20.

In figure XI-20 the projected emissions characteristics of the VSCE have been updated to reflect the duct burner emissions measurements from both the segment rig and testbed engine tests. The data used for projecting the emissions of the main burner were based on results from the Clean Combustor program, and the main burner was assumed to be a two-stage vorbix concept. Figure XI-20 shows the projected emissions levels for both the airport vicinity and at altitude cruise. The shaded area depicts emissions from the main burner, while the unshaded area shows the emissions from the duct burner. The results at the airport indicate that the engine is capable of meeting the 1984 emissions requirement for the class T5 advanced supersonic transport engines. The NO_x emissions at high altitude cruise are higher than the proposed Climatic Impact Assessment Program (or CIAP) goal of 3.0. Although the requirements for altitude NO_x are not yet established, if they are constrained to this proposed CIAP level, more advanced emissions-reduction technology must be employed to meet the goal. This is particularly true for the main burner, since it produces nearly 90 percent of the total NO_x emissions at altitude cruise.

One of the major concerns with a duct burner is its starting problem and how that influences fan stability. This problem was addressed in this concept by designing the pilot prechamber stage to operate at a very low fuel-air ratio. Soft lights have been demonstrated with no significant pressure disturbance at the design starting fuel-air ratio of 0.002. Another concern was screech. No acoustic instabilities have been encountered to date after 46 hours of duct burner operation. The cooling system was worked out, and the duct burner was able to operate on all three stages for periods of several hours. As mentioned previously, the performance and emissions characteristics have been very good. Combustion efficiencies are near a value of 1.0. The thrust efficiency at the cruise condition was better than 97 percent, which was well above the design goal of 94.5 percent. Thrust efficiency is a measure of the uniformity of the temperature distribution at the fan duct nozzle exit plane. The temperature profile should be as uniform as possible to produce the maximum thrust. However, the uniformity of the exit temperature profile is limited by the necessity of cooling the nozzle. A thrust efficiency of 97 percent is considered excellent.

A photograph of the testbed engine installed in the test stand at East Hartford is shown in figure XI-21. This is a rear view of the testbed with the ejector nozzle removed. A photograph of the exhaust flow with the duct burner lit is shown in figure XI-22. It is evident that the exhaust flow is extremely clean.

Program status. - The component testbed program at Pratt & Whitney is in the fourth year of a total five-year program. The emissions and performance testing of the baseline duct burner configuration on the testbed engine is nearly completed. There are still items to be done in the present program. The model nozzle program is continuing with an effort to improve nozzle performance, especially at the off-design conditions where the measured performance to date has been poor. Duct burner segment rig tests will continue to refine the three-stage vorbix concept and to initiate work on a more simplified configuration. This effort will lead to a second emissions test on the testbed engine. The large-scale aero/acoustic test of the coannular nozzle on the testbed engine and the measurement of duct burner combustion noise levels remain to be completed.

In summary, the performance and emissions measurements obtained to date from the component testbed program at Pratt & Whitney have been very encouraging. Successful operation of these advanced and unique engine components will remove some of the technical barriers that now inhibit the development of an advanced supersonic cruise aircraft.

Double Bypass Engine

The General Electric Company's VCE, previously identified as their most promising concept from the NASA-sponsored SCR propulsion studies, is a double bypass turbofan - so called because the fan has been split into two blocks. A schematic drawing of this engine is shown in figure XI-23. Each fan block has its own separate bypass duct; hence, the terminology double bypass engine. Splitting the fan apart gives the designer additional freedom in sizing this component and additional control over bypass ratio.

Description of concept. - Some of the unique features of this engine, which help control the flow, are illustrated in figure XI-23. The split fan consists of an enlarged front block, which is designed to accommodate all the airflow required for takeoff with low jet noise, and a smaller, lower capacity rear block, or third-stage fan, which has variable inlet guide vanes for additional flow control. They are partially closed to divert flow through the outer duct in double bypass operation, which is the mode shown in the view above the engine centerline in figure XI-23. This third-stage fan is driven by the high-pressure turbine, as opposed to the more normal low-pressure turbine drive system. This unique drive arrangement provides a better turbine work split between the high- and low-pressure spools and allows the fan tip diameter to be reduced because of the higher core shaft speed. The improved work split also reduces the cooling air required for the low-pressure turbine because more energy is extracted from the high-pressure turbine.

Another unique component is the forward bypass control valve, which is located immediately downstream of the split fan at the juncture of the two bypass streams. In double bypass operation, it varies the discharge opening of the inner bypass duct to balance the static pressure in this duct with that of the outer bypass stream so that they can be combined at minimum loss into a single stream. This flow is then brought to the crossover struts; these struts support the nozzle plug and channel the flow through the hot stream when the inner plug is translated open. This setup provides the inverted flow with the hot gas on the outside and the cold fan air on the inside for the maximum jet acoustic benefit.

The more conventional single bypass operating mode of this engine is shown below the centerline in figure XI-23. The outer bypass duct is closed off by the bypass selector valve, and the inlet guide vanes on the third-stage fan are opened so that this stage can accommodate all the flow from the front block fan. In this case, the nozzle inner cone is translated aft to block any cold flow from discharging through the inner nozzle. The rear bypass control valves, located between the crossover struts, are opened to allow the bypass flow to be mixed with the main engine exhaust flow to provide a uniform jet velocity profile.

The simplified schematic drawings in figure XI-24 illustrate the three critical flight conditions referred to in the previous section about the Pratt & Whitney VCE: takeoff, subsonic cruise, and supersonic cruise. At takeoff, the General Electric engine is operated in the double bypass mode with the fan at an overspeed condition to maximize airflow for reduced jet noise. Unlike the Pratt & Whitney VCE, this engine does not have a duct burner to provide the inverted jet velocity profile desirable for low noise; instead, it relies on the flow inversion of the engine and fan exhaust streams for this effect.

At subsonic cruise, the engine is throttled back and is again operated in the double bypass mode at high flow. The higher bypass ratio improves the specific fuel consumption at this flight condition. Because the airflow is kept high, the throttle dependent installation losses remain low. Most of the fan discharge air is mixed with the main exhaust flow ahead of the nozzle to obtain a uniform, low-velocity jet profile, which is desirable for good propulsive efficiency.

At supersonic cruise, the engine operates as a conventional single bypass mixed-flow turbofan for high specific thrust. The bypass and core exhaust streams are mixed ahead of the exhaust nozzle to obtain a single uniform jet for high propulsive efficiency.

Early acoustic test program. - The early acoustic testbed engine, shown schematically in figure XI-25, was assembled to assess the

feasibility of some of the most critical technologies relevant to the double bypass VCE concept, especially with respect to the operation of the coannular exhaust system and the unique inverted velocity profile desirable for low jet noise. A series of aero/acoustic tests with the testbed engine was completed in October 1978 at a General Electric test facility at Edwards, California. Prior tests were conducted with this engine using a conventional mixed-flow exhaust at a General Electric test cell at Lynn, Massachusetts. To save costs and to get an earlier test date, the NASA program started with a Navy-modified YJ101 split fan VCE configuration with double bypass flows. The forward bypass control valve system was then added for the Lynn tests and the coannular plug exhaust system was later added for the Edwards test. The reduced size YJ101/testbed engine design is obviously very similar to the advanced study engine shown in figure XI-23. The third-stage fan, however, is driven by the low-pressure turbine, and the front block is not enlarged but is the same flow size as the rear block. Also, losses in the testbed engine might be expected to be somewhat higher because of the increased bypass stream turning in the vicinity of the forward bypass control valving and the increased fan block spacing necessitated by the use of existing YJ101 hardware. In spite of these differences, takeoff exhaust conditions of the advanced study engine can be simulated by the testbed engine.

A photograph of the testbed engine on the Edwards test stand is shown in figure XI-26. A large protective screen is shown ahead of a bellmouth inlet. In this photograph the engine is set up for the initial calibration testing with a baseline single-stream conic mixed-flow nozzle. Figure XI-27 is a photograph of the engine on the stand with the coannular plug exhaust nozzle installation. A laser velocimeter is shown to the side of the exhaust nozzle. It was used to make a velocity survey of the jet plume at various positions downstream of the exit plane. Two laser beams can be seen emanating from the laser velocimeter, which is on a track-mounted traversing system. Through a combination of different plug crowns and outer nozzle shrouds, tests were conducted with three different outer nozzle radius ratios at a constant throat area. The effect of nozzle area ratio was also investigated by translating the inner cone of the plug nozzle to vary the exit area of the inner stream. Both conic and convergent-divergent outer nozzle terminations were investigated.

Figure XI-28 shows the thrust loss resulting from bypass system pressure losses. In this bargraph, thrust loss is compared at typical takeoff exhaust conditions for both single and double bypass operation. The single bypass case represents an exhaust condition with a mass-averaged jet velocity of 2300 feet per second and an inner to outer area ratio of 0.1. In other words, even though the fan is operated in the single bypass mode, a small amount of bypass air is allowed to flow through the crossover struts and out through the inner plug to obtain an area

ratio of interest from the VCE conceptual engine studies. The cycle limitations of the testbed, which was constrained by the use of YJ101 hardware, necessitated operation in the single bypass mode to obtain this high a level of jet velocity; the conceptual study engines, however, would obtain this exhaust condition in the double bypass mode. The double bypass case, represented by the second pair of bars in figure XI-28, is for a mass-averaged jet velocity of 2000 feet per second at an area ratio of 0.4. The highest losses would be anticipated at these conditions since the strut flow is at a maximum, as evidenced by the higher area ratio.

Bypass system losses were of some concern prior to the Edwards testing because of the rather tortuous flowpath from the fan discharge through the bypass ducting and the crossover struts to the inner plug nozzle entrance. There was concern that these losses might be higher than analytical prediction techniques indicated, thereby detracting from an otherwise attractive concept. These predictions, as well as the actual testbed engine results, are shown in figure XI-28. For single bypass operation, the predicted losses are in close agreement with the actual test results and are fairly inconsequential. For double bypass operation at the strut design flow condition, the predicted thrust losses were around 2 percent, but the actual measured loss was only slightly greater than for single bypass - a very encouraging test result.

Figure XI-29 shows engine specific fuel consumption as a function of fan airflow on the test stand at part throttle conditions with constant thrust. This type of operation is representative of cutback at the takeoff flyover noise measuring station or subsonic cruise. It shows that a 29-percent increase in airflow is possible for double bypass operation compared to the normal single bypass operation without exceeding the minimum specific fuel consumption in single bypass. At cutback, this could mean a 6 to 10 perceived noise decibel (PNdB) reduction in jet noise because of the lower jet velocity. At subsonic cruise, the greater mass flow implies reduced throttle-dependent installation drag because the inlet spillage and nozzle boattail are reduced. Trades are possible, however, between increased airflow in double bypass and lower uninstalled specific fuel consumption. For instance, an uninstalled specific fuel consumption about 5 percent lower could be obtained at an airflow about 13 percent greater than at the single bypass minimum specific fuel consumption point.

Incidentally, another important objective in these tests was met by successful transitions between single and double bypass modes, and vice versa, without engine stall over a wide range of power settings.

The acoustic test results for both the coannular plug nozzle and the baseline single-stream conic nozzle are shown in figure XI-30. Perceived noise level (PNL) is plotted at the peak sideline

angle against the mass-averaged jet velocity. The data shown here have been scaled to study engine size, and the distance has been scaled to the sideline measuring station in a flight situation. All the coannular data shown are for an inner to outer nozzle area ratio of 0.2. The outer nozzle has a convergent-divergent termination designed for a 2.9 pressure ratio. Its radius ratio was 0.85. The acoustic benefit of the coannular plug is about 6 PNdB relative to the conic at the higher jet velocities representative of takeoff conditions. A velocity ratio of approximately 1.5 between the hot and cold exhaust streams was maintained above a mass-averaged velocity of about 1750 feet per second. Below this velocity, the velocity ratio and the coannular benefit began to deteriorate because of the fixed nozzle areas used in this test.

The sideline directivity of the PNL observed in the Edwards testing is shown in figure XI-31 at various angles measured from the inlet axis. Test data are shown for both the reference mixed conic and the coannular plug nozzles. The peak sideline PNL occurs in the aft quadrant at an angle of 130° where the coannular nozzle is about 6 PNdB quieter than the baseline conic, the same result shown in the preceding figure for this mass-averaged jet velocity of 1950 feet per second. In the forward quadrant there also appears to be about 7 PNdB in shock noise reduction from the coannular nozzle. Small-scale model coannular data are also shown for the coannular plug as a broken line. Very close agreement was obtained between the model and testbed engine data when both are scaled to full size and a common distance.

Core-driven fan stage VCE testbed. - The acoustic test of the initial testbed engine configuration shown in figure XI-25 was completed in October 1978. Figure XI-32 shows a testbed engine now being built which is more similar to the advanced double bypass study engine. This engine, to be tested in 1980, will have a core-driven third-stage fan, closer spacing between the fan blocks and compressor, and certain exhaust system modifications to allow for testing a simple outer stream mechanical suppressor. Figure XI-33 shows a retractable shallow-chute suppressor as it might be applied to the outer stream of the advanced double bypass study engine. Such a lightweight, low-loss suppressor could probably be added to a flight-type engine with very little penalty to the aircraft mission or cost effectiveness. Further reductions to the sideline and community cutback noise would result relative to that obtained with only the coannular inverted velocity profile benefit alone. Studies are now underway to determine the mission/acoustic trades possible with such systems. Using suppressors such as these should bring the projected noise levels closer to those specified by FAR 36 (1978). The version to be used on the testbed is still in the initial design phase, but it would be a similar, although nonretractable, boilerplate design. Model scale suppressor work, which is now starting, should provide some further design information for this suppres-

sor, in addition to that available from the previous DOT/FAA-funded experimental studies done by General Electric.

Program status. - The accomplishments of the General Electric component testbed program have, thus far, been very encouraging. The coannular jet noise relief of 6 PNdB obtained at the sideline condition verified the acoustic predictions based on the scale model work. The part-power airflow extension capabilities at lower specific fuel consumptions in the double bypass mode have demonstrated another of the variable cycle benefits. Successful transitions between double and single bypass modes have also been accomplished. Furthermore, the bypass system losses from the fan discharge through the crossover struts to the inner nozzle were less than expected. Next year, a major goal in the General Electric program is to verify the unique core-drive fan system and evaluate any additional acoustic benefit derived from a simple outer stream suppressor.

SUPERSONIC CRUISE INLETS

So far in this discussion only the engine and the exhaust nozzle have been discussed. Another important element of the propulsion package is the engine inlet. At the supersonic cruise speeds of interest, the inlet develops a pressure ratio of up to 20 to 1, thus generating over half of the propulsive thrust.

Basic Inlet Properties

There are several design factors that an inlet designer must consider when designing an inlet. Each of these factors tries to shape the inlet its own way. These factors are shown around the outside of figure XI-34, while the basic inlet properties which the designer must select are shown inside the box. Each of these basic properties will be described, and the factors will be discussed as appropriate.

Geometry type. - The first and most basic inlet property is geometry type. The inlet would really like to be made of rubber so that it could change its shape to just match the airflow requirements at each aircraft speed. But, to be practical, a basic shape must be selected as well as a method of varying the internal flow area. Figure XI-35 shows the trend of three inlet properties for three typical geometry types. One curve shows the trend of inlet complexity and the other curve shows the trend of both inlet weight and inlet off-design airflow capacity.

The inlet on the left is a twin duct two-dimensional expanding wedge inlet. A photograph of this inlet type with the ramps in a vertical orientation is shown in figure XI-36. This photograph was taken from a position ahead of and below the inlet with the

flow going into the page. The internal area of this inlet is varied by a simple doorlike movement of the aft portion of the ramp, about a hingeline on the ramp surface. The curves in figure XI-35 show that this inlet tends to be the least complex. It also has the largest off-design airflow capacity due to its large throat area capability. However, it does tend to be the heaviest.

The middle inlet in figure XI-35 is an axisymmetric expanding (axi expanding) centerbody inlet which is also known as a collapsing centerbody inlet. A photograph of this inlet type is shown in figure XI-37. The internal area of this inlet is varied by the movement of overlapping leaves about a hingeline on the cone surface. This mechanization is similar to that of an iris nozzle. Figure XI-35 shows that this inlet tends to be the most complex. But it is lighter than the expanding wedge inlet and it has a moderate off-design airflow capacity.

The inlet on the right in figure XI-35 is an axisymmetric translating (axi-translating) centerbody inlet. A photograph of this inlet type is shown in figure XI-38. The internal area of this inlet is varied by translating the centerbody along a support tube. Figure XI-35 shows that the basic axi-translating inlet (lower edge of shaded bands) tends to be somewhat more complex than the expanding wedge inlet. It tends to have the lowest weight, but it also has the least off-design airflow capacity. In fact, at speeds near Mach 1, the axi-translating inlet may not be able to supply enough airflow to the engine. The addition of auxiliary (AUX) devices, such as auxiliary inlets, can increase its airflow capacity, but these devices will also make it heavier and more complex. All three SCR airframers presently show some type of axi-translating inlet on their aircraft. Also, all the VCE engines have been matched to this inlet type. But it must be remembered that its potential lack of off-design airflow capacity may result in marginal or inadequate transonic thrust.

Compression split. - The second inlet property is compression split and is described in figure XI-39. The upper sketches will be used to define some terms. The left sketch shows that at supersonic cruise the inlet uses multiple shock waves to slow the air to subsonic speeds before it enters the engine. The oblique shocks are produced by the inlet flow area contraction. The final wave is a normal shock which sits downstream of the minimum area called the inlet throat. External compression is defined as the flow area contraction occurring ahead of the cowl lip, and internal compression is that occurring between the cowl lip and the throat. The inlet is said to be started when the shocks are in this high-performance position. But if the normal shock is pushed into the converging area ahead of the throat, by something like increased angle-of-attack or a control error, it is unstable and will be abruptly expelled to a point in front of the cowling, as shown on the right. This process is called an inlet unstart. The unstart transient can be very violent and the unstarted re-

covery very low. These unstart characteristics impart large unsymmetric forces on the aircraft.

The curves in figure XI-39 show that the desire for higher recovery and lower cowl drag will push the inlet designer toward high internal compression. The penalties will be greater bleed drag, lower angle-of-attack (α) tolerance before unstart, greater unstart severity, and lower unstarted recovery. The figure also indicates the amount of internal compression that would be employed by the translating and expanding inlet concepts. The axi-translating (TRANS) inlet must employ high internal compression. The high internal compression is required so the translating inlet can obtain the needed off-design area variation. The expanding (EXP) concepts allow the choice of more modest amounts of internal compression. The choice would be the least amount of internal compression consistent with relatively good recovery and cowl drag, thus reducing the bleed drag and unstart penalties.

Variable geometry features. - The third inlet property, required variable geometry features, is described in figure XI-40. This figure shows the gyrations of an axi-translating centerbody inlet during a typical mission. The supersonic cruise shock structure has already been described. Since the inlets are normally sized at cruise speed, the inlet is always matched to the engine at this condition.

The supersonic throat is too small in the off-design speed range and must be increased by extending the centerbody. The throat now occurs near the cowl lip and the terminal shock sits in front of the cowling. Toward the upper end of this speed range, bypass may be needed to spill air the engine cannot use. However, as speed is further reduced to near Mach 1, the bypass will be closed. At this point, as mentioned before, the translating inlet has difficulty obtaining all the flow area the engine demands.

The inlet must deliver a large quantity of high recovery airflow to the engine at takeoff so as to reduce jet noise. However, a sharp lip separation is present at this condition which forces the addition of auxiliary inlet airflow to supply enough good quality air to the engine.

Fan noise suppression of up to 20 decibels may be required in the terminal area. This suppression will most likely be accomplished by a combination of acoustic treatment on the internal walls, similar to that described by the noise reduction panel, and operation of the inlet at high throat Mach numbers near choke. The auxiliary inlets will have to be open for some noise suppression conditions in order to supply enough air to the engine. Therefore, in addition to the main duct, the auxiliary inlets will also have to incorporate some form of noise suppression for these conditions. This figure shows what a complex machine the inlet can be.

Design Factors

Now that the basic inlet properties have been described, the design factors of figure XI-34 will be discussed. Noise suppression, cruise speed, performance, weight, and alpha tolerance have already been covered. The need for good shock stability has also been implied. But it should also be mentioned that shock stability systems are being studied that will tend to prevent unstarts, or at least reduce their frequency of occurrence. But these shock stability systems will add complexity. The engine cycle is also an important driver on inlet selection. For a VCE to operate as advertised, it must be matched to an inlet which can efficiently provide the airflow that the engine demands over the full speed range. The mission is important as it defines such things as the need for subsonic cruise legs which in turn can dictate the required inlet throat area. The nacelle location dictates the Mach number and flow angles at the inlet station. Good compatibility and controlability are required for any supersonic cruise vehicle and must be considered early in the inlet selection process. Maintainability and reliability of the various inlet systems are nebulous quantities, particularly early in a development cycle, but can be all important to a final inlet selection.

Axi-Expanding Inlet Evaluation

The previous review of supersonic cruise inlets has alluded to some potential airflow and low internal compression advantages of the axi-expanding inlet. In 1978 it was decided to further explore these potential advantages by having the three SCR airframers - Boeing, Douglas, and Lockheed - conduct preliminary axi-expanding inlet evaluation studies. Each airframer was to aerodynamically and mechanically design an axi-expanding inlet to match their aircraft and VCE. Then they were to estimate its performance, weight, complexity, and operating characteristics and define any unique features associated with this inlet concept. They were then to compare all of these characteristics with those of their present axi-translating inlets. Finally, they were asked to identify inlet technology areas that require future effort. Since each airframer was studying a different aircraft at a different Mach number, three different answers might be expected.

General agreement. - There were several items on which all three contractors agreed. They agreed that the axi-expanding inlet requires less bleed, has a greater alpha tolerance and a milder unstart, and can deliver a larger off-design airflow. The axi-expanding inlet has a less complex centerbody bleed system, but it does have complex centerbody leaf seals with possible leakage problems. Since very little is known about noise suppression in supersonic cruise inlets, the relative suppression advantages of the two inlets could not be identified. All of the contractors

felt fan noise suppression testing is required. The other findings of each contractor are now reviewed in order of increasing design Mach number.

Douglas evaluation. - Figure XI-41 shows simplified cross sections of the two inlet types for the Douglas Mach 2.2 aircraft. The bypass and auxiliary inlet systems are shown in different positions on the top and bottom of the cowl to illustrate movement. The axi-translating inlet incorporates two unique features. One is a telescoping centerbody for added transonic airflow. The aft portion of the centerbody is translated forward, with the spike tip in the full aft position, in order to open an auxiliary flow path through the centerbody. The other unique feature is the forward translating cowl auxiliary inlet system which is used for added takeoff airflow. An aft bypass door system is also employed in which the doors rotate about an axial axis, somewhat like a furnace damper. The axi-expanding inlet, shown on the bottom, also incorporates the translating cowl auxiliary inlet system and the aft bypass rotating system. The bleed system on this inlet is much simpler than the bleed systems on the axi-translating inlet.

Douglas found that the axi-expanding inlet resulted in 3.3 percent more range due to the 27 percent less weight, a better supersonic cruise specific fuel consumption, and more climb thrust. It also required fewer operating mechanisms. A negative factor on the axi-expanding inlet was less area for acoustic treatment due to the shorter length and overlapping leaves. Douglas found that the axi-expanding inlet is a valid VCE concept but that verification is required. Also, since all the VCE's have been matched to an axi-translating inlet, Douglas recommends that VCE cycles should be pursued that might take better advantage of the added flow capacity of the axi-expanding inlet.

Boeing evaluation. - The Boeing inlet geometries for their Mach 2.4 aircraft are shown in figure XI-42. The Boeing axi-translating inlet is a typical translating design. The aft door system, which is used on both inlets, is a combination bypass and auxiliary inlet system. This aft door system rotates out for bypass and in for auxiliary inlet operation. The axi-expanding inlet incorporates the unique feature of an added hinge point in the subsonic diffuser in order to obtain better throat position and area control. Again, the bleed system on the axi-expanding inlet is much simpler than those on the axi-translating inlet.

Boeing found that the axi-expanding inlet resulted in 1.7 percent less range; this was due mainly to the inlet's 42 percent greater weight even though it provided better SFC at cruise and climb. Although they felt that the axi-expanding inlet would have greater benefit for the lower cruise speeds and that it is a valid VCE concept, they also felt that verification is required, particularly on the subsonic diffuser. Boeing's main near term

interest, however, is in combining existing three-dimensional flow codes into the three-dimensional analytical models needed to design supersonic cruise inlets and their associated control systems. They would prefer to use an existing axi-translating wind tunnel model, which has a large available data bank, to experimentally verify these analytical models.

Lockheed evaluation. - The Lockheed inlet geometries for their Mach 2.55 aircraft that incorporates overwing and underwing inlets are shown in figure XI-43. Both the over and under inlets are designed for the local Mach number at the overwing position of 2.75. The axi-translating inlet is a typical translating design. The aft door system, which is used on both inlets, is a combination bypass and auxiliary inlet system. The aft door system opens as one door for bypass but opens several small louvers for takeoff auxiliary airflow. The axi-expanding inlet is unique in that it incorporates translation to maintain better shock position and airflow control. Again, the bleed system on the axi-expanding inlet is much simpler than those on the axi-translating inlet.

Lockheed found that the axi-expanding inlet had a 3 percent range advantage due to its better supersonic cruise SFC and better climb engine flow match. A better takeoff recovery is also obtained with the axi-expanding inlet. The absence of cowl bleed on the axi-expanding inlet permits the installation of acoustic treatment between the engine face and the auxiliary inlets and also gives increased auxiliary inlet position options. However, the axi-expanding inlet was 21 percent heavier. Lockheed felt that, within the scope of this study, the axi-expanding inlet was their preferred inlet but that concept screening should continue.

Evaluation summary. - The three SCR airframers reached the following conclusions:

(1) The range of an aircraft with an axi-expanding inlet was comparable to the range of an aircraft with a axi-translating inlet.

(2) Factors other than performance were more important as decision criteria in selecting an inlet type. These items include engine flow matching, angle-of-attack tolerance, noise suppression characteristics, and complexity.

(3) The axi-expanding inlet is a viable SCR inlet candidate which adds a VCE flow match option.

The three airframers recommended the following:

(1) Experimental verification of the potential advantages of the axi-expanding inlet should be obtained.

(2) New inlet concepts should be screened or old concepts revised so as to generate new and perhaps better inlet-VCE combinations.

(3) Early testing is needed to define the low-speed performance and fan noise suppression characteristics of supersonic cruise inlets.

CONCLUSIONS

The objective of the Supersonic Cruise Research program is to provide this country with an advanced technology data base to support possible future civilian and military supersonic cruise aircraft.

This report has shown some of the recent technical advancements in supersonic propulsion that indicate cost and environmental improvements are possible in a second generation supersonic transport. The paper has also described, in some detail, the work being done on variable cycle engines. These unique propulsion concepts, together with advanced supersonic inlets and low noise coannular nozzles, promise to provide good operating performance at both supersonic and subsonic flight, are reasonably quiet during takeoff and landing, and have acceptable exhaust emissions.

SUPERSONIC CRUISE RESEARCH

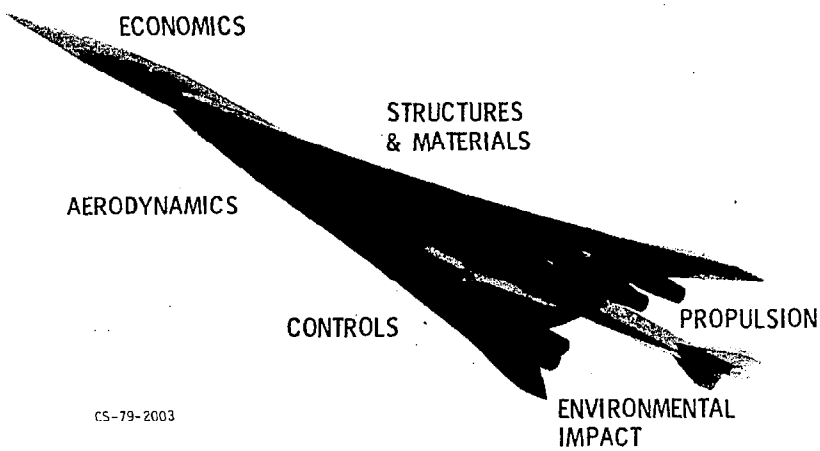

Figure XI-1

ADVANCED SUPERSONIC CRUISE AIRCRAFT CONFIGURATIONS

BOEING

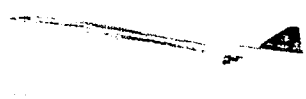

McDONNELL DOUGLAS

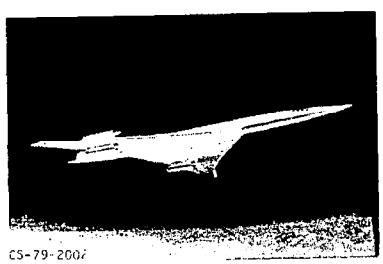

LOCKHEED

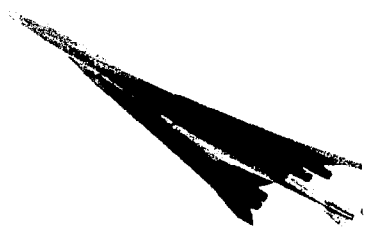

NASA LANGLEY

Figure XI-2

1971 PROPULSION STATUS

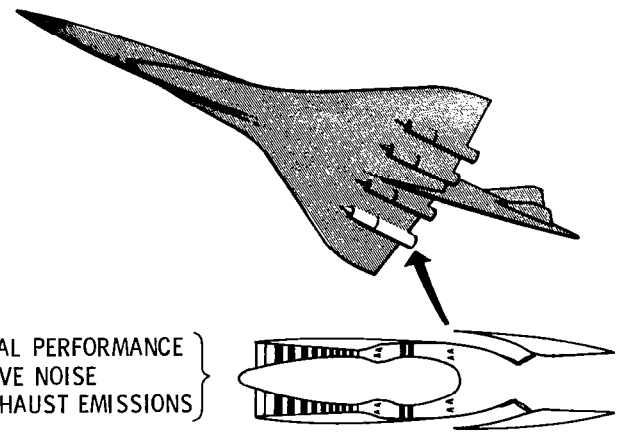

- MARGINAL PERFORMANCE
- EXCESSIVE NOISE
- HIGH EXHAUST EMISSIONS

CS-79-1639

GE-4 AFTERBURNING TURBOJET

Figure XI-3

ENGINE REQUIREMENTS

TYPICAL SUPERSONIC TRANSPORT

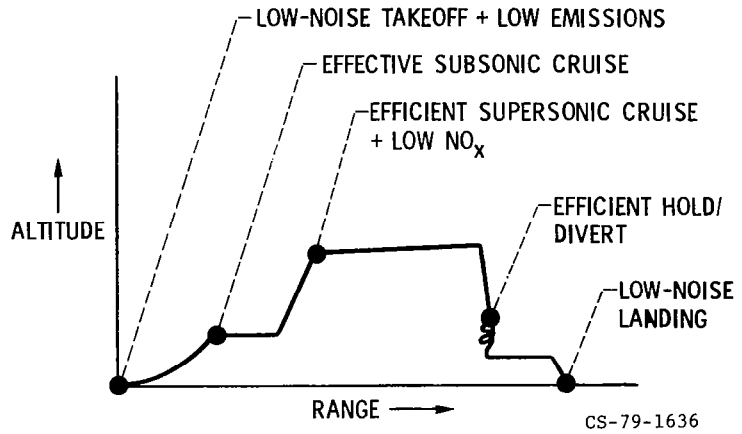

Figure XI-4

EVOLUTION OF ENGINE STUDIES

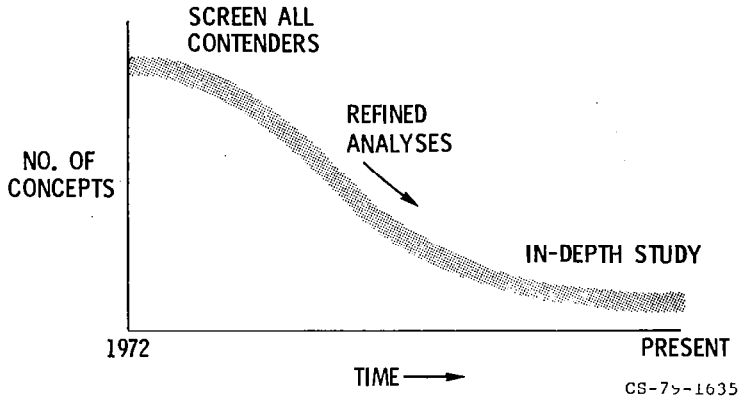

Figure XI-5

PROPULSION PROGRAM

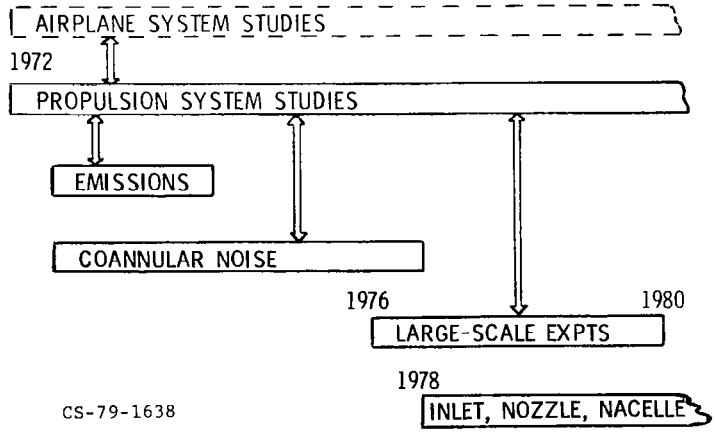

Figure XI-6

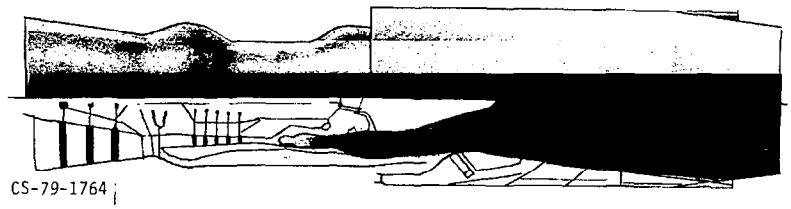

CS-79-1764

LOW BYPASS ENGINE (LBE)

Figure XI-7

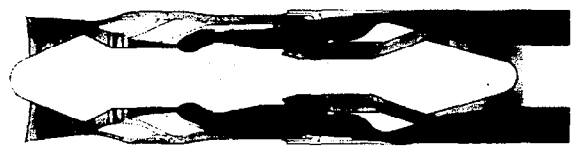

DOUBLE BYPASS ENGINE (DBE)

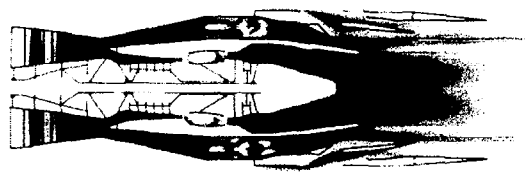

VARIABLE STREAM CONTROL ENGINE (VSCE)

Figure XI-8

COMPARISON OF ENGINES

M = 2.4; ALL SUPERSONIC CRUISE
292 PASSENGERS
RANGE, 4500 n mi

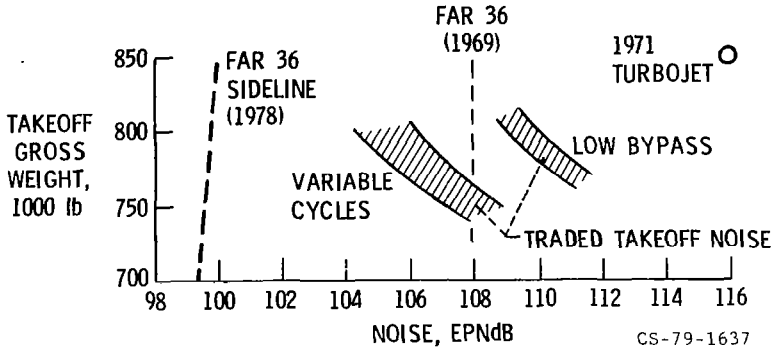

Figure XI-9

AIRCRAFT NOISE LEVELS

G.E. DOUBLE BYPASS ENGINE

EXHAUST

□ COANNULAR
▩ COANNULAR/SUPPRESSED

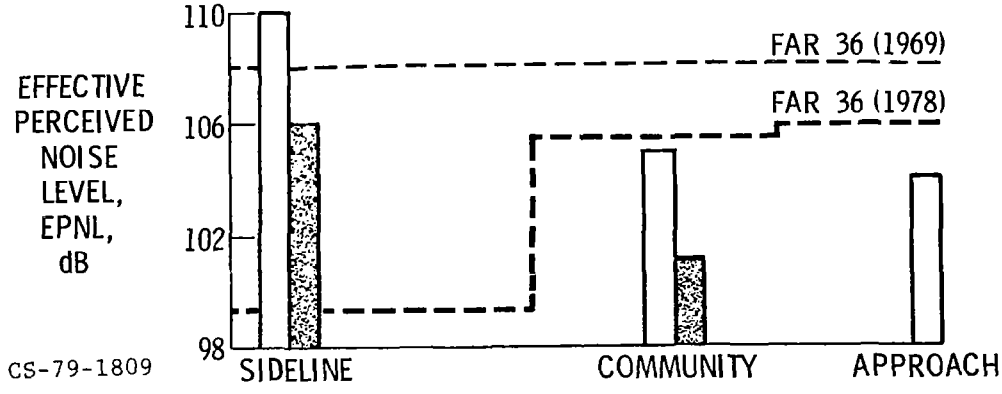

Figure XI-10

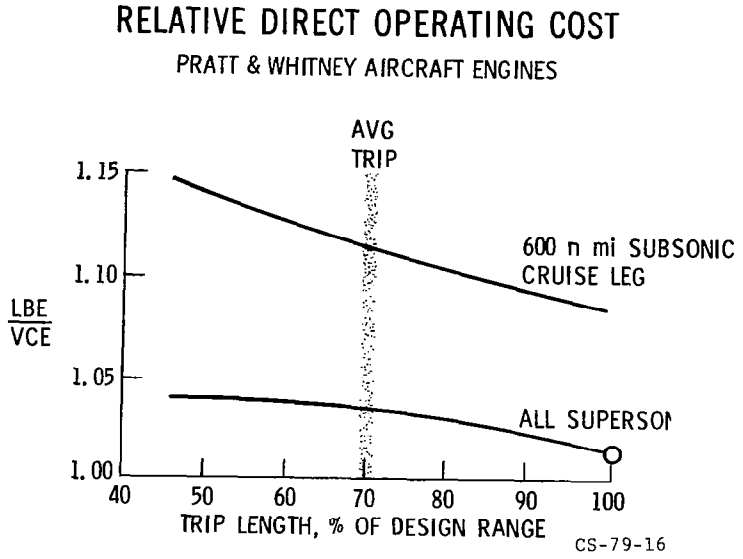

Figure XI-11

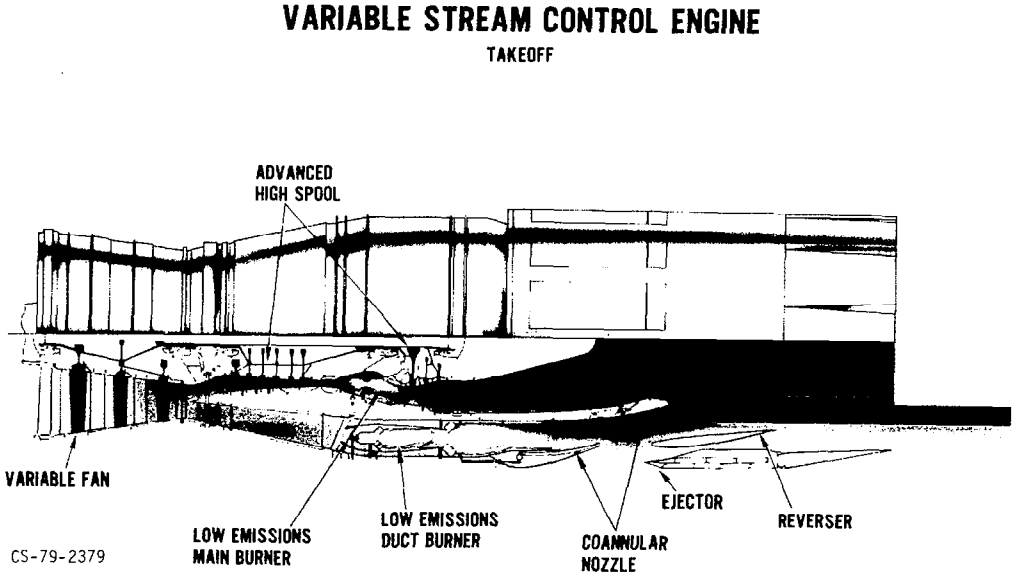

Figure XI-12

PRATT AND WHITNEY AIRCRAFT
VARIABLE STREAM CONTROL ENGINE

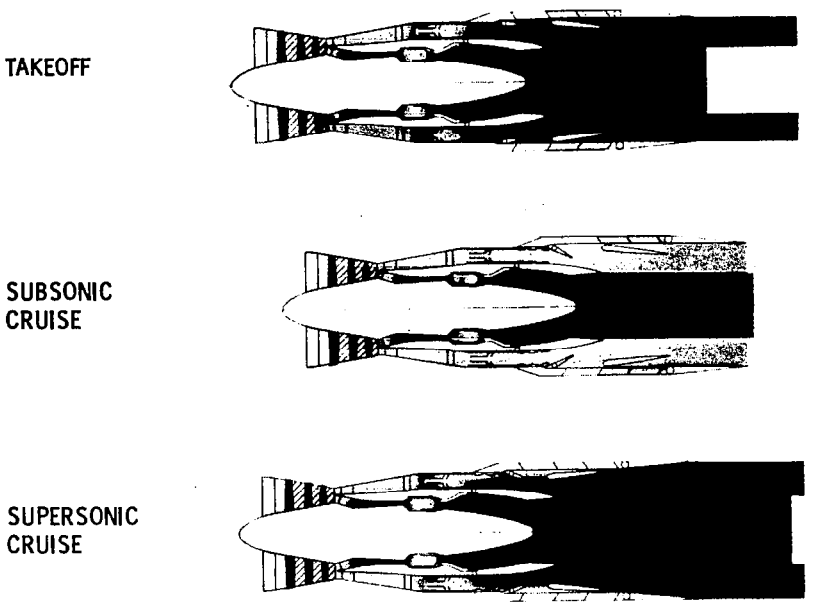

Figure XI-13

COMPARISON OF VSCE-502B AND TESTBED CONFIGURATION

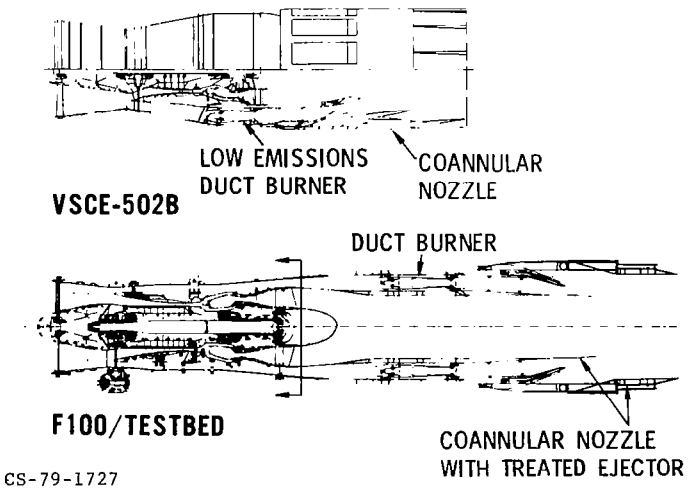

CS-79-1727

Figure XI-14

VSCE-502B EJECTOR NOZZLE

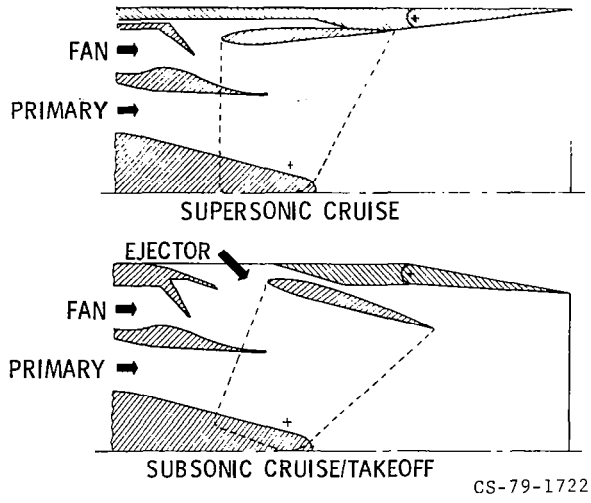

Figure XI-15

VSCE-502B NOZZLE IN 8'X6' SUPERSONIC WIND TUNNEL

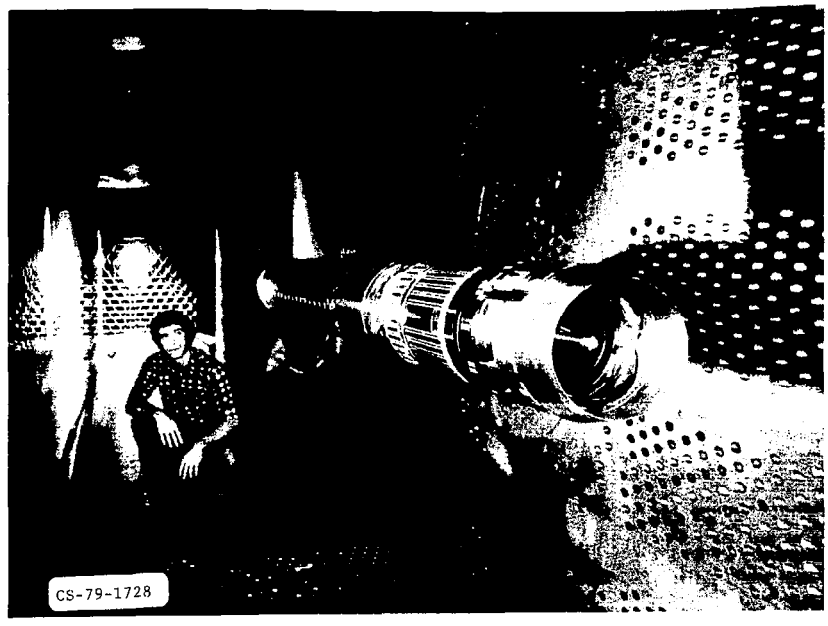

Figure XI-16

VSCE-502B NOZZLE THRUST PERFORMANCE

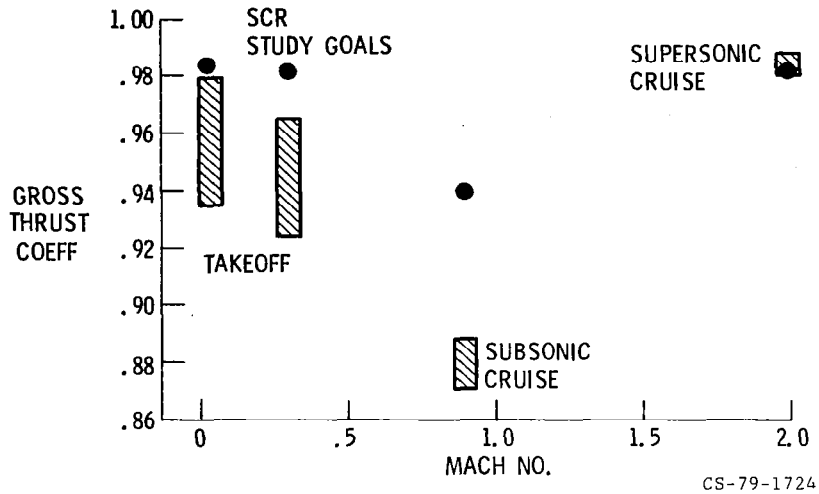

Figure XI-17

THREE-STAGE VORBIX DUCT BURNER

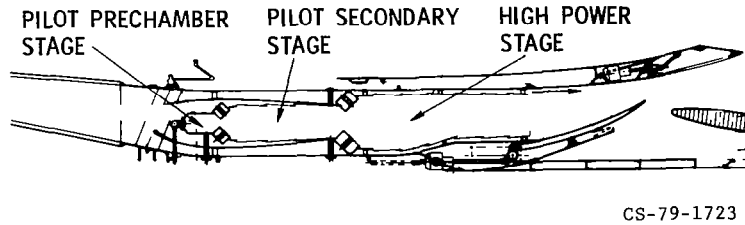

Figure XI-18

MEASURED DUCT BURNER EMISSIONS

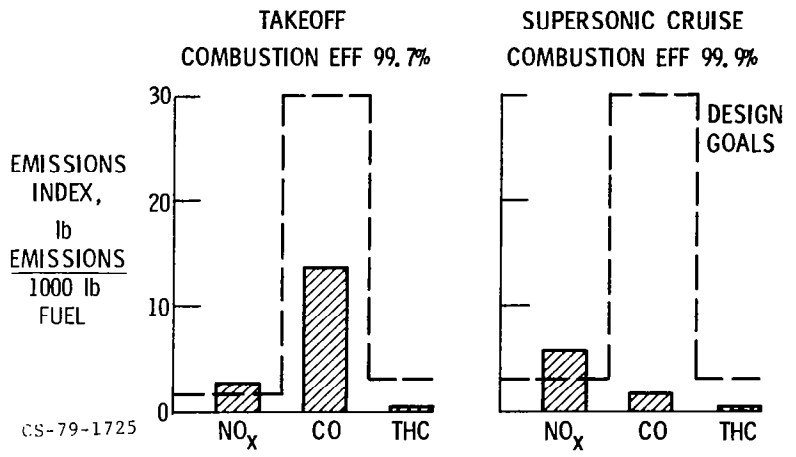

Figure XI-19

VSCE-502B EXHAUST EMISSIONS ESTIMATES

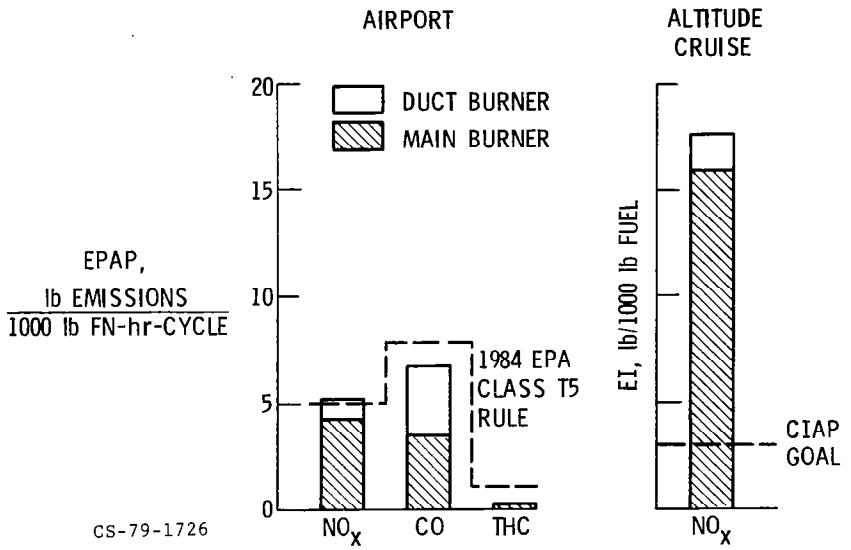

Figure XI-20

VSCE/F-100 COMPONENT TESTBED
INSTALLED IN X-16 STAND

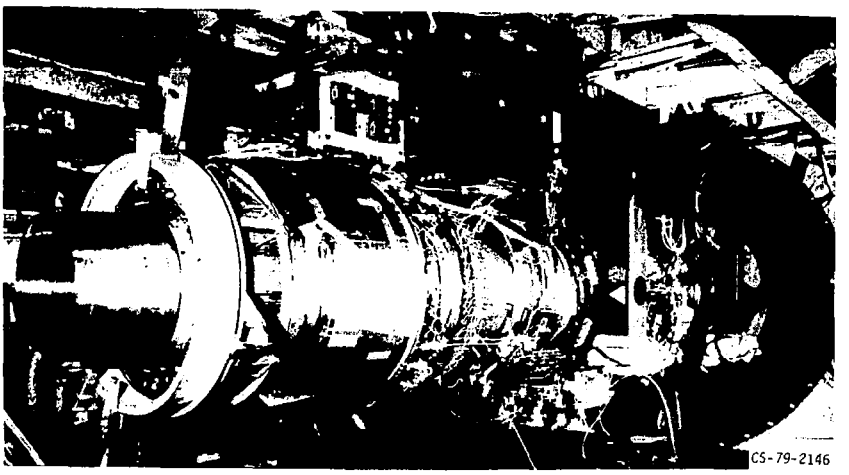

Figure XI-21

VSCE/F-100 COMPONENT TESTBED
WITH DUCT BURNER OPERATING

Figure XI-22

DOUBLE BYPASS ENGINE

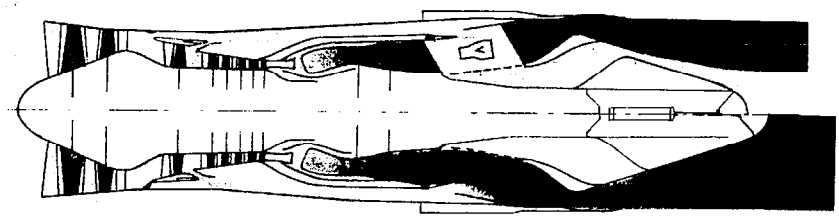

CS-79-1996

Figure XI-23

DOUBLE BYPASS ENGINE
GENERAL ELECTRIC CO.

TAKEOFF

SUBSONIC CRUISE

SUPERSONIC CRUISE

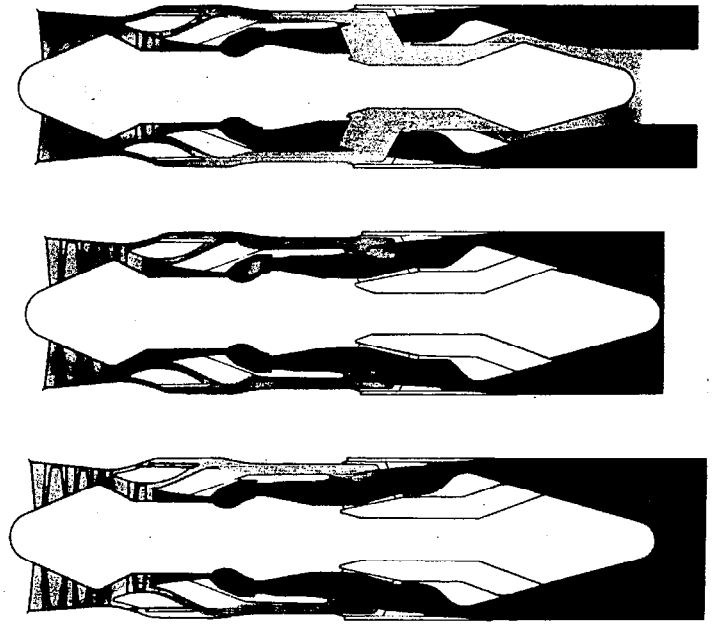

CS-79-1998

Figure XI-24

YJ101/EARLY ACOUSTIC TESTBED ENGINE

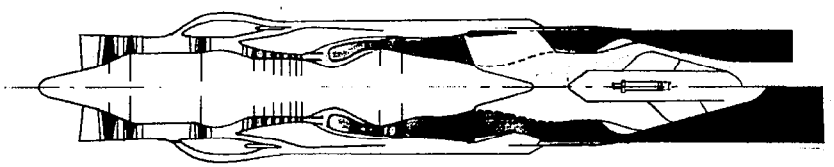

CS-79-2001

Figure XI-25

CALIBRATION NOISE TEST OF GE ENGINE

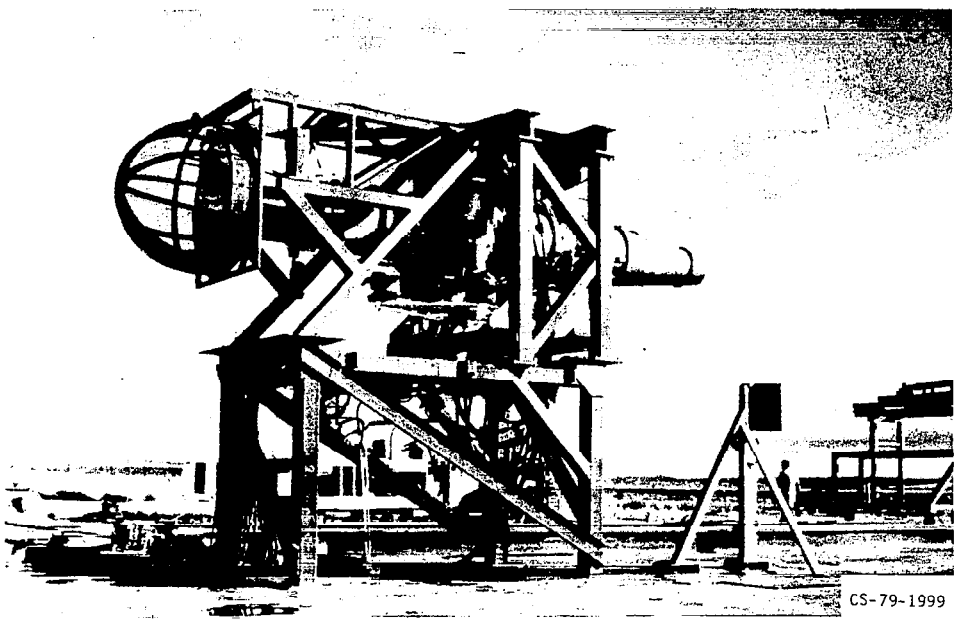

CS-79-1999

Figure XI-26

COANNULAR NOISE TEST OF GE ENGINE

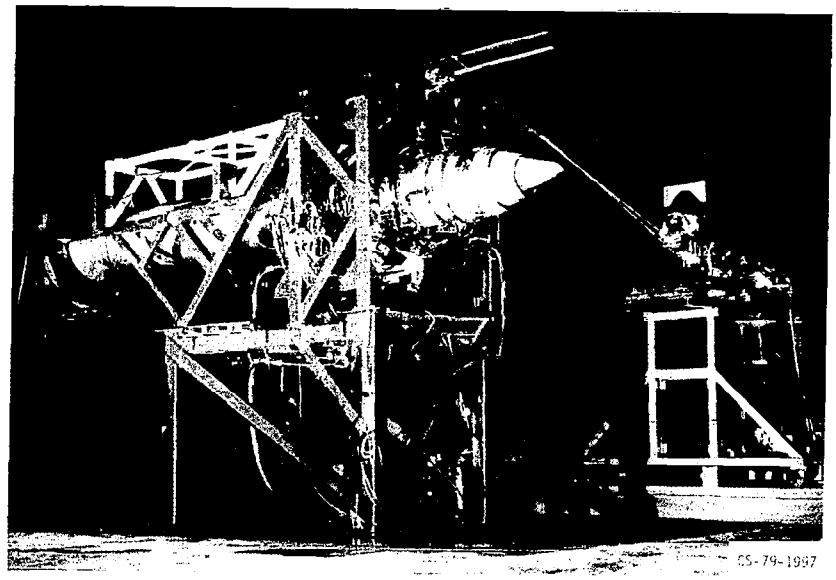

Figure XI-27

BYPASS SYSTEM LOSS COMPARISON

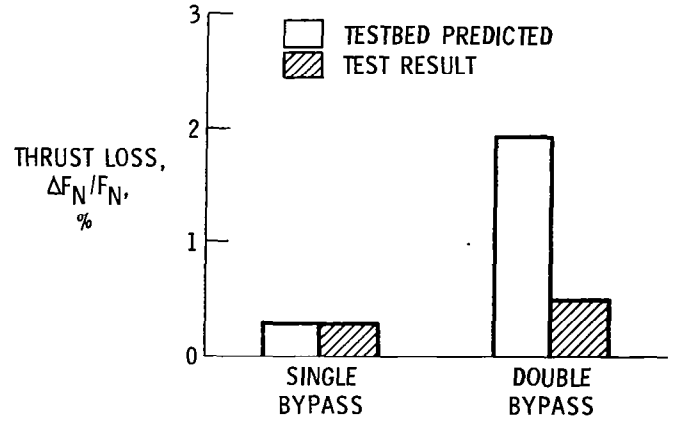

Figure XI-28

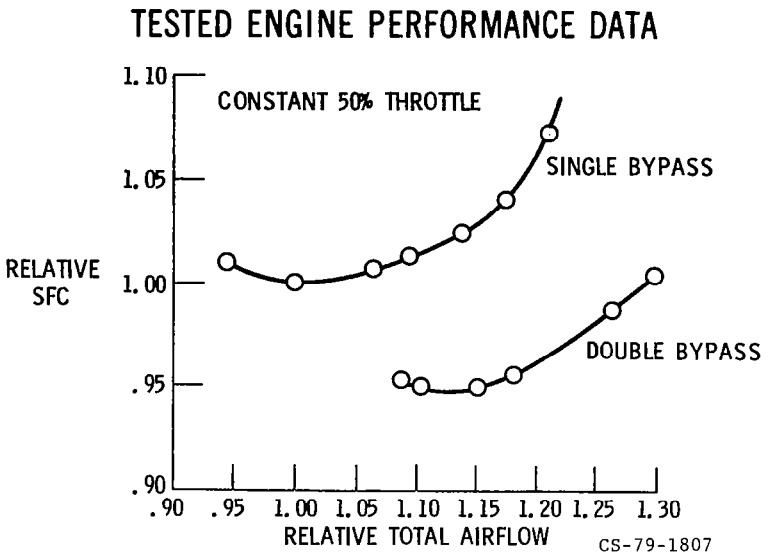

Figure XI-29

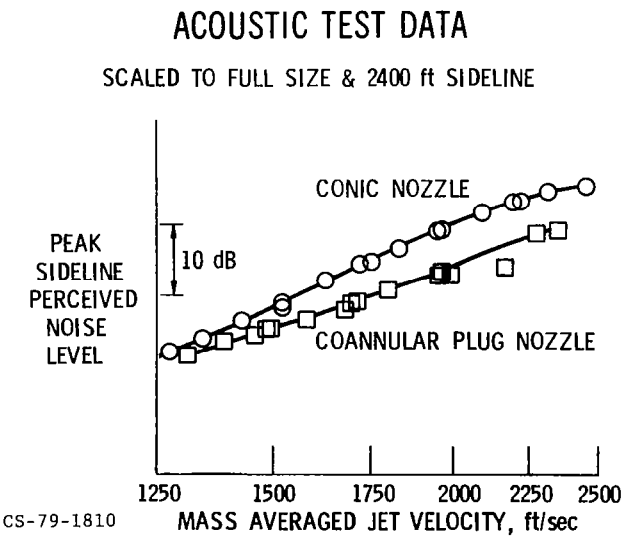

Figure XI-30

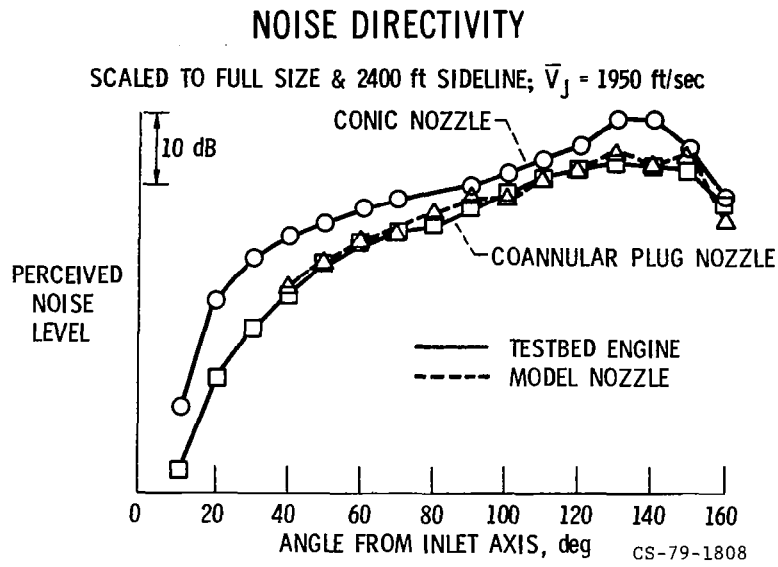

Figure XI-31

YJ101/CORE-DRIVEN TESTBED ENGINE

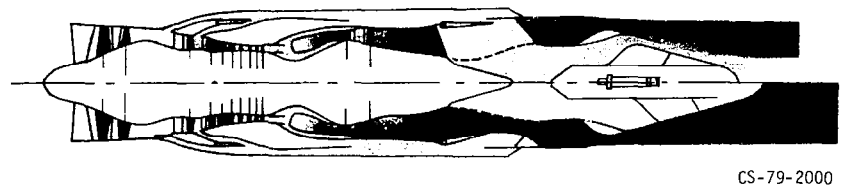

Figure XI-32

COANNULAR NOZZLE WITH SIMPLE SHALLOW CHUTE SUPPRESSOR

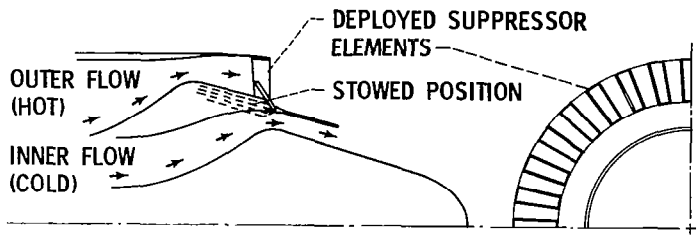

Figure XI-33

INLET DESIGN FACTORS

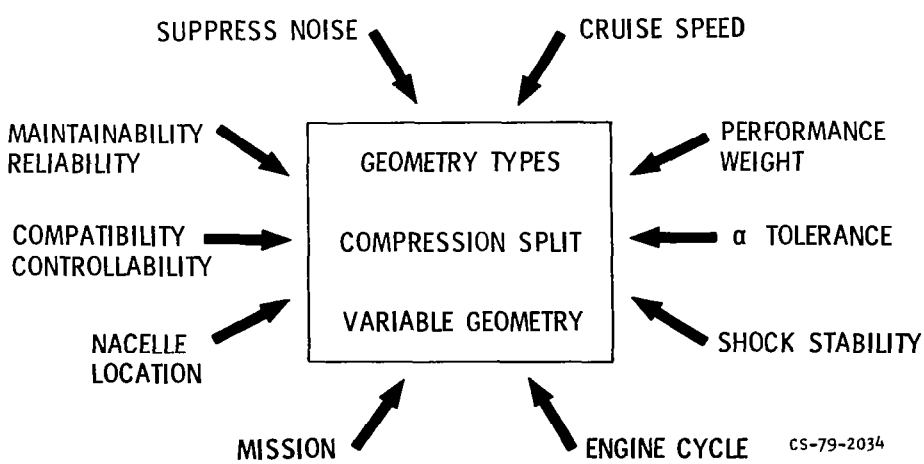

Figure XI-34

INLET GEOMETRY TYPES

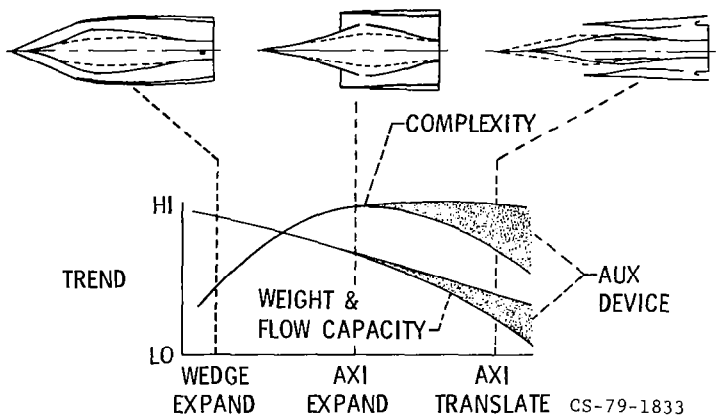

Figure XI-35

EXPANDING WEDGE INLET

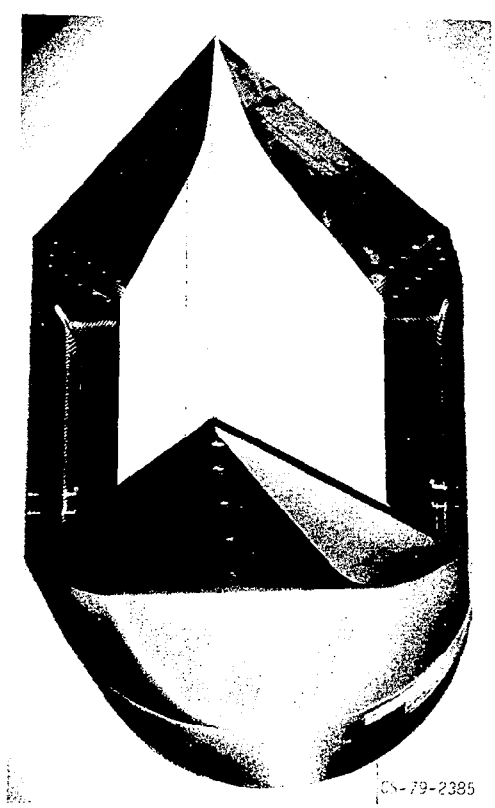

Figure XI-36

EXPANDING AXI INLET

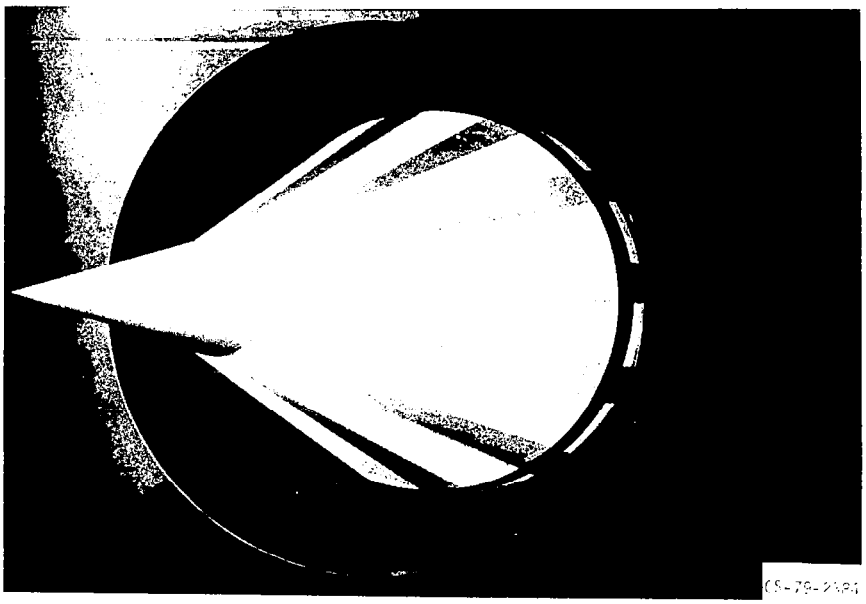

Figure XI-37

AXI-TRANSLATING INLET

Figure XI-38

EFFECT OF INLET INTERNAL COMPRESSION

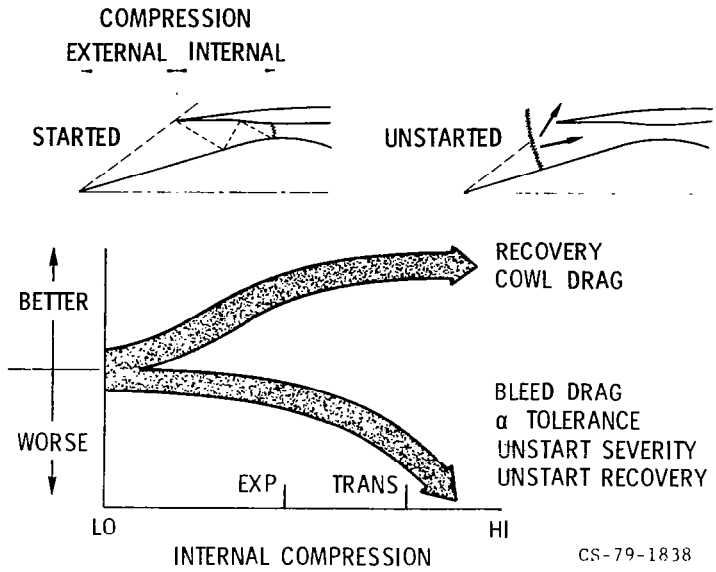

Figure XI-39

INLET VARIABLE GEOMETRY

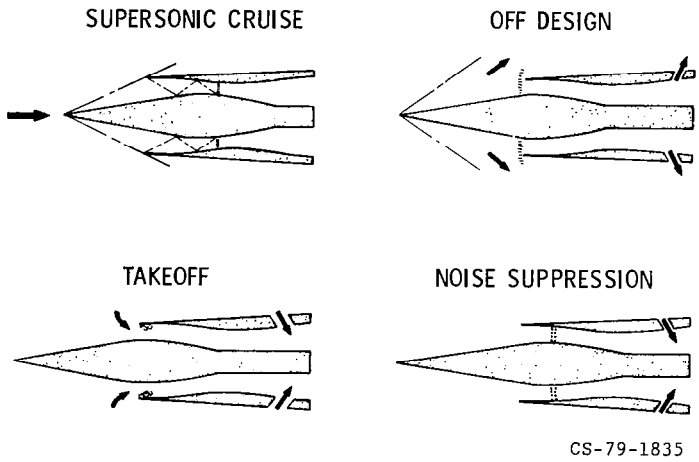

Figure XI-40

DOUGLAS INLET GEOMETRIES

CRUISE MACH = 2.2

TRANSLATING

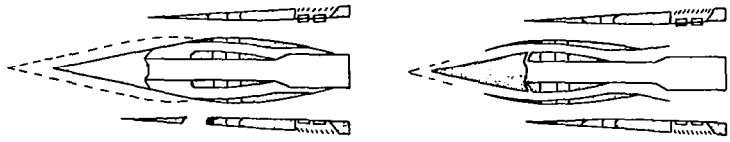

EXPANDING

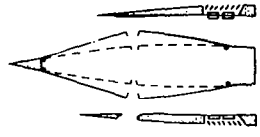

CS-79-1836

Figure XI-41

BOEING INLET GEOMETRIES

CRUISE MACH 2.4

TRANSLATING

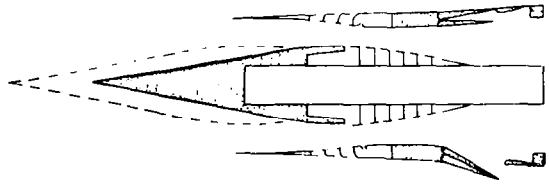

EXPANDING

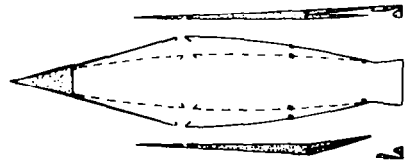

CS-79-1837

Figure XI-42

LOCKHEED INLET GEOMETRIES

CRUISE MACH = 2.55

TRANSLATING

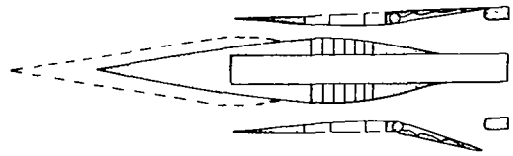

EXPANDING

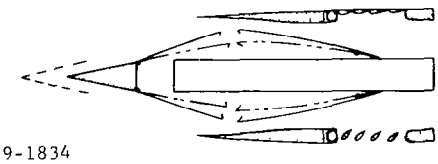

CS-79-1834

Figure XI-43

XII. HYPERSONIC PROPULSION

H. Lee Beach, Jr.

National Aeronautics and Space Administration
Lewis Research Center

Research at NASA on vehicles and propulsion systems for hypersonic flight in the atmosphere is aimed at providing viable technological options for future civil and military applications. Within the uncertain framework of social, economic, defense, and environmental issues, a wide spectrum of possibilities exists. It is imperative, therefore, that key technologies be pursued that can provide the alternatives when they are required. Various airbreathing and rocket propulsion system alternatives are shown in figure XII-1. Of the airbreathing systems, turbojets have the highest performance (as measured by specific impulse) up to Mach numbers of approximately 3. Above this speed, turbine inlet temperature constrains performance, and ramjets become more attractive. About Mach 6, dissociation losses caused by slowing the high-velocity stream to subsonic speeds greatly reduce ramjet performance. It is then more efficient to allow the engine internal flow to remain supersonic and the engine to operate as a scramjet (supersonic combustion ramjet). All systems in figure XII-1 except the turbojet are shown for both hydrocarbon and hydrogen fuels.

Hypersonic propulsion research is concerned with Mach numbers of 4 to 6 and beyond. At these speeds, the scramjet is the primary system of interest because of its obvious performance advantages. Specifically, the research program now under way at the NASA Langley Research Center deals with hydrogen-fueled scramjets. Hydrogen is being studied because it provides a very large performance benefit that yields specific impulse levels at Mach 7 comparable to those of JP-fueled turbojets at about Mach 2. Hydrogen also has the excellent and necessary capability to cool both the engine and parts of the airframe in high Mach number flight.

This paper discusses the current NASA program in hypersonic propulsion. The program is first put into context by a brief discussion of past and other ongoing scramjet programs. The status of the research is then discussed; and emphasis is given to component developments, computational methods, and preliminary ground tests at Mach 4 and 7 of subscale scramjet engine modules.

BACKGROUND

The United States' commitment to scramjet research began in the early 1960's and has continued at various levels of effort through support from NASA, the U.S. Navy, and the U.S. Air Force. Much work has been done, and considerable progress can be claimed in all pertinent technology areas. An excellent review of scramjet development efforts in the United States is given in reference 1. Much of the discussion in the next section is derived from that reference.

Brief Review of Scramjet Research

The U.S. Air Force became involved with scramjets 20 years ago through interest in external-burning and single-stage Earth-to-orbit vehicles. Engine development programs were sponsored with the United Aircraft Research Laboratory, the General Electric Co., General Applied Science Laboratories, and the Marquardt Co. Four research engines were built and ground tested in the 1960's. These engines were hydrogen fueled and generally achieved the internal performance levels that had been predicted. Features included in one or more of these engines were the variable-geometry inlet; staged fuel injection for operating over a wide Mach number range; rearward-facing steps for combustor-inlet isolation; and thermal compression. At the conclusion of these test programs, the Air Force began concentrating on smaller missile systems that used hydrocarbon fuels. Subsequent research has been related to piloting such missile systems.

U.S. Navy-sponsored scramjet research has continued since the early 1960's under the direction of Johns Hopkins University's Applied Physics Laboratory (APL). This work has been missile related, with emphasis on unmanned systems that are constrained by the launching and handling requirements of ships. Such systems are volume limited; therefore, storable fuels and passive cooling are most desirable. The research has included testing of both engine components and complete engine models. Inlet developments have resulted in inverted, internal, axisymmetric compression flow fields split into three or four modules. These inlets appear to perform well and use sweep to minimize heat-transfer problems. The combustor configuration that has evolved from many tests of autoignitible hydrocarbon fuel uses a rearward-facing step, a constant-area isolation section, and a conical section that expands to an area ratio of 2. Free-jet tests of engine models with these features have been conducted at Mach numbers of 5, 5.8, and 7. Net thrust (thrust greater than engine drag) was measured for at least one configuration at all three Mach numbers. More recent research at APL has focused on an integral-rocket, dual-combustion ramjet for the volume-limited missions. This concept uses an embedded dump-combustor

ramjet system to serve as a fuel-rich, hot-gas generator for a primary scramjet system (ref. 2).

NASA also began its scramjet research in the 1960's with a program to advance the technology for manned vehicles. The Hypersonic Research Engine (HRE) project provided the focus for this effort; the original goal was to test a regeneratively cooled, flight-weight engine on the X-15 research airplane. Although the cancellation of the X-15 program precluded the achievement of this goal, two engines were designed and built by Garrett AiResearch and ground tested. The HRE was axisymmetric and used a translating spike to position the shocks and to control the inlet airflow over a Mach number range of 4 to 8. Combustor operation was controlled by staging fuel injection streamwise over the Mach number range. Structural, nonburning tests of a complete flight-weight, regeneratively cooled version of this engine were made in the Langley Research Center's 8-Foot High-Temperature Structures Tunnel. Thrust performance was determined in separate tests at the Lewis Research Center's Plum Brook Station of a water-cooled, heavy-walled version of the engine. The measured internal performance at Mach 5 to 7 was very close to the design goal. These two sets of tests verified the structural and cooling design and manufacturing techniques and demonstrated the feasibility of good internal thrust over a range of flight speeds.

Although good internal thrust performance remains a primary goal for any propulsion system, it must also achieve high installed performance (internal thrust minus external drag). This fact has driven the emphasis of scramjet research away from most of the engine types examined in the 1960's to concepts that are intimately integrated with the vehicles on which they are installed.

Airframe-Integrated Scramjet Concept

The meaning of airframe - propulsion-system integration for scramjets is illustrated in figure XII-2. In this concept, the entire undersurface of the vehicle is part of the propulsion system. Integration is needed at high Mach numbers because almost all the airflow between the vehicle and its bow shock is required for good performance. This suggests an inlet capture area with an annular shape. By splitting the annular area into smaller rectangular modules, the primary engine becomes a system of identical units of a size and shape appropriate for testing in ground facilities. Within this framework, the vehicle forebody performs a significant part of the inlet function, and the afterbody becomes the nozzle expansion surface. Engine module external surfaces can therefore be easily shaped to minimize installation losses, and the vehicle base region can provide the large expansion ratios that are necessary.

The rectangular module concept that takes advantage of this approach is shown in the center of figure XII-2. Since the vehicle compresses the flow in the vertical direction, the module inlet side walls have wedge shapes to compress the flow horizontally. This tends to minimize flow distortion over a flight Mach number range. Sweep of these wedges, in combination with a recess in the cowl, allows spillage to occur efficiently with fixed geometry. Inlet compression is completed by three wedge-shaped struts located at the minimum-area section of the module. These struts also provide multiple planes for fuel injection and therefore shorten the required combustor length. A cross-sectional view of the strut region, shown to the left in figure XII-2, illustrates the technique used to control the distribution of heat release in the combustor. At Mach numbers of 7 and higher, almost all the fuel is injected perpendicular to the airflow over the struts. This is an inherently fast mixing process and results in rapid heat release close to the struts for maximum performance. At Mach numbers below 6, too much perpendicular injection produces too rapid mixing and reaction, and the flow thermally chokes. To prevent this, most of the fuel is injected from the base of the struts parallel to the local flow direction. Mixing thus occurs much more slowly, and the heat release is stretched out over the length of the combustor.

The scramjet concept now under investigation is therefore a fixed-geometry module using three dimensionality and mixed-mode fuel injection to allow flight over a wide Mach number range. The sections that follow describe the nature and status of the research program to support this concept.

THE AIRFRAME-INTEGRATED RESEARCH PROGRAM

The NASA Langley Research Center is currently engaged in a broad-based research program (refs. 3 and 4) to establish the aerothermodynamic lines and performance potential of this scramjet airframe-integrated module concept. The program includes research on engine components (inlets, combustors, and nozzles), computational fluid mechanics for internal flows, component integration (subscale engines), structures, and flow diagnostics. The performance of the module itself is the key technology area and is the focus of the remaining discussion. Airframe integration (including nozzles) and structures are also briefly covered for completeness.

Inlet Research

Four generations of aerodynamic tests over a period of years have brought the inlet concept to a relatively mature state of development (refs. 5 and 6). Figure XII-3 shows one of the test

models. A foreplate with boundary-layer trips was installed to partially simulate the boundary layer on the undersurface of a vehicle. One side wall of the model has been removed to show the struts and instrumentation rake used to measure flow profiles at the throat.

Tests were conducted at Mach numbers ahead of the inlet from 2.3 to 6, corresponding to flight Mach numbers from 3 to 8. Results were presented in the proceedings of the 1975 Aeropropulsion Conference (ref. 7) and indicated variations in throat Mach number, contraction ratio, mass capture, and pressure recovery similar to those of a variable-geometry inlet. It appears that the vehicle boundary layer can be ingested without separation or other problems, at least as long as the effects of the combustor flow do not feed forward.

Although some inlet testing has taken place in the last few years, the basic inlet has not changed significantly. Its performance is considered to be excellent; the key remaining question is that of inlet-combustor interaction, which is discussed in a later section.

Combustor Research

The difficulties in achieving rapid mixing and combustion in the fraction-of-a-millisecond residence times available in a supersonic combustor have dictated that considerable research be conducted on the physics and thermodynamics of such flows. Fuel injector and combustor configurations are experimentally evaluated by direct-connect tests in a combustion-heated facility (refs. 8 and 9). The facility burns a mixture of hydrogen, oxygen, and air to form a high-enthalpy test gas with an oxygen mole fraction identical to that of air. Stagnation conditions up to 500 psi and 4700° R can be produced; such values are representative of Mach 8 flight.

A large number of configurations has been tested over the past 8 years. These have included fuel injection from walls (refs. 10 to 12), from single struts with perpendicular or parallel injection (ref. 13), from multiple struts (ref. 14), and from swept struts (refs. 15 and 16). Through these tests, the mixing performance of the baseline concept has been established. Mixed-mode, perpendicular and parallel injection appears to provide a viable mechanism to control mixing and heat-release, and the design length of the module combustor appears to be adequate for approximately 95 percent mixing.

An interesting issue of potential importance emerged from several of these tests, as well as from the subscale engine tests discussed later. Inconsistencies in ignition and flameholding behavior were noted. For example, much-delayed ignition was

sometimes observed when rapid autoignition was expected. A simple autoignition test program was begun (ref. 17) to investigate these inconsistencies and to solve the ignition and flameholding problems without altering the basic mixing performance that had evolved through years of research.

The model used in these tests is shown schematically in figure XII-4. A Mach 2.7 nozzle was mounted at the exit of the combustion heater described previously. The injector model was a simple flat plate on which fuel injectors (usually three) were drilled near a rearward-facing step. Such steps are used on the fuel injection struts in the engine concept to help isolate the inlet from the combustor and to help stabilize the flame. The step is shown swept to simulate sweep in the engine. Variables in the test program were free-stream conditions, fuel temperature, wall temperature, sweep angle, boundary-layer thickness, and various injection parameters such as injector location relative to the step, injector size, and step size.

Figure XII-5 shows three typical photographs taken during the tests. All are for Mach 7-simulated conditions with a stagnation temperature of 4000° R and a static pressure of 1 atmosphere. The flow is from left to right in these photographs, and the step location has been indicated with an arrow. For injection 1.67 step heights upstream of the step ($x/h_s = -1.67$), ignition occurs at the point of injection, and the fuel continues to burn as it expands over the step. The problem with this configuration is its relatively high susceptibility to inlet-combustor interaction through boundary-layer feedback. When the injectors were moved just downstream of the step to $x/h_s = 1$, the base region apparently became too fuel rich, and ignition was severely delayed. This can, of course, have serious implications for engine performance. By moving the injectors an additional 2 step heights downstream to $x/h_s = 3$, this problem was alleviated. Ignition began near the injectors, and the flame stabilized at the step; this condition is the one desired for the engine. The 3-step-height criterion proved to be an optimum for locating the injectors, independent of sweep, as long as the distance was measured perpendicular to the sweep line.

Several other important results were produced by the ignition tests. There was a very large effect of boundary-layer (energy) thickness on the temperature required for ignition. For example, up to 1200 degrees R higher temperatures were needed to ignite the fuel with a thick (0.15 in.) boundary layer than with a boundary layer five times thinner. In addition, up to 700-degree R differences in ignition temperature were found for wall temperature differences of 200 degrees R, where the boundary-layer thicknesses were about the same. Heating the hydrogen fuel had only a small effect. However, the hydrogen temperature was always much lower than the air temperature, and mixture tem-

peratures near the ignition point were therefore not affected substantially. Interestingly, the pressure-scale product was confirmed in these tests to be a scaling parameter for ignition in scramjet flow fields.

The results of this simple test program have explained inconsistencies observed in various tests and have provided valuable design and scaling information for use in future configurations. It is clear that sensitivities are large, and that extreme care must be taken in controlling boundary-layer thickness, exact injector location, and wall temperature for effective ground simulation.

Computational Fluid Mechanics Research

To support the inlet and combustor component research, a significant effort in computational fluid mechanics for scramjets has been under way for several years. The objective is to provide reasonably detailed and reasonably accurate computational tools for engine design and analysis, with emphasis on such performance parameters as combustion efficiency and heat-release control. The scramjet environment is an extremely challenging one for analysis since the flow field is highly three-dimensional and has turbulent mixing and chemical reaction, regions of separation and recirculation, and shock waves throughout the inlet and combustor. Relative to other propulsion systems, however, the scramjet presents a unique opportunity. Because the hydrogen is injected as a gas, the combustor flow is single phase. In addition, hydrogen-air chemistry is the most studied and best understood of any fuel. The geometry is also quite simple (relative to turbojets), and the fact that the flow remains largely supersonic gives several computational advantages.

Because of the relative lack of understanding of the combustor flow field, recent emphasis has been on the combustor. Three-dimensional codes have been developed (refs. 18 and 19) for computing scramjet flows downstream of the fuel-injector struts, where separation and recirculation no longer occur, and the equations describing the flow are parabolic. These codes are spatially marching, require two-dimensional storage, and give good agreement with experimental data (refs. 20 and 21). The most serious problem in applying them is the specification of initial conditions, which must come from experimental data or some other analysis describing the injector-strut near field. Research is now under way to address this near-field analysis problem.

Figure XII-6 shows the sample problem being used for near-field focus. It depicts the sonic, underexpanded injection of a hydrogen jet into a supersonic crossflow. The features include

jet shocks from the underexpansion, separation of the boundary layer ahead of the jet, recirculation zones ahead of and behind the jet, and bow shocks off the separated zone and the jet. Several methods are being used to solve this problem. A semi-empirical method (ref. 22) has been shown to give acceptable results for certain cases; a more exact method to solve the Navier-Stokes equations describing the flow is also being pursued. In the latter case, the differential equations are elliptic, and the computing requirements increase tremendously over cases with parabolic equations. For example, complete computer storage is required for each spatial dimension. Full three-dimensional storage is therefore needed for three-dimensional problems. Computer run times also tend to increase dramatically because time-relaxation techniques requiring many steps are necessary.

The problem shown in figure XII-6 has recently been analyzed two dimensionally (ref. 23); that is, the fuel injector was a slot rather than a discrete orifice. Velocity vectors from such an analysis with an air Mach number of 2.5 are shown in figure XII-7. The top and bottom of the plot correspond to the bounding walls. The direction of the arrow indicates flow direction, and the arrow length indicates relative velocity. Some of the flow-field structure shown in figure XII-6 has been superimposed for clarity. Both the front and rear recirculation zones have been computed as shown by the vectors turning around. The vectors also turn up, then back, as the flow crosses the up-running bow shock and its down-running reflection. The bow shock for this particular calculation was strong enough to separate the top-surface boundary layer. Fuel mass contours are shown in figure XII-8. The lines are for constant mass fraction and are useful to indicate where the fuel is going. Similar plots are, of course, generated for temperature, pressure, and other flow variables.

This two-dimensional analysis has progressed to the point that comparisons with experimental data are now being made, and plans to extend the technique to three dimensions are being formulated. The ultimate objective is to couple this near-field approach (or a semi-empirical one) with the three-dimensional downstream approach to provide a complete combustor analysis capabilty. It should be emphasized that in all computations of this type, the results are only as reliable as the turbulence and reaction models that go into them. Such modeling is perhaps the weakest link of all in the analysis of scramjet flows. Currently, two-equation turbulence models are being used in the parabolic codes, and the elliptic code uses an algebraic model. Reaction schemes ranging from complete reaction to full finite-rate chemistry are being used, and modeling to account for combined turbulence and reaction effects is also being done. It is

clear that computational fluid mechanics for scramjets has come a long way in the last several years. Complex two- and three-dimensional flows are being computed, and these calculations are now beginning to affect both scramjet analysis and design. For example, strut contours in the latest subscale engine model were designed with such analyses, and detailed mixing and performance data from direct-connect tests are now being analyzed. The future importance of computational fluid mechanics for scramjets therefore appears to be large.

Component Integration Research

Concepts, results, and experience in component testing have been assembled in the form of component integration, or subscale engine modules. Initial wind-tunnel tests at flight-simulated Mach numbers of 4 and 7 have been conducted in two ground facilities (ref. 24). These tests are the first known for an airframe-integrated concept and were intended for research rather than performance demonstration. Mach 4 testing was done at the General Applied Science Laboratories (GASL), Inc., Westbury, N.Y.; to date, there have been approximately 70 tests totaling 12 minutes test time. Mach 7 testing was conducted in the Langley Scramjet Test Facility; to date, there nave been approximately 100 tests totaling about 25 minutes test time. Both flight Mach numbers were simulated because they represent engine operation over a wide Mach number range. At Mach 7, almost all the captured flow passes through the engine, most of the fuel is injected perpendicular to the airflow coming by the struts, and the fuel will probably autoignite. In contrast, Mach 4 spillage can be as much as 40 percent, most of the fuel is injected parallel to the airflow, and the fuel will not autoignite. The susceptibility to inlet combustor interactions should also be quite different at the two Mach numbers.

The model being tested at Mach 7 is shown in figure XII-9. It is constructed of copper and is primarily a heat-sink design with water cooling only in high-heat-flux areas such as leading edges. The engine is heavily instrumented to measure internal wall static pressures, temperatures, and heating rates. It is mounted in the test facility on a one-component force balance to measure thrust and drag. Attention was given in the design to allow research on different configurations by changing or substituting components. The model is 6.4 inches wide, 8 inches high, and about 5 feet long. The primary differences in the Mach 4 engine are that it is constructed of nickel and is entirely a heat sink.

The Langley Scramjet Test Facility is shown in figure XII-10. It is an arc-heated facility, supplying 10 megawatts of power to provide Mach 7 simulation of 4000° R stagnation temperature and 116 000 feet altitude. The front part of the model is

visible in the test-section viewing port. In these tests, vehicle bow-shock precompression that would occur in flight is simulated by expanding the Mach 7 energy flow to only Mach 6. The facility at GASL uses a hydrogen combustion heater and expands to Mach 3.4 for a Mach 4 simulation of 1600° R and 70 000 feet. Ingestion of the vehicle undersurface boundary layer is simulated at both Mach numbers by alining the engine top surface with the nozzle exit so as to ingest the facility boundary layer. This is shown more clearly in the facility schematic at the top of figure XII-11.

Preliminary scramjet engine performance is shown at the bottom of figure XII-11. The performance parameter ΔF, defined as the difference in the thrust balance reading with and without fuel, is plotted as a function of fuel-air ratio (percent stoichiometric). The symbols represent selected experimental data, and the lines are theoretical predictions representing performance levels that would be required to cruise a hypersonic aircraft. For ratios less than 50 percent, the experimental data approach the predicted performance levels. This is a very encouraging result from preliminary tests. For flight application, however, it will be necessary to operate at equivalence ratios near 1. No experimental data are shown at higher ratios because at both Mach numbers inlet-combustor interactions occurred that adversely affected performance. These interactions were not surprising, particularly at Mach 4, and appear to be caused by a combination of boundary-layer feedback effects and local thermal choking leading to complete engine unstart.

The challenge for future tests is obviously to raise the fuel-air ratio without causing inlet-combustor interactions. To help insure that this will occur, inlet and combustor component tests to examine various aspects of the interaction problem have been started. The objective for the component integration research is to demonstrate useful levels of thrust within the next several years. Two more generations of models and tests will probably be required to accomplish this.

Other Related Research

Several areas of research relating directly to the scramjet module developments already discussed involve significant commitments in other disciplines. These include airframe integration, structures, and flow diagnostics.

As stated earlier, intimate propulsion-system - airframe integration is necessary for efficient hypersonic cruise. This involves careful design of the vehicle forebody so as to provide aerodynamic efficiency and high-quality flow to the module inlet. It also involves extremely careful design of the aft

vehicle surface (or engine nozzle), which at Mach 6 generates about half the net thrust of the propulsion system. The nozzle flow is supersonic and must account for interactions between module wakes, spillage from the inlet, and other effects that change with altitude and flight Mach number. These very complex problems are currently being studied through a combination of sophisticated computational methods (ref. 25) and experimental simulation (ref. 26).

Structural concepts for regeneratively cooled scramjets are also being developed. The starting point for the current research was the HRE technology mentioned previously. The HRE used a Hastelloy skin backed by an integral offset-fin heat exchanger through which the hydrogen fuel was circulated for cooling. Thermal cycle life was estimated to be approximately 100 for that design. As discussed in reference 27, this is extended to about 500 cycles by changing to the airframe-integrated design approach. An additional 500 cycles can be realized by improved fabrication techniques in which fin coolant passages are photochemically etched into the aerodynamic skin and hot-skin brazing is eliminated. Future improvements in materials could raise the expected engine cycle life at least another order of magnitude. These and other structural problems related to scramjets and fuel injection struts are now being investigated by AiResearch (ref. 28).

Flow diagnostic limitations for both combustor and engine flow fields continue to affect both the kind and quality of experimental data acquired. In-stream probes for reacting flows tend to be quite large, since they must be water cooled, and they almost invariably perturb the state of the stream in which they are attempting measurements. Using nonintrusive techniques is therefore very desirable. In response to the need for more and better measurements in reacting systems, several nonintrusive approaches are being examined to measure static temperature and/or species concentration. Infrared and sodium-line-reversal techniques have either been tried or are being implemented, although neither is expected to give the kind of detailed data that are being sought. A method that appears to have promise for making temperature measurements uses the low-resolution absorption spectra of the OH (hydroxyl) radical associated with electronic transitions in the ultraviolet (ref. 29). The near-term application of this technique will involve spatially averaged measurements across a combustion duct at several streamwise stations. For spatially resolved measurements, a fiber-optics probe that reduces the optical path length to approximately 0.5 centimeter is being designed. Ultimately, the solution to combustion measurement problems may be found in coherent anti-Stokes Raman spectroscopy (CARS). The signal strength and laser-like signal character of CARS give inherent advantages over conventional Raman spectroscopy. The feasibility of using this technique to make temperature and species measurements in

supersonic combustion flow fields is currently being examined under an NASA contract (NAS1-15491) with United Technologies Research Center and Dr. Alan Eckbreth. A conceptual CARS system design for the Langley Scramjet Test Facility has been formulated.

CONCLUDING REMARKS

Over the past several years, considerable progress has been made toward the goal of developing a viable airframe-integrated scramjet concept. The fixed-geometry inlet has been demonstrated to give good performance over a wide range of Mach numbers. Also, mixed-mode perpendicular and parallel fuel injection has been shown to be an acceptable way to control heat release over a Mach number range. Initial research tests of two subscale engine modules have been conducted, and results look quite promising. In addition, detailed analytical approaches to supersonic combustion are now beginning to affect design, and the related technologies of airframe integration, structures, and flow diagnostics have continued to advance.

It is clear, however, that many challenges remain. Operation at high fuel-air ratios must be achieved without inlet-combustor interactions. The aerothermodynamic design must be optimized, although the detailed design might be mission dependent. Ultimately, the airframe-integrated scramjet technology must be demonstrated both on the ground and in flight. Flight tests will be required since the vehicle is actually an important part of the propulsion system. Such demonstrations are expected to verify the viability of an airframe-integrated scramjet propulsion system option for future systems.

REFERENCES

1. Waltrup, P. J.; Anderson, G. Y.; and Stull, F. D.: Supersonic Combustion Ramjet (Scramjet) Engine Development in the United States. Proceedings of Third International Symposium on Air Breathing Engines, DGLR-Fachbuch, Vol. 6, Deutsche Gesellschaft fuer Luft- und Raumfanrt, Cologne, 1976, pp. 835-861.

2. Billig, F. S.; Waltrup, P. J.; and Stockridge, R. D.: The Integral-Rocket, Dual-Combustion Ramjet: A New Propulsion Concept. Fourth International Symposium on Air Breathing Engines, American Institute of Aeronautics and Astronautics, Inc., 1979, AIAA Paper 79-7044, pp. 433-444.

3. Jones, R. A.; and Huber, P. W.: Toward Scramjet Aircraft. Astronautics and Aeronautics, vol. 16, no. 2, Feb. 1978, pp. 38-48.

4. Jones, R. A.; and Huber, P. W.: Airframe-Integrated Propulsion System for Hypersonic Cruise Vehicles. Recent Advances in Structures for Hypersonic Flight, NASA CP-2065-Pt. 1, 1978, pp. 39-45.

5. Trexler, C. A.; and Souders, S. W.: Design and Performance at a Local Mach Number of 6 of an Inlet for an Integrated Scramjet Concept. NASA TN D-7944, 1975.

6. Trexler, C. A.: Inlet Performance of the Integrated Langley Scramjet Module. AIAA Paper 75-1212, Sept. 1975.

7. Anderson, G. Y.: Hypersonic Propulsion. Aeronautical Propulsion, NASA SP-381, 1975, pp. 459-474.

8. Russin, W. R.: Performance of a Hydrogen Burner to Simulate Air Entering Scramjet Combustors. NASA TN D-7567, 1974.

9. Eggers, J. M.: Composition Surveys of Test Gas Produced by a Hydrogen-Oxygen-Air Burner. NASA TM X-71964, 1974.

10. Rogers, R. C.; and Eggers, J. M.: Supersonic Combustion of Hydrogen Injected Perpendicular to a Ducted Vitiated Airstream. AIAA Paper 73-1322, Nov. 1973.

11. Anderson, G. Y.; et al.: Investigation of Step Fuel Injection for an Integrated Modular Scramjet Engine. Thirteenth JANNAF Combustion Meeting, Vol. 3, CPIA Publ-281, 1976, pp. 175-189.

12. Rogers, R. C.: Influence of Fuel Temperature on Supersonic Mixing and Combustion of Hydrogen. AIAA Paper 77-17, Jan. 1977.

13. Anderson, G. Y.; and Gooderum, P. B.: Exploratory Tests of Two Strut Fuel Injectors for Supersonic Combustion. NASA TN D-7581, 1974.

14. McClinton, Charles R.; and Gooderum, P. B.: Direct-Connect Test of a Hydrogen-Fueled, Three-Strut Injector for an Integrated Modular Scramjet Engine. Fourteenth JANNAF Combustion Meeting, Vol. 2, CPIA Publ-292, 1977, pp. 489-505.

15. Anderson, G. Y.; et al.: Experimental Investigation of a Swept-Strut Fuel-Injector Concept for Scramjet Application. NASA TN D-8454, 1977.

16. Northam, G. B.; Trexler, C. A.; and Anderson, G. Y.: Characterization of a Swept-Strut Hydrogen Fuel Injector for Scramjet Applications. Presented at the 15th JANNAF Combustion Meeting, Newport, Rhode Island, Sept. 11-15, 1978.

17. McClinton, C. R.: Autoignition of Hydrogen Injected Transverse to a Supersonic Airstream. AIAA Paper 79-1239, June 1979.

18. Markatos, N. C.; Spalding, D. B.; and Tatchell, D. G.: Combustion of Hydrogen Injected into a Supersonic Airstream (The SHIP Computer Program). NASA CR-2802, 1977.

19. Pan, Y. S.: The Development of a Three-Dimensional Partially Elliptic Flow Computer Program for Combustor Research. NASA CR-3057, 1978.

20. Pan, Y. S.; Drummond, J. P.; and McClinton, C. R.: Comparison of Two Computer Programs by Predicting Turbulent Mixing of Helium in a Ducted Supersonic Airstream. NASA TP-1166, 1978.

21. Pan, Y. S.: Evaluation of the Three-Dimensional Parabolic Flow Computer Program SHIP. NASA TM-74094, 1978.

22. Rogers, R. C.: A Model of Transverse Fuel Injection Applied to the Computation of Supersonic Combustor Flow. AIAA Paper 79-0359, Jan. 1979.

23. Drummond, J. P.: Numerical Solution for Perpendicular Sonic Hydrogen Injection into a Ducted Supersonic Airstream. AIAA J., vol. 17, no. 5, May 1979, pp. 531-533.

24. Guy, R. W.; and Mackley, E. A.: Initial Wind Tunnel Tests at Mach 4 and 7 of a Hydrogen-Burning, Airframe-Integrated Scramjet. Fourth International Symposium on Air Breathing Engines. American Institute of Aeronautics and Astronautics, Inc., 1979, AIAA Paper 79-7045, pp. 347-358.

25. Dash, S. M.; and Del Guidice, P. D.: Numerical Methods for the Calculation of Three-Dimensional Nozzle Exhaust Flow Fields. Aerodynamic Analyses Requiring Advanced Computers, Part 1, NASA SP-347-Pt-1, 1975, pp. 659-701.

26. Cubbage, J. M.; Talcott, N. A.; and Hunt, J. L.: Scramjet Exhaust Simulation for Hypersonic Aircraft Nozzle Design and Aerodynamic Tests. AIAA Paper 77-82, Jan. 1977.

27. Kelly, H. N.; et al.: Recent Advances in Convectively Cooled Engine and Airframe Structures for Hypersonic Flight. Eleventh Congress of the International Council of the Aeronautical Sciences, J. Singer and R. Staufenbiel, eds., International Council of the Aeronautical Sciences Secretariat, Cologne, West Germany, 1978, pp. 137-151.

28. Killackey, J. J.; et al.: Thermal-Structural Design Study of an Airframe-Integrated Scramjet. (AIRESEARCH-77-13967, AiResearch Mfg. Co.; NASA Contract NAS1-13984.) NASA CR-145368, 1978.

29. Burde, D. H.; and Neer, M. E.: The Advanced Development of a High Frequency Response Spectroscopic Probe for Analysis of Supersonic Combustor Flow Fields. (ARAP-335, Aeronautical Research Associates of Princeton, Inc.; NASA Contract NAS1-14853.) NASA CR-145363, 1978.

PROPULSION ALTERNATIVES

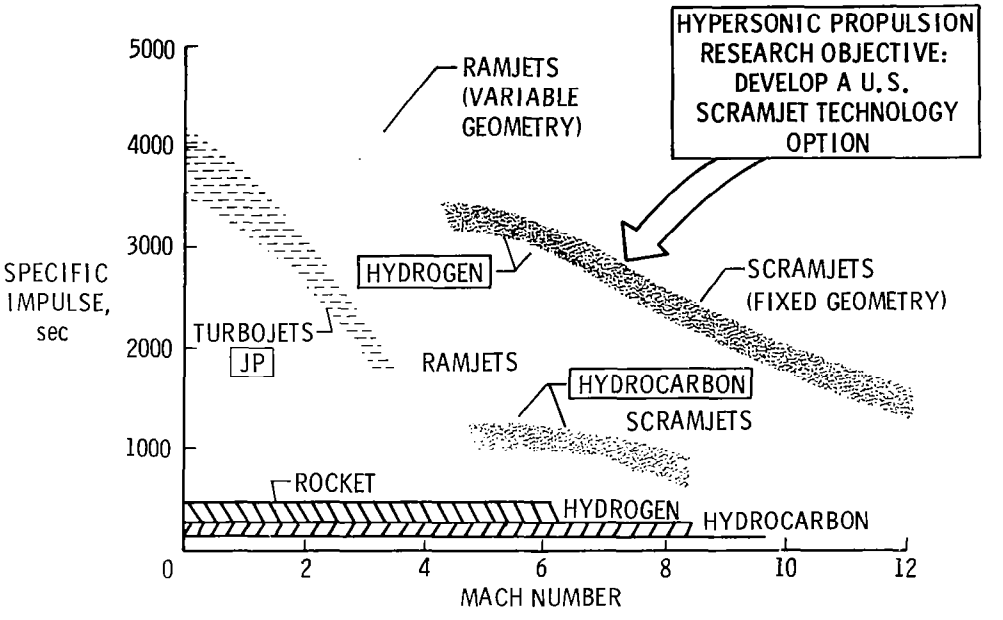

Figure XII-1

AIRFRAME-INTEGRATED SUPERSONIC COMBUSTION RAMJET

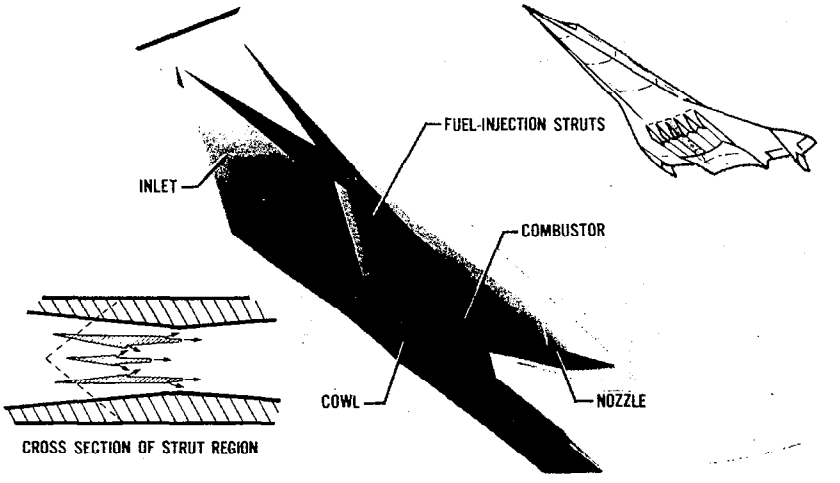

Figure XII-2

AIRFRAME-INTEGRATED INLET MODEL

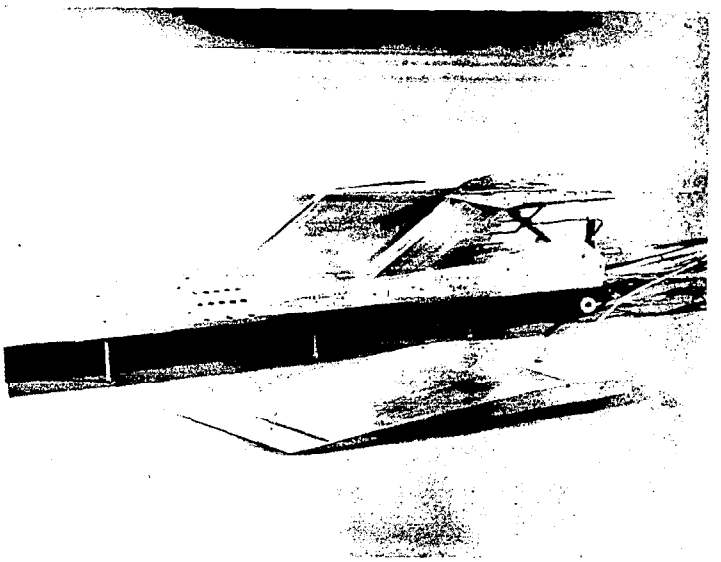

Figure XII-3

DIRECT-CONNECT AUTOIGNITION MODEL

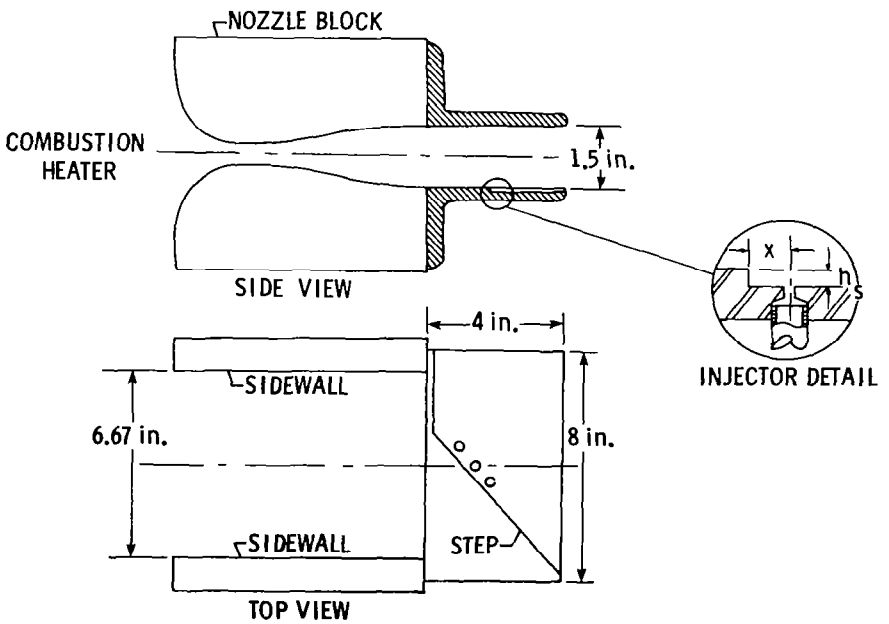

Figure XII-4

EFFECT OF INJECTOR LOCATION ON IGNITION

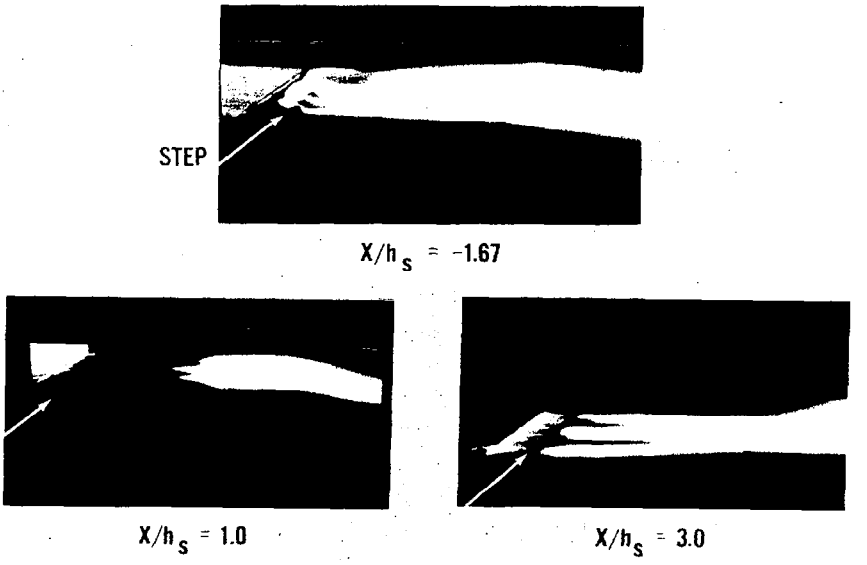

Figure XII-5

FUEL INJECTOR FLOW-FIELD SCHEMATIC

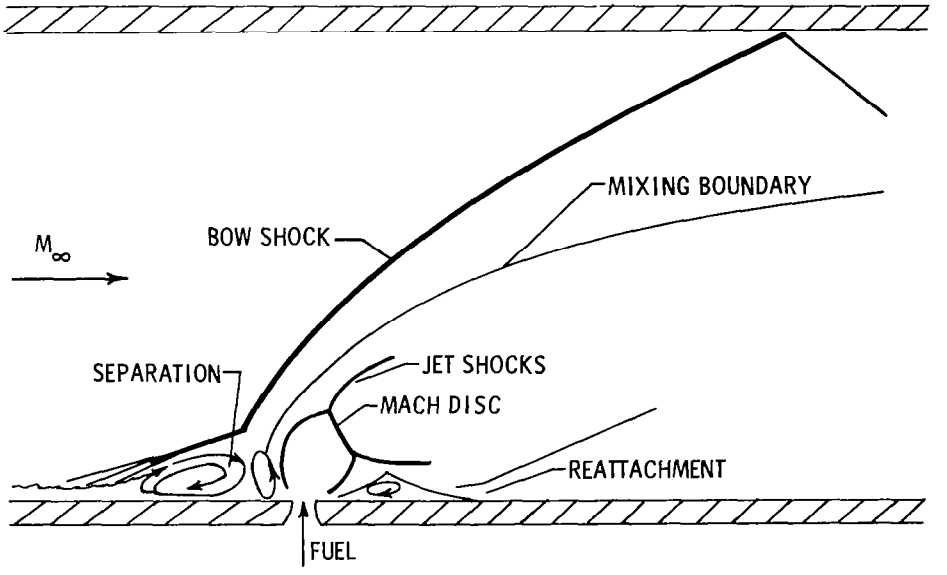

Figure XII-6

VELOCITY VECTORS FROM ELLIPTIC ANALYSIS

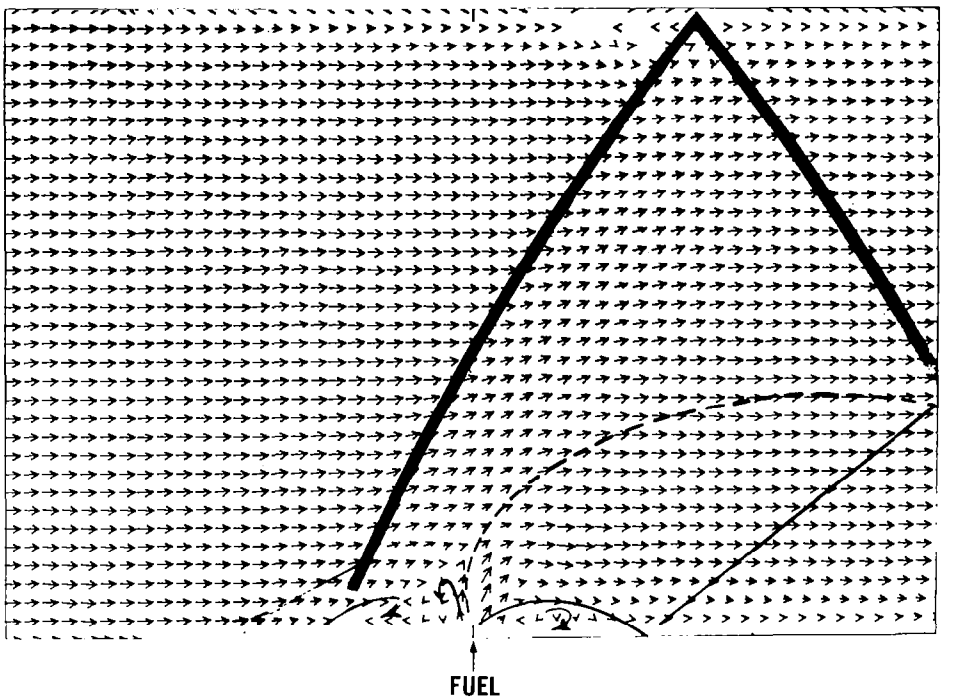

Figure XII-7

FUEL MASS CONTOURS FROM ELLIPTIC ANALYSIS

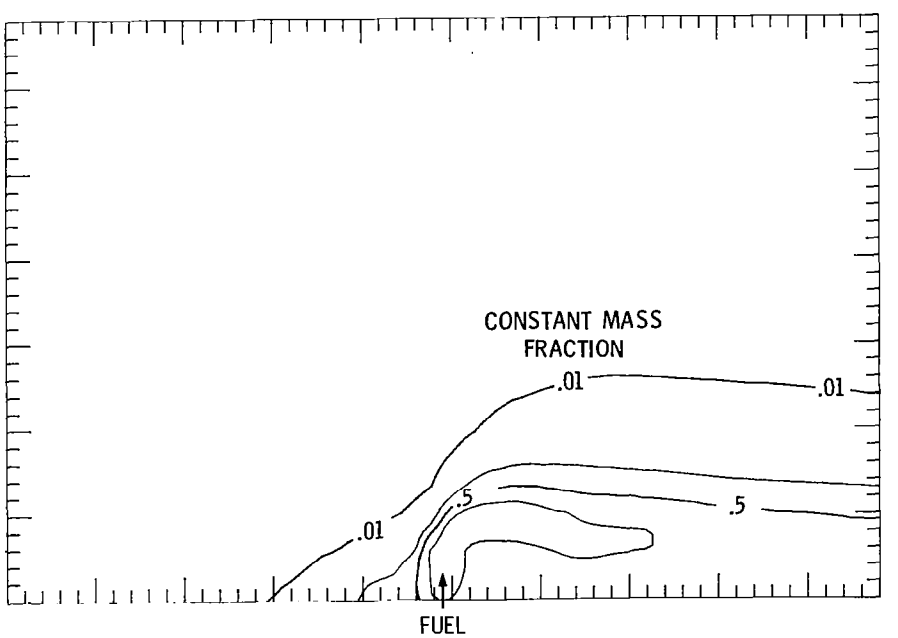

Figure XII-8

COMPONENT INTEGRATION MODEL

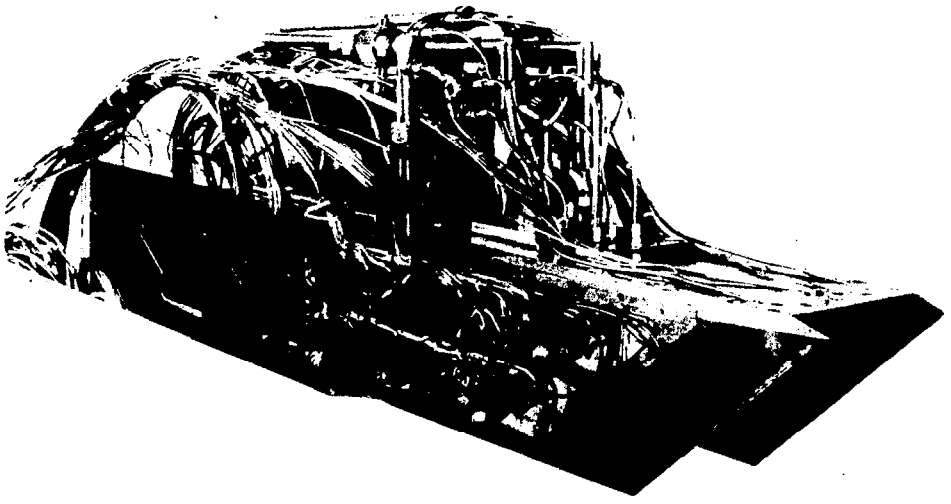

Figure XII-9

LANGLEY SCRAMJET TEST FACILITY

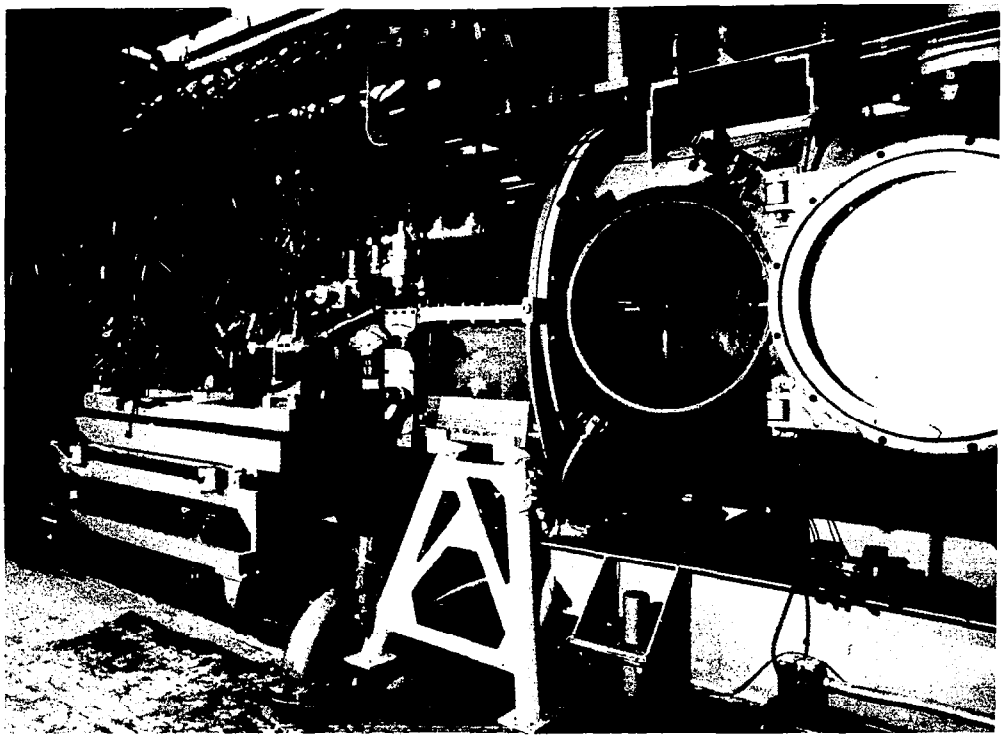

Figure XII-10

PRELIMINARY SCRAMJET ENGINE PERFORMANCE

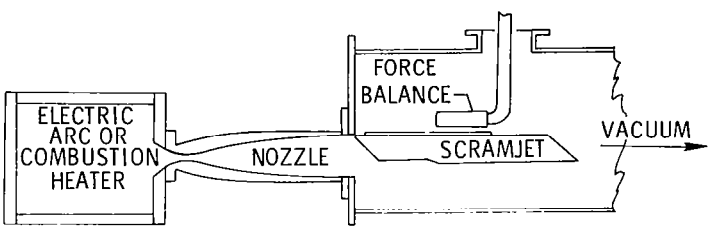

DIRECT THRUST MEASUREMENT AND SIMULATED AIRCRAFT FOREBODY INTEGRATION

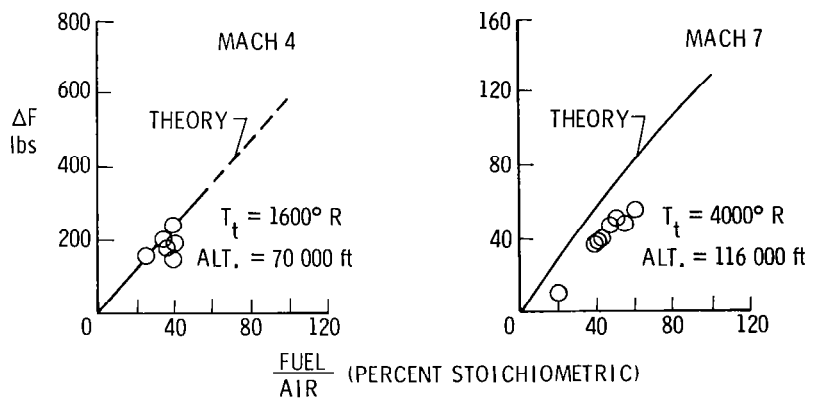

Figure XII-11

XIII. VERTICAL TAKEOFF AND LANDING (VTOL) PROPULSION TECHNOLOGY

Carl C. Ciepluch, John M. Abbott, Royce D. Moore, and James F. Sellers

National Aeronautics and Space Administration
Lewis Research Center

The propulsion systems of vertical-takeoff-and-landing (VTOL) aircraft present some challenging problems. Accordingly, an adequate propulsion technology base will be a key factor in developing these aircraft for either military or commercial use. This paper identifies the unique propulsion problems and advanced-technology requirements of VTOL aircraft. It also discusses programs in this area currently under way at the Lewis Research Center.

VTOL PROPULSION TECHNOLOGY REQUIREMENTS

The propulsion-system technical challenge is illustrated by several VTOL aircraft concepts. Figure XIII-1 shows one of several concepts for a Navy subsonic, multimission VTOL aircraft. Vertical lift is obtained by rotating the engine nacelles to a vertical attitude and by incorporating a lift fan in the aircraft nose. This concept is usually referred to as the tilting-nacelle approach.

In addition to providing the aircraft lift, the VTOL propulsion system must provide aircraft control during landing and takeoff. This is a new and relatively complex requirement for aircraft propulsion systems and their controls. Roll is controlled by modulating the thrust of the engines on either side of the fuselage. Pitch is controlled by modulating the thrust of the nose fan relative to that of the main engines. Aircraft yaw is usually controlled by using aerodynamic vanes in the propulsion exhaust.

Another unique requirement of the VTOL propulsion system is that its thrust response must be much faster than that available by the usual method of varying engine speed. Fast thrust response can be obtained by using either a variable-pitch fan or a variable-inlet-guide-vane fan.

The Navy aircraft (fig. XIII-1) is designed to land safely if a main engine core has to be shut down or fails. The engine fans

are mechanically interconnected through shafts and gearing, and the cores are sized so that either could land the aircraft. The power for driving the nose fan is also provided through shafting and gearing. This shafting and gearing must be capable of transmitting 15 000 horsepower and also must be lightweight and reliable. The gear and bearing research reported in paper VIII, MECHANICAL COMPONENTS, of this conference publication is contributing to the VTOL propulsion-system technology base.

During landing and takeoff the vertical attitude of the nacelles coupled with the aircraft forward velocity results in a very severe inlet flow angle of attack. Lightweight, compact advanced-technology inlets are therefore necessary for acceptable pressure recovery and low flow distortion to the fan.

Another class of VTOL aircraft is characterized by fixed nacelles rather than the tilting nacelles shown in figure XIII-1. A representative fixed-nacelle VTOL aircraft is shown in figure XIII-2. Vertical lift is obtained with this type of propulsion-system installation by deflecting the engine exhaust downward with deflector nozzles. These nozzles must be not only aerodynamically efficient, but also lightweight and compact. They therefore represent another advanced-technology area for VTOL propulsion systems.

This particular fixed-nacelle aircraft has a tandem-fan propulsion system. In this concept, each engine has two interconnected fans. The deflected flow from the forward-located fan produces a lift force forward of the aircraft center of gravity, and the deflected flow from the aft-located fan and the engine exhaust produce a lift force aft of the center of gravity. Aircraft pitch is controlled by modulating the forward and aft lift forces.

Although the inlet flow environment is less severe for the fixed-nacelle aircraft, the tandem-fan propulsion concept illustrated in figure XIII-2 presents a special inlet problem because two closely coupled inlets are required for each nacelle.

These are some of the special propulsion problems associated with subsonic VTOL aircraft. The following sections of this paper present results of the Lewis Research Center VTOL technology program that addresses these problems. To be discussed are high-angle-of-attack-capability inlets, rapid-thrust-modulation fans, and propulsion-system - aircraft-control integration.

INLETS

The aerodynamic performance of inlets for all types of VTOL aircraft is being investigated at Lewis. This discussion is concentrated on the tilting-nacelle inlet because it encounters

more extreme flow conditions than the fixed-nacelle inlet. A tilting-nacelle V/STOL aircraft is shown in figure XIII-3 in two configurations: with the nacelles level for cruise, and with the nacelles tilted back 90° as they would be during vertical operation. For this particular example, the aircraft is shown as it would be configured during a portion of the landing approach. The nacelles are tilted back 90°, the aircraft is descending, and the resultant inflow angle to the inlet is 120°.

Inlet Requirements

A typical landing-approach flightpath for a tilting-nacelle VTOL aircraft is shown in figure XIII-4. As the aircraft begins its landing approach, the nacelles begin to tilt back at a forward velocity V_0 of about 160 knots. The inlet reaches a maximum angle of attack of 120° at 40 knots forward velocity. This is the example that is illustrated in figure XIII-3. The inlet airflow also varies during the approach with the necessary variation in engine thrust.

The primary objective of the inlet designer for a tilting-nacelle aircraft is to design an inlet that provides separation-free airflow to the engine at all operating conditions. Inlet internal-flow separation is to be avoided because the resulting sudden high pressure losses and high pressure distortions can lead to sudden changes in engine thrust and to fan or compressor blade stresses.

The inlet is most likely to encounter internal-flow separation at a forward velocity of 120 knots, an inlet angle of attack of 60°, and an inlet airflow of 56 percent of maximum. This flow condition is labeled "critical" in figure XIII-4. An inlet that operates separation free at this critical flow condition will operate separation free at all other flow conditions encountered during approach and takeoff. At conditions prior to the critical condition, the inlet angle of attack is lower and inlet operation is therefore more stable. At conditions beyond this critical condition, the forward velocity is lower and the inlet airflow is higher. Therefore these later conditions are less critical, even though the inlet angle of attack is actually higher. For the remainder of the discussion, this critical point in the landing approach is called the tilting-nacelle-inlet design requirement.

Inlet Performance

In designing an inlet to operate with unseparated internal flow at this critical condition, the first approach that comes to mind is to provide enough inlet lip thickness to effectively

turn the flow into the inlet (refs. 1 to 6). To determine just how much lip thickness is needed for effective flow turning, Lewis conducted an experimental test program on both 12- and 20-inch-diameter inlets (refs. 7 to 11).

The 20-inch-diameter inlets were tested on a 20-inch-diameter model fan installed in the Lewis 9- by 15-Foot Low-Speed Wind Tunnel (fig. XIII-5). The model fan has a pressure ratio of about 1.2 and is powered by a core turbine driven by high-pressure air supplied through the support post and pylon. A typical tilting-nacelle inlet is shown installed on the fan. The inlet was instrumented to determine its aerodynamic performance. The model-fan blades were also instrumented with strain gages, and blade stress data were gathered as part of the research data.

The results of the test program to determine lip-thickness requirements for tilting-nacelle inlets are shown in figure XIII-6. The figure illustrates how the inlet-lip contraction ratio affects the angle of attack at which the internal flow separates. The lip contraction ratio A_{HL}/A_T is defined as the ratio of the inlet highlight or leading-edge area A_{HL} to the inlet throat area A_T and is hence a direct indication of inlet-lip thickness. The higher the contraction ratio, the thicker the lip. The data are for the critical flow condition described earlier: a forward velocity of 120 knots and an inlet airflow of 56 percent of maximum. The inlet angle of attack at which the internal flow separates from the inlet lower lip α_{SEP} is plotted against the inlet-lip contraction ratio. The horizontal line drawn on the figure is the 60°-angle-of-attack tilting-nacelle-inlet design requirement.

The data in figure XIII-6 suggest that for separation-free inlet flow, the lip contraction ratio must be about 1.65. Thinner lips, those with contraction ratios below this value, have separated internal flow at the critical 60° angle of attack. Hence, by making the inlet lip thick enough, a tilting-nacelle inlet can be designed to operate at this most critical condition in the aircraft landing approach. It will then, of course, operate effectively over the entire approach and takeoff flightpaths.

Effect of Inlet Flow Separation on Fan Blade Stress

How the fan blade stress is affected by separated inlet flow is shown in figure XIII-7. Blade stress levels from the 20-inch-diameter model fan are plotted against inlet-air weight flow. The data are for the same flow conditions as those in figure XIII-6. Two curves are shown: one for a relatively thin inlet with a contraction ratio of 1.46, and one for a relatively thick inlet with a contraction ratio of 1.76. The 1.46-contraction-

ratio inlet has separated flow at these conditions. The resulting fan blade stresses increase with increasing inlet-air weight flow and exceed the limit at the required 56 percent airflow. The thicker, 1.76-contraction-ratio inlet initially has separated flow at low inlet-air weight flows and the fan blade stresses begin to increase. But the flow attaches before the critical inlet weight flow of 56 percent is reached, and the blade stress then decreases to low levels. The spike in the blade stress curve after the initial attachment point corresponds to a first-bending-mode excitation of the fan blades. It results from the inlet flow not being completely attached along the entire length of the inlet internal surface. The point to be made is that, when the inlet flow is separated, the fan blade stresses can be unacceptable and, when the inlet flow is attached, fan blade stresses are not a problem.

Methods to Prevent Flow Separation and Minimize Inlet-Lip Thickness

Lip thickness can be increased to the point where an inlet will meet the requirements of a tilting-nacelle VTOL aircraft. A thicker lip, however, does have some disadvantages in that weight, surface area, and hence cruise drag will increase. These disadvantages can be minimized by making the inlet unsymmetrical - thick on the bottom, where angle of attack is important, and thinner on the sides and top.

In the interst of reducing inlet weight and surface area even further, however, it would be desirable to somehow make the lower lip as thin as possible. That leads to considering methods by which the angle-of-attack capability of an inlet with a given lower lip thickness can be extended. Several methods are illustrated in figure XIII-8: an extended centerbody, lower-lip blowing, a scarf inlet, lower-lip suction, a lower-lip slot, and lower-lip vortex generators. Each method is intended to improve the inlet lower-lip performance to the point where a given angle-of-attack capability can be attained with a thinner lip. Results for the first three methods are discussed here; the performance of the other methods will be evaluated in future tests.

Extended centerbody. - The effect of extending the inlet centerbody on inlet flow separation is shown in figure XIII-9. The data are shown in the same format and at the same flow conditions as figures XIII-6 and XIII-7, with the angle of attack at flow separation being plotted against the lip contraction ratio. The lip-thickness-effect data with a short centerbody are repeated here and labeled as "reference." As indicated, extending the centerbody forward increases the flow separation angle by about 10^{o} for a 1.46-contraction-ratio inlet - a significant improvement. The method works by changing the area distribution within the inlet duct to make it more favorable to

the inlet internal flow, thereby extending the separation angle. Additional results are reported in reference 8.

Lower-lip blowing. - The effect of lower-lip blowing is shown in figure XIII-10. The plot format is again the same, and the data indicate that lower-lip blowing can extend the separation angle for a 1.46-contraction-ratio inlet by an impressive 20° to a value very close to the tilting-nacelle-inlet requirement. This large improvement in angle-of-attack capability results from the flowing air energizing the lower-lip boundary layer and thereby making the flow less likely to separate. This result was attained with a blowing-air pressure of 1.1 times atmospheric and a blowing-air mass flow of about 6 percent of the inlet flow. Additional results are reported in reference 12.

Scarf inlet. - The third method of extending the inlet flow separation angle is shown in figure XIII-11. The data indicate that extending the inlet lower lip to form a scarf inlet can increase the flow separation angle for a 1.44-contraction-ratio inlet by about 20° - the same amount that was attained with lower-lip blowing. This method works because a scarf inlet draws in air more from above than from below. This effectively reduces the local angle of attack on the lower lip of the inlet and thereby permits a higher inlet angle of attack to be attained before the internal flow separates. Additional results are reported in reference 13.

Benefit of thin lip. - As stated previously, these different methods for extending the flow-separation angle of attack are being investigated so that a thinner inlet lip can be used to meet the tilting-nacelle-inlet design requirement. As an example of the potential benefit of a thinner inlet lip, figure XIII-12 shows two nacelle layouts - the top one without lip blowing, the bottom one with lip blowing. Both inlets have been designed to provide exactly the same angle-of-attack capability. Without lip blowing, the inlet lower lip is relatively thick, and it is therefore relatively heavy and has higher cruise drag. With lip blowing, however, the angle-of-attack requirement is attained with a thinner lip and the inlet is lighter and has less cruise drag. In addition, the lip-blowing inlet is somewhat shorter. The inlet thickness also affects the nacelle thickness aft of the inlet. All in all, from a nacelle-weight and cruise-drag standpoint, it is highly desirable to design an inlet that meets the tilting-nacelle-inlet flow design requirement and is as thin as possible.

In summary, the tilting-nacelle VTOL aircraft concept presents the most challenging low-speed inlet design problems. Tests at Lewis have shown that, by increasing inlet lower-lip thickness enough, the inlet can be made to provide separation-free internal flow over the full aircraft operating range. Other test results have shown the promising potential of various methods to

provide a given angle-of-attack capability with a thinner inlet lip. A strong motivation exists to use thin inlet lips since thinness results in reductions in overall nacelle weight and length and in cruise drag.

Lewis is also doing some work on non-tilting-nacelle inlets. A fixed-nacelle VTOL inlet that has been tested at Lewis is shown in figure XIII-13. This is a tandem-fan propulsion system inlet model that is compatible with the fixed-nacelle, tandem-fan VTOL aircraft described previously. The model is shown installed in the Lewis 10- by 10-Foot Supersonic Wind Tunnel, where low-speed tests were just recently completed. The model is composed of two inlets - the front axisymmetric inlet for the front fan, and the top S-duct inlet for the aft fan. Only the top inlet has been tested, in isolation, with the front inlet faired over. The test results indicated only a 4 percent loss in total pressure and an 8 percent distortion in total pressure at the most extreme condition tested. Plans include testing the model as shown in the figure with two fans, one for each inlet, in order to determine the aerodynamic interaction of the two inlets.

RAPID-THRUST-MODULATION FANS

As already stated in this paper, either a variable-pitch fan or a variable-inlet-guide-vane (IGV) fan is being considered to provide the rapid thrust modulation needed for aircraft stability and roll control. A sketch of a variable-pitch fan is shown in figure XIII-14. The variable-pitch mechanism, located in the rotor hub region, is quite complicated. There has been some concern about the durability and reliability of variable-pitch rotor blades, and therefore some approaches favor a fixed-pitch fan with variable IGV's. A sketch of a variable-inlet-guide-vane fan stage is shown in figure XIII-15. The rotor blades are at a fixed setting angle. The IGV angle-changing mechanism is much simpler; a geared motor and a synchronous ring are shown. Since the mechanism is located on the outer casing, the engine thrust controls can easily be incorporated into the variable-IGV systems.

All VTOL two-engine configurations must be capable of safe operation with one engine out. The fan stages in both nacelles must be capable of being driven by one engine and must each provide the required thrust for all modes of operation. The thrust level of either propulsion system can be controlled individually by adjusting its variable blade during constant-speed, one-engine-out operation. Both a variable-pitch-rotor-blade fan stage and a variable-IGV fan stage were tested at Lewis in order to determine the feasibility of such designs for rapid thrust modulation (refs. 14 and 15).

Variable-pitch fan stages. - The variable-pitch fan stage was designed and fabricated by the Hamilton Standard Division of United Technologies Corp. The stage was designed for a pressure ratio of 1.38 at a flow of 65.3 pounds per second, which corresponds to a specific flow of 41 pounds per second per square foot of annulus area. The design tip speed was 950 feet per second.

The rotor is shown in figure XIII-16, and the stators are shown mounted in the casing in figure XIII-17. The 20-inch-diameter rotor has a hub-tip ratio of 0.52. The 19 variable-pitch rotor blades have an aspect ratio of 1.26. The rotor-blade setting angle was changed manually. The 38 stator blades were spaced about 2 rotor chords downstream of the rotor trailing edge.

So that the variable-pitch rotor blades can turn to feather, the blade tip contour is basically a circular arc (fig. XIII-18) in the chordwise direction. In an attempt to reduce the effects of tip clearance, the casing above the rotor was recessed as shown. The radius at the blade leading and trailing edges is equal to the nominal casing radius. At the blade radial axis of rotation, the blade tip radius is greater than the nominal casing radius. In an actual engine application, this configuration has the disadvantage that a split casing would have to be used to allow for rotor removal.

Variable-inlet-guide-vane fan. - Hamilton Standard designed a set of IGV's (fig. XIII-19) to be added to the variable-pitch stage so that the effects of variable IGV's on performance could be investigated. NACA-63-series airfoil shapes where used for the IGV elements. The front portion of the vanes was fixed and only the rear portion rotated. For this series of tests, the rotor blades were set at an angle of 6° closed. Both stage configurations were tested in the Lewis single-stage compressor test facility described in paper VII, TURBOMACHINERY TECHNOLOGY, of this conference publication.

Performance with Variable-Pitch Fan

The performance with the variable-pitch fan is shown in figure XIII-20. Pressure ratio is plotted as a function of weight flow for several delta blade setting angles. The data presented are for design speed. Also shown in the figure are the stall line and an assumed operating line that corresponds to a constant-throttle valve position. The definition of blade setting angle is presented in figure XIII-21. Positive setting angles close the blade passages from the design setting and reduce the flow. Negative setting angles open the blade passages and increase the flow. At the design setting angle (0°), the measured performance agrees reasonably well with design (fig. XIII-20). However, the stall margin is only 5 percent. The stall margin

based on the operating-line performance is 10 percent. As shown in the performance plots, the fan can operate over a wide range of blade setting angles. At high positive angles, the operating line crosses the low-pressure-ratio side of the performance curves. At -8°, the operating line is very close to the stall line with only about a 2 percent stall margin.

The effect of blade setting angle on static thrust is shown in figure XIII-22. The operating-line calculated static thrust is plotted as a function of the delta blade setting angle. The static thrust varies from about 100 pounds at an angle of 25° to about 1800 pounds at an angle of -8°.

Variable-pitch rotor blades show promise for VTOL application because the thrust of each fan can be independently varied while the engine is operating at a constant speed. However, for this particular fan, the stall margin at negative blade setting angles is low. If the expected inlet flow distortions occur, the stall margin will be inadequate.

In an effort to improve the stall margin, several modifications were made to the rotor (ref. 14). First, the blade leading edge was recoined in the tip region. This resulted in only a slight improvement in stall margin. Next (fig. XIII-23), the recessed contour above the rotor was replaced by a cylindrical insert and the blade tips were trimmed. Finally, the skewed-slot casing treatment shown in figure XIII-24 was inserted above the rotor tip. This insert replaced the cylindrical solid insert shown in figure XIII-23. The axial location of the fence separating the two rows of slots corresponds to the rotor-blade axis of rotation. Its slots are skewed 60° from radial in the direction of rotation. The performance with both the solid casing and the skewed-slot casing treatment is presented in figure XIII-25. Pressure ratio is plotted as a function of weight flow for three blade setting angles. The operating line is the same as that shown in figure XIII-20. At the high flow blade angles, casing treatment substantially increased stall margin. At 15°, casing treatment did not affect the stall point. The blade-element data show that the rotor-tip element was not controlling stall at that angle, and thus the casing treatment provided no benefit. At the design angle, the casing treatment increased the stall margin by 13 percent. However, there was a 4 percent loss in efficiency. Further studies are required to determine a casing treatment that will give the improved stall margin with better efficiency.

Performance with Variable-Inlet-Guide-Vane Fan Stage

The effects of the variable-inlet-guide-vane fan stage on overall performance are shown in figure XIII-26. Pressure ratio at design speed is plotted as a function of weight flow at several

IGV angles. The stall line and the operating line are also shown. The operating line corresponds to a constant throttle-valve position, and it is different from that obtained with the variable-pitch stage.

The definitions of vane setting angle are illustrated in figure XIII-27. Positive IGV angles turn the flow in the direction of blade rotation and close the rotor-blade passage. Negative IGV angles turn the flow opposite to the direction of rotation.

The operating line of the variable-inlet-guide-vane stage is limited at low flows by stall. At the high flows, the stage experiences a maximum flow condition, as illustrated by the -17.5° and -25° IGV angles having the same performance (fig. XIII-26). This is a result of the very high losses associated with the high, negative IGV angles. Figure XIII-28 shows the effect of vane setting angle on the calculated static thrust and compares the thrust with that for the variable-pitch stage. The operating-line static thrust, as a percentage of that obtained at design angle, is plotted as a function of delta setting angle. The change in thrust with angle is not as great with the IGV's as with the variable-pitch rotor. At the positive angles, thrust is limited by stall; at the negative angles, thrust is limited by choke.

In summary, both the variable-pitch and variable-inlet-guide-vane fan stages show promise for VTOL application because the thrust of each fan can be independently varied while the engine is operated at a constant speed. The type of fan stage selected will probably depend on the specific application. The variable-pitch fan gives a much greater thrust modulation. However, if the required thrust modulation is about ± 20 percent, the variable-inlet-guide-vane fan might be chosen because of its simpler design. From the data shown, it is obvious that much more work is needed before the optimum fan configuration for a paricular application can be identified.

In addition to the model-fan program just described, Lewis also has in progress a large-scale evaluation of the variable-IGV thrust modulating concept. A variable-IGV module has been installed in the TF-34 engine, as shown in figure XIII-29. The variable IGV's are designed to affect only the bypass flow and not engine-core supercharging. This is to prevent the core from being desupercharged when the guide vanes are adjusted to reduce engine thrust. The variable IGV's are shown in figure XIII-30. This view of the engine front face shows the inner ring to which the end of each guide vane is attached. The trailing edges of the vanes articulate, but the leading edges are fixed.

The thrust-modulating experiments are being conducted in one of Lewis' altitude test facilities. The engine installation is shown in figure XIII-31. This program, which has been under way

for only several months, is investigating the variable-IGV-fan thrust modulation range, stall margin, and blade stress over a range of inlet-guide-vane deflection angles.

PROPULSION CONTROL

Some of the propulsion control problems of VTOL aircraft have already been discussed, for example, the use of variable-geometry fans to obtain rapid thrust response. Some of the methods used to integrate the controls of these complex propulsion systems are discussed here. During hovering flight, a VTOL propulsion system has to do the same job that the wings and control surfaces do during conventional flight. Therefore a much higher degree of aircraft - propulsion control integration is required in VTOL aircraft than in more conventional aircraft.

Piloted Simulators

The success of the control-system design for a VTOL airplane is measured by the pilot's ability to land the airplane safely on a small landing pad. In studying this problem, it is necessary to consult the pilot for his opinion on aircraft handling qualities. The safest and most economical way to do this is to use piloted simulators like the one shown in figure XIII-32. This facility is located at the NASA Ames Research Center and is called the flight simulator for advanced aircraft (FSAA). The pilot sits inside the enclosed cab at the left of the figure. The cab is driven by actuators that simulate actual aircraft moments. The actuators are positioned by a digital computer that solves the aircraft equations of motion.

Inside the cab, the pilot is provided with a complete set of controls and displays. His view of the landing area is provided by a television screen. This screen displays a picture taken by a camera that traverses a scale model of the landing area. The television camera is operated by the same computer that operates the cab.

For proper simulation of VTOL operations, the FSAA's computer should be capable of solving the equations that model propulsion-system dynamics, ground effects, and even ship motion for Navy operations. At present, the computer does not have enough capacity to handle all these calculations in real time. Plans are to expand the computer's capacity; however, for the present, investigations have been confined to propulsion systems that are somewhat simpler than those required for VTOL aircraft. These investigations are nonetheless relevant to VTOL research since VTOL aircraft belong to the general class of powered-lift aircraft. This class of aircraft includes STOL aircraft and heli-

copters as well as VTOL aircraft, and these types of aircraft share many similar problems.

For all these types of aircraft, power modulation is used to control aircraft lift. This implies that aircraft maneuvers cause changes in engine speeds, temperatures, and surge margins. Monitoring of these internal engine variables is important for an adequate integrated-control-system design. The pilot becomes an important element in the overall system, and consequently pilot opinion has a critical effect on propulsion control requirements. The pilot has to be satisfied with the thrust response since he uses the engines to maneuver the airplane. Engine failures are also a critical problem for all powered-lift aircraft since engine failures limit the lift available for controlling the flightpath.

STOL Aircraft Simulation

These problems were investigated by performing a piloted simulation of the STOL propulsion system shown in figure XIII-33. This system is the Quiet Clean Short-Haul Experimental Engine (QCSEE). This engine has such VTOL technology features as a variable-pitch fan and a digital control. The hydromechanical backup control is designed to provide engine protection in case of a digital control failure. Since QCSEE was designed for a powered-lift aircraft, it was a good candidate for a piloted simulator evaluation. In cooperation with NASA Ames, the Lewis Research Center developed a simulation of QCSEE suitable for use on the FSAA.

The engine simulation was combined with a simulation of the aircraft shown in figure XIII-34. This is an externally blown-flap STOL airplane. As for a VTOL airplane, one of its critical problems is engine failure during a landing approach. This particular airplane experiences rolling and yawing moments after an engine failure.

The piloted simulator is quite safe, in contrast to actual aircraft flight testing, so it is an ideal tool for investigating the pilot's reaction to propulsion-system failures. A number of failure modes were investigated in this experiment, including failure of the QCSEE digital control and engine failure. The pilot could easily compensate for failure of the QCSEE digital control. The hydromechanical backup system proved adequate to prevent a serious loss of thrust. Total engine failure, which did cause a thrust loss, was considerably more difficult for the pilot to handle. Some results of simulated engine failures are discussed here because they illustrate the importance of the pilot's role in overall system performance and because they demonstrate the need for adequate modeling of internal engine behavior.

A typical result of an engine failure is shown in figure XIII-35. The upper trace shows distance from the center of the runway in feet as a function of time. The lower trace shows changes in engine turbine-inlet temperature. The vertical dotted line indicates when engine failure occurs. The pilot's first warning of failure comes from a light that illuminates when the engine pressure ratio drops below a specified value. He must compensate for the failure manually. The engine failure causes the airplane to veer off the center of the runway by about 80 feet. There is a slight increase in turbine-inlet temperature about 1 second after the failure, when the pilot advances the throttle. For this flight, the temperature variations were small but flightpath control was marginal.

An automatic thrust control system was devised to help the pilot correct for engine failure. The automatic system was designed to keep the sum of all four engine thrusts at a level requested by the pilot. The automatic system was engaged at all times; so, when an engine failed, it would automatically increase the thrusts of the working engines.

This system was evaluated with the piloted simulator. The results are shown in figure XIII-36. When unexpected failures are simulated, it is impossible to draw any final conclusions from the results of only two flights, but some general observations can be made. First, it appears that the automatic system was helpful since the airplane stayed near the center of the runway. From the flightpath information alone, the automatic system appears to be highly successful. However, this conclusion is questionable when the time history of turbine-inlet temperature is considered. The range of temperature variation is about 900 degrees F, much greater than for the manual system. The reason for this was the high gain of the automatic control and also the fact that the automatic system felt different to the pilot. As a result, his throttle activity was greater than with the manual system. Another surprising result was that the pilot used the throttle more before the failure than after. When the failure occurred, he turned his attention to the flight controls and let the automatic system take care of thrust.

At present, it is not possible to determine exactly what these temperature variations mean. A likely problem is an excessive reduction of engine thermal fatigue life. Lewis has begun a study to determine whether the complex process of engine fatigue life prediction can be simplified enough to provide system design criteria.

Future Controls Research

The results discussed in the preceding sections are for a STOL aircraft landing on a 2000-foot runway. The problems will be

even more severe for VTOL aircraft landing on small pads. Lewis is currently trying to simulate more complex VTOL propulsion systems, like the one shown in figure XIII-37. This system includes variable-pitch fans connected by cross shafts and high-angle-of-attack inlets. In cooperation with NASA Ames, Lewis will investigate problems similar to those discovered in the STOL aircraft simulation. These problems include thrust response, engine failure, and low-cycle fatigue. Lewis will also continue to use the piloted simulator as a tool for investigating VTOL propulsion control problems without the safety hazards and cost of actual aircraft flight testing.

SUPERSONIC VTOL PROPULSION TECHNOLOGY

The previous discussion dealt primarily with subsonic VTOL aircraft technology programs. Because of the military's interest in VTOL fighter aircraft, Lewis is also conducting advanced-technology programs applicable to supersonic VTOL propulsion systems. Work is beginning on inlets, nozzles, and propulsion controls. The inlet must function efficiently at both supersonic and subsonic speeds, where it will encounter a relatively severe angle-of-attack environment during takeoff and landing. Ejectors could improve the performance of remote burner nozzles and aircraft control jets. The ejector could also reduce the problems associated with remote burner hot-gas impingement and reingestion during takeoff and landing. And finally, integration of the propulsion system and the aircraft controls will be studied, and programs to improve control-system reliability will be undertaken.

CONCLUDING REMARKS

This paper has reviewed the unique propulsion problems and technology requirements associated with VTOL aircraft. The Lewis Research Center is currently active in technological development applicable to subsonic VTOL aircraft and is also beginning work applicable to supersonic VTOL aircraft. The objective of this overall program is to provide an adequate technology base so that the development of military and commercial VTOL aircraft can be undertaken with a reasonable degree of risk.

REFERENCES

1. Albers, James A.; Stockman, Norbert O.; and Hirn, John J.: Aerodynamic Analysis of Several High Throat Mach Number Inlets for the Quiet Clean Short-Haul Experimental Engine. NASA TM X-3183, 1975.

2. Stockman, Norbert O.: Potential and Viscous Flow in VTOL, STOL, or CTOL Propulsion System Inlets. AIAA Paper 75-1186, Sept. 1975.

3. Jakubowski, A. K.; and Luidens, R. W.: Internal Cowl-Separation at High Incidence Angles. AIAA Paper 75-64, Jan. 1975.

4. Boles, M. A.; and Stockman, N. O.: Use of Experimental Limits in the Theoretical Design of V/STOL Inlets. AIAA Paper 77-878, July 1977.

5. Chou, D. C.; Luidens, R. W.; and Stockman, N. O.: Prediction of Laminar and Turbulent Boundary Layer Flow Separation in V/STOL Engine Inlets. NASA TM X-73575, 1977.

6. Hawk, J. Dennis; and Stockman, Norbert O.: Theoretical Study of VTOL Tilt-Nacelle Axisymmetric Inlet Geometries. NASA TP-1380, 1979.

7. Miller, Brent A.; Dastoli, Benjamin J.; and Wesoky, Howard L.: Effect of Entry-Lip Design on Aerodynamics and Acoustics of High Throat-Mach-Number Inlets for the Quiet, Clean, Short-Haul Experimental Engine. NASA TM X-3222, 1975.

8. Burley, R. R.: Effect of Lip and Centerbody Geometry on Aerodynamic Performance of Inlets for Tilting-Nacelle VTOL Aircraft. AIAA Paper 79-0381, Jan. 1979.

9. Shaw, R. J.; Williams, R. C.; and Koncsek, J. L.: VSTOL Tilt Nacelle Aerodynamics and Its Relation to Fan Blade Stresses. AIAA Paper 78-958, July 1978.

10. Potonides, H. C.; Cea, R. A.; and Nelson, T. F.: Design and Experimental Studies of a Type 'A' V/STOL Inlet. AIAA Paper 78-956, July 1978.

11. Abbott, John M.; Diedrich, James H.; and Williams, Robert C.: Low-Speed Aerodynamic Performance of 50.8-Centimeter-Diameter Noise-Suppressing Inlets for the Quiet, Clean, Short-Haul Experimental Engine (QCSEE). NASA TP-1178, 1978. Proj. FEDD.

12. Johns, A. L.: The Effect of a Diffuser Blowing on the Performance of a Short V/STOL Tilt Nacelle Inlet. AIAA Paper 79-1163, June 1979.

13. Abbott, J. M.: Aerodynamic Performance of Scarf Inlets. AIAA Paper 79-0380, Jan. 1979.

14. Moore, Royce D.; and Osborn, Walter M.: Aerodynamic Performance of a 1.38-Pressure-Ratio, Variable-Pitch Fan Stage. NASA TP-1502, 1979.

15. Moore, Royce C.; and Reid, Lonnie: Aerodynamic Performance of Axial-Flow Fan Stage Operated at Nine Inlet Guide Vane Angles. NASA TP-1510, 1979.

REPRESENTATIVE TILTING-NACELLE VTOL AIRCRAFT

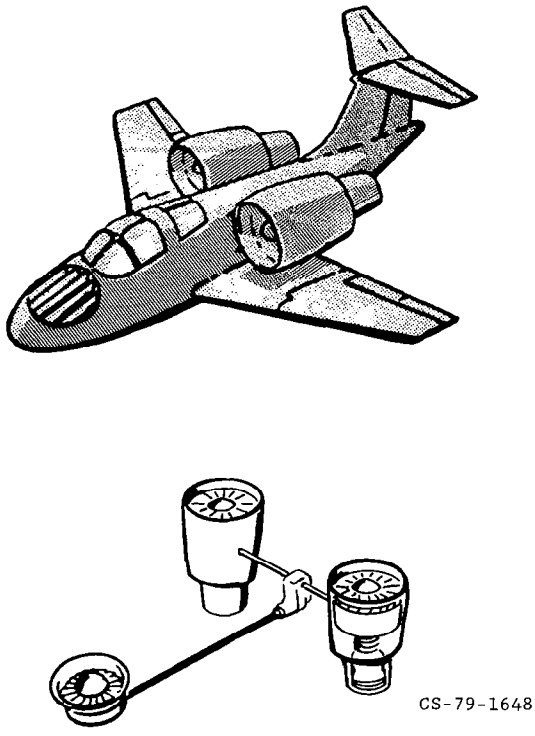

CS-79-1648

Figure XIII-1

REPRESENTATIVE FIXED-NACELLE VTOL AIRCRAFT

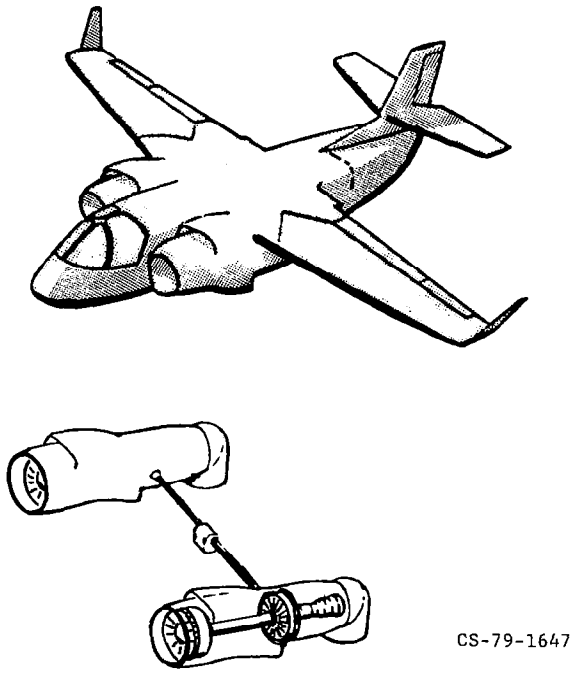

CS-79-1647

Figure XIII-2

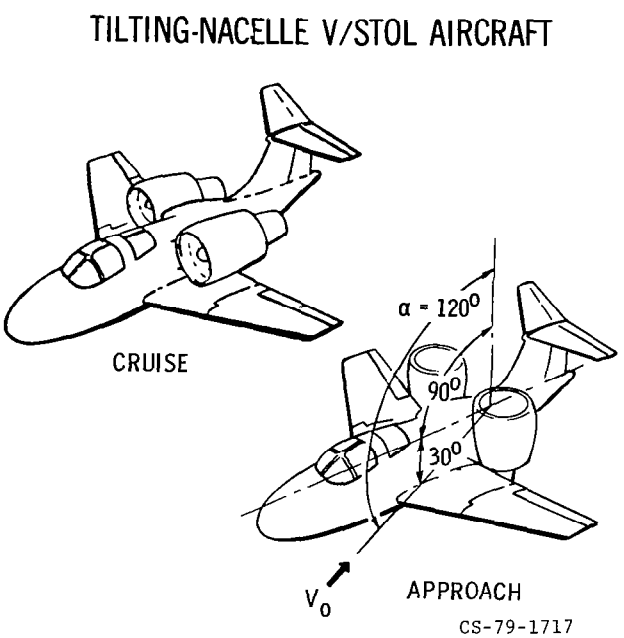

Figure XIII-3

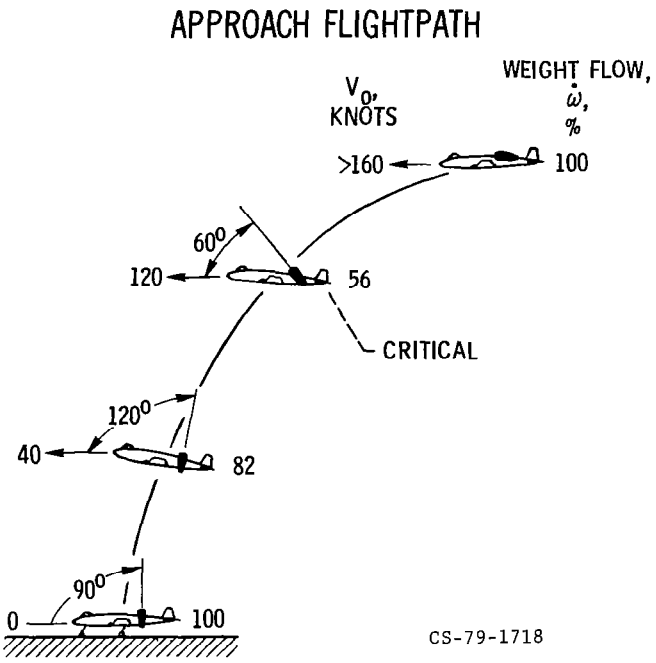

Figure XIII-4

Figure XIII-5

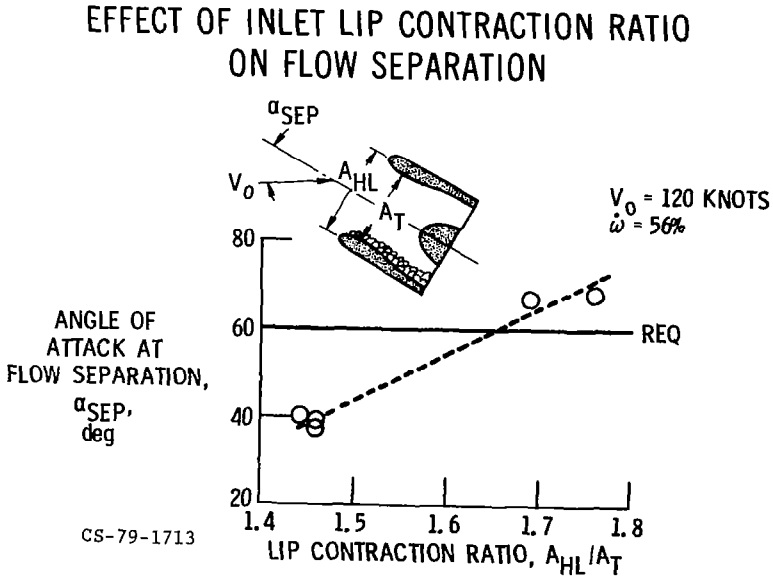

Figure XIII-6

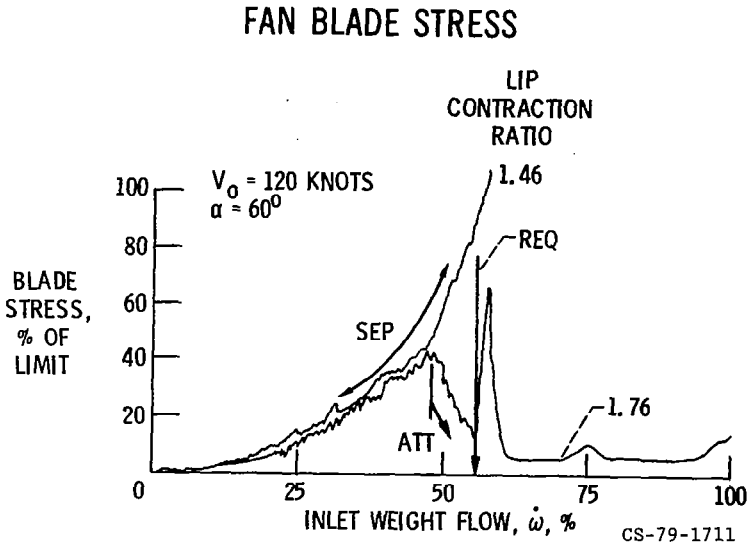

Figure XIII-7

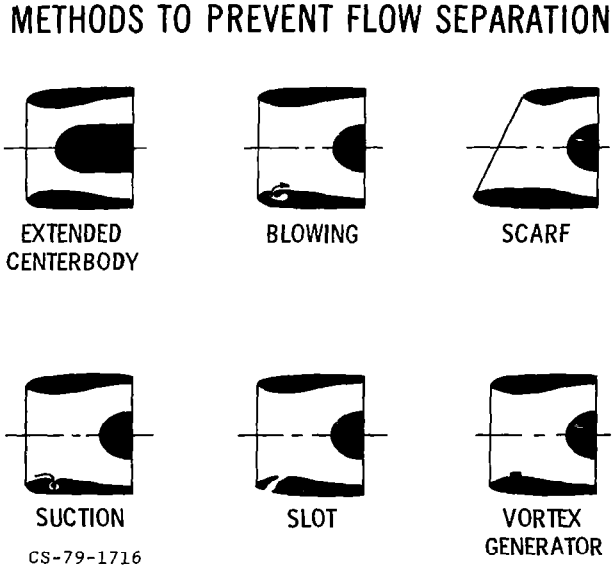

Figure XIII-8

EFFECT OF EXTENDED CENTERBODY

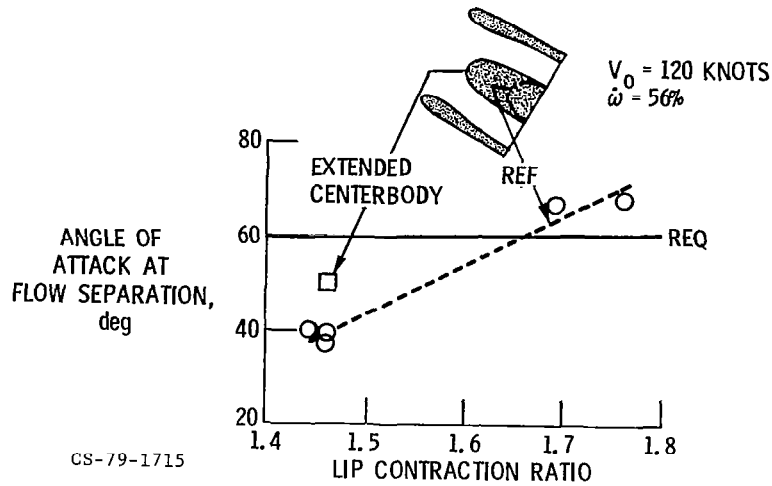

Figure XIII-9

EFFECT OF BLOWING

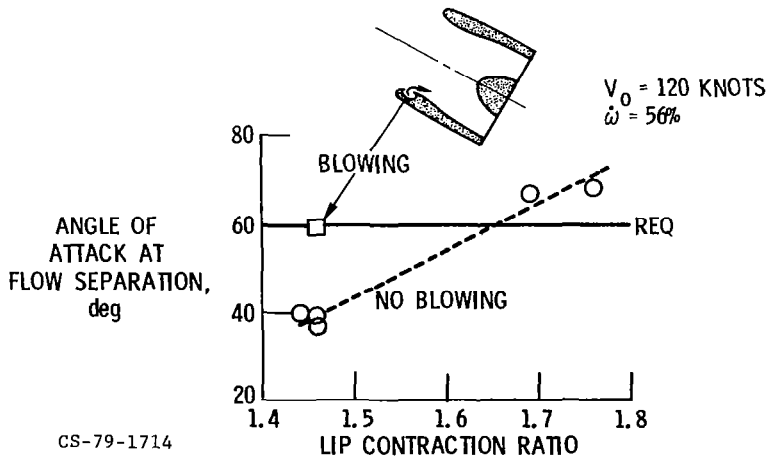

Figure XIII-10

EFFECT OF SCARF INLET

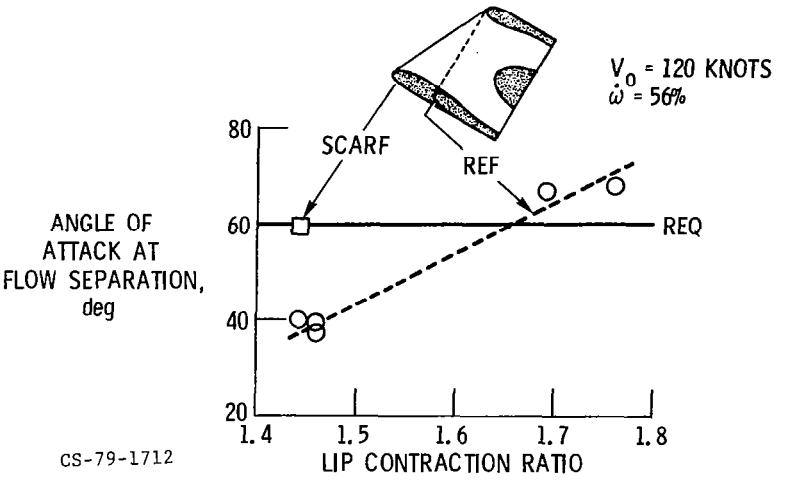

Figure XIII-11

BENEFIT OF BLOWING

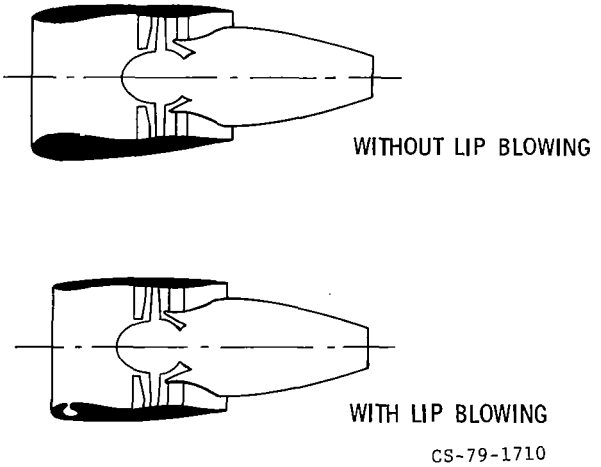

Figure XIII-12

TANDEM FAN INLET MODEL

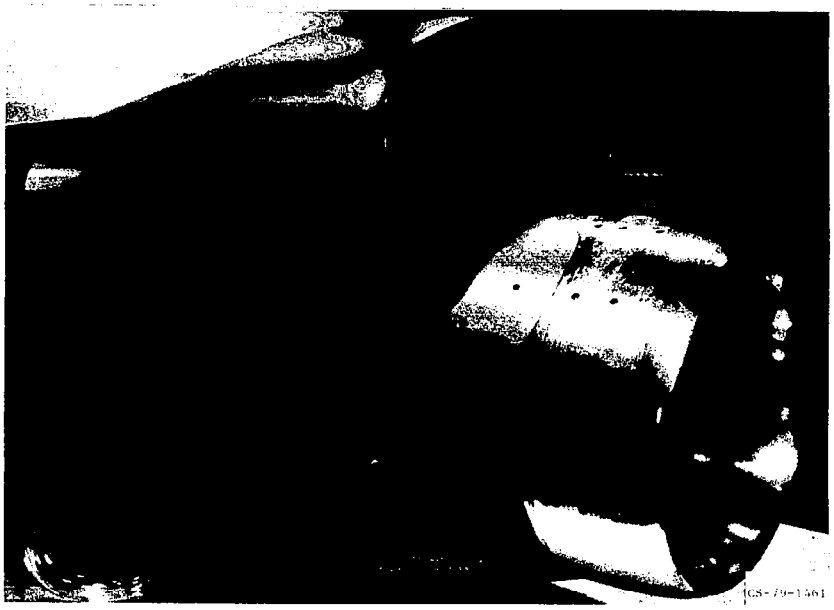

Figure XIII-13

VARIABLE-PITCH FAN STAGE

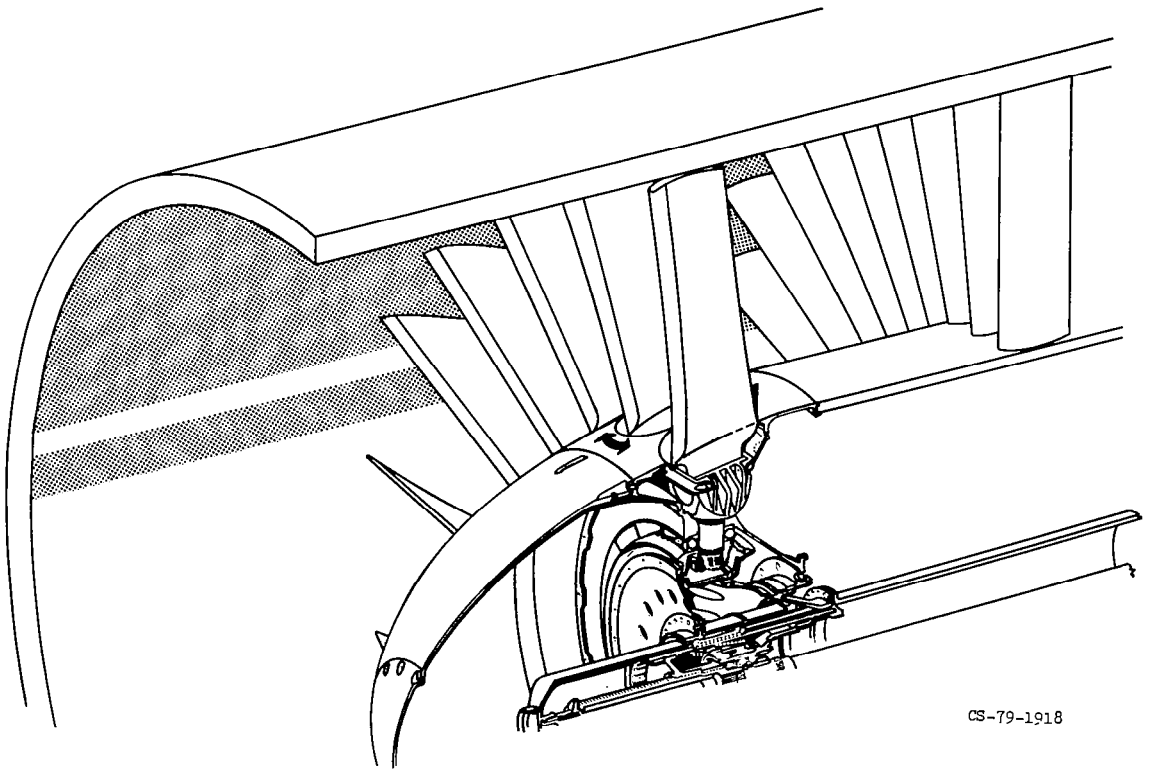

Figure XIII-14

VARIABLE-INLET-GUIDE-VANE FAN STAGE

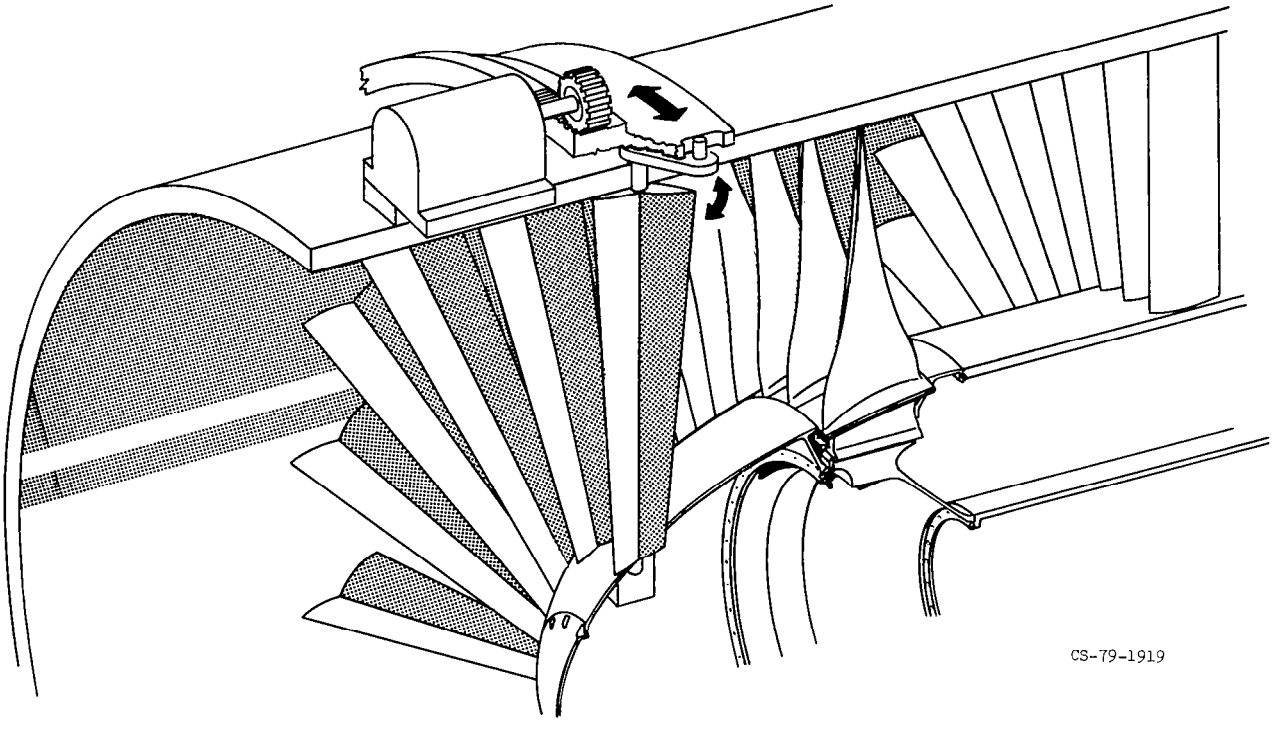

Figure XIII-15

VARIABLE-PITCH ROTOR

Figure XIII-16

STATOR

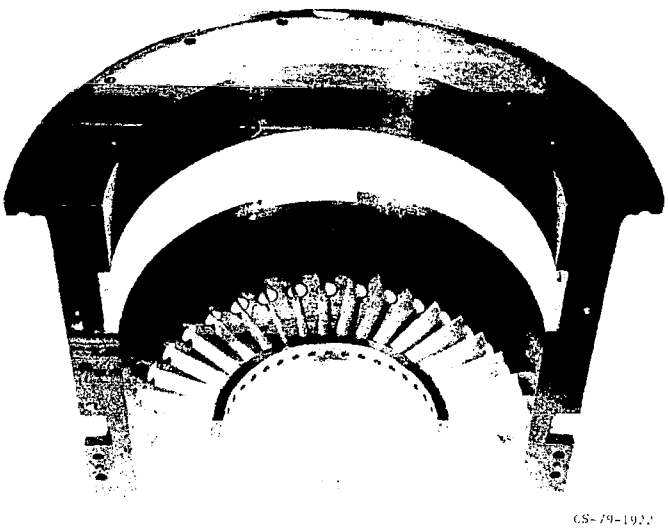

Figure XIII-17

CASING-ROTOR TIP CONTOUR

Figure XIII-18

VARIABLE-INLET-GUIDE-VANE FAN STAGE

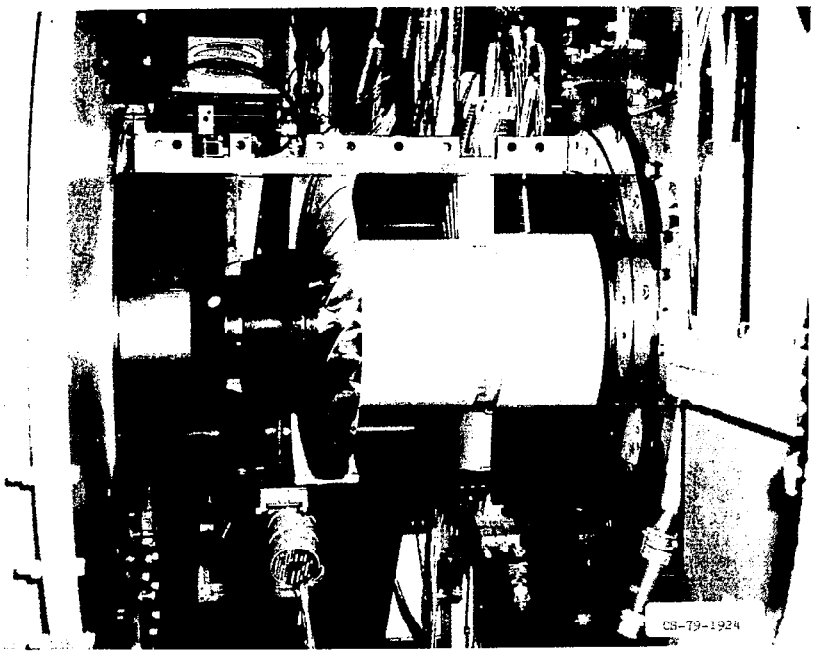

Figure XIII-19

EFFECT OF SETTING ANGLE ON PERFORMANCE

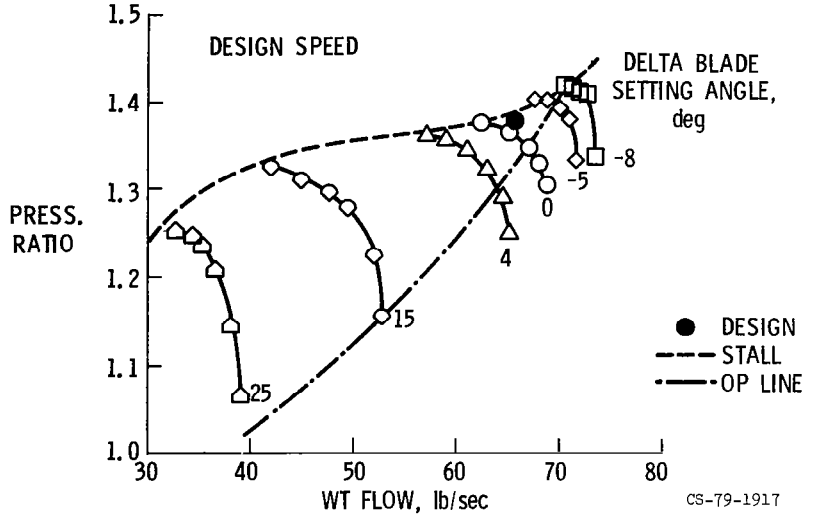

Figure XIII-20

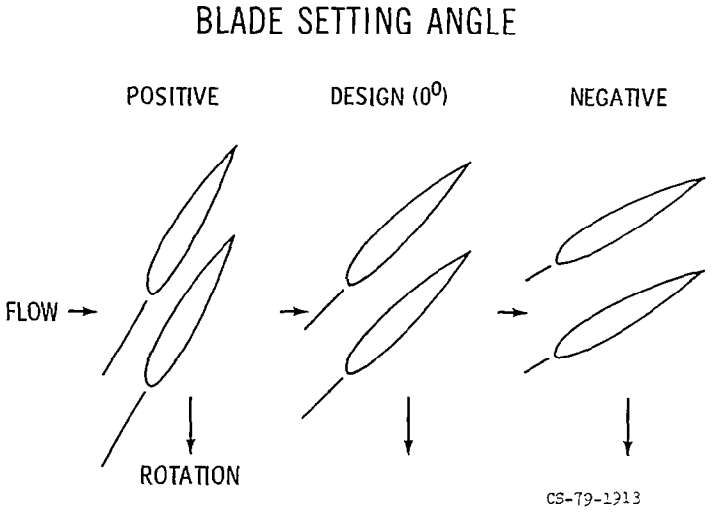

Figure XIII-21

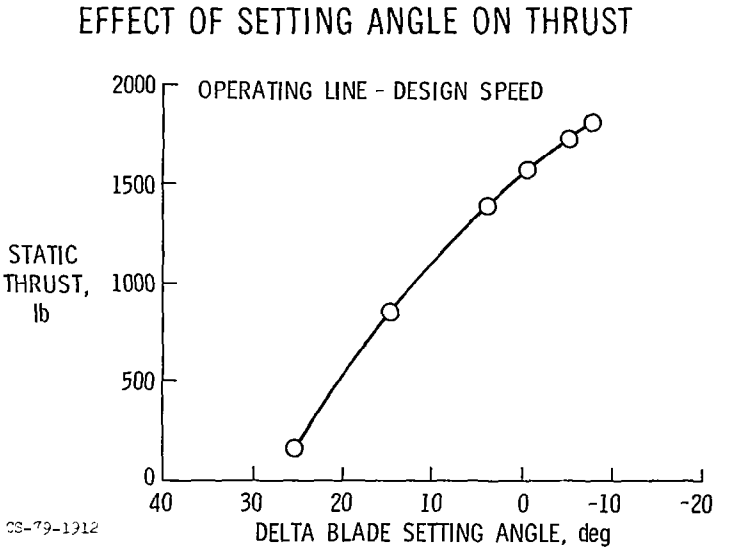

Figure XIII-22

CYLINDRICAL INSERT

Figure XIII-23

CASING TREATMENT INSERT

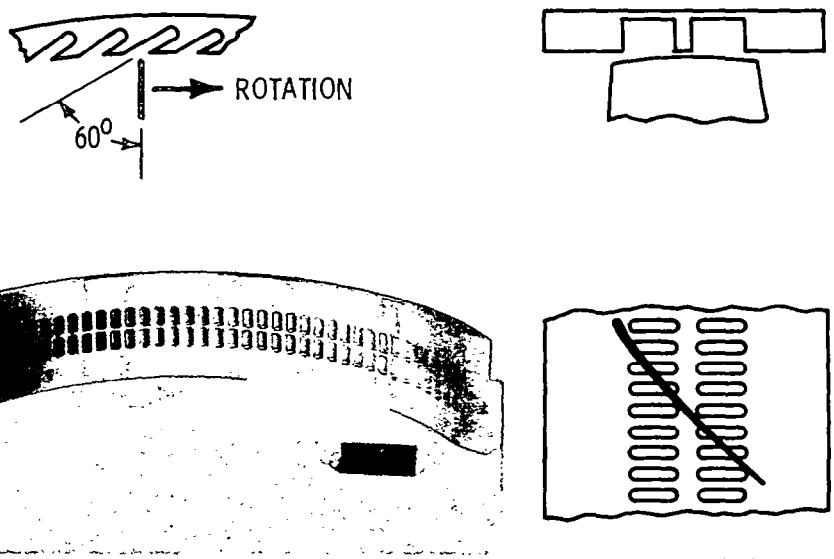

Figure XIII-24

EFFECT OF CASING TREATMENT ON PERFORMANCE

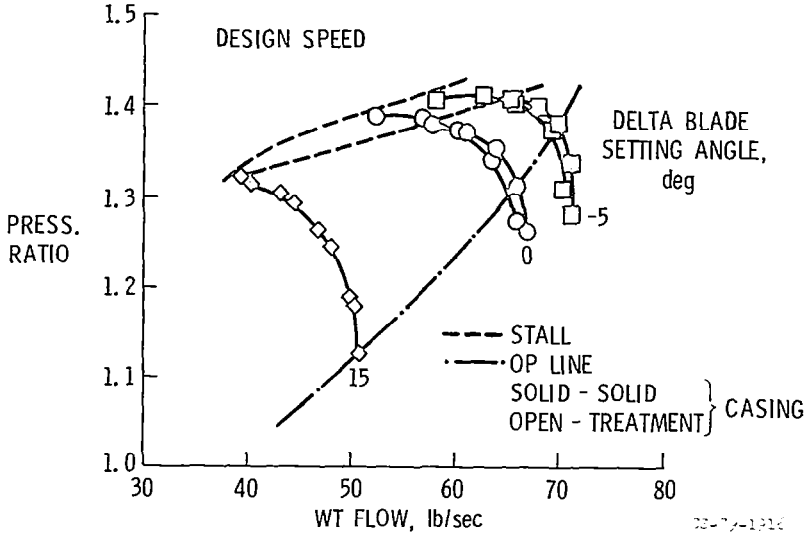

Figure XIII-25

EFFECT OF VANE ANGLE ON PERFORMANCE

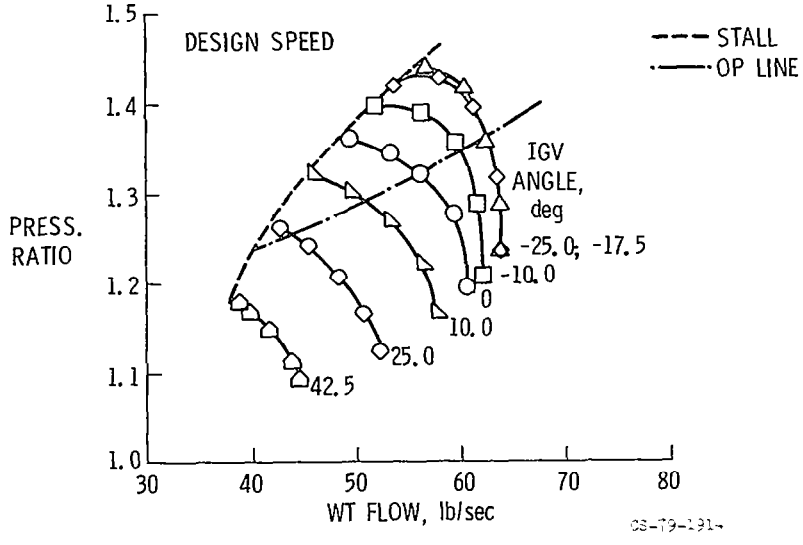

Figure XIII-26

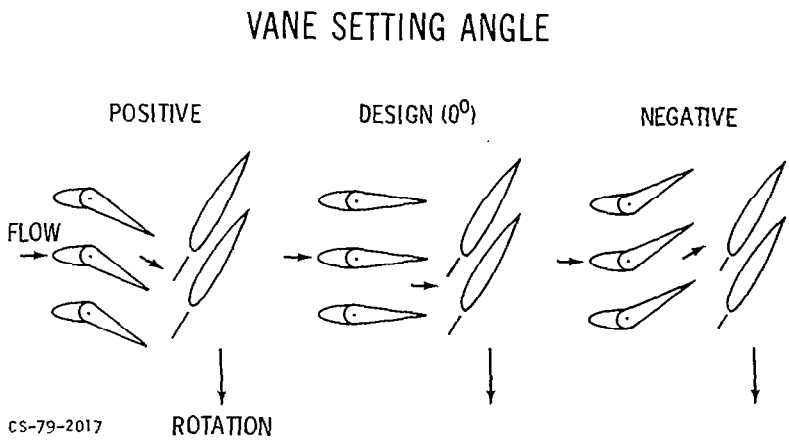

Figure XIII-27

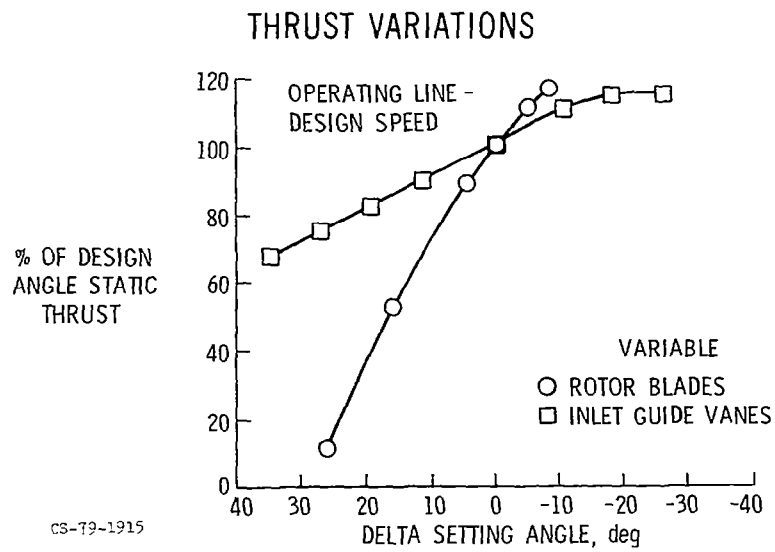

Figure XIII-28

VARIABLE INLET GUIDE VANE ON TF 34 ENGINE

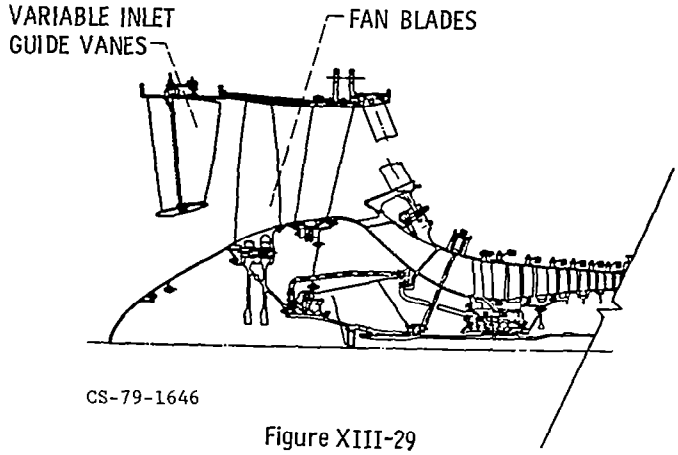

Figure XIII-29

VARIABLE INLET GUIDE VANES MOUNTED ON TF-34 ENGINE

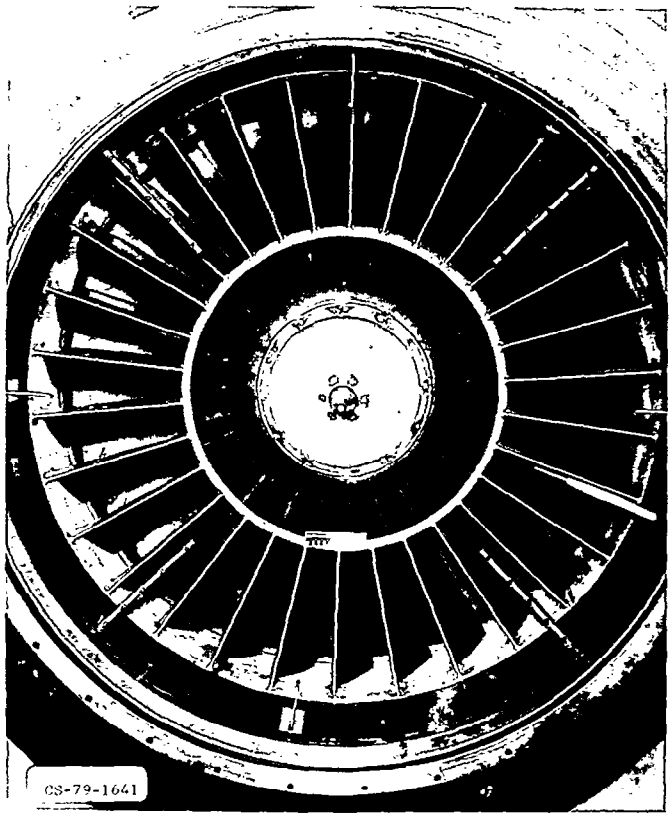

Figure XIII-30

VARIABLE-INLET-GUIDE-VANE TF-34 ENGINE IN TEST FACILITY

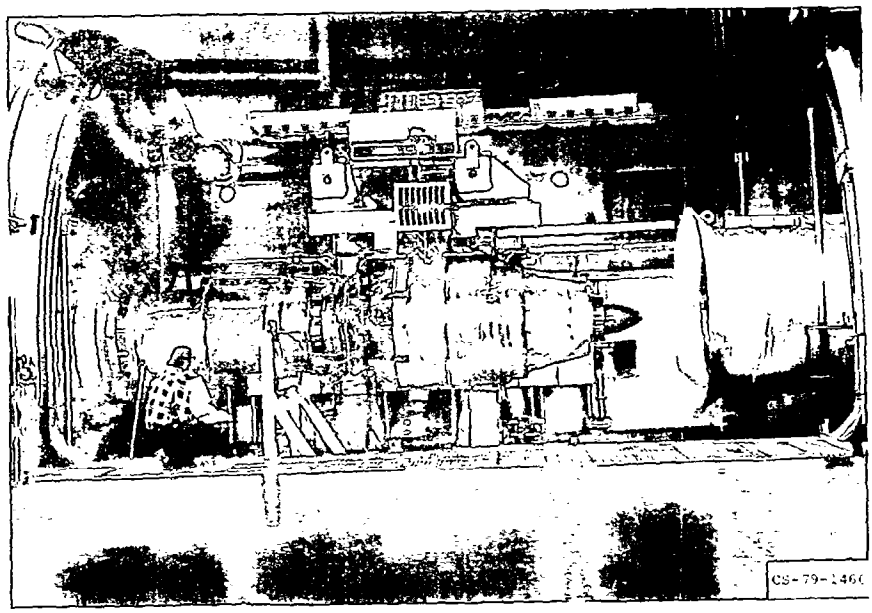

Figure XIII-31

FLIGHT SIMULATOR FOR ADVANCED AIRCRAFT (FSAA)

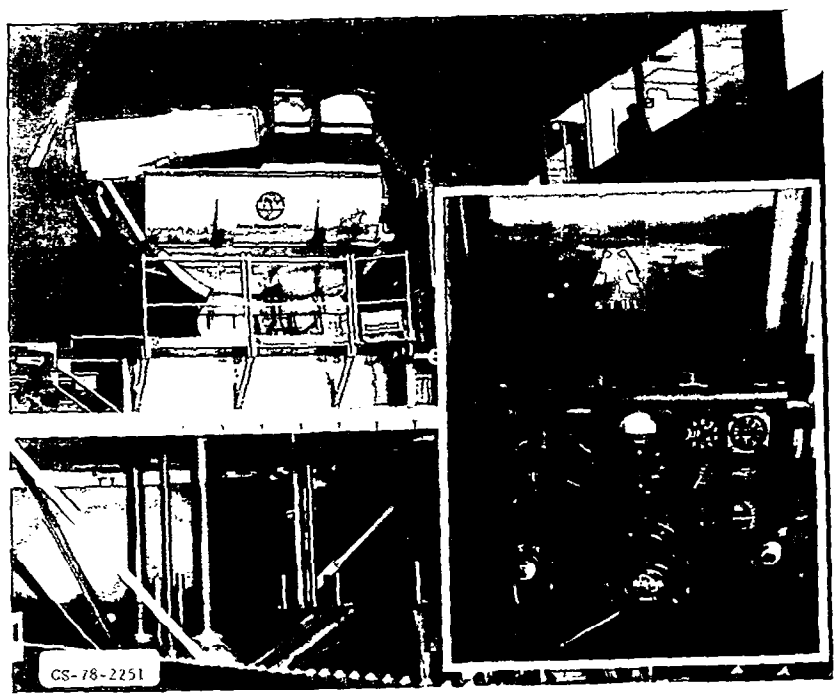

Figure XIII-32

QCSEE EXPERIMENTAL PROPULSION SYSTEM

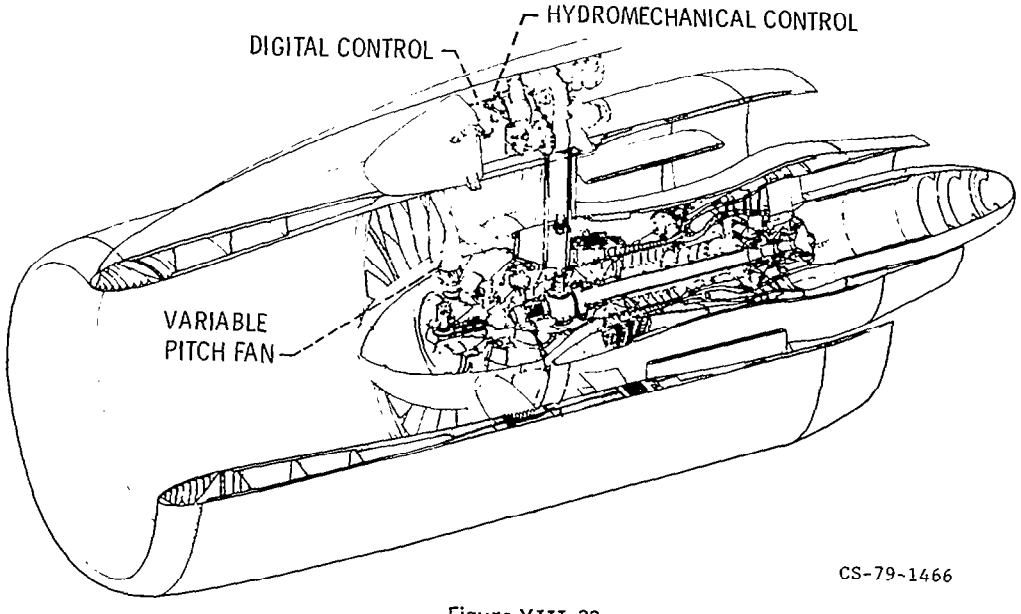

Figure XIII-33

CONCEPTUAL UTW SHORT-HAUL AIRCRAFT

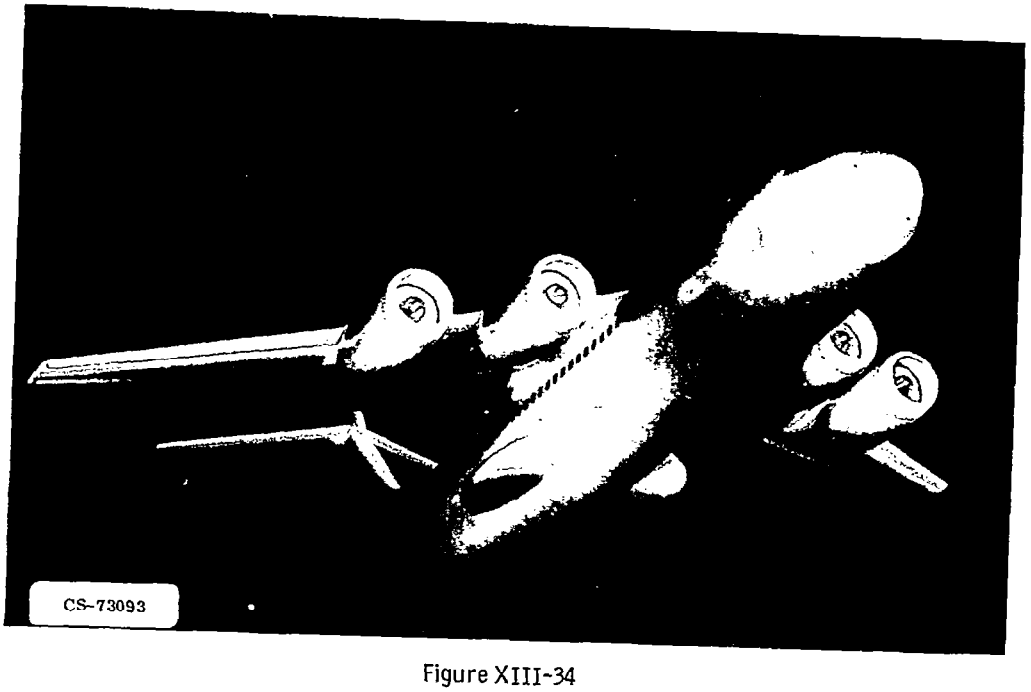

Figure XIII-34

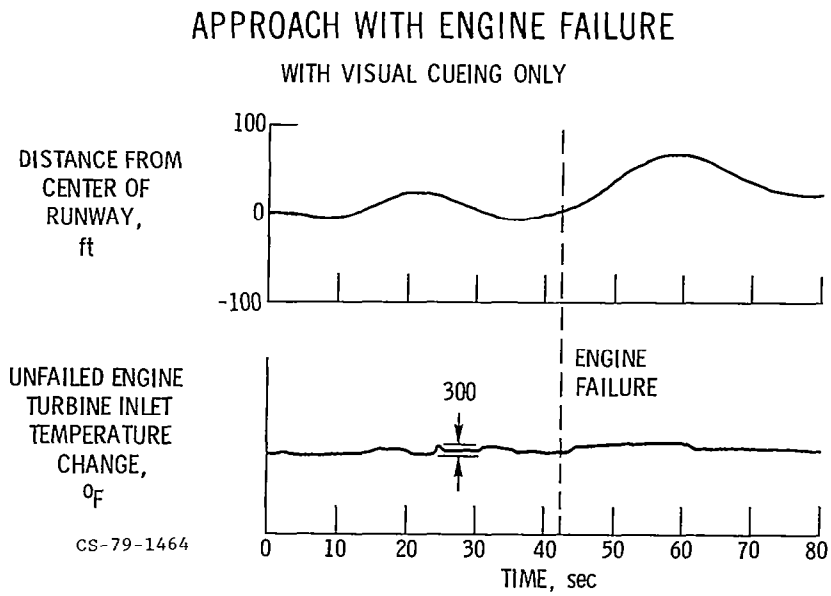

Figure XIII-35

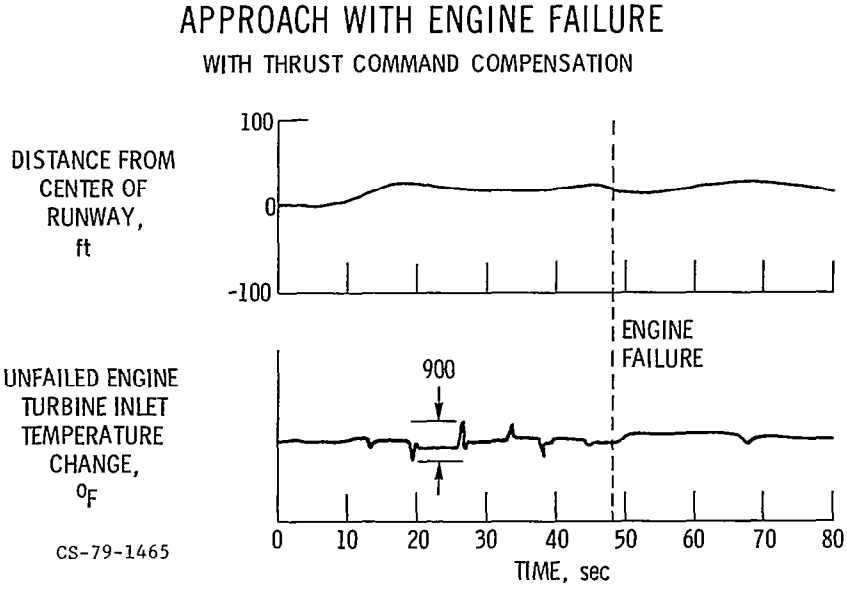

Figure XIII-36

CONTROLS ANALYSIS FOR SUBSONIC VTOL PROPULSION SYSTEM

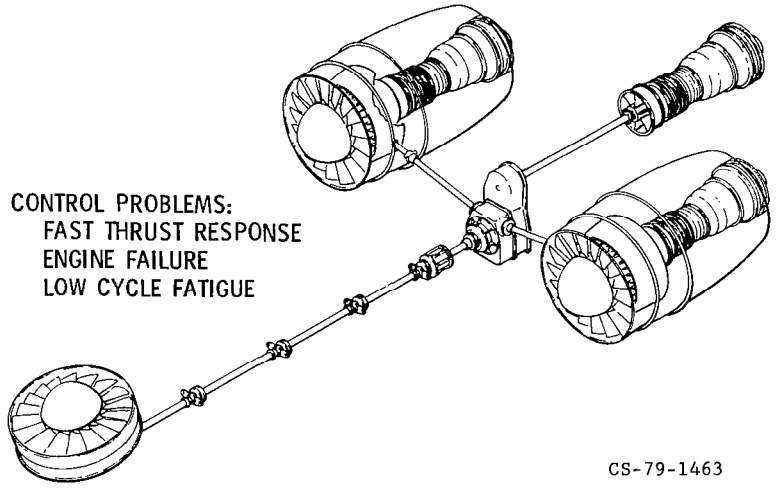

Figure XIII-37

XIV. HIGH-PERFORMANCE-VEHICLE TECHNOLOGY

Louis A. Povinelli

National Aeronautics and Space Administration
Lewis Research Center

This paper discusses some of the special needs of one of the most important types of aircraft, the high-performance military fighter. Figure XIV-1 shows a modern aircraft of this type used by the Air Force, the F-15. Such aircraft use highly advanced technology in all systems, especially in propulsion, to perform important functions in national defense. Aircraft of this general class may also constitute a major portion of international sales of U.S. manufacturers. The discussion in this paper is limited to the following propulsion-related topics: (1) inlet performance, (2) nozzle performance and cooling, and (3) afterburner performance.

The discussion indicates trends in future concepts and describes some NASA activities to supplement those of the military agencies and industry to further advance the technology required for high-performance aircraft.

INLET PERFORMANCE

First consider the type of inlet that is required. Figures XIV-2 to XIV-4 show three current high-performance aircraft and illustrate the fact that inlet geometry differs significantly with aircraft design. Figure XIV-2 shows the Air Force F-16. For the F-16, which is a single-engine aircraft, the inlet has a "smile" configuration at the entrance, is vertically offset, and is mounted beneath the fuselage. Figure XIV-3 shows the F-18, a Navy aircraft. The twin-engine F-18 has a D-shape inlet, the offset is primariy in the horizontal direction, and a wing root mounting is used. In both aircraft, the inlet concept is unique.

A special research aircraft is shown in figure XIV-4. It is the new Air Force/NASA highly maneuverable aircraft technology (HiMAT) vehicle for a flight research program. It is remotely piloted. The inlet has similarities to that for the F-16: it is fuselage mounted, vertically offset, and "smile" shaped.

Figure XIV-5 gives examples of a concept that may be needed for future Air Force missions; it illustrates some interesting results of recent study contracts of stealthy configurations. In each case, portions of the airframe are used to hide the inlet so that it can be less easily detected by ground radar. Inlets act as beacons, reflecting radar signals in a very focused manner, whereas the convex underside of a fuselage and wing scatter the radar signals. Again the inlet geometry (fig. XIV-5) is different from any other.

There are, however, some common geometrical and operational requirements for inlets, which can be summarized as follows:

(1) High degree of integration with airframe

(2) Simple, lightweight design, short length, large offset, and geometric transition

(3) Wide range of Mach number and angle of attack

(4) Stall- and buzz-free operation

(5) Low radar cross section

It is important at this point to inquire as to the consequences of these requirements on the aerodynamics. The progression from rather conservative toward more advanced inlets may cause serious problems with the internal flow. Typical problems are shown in figure XIV-6. Of particular importance are a strong shock - boundary-layer interaction at the entrance to the inlet, which could cause flow separation, and another tendency for flow separation farther downstream in the subsonic diffuser that results from the curvature of the duct. It is necessary to achieve reattachment of the flow at the entrance so that shock stability can be assured and also so that pressure recovery and distortion of the flow at the engine face are established at acceptable values.

Boundary-layer control techniques are discussed in the previous paper (ref. 1) and are listed at the bottom of figure XIV-6. These techniques have been useful in the past and will undoubtedly be even more so in the future. The applications of these techniques have historically been developed through experimental research for each unique inlet. Analytical methods to guide experimental research in applying vortex generation, bleeding, and blowing are now becoming sufficiently advanced so that they will play a greater role in guiding the experimental work than they have in the past. As an example of the use of analysis, consider the use of one of the viscous computer codes discussed by the panel on computational fluid mechanics (ref. 2). It is called the Annular Diffuser Deck (ref. 3) and was developed under contract by United Technologies Research Corporation. One of the

configurations it was applied to is shown in figure XIV-7. It is the F-16 inlet model which was tested in the Lewis 8- by 6-foot supersonic wind tunnel. In order to perform the calculation, several assumptions were required regarding the F-16 geometry. The method of analysis was developed by this author. It was assumed that the passage was an annulus having a centerbody shaped like the ramp surface. A number of radial struts which extended through the length of the inlet divided the flow into compartments. The flow through each of these compartments resembled the F-16 flow. The proper entrance-exit area ratio was matched as well as the correct contour on the ramp and cowl surfaces. The offsets between the entrance and the exit on the cowl and ramp surfaces were also matched to those of the F-16. Figure XIV-8 shows results for this duct obtained from the computer analysis by using the Annular Diffuser Deck. Shown at the top are velocity profiles for the flow between the throat and the compressor face. An accurate indication of flow separation is the corresponding calculation of local skin friction on the ramp and cowl surfaces. As shown at the bottom of the figure, the coefficient was positive at all locations and, hence, would not be expected to separate. No separation was observed in this portion of the flow in the model tests.

Compared with the F-16 inlet, the HiMAT inlet is considered to be a more aggressive design in that it combines a large amount of offset with a short length; it is required to perform over a wide attitude and speed range. Figure XIV-9 shows the test model of the HiMAT mounted in the Lewis 8- by 6-foot supersonic wind tunnel. The same computer program used for the F-16 was used for the HiMAT duct, with the same assumptions. The corresponding analytical results are shown in figure XIV-10. Velocity profiles are at the top, and skin friction is at the bottom. A tendency for flow separation was predicted on the ramp side and, in fact, was observed in the model test. The analysis, therefore, predicted the location of the flow separation. Unfortunately parabolic marching procedures do not calculate beyond the separation point, and, hence, reattachment cannot be determined. Navier-Stokes analyses or some type of empirical modeling through the separated region would be required in order to calculate the entire flow. The current marching solutions do, however, predict where separation will occur and, therefore, where boundary-layer controls should be employed in order to prevent separation. The distortion at the HiMAT compressor face resulting from the separation was not so severe that engine stall would necessarily result. The tendency for separation was easily suppressed with vortex generators, which were designed before the test in anticipation of the problem as predicted by the analysis. Without question, this and other analysis methods will play a significant role in future inlet development efforts.

NOZZLE PERFORMANCE AND COOLING

Consider now the other end of the engine - the exhaust system. As in the case of inlets, there also exist geometrical and operational requirements for nozzles. Some of the special requirements of current interest for the nozzle are

(1) High degree of integration with airframe

(2) Stealth considerations

(3) Thrust deflection and reversal

An important item is a high degree of integration with the airframe. Studies at the Langley Research Center have underscored the growing interest in nonaxisymmetric nozzles for this purpose. Illustrated in figure XIV-11 are some study concepts that demonstrate the dramatic effect that can be achieved in aircraft design. On the left is a twin-engine axisymmetric nozzle concept that quite likely will encounter external flow separation. On the right are wedge or two-dimensional nozzles that would clean up the external lines very effectively. In addition, requirements (2) and (3) may be more easily met. In particular, thrust deflection and reversal may be implemented with less mechanical complexity. Deflection and reversal capabilities are of growing interest in order to increase flight maneuverability and decrease ground roll after landing. Although the wedge nozzle provides an important simplification of the external flow field of the aircraft, it may also lead to complexities of the internal flow field of the jet. To illustrate, figure XIV-12 shows some Langley results (ref. 4). At the top of figure XIV-12 is shown the jet flow on the lower side of the wedge nozzle. The sketch indicates the emergence of the jet at an off-design pressure ratio where overexpansion shock waves are present in the flow. Beneath that are plan views of the wedge surface and shock patterns for nozzle pressure ratios of 3 and 6. The position and nature of these shocks were determined experimentally by the use of oil patterns on the wedge surfaces. At the lower pressure ratio, the flow is basically two-dimensional. At the higher pressure ratio, three-dimensional flow is indicated by the unexpectedly complex shock pattern. The planar shocks become curved, recirculation patterns appear, and vortex slip lines emanate downstream of the shock interaction points.

The pressures measured along the centerline of the nozzle on the wedge surface are plotted at the botton in figure XIV-12. For comparison, the results of a two-dimensional, inviscid, time-dependent computer program by Cline (ref. 5) are also shown. At the lower pressure ratio, the agreement between theory and experiment is excellent. At the higher pressure ratio, the same comparison shows that the analysis does not predict the pressures

correctly. Additional work on the analysis is required, and work is under way at Langley to develop a three-dimensional computer program for this flow.

Another problem of the jet internal flow that is being studied at Lewis is film cooling of the nozzle walls to protect them from the hot flow resulting from afterburner operation (ref. 6). In a preliminary phase of this effort, a simple axisymmetric plug nozzle is being used; for a later phase, a more complex two-dimensional nozzle is being procured. Figure XIV-13 shows the axisymmetric plug nozzle mounted on a J-85 engine in an altitude test cell.

Figure XIV-14 shows the plug nozzle during afterburner operation. Film coolant is injected just downstream of the cowl. Overexpansion shock waves are clearly evident in this flow. Figure XIV-15 shows the variation in local film cooling effectiveness as a function of a nondimensionalized parameter which includes length, coolant mass flow ratio, and slot height. The data correlate well with an empirical design curve except for specific points well below the design curve. These points correspond to conditions where shock waves in the jet disrupt the flow of the cooling film. Additional effort is required for correlation of these effects. A future phase of this cooling research program will progress to nonaxisymmetric nozzles of the type illustrated in figure XIV-16.

This two-dimensional, convergent-divergent exhaust nozzle may be used in a variety of operating positions. This nozzle concept was developed by General Electric under contract to Lewis. On the model shown in the figure, one of the side plates is removed. The geometry at the top of the nozzle is set for low pressure ratios. The top and bottom plates are adjustable for changes in power and pressure ratios. At the left in the figure the plates are rotated and the nozzle is positioned for thrust deflection. On the right in the figure, rotation of a clamshell-like arrangement closes off the normal exhaust path. The two halves of the clamshell turn the flow. Top and bottom ports are opened when the clamshell is rotated. These ports allow the flow to exit in the forward direction. This nozzle will be used on a J-85 engine, and both cooling requirements and thrust characteristics will be evaluated.

An alternative concept for thrust reversal is to use external flaps in conjunction with wedge nozzles (ref. 7). In this case, the reversal is accomplished externally rather than internally as in the two-dimensional clamshell geometry. Figure XIV-17 shows a model of the F-18 aircraft with a twin-wedge nozzle installation. Deflection plates are installed on the top and bottom surfaces of both wedges. The plates are stored in the retracted position when no thrust deflection is required. Deployment of the plates provides increased maneuverability or thrust reversal. This

study at the Langley Research Center evaluated the effect of flap geometry, for example, the effect of sideplates on the deflection flaps. A sideplate is used on both sides of each of the flaps so that the cross section is U-shaped. Flaps with sideplates were more effective than flaps without sideplates for increasing the amount of thrust reversal.

AFTERBURNER PERFORMANCE

The first goal of the afterburner program conducted at Lewis (refs. 8 and 9) was to increase altitude limits for stable combustion without rumble. Rumble is defined as a traveling pressure disturbance of 20 to 300 hertz. Operation of the afterburner in high-amplitude rumble causes fatigue failure of the afterburner with subsequent nozzle damage in a matter of minutes.

The second goal was to increase blowout limits for transients from idle to maximum augmentation throttle. For this work, an F-100 engine was used.

Figure XIV-18 shows the research afterburner. The flameholder and injection rings can be seen. The novel feature of this afterburner was the introduction of swirl in the core flow. The method used is shown in figure XIV-19. The standard production augmentor is shown at the top of the figure, and the new swirl augmentor at the bottom. The latter is called a partial swirl augmentor, since only the core flow is swirled, not the fan flow. The 20^{o} of core swirl around the centerbody was achieved by recambering the turbine exit guide vanes. Additional pressure loss was created by the presence of this swirl. However, swirling allowed the removal of the flameholder fingers and thereby eliminated some pressure loss. The net result was no overall performance penalty. A digital electronic engine control system was also added in order to control fuel flow rates and nozzle opening more precisely. Performance results are shown in figure XIV-20. The outer lines show the altitude and Mach number operating envelope of the engine without afterburning. The engine operates at any point inside this envelope. The limits of the productuion afterburner are shown by the inner lines, which indicate a loss in rumble free operational capability for very high altitudes at low Mach numbers. As indicated by the cross-hatched region, the swirl afterburner pushed the operating limit to much higher altitudes - increased it as much as 15 000 feet. Although not shown in this figure, the transient blowout altitude limit was simultaneously increased by a minimum of 8000 feet. This research afterburner may be flight tested in an F-15 at the Dryden Flight Research Center in the near future.

CONCLUDING REMARKS

A few areas of NASA work which are related to high-performance vehicles have been discussed. Unique inlet concepts will continue to evolve, but their design will be aided by computational methods to a greater extent than in the past. Nonaxisymmetric nozzles will provide cleaner external lines and enhanced maneuverability, but the internal flows will be more complex. And finally, novel concepts for swirl afterburners show promise for enanced performance in the high-altitude, low Mach number region.

REFERENCES

1. Ciepluch, C. C.; et al.: Vertical Takeoff and Landing (VTOL) Propulsion Technology. Presented at the Aeropropulsion 1979 Conference (Cleveland, Ohio), May 15-16, 1979.

2. Bowditch, D. N.; et al: Computational Fluid Mechanics of Internal Flow. Presented at the Aeropropulsion 1979 Conference (Cleveland, Ohio), May 15-16, 1979.

3. Anderson, O. L.: Finite-Difference Solution for Turbulent Swirling Compressible Flow in Axisymmetric Ducts with Struts. NASA CR-2365, 1974.

4. Carson, G. T., Jr.; and Mason, M. L.: Experimental and Analytical Investigation of a Nonaxisymmetric Wedge Nozzle at Static Conditions. NASA TP-1188, 1978.

5. Cline, M. C.: NAP: A Computer Program for the Computation of Two-Dimensional, Time-Dependent, Inviscid Nozzle Flow. LA-5984, Los Alamos Scientific Laboratory, 1977.

6. Straight, D. M.: Effect of Shocks on Film Cooling of a Full Scale Turbojet Exhaust Nozzle Having an External Expansion Surface. NASA TM-79157, 1979.

7. Capone, F. J.; Gowadia, N. S.; and Wooten, W. H.: Performance Characteristics of Nonaxisymmetric Nozzles Installed on the F-18 Airplane. AIAA Paper 79-0101, Jan. 1979.

8. Egan, W. J., Jr.; and Schadowen, J. H.: Design and Verification of a Turbofan Swirl Augmentor. AIAA Paper 78-1040, July 1978.

9. Hanloser, K. J.; and Cullom, R. R.: Test Verification of a Partial Swirl Afterburner. AIAA Paper 79-1199, June 1979.

F-15 AIRCRAFT

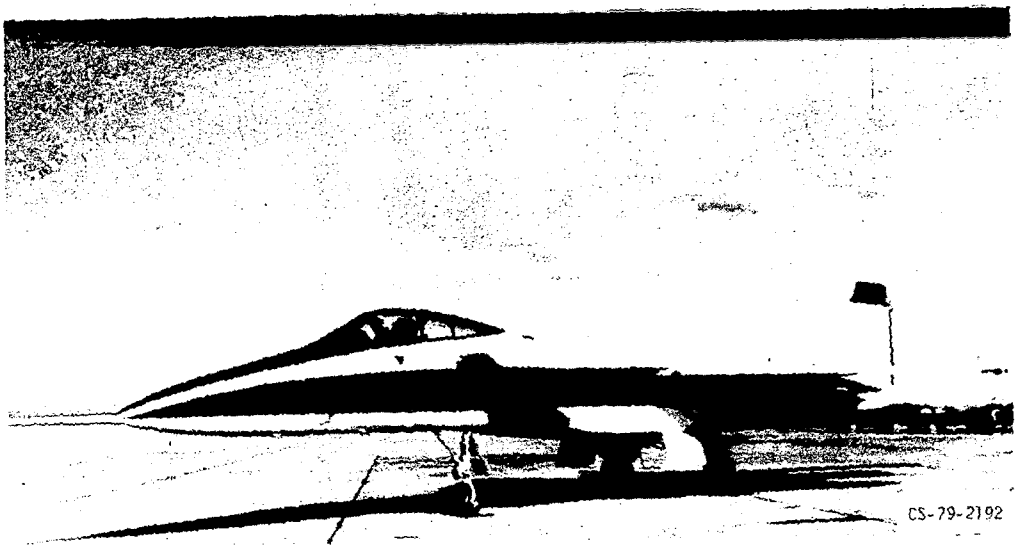

Figure XIV-1

F-16

Figure XIV-2

F-18

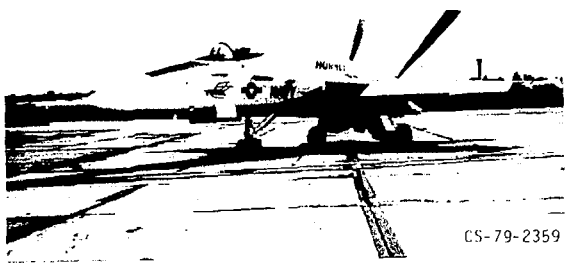

Figure XIV-3

HiMAT

Figure XIV-4

STEALTH CONFIGURATIONS

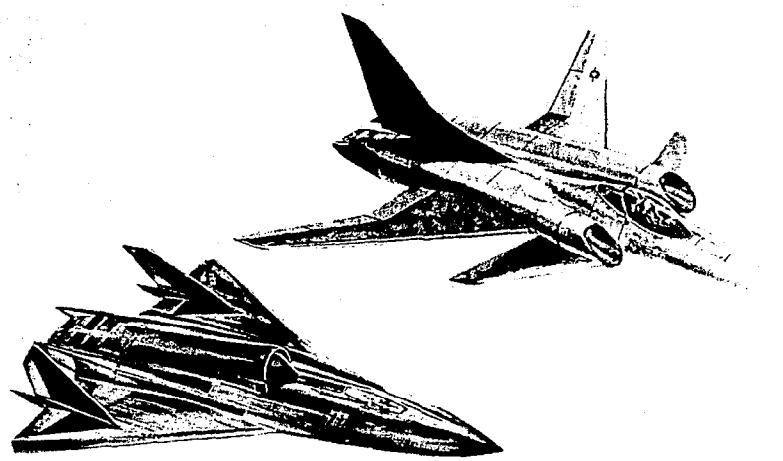

CS-79-1732

Figure XIV-5

AERODYNAMIC FEATURES OF ADVANCED INLETS

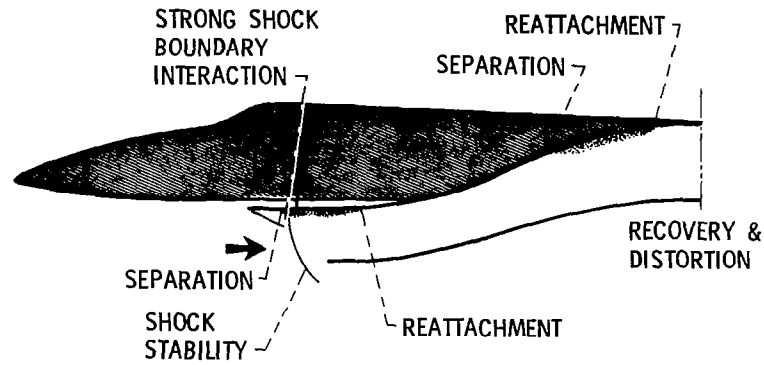

BOUNDARY LAYER CONTROL TECHNIQUES
- VORTEX GENERATORS
- BLEEDING
- BLOWING

CS-79-2202

Figure XIV-6

F-16 INLET MODEL TESTING IN LEWIS 8X6 TUNNEL

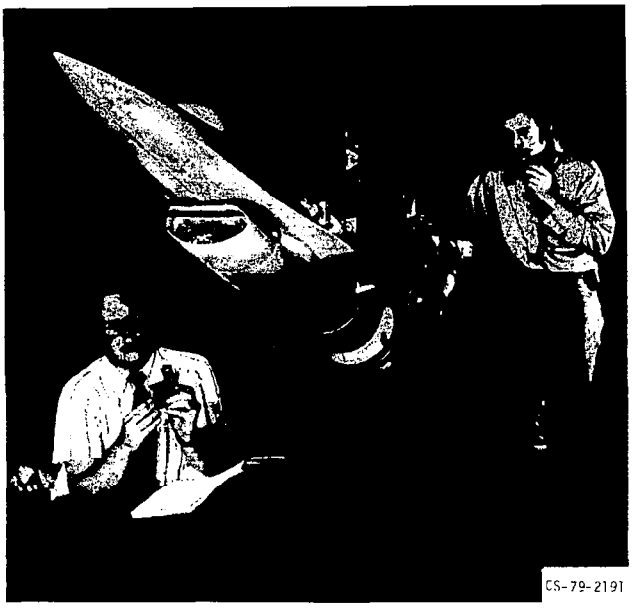

Figure XIV-7

COMPUTER ANALYSIS OF F-16 INLET

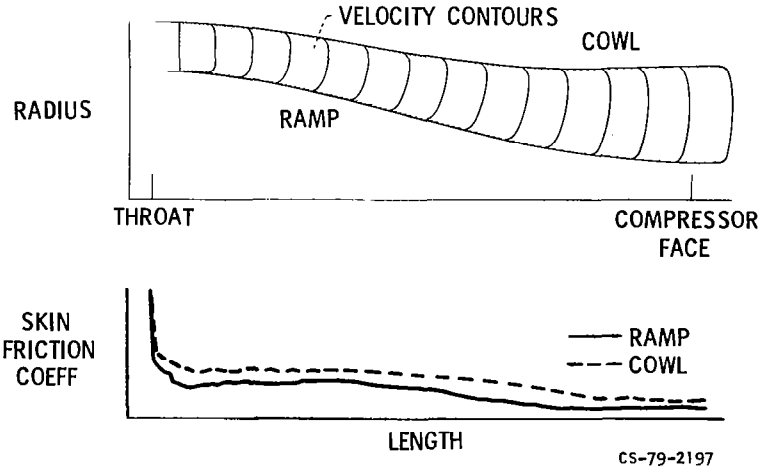

Figure XIV-8

HiMAT INLET TEST IN 8X6 TUNNEL

Figure XIV-9

COMPUTER ANALYSIS OF HiMAT INLET

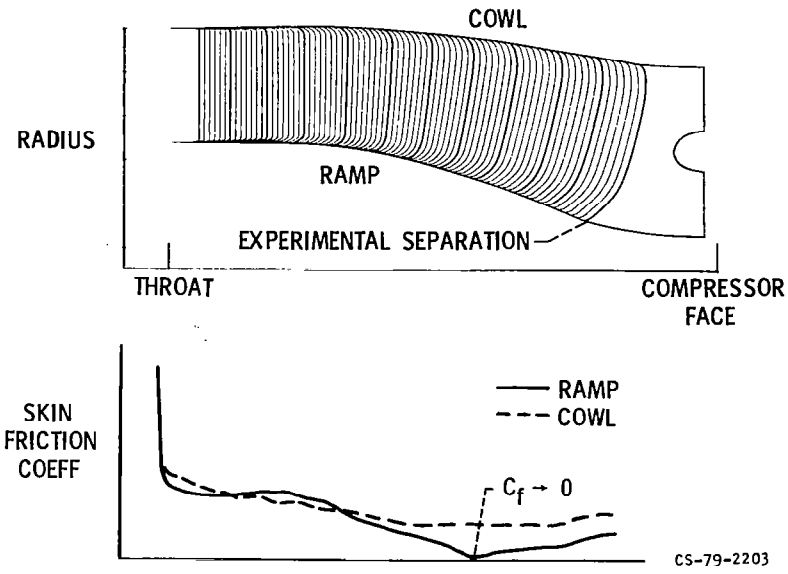

Figure XIV-10

TWIN AXISYMMETRIC AND WEDGE NOZZLE INSTALLATION

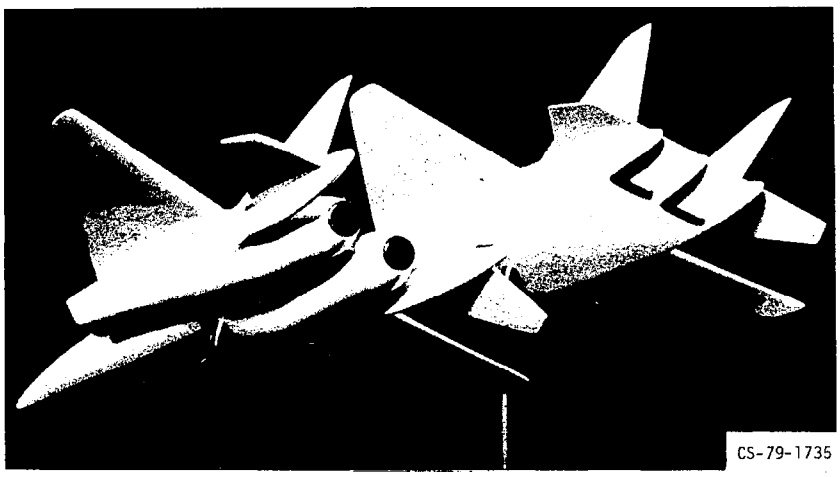

Figure XIV-11

WEDGE NOZZLE AERODYNAMICS

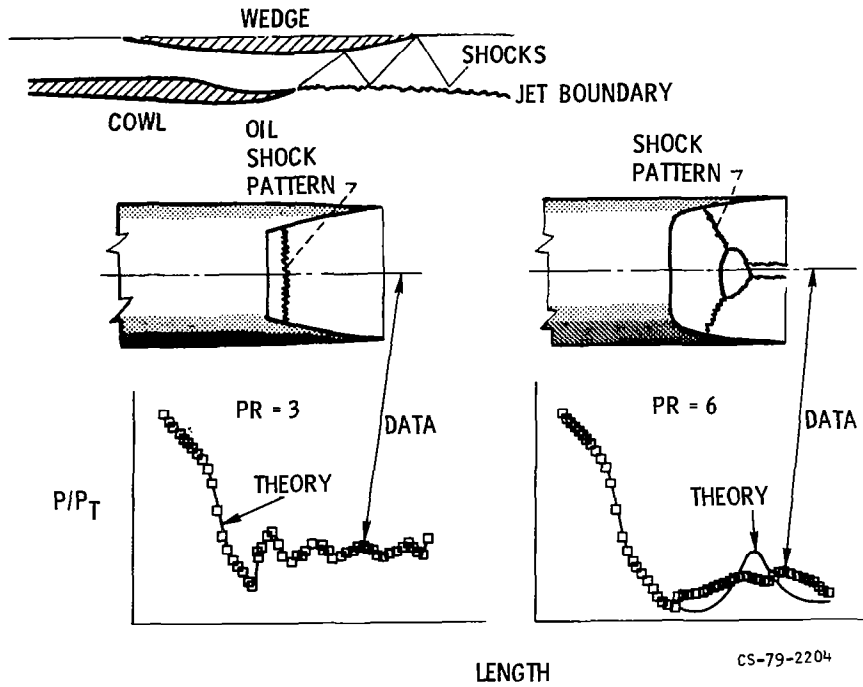

Figure XIV-12

FILM COOLED PLUG APPARATUS

J-85 ENGINE

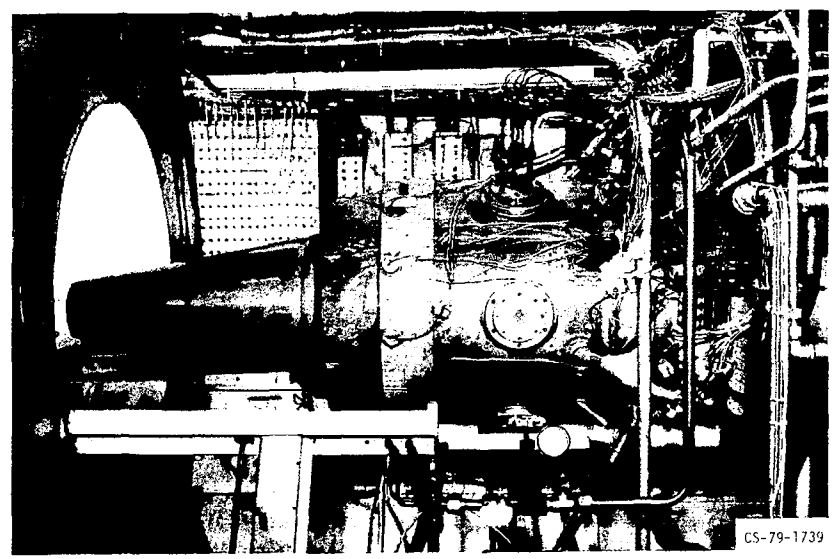

Figure XIV-13

AXISYMMETRIC FILM COOLED PLUG NOZZLE

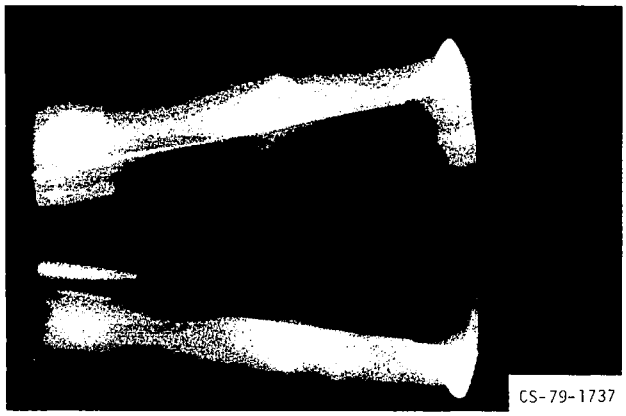

PR = 3.1

Figure XIV-14

EXPERIMENTAL FILM COOLING RESULTS

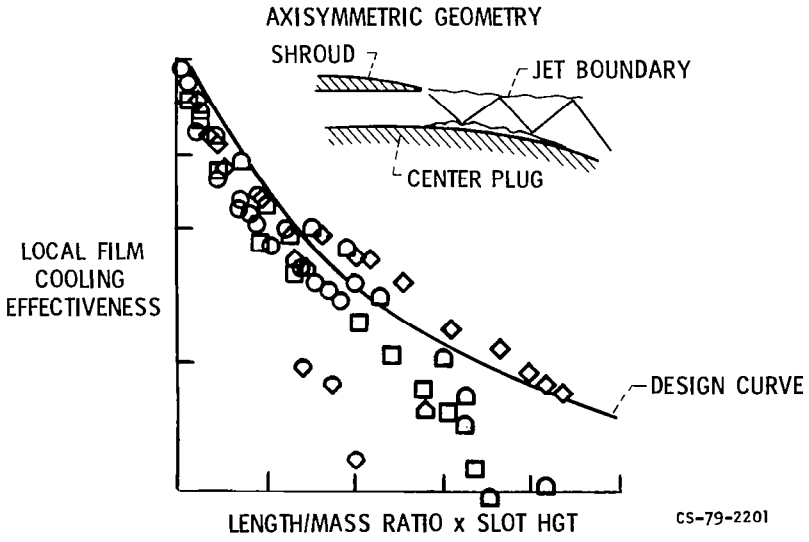

Figure XIV-15

2D CD VERSATILE EXHAUST NOZZLE MODEL

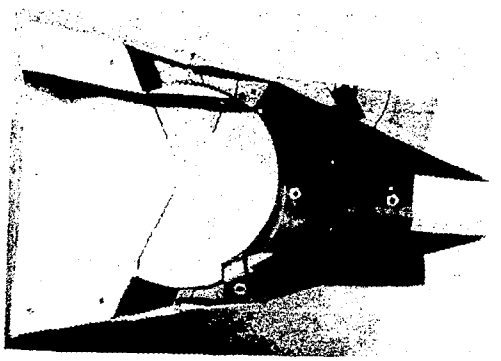

NORMAL OPERATION

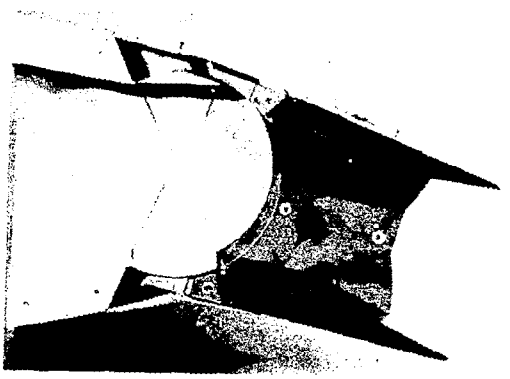

THRUST DEFLECTION

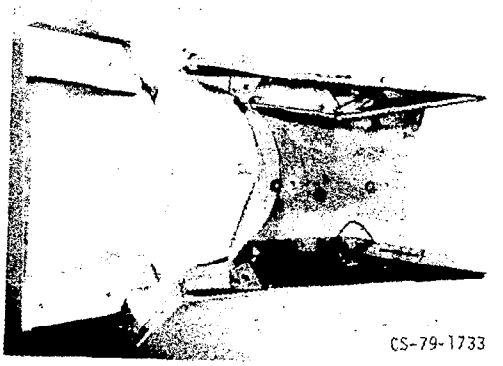

THRUST REVERSAL

Figure XIV-16

F-18 MODEL WITH TAB REVERSERS

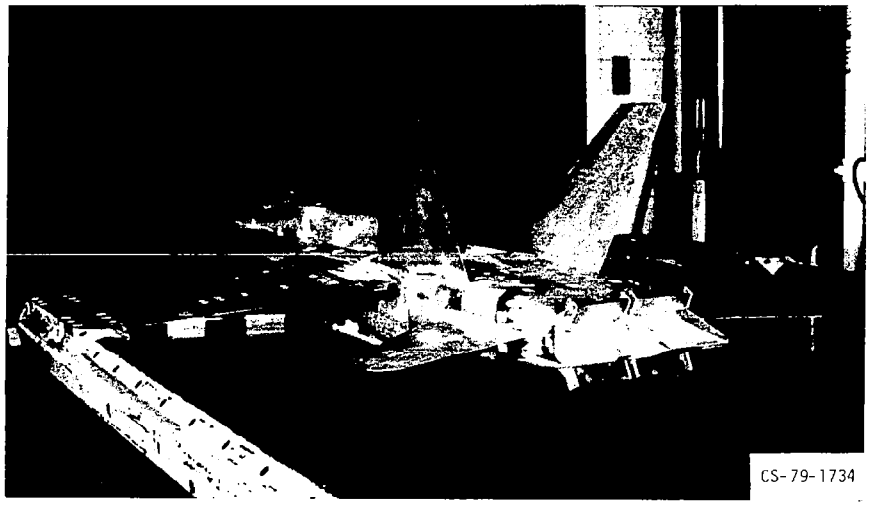

Figure XIV-17

AFTERBURNER VIEW OF F-100 ENGINE

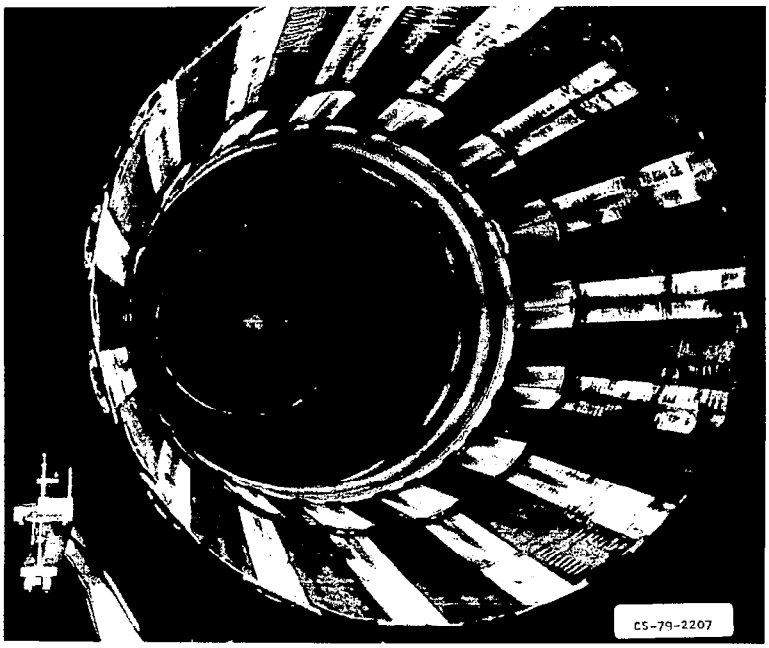

Figure XIV-18

SWIRL AND PRODUCTION AUGMENTOR COMPARISON

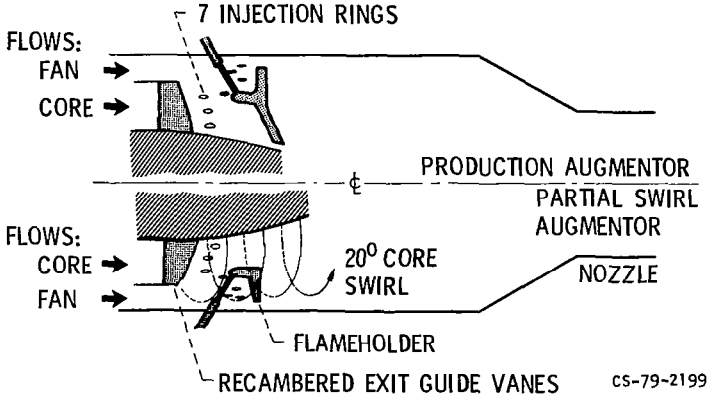

Figure XIV-19

EFFECT OF SWIRL ON AFTERBURNER

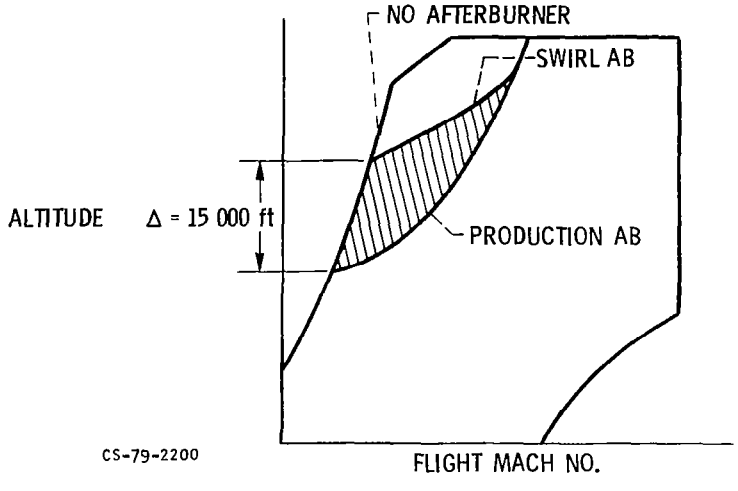

Figure XIV-20

RESEARCH AND DEVELOPMENT CONTRACTORS AND GRANTEES

NASA relies heavily on the support and expertise of industry, universities, and research organizations in conducting its research and technology programs in aeronautical propulsion. The following is a list of contractors and grantees who are currently supplementing the in-house efforts of the NASA Lewis Research Center in this program area. In view of the large number of organizations involved, inadvertent omissions are possible, for which apology is duly expressed.

Industry

Aeromexico
Aeronautical Research Associates of Princeton, Inc.
AiResearch Manufacturing Co.
Air New Zealand, Ltd.
American Airlines, Inc.
Atlas Consortium
Avco Corp., Avco Lycoming Division
The Boeing Co.
Bolt, Beranek, & Newman, Inc.
Chandler Evans, Inc.
Colt Industries, Inc.
Continental Air Lines, Inc.
Cooper Airmotive, Inc.
Detroit Diesel Allison Div., GMC
Douglas Aircraft Co.
Eastern Air Lines, Inc.
Exxon Research and Engineering Corp.
Finnair OY
Flow Research
Flow Simulators, Inc.
Fluidyne Engineering Corp.
Frontier Airlines
Garrett AiResearch Aviation Co.
General Applied Science Laboratories, Inc.
General Dynamics Corp.
General Electric Co.
Grumman Aerospace Corp.
Hamilton Standard
Hersh Acoustical Engineering
Honeywell, Inc.
Industrial Tetronics, Inc.
International Nickel Co.
KSSU Consortium
Arthur D. Little, Inc.
Lockheed Aircraft Corp.
Lockheed Missiles & Space Co.
McDonnell Douglas Corp.
Mechanical Technology, Inc.
National Airlines
Northwest Airlines, Inc.
Nielsen Engineering
Pacific Airmotive Corp.
Pan American World Airways, Inc.
Pratt & Whitney Aircraft Group
Rockwell International Corp.
Scientific Research Associates
Solar, Division of International Harvester Co.
Solar Turbines International
Southwest Research Institute
Systems Control, Inc. (VT)
Tech Development, Inc.
Thermo Mechanical Systems, Inc.
Trans World Airlines, Inc.
TRW, Inc.
United Air Lines, Inc.
United Technologies Corp.
United Technologies Research Center
Vought Systems Div., LTV Aerospace Corp.
Western Air Lines
Western Gear Corp.

Educational and Research Institutions

Arizona State University
Battelle Memorial Institute, Columbia Laboratory
Case Western Reserve University
Cornell University
George Washington University
Georgia Institute of Technology
Illinois Institute of Technology
Iowa State University
Massachusetts Institute of Technology
New York University at Westbury
Pennsylvania State University
Purdue University
Stanford University
State University of New York at Stoneybrook
Trenton State University
University of California at Los Angeles
University of Colorado
University of Michigan
University of Missouri
University of Notre Dame
University of Texas
Wichita State University

Federal Agencies

Federal Aviation Administration
U.S. Air Force Aeropropulsion Laboratory
U.S. Army Research & Development Command
U.S. Army Research & Technology Laboratories (AVRADCOM)
U.S. Naval Air Propulsion Center
U.S. Naval Sea System Command (NAVSEA)

1. Report No.	2. Government Accession No.	3. Recipient's Catalog No.
NASA CP-2092		

4. Title and Subtitle	5. Report Date
AEROPROPULSION 1979	October 1979
	6. Performing Organization Code
7. Author(s)	8. Performing Organization Report No. E-079
	10. Work Unit No.
9. Performing Organization Name and Address National Aeronautics and Space Administration Lewis Research Center Cleveland, Ohio 44135	11. Contract or Grant No.
	13. Type of Report and Period Covered Conference Publication
12. Sponsoring Agency Name and Address National Aeronautics and Space Administration Washington, D.C. 20546	14. Sponsoring Agency Code

15. Supplementary Notes

16. Abstract

A two-day conference was held at the NASA Lewis Research Center on May 15 and 16, 1979, to provide leaders from government, industry, and universities with the latest results of NASA programs in aeronautical propulsion. Fourteen papers were presented on topics including emission and noise reduction, alternative fuels, computational fluid mechanics, and hypersonic propulsion. The proceedings contains all the papers presented.

17. Key Words (Suggested by Author(s))	18. Distribution Statement
Propulsion efficiency; Emission; Noise reduction; Aircraft fuels; Ceramic coatings; Materials science; Turbomachinery; Bearings; Gears; Microelectronics; Optical measurement; Engine control; Supersonic turbines; Hypersonic inlets; Supersonic combustion ramjet engines; Vertical takeoff aircraft	Unclassified - unlimited STAR Category 07

19. Security Classif. (of this report)	20. Security Classif. (of this page)	21. No. of Pages	22. Price*
Unclassified	Unclassified	467	A20

* For sale by the National Technical Information Service, Springfield, Virginia 22161

NASA-Langley, 1979